Journal of Nanomaterials

# Nanomechanics and Nanostructured Multifunctional Materials: Experiments, Theories, and Simulations

Guest Editors: Jun Lou and Junlan Wang

# Nanomechanics and Nanostructured Multifunctional Materials: Experiments, Theories, and Simulations

Journal of Nanomaterials

# Nanomechanics and Nanostructured Multifunctional Materials: Experiments, Theories, and Simulations

Guest Editors: Jun Lou and Junlan Wang

# Contents

**Nanomechanics and Nanostructured Multifunctional Materials: Experiments, Theories, and Simulations**, Jun Lou and Junlan Wang
Volume 2008, Article ID 408606, 1 page

**Green Synthesis of Ag and Pd Nanospheres, Nanowires, and Nanorods Using Vitamin $B_2$: Catalytic Polymerisation of Aniline and Pyrrole**, Mallikarjuna N. Nadagouda and Rajender S. Varma
Volume 2008, Article ID 782358, 8 pages

**Templated Fabrication of InSb Nanowires for Nanoelectronics**, M. Ibrahim Khan, Xu Wang, Krassimir N. Bozhilov, and Cengiz S. Ozkan
Volume 2008, Article ID 698759, 5 pages

**Direct Oxidation Growth of CuO Nanowires from Copper-Containing Substrates**, Benjamin J. Hansen, Ganhua Lu, and Junhong Chen
Volume 2008, Article ID 830474, 7 pages

**Growth of ZnO Nanowires in Aqueous Solution by a Dissolution-Growth Mechanism**, Shaojing Bu, Chunxiang Cui, Qingzhou Wang, and Ling Bai
Volume 2008, Article ID 610541, 5 pages

**Pressure and Temperature Effects on Stoichiometry and Microstructure of Nitrogen-Rich TiN Thin Films Synthesized via Reactive Magnetron DC-Sputtering**, E. Penilla and J. Wang
Volume 2008, Article ID 267161, 9 pages

**Studies on Nanocrystalline TiN Coatings Prepared by Reactive Plasma Spraying**, Dong Yanchun, Yan Dianran, He Jining, Zhang Jianxin, Xiao Lisong, and Li Xiangzhi
Volume 2008, Article ID 690951, 8 pages

**Nanomechanics of Single Crystalline Tungsten Nanowires**, Volker Cimalla, Claus-Christian Röhlig, Jörg Pezoldt, Merten Niebelschütz, Oliver Ambacher, Klemens Brückner, Matthias Hein, Jochen Weber, Srdjan Milenkovic, Andrew Jonathan Smith, and Achim Walter Hassel
Volume 2008, Article ID 638947, 9 pages

**Synthesis and Elastic Characterization of Zinc Oxide Nanowires**, M. P. Manoharan, A. V. Desai, G. Neely, and M. A. Haque
Volume 2008, Article ID 849745, 7 pages

**Atomic Force and Optical Microscopy Characterization of the Deformation of Individual Carbon Nanotubes and Nanofibers**, Terry P. Bigioni and Brett A. Cruden
Volume 2008, Article ID 352109, 7 pages

**Toward a Detailed Understanding of Si(111)-7 $\times$ 7 Surface and Adsorbed Ge Nanostructures: Fabrications, Structures, and Calculations**, Ye-Liang Wang, Hai-Ming Guo, Zhi-Hui Qin, Hai-Feng Ma, and Hong-Jun Gao
Volume 2008, Article ID 874213, 18 pages

**Improving the Performance of Lithium-Ion Batteries by Using Spinel Nanoparticles**, J. C. Arrebola, A. Caballero, L. Hernán, and J. Morales
Volume 2008, Article ID 659397, 10 pages

**Membranes of Polyvinylidene Fluoride and PVDF Nanocomposites with Carbon Nanotubes via Immersion Precipitation**, Gaurav Mago, Dilhan M. Kalyon, and Frank T. Fisher
Volume 2008, Article ID 759825, 8 pages

**Morphology and Properties of Aminosilane Grafted MWCNT/Polyimide Nanocomposites**, Siu-Ming Yuen, Chen-Chi M. Ma, Chin-Lung Chiang, and Chih-Chun Teng
Volume 2008, Article ID 786405, 15 pages

**Properties Enhancement of PS Nanocomposites through the POSS Surfactants**, Huei-Kuan Fu, Shiao-Wei Kuo, Ding-Ru Yeh, and Feng-Chih Chang
Volume 2008, Article ID 739613, 7 pages

**Effect of Rare Earth Y on Properties of Nanosized 90W-7Ni-3Fe Composite Powder Fabricated by Spray Drying-Hydrogen Reduction**, Y.-Z. Ma, Liu Wensheng, Huang Baiyun, and Fan Jinglian
Volume 2008, Article ID 459093, 4 pages

**Structure and Property Investigation of Composite ZnO/$SnO_2$ Nanocrystalline Particles after High-Pressure Treatment**, Sun Zhenya, Deng Yundi, and Zhang Weiying
Volume 2008, Article ID 286069, 5 pages

**Synthesis of Nanostructured Nanoclay-Zirconia Multilayers: A Feasibility Study**, Hao Chen, Guoping Zhang, Kathleen Richardson, and Jian Luo
Volume 2008, Article ID 749508, 8 pages

**Mechanisms of Nanoindentation on Multiwalled Carbon Nanotube and Nanotube Cluster**, Ling Liu, Guoxin Cao, and Xi Chen
Volume 2008, Article ID 271763, 12 pages

**Buckling of Single-Crystal Silicon Nanolines under Indentation**, Min K. Kang, Bin Li, Paul S. Ho, and Rui Huang
Volume 2008, Article ID 132728, 11 pages

**Dislocation Nucleation and Pileup under a Wedge Contact at Nanoscale**, Y. F. Gao and J. Lou
Volume 2008, Article ID 380961, 5 pages

**Statistical Molecular Dynamics Study of (111) and (100) Ni Nanocontacts: Evidences of Pentagonal Nanowires**, P. García-Mochales, R. Paredes, S. Peláez, and P. A. Serena
Volume 2008, Article ID 361464, 9 pages

**Mineral and Protein-Bound Water and Latching Action Control Mechanical Behavior at Protein-Mineral Interfaces in Biological Nanocomposites**, Pijush Ghosh, Dinesh R. Katti, and Kalpana S. Katti
Volume 2008, Article ID 582973, 8 pages

Hindawi Publishing Corporation
Journal of Nanomaterials
Volume 2008, Article ID 408606, 1 page
doi:10.1155/2008/408606

*Editorial*

# Nanomechanics and Nanostructured Multifunctional Materials: Experiments, Theories, and Simulations

**Jun Lou[1] and Junlan Wang[2]**

[1] *Department of Mechanical Engineering and Materials Science, Rice University, Houston, TX 77005, USA*
[2] *Department of Mechanical Engineering, University of California - Riverside, Riverside, CA 92521, USA*

Correspondence should be addressed to Jun Lou, jlou@rice.edu

Received 30 April 2008; Accepted 30 April 2008



The rapid advances of modern technology require a thorough understanding of mechanics of materials, structures, and processes at the micro- and nanoscales. Carbon nanotubes, nanowires, nanocomposites, nanoscale thin films and coatings, micro- and nano electromechancial systems (MEMS and NEMS), micro- and nanofabrication processes are all examples of materials systems, technologies, and processes whose continuous advancement depends upon fundamental understandings of material properties at small length scales. In order to help them fulfill their promises, mechanics at nanometer length scale must be developed to understand the deformation and failure mechanisms of these small material structures. In addition, advances in the development of new materials for multifunctional applications will require design, fabrication, and characterization at the nanometer length scale. Nanostructured materials that can be tailored to achieve greater mechanical properties along with their electrical, optical, thermal, and other functional properties are essential for future applications in many industry sectors. To achieve the overwhelming potential of nanostructured multifunctional materials, advances in the synthesis of materials with multifunctional capabilities through incorporating nanoscale constituents such as nanotubes, nanofibers, and nanoclays, as well as the development of novel methods and techniques to characterize the mechanical and multifunctional behavior of these materials under application conditions are clearly of critical importance.

The goal of this special issue is to provide a platform for researchers working at the frontier of nanomechanics and nanostructured multifunctional materials to present and discuss exciting new developments on various topics in this area, which include work focused on experiments, theories, and simulations. The special issue with a total of twenty-two papers covers a wide range of topics related to fabrication of nanoscale building blocks such as nanosphere, nanowires, nanorods, and nanoscale thin films; development and application of nanomechanical characterization methods for nanomaterials and other advanced characterization techniques to probe important physical/chemical properties of multifunctional nanomaterial systems; processing and property evaluation of various polymer, ceramic, and metal-based nanocomposites; and finally nanomechanical modeling and simulations from continuum micromechanics-based modeling to molecule dynamic-based simulations. We sincerely hope such a broad representation of important topics in these vibrant and fast growing research areas would be of interest to the readership.

## ACKNOWLEDGMENTS

The editors would like to acknowledge those who assisted in putting together this special issue, including our invited and contributing authors, reviewers, staff members of Hindawi Publisher, and the Editor in-Chief of Journal of Nanomaterials, Dr. Michael Z. Hu.

*Jun Lou*
*Junlan Wang*

Hindawi Publishing Corporation
Journal of Nanomaterials
Volume 2008, Article ID 782358, 8 pages
doi:10.1155/2008/782358

*Research Article*

# Green Synthesis of Ag and Pd Nanospheres, Nanowires, and Nanorods Using Vitamin $B_2$: Catalytic Polymerisation of Aniline and Pyrrole

**Mallikarjuna N. Nadagouda and Rajender S. Varma**

*Sustainable Technology Division, US Environmental Protection Agency, National Risk Management Research Laboratory, 26 West Martin Luther King Drive, MS 443, Cincinnati, OH 45268, USA*

Correspondence should be addressed to Rajender S. Varma, varma.rajender@epa.gov

Received 10 May 2007; Revised 23 August 2007; Accepted 4 October 2007

Recommended by Jun Lou

For the first time, we report green chemistry approach using vitamin $B_2$ in the synthesis of silver (Ag) and palladium (Pd), nanospheres, nanowires, and nanorods at room temperature without using any harmful reducing agents, such as sodium borohydride ($NaBH_4$) or hydroxylamine hydrochloride and any special capping or dispersing agent. Vitamin $B_2$ was used as reducing agent as well as capping agent due to its high-water solubility, biodegradability, and low-toxicity compared with other reducing agents. The average particle size of nanoprticle was found to be Ag (average size $6.1 \pm 0.1$ nm) and Pd (average size $4.1 \pm 0.1$ nm) nanoparticles in ethylene glycol and Ag (average size $5.9 \pm 0.1$ nm, and average size $6.1 \pm 0.1$) nanoparticles in acetic acid and NMP, respectively. The formation of noble multiple shape nanostructures and their self assembly were dependent on the solvent employed for the preparation. When water was used as solvent media, Ag and Pd nanoparticles started to self-assemble into rod-like structures and in isopropanol Ag and Pd nanoparticles yielded wire-like structures with a thickness in the range of 10 to 20 nm and several hundred microns in length. In acetone and acetonitrile medium, the Ag and Pd nanoparticles are self-assembled into a regular pattern making nanorod structures with thicknesses ranging from 100 to 200 nm and lengths of a few microns. The so-synthesized nanostructures were characterized using scanning electron microscopy (SEM), transmission electron microscopy (TEM), energy dispersive X-ray (EDX) analysis, and UV spectroscopy. The ensuing Ag and Pd nanoparticles catalyzed the reactions of aniline and pyrrole to generate polyaniline and polypyrrole nanofibers and may find various technological and biological applications. This single-step greener approach is general and can be extended to other noble metals and transition metal oxides.



## 1. INTRODUCTION

Recently, much effort has been devoted to the controlled synthesis of nanostructured materials because of their unique chemical and physical properties that are different from those of the bulk materials [1]. Particularly, metal nanomaterials have attracted considerable attention because of their unique magnetic, optical, electrical, and catalytic properties and their potential applications in nanoelectronics [2]. Hierarchical assembly of solution-based nanocrystals as building blocks is of great interest because of their potential in controlling morphologies of nanostructures, and hence their properties [3–6] wherein structured nanoparticle assemblies such as wires, rings, and superlattices, can be prepared [7–13]. However, the challenge of synthetically controlling particle shape had limited success. Nevertheless, some physical and solid state chemical methods have been developed for making semiconductor, metal nanowires, nanobelts, and nanodots [14–18] in addition to wet-chemical methods [19–26]. Presently there are some methods available for making rods with controllable aspect ratio using seeding approaches [27], electrochemical and membrane-templated syntheses [28–30]. In solution phase, pH-dependent assembly of gold nanorods [31] and streptavidin-linked nanorods [32] is possible but requires elevated temperatures and, in most cases they afford poor yield of desired particle shape. Thus, the developments of bulk solution synthetic methods that offer shape control are very desirable to realize the full potential

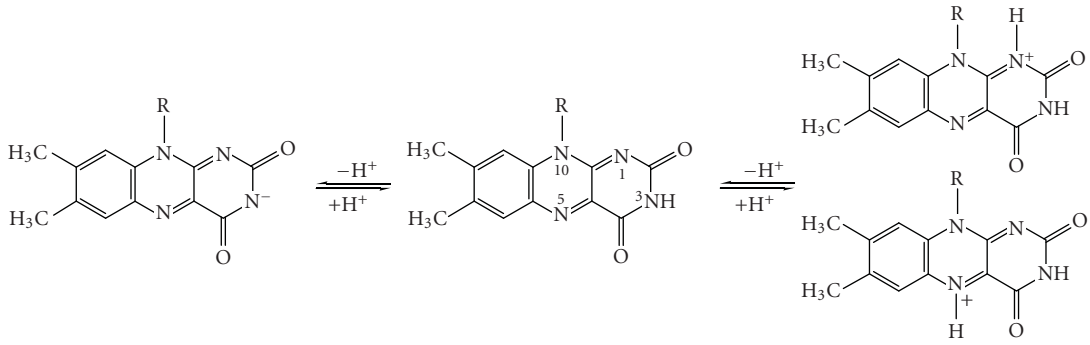

Scheme 1: Structure of anionic (left), neutral (center), and cationic (right) vitamin $B_2$ species in the fully oxidized redox state ($R = -CH_2(CHOH)_3CH_2OH$).

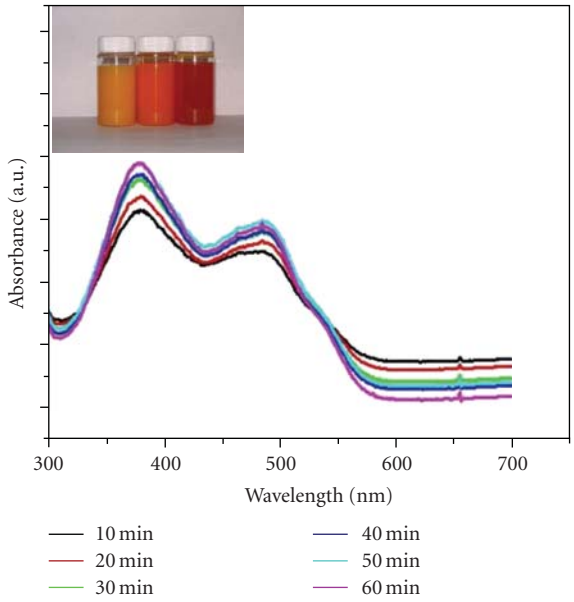


Figure 1: Reaction of vitamin $B_2$ with silver nitrate over the time in water media. The inset figure shows control vitamin $B_2$ (from left), reduced silver nanoparticles in water, and NMP solvent media after 60 minutes.

of these materials. Herein, we report a simple strategy using different solvents under which noble metal nanoparticles effectively self-assemble into spheres, nanowires, and nanorods in presence of vitamin $B_2$ (Riboflavin) and the ensuing self-assembled Ag and Pd nanoparticles can catalyze monomers such as pyrrole and aniline to afford conducting polymer nanocomposites. The study also serves the need for a greener protocol as there is a renewed interest in using green chemistry to synthesize metal nanoparticles [6, 33] Green chemistry is the design, development, and implementation of chemical products and the process to reduce or eliminate the use and generation of substances hazardous to human health and the environment[34–37]. Strategies to address mounting environmental concerns with current approaches include the use of environmentally benign solvents, biodegradable polymers, and nontoxic chemicals [34–37]. In the synthesis of metal nanoparticles by reduction of the corresponding metal ion salt solutions, there are three areas of opportunity to engage in green chemistry: (i) choice of solvent, (ii) the reducing agent employed, and (iii) the capping agent (or dispersing agent). In this area, there has also been increasing interest in identifying environmentally friendly materials that are multifunctional. For example, the vitamin $B_2$ used in this study functions both as a reducing and capping agent for Ag and palladium nanostructures, in addition to its high-water solubility, low toxicity and biodegradability; and water serves as a benign media. Herein, we describe a general method to prepare noble nanostructures such as Ag and Pd and their catalytic application to make polyaniline and polypyrrole nanofiber nanocomposites. This greener and general approach used to produce multiple shaped nanostructures such as Ag and Pd and their nanocomposites could find newer technological and medicinal applications.

## 2. EXPERIMENTAL PROCEDURE

All reagents were used as received without further purification. Vitamin $B_2$ (Riboflavin), silver nitrate (99.99%), and palladium chloride (99.99%) were purchased from Aldrich. In all experiments, Milli-Q water was used. The synthesis and self-assembly were accomplished by reacting respective metal salts with vitamin $B_2$ dissolved in solvents of different chemical nature. The reaction mixture was allowed to stand for 24 hours at room temperature and then analyzed. In particularly, 50 mg of Riboflavin was dissolved in 20 mL (glass vial) of solvents such as ethylene glycol, acetic acid, *N*-methylpyrrolidinone (NMP), water, isopropanol, acetone, and acetonitrile in separate experiments. To this, 2 mL of aqueous solution containing $1 \times 10^{-1}$ M $AgNO_3$ were added at room temperature, hand-shaken for a minute and allowed to settle. The solution turned orange immediately after the addition of $AgNO_3$ and the formation of silver nanoparticles was confirmed using UV spectroscopy and energy dispersive X-ray analysis (EDX). Similarly, experiments were conducted using $1 \times 10^{-1}$ M $PdCl_2$. TEM specimens were prepared by placing 1 $\mu$L of the particle solution on a carbon-coated copper grid and dried at room temperature. Transmission electron microscopy (TEM) was performed with a JEOL-1200 EX II microscope operated at 120 kV.

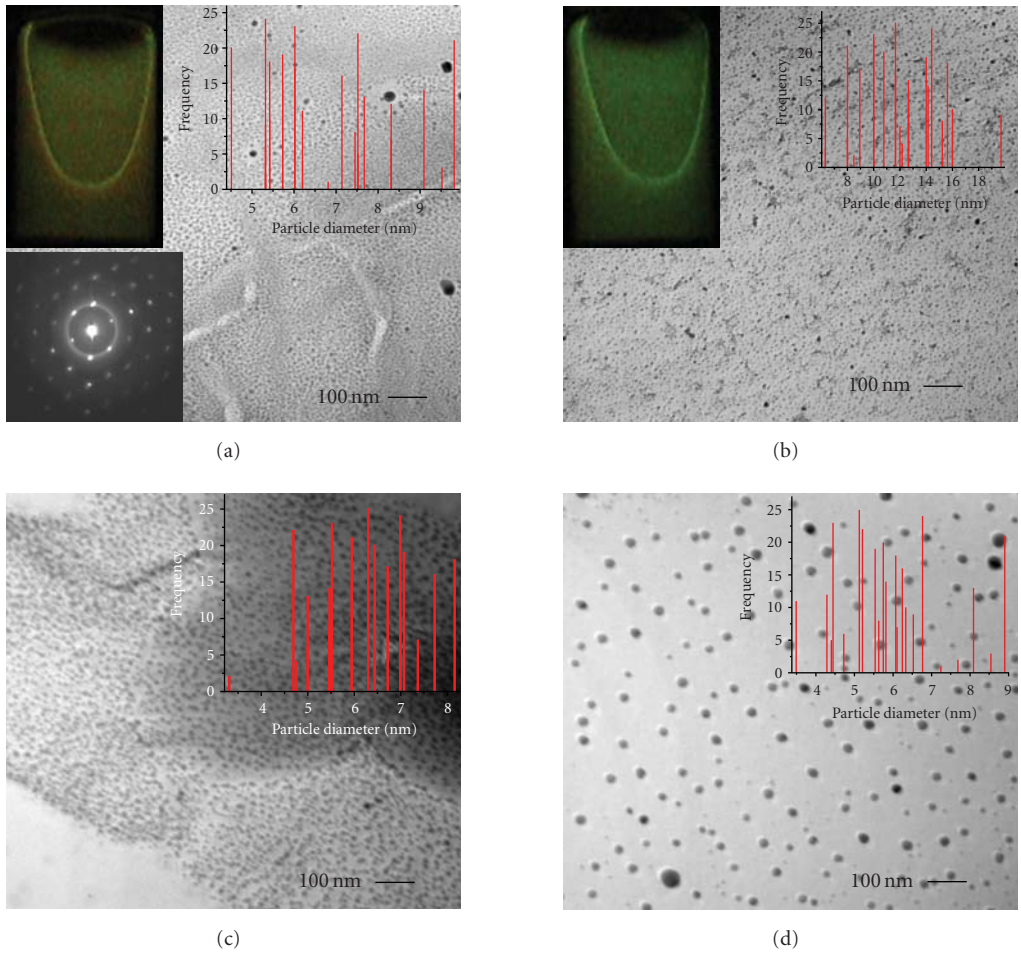


FIGURE 2: TEM image of Ag and Pd nanoparticles synthesized using vitamin $B_2$. (a) Ag (average size 6.1 ± 0.1 nm), (b) Pd (average size 4.1 ± 0.1 nm) nanoparticles in ethylene glycol, and (c), (d) Ag (average size 5.9 ± 0.1 nm, and average size 6.1 ± 0.1) nanoparticles in acetic acid and NMP, respectively. Inset shows corresponding particle size distribution, electron diffraction, and UV excitation.

## 3. RESULTS AND DISCUSSION

Vitamin $B_2$ is the most frequently encountered organic cofactor in nature and it can assume three different redox states: fully oxidized, one-electron reduced, and fully reduced [38]. Each of these redox states exists in a cationic, neutral, and anionic form (see Scheme 1) depending on the pH of the solution. The reduction potential of vitamin $B_2$ is −0.3 V versus SCE [39] which is sufficient to reduce palladium (Pd, reduction potential 0.915 V versus SCE) and silver (Ag, 0.80 V versus SCE).

The formation of noble nanostructures with vitamin $B_2$ probably occurs as follows: (i) vitamin B complexation with noble metal salts; (ii) simultaneous reduction of noble metal salts such as Ag (Ag, 0.80 V versus SCE) and Pd (Pd, reduction potential 0.915 V versus SCE) and formation of capping with oxidized vitamin $B_2$; (iii) solvent chemical nature with self-assembly of nanoparticles to form spheres, nanowires, and nanorods. The reaction of respective metal salts with vitamin $B_2$ in different solvents resulted in the reduction of metal and simultaneous oxidation and capping of vitamin $B_2$ as confirmed by UV spectroscopy (see Figure 1 for Ag). The increase in intensity over the time indicates the completion of the reaction. Plasmon absorption spectroscopy is usually used to examine the size- and shape-controlled nanoparticles because of their optical properties in aqueous suspensions related to these properties [40]. For example, the UV-vis spectrum for the colloidal solution of spherical Ag nanoparticles prepared shows a peak at approximately 375 nm. This broad extinction peak potentially results from inhomogeneity in morphology for the sample [40]. However, the plasmon absorption peak of the nanorods showed a more complex absorption pattern due to the absorption of visible light both along the length of the nanorods (the longitudinal plasmon band) and along the width of the nanorods (the transverse plasmon band). As the aspect ratio increases, the longitudinal surface plasmon resonance (SPR) band ($\lambda_1$) should be red-shifted significantly, whereas the transverse SPR($\lambda_T$) band should only show a slight blue-shift [40].

The size of the Ag and Pd nanoparticles decreased with use of ethylene glycol and acetic acid. Solvents such as ethylene glycol yielded nanoparticles with average sizes of

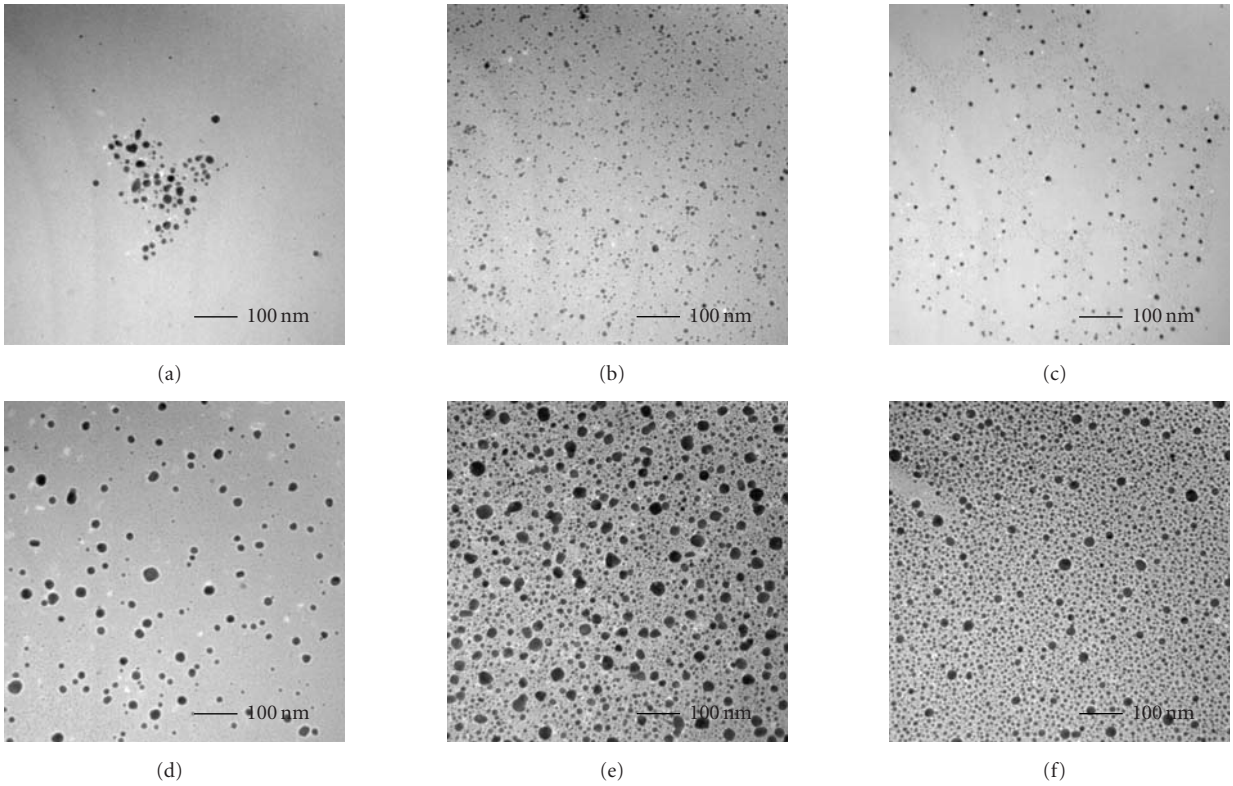


Figure 3: TEM micrographs of (a)–(c) Ag nanoparticles and (e), (f) Pd nanoparticles synthesized using vitamin $B_2$ in acetic acid, ethylene glycol, and NMP with sucrose as a capping agent, respectively.

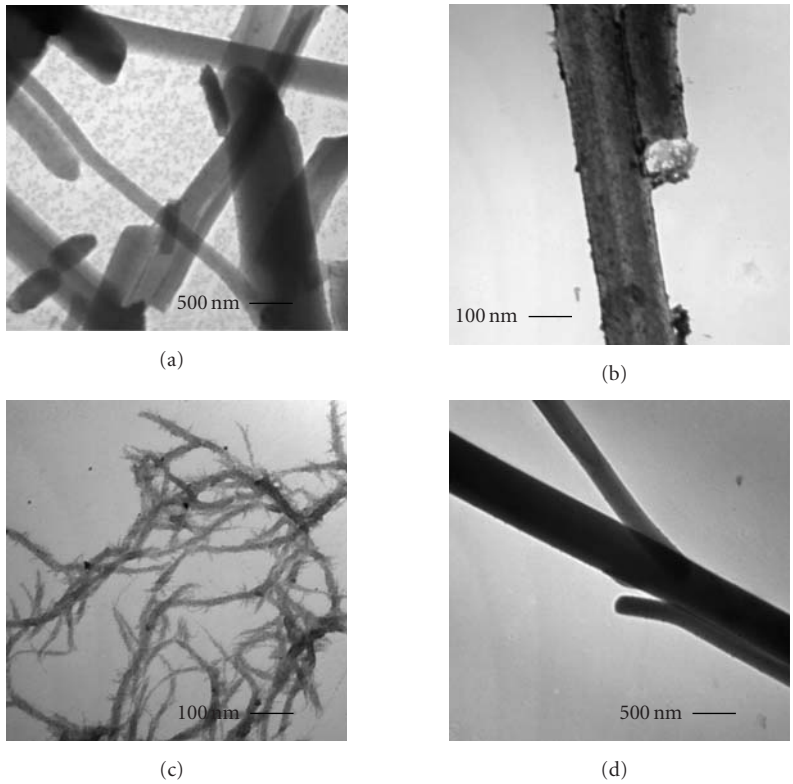


Figure 4: TEM micrographs of (a), (b) Ag and Pd nanostructures synthesized using vitamin $B_2$ in water and (c), (d) in isopropanol, respectively.

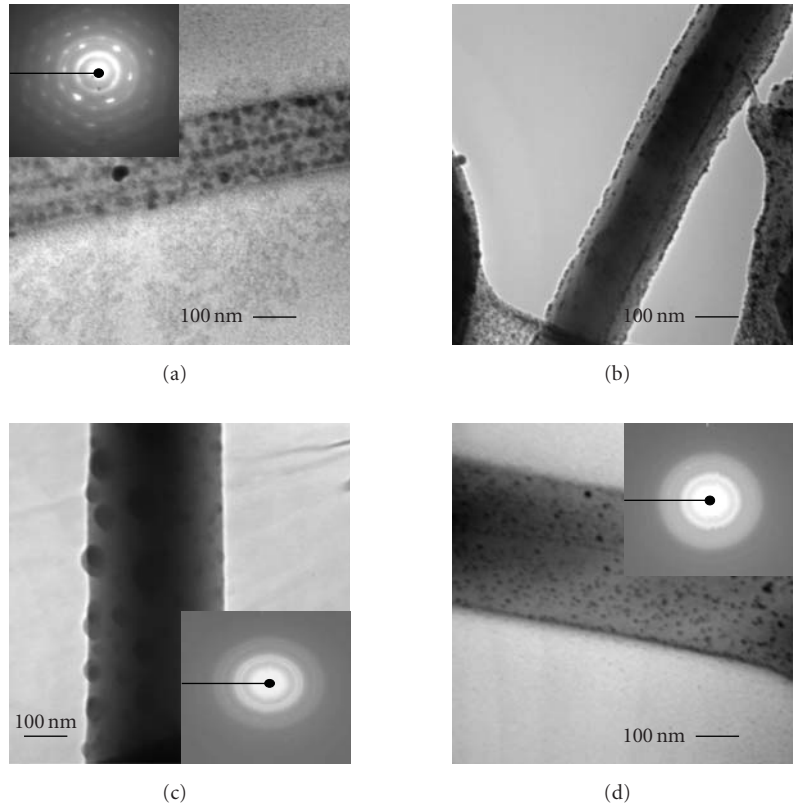


FIGURE 5: TEM image of self-assembled Ag and Pd nanowires/nanorods synthesized using vitamin $B_2$. (a), (b) Ag and Pd nanorods in acetone and (c), (d) Ag and Pd nanowires/nanorods in acetonitrile. Inset shows corresponding selected area electron diffraction patterns.

6.1 ± 0.1 nm for Ag (Figure 2(a)) and 4.1 ± 0.1 nm for Pd (Figure 2(b)). Acetic acid afforded nanoparticles ranging from 3 to 8 nm with an average of 5.9 ± 0.1 nm for Ag (Figure 2(c)) and 1 to 7 with an average size of 4.1 ± 0.1 nm for Pd (see Supplementary Material 1 Available online at doi:10.1155/2008/782358). Changing solvent, for example, using *N*-methylpyrrolidinone (NMP), yielded nanoparticles ranging from 3 to 9 nm with an average of 6.1 ± 0.1 nm for Ag (Figure 3(d)) and 5 to 13 nm with an average of 9.2 ± 0.2 nm for Pd (see Supplementary Material).

Solvents such as ethylene glycol, acetic acid, and NMP are not mere solvents but can modify the reaction conditions by virtue of their reducing character and pH, and so forth, and thereby change size and shape of the particles. For example, ethylene glycol is essentially a reducing agent and can help to reduce noble salts to corresponding metals when compared with other solvents such as NMP, water, and so forth. The more reduction nature atmosphere, the bigger the particle size formation. In contrast, NMP can form complexes with noble salts and can slow the metal reduction rate and hence, decrease in particle size. However, other solvents do not interfere a great deal in the reduction. In this context, we conducted control experiments using sucrose as a capping agent wherein we observed only nanoparticles with higher particle size (see Figure 3). This is due to masking of solvent effect (reducing and complexing behavior) on nanoparticles and hence the formation of bigger particle size. The TEM micrographs of Ag and Pd nanoparticles self-assembled in water and isopropanol are shown in Figure 4.

In water, Ag, and Pd nanoparticles started to self-assemble into rod-like structures. In isopropanol, Ag and Pd nanoparticles yielded wire-like structures with a thickness in the range of 10 to 20 nm and several hundred microns in length. In acetone and acetonitrile medium, the Ag and Pd nanoparticles are self-assembled into a regular pattern making nanorod structures with thicknesses ranging from 100 to 200 nm and lengths of a few microns (see Figures 5(a)–5(d)). The formation of self-assembly was due to strong inter-particle van-der-Waals interactions and hydrophobic interactions in aqueous solutions. Irrespective of solvent used Ag and Pd crystallized in fcc symmetry. To take the advantage of self-assembly, we were able to measure two-probe conductivity. For instance, Ag nanorods prepared from acetonitrile solvent casted on a gold electrodes 5 $\mu$m apart gave a conductivity of (40 to 80) $\times$ $10^6$ depending on electrode contact which is very much comparable to conductivity of the bare Ag reported [41]. It is interesting to note that self-assembled Pd nanoparticles can catalyze monomers such as pyrrole and aniline to afford polypyrrole and polyaniline nanocomposites (see Figure 6 for SEM and UV spectra and Figure 7 for TEM images). In the present study, Pd- and Ag-catalyzed polypyrrole yielded nanofiber nanocomposite formation in contrast with the literature reports that deliver spherical nanoparticle composites [42].

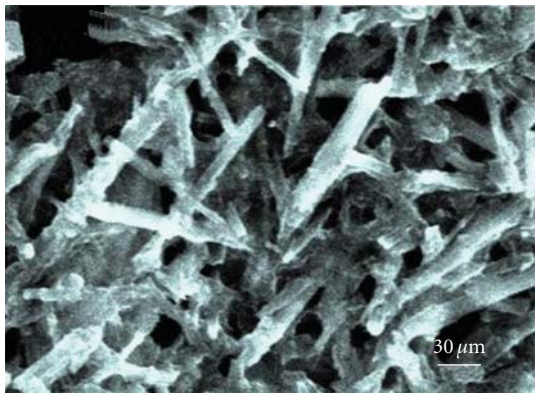


(a)

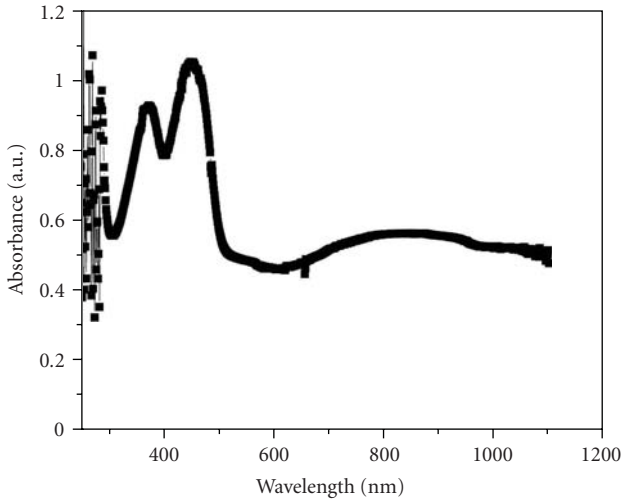


(b)

Figure 6: (a) SEM image of polypyrrole nanocomposites catalyzed by self-assembled Pd nanoparticles synthesized in water media using vitamin $B_2$ and (b) corresponding UV spectra.

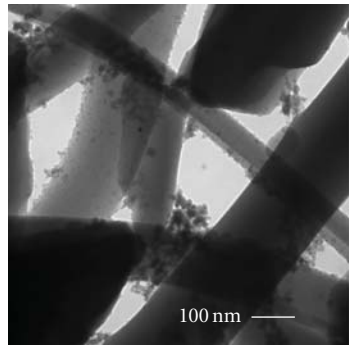


(a)

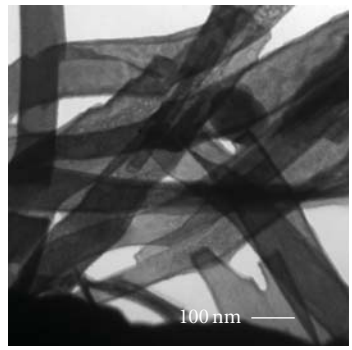


(b)

Figure 7: TEM image of (a) polypyrrole nanocomposites and (b) polyaniline nanocomposites catalyzed by self-assembled Pd nanoparticles synthesized in water media.

The broad absorption spectrum from 600 to 900 nm is due to the characteristic peak of polypyrrole formation [43]. We believe these one-dimensional fiber nanocomposites filled with noble nanoparticles may find applications in sensors, hydrogen-storage material, fuel cell membranes, catalysis, and other biological applications.

In summary, we report the following.

(i) High yield, room temperature, solvent-assisted self-assembly to prepare noble nanostructures such as Ag and Pd nanospheres, nanowires, and nanorods using vitamin $B_2$ in different solvent media thereby providing new opportunities in a myriad of applications, such as catalysis, antibacterial coatings, fuel cell membranes, and so forth.

(ii) The method employed no special capping, dispersing, or polymer as a coating agent.

(iii) Formation of noble nanostructure multiple shapes and their self-assembly depended on the solvent used for the preparation.

(iv) This single-step greener approach (when used in water) is general and may be extended to other transition metal oxides.

(v) Self-assembled Ag and Pd nanoparticles catalyzed reactions of aniline and pyrrole to generate polyaniline and polypyrrole nanocomposites.

## ACKNOWLEDGMENTS

MNN was supported, in part, by the Postgraduate Research Program at the National Risk Management Research Laboratory administered by the Oak Ridge Institute for Science and Education through an interagency agreement between the US Department of Energy and the US Environmental Protection Agency. We thank Christina Bennett-Stamper, EPA Electron Microscopy Facility, for her assistance.

## REFERENCES

[1] M. P. Pileni, "Control of the size and shape of inorganic nanocrystals at various scales from nano to macrodomains," *Journal of Physical Chemistry C*, vol. 111, no. 26, pp. 9019–9038, 2007.

[2] J. Chen, B. J. Wiley, and Y. Xia, "One-dimensional nanostructures of metals: large-scale synthesis and some potential applications," *Langmuir*, vol. 23, no. 8, pp. 4120–4129, 2007.

[3] C. G. Sztrum, O. Hod, and E. Rabani, "Self-assembly of nanoparticles in three-dimensions: formation of stalagmites,"

*Journal of Physical Chemistry B*, vol. 109, no. 14, pp. 6741–6747, 2005.

[4] E. Rabani, D. R. Reichman, P. L. Geissler, and L. E. Brus, "Drying-mediated self-assembly of nanoparticles," *Nature*, vol. 426, no. 6964, pp. 271–274, 2003.

[5] A. Tao, F. Kim, C. Hess, et al., "Langmuir-Blodgett silver nanowire monolayers for molecular sensing using surface-enhanced Raman spectroscopy," *Nano Letters*, vol. 3, no. 9, pp. 1229–1233, 2003.

[6] M. N. Nadagouda and R. S. Varma, "Green and controlled synthesis of gold and platinum nanomaterials using vitamin $B_2$: density-assisted self-assembly of nanospheres, wires and rods," *Green Chemistry*, vol. 8, no. 6, pp. 516–518, 2006.

[7] L. Zheng and J. Li, "Self-assembly of ordered 3D Pd nanospheres at a liquid/liquid interface," *Journal of Physical Chemistry B*, vol. 109, no. 3, pp. 1108–1112, 2005.

[8] S. H. Park, R. Barish, H. Li, et al., "Three-helix bundle DNA tiles self-assemble into 2D lattice or 1D templates for silver nanowires," *Nano Letters*, vol. 5, no. 4, pp. 693–696, 2005.

[9] M. M. Maye, I.-I. S. Lim, J. Luo, et al., "Mediator-template assembly of nanoparticles," *Journal of the American Chemical Society*, vol. 127, no. 5, pp. 1519–1529, 2005.

[10] F. Gao, Q. Lu, and S. Komarneni, "Interface reaction for the self-assembly of silver nanocrystals under microwave-assisted solvothermal conditions," *Chemistry of Materials*, vol. 17, no. 4, pp. 856–860, 2005.

[11] N. R. Jana, "Shape effect in nanoparticle self-assembly," *Angewandte Chemie International Edition*, vol. 43, no. 12, pp. 1536–1540, 2004.

[12] C. Burda, X. Chen, R. Narayanan, and M. A. El-Sayed, "Chemistry and properties of nanocrystals of different shapes," *Chemical Reviews*, vol. 105, no. 4, pp. 1025–1102, 2005.

[13] Z. W. Pan, Z. R. Dai, and Z. L. Wang, "Nanobelts of semiconducting oxides," *Science*, vol. 291, no. 5510, pp. 1947–1949, 2001.

[14] J. Hu, T. W. Odom, and C. M. Lieber, "Chemistry and physics in one dimension: synthesis and properties of nanowires and nanotubes," *Accounts of Chemical Research*, vol. 32, no. 5, pp. 435–445, 1999.

[15] C. L. Haynes and R. P. Van Duyne, "Nanosphere lithography: a versatile nanofabrication tool for studies of size-dependent nanoparticle optics," *Journal of Physical Chemistry B*, vol. 105, no. 24, pp. 5599–5611, 2001.

[16] P. V. Kamat, "Photophysical, photochemical and photocatalytic aspects of metal nanoparticles," *Journal of Physical Chemistry B*, vol. 106, no. 32, pp. 7729–7744, 2002.

[17] K. G. Thomas and P. V. Kamat, "Chromophore-functionalized gold nanoparticles," *Accounts of Chemical Research*, vol. 36, no. 12, pp. 888–898, 2003.

[18] J. E. Millstone, S. Park, K. L. Shuford, L. Qin, G. C. Schatz, and C. A. Mirkin, "Observation of a quadrupole plasmon mode for a colloidal solution of gold nanoprisms," *Journal of the American Chemical Society*, vol. 127, no. 15, pp. 5312–5313, 2005.

[19] S. F. Sweeney, G. H. Woehrle, and J. E. Hutchison, "Rapid purification and size separation of gold nanoparticles via diafiltration," *Journal of the American Chemical Society*, vol. 128, no. 10, pp. 3190–3197, 2006.

[20] N. R. Jana, L. Gearheart, and C. J. Murphy, "Wet chemical synthesis of silver nanorods and nanowires of controllable aspect ratio," *Chemical Communications*, no. 7, pp. 617–618, 2001.

[21] C. J. Murphy, T. K. Sau, A. M. Gole, et al., "Anisotropic metal nanoparticles: synthesis, assembly, and optical applications," *Journal of Physical Chemistry B*, vol. 109, no. 29, pp. 13857–13870, 2005.

[22] J. Chen, T. Herricks, and Y. Xia, "Polyol synthesis of platinum nanostructures: control of morphology through the manipulation of reduction kinetics," *Angewandte Chemie International Edition*, vol. 44, no. 17, pp. 2589–2592, 2005.

[23] S. H. Im, Y. T. Lee, B. Wiley, and Y. Xia, "Large-scale synthesis of silver nanocubes: the role of HCl in promoting cube perfection and monodispersity," *Angewandte Chemie International Edition*, vol. 44, no. 14, pp. 2154–2157, 2005.

[24] Y. Sun and Y. Xia, "Shape-controlled synthesis of gold and silver nanoparticles," *Science*, vol. 298, no. 5601, pp. 2176–2179, 2002.

[25] K. K. Caswell, C. M. Bender, and C. J. Murphy, "Seedless, surfactantless wet chemical synthesis of silver nanowires," *Nano Letters*, vol. 3, no. 5, pp. 667–669, 2003.

[26] M. N. Nadagouda and R. S. Varma, "A greener synthesis of core (Fe, Cu)-shell (Au, Pt, Pd, Ag) nanocrystals using aqueous vitamin C," *Crystal Growth & Design*, vol. 7, no. 12, pp. 2582–2587, 2007.

[27] B. Nikoobakht, Z. L. Wang, and M. A. El-Sayed, "Self-assembly of gold nanorods," *Journal of Physical Chemistry B*, vol. 104, no. 36, pp. 8635–8640, 2000.

[28] Y.-Y. Yu, S.-S. Chang, C.-L. Lee, and C. R. C. Wang, "Gold nanorods: electrochemical synthesis and optical properties," *Journal of Physical Chemistry B*, vol. 101, no. 34, pp. 6661–6664, 1997.

[29] C. A. Foss, G. L. Hornyak, J. A. Stockert, and C. R. Martin, "Template-synthesized nanoscopic gold particles: optical spectra and the effects of particle size and shape," *Journal of Physical Chemistry*, vol. 98, no. 11, pp. 2963–2971, 1994.

[30] J. Aizpurua, G. W. Bryant, L. J. Richter, F. J. García de Abajo, B. K. Kelley, and T. Mallouk, "Optical properties of coupled metallic nanorods for field-enhanced spectroscopy," *Physical Review B*, vol. 71, no. 23, Article ID 235420, 13 pages, 2005.

[31] C. J. Orendorff, P. L. Hankins, and C. J. Murphy, "pH-triggered assembly of gold nanorods," *Langmuir*, vol. 21, no. 5, pp. 2022–2026, 2005.

[32] K. K. Caswell, J. N. Wilson, U. H. F. Bunz, and C. J. Murphy, "Preferential end-to-end assembly of gold nanorods by Biotin-Streptavidin connectors," *Journal of the American Chemical Society*, vol. 125, no. 46, pp. 13914–13915, 2003.

[33] P. Mukherjee, S. Senapati, D. Mandal, et al., "Extracellular synthesis of gold nanoparticles by the fungus *Fusarium oxysporum*," *ChemBioChem*, vol. 3, no. 5, pp. 461–463, 2002.

[34] P. T. Anastas and J. C. Warner, *Green Chemistry: Theory and Practice*, Oxford University Press, Oxford, UK, 1998.

[35] C.-J. Li and L. Chen, "Organic chemistry in water," *Chemical Society Reviews*, vol. 35, no. 1, pp. 68–82, 2006.

[36] D. Dallinger and C. O. Kappe, "Microwave-assisted synthesis in water as solvent," *Chemical Reviews*, vol. 107, no. 6, pp. 2563–2591, 2007.

[37] J. Chen, S. K. Spear, J. G. Huddleston, J. D. Holbrey, R. P. Swatloski, and R. D. Rogers, "Application of poly(ethylene glycol)-based aqueous biphasic systems as reaction and reactive extraction media," *Industrial and Engineering Chemistry Research*, vol. 43, no. 17, pp. 5358–5364, 2004.

[38] P. V. Jaiswal, V. S. Ijeri, and A. K. Srivastava, "Voltammetric behaviour of certain vitamins and their determination in surfactant media," *Analytical Sciences*, vol. 17, pp. i741–i744, 2001.

[39] V. Massey, "The chemical and biological versatility of riboflavin," *Biochemical Society Transactions*, vol. 28, no. 4, pp. 283–296, 2000.

[40] B. Wiley, T. Herricks, Y. Sun, and Y. Xia, "Polyol synthesis of silver nanoparticles: use of chloride and oxygen to promote the formation of single-crystal, truncated cubes and tetrahedrons," *Nano Letters*, vol. 4, no. 9, pp. 1733–1739, 2004.

[41] M. N. Nadagouda and R. S. Varma, "Microwave-assisted shape-controlled bulk synthesis of noble nanocrystals and their catalytic properties," *Crystal Growth & Design*, vol. 7, no. 4, pp. 686–690, 2007.

[42] N. H. Dryden, J. J. Vittal, and R. J. Puddephatt, "New precursors for chemical vapor deposition of silver," *Chemistry of Materials*, vol. 5, no. 6, pp. 765–766, 1993.

[43] P. Rapta, A. Neudeck, A. Petr, and L. Dunsch, "*In situ* EPR/UV-VIS spectroelectrochemistry of polypyrrole redox cycling," *Journal of the Chemical Society, Faraday Transactions*, vol. 94, no. 24, pp. 3625–3630, 1998.

Hindawi Publishing Corporation
Journal of Nanomaterials
Volume 2008, Article ID 698759, 5 pages
doi:10.1155/2008/698759

*Research Article*

# Templated Fabrication of InSb Nanowires for Nanoelectronics

**M. Ibrahim Khan,[1] Xu Wang,[2] Krassimir N. Bozhilov,[3] and Cengiz S. Ozkan[1]**

[1] *Department of Mechanical Engineering, University of California Riverside, Riverside, CA 92521, USA*
[2] *Department of Chemical Engineering, University of California Riverside, Riverside, CA 92521, USA*
[3] *Central Facility for Advanced Microscopy and Microanalysis, University of California Riverside, Riverside, CA 92521, USA*

Correspondence should be addressed to Cengiz S. Ozkan, cozkan@engr.ucr.edu

Received 5 November 2007; Accepted 11 February 2008

Recommended by Junlan Wang

Among various ways to produce nanowires, anodic alumina membrane- (AAM-) based synthesis has constantly received much attention, because AAM has a uniform and parallel porous nanostructure which makes it an ideal template material for fabricating highly ordered nanostructures. In this paper, we report fabrication of InSb nanowire arrays with diameter of 200 nm and 30 nm by direct current electrodeposition inside the nanochannels of anodic alumina membranes without subsequent annealing. The nanowires have four major growth directions, (220) being the most dominant with structure defects such as twins. The transmission electron microscopy (TEM) and scanning electron microscopy (SEM) results demonstrate that these InSb nanowires are uniform with diameters about 200 nm and 30 nm, corresponding to the pore diameter of the AAMs. The I-V measurement of a single nanowire is also reported with encouraging preliminary results.



## 1. INTRODUCTION

InSb is well known for its direct narrow band gap (0.18 eV at 300 K) and various applications in electronic and optoelectronic devices with a very high-electron mobility ($8 \times 10^4\ \mathrm{cm^2V^{-1}s^{-1}}$at 300 K), electron velocity, and ballistic length (up to 0.7 $\mu$m at 300 K), and ideal candidates for detector arrays operating in the infrared wavelength, high-speed electronic devices, and magneto resistive sensors [1]. In the past few years, there has been increasing interest in nanostructure III-V semiconducting materials due to their potential applications. Different methods have been used to fabricate the nanowires, such as vapor-liquid-solid (VLS), physical vapor deposition (PVD), and hydrothermal methods [2–10]. Comparatively, the pulsed electrodeposition process, using anodic alumina membranes (AAM) as template, is an effective and inexpensive method to fabricate nanowires. However, although it is considered that the electrodeposition of high-quality compound InSb with precise stoichiometry at ambient temperature from aqueous solutions is a challenge, it is surprising that only a few studies on this important issue have been reported [11–13]. Other than thin films on a substrate [14–16], fabrication of InSb nanowires and nanocables by simple electrodeposition in anodic alumina membranes was reported [17]. Transport properties along with thermal properties of InSb nanowires have been shown very recently [18–22]. But these properties were reported only for the whole template or membrane embedded with nanowires and single nanowire properties are not measured or reported so far. Also, no attention has been given to the photoconduction properties of InSb nanowires despite the exciting possibilities for using InSb nanowires in optoelectronic circuits or as infrared detectors. We have synthesized InSb nanowires with single-crystal structures, diameters as small as from 30 to 200 nanometers by electrochemical deposition in the porous anodic alumina template and exploring the possible applications for nanoelectronics devices such as field effect transistors and Infrared photodetectors [23–28].

## 2. EXPERIMENTAL PROCEDURES

### 2.1. Synthesis

The AAMs were purchased from Whatman Inc. Florham Park, NJUSA and Synkera Technologies, Inc. (Longmont, Colo, USA). The diameters of the pores in the AAMs are about 30 nm and 200 nm, and the thickness of all AAMs

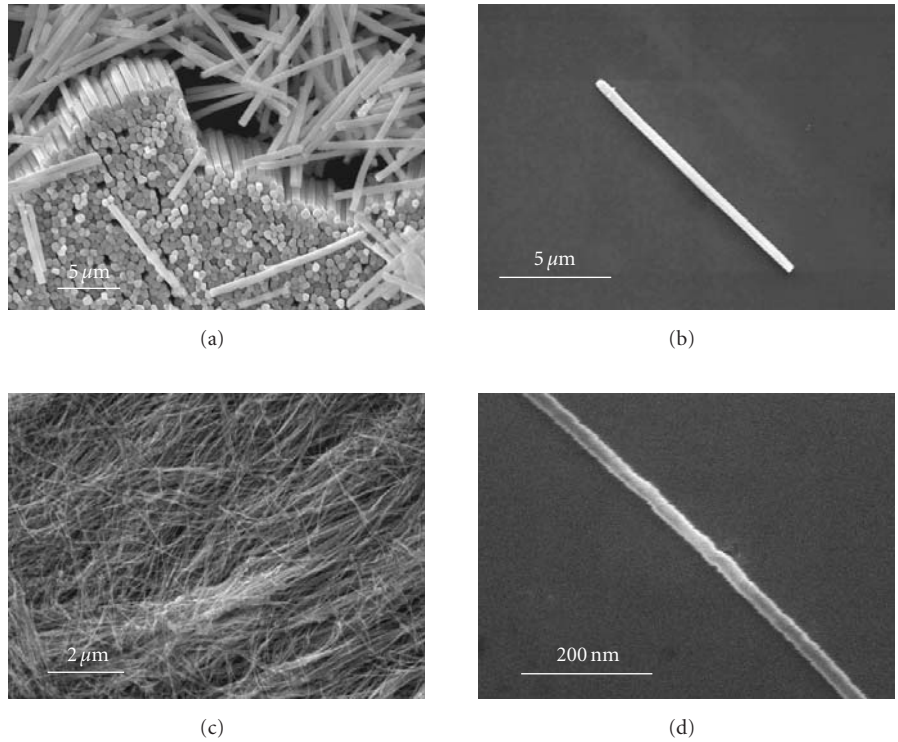


Figure 1: (a) SEM of a bundle of aligned nanowires released from AAM with 200 nm pores, (b) SEM of a single 200 nm-diameter InSb nanowire, (c) SEM of a bundle of nanowires after they are removed from the template with 30 nm pores, and (d) SEM of one single isolated 30 nm-diameter InSb nanowire.

used here is about 60 $\mu$m. A layer of Au about 200 nm in thickness was sputtered onto the bottom side of the AAMs to serve as a conduction contact. The electrodeposition was carried out in a typical three-electrode electrochemical cell equipped with a platinum electrode as the counter electrode, Ag/AgCl as reference electrode, and the AAMs with Au back layer as the working electrode controlled by a potentiostat/galvanostat (Princeton Applied Research Company (Oak Ridge, Tenn, USA), model: Potentiostat 263A). All chemicals were analytical grade used without further purification. We had performed a series of experiments and optimized the deposition parameters as follows: 0.1 M $SbCl_3$, 0.15 M $InCl_3$, 0.36 M citric acid, and 0.17 M potassium citrate at pH 1.8. The citrate ions are used as the complexion agents to bring the deposition potential of In and Sb closer to maintain binary growth. The deposition was conducted for 40 minutes under the deposition potential of $-1.5$ V versus Ag/AgCl reference electrode at room temperature. After the deposition, the sample was washed several times in distilled water and rinsed with acetone.

### 2.2. Characterization

The as-synthesized products were characterized by X-ray diffraction (XRD) machine (BRUKER AXS, Inc. Madison, WI USA, model: D8 Advance), transmission electron microscope (FEI Company (Hillsboro, Ore, USA), model: CM 300), and Scanning electron microscope (JEOL Company (Tokyo, Japan), model: JSM-6300) equipped with energy dispersive X-ray spectroscopy. For TEM analysis, the products were immersed in 3 M NaOH solution for several minutes to centrifuge and were washed with distilled water to remove the dissolved AAMs and the remaining NaOH solution; the nanowires were dispersed in deionized water. Then, drops of the solution were dripped onto copper grids coated with holey carbon film. For SEM observation, the products were treated with 3 M NaOH for about 30 minutes and washed with distilled water then was placed on Si substrate.

## 3. RESULTS AND DISCUSSION

SEM observations in Figure 1(a) show that the InSb nanowires are uniformly distributed, highly ordered, parallel to each other, and their diameters are all about 200 nm, corresponding to the pore diameter of the AAM used. It can be seen in Figure 1(b) that the nanowires are uniform in diameter and have a smooth surface. Figures 1(c) and 1(d) show the bundles of nanowires after removing from a membrane with 30 nm pores. Depending on the pore diameter of the AAM, InSb nanowire arrays with different diameters can be obtained. The length of InSb nanowires varies between 5 $\mu$m to 20 $\mu$m, which corresponds with the deposition time used and also the speed of the centrifuge during cleaning. The length of the nanowires can be modulated by changing the thickness of the AAM or the pulsed deposition time. Figures 2(a) and 2(b) show a typical EDS spectrum of InSb nanowire and the XRD patterns, respectively. The diffraction peaks can be indexed to a cubic zinc-blended phase of InSb

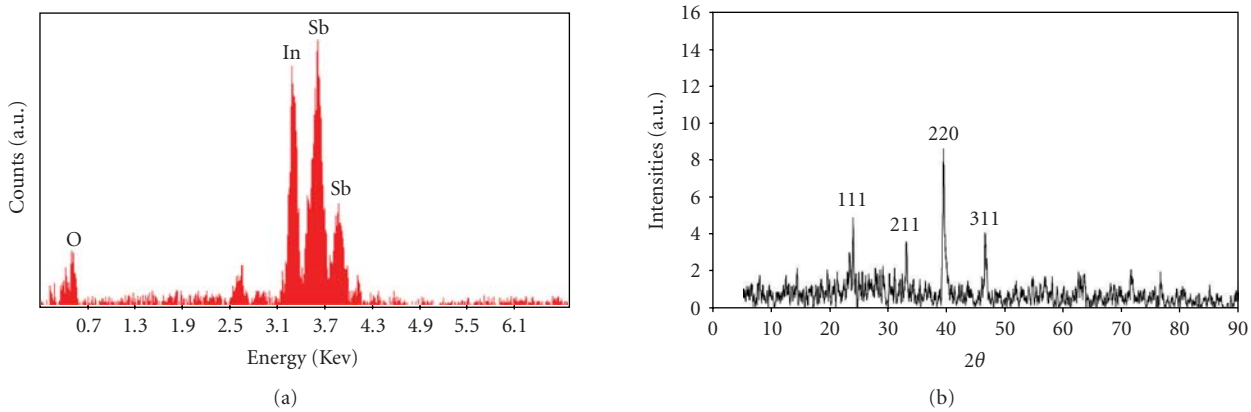


Figure 2: (a) Energy dispersive spectrum of a single InSb nanowire, (b) XRD pattern of InSb nanowire arrays show four preferred directions of growth.

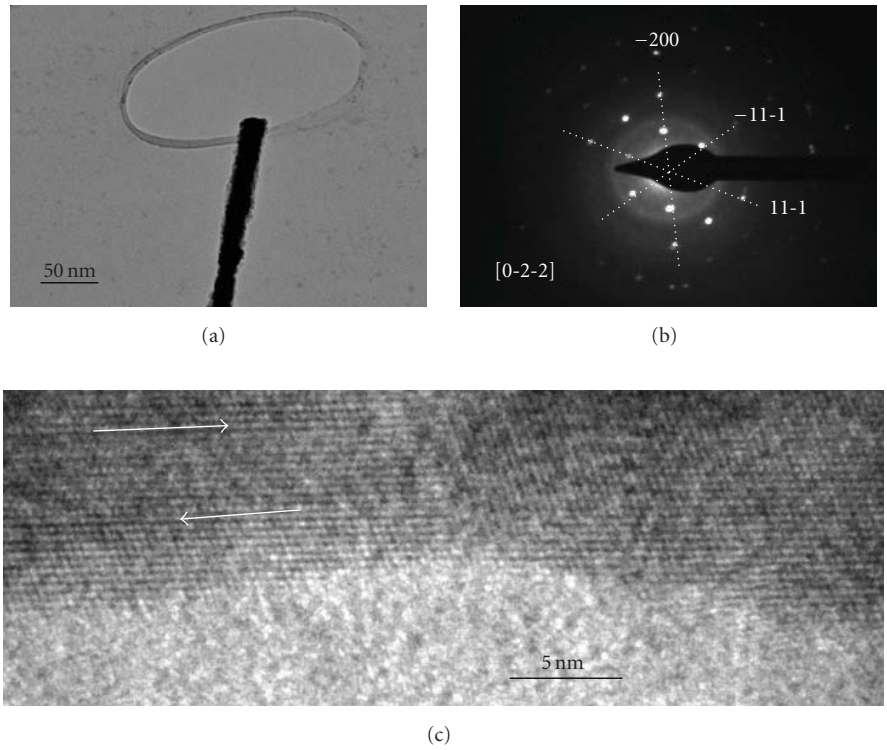


Figure 3: (a) Electron transparent edge of an InSb nanowire in a TEM bright field image, (b) selected area diffraction pattern (SAED) shows hexagonal pattern on a (0-2-2) zone axis, and (c) high-resolution TEM image of the junction between an atomically abrupt inter-twinning. The arrows are showing the junctions.

crystal from the American Mineralogist Crystal Structure Database (AMCSD). One can see that the intensity of the diffraction peak at $2\theta = 39.34^\circ$ is relatively stronger than the other diffraction peaks, demonstrating that the InSb nanowires deposited in AAM grow preferentially along (220) crystal direction.

The transmission electron microscope (TEM) images of one single InSb nanowire released from AAMs is shown in Figure 3(a). The corresponding selected-area electron diffraction (SAED) pattern indicates that the InSb nanowires are single crystalline in Figure 3(b). The SAED pattern was taken along the nanowires, but changes along the length of the nanowires. This means that the nanowires are single crystal with a slight structural deformation along the length which is seen in the high resolution TEM (HRTEM) image in Figure 3(c). The HRTEM obtained from the nanowire shown in Figure 3(a) is shown in Figure 3(c) depicting the twinning pattern present in the crystal structure. The deformations may be due to the release process of nanowires from the membrane, which involves etching with NaOH, washing

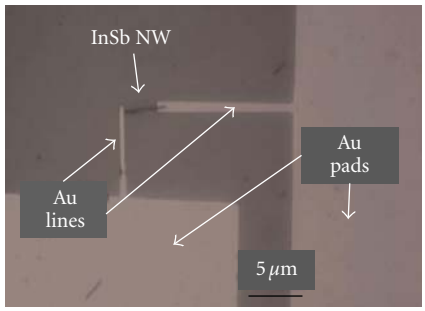


(a)

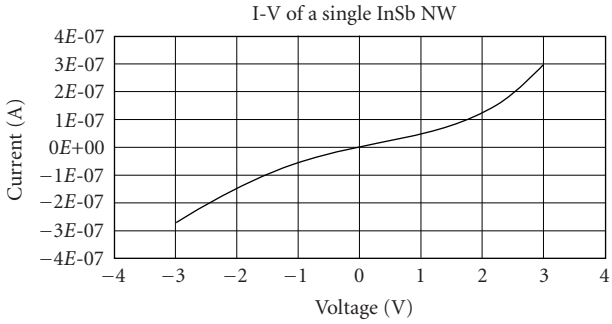


(b)

Figure 4: (a) Au-InSb-Au contacts (Schottky) made by electron beam lithography (EBL) technique for a single NW, (b) I-V characteristics show the nonlinear rectifying effect due to the metal-semiconductor-metal contacts.

with acetone and isopropanol and finally centrifuging in deionized water.

Numbered grids were written onto a silicon wafer using electron beam lithography technique (EBL) for fabricating test beds for electrical measurements. The synthesized InSb nanowires were suspended in deionized water and transferred onto each grid. A scanning electron microscope was used to locate and image the deposited wires. With the images as reference, contacts to the nanowires were designed using an SEM/E-beam Lithography system (Carl Zeiss Company, model: Leo SUPRA 55). The Si chip was spin-coated with a polymer resist layer (PMMA) for using with electron beam lithography, which involves exposing the resist layer to high-energy electrons in a pattern defined by the drawing programmed in the lithography system. Through developing, the resist is removed from the exposed areas. A layer of Au is evaporated for making contact patterns to the measurement devices. After metals are deposited, the remaining polymer is removed using acetone and the EBL patterns of gold lines were found on top of the nanowires at the desired sites (Figure 4(a)). Electrical measurements were made using a semiconductor parameter analyzer (Agilent Technologies, Inc. Santa Clara, CA USA, model: 4155C) coupled with a probe station (Signatone Corporation Gilroy, CA USA, model: H 100) by applying a constant voltage across the nanowire and current was measured. Figure 4(b) shows that the I-V curves exhibit a nonlinear characteristic and might be referred to the Au/InSb/Au junction structure. It is well known that contacts made by EBL shows rectifying behavior which can be explained considering the existence of two back-to-back Schottky barriers connected in series to both extremes of the nanowire, that is, Au-InSb-Au. The observed rectifying behavior at room temperature tends to disappear at higher temperatures which is being studied at present and will be reported in near future. Nevertheless, it could be ascertained to the fact that conduction electrons possess enough mobility to overcome the energy barrier existing in Schottky junctions.

## 4. CONCLUSION

In summary, near-stoichiometric InSb nanowires have been synthesized by using dc electrodeposition inside the nanochannels of AAMs without subsequent annealing. Achievement of better control of stoichiometry than demonstrated here may be possible and will be important for future device applications. The nanowires also conduct almost no current in the dark, but when hit with light, they conduct 10000 times more current which was also found recently. This photoconduction property could lead to a variety of tiny optoelectronic devices potentially useful in future generations of nanoelectronics, chemical sensors, and eventually provide clues to the fabrication of tiny solar cells. The light-induced conductivity increase and the temperature dependent behavior of the nanowires will be reported in near future.

## ACKNOWLEDGMENT

This work was supported by the financial support from the Focus Center Research Program (FCRP) on Functional Engineered Nano Architectonics (FENA).

## REFERENCES

[1] D. G. Avery, D. W. Goodwin, and M. A. E. Renni, "New infrared detectors using indium antimonide," *Journal of Scientific Instruments*, vol. 34, pp. 394–395, 1957.

[2] A. Huczko, "Template-based synthesis of nanomaterials," *Applied Physics A*, vol. 70, no. 4, pp. 365–376, 2000.

[3] M. Law, J. Goldberger, and P. Yang, "Semiconductor nanowires and nanotubes," *Annual Review of Materials Research*, vol. 34, pp. 83–122, 2004.

[4] C. N. R. Rao and A. Govindaraj, "Nanotubes and nanowires," *Journal of Chemical Sciences*, vol. 113, no. 5-6, pp. 375–392, 2001.

[5] S. A. Solin, D. R. Hines, A. C. H. Rowe, et al., "Nonmagnetic semiconductors as read-head sensors for ultra-high-density magnetic recording," *Applied Physics Letters*, vol. 80, no. 21, pp. 4012–4014, 2002.

[6] H. Masuda and K. Fukuda, "Ordered metal nanohole arrays made by a two-step replication of honeycomb structures of anodic alumina," *Science*, vol. 268, no. 5216, pp. 1466–1468, 1995.

[7] J. Hu, M. Ouyang, P. Yang, and C. M. Lieber, "Controlled growth and electrical properties of heterojunctions of carbon nanotubes and silicon nanowires," *Nature*, vol. 399, no. 6731, pp. 48–51, 1999.

[8] X. Duan, Y. Huang, Y. Cui, J. Wang, and C. M. Lieber, "Indium phosphide nanowires as building blocks for nanoscale electronic and optoelectronic devices," *Nature*, vol. 409, no. 6816, pp. 66–69, 2001.

[9] N. K. Udayashankar and H. L. Bhat, "Growth and characterization of indium antimonide and gallium antimonide crystals," *Bulletin of Materials Science*, vol. 24, no. 5, pp. 445–453, 2001.

[10] S. J. Hurst, E. K. Payne, L. Qin, and C. A. Mirkin, "Multisegmented one-dimensional nanorods prepared by hard-template synthetic methods," *Angewandte Chemie International Edition*, vol. 45, no. 17, pp. 2672–2692, 2006.

[11] D. Lincot, "Electrodeposition of semiconductors," *Thin Solid Films*, vol. 487, no. 1-2, pp. 40–48, 2005.

[12] T. Fulop, C. Bekele, U. Landau, J. Angus, and K. Kash, "Electrodeposition of polycrystalline InSb from aqueous electrolytes," *Thin Solid Films*, vol. 449, no. 1-2, pp. 1–5, 2004.

[13] G. Mengoli, M. M. Musiani, F. Paolucci, and M. Gazzano, "Synthesis of InSb and $In_xGa_{1-x}Sb$ thin films from electrodeposited elemental layers," *Journal of Applied Electrochemistry*, vol. 21, no. 10, pp. 863–868, 1991.

[14] L. P. Chen, J. J. Lou, T. H. Liu, Y. M. Pang, and S. J. Yang, "Evaluation of low dark current InSb photovoltaic detectors," *Solid-State Electronics*, vol. 35, no. 8, pp. 1081–1084, 1992.

[15] J.-J. McChesney, J. Haigh, I. M. Dharmadasa, and D. J. Mowthorpe, "Electrochemical growth of GaSb and InSb for applications in infra-red detectors and optical communication systems," *Optical Materials*, vol. 6, no. 1-2, pp. 63–67, 1996.

[16] M. Oszwaldowski and T. Berus, "Doping of InSb thin films with lead," *Journal of Physics and Chemistry of Solids*, vol. 61, no. 6, pp. 875–885, 2000.

[17] M. J. Zheng, L. D. Zhang, G. H. Li, X. Y. Zhang, and X. F. Wang, "Ordered indium-oxide nanowire arrays and their photoluminescence properties," *Applied Physics Letters*, vol. 79, no. 6, pp. 839–841, 2001.

[18] Y. Zhang, G. Li, Y. Wu, B. Zhang, W. Song, and L. Zhang, "Antimony nanowire arrays fabricated by pulsed electrodeposition in anodic alumina membranes," *Advanced Materials*, vol. 14, no. 17, pp. 1227–1230, 2002.

[19] M. V. Vedernikov, O. N. Uryupin, B. M. Goltsman, Yu. V. Ivanov, and Yu. A. Kumzerov, "Experimental thermopower of quantum wires," *Materials Research Society Symposium Proceedings*, vol. 691, pp. 301–306, 2002.

[20] N. Mingo, "Thermoelectric figure of merit and maximum power factor in III-V semiconductor nanowires," *Applied Physics Letters*, vol. 84, no. 14, pp. 2652–2654, 2004.

[21] K. H. Lee, J. Y. Lee, and W. Y. Jeung, "III-V compound semiconductor InSb films electrodeposited from aqueous citric solutions," in *Proceedings of the 206th Meeting of the Electrochemical Society (ECS '04)*, Honolulu, Hawaii, USA, October 2004, Abs. 48.

[22] I. M. Dharmadasa and J. Haigh, "Strengths and advantages of electrodeposition as a semiconductor growth technique for applications in macroelectronic devices," *Journal of the Electrochemical Society*, vol. 153, no. 1, pp. G47–G52, 2006.

[23] Y. Yang, L. Li, X. Huang, M. Ye, Y. Wu, and G. Li, "Fabrication of InSb-core/alumina-sheath nanocables," *Materials Letters*, vol. 60, no. 4, pp. 569–571, 2006.

[24] X. Zhang, Y. Hao, G. Meng, and L. Zhang, "Fabrication of highly ordered InSb nanowire arrays by electrodeposition in porous anodic alumina membranes," *Journal of the Electrochemical Society*, vol. 152, no. 10, pp. C664–C668, 2005.

[25] Y. Yang, L. Li, X. Huang, G. Li, and L. Zhang, "Fabrication and optical property of single-crystalline InSb nanowire arrays," *Journal of Materials Science*, vol. 42, no. 8, pp. 2753–2757, 2007.

[26] E. C. Walter, R. M. Penner, H. Liu, K. H. Ng, M. P. Zach, and F. Favier, "Sensors from electrodeposited metal nanowires," *Surface and Interface Analysis*, vol. 34, no. 1, pp. 409–412, 2002.

[27] H. Kind, H. Yan, B. Messer, M. Law, and P. Yang, "Nanowire ultraviolet photodetectors and optical switches," *Advanced Materials*, vol. 14, no. 2, pp. 158–160, 2002.

[28] J. H. He, W. W. Wu, S. W. Lee, L. J. Chen, Y. L. Chueh, and L. J. Chou, "Synthesis of blue-light-emitting $Si_{1-x}Ge_x$ oxide nanowires," *Applied Physics Letters*, vol. 86, no. 26, Article ID 263109, 3 pages, 2005.

Hindawi Publishing Corporation
Journal of Nanomaterials
Volume 2008, Article ID 830474, 7 pages
doi:10.1155/2008/830474

*Research Article*

# Direct Oxidation Growth of CuO Nanowires from Copper-Containing Substrates

**Benjamin J. Hansen, Ganhua Lu, and Junhong Chen**

*Department of Mechanical Engineering, University of Wisconsin-Milwaukee, Milwaukee, WI 53211, USA*

Correspondence should be addressed to Junhong Chen, jhchen@uwm.edu

Received 20 September 2007; Accepted 3 January 2008

Recommended by Junlan Wang

Controlling the growth of semiconducting nanowires with desired properties on a reproducible basis is of particular importance in realizing the next-generation electronic and optoelectronic devices. Here, we investigate the growth of cupric oxide (CuO) nanowires by direct oxidation of copper-containing substrates at 500°C for 150 minutes at various oxygen partial pressures. The substrates considered include a low-purity copper gasket, a high-purity copper foil, compacted CuO and $Cu_2O$ thin layers, and layered Cu/CuO and Cu/$Cu_2O$ substrates. The morphology, composition, and structure of the product CuO nanowires were analyzed using scanning electron microscopy, energy-dispersive X-ray spectroscopy, transmission electron microscopy, selected area electron diffraction, X-ray diffraction, and UV-Visible absorption. Selected oxidation processes have been monitored using a thermogravimetric analyzer. The layering structure of the substrate after oxidation was analyzed to elucidate the growth mechanism of CuO nanowires.



## 1. INTRODUCTION

One-dimensional nanostructures that can efficiently transport electrical carriers have been an exciting area of research due to their potential applications in next-generation optoelectronic [1], electronic [1], bio- [2], and gas- [3] sensing devices. Research in the controlled growth of semiconducting nanowires (NWs) is of particular importance in achieving the desired properties on a reproducible basis. Various growth techniques have been employed, including the vapor-liquid-solid growth [4], epitaxial growth [5], vapor-solid growth [6], wet chemical methods [7], and electrospinning [8]. For vapor-solid growth, it has been known since the 1950s that the oxidation of various metals, including copper, iron, zinc, and tantalum, at intermediate temperatures, results in a parallel oxide layering with high-density oxide wires/whiskers at the surface [9]. However, only recently with the advent of advanced characterization and assembly techniques has this phenomenon revived interest. The simplicity of the vapor-solid technique, together with its high NW yield and potential for controllability, makes it an attractive avenue for NW growth.

Cupric oxide (CuO) has been extensively studied due to its application in high Tc superconductors [10] and as a heterogeneous catalyst [11]. In addition, bulk CuO with a known band gap of 1.2 eV has an interesting monoclinic crystal structure belonging to the Mott insulator material class whose electronic structure cannot be described by conventional band theory [12]. CuO NW arrays have been recently applied to various applications including gas sensing [3], field emission [13, 14], and photovoltaic devices [7]. The vapor-solid oxidation technique has been widely used to grow CuO NWs [6, 14–17] from copper substrates. Recent studies on CuO NWs have focused on the influence of temperature, growth time, and oxidative environment on the growth rate, size distribution, and areal density of CuO nanowires [6, 14, 15]. It has been shown that the growth time can be used to control NW length distribution, the growth temperature can be used to control the NW diameter distribution [6], and the $O_2$ and $H_2O$ partial pressures strongly affect the NW areal density [15, 16]. The surface condition of the copper substrate was also shown to significantly affect the nanowire growth [17].

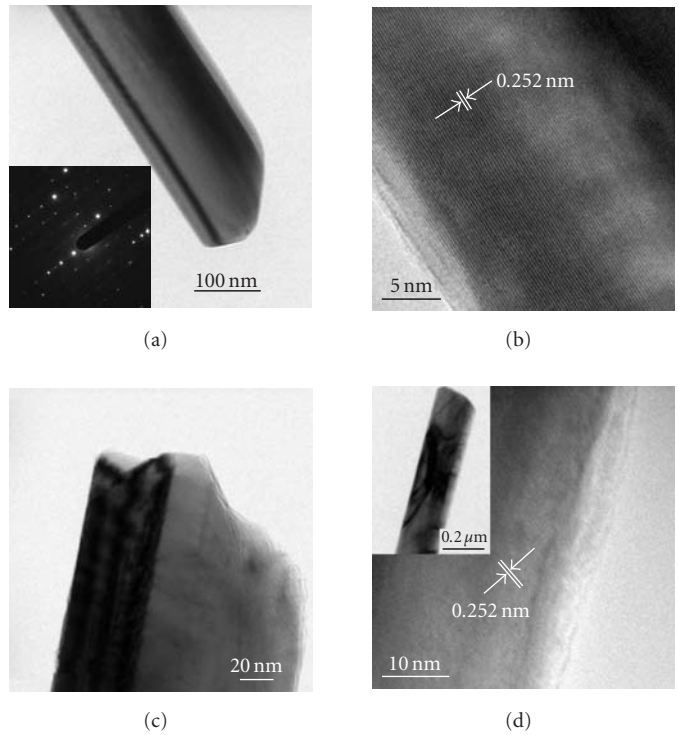


Figure 1: Bright field TEM (a) and HRTEM (b) images of a nanowire grown from a high-purity Cu foil with the inset of (a) being a SAED pattern; (c) BF TEM image of a nanowire grown from a low-purity Cu gasket; and (d) HRTEM image of a nanowire (the inset) shows fringes that are not parallel to the nanowire axis.

A common problem with the vapor-solid oxidation growth of CuO NWs from copper substrates is that the mismatching stress between the substrate and the oxide layer leads to the flaking of the oxide layer and hence the poor electrical contact between the NW and the substrate. Herein, we investigate the growth of CuO NWs directly from copper-containing substrates, such as CuO and $Cu_2O$ layers with and without a Cu substrate. In addition, the effect of $O_2$ partial pressure on NW areal density is investigated. The layering of the substrate after oxidation is analyzed to elucidate the growth mechanism. The resulting CuO NWs on a conducting/semiconducting substrate can be directly used for electronic applications.

## 2. EXPERIMENTAL DETAILS

Both copper substrates and copper-containing substrates were used for the growth of CuO NWs. Copper substrates used include a low-purity Cu gasket with high surface roughness and a high-purity Cu foil (5Ns, 0.2 mm thick) with low surface roughness. Before the NW growth, the Cu substrates were cleaned in 1 M HCl solution for ~30 seconds, then rinsed in deionized water, and finally dried in a dry airflow. Copper-containing substrates used include CuO and $Cu_2O$ thin layers that were created by compacting commercial CuO (3Ns, <74 $\mu$m) and $Cu_2O$ (2Ns, <74 $\mu$m) powders under 103 MPa for ~2 minutes. Likewise, CuO and $Cu_2O$ powders were deposited onto high-purity Cu foils and compacted to create Cu/CuO and Cu/$Cu_2O$ layered substrates.

CuO NWs were grown by direct oxidation of the above substrates in pure $O_2$ or Ar–$O_2$ mixtures. The oxidation processes were normally carried out inside a Lindberg/Blue Mini-Mite tube furnace. However, to monitor the oxidation process, a few substrates were oxidized using a TA Instrument SDT 2960 horizontal thermogravimetric analyzer (TGA). During a typical oxidation procedure, a substrate was exposed to an Ar–$O_2$ gas mixture of 5 lpm with the desired $O_2$ partial pressure, then heated at ~50°C/min to an isotherm of 500°C and held for 150 minutes. Upon cooling down, a pure inert gas flow was introduced to prevent the further oxidation. The $O_2$ partial pressures were controlled at 10%, 15%, 20%, and 100% (pure $O_2$) by mixing $O_2$ with Ar at appropriate flow rates using mass flow controllers.

Following the oxidation process, each sample was analyzed using a Topcon ABT-32 scanning electron microscope (SEM) equipped with an energy dispersive X-ray (EDX) spectrometer. SEM images were used to analyze the NW morphology and oxide layering and the EDX was used to determine the elemental composition of the sample. The as-produced NW samples were first scratched off their growing substrates, and then transferred onto copper grids and analyzed using a Hitachi H 9000 NAR transmission electron microscope (TEM) for bright field (BF) TEM and high-resolution TEM (HRTEM) imaging and selected area electron diffraction (SAED). A Scintag XDS 2000 X-ray diffractometer (XRD) was used for further analyzing the crystal structure of the samples. An Ocean Optics 2000 UV-Visible spectrometer was used to obtain the absorption spectrum

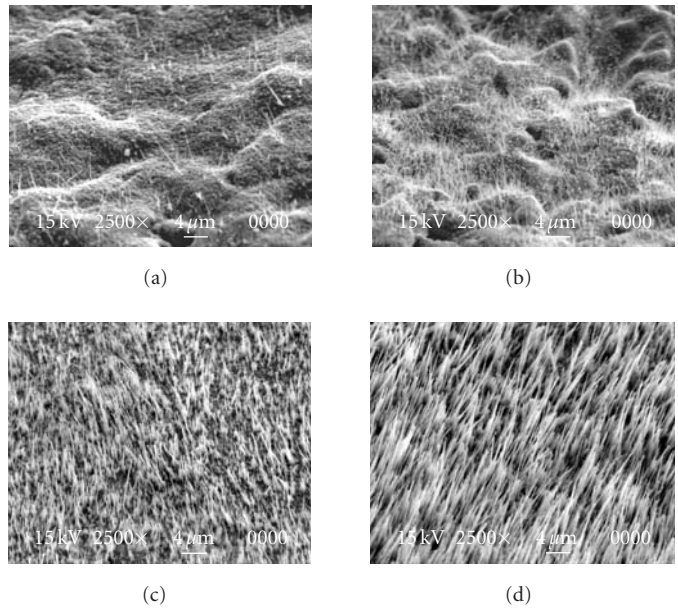


Figure 2: SEM images of oxidized copper substrates at various $O_2$ partial pressures: (a) 10%, (b) 15%, (c) 20%, and (d) 100%.

(reflection mode) of an as-grown high-density NW array. The reflection from a high-quality mirror was used as the reference.

## 3. RESULTS AND DISCUSSION

Figures 1(a) and 1(c) show low-magnification TEM images of nanowires grown in pure $O_2$ from a high-purity Cu foil and a low-purity Cu gasket, respectively. The corresponding HRTEM images of the NWs are shown in Figures 1(b) and 1(d), respectively. The visible stripes identified with different contrasts in Figures 1(a) and 1(c) indicate that as-grown nanonwires bear faceted instead of circular cross-sections. The SAED pattern of the NW in the inset of Figure 1(a) confirms the crystallinity of product nanowires and the direction of diffraction spots is consistent with the fringe direction shown in the HRTEM image of Figure 1(b). The lattice spacing of the NWs was measured as 0.252 nm, corresponding to the $(\bar{1}11)$ plane of CuO. The direction of the fringes in Figure 1(b) is in parallel with the nanowire axis, while the fringes shown in Figure 1(d) are not parallel to the wire axis, with a similar angle of 50° reported in [9]. The two observed fringe directions may be attributed to the difference in surface orientation or surface roughness of the corresponding substrates [18, 19]. The direction in which a crystal grows on a substrate is dependent on the orientation of the seed crystal. As CuO NWs grow from a Cu foil, which is polycrystalline and consists of grains with varying crystallographic orientations, their growth directions would be different from each other, leading to dissimilar fringes of the NWs in HRTEM images.

The low-purity copper substrates were oxidized at four different $O_2$ partial pressures of 10%, 15%, 20%, and 100%. Upon inspection after oxidation, the surfaces of the copper substrates were tarnished from light to dark grey with respect to the 10% to 20% $O_2$ partial pressures, whereas the substrate oxidized in 100% $O_2$ was tarnished almost completely black with only several small grey areas. The SEM images of the oxidized copper substrates are shown in Figures 2(a)–2(d). Since the NW density varies throughout the surface of each individual substrate, the images shown are those representative areas with more uniformly dense NWs on each substrate. The NW density and the vertical alignment increase with increasing $O_2$ partial pressures, while the average length and diameter of the NWs seem to decrease with decreasing $O_2$ partial pressures. Most NWs appear to be tapered like a needle or whisker, which may be due to the high roughness of the substrate and the subsequent merging of multiple NWs into one NW during the growth. In the case of pure $O_2$, the areas of highest NW

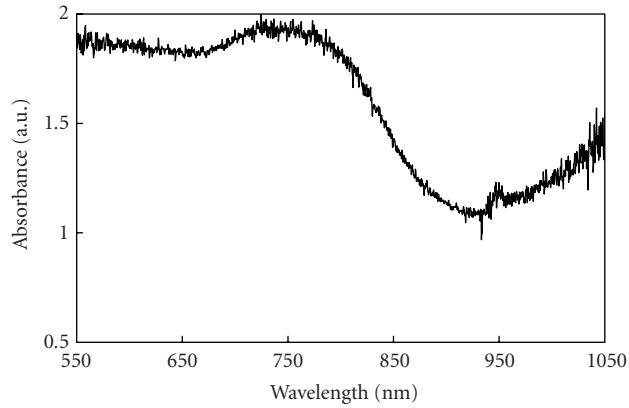


Figure 3: UV-Visible absorption spectrum of a CuO nanowire array.

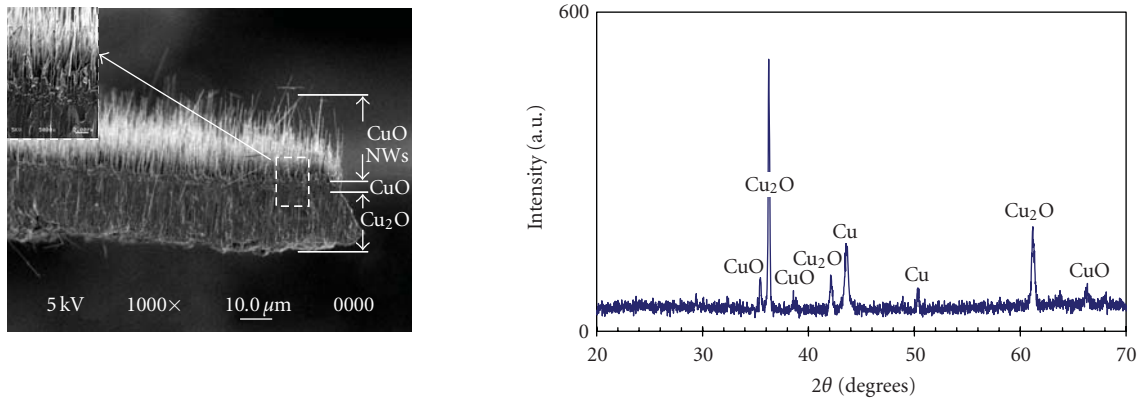


Figure 4: (a) SEM images and (b) XRD spectrum of an oxidized copper substrate.

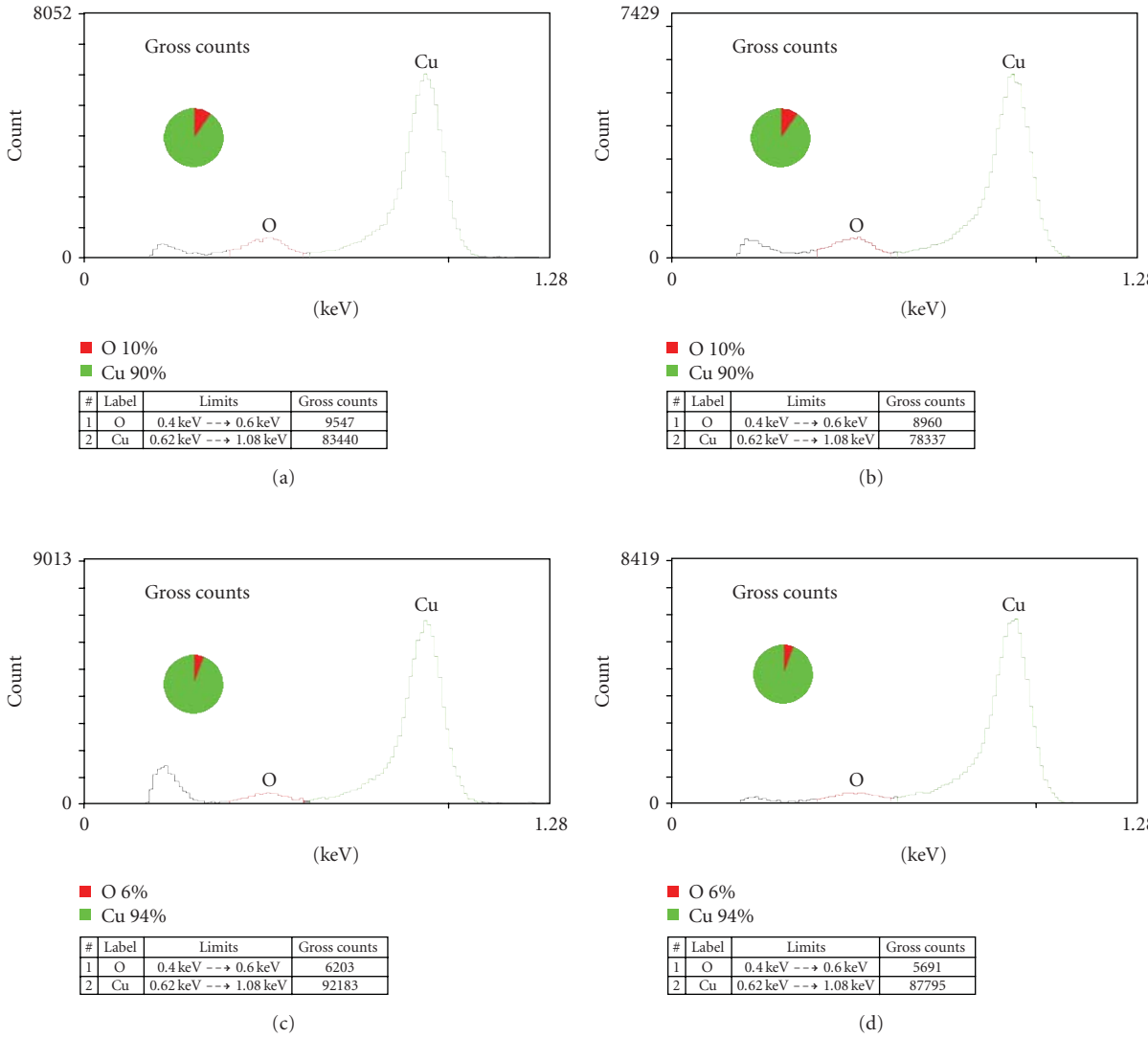


Figure 5: EDX spectra and region analysis: (a) CuO standard; (b) top of the oxide flake; (c) $Cu_2O$ standard; and (d) bottom of the oxide flake.

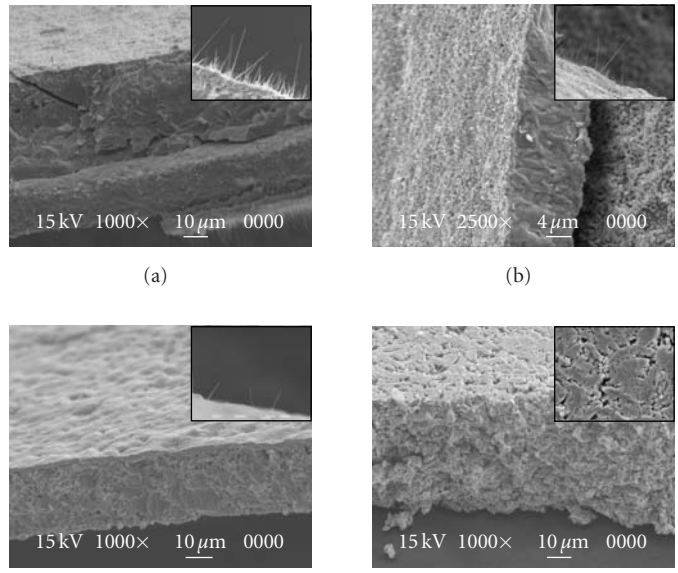


FIGURE 6: SEM images of the substrates after oxidation: (a) $Cu/Cu_2O$, (b) Cu/CuO, (c) $Cu_2O$ thin layer, and (d) CuO thin layer. The insets show the amplified top surface details of the corresponding substrates.

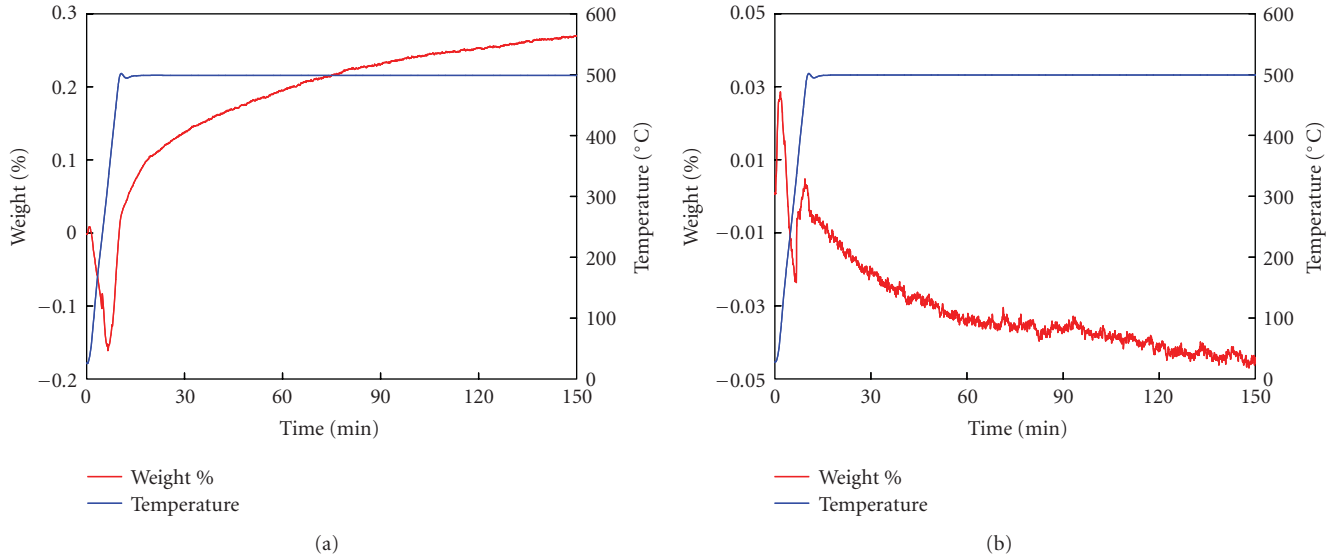


FIGURE 7: TGA results of the oxidation process from (a) $Cu_2O$ thin layer (initial mass: 49.598 mg) and (b) CuO thin layer (initial mass: 38.061 mg).

density were those that tarnished black. And the light to dark grey samples with 10 to 20% $O_2$ partial pressures correspond to the low to medium NW density. Since bulk CuO is known to be grey to black in color and $Cu_2O$ is red, it can be roughly inferred that the oxide surface and possibly the NWs are CuO. However, in many cases the color of nanostructures is very different from that of their corresponding bulk structures due to morphology-induced interference and scattering. Thus, the observed color can only be used as a rough guide and the actual composition of the surface and the NWs must be obtained with the aid of advanced characterization techniques. A UV-Visible absorption spectrum of a high-density NW array similar to the sample shown in Figure 2(d) is presented in Figure 3. The band gap of the as-grown NWs was estimated from the absorption spectrum by fitting a tangential line passing the midpoint of the first absorption edge (750–940 nm) and reading out the $x$-intercept. In this way, a band gap of approximately 1.2 eV (1030 nm) corresponding to bulk CuO can be extracted.

To further analyze the oxide layering structure, an oxide flake was carefully removed from a copper substrate oxidized in pure $O_2$. The SEM image of the flake is shown

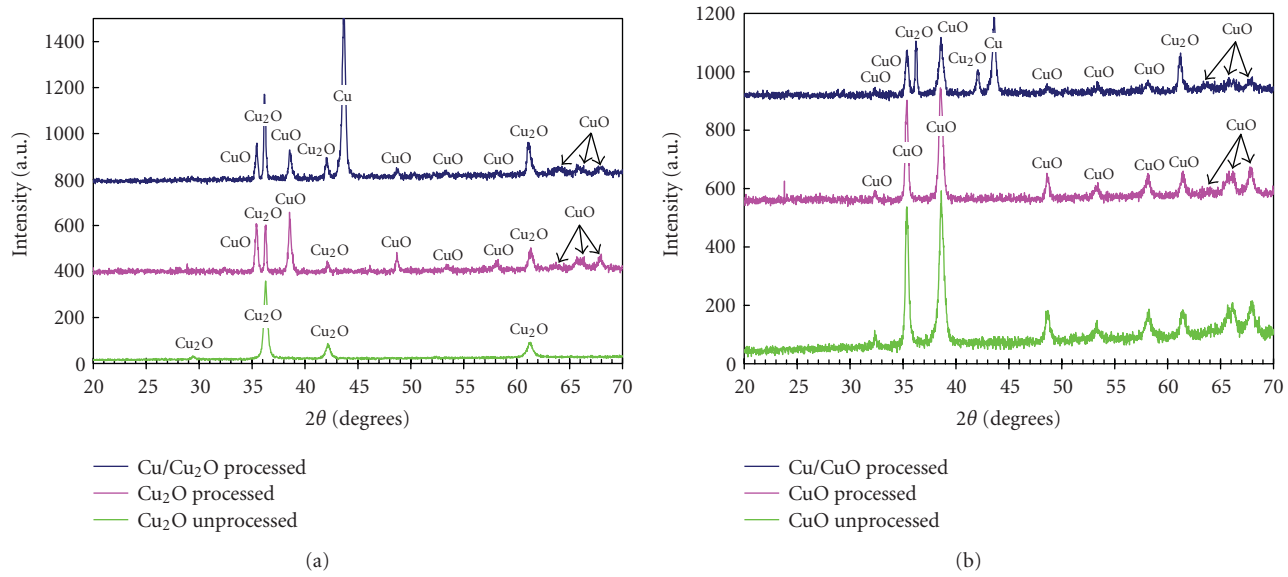


Figure 8: XRD spectra of the substrates involving $Cu_2O$ (a) and CuO (b).

in Figure 4(a), with an amplified figure shown in the inset. Three layers can be distinguished: a bottom layer that lies directly above the copper substrate, an intermediate layer that the NWs grow from, and a top NW layer. The XRD spectrum of an oxidized Cu substrate is shown in Figure 4(b), which indicates the presence of both $Cu_2O$ and CuO. However, no information on the individual layer composition can be extracted. The theoretical layering composition (labeled in Figure 4(a)) has been discussed in [8, 9] with CuO as the NWs and the intermediate layer and $Cu_2O$ as the bottom layer. The theoretical hypothesis on the NWs has been proved by our experiments.

To confirm the rest of the layering composition, EDX spectra were obtained from the top and the bottom surfaces of an oxide flake similar to that shown in Figure 4. In addition, EDX standards were produced from compacted CuO (3Ns) and $Cu_2O$ (2Ns) powders. The resulting spectra and region analysis are presented in Figure 5. The spectra were made up of ~100 000 counts, taken at identical parameters of 5 keV and 10 000 × magnification with a 60 degree sample tilt. Regions of 0.400–0.600 keV and 0.620–1.080 keV were created about the OK$\alpha$ and CuL$\alpha$ peaks, respectively, and the number and the percentage of gross counts in each region was determined. The relatively small fraction of oxygen counts detected is due to the low energy X-rays produced and the subsequent reabsorption upon exiting the sample material. The results indicate that the percent of gross counts for oxygen and copper taken from the bottom of the flake matched that of the standard $Cu_2O$. Likewise, the percent of gross counts for oxygen and copper taken from the top of the flake matched that of the standard CuO. Furthermore, a simple calibration has been carried out to correlate the gross count ratio of oxygen to copper with the molar ratio of O to Cu (or $x$ value of $CuO_x$, where $x$ equals 0, 0.5 and 1 for Cu, $Cu_2O$, and CuO, resp.) in standard reference samples. The resulting $x$ value is 0.99 for the top layer and 0.48 for the bottom layer in our sample. Our experimental results indicate distinct oxide layers and directly agree with the theoretical speculation [8, 9] of the bottom layer of $Cu_2O$ and the intermediate layer of CuO. The layering structures can be used to interpret the CuO NW growth mechanism as elaborated in [6]: $Cu_2O$ acts as a precursor for the second oxidation step to CuO where the slow production rate of CuO results in a localized CuO vapor pressure and a continuous growth mode for CuO NWs by means of the vapor-solid growth mechanism.

Compacted CuO and $Cu_2O$ layers with and without the Cu foil support were also used to grow CuO NWs in pure $O_2$ at 500°C for 150 minutes. The SEM images of the oxidized substrates are presented in Figure 6. High-density NW growth on the $Cu/Cu_2O$ substrate, medium NW growth on the Cu/CuO substrate, low NW growth on the $Cu_2O$ substrate, and no NW growth on the CuO substrate have been observed. The results indicate the importance of $Cu_2O$ to CuO conversion for the growth of CuO NWs as well as the presence of a Cu substrate for high-density NW growth. The importance of the Cu substrate is possibly in its role as a Cu ion source and in establishing a chemical potential gradient for the diffusion of Cu ions to the substrate surface. In Figure 6(a), the relatively thick compacted $Cu_2O$ layer with high-density NWs at its surface is seen at the top side of the Cu substrate and the familiar layering scheme is observed at the bottom of the substrate. Also note that the oxide layers of Figures 6(a)–6(c) are uniformly structured with less or without pores, whereas the presumably unchanged CuO sample in Figure 6(d) has a porous structure consistent with compacted powders.

To determine if the oxidation took place, the $Cu_2O$ and CuO thin layers were processed separately in a TGA. From the TGA results shown in Figure 7, it is clear that the $Cu_2O$ thin layer oxidized whereas the CuO thin layer did not. The small decrease in the weight for the CuO thin layer is

a consequence of the thermal expansion of the TGA and can be ignored. XRD spectra were also obtained from each sample and compared to those of unprocessed $Cu_2O$ and CuO in Figure 8. For those samples which oxidized to form CuO NWs ($Cu_2O$, Cu/$Cu_2O$, Cu/CuO), the XRD spectra indicate the presence of both CuO and $Cu_2O$, suggesting the importance of the oxide layering on NW growth.

## 4. CONCLUSION

CuO NWs have been successfully grown from both copper and copper-containing substrates through direct oxidation of the substrates in oxidative environments. The as-grown NWs have a band gap of ~1.2 eV (1030 nm) corresponding to bulk CuO. Oxygen partial pressure was found to significantly affect NW growth. The vertical alignment of the NW increases with increasing $O_2$ partial pressures, while the average length and diameter of the NWs seem to decrease with decreasing $O_2$ partial pressures. Analyses on the oxidized substrates indicate CuO as the NWs and the intermediate layer and $Cu_2O$ as the bottom layer. The oxidation of compacted CuO and $Cu_2O$ layers with and without a Cu substrate suggests the importance of $Cu_2O$ to CuO conversion for the growth of CuO NWs, as well as the importance of a Cu substrate for high-density NW growth.

## ACKNOWLEDGMENTS

This work was supported by National Science Foundation (DMI-0609059), WiSys Technology Foundation, as well as the University of Wisconsin-Milwaukee (UWM) Advanced Analysis Facility (AAF) Summer Internship Program. The authors thank Steven Hardcastle for assistance with SEM, EDX, and XRD analyses, which were carried out at the AAF of UWM. TEM analyses were performed at the UWM HRTEM Laboratory. The authors also thank the anonymous reviewers for their valuable comments and suggestions.

## REFERENCES

[1] Y. Li, F. Qian, J. Xiang, and C. M. Lieber, "Nanowire electronic and optoelectronic devices," *Materials Today*, vol. 9, no. 10, pp. 18–27, 2006.

[2] F. Patolsky, G. F. Zheng, and C. M. Lieber, "Nanowire-based biosensors," *Analytical Chemistry*, vol. 78, no. 13, pp. 4260–4269, 2006.

[3] C. Wang, X. Q. Fu, X. Y. Xue, Y. G. Wang, and T. H. Wang, "Surface accumulation conduction controlled sensing characteristic of p-type CuO nanorods induced by oxygen adsorption," *Nanotechnology*, vol. 18, no. 14, Article ID 145506, 5 pages, 2007.

[4] R. S. Wagner and W. C. Ellis, "Vapor-liquid-solid mechanism of single crystal growth," *Applied Physics Letters*, vol. 4, no. 5, pp. 89–90, 1964.

[5] G.-C. Yi, C. Wang, and W. I. Park, "ZnO nanorods: synthesis, characterization and applications," *Semiconductor Science and Technology*, vol. 20, no. 4, pp. S22–S34, 2005.

[6] X. Jiang, T. Herricks, and Y. N. Xia, "CuO nanowires can be synthesized by heating copper substrates in air," *Nano Letters*, vol. 2, no. 12, pp. 1333–1338, 2002.

[7] S. Anandan, X. Wen, and S. Yang, "Room temperature growth of CuO nanorod arrays on copper and their application as a cathode in dye-sensitized solar cells," *Materials Chemistry and Physics*, vol. 93, no. 1, pp. 35–40, 2005.

[8] H. Wu, D. Lin, and W. Pan, "Fabrication, assembly, and electrical characterization of CuO nanofibers," *Applied Physics Letters*, vol. 89, no. 13, Article ID 133125, 2006.

[9] K. Hauffe, *Oxidation of Metals*, Plenum Press, New York, NY, USA, 1965.

[10] K.-H. Muller, *High-Tc Superconductors and Related Materials*, vol. 86, Kluwer Academic, Dordrecht, The Netherlands, 2001.

[11] O. A. Chaltykyan, *Copper-Catalytic Reactions*, Consultants Bureau, New York, NY, USA, 1966.

[12] P. A. Cox, *Transition Metal Oxides: An Introduction to Their Electronic Structure and Properties*, Oxford University Press, New York, NY, USA, 1992.

[13] S.-C. Yeon, W.-Y. Sung, W.-J. Kim, S.-M. Lee, H.-Y. Lee, and Y.-H. Kim, "Field emission characteristics of CuO nanowires grown on brown-oxide-coated Cu films on Si substrates by conductive heating in air," *Journal of Vacuum Science & Technology B*, vol. 24, no. 2, pp. 940–944, 2006.

[14] Y. W. Zhu, T. Yu, F. C. Cheong, et al., "Large-scale synthesis and field emission properties of vertically oriented CuO nanowire films," *Nanotechnology*, vol. 16, no. 1, pp. 88–92, 2005.

[15] C. H. Xu, C. H. Woo, and S. Q. Shi, "The effects of oxidative environments on the synthesis of CuO nanowires on Cu substrates," *Superlattices and Microstructures*, vol. 36, no. 1–3, pp. 31–38, 2004.

[16] R. Haugsrud, "The influence of water vapor on the oxidation of copper at intermediate temperatures," *Journal of the Electrochemical Society*, vol. 149, no. 1, pp. B14–B21, 2002.

[17] C.-T. Hsieh, J.-M. Chen, H.-H. Lin, and H.-C. Shih, "Synthesis of well-ordered CuO nanofibers by a self-catalytic growth mechanism," *Applied Physics Letters*, vol. 82, no. 19, pp. 3316–3318, 2003.

[18] M. Mattila, T. Hakkarainen, H. Jiang, E. I. Kauppinen, and H. Lipsanen, "Effect of substrate orientation on the catalyst-free growth of InP nanowires," *Nanotechnology*, vol. 18, no. 15, Article ID 155301, 5 pages, 2007.

[19] T. G. Woodcock, J. S. Abell, J. Eickemeyer, and B. Holzapfel, "Crystal orientation mapping of NiO grown on cube textured Ni tapes," *Journal of Microscopy*, vol. 216, no. 2, pp. 123–130, 2004.

Hindawi Publishing Corporation
Journal of Nanomaterials
Volume 2008, Article ID 610541, 5 pages
doi:10.1155/2008/610541

*Research Article*

# Growth of ZnO Nanowires in Aqueous Solution by a Dissolution-Growth Mechanism

**Shaojing Bu, Chunxiang Cui, Qingzhou Wang, and Ling Bai**

*School of Materials Science and Engineering, Hebei University of Technology, Dingzigu, Road No.1, Hongqiao District, Tianjin 300130, China*

Correspondence should be addressed to Chunxiang Cui, hutcui@hebut.edu.cn

Received 22 May 2007; Revised 5 December 2007; Accepted 18 December 2007

Recommended by Junlan Wang

A novel methodology based on the dissolution-growth mechanism was developed to prepare ZnO nanowire films. The film morphology and structure were investigated by using field emission scanning electron microscopy, high-resolution transmission electron microscopy, and X-ray diffraction analysis methods. The results show that the ZnO nanowires are single crystalline *c*-oriented wurtzite. The ZnO rod crystals were eroded to provide the growth primitive of ZnO nanowires, which formed on top of the rod crystals when the erosion reaction got the equilibrium. The length of the resultant nanowires is rather large because the successive erosion of the rod crystals maintains the low concentration of $Zn_2O(OH)_{2n-2}$ in the aqueous solution.



## 1. INTRODUCTION

One-dimensional zinc oxide represents an important basic material due to its low-cost, large-band [1], and luminescent properties and has wide applications in photocatalyst [2], gas sensor [3], varistor [4], transparent conductive coating [5], and solar cells [6]. The fabrication of one-dimensional zinc oxide has been widely studied by different methods. For example, vapor-liquid-solid epitaxial (VLSE) mechanism [7], thermal evaporation [8], hydrothermal methods [9], template-based growth [10], chemical vapor deposition [11], and pulsed laser deposition [12] have been successful in creating 2D-oriented arrays of ZnO rods. Among these methods, solution process has been demonstrated to be a facile method for synthesizing ZnO due to its own advantages such as simplicity, reproducibility, non-hazardousness, cost effectiveness, being suitable for producing large-area thin films. Various morphologies have been achieved by aqueous solution method, for example, rod-like [13], tube-like, flower-like crystals [14], and so on.

But up to now, growth of nanowire with large length has not been achieved by aqueous solution method. The diameter of ZnO nanocrystals is dependent on the concentration of the solution [13, 15]; nanorods can be obtained when the concentration is relatively low, but nanowires cannot because the concentration of the solution will decrease greatly with the crystal growth. So it is essential to maintain the concentration of the solution during the whole growth process to get nanowires with larger length. In this paper, a novel method was developed to obtain large-scale ZnO nanowires based on the basic dissolution-growth mechanism. The successive erosion of rod crystals was used to maintain the zinc concentration in the solution.

## 2. EXPERIMENTAL

ZnO rod films were fabricated in aqueous solution using the method in [13, 16]. To prepare ZnO nanowires, 1 M $NH_3 \cdot H_2O$ aqueous solution was added in a 25 mL beaker, and stirred for several minutes. Then ZnO rod films ($2 \times 1$ cm) were inserted in the solution and the beaker was sealed. After the beakers were kept in an oven at 80°C for 2−6 hours, the films were removed from the solution and dried under vacuum at 80°C. The pH value of the initial solution was 11.5, and it decreased slightly to 11.2 after the erosion for 6 hours.

The ZnO nanowires were characterized by using field emission scanning electron microscopy (FESEM, JEOL 6700, 200 kV), high-resolution transmission electron microscopy (HRTEM, PHILIPS TECNAI G2 F20, 300 kV). X-ray diffraction was recorded by Rigaku D/max-2500 X-ray diffractometer (30 kV, 20 mA) with copper targets ($\lambda = 0.154059$ nm).

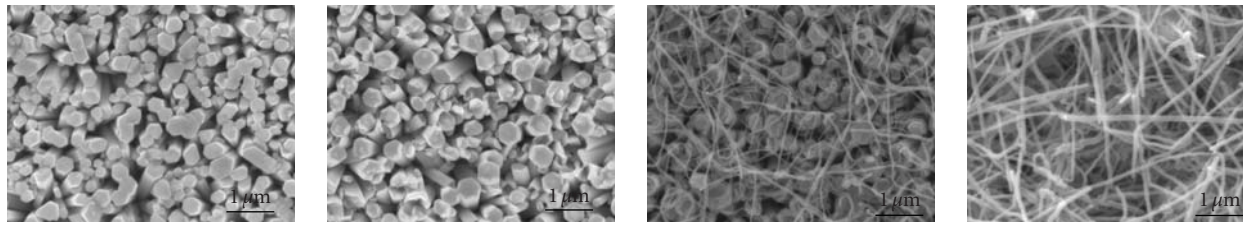


(a) (b) (c) (d)

Figure 1: FESEM photographs of ZnO films eroded for different periods: (a) 0 hour, (b) 2 hours, (c) 4 hours, and (d) 6 hours.

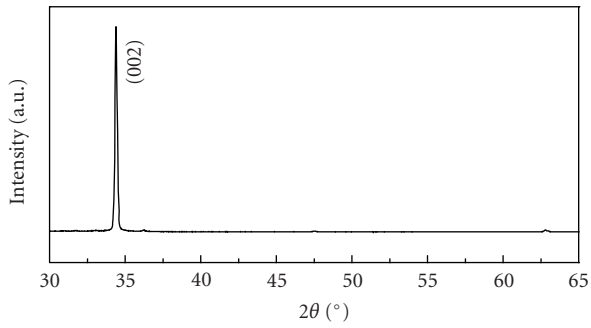


Figure 2: XRD pattern of ZnO film obtained after erosion for 6 hours in the ammonia solution.

## 3. RESULTS AND DISCUSSION

Morphology of ZnO films obtained in ammonia solutions with different reaction times is shown in Figure 1. Figure 1(a) illustrates the FESEM image of the as-grown ZnO rod films, from which it can be seen that the substrate was covered with hexagonal rod crystals with the diameter of 0.2−0.6 $\mu$m. The morphology evolution during the erosion process is shown in Figures 1(b), 1(c), and 1(d). As depicted in Figure 1(b), after 2 hours of reaction, hexagonal pits with the wall thickness of ~30 nm formed on top of the rod crystals. This process is similar to the rod crystals growth, which we have found previously [15], namely, both erosion and growth begin from the center at (0001) plane of the rod crystals. As the period of the process was prolonged to 4 hours, nanowires appeared on surface of the films, of which the diameter was about 25 ~ 40 nm (as seen in Figure 1(c)). The nanowires became longer and thicker when the reaction time was increased to 6 hours (Figure 1(d)).

Figure 2 shows the XRD pattern of the ZnO film illustrated in Figure 1(d). The high (002) peak is indexed as the wurtzite structure of ZnO, indicating that the nanowires are highly *c*-oriented. An energy dispersive spectroscopic (EDS) analysis of the film (Figure 3) shows that the products are mainly composed of Zn and O elements, consistent with the result of XRD.

Figure 4 shows the HRTEM image of a part of a typical ZnO nanowire. The diameter and length of the nanowire are 30 nm and more than 5 $\mu$m, respectively. So the aspect ratio of the nanowire is more than 160, which is the typical characteristic of nanowire.

Figure 5 shows HRTEM and TEM (inset) images of a ZnO nanowire, demonstrating the single-crystalline structure of the nanowire. The lattice spacing of 0.28 nm shown in the HRTEM image of Figure 5 corresponds to a *d*-spacing of $(\bar{1}0\ 0)$ crystal planes, confirming that the nanowire is *c*-oriented.

The growth of ZnO nanowire can be described based on the chemical equilibrium of dissolution-regrowth in the solution. Yamabi and Imai [17] and Peterson and Gregg [18] found that $ZnO_{(s)}$ only formed at small region in the phase diagram, thus suitable pH value and Zn species concentration is necessarily required. In aqueous solutions at pH > 9, Zn (II) soluble species in the form of hydroxyl complexes such as $Zn(OH)_2$ (aq) and $Zn(OH)_4^{2-}$ increase [16], the thermodynamic equilibrium for $ZnO_{(s)}$-$H_2O$ system can be represented by

$$ZnO_{(s)} + (n-1)H_2O \longleftrightarrow Zn(OH)_n^{2-n}{}_{(aq)} + (n-2)H^+. \quad (1)$$

As is well known, supersaturation is required for crystal growth in solution. In our system, the erosion should stop when the process achieves the equilibrium according to (1). However, the growth of nanowire indicates that the solution is supersaturated, which suggests that the erosion and growth proceed simultaneously when the reaction get the equilibrium.

When $ZnO_{(s)}$ is introduced into the basic solution, the equilibrium in (1) moves to the right because of the low $Zn(OH)_n^{2-n}{}_{(aq)}$ concentration and $H^+$ consumption. Thus the $ZnO_{(s)}$ will be eroded. As the erosion time increases, the concentration of $Zn(OH)_n^{2-n}{}_{(aq)}$ increases and approaches to the critical supersaturation. Peterson and Gregg [18] and Yamabi and Imai [19] have found that $Zn(OH)_n^{2-n}{}_{(aq)}$ can form polyhydroxyl zinc complex, which was represented by

$$[Zn(OH)_n]^{2-n} + [Zn(OH)_n]^{2-n} \longrightarrow [Zn_2O(OH)_{2n-2}]^{4-2n} + H_2O, \quad (2)$$

where $n = 2$ or 4, $Zn_2O(OH)_{2n-2}$ supplies the source of the heterogeneous nucleation and growth of ZnO nanowires. The concentration of $Zn(OH)_n^{2-n}{}_{(aq)}$ and $Zn_2O(OH)_{2n-2}$ increases with the erosion of the rod crystals and then the reaction achieves the equilibrium. The erosion process continues,

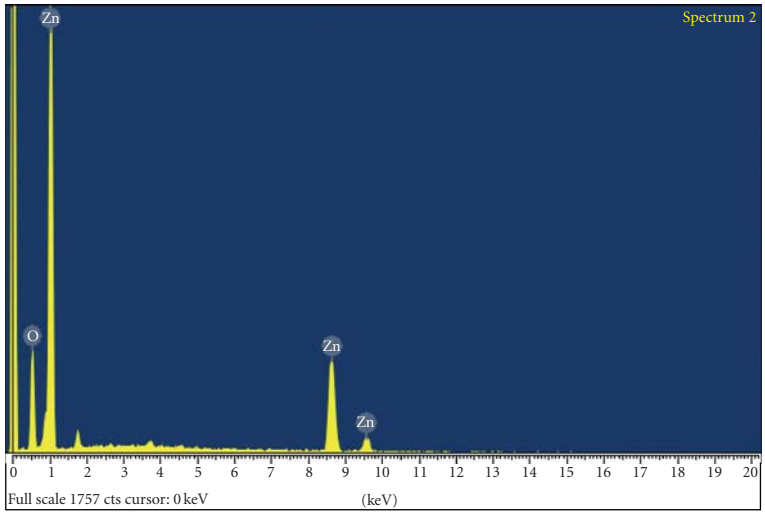


Figure 3: EDS picture of the ZnO film obtained after erosion for 6 hours.

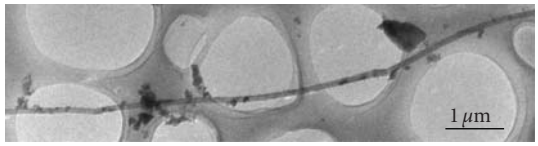


Figure 4: HRTEM photograph of a typical ZnO nanowire.

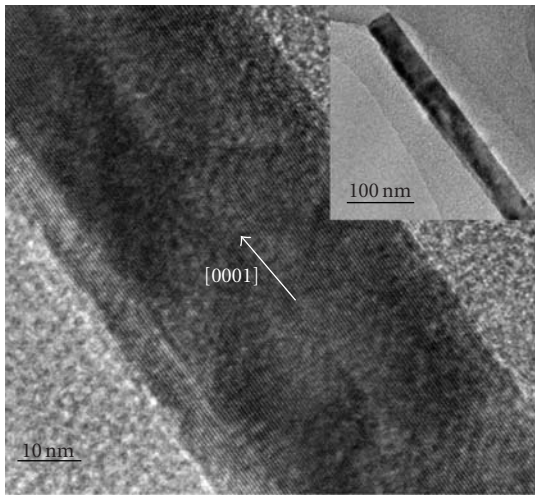


Figure 5: TEM (inset) and HRTEM photograph of a ZnO nanowire.

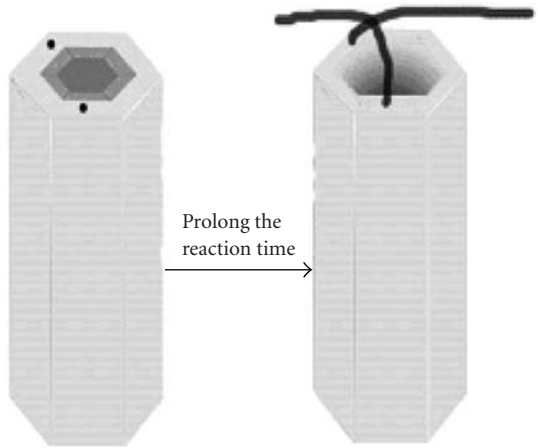


Figure 6: Nucleation and growth of the ZnO nanowire by dissolution-growth mechanism.

then new ZnO nuclei form on top of the ZnO rod because the solution is supersaturated. In previous work, we have found that the diameter of ZnO rods, which were fabricated by aqueous solution method decreased with the reduction of the zinc precursor concentration, due to the shift of chemical equilibrium in the solution [15]. As a result of the low zinc concentration in the solution, the diameter of the crystals obtained in this work is in nanoscale [13]. The nanocrystals transform to nanowires with the increase of growth time for the successive erosion of ZnO rod, which maintains the rather low concentration of $Zn_2O(OH)_{2n-2}$. Figure 6 gives the sketch of the growth mechanism.

In addition, the growth manner of the nanowires can be analyzed by the aid of TEM and HRTEM characterization. Three typical fractions of the ZnO nanowire were observed in the film eroded for 6 hours (Figure 7(a)). For the first fraction (as shown in Figure 7(b)), nanowire was composed of nanoparticles with the diameter of 5~8 nm, between which there are many mesopores. No crystalline fringe can be detected in these nanoparticles, suggesting the amorphous nature of the nanowire. As for the second fraction (Figure 7(c)), it can be seen that almost all of the nanoparticles are crystalline grains, and many of them begin to attach with each other along *c*-axis. The densification of the nanowire can be

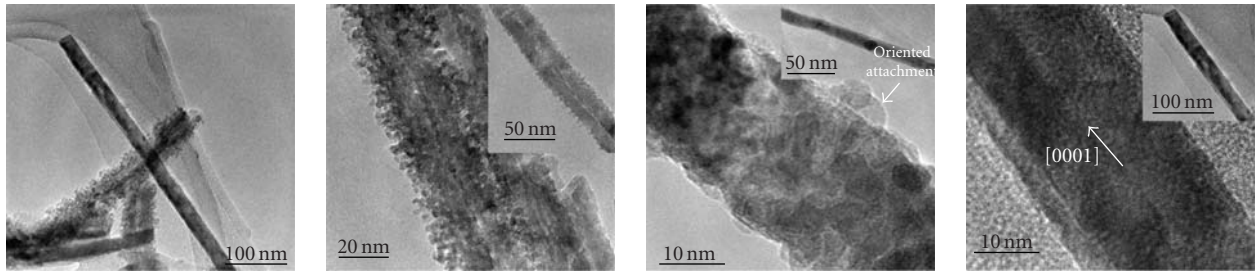


Figure 7: (a) A typical TEM image of ZnO nanowire fractions, three kinds of fractions with different crystallinity were shown. (b) A typical HRTEM image of a ZnO nanowire fraction in the early growth stage and its TEM image (inset). (c) A typical HRTEM image of a ZnO nanowire fraction in the medium growth stage and its TEM image (inset), the arrowhead indicates the oriented attachment. (d) The HRTEM image of a typical crystallized ZnO nanowire fraction and its TEM image (inset).

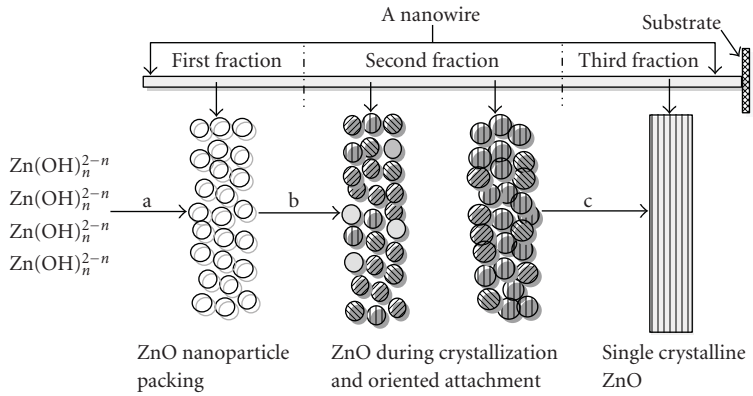


Figure 8: Schematic disorder-order growth process of ZnO nanowire: (a) nanoparticle packing, (b) crystallization and oriented attachment of small grain domains, and (c) formation of single crystalline ZnO nanowire.

inferred according to disappearance of the pores. But the interfaces among the nanoparticle packing are still visible. A similar oriented attachment has also been found by Searson et al. [20] when preparing $TiO_2$ nanoparticles under hydrothermal condition. The driving force for the disorder-order assembly process is the reduction of surface energy, and this mechanism has been reported previously [21, 22]. The third kind of nanowire fraction is very smooth and compact (Figure 7(d) (inset)). Its HRTEM image shows that a large quantity of small grain domains has transformed into a single crystalline nanowire. According to these observed results, the proposed growth mechanism of ZnO nanowire can be illustrated in Figure 8. Based on the growth period, there are three different fractions in one nanowire, corresponding to three growing stages of the nanowire. Step (a) is nanoparticle packing process. Step (b) is the process of crystallization and oriented attachment. In Step (c), the single crystalline nanowire forms.

## 4. CONCLUSIONS

ZnO nanowires were synthesized in aqueous solution by a dissolution-growth mechanism. The nanowires are single crystalline *c*-oriented wurtzite. The ZnO rod crystals were eroded to provide the growth primitive of ZnO nanowire. The nanowire formed on top of the rod crystals when the erosion reaction achieved the equilibrium. The growth manner of nanowires has been discussed based on the TEM and HRTEM results. The length of the nanowire is rather large because the successive erosion of the rod crystals maintains the low concentration of $Zn_2O(OH)_{2n-2}$.

As we all know, ZnO nanowires have great application potential in the photoelectric field, such as luminescence, window and electrode material for solar cells, phosphors, piezoelectric transducers and actuators, surface acoustic coatings, varistors, and sensors. This strategy can provide a novel and simple route to obtain ZnO nanowires, even ultralong ZnO nanowires which may improve the properties of nanowire-based devices.

## ACKNOWLEDGMENTS

The authors gratefully acknowledge the financial support of a grant for Ph.D. research startup, from Hebei University of Technology. This paper was aided financially by Natural Science Foundation of Hebei Province (Project

no. E2006000025), Natural Science Innovation Project of China (Project no. 02CJ-020218), Key Project and International Cooperation Research Project of Natural Science Foundation of Tianjin (Projects no. 05YFJZJC02200 and no. 05YFGHHZ01200).

## REFERENCES

[1] V. Srikant and D. R. Clarke, "On the optical band gap of zinc oxide," *Journal of Applied Physics*, vol. 83, no. 10, pp. 5447–5451, 1998.

[2] K. Yubuta, T. Sato, A. Nomura, K. Haga, and T. Shishido, "Structural characterization of ZnO nano-chains studied by electron microscopy," *Journal of Alloys and Compounds*, vol. 436, no. 1-2, pp. 396–399, 2007.

[3] K.-S. Weißenrieder and J. Müller, "Conductivity model for sputtered ZnO-thin film gas sensors," *Thin Solid Films*, vol. 300, no. 1-2, pp. 30–41, 1997.

[4] V. Tohver, S. L. Morissette, J. A. Lewis, B. A. Tuttle, and J. A. Voigt, "Direct-write fabrication of zinc oxide varistors," *Journal of the American Ceramic Society*, vol. 85, no. 1, pp. 123–128, 2002.

[5] J.-H. Lee, K.-H. Ko, and B.-O. Park, "Electrical and optical properties of ZnO transparent conducting films by the sol-gel method," *Journal of Crystal Growth*, vol. 247, no. 1-2, pp. 119–125, 2003.

[6] M. Law, L. E. Greene, J. C. Johnson, R. Saykally, and P. Yang, "Nanowire dye-sensitized solar cells," *Nature Materials*, vol. 4, no. 6, pp. 455–459, 2005.

[7] J. B. Baxter and E. S. Aydil, "Nanowire-based dye-sensitized solar cells," *Applied Physics Letters*, vol. 86, no. 5, Article ID 053114, 3 pages, 2005.

[8] M. H. Huang, S. Mao, H. Feick, et al., "Room-temperature ultraviolet nanowire nanolasers," *Science*, vol. 292, no. 5523, pp. 1897–1899, 2001.

[9] L. Wu and Y. Wu, "Synthesis and optical characteristic of ZnO nanorod," *Journal of Materials Science*, vol. 42, no. 1, pp. 406–408, 2007.

[10] Z. R. Tian, J. A. Voigt, J. Liu, et al., "Complex and oriented ZnO nanostructures," *Nature Materials*, vol. 2, no. 12, pp. 821–826, 2003.

[11] Y. Li, G. W. Meng, L. D. Zhang, and F. Phillipp, "Ordered semiconductor ZnO nanowire arrays and their photoluminescence properties," *Applied Physics Letters*, vol. 76, no. 15, pp. 2011–2013, 2000.

[12] Y. Sun, G. M. Fuge, and M. N. R. Ashfold, "Growth of aligned ZnO nanorod arrays by catalyst-free pulsed laser deposition methods," *Chemical Physics Letters*, vol. 396, no. 1–3, pp. 21–26, 2004.

[13] L. Vayssieres, "Growth of arrayed nanorods and nanowires of ZnO from aqueous solutions," *Advanced Materials*, vol. 15, no. 5, pp. 464–466, 2003.

[14] Z. Wang, X.-F. Qian, J. Yin, and Z.-K. Zhu, "Large-scale fabrication of tower-like, flower-like, and tube-like ZnO arrays by a simple chemical solution route," *Langmuir*, vol. 20, no. 8, pp. 3441–3448, 2004.

[15] X. Liu, Z. Jin, S. Bu, J. Zhao, and Z. Liu, "Growth of ZnO films with controlled morphology by aqueous solution method," *Journal of the American Ceramic Society*, vol. 89, no. 4, pp. 1226–1231, 2006.

[16] W. Stumm and J. J. Morgan, *Aquatic Chemistry*, Wiley-Interscience, New York, NY, USA, 1995.

[17] S. Yamabi and H. Imai, "Growth conditions for wurtzite zinc oxide films in aqueous solutions," *Journal of Materials Chemistry*, vol. 12, no. 12, pp. 3773–3778, 2002.

[18] R. B. Peterson, C. L. Fields, and B. A. Gregg, "Epitaxial chemical deposition of ZnO nanocolumns from NaOH solutions," *Langmuir*, vol. 20, no. 12, pp. 5114–5118, 2004.

[19] S. Yamabi, J. Yahiro, S. Iwai, and H. Imai, "Formation of cellular films consisting of wurtzite-type zinc oxide nanosheets by mediation of phosphate anions," *Thin Solid Films*, vol. 489, no. 1-2, pp. 23–30, 2005.

[20] G. Oskam, A. Nellore, R. L. Penn, and P. C. Searson, "The growth kinetics of $TiO_2$ nanoparticles from titanium(IV) alkoxide at high water/titanium ratio," *Journal of Physical Chemistry B*, vol. 107, no. 8, pp. 1734–1738, 2003.

[21] R. L. Penn, G. Oskam, T. J. Strathmann, P. C. Searson, A. T. Stone, and D. R. Veblen, "Epitaxial assembly in aged colloids," *Journal of Physical Chemistry B*, vol. 105, no. 11, pp. 2177–2182, 2001.

[22] R. L. Penn and J. F. Banfield, "Imperfect oriented attachment: dislocation generation in defect-free nanocrystals," *Science*, vol. 281, no. 5379, pp. 969–971, 1998.

Hindawi Publishing Corporation
Journal of Nanomaterials
Volume 2008, Article ID 267161, 9 pages
doi:10.1155/2008/267161

*Research Article*

# Pressure and Temperature Effects on Stoichiometry and Microstructure of Nitrogen-Rich TiN Thin Films Synthesized via Reactive Magnetron DC-Sputtering

**E. Penilla and J. Wang**

*Department of Mechanical Engineering, Bourns College of Engineering, University of California, Riverside, CA 92521, USA*

Correspondence should be addressed to J. Wang, wang@engr.ucr.edu

Received 01 September 2007; Accepted 11 January 2008

Recommended by Jun Lou

Nitrogen-rich titanium nitride (TiN) thin films containing excess nitrogen up to 87.0 at.% were produced on (100) Si substrates via the reactive magnetron DC-sputtering of a commercially available 99.995 at.% pure Ti target within an argon-nitrogen ($Ar$-$N_2$) atmosphere with a 20-to-1 gas ratio. The process pressure ($P_P$) and substrate temperature ($T_S$) at which deposition occurred were varied systematically between 0.26 Pa–1.60 Pa and between 15.0°C–600°C, respectively, and their effects on the chemical composition, surface morphology, and preferred orientation were characterized by energy dispersive X-ray spectroscopy (EDS), field emission scanning electron microscopy (FE-SEM), and X-ray diffraction (XRD). The EDS analysis confirms increasing nitrogen content with increasing $P_P$ and $T_S$. The SEM images reveal a uniform and crystallized surface morphology as well as a closely packed cross-sectional morphology for all crystalline films and a loosely packed cross-sectional morphology for amorphous films. Films produced at lower $P_P$ and $T_S$ have a pyramidal surface morphology which transitions to a columnar and stratified structure as $P_P$ and $T_S$ increase. The XRD analysis confirms the existence of only the $\delta$-TiN phase and the absence of other nitrides, oxides, and/or sillicides in all cases. It also indicates that at lower $P_P$ and $T_S$, the preferred orientation relative to the substrate is along the (111) planes, and that it transitions to a random orientation along the (200), (220), and (311) planes as $P_P$ and $T_S$ increase and these results correlate with and qualify those observed by SEM.



## 1. INTRODUCTION

Various transition metal nitrides such as TiN thin films have attracted considerable attention from researchers spanning the spectrum of the physical sciences. This is a testament to the myriad of potential applications that the TiN system affords because of its unique properties. They have been used as wear-resistant coatings on high-speed cutting tools [1–3], as infrared filtering coatings on windows [4], and as inexpensive decorative coatings on pens, watch dials, and so on [5] because of their golden luster. TiN thin films have also been used as microelectronic contacts [6], resistors [7], and, because of their high-chemical stability, as diffusion barriers [8, 9] between interconnects of microchips. A most recent application makes use of their biocompatibility and hemocompatability [10, 11], as they have been integrated as surface layers within orthopedic prostheses and cardiac valves [12, 13].

TiN thin films have been produced by various techniques, all derivatives of those used in semiconductor processing, such as electroplating [14], laser ablation [15, 16], chemical vapor deposition (CVD) [17], as well as the physical vapor deposition (PVD) techniques of evaporation and sputtering, reactive or otherwise [18–22]. Much of the problem associated with their production has been the need for high voltages and temperatures, which limit their integration within CMOS process flows. As of late, however, the commercial availability of TiN sputtering targets has facilitated their use within certain scenarios, where sputtering thin films is an option.

Although many practical applications, synthesis techniques, and deposition methods have been developed for TiN thin films, the literature seems to indicate that the basic metallurgy and physics of the TiN system are not completely understood [1, 23, 24]. The literature indicates that the first attempts to derive the TiN phase diagram were conducted

by Wriedt and Murray as recently as 1987, but the complete phase diagram covering the full compositional spectrum was not reported herein, namely, the data pertaining to overstoichiometric TiN was not reported [24]. Additional studies by Ristolainen et al. report the stability of TiN films with excess nitrogen contents up to 62 at.% via triode ion plating techniques [23]. Nonetheless, the limit of nitrogen solubility in TiN still appears uncertain as do the properties of such nitrogen-rich films as well as the effects of processing parameters on the basic metallurgy and physics.

All of the TiN films synthesized for this work, whose phase existence is confirmed by EDS and XRD analyses, have an excess nitrogen content of at least 70.4 at.% and up to 87 at.% and it is believed that this is the first report of such produced films. This belief in tandem with the wide range of potential applicability within industry and academia prompted the authors' interest in characterizing some of the films' fundamental physics. Scanning electron microscopy was used to elucidate the surface and cross-sectional characteristics, and SEM in concert with EDS and XRD was instrumental in determining the chemistry and crystallography.

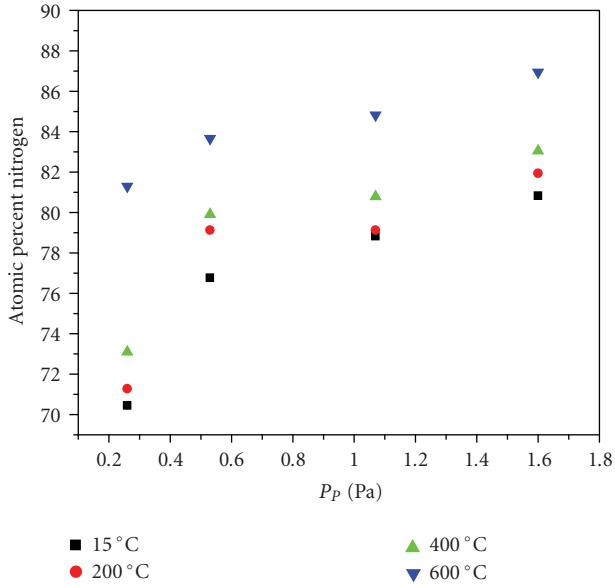


FIGURE 1: Effect of $P_P$ and $T_S$ variations on nitrogen solubility.

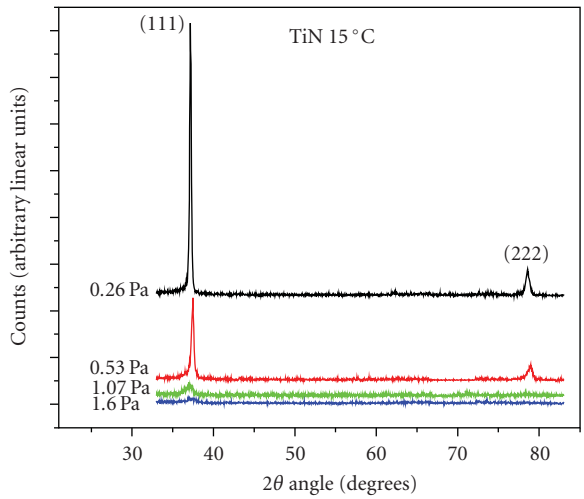


FIGURE 2: XRD spectra of increasing $P_P$ for $T_S$ = 15°C.

## 2. EXPERIMENTAL PROCEDURE

### 2.1. Preparation of TiN films

TiN films with high nitrogen content were deposited onto polished (100) Si substrates with a native oxide layer and overall thicknesses of 480 $\mu$m by sputtering a commercially developed 99.995 at.% Ti target (50.8 mm diameter × 6.35 mm thick) within an Ar-$N_2$ atmosphere. The target was mechanically clamped to a water-cooled direct-current magnetron cathode of an ultrahigh vacuum sputtering system (Orion 5 UHV sputtering system, AJA International, Inc., North Scituate, Mass, USA). The target must remain at a constant temperature throughout because the sputter yield and, as a consequence, the deposition rate are functions of target temperature [25]. Target poisoning also becomes an issue with the elevation of target temperature [25]. A DC-potential of 466 V was coupled to the cathode and this resulted in a driving current of 536 mA and a power dissipation of 250 W. All depositions occurred at a target to substrate distance of 178 mm and lasted 6300 seconds.

The purity of the gases was 99.9995% and the Ar-$N_2$ ratio was 20 to 1 in all cases. Gas flow was controlled by 2 independently calibrated mass flow controllers (MFC) capable of delivering up to 20 SCCM of gas. The MFCs are integrated within a computer-controlled feedback loop to ensure constant flow and gas mixture throughout the entire deposition process. At full gas flow, $P_P$ was controlled by adjusting a three-position throttle valve, which is placed in series between the preparation chamber and a 500 L turbomechanical pump, allowing for the adjustment of conductance between the two. Films were synthesized with $P_P$ set points of 0.26 Pa, 0.53 Pa, 1.07 Pa, and 1.60 Pa.

Before sputtering, the substrates were subjected to a series of ultrasonicated chemical baths including acetone, isopropanol (IPA) and deionized (DI) water. They were then blown dry and inserted into a prevacuum load-lock chamber until reaching a pressure of $10^{-4}$ Pa. This is followed by insertion into the main preparation chamber where the substrates were pumped on until the preparation chamber reached a base pressure of $10^{-6}$–$10^{-7}$ Pa. Further cleaning was achieved by subjecting the substrates to an RF-etching bias (13.52 MHz) of 50 W for 10 minutes in a pure Ar plasma. The process pressure during etching was 0.53 Pa. This also removes the native oxide layer, ensuring a maximum absence of oxygen within the preparation chamber whose presence could have become an issue, especially during those depositions at elevated $P_P$ and $T_S$.

Following chamber and substrate conditioning, the substrates were heated to the desired set points via a pair of 1 kW quartz heating elements that are coupled to a proportional with integral and derivative (PID) controller capable of

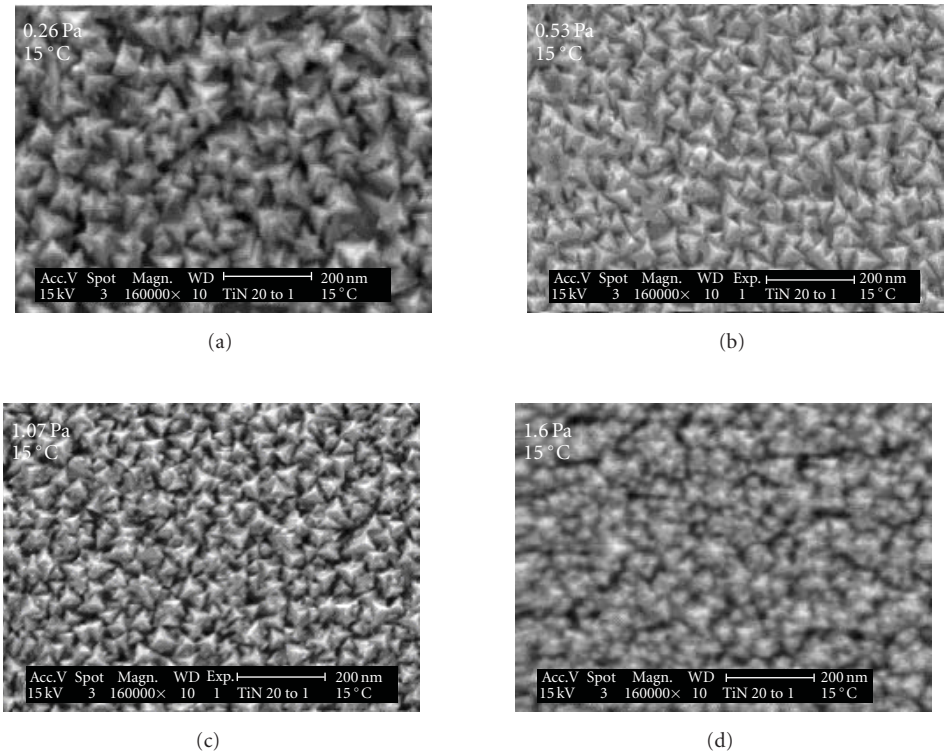


FIGURE 3: SEM images of increasing $P_P$ at $T_S = 15°C$ with a) 0.26 *Pa*, b) 0.53 *Pa*, c)1.07 *Pa* and d) 1.60 *Pa*.

maintaining set point ±1°C. $T_S$ is monitored throughout by a *k*-type thermocouple which is integrated within a feedback loop with the heating elements and the PID controller. Depositions were performed with $T_S$ held constant during the entire processes at set points of 15°C, 200°C, 400°C, and 600°C for each of the $P_P$ set points denoted above. Therefore, a total of 16 samples were synthesized by this technique for characterization.

### 2.2. Film characterization

All films were characterized ex situ and at room temperature. Film thicknesses, $t_f$, were experimentally confirmed by scanning probe profilometry (SPP) and SEM of their cross-sections to be ~500 nm with no significant variation from film to film. It is important to make this conclusion because it is well known that process pressure and substrate temperature have an effect on the sputter yield and the eventual film thickness [25] and that it has also been shown that the physical properties of TiN films are dependent on film thickness [26].

The surface and cross-sectional morphology were qualitatively ascertained by the implementation of FE-SEM. For cross-sectional characterization, the samples were cleaved in order to expose their underlying microstructure. The instrument used was a Phillips XL30. All samples were imaged with a 15 kV accelerating potential, 50 nm spot size, 30 $\mu$m aperture, at a working distance of 10 mm, and all images were gathered by the secondary electron (SE) detector.

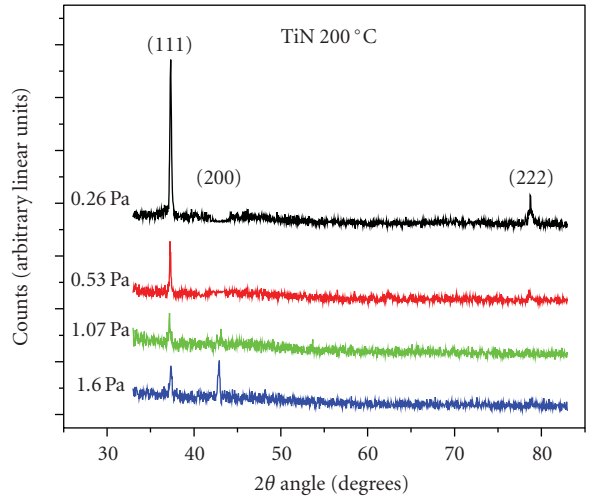


FIGURE 4: XRD spectra of increasing $P_P$ for $T_S = 200°C$.

EDS of all samples was conducted within the Phillips XL30 using the same parameters as above, which produced a projected interaction volume ~500 nm$^3$ allowing for full cross-sectional analysis of the synthesized TiN films. Counts were taken for 90 seconds and the spectra were analyzed with Phillips EDXi software, which allows for background signal removal, peak identification, and peak quantification.

Nondestructive XRD was performed on a Bruker AXS D8 advanced X-ray diffractometer which implements a Cu

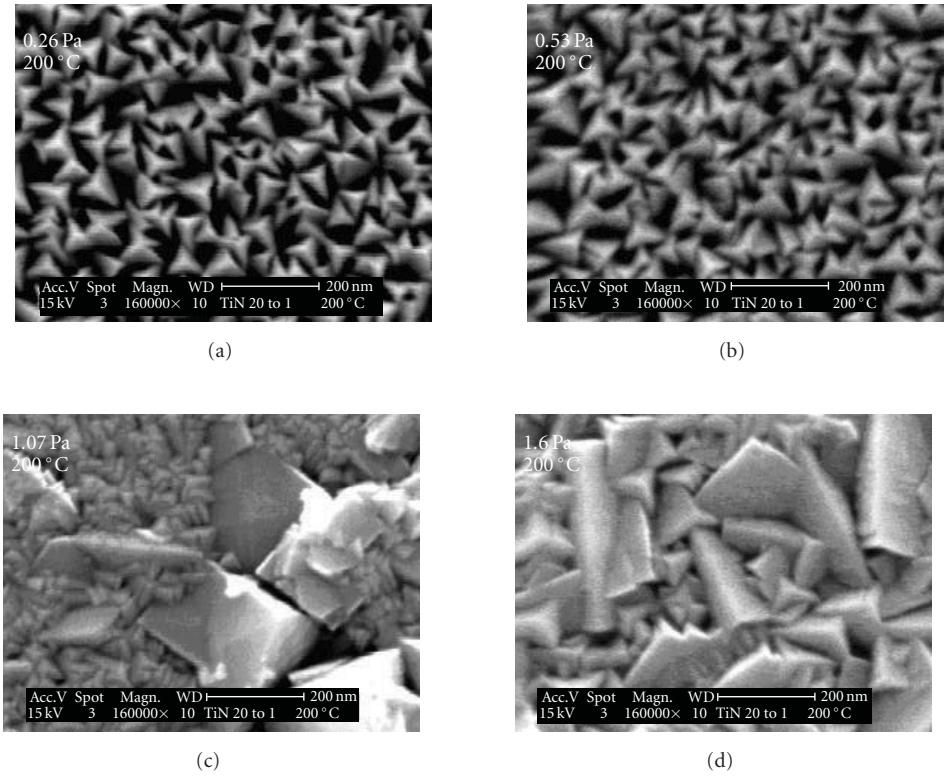


Figure 5: SEM images of increasing $P_P$ at $T_S = 200°C$ with a) 0.26 *Pa*, b) 0.53 *Pa*, c) 1.07 *Pa* and d) 1.60 *Pa*.

$K\alpha_1$ ($\lambda = 1.54058\,Å$) radiation operated at 40 kV and 40 mA. All scans were taken in continuous mode for a $2\theta$ range of 33°–83°, a step size of .02°, and time step of 2 seconds. All peaks derived beyond this range are secondary and therefore scans beyond this range are not strictly necessary for crystallographic and/or chemical identification.

## 3. RESULTS AND DISCUSSION

### 3.1. Chemical composition

EDS analysis was implemented to elucidate the stoichiometric composition of the reactively sputtered TiN films and it reveals an increasing nitrogen content within the films with increasing process pressure and substrate temperature as is shown in Figure 1. It is important to note that surface roughness has an effect on EDS results with decreased reliability as the root mean square surface roughness approaches the micron scale. As will be disclosed in Section 3.2, the feature size of the produced films is nanometric and, therefore, localized EDS analysis is minimally affected by the film surface roughness [27]. The film produced at $P_P = 0.26$ Pa and $T_S$ =15.0°C contained 70.4 at.% nitrogen and the film produced at $P_P = 1.60$ Pa and $T_S = 600°C$ had a nitrogen content of 87.0 at.%, and these were the minimum and maximum nitrogen contents of all of the produced films. This indicates that the combined effects of increasing $P_P$ and $T_S$ to the upper limit resulted in a 16.6 at.% increase in the nitrogen content of the TiN films.

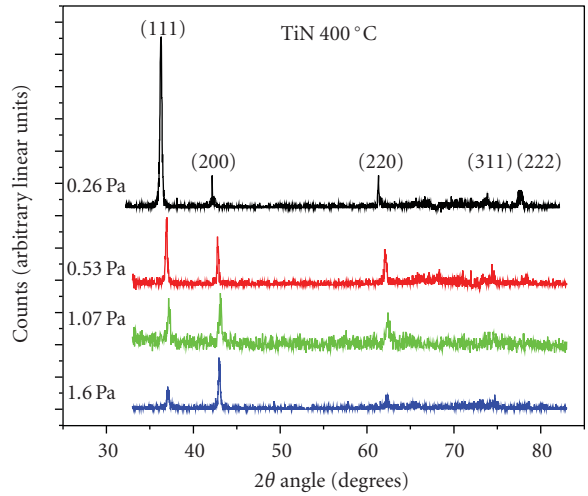


Figure 6: XRD spectra of increasing $P_P$ for $T_S = 400°C$.

The increase in $P_P$ from 0.26 Pa to 1.60 Pa at a constant $T_S$ resulted in a maximum increase in nitrogen content of 10.7 at.%. This value is obtained by taking the difference of the maximum and minimum nitrogen contents for the denoted process pressure range at each substrate temperature. The average increase in nitrogen content as a function of $P_P$ was 9.16 at.% over the entire temperature range.

Similarly, increasing $T_S$ from 15°C to 600°C with $P_P$ held constant at 0.26 Pa caused the nitrogen content to increase

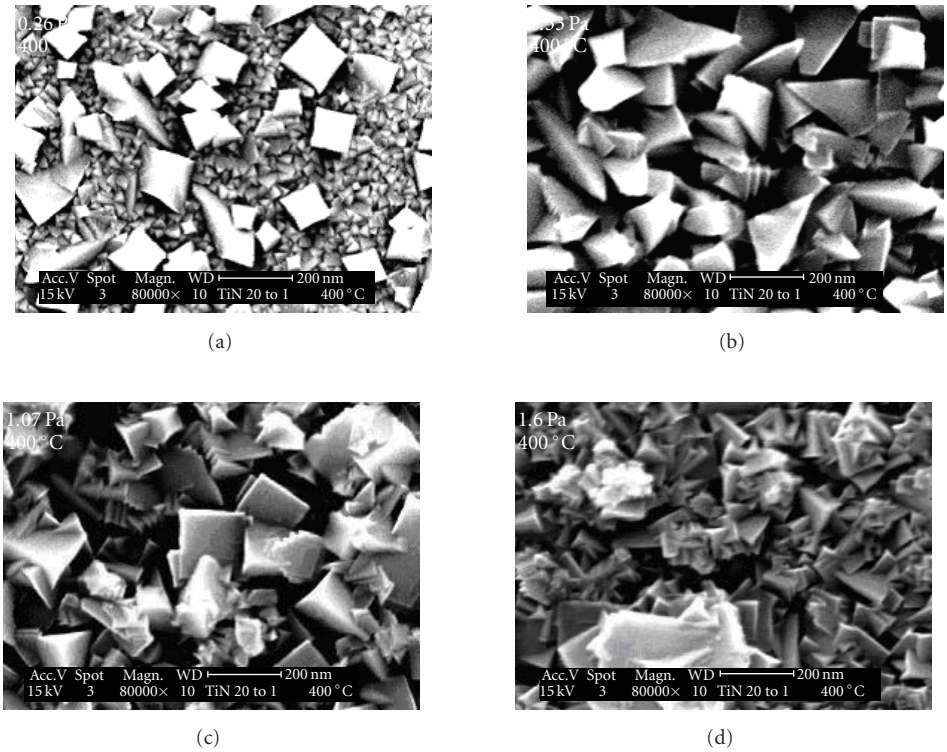


FIGURE 7: SEM images of increasing $P_P$ at $T_S = 400°C$. with a) 0.26 *Pa*, b) 0.53 *Pa*, c) 1.07 *Pa* and d) 1.60 *Pa*

from 70.4 at.% to 81.3 at.%, a maximum increase of 10.9 at.%. On average, the increased substrate temperature was responsible for a 7.46 at.% increase in nitrogen content. There appears to be no sign of asymptotic behavior with respect to nitrogen solubility as a function of either $P_P$ or $T_S$; nonetheless logic indicates that there must exist an upper limit to nitrogen saturation.

### 3.2. *Surface morphology and preferred orientation: effects of increasing $P_P$ and $T_S$*

The XRD analysis of the four samples deposited with $T_S$ = 15°C at each of the defined $P_P$ set points indicates that the synthesized material is indeed titanium nitride, namely, the $\delta$-TiN phase (cubic NaCl structure, $a = 4.244\,Å$) [28], and that the preferred orientation of the films is along the (111) planes ($2\theta = 36.9°$) relative to the (100) Si substrates in all cases (Figure 2). The smaller peaks at $2\theta = 78.9°$ correspond to the secondary (222) planes. Nominally, these peaks are not necessary for crystallographic and/or chemical phase identification, but in this case there is only the emergence of a single primary peak, making it difficult to qualify the data. Hence the presence of the secondary peak in its expected location along with the presence of the primary peak allows for reliable spectrum qualification.

It is also important to notice that the spectra indicate that no other nitrides, oxides, or sillicides of titanium or permutations thereof were synthesized even at increased process pressures and therefore that the films produced are nitrogen-rich TiN indeed.

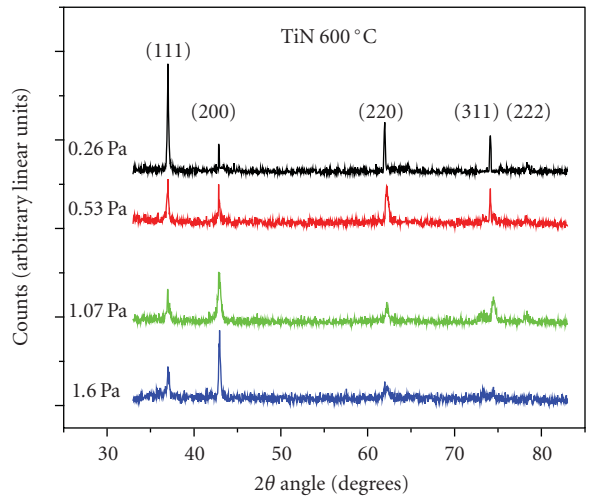


FIGURE 8: XRD spectra of increasing $P_P$ for $T_S = 600°C$.

The sharpness of the XRD peaks indicates an ordered crystalline structure. This can be qualitatively seen in the SEM images in Figure 3, which indicates that the nanostructured morphology is densely and uniformly packed throughout with an approximate feature size of 75 nm. The intensity of the (111) peaks decreases with increasing pressure and is almost indiscernible for the spectrum corresponding to the 1.60 Pa film. This indicates that increasing $P_P$ at this temperature results in a transition from the (111) orientations to a quasiamorphous phase.

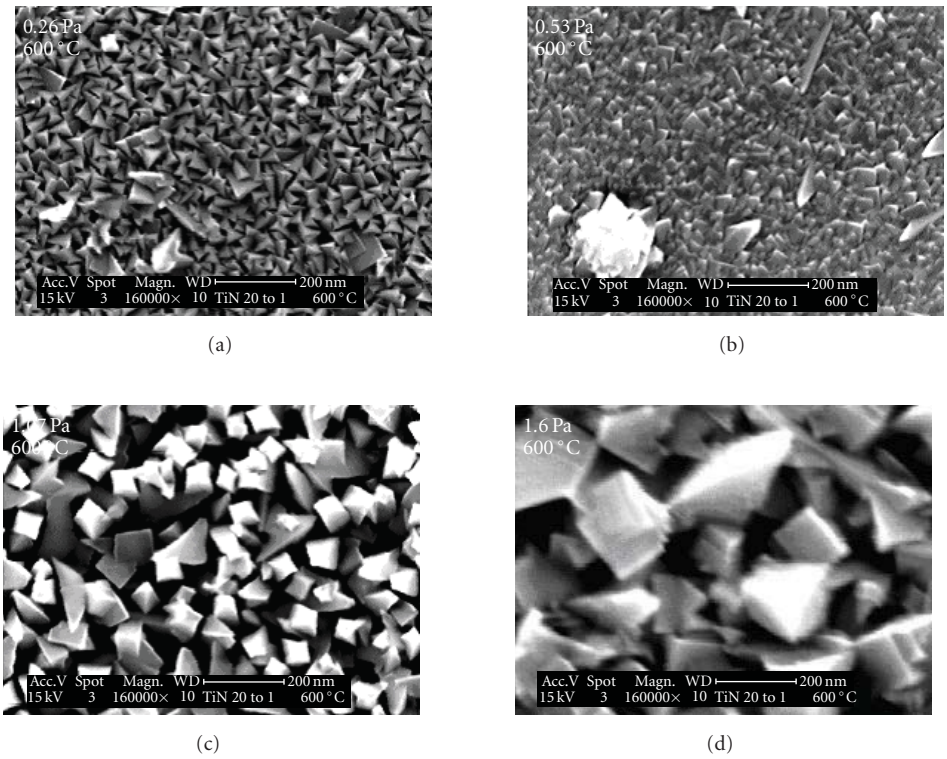


FIGURE 9: SEM images of increasing $P_P$ at $T_S = 600^\circ$C with a) 0.26 *Pa*, b) 0.53 *Pa*, c) 1.07 *Pa* and d) 1.60 *Pa*.

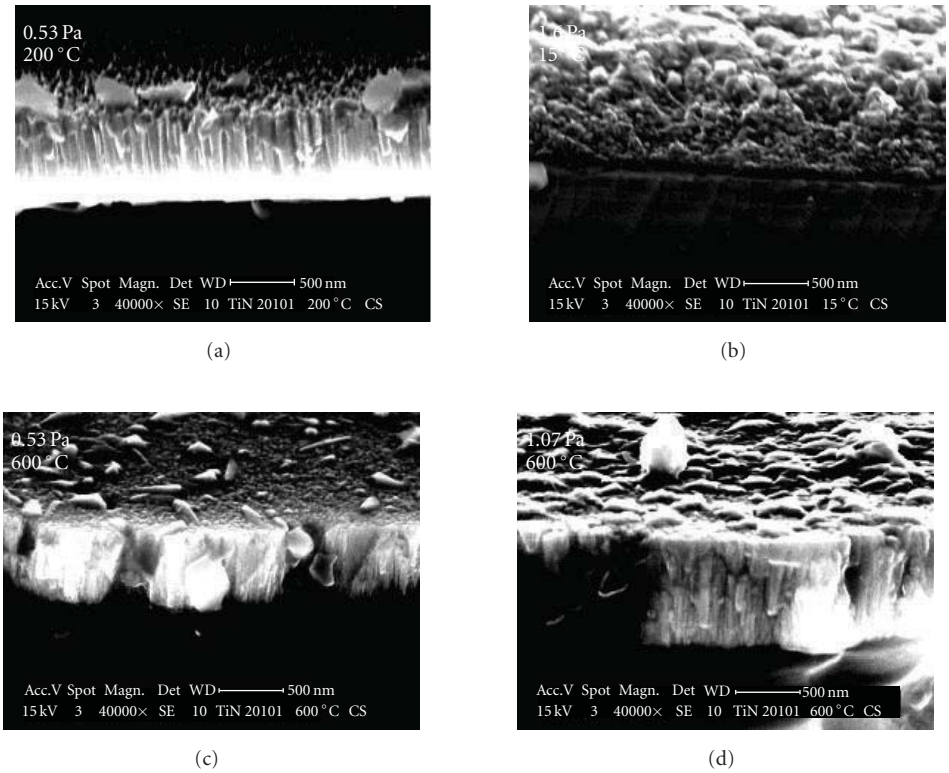


FIGURE 10: SEM images of typical film cross-sections: (a) pyramidal surface with $P_P = 0.53\,Pa$ and $T_s$ =200 °C , (b) amorphous surface with $P_P = 1.06\,Pa$ and $T_s$ =15 °C, (c) transitional surface with $P_P = 0.53\,Pa$ and $T_s$ = 600 °C, and (d) columnar/stratified surface with $P_P = 1.07\,Pa$ and $T_s$ = 600 °C.

The SEM images in Figure 3 of these produced films display the variation in their surface morphology. It quickly becomes evident that the films deposited with 0.26 Pa $\leq P_P \leq$ 1.07 Pa have a pyramidal surface structure with uniformity in the long range and that the surface morphology becomes less distinctive when $P_P$ = 1.60 Pa. Based on the information collected by XRD, it is apparent that these pyramids are single crystals of TiN growing with their (111) planes parallel to the substrate. In effect, we are seeing the ⟨100⟩ family planes as the sides of these pyramids. The image of the 1.60 Pa film supports the conclusion drawn from the XRD spectrum that this film is an amorphous structure with intermittent pyramidal, that is, isolated (111) single crystals.

The overlain spectra of the films produced at a substrate temperature of 200°C, (Figure 4), indicate that the $\delta$-TiN phase transitions from the (111) orientations to a combination of (111) and (200) orientations ($2\theta$ = 42.8°) as the process pressure is taken to the upper limit. The scanning electron micrographs in Figure 5 for the 0.26 Pa and 0.53 Pa films display almost no difference between those films produced at similar pressures but at 15°C. Again, we see a highly uniform and pyramidal surface structure with no real discerning attributes between one and another. The transition in surface morphology and preferred orientation does not occur at $T_S$ = 200°C until $P_P \geq$ 1.07 Pa. In this case, the elevated pressures do not cause amorphicivity, instead we see the formation of large (∼200 nm) $\delta$-TiN (200) single crystals coexisting with the familiar (111) crystals, especially in the film produced at $P_P$ = 1.07 Pa. The (200) and (220) planes are referenced and analyzed because the (100) and (110) planes are necessarily forbidden in the $\delta$-TiN XRD spectrum even though they are of the same family because $\delta$-TiN has a cubic NaCl structure and these planes have mixed Miller indices. Refer to [28] for a complete discussion. As the process pressure is taken to the upper limit, the intensity of the (200) peaks is dominant over the (111) peaks. This is qualitatively confirmed by SEM imaging, whereby the majority of the crystals seen are not the pyramidal (111) crystals but the larger (200) crystals, however, this film is yet completely homogenous.

The films produced at a substrate temperature of 400°C exhibit further transition in their preferred orientation and surface morphology. With this set of films, we again see the prominence of the (111) peaks decreasing as the process pressure is elevated. Again, the emergence of the (200) peaks results in these spectra, yet the interesting result here is that the increase in substrate temperature has allowed this transition to occur at a $P_P$ of 0.26 Pa, moreover peaks at $2\theta$ = 61.7° and 74.4°, corresponding to the (220) and (311) planes, respectively, emerge and increase in intensity with the elevation in the process pressure as shown in Figure 6. Interestingly enough, the SEM images shown in Figure 7 again parallel the XRD results. The surface morphology of the 0.26 Pa film is unmistakably comprised of pyramidal (111) crystals intermixed with rectangular (200), and parallelogram (220) and (311) crystals. And as the process pressure is increased to 1.60 Pa, the films become less columnar and more stratified with the crystalline planes growing parallel to each other, indicating the increased prevalence of the (200), (220), and (311) orientations over a (111) alignment. The stratified crystals are the (200) crystals growing atop one another.

Again, the feature size is also affected with those films synthesized at elevated set points exhibiting features that are 200–500 nm in size as opposed to those produced at lower pressures which still contain (111) oriented crystals of approximately 75–100 nm.

Based on the observed trend, it would seem likely that further increasing the substrate temperature would completely eliminate the (111) orientations regardless of the applied process pressure set point, but surprisingly, the films produced at $T_s$ =600°C with $P_P$ = 0.26 Pa are still dominantly oriented along the (111) planes, as can be seen in the XRD and SEM results displayed in Figures 8 and 9, respectively. As expected, however, grain coarsening and stratification are activated by increased process pressures as in previous cases. The ultimate conclusion is that the change in surface morphology and preferred orientation are a result of the coupled parametric variations in $P_P$ and $T_S$.

### 3.3. Cross-sectional morphology

As has been discussed, films produced at lower $P_P$ and $T_S$ were preferably oriented along the (111) planes and that an increased $P_P$ at low $T_S$ results in the amorphization of the films as shown in Figures 2 and 3. Moreover, a combined increase in $P_P$ and $T_S$ results in a transition from the pyramidal (111) orientations to stratified and columnar orientations. Field emission scanning electron microscopy of the as-cleaved cross-sections was implemented to qualify and correlate the cross-sectional microstructure of each typical film type.

The scanning electron micrographs reveal a closely packed and columnar cross-section for those films with a preferred orientation along the (111) planes as shown in Figure 10(a). In essence, the columnar cross-sectional microstructure supports the conclusion that the pyramidal structures are in fact the ⟨100⟩ family of planes and that the film is growing with the (111) planes parallel to the substrate.

Interestingly, the scanning electron micrographs of the cross-sections of the amorphous film reveal a quasiloosely packed underlying microstructure (Figure 10(b)), again correlating as expected with the results derived from XRD and surface SEM.

SEM images of the cross-sections of those films that are transitioning from the (111) preferred orientation to the stratified and columnar orientations as well as those which are fully stratified and columnar are shown in Figures 10(c) and 10(d). The micrographs again reveal a closely packed and columnar cross-section with the absence of pockets or voids. This is in fact the expectation since all of these films are crystalline and are being produced via a PVD route, where films grow from the substrate layer by layer.

## 4. CONCLUSIONS

Reactive magnetron DC-sputtering of titanium was implemented for the synthesis of TiN thin films. EDS analysis of the as-synthesized films confirmed an overstoichiometric chemical composition with excess nitrogen contents ranging between 70.4 at.% and 87.0 at.%. XRD analysis indicates the independent existence of the $\delta$-TiN phase, and that indeed the films produced were a solid solution of the TiN constituents. The effects of increasing $P_P$ and $T_S$ set points during deposition affected nitrogen solubility within titanium. Increasing $P_P$ from 0.26 Pa to 1.60 Pa was responsible for a maximum nitrogen content increase of 10.7 at.% and on average the variation in the $P_P$ increased the nitrogen content by 9.16 at.%. Varying $T_S$ between 15.0°C–600°C resulted in an increased nitrogen content of up to 10.9 at.% and an average increase of 7.46 at.%. The nitrogen content in the films increased by 16.6 at.%, when both $P_P$ and $T_S$ were taken to their maximum set points.

The surface morphology and preferred orientation were also affected by these parametric variations. Scanning electron microscopy reveals nanometric surface roughness, and that increased $P_P$ and $T_S$ resulted in a columnar and stratified surface morphology with long-range uniformity. This columnation and stratification are explained by XRD analysis which indicates that the preferred orientation of these films relative to the substrate is along the (200), (220), and (311) planes. Those films produced at lower set points had a pyramidal surface morphology, that is, the preferred orientation is along the (111) planes. Scanning electron microscopy of the as-cleaved cross-sections reveals a closely packed and columnar underlying microstructure for all crystalline films and a loosely packed cross-section for amorphous films.

## ACKNOWLEDGMENTS

This work is sponsored by awards from the University of California, Academic Senate, and the Department of Defense DURIP (ARO/W911NF-07-1-0213).

## REFERENCES

[1] J. M. Molarius, A. S. Korhonen, and E. O. Ristolainen, "Ti-N phases formed by reactive ion plating," *Journal of Vacuum Science & Technology A*, vol. 3, no. 6, pp. 2419–2425, 1985.

[2] W. D. Münz, D. Hoffamn, and K. Hartig, "A high rate sputtering process for the formation of hard friction-reducing TiN coatings on tools," *Thin Solid Films*, vol. 96, no. 1, pp. 79–86, 1982.

[3] R. Buhl, H. K. Pulker, and E. Moll, "TiN coatings on steel," *Thin Solid Films*, vol. 80, no. 1–3, pp. 265–270, 1981.

[4] R. L. Hatschek, "Coatings: revolution in HSS tools," Special Report 752, American Machinist, March 1983.

[5] S. Niyomsoan, W. Grant, D. L. Olson, and B. Mishra, "Variation of color in titanium and zirconium nitride decorative thin films," *Thin Solid Films*, vol. 415, no. 1-2, pp. 187–194, 2002.

[6] C. N. Kirchner, K. H. Hallmeier, R. Szargan, T. Raschke, and C. Radehaus, "Contents: electroanalysis 10/2007," *Electroanalysis*, vol. 19, no. 10, pp. 1019–1021, 2007.

[7] M. Tao, D. Udeshi, S. Agarwal, E. Maldonado, and W. P. Kirk, "Negative Schottky barrier between titanium and n-type Si(0 0 1) for low-resistance ohmic contacts," *Solid-State Electronics*, vol. 48, no. 2, pp. 335–338, 2004.

[8] L. A. Cyster, D. M. Grant, K. G. Parker, and T. L. Parker, "The effect of surface chemistry and structure of titanium nitride (TiN) films on primary hippocampal cells," *Biomolecular Engineering*, vol. 19, no. 2–6, pp. 171–175, 2002.

[9] I. Suni, M. Mäenpää, M. A. Nicolet, and M. Luomajärvi, "Thermal stability of hafnium and titanium nitride diffusion barriers in multilayer contacts to silicon," *Journal of the Electrochemical Society*, vol. 130, no. 5, pp. 1215–1218, 1983.

[10] Y. L. Jeyachandran, Sa. K. Narayandass, D. Mangalaraj, S. Areva, and J. A. Mielczarski, "Properties of titanium nitride films prepared by direct current magnetron sputtering," *Materials Science & Engineering: A*, vol. 445-446, pp. 223–236, 2007.

[11] Y. L. Jeyachandran, S. Venkatachalam, B. Karunagaran, et al., "Bacterial adhesion studies on titanium, titanium nitride and modified hydroxyapatite thin films," *Materials Science & Engineering: C*, vol. 27, no. 1, pp. 35–41, 2007.

[12] K. H. Chung, G. T. Liu, J. G. Duh, and J. H. Wang, "Biocompatibility of a titanium-aluminum nitride film coating on a dental alloy," *Surface and Coatings Technology*, vol. 188-189, pp. 745–749, 2004.

[13] W. Franks, I. Schenker, P. Schmutz, and A. Hierlermann, "Impedance characterization and modeling of electrodes for biomedical applications," *IEEE Transactions on Biomedical Engineering*, vol. 52, no. 7, pp. 1295–1302, 2005.

[14] Y. Y. Guu, J. F. Lin, and C.-F. Ai, "The tribological characteristics of titanium nitride, titanium carbonitride and titanium carbide coatings," *Thin Solid Films*, vol. 302, no. 1-2, pp. 193–200, 1997.

[15] J. Bonse, P. Rudolph, J. Krüger, S. Baudach, and W. Kautek, "Femtosecond pulse laser processing of TiN on silicon," *Applied Surface Science*, vol. 154-155, pp. 659–663, 2000.

[16] J. Bonse, H. Sturm, D. Schmidt, and W. Kautek, "Chemical, morphological and accumulation phenomena in ultrashort-pulse laser ablation of TiN in air," *Applied Physics A*, vol. 71, no. 6, pp. 657–665, 2000.

[17] A. Intemann, H. Koemer, and F. Koch, "Film Properties of CVD titanium nitride deposited with organometallic precursors at low pressure using inert gases, ammonia, or remote activation," *Journal of the Electrochemical Society*, vol. 140, no. 11, pp. 3215–3222, 1993.

[18] C. Carney and D. Durham, "Optimization of hardness by the control of microwave power in TiN thin film deposited by electron cyclotron resonance assisted sputtering in a nitrogen plasma," *Journal of Vacuum Science & Technology A*, vol. 17, no. 5, p. 2535, 1999.

[19] H. Köstenbauer, G. A. Fontalvo, M. Kapp, J. Keckes, and C. Mitterer, "Annealing of intrinsic stresses in sputtered TiN films: the role of thickness-dependent gradients of point defect density," *Surface and Coatings Technology*, vol. 201, no. 8, pp. 4777–4780, 2007.

[20] J.-H. Huang, K.-W. Lau, and G.-P. Yu, "Effect of nitrogen flow rate on structure and properties of nanocrystalline TiN thin films produced by unbalanced magnetron sputtering," *Surface and Coatings Technology*, vol. 191, no. 1, pp. 17–24, 2005.

[21] S.-S. Yang, Y.-R. Lin, and S.-T. Wu, "Room temperature epitaxial growth of TiN on SiC," *Surface and Coatings Technology*, vol. 201, no. 9–11, pp. 4850–4853, 2007.

[22] S. H. Ahn, J. H. Hong, J. G. Kim, and J. G. Han, "Effect of microstructure on corrosion behavior of TiN hard coatings

produced by a modified two-grid attachment magnetron sputtering process," *Thin Solid Films*, vol. 515, no. 17, pp. 6878–6883, 2007.

[23] E. O. Ristolainen, J. M. Molarius, A. S. Korhonen, and V. K. Lindroos, "A study of nitrogen-rich titanium and zirconium nitride films," *Journal of Vacuum Science & Technology A*, vol. 5, no. 4, pp. 2184–2189, 1987.

[24] H. A. Wriedt and J. L. Murray, "The N-Ti (nitrogen-titanum) system," *Bulletin of Alloy Phase Diagrams*, vol. 8, no. 4, pp. 378–388, 1987.

[25] M. Ohring, *The Materials Science of Thin Films*, Academic Press, San Diego, Calif, USA, 1992.

[26] L. Combadiere and J. Machet, "Reactive magnetron sputtering deposition of TiN films. I. Influence of the substrate temperature on structure, composition and morphology of the films," *Surface and Coatings Technology*, vol. 88, no. 1–3, pp. 17–27, 1997.

[27] L.-M. Peng, S. L. Dudarev, and M. J. Whelan, *High-Energy Electron Diffraction and Microscopy*, Oxford University Press, New York, NY, USA, 2004.

[28] B. D. Cullity, *Elements of X-Ray Diffraction*, Addison-Wesley, Menio Park, Calif, USA, 2nd edition, 1978.

Hindawi Publishing Corporation
Journal of Nanomaterials
Volume 2008, Article ID 690951, 8 pages
doi:10.1155/2008/690951

*Research Article*

# Studies on Nanocrystalline TiN Coatings Prepared by Reactive Plasma Spraying

**Dong Yanchun, Yan Dianran, He Jining, Zhang Jianxin, Xiao Lisong, and Li Xiangzhi**

*School of Material Science and Engineering, Hebei University of Technology, Tianjin 300130, China*

Correspondence should be addressed to Dong Yanchun, dongrunyanchun@126.com

Received 21 May 2007; Revised 5 November 2007; Accepted 19 December 2007

Recommended by Junlan Wang

Titanium nitride (TiN) coatings with nanostructure were prepared on the surface of 45 steel (Fe-0.45%C) via reactive plasma spraying (denoted as RPS) Ti powders using spraying gun with self-made reactive chamber. The microstructural characterization, phases constitute, grain size, microhardness, and wear resistance of TiN coatings were systematically investigated. The grain size was obtained through calculation using the Scherrer formula and observed by TEM. The results of X-ray diffraction and electron diffraction indicated that the TiN is main phase of the TiN coating. The forming mechanism of the nano-TiN was characterized by analyzing the SEM morphologies of surface of TiN coating and TiN drops sprayed on the surface of glass, and observing the temperature and velocity of plasma jet using Spray Watch. The tribological properties of the coating under nonlubricated condition were tested and compared with those of the AISI M2 high-speed steel and $Al_2O_3$ coating. The results have shown that the RPS TiN coating presents better wear resistance than the M2 high-speed steel and $Al_2O_3$ coating under nonlubricated condition. The microhardness of the cross-section and longitudinal section of the TiN coating was tested. The highest hardness of the cross-section of TiN coating is $1735.43HV_{100\,g}$.



## 1. INTRODUCTION

Titanium nitride (TiN) coatings are extensively applied in machinery industry due to their high hardness, low friction coefficient, beautiful color, excellent chemical stability, and wear resistance [1–6]. TiN has been produced by several techniques, which include direct nitridation of titanium metal, reductive nitridation of $TiCl_4$, plasma synthesis, and laser synthesis. Direct nitridation of titanium metal powder by nitrogen has been well studied [5, 6]. The formation of TiN is highly exothermic and the nitridation can be sustained to completion even at relatively low pressures of nitrogen. Chemical vapor deposition and plasma synthesis of titanium nitride involve the use of TiCl using ammonia as the nitriding agent. A vapor-phase chemical route using titanium tetrachloride, magnesium or sodium, and nitrogen in the temperature range 750–1050°C has been used in many studies [7–10]. Plasma processing in RF plasma torches has also been used to prepare titanium nitride [11–13]. The process involves the use of titanium halide or titanium metal powder with ammonia or nitrogen as the reactive gas. These coatings have deadly disadvantage, too. Namely, deposited efficiency is low (about $2\sim10\,\mu$m/h), and producing complicated structural part is very difficult, and wear resistance in the high loading weight is not acceptable, therefore the application of TiN is restricted.

As known, bulk TiN has such an excellent corrosion resistance that most acidic and alkaline solutions cannot corrode it [14]. However, thin TiN coatings are not corrosion resistant to aqueous or gaseous media due to some pinholes existing in the coating [10, 11, 14, 15]. Rickerby and Burnett found that the wear resistance of the coating improved as the thickness of the coating increased [16].

The disadvantage of these coatings can be overcome when TiN coating is prepared by plasma spraying. Because the deposited efficiency of plasma spraying is higher than that of other ways, and the thickness of coatings prepared by plasma spraying is bigger than that of other ways. The reactive plasma spraying (RPS) technology has been introduced in recent years as a promising way to develop dense composite coatings with a metallic or an intermetallic matrix and finely dispersed ceramic phases [17–19]. The wear

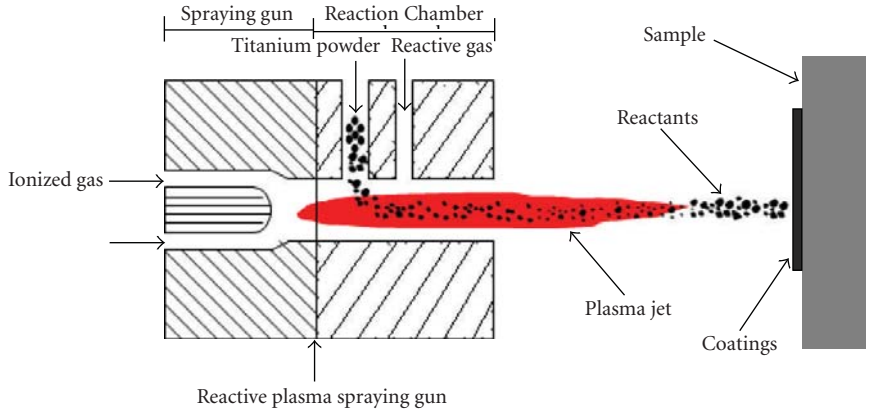


Figure 1: Sketch of the reactive plasma spraying gun.

resistance of plasma sprayed coatings can be enhanced by means of RPS techniques. Titanium nitride coatings developed via RPS are characterized by a considerable hardness, over 1500 HV, without the characteristic brittleness of TiN coatings obtained by physical vapor deposition (PVD), or chemical vapor deposition (CVD) [20, 21]. In this paper, nanocrystalline TiN coating is prepared by spraying Ti powder with size of 30~40 $\mu$m using plasma spray gun with self-made reactive chamber which is filled with $N_2$. The microstructure and property of nano-TiN coating are investigated in this paper.

## 2. EXPERIMENTS

### 2.1. Materials

The spraying equipment is LP-50B type, which is made in Jiujiang, China, and its standard power is 50 Kw. The spraying gun is assembled using a BT-G3 type plasma spraying gun and a reactive chamber which is self-designed and prepared [22]. The sketch of reactive plasma spraying gun is shown in Figure 1. The pure titanium powder used in the present work is commercially available and produced by Beijing General Research Institute of Mining and Metallurgy, China. The average particle size distribution of the titanium powder is about 30~40 $\mu$m. The substrate material is 45 (Fe-0.45wt.%C) steel, which is machined into samples of 30 mm $\times$ 25 mm $\times$ 10 mm and ground to rough surfaces. Prior to spraying TiN coating, Ni-10 wt.%Al self-melting alloy bond layer with a thickness of about 100 $\mu$m is sprayed onto surfaces of samples, for increasing the adhesive strength between the TiN coating and substrate.

### 2.2. Fabrication and characterization of the TiN coating

During spraying, the titanium powders, the micrograph of which was shown in Figure 2, were carried by nitrogen gas into the reactive chamber of the RPS gun, where pure nitrogen gas was also introduced. Ti and $N_2$ reacted in the reactive chamber, the product, which was TiN, deposited

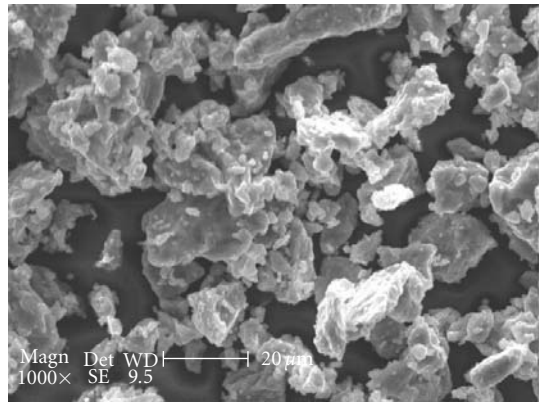


Figure 2: SEM micrograph of the original Ti powders.

on the substrate. Thus, a coating with a thickness of at least 400 $\mu$m was fabricated within a few minutes. The morphology of the as-sprayed TiN coating was observed by means of a PHILIPS XL30/TMP scanning electron microscope (SEM) and PHILIPS TECNAI F20 transmission electron microscope (TEM). The JEOL Rigaku X-ray diffractometer 2500/PC diffraction instrument with Cu target was adopted to analyze the phase composition of the coating's exposed surface and cross-section. The grain size of the TiN coating was calculated according to Scherrer formula [23]:

$$D_{hkl} = \frac{k\lambda}{B\cos\theta}, \qquad B = \sqrt{B_1^2 - B_2^2}, \tag{1}$$

where "$D_{hkl}$" is the average diameter in nm, "$k$" is the shape factor (0.9), "$B$" is the broadening of the diffraction line measured half of its maximum intensity in "radians," "$B_1$" is the half peak breadth of the diffraction line of test sample, "$B_2$" is half peak breadth of the diffraction line of micron crystal TiN specimen prepared by other way, "$\lambda$" is the wave length of X-ray, and "$\theta$" is the Bragg diffraction angle.

Spray Watch used during spraying is observation system for thermal spraying, made by Oseir Co., Ltd., Finland.

### 2.3. Hardness test

Microhardness of the cross and longitudinal sectional TiN coating was measured using the digital Vickers microhardness tester, which is made in Shanghai Taiming Optical Instrument Co., Ltd., China. Loads ranging from 25 to 1000 g and a dwell time of 15 seconds were selected. Approximately, 10 indentations were made for each load. The distance between every two indentations was controlled three times longer than the indentation diagonal, so the stress field effect near the indentation can be eliminated. The average microhardness is selected for discussion in this paper.

### 2.4. Wear tests

Friction and wear tests of the TiN coated specimens were performed using a block-on-ring sliding apparatus, under nonlubricated condition. The MM-200 wear test machine, made by Xuanhua Material Test Machine Co., Ltd., China, was operated with the sliding speed of 0.4 $ms^{-1}$. The test specimens were fixed by a sample holder; the wear rings were placed under the specimens; loads ranging from 100 to 1470 N were vertically applied at the top of specimens. For each load, three specimens were tested, and the average wear volume loss was taken. The wear ring used was AISI E52100 steel (0.95–1.05C, 0.2–0.4 Mn, 0.15–0.35 Si, 1.3–1.65 Cr, 0.3 Ni, 0.25 Cu, and bal Fe) (in wt.%). The ring is 38 mm in external diameter and 10 mm in thickness, which was heat-treated to an average hardness of about 60 HRC. Each wear test was conducted for 60 minutes. Wear loss of TiN coating, $Al_2O_3$ coating, and the AISI M2 steel specimens were obtained by measuring the volumetric loss after each test according to (2). The friction coefficient (FC) of the specimens was given by (3):

$$\Delta V = B \times \left[ r^2 \times \mathrm{Sin}^{-1}\left(\frac{b}{2r}\right) - \frac{b}{2}\left(r^2 - \frac{b^2}{4}\right)^{1/2} \right], \quad (2)$$

$$\mu = \frac{T}{r \cdot P} \times \frac{\alpha + \sin\alpha \cdot \cos\alpha}{2\sin\alpha}, \quad (3)$$

where $\Delta V$ is the volumetric loss of specimens; $B$ and $r$ are, respectively, the thickness and radius of the ring; $b$ is the width of worn scars; $T$ is the wear moment; $P$ is the load employed; $\alpha$ is the contacted angle, according to $\alpha = \sin^{-1}(b/2r)$, and $\mu$ is friction coefficient.

## 3. RESULTS

### 3.1. Phases constitute of the TiN coating

Figure 3 is XRD pattern of the TiN coating sprayed on the surface of substrate and pure Ti powders. The coating is mainly composed of two phases, TiN and small quantities of $Ti_3O$, without pure Ti. Observing the spectrum, five sharp TiN diffraction peaks appeared, and the diffraction planes are (111), (200), (220), (311), and (222). Intensities of $Ti_3O$ are very low, the diffraction planes of the $Ti_3O$ phase are (103), (113), (116), and (223). According to the Scherrer formula, the grain size of TiN coating was estimated, which was shown in Table 1. The grain size of the TiN coating

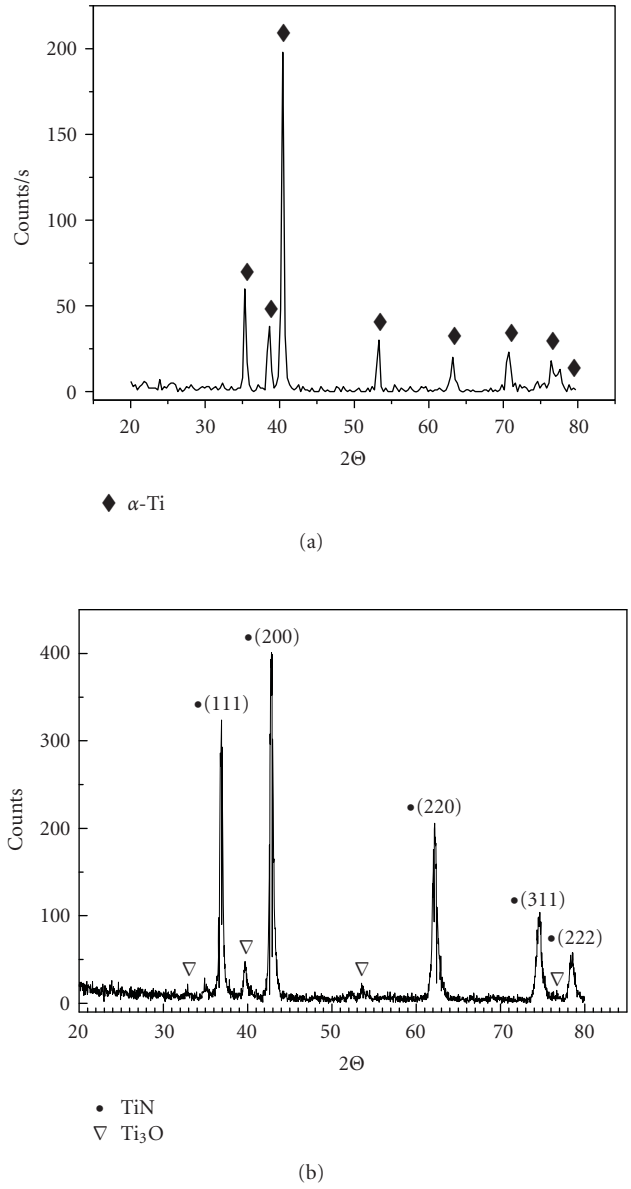


Figure 3: Surface XRD pattern of original Ti powders and the reactive plasma sprayed TiN coating.

ranged 78∼97 nm, which is consistent with what is observed by TEM (see Figure 5). Pure Ti diffraction does not appear in the coating, which proves that the Ti and $N_2$ react fully in RPS process. This is consistent with literature [9]. $Ti_3O$ is metastable solid solution, which comes from Ti unsufficient oxidation at temperature of 650∼750°C and decomposes when temperature exceeds 750°C [24]. The $Ti_3O$ in the coating is product of the oxidation of TiN and exists in the coating for shock cooling under plasma spraying condition.

### 3.2. Microstructural characterization of the TiN coating

The SEM photograph of the TiN coating cross-section is shown in Figure 4. The entire cross-sectional morphology of

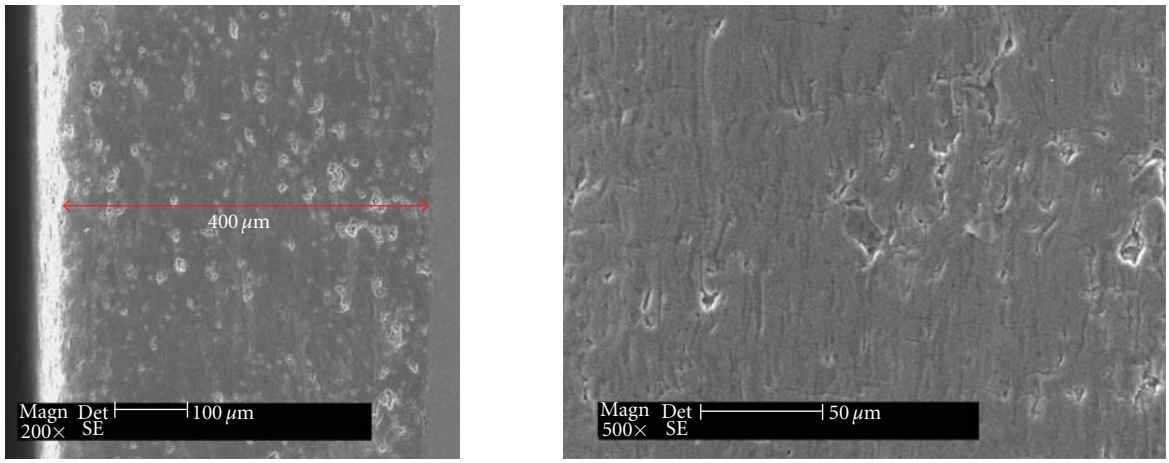


(a) (b)

Figure 4: The cross-sectional morphologies of the RPS TiN coating, (b) is partial enlarged drawing of (a).

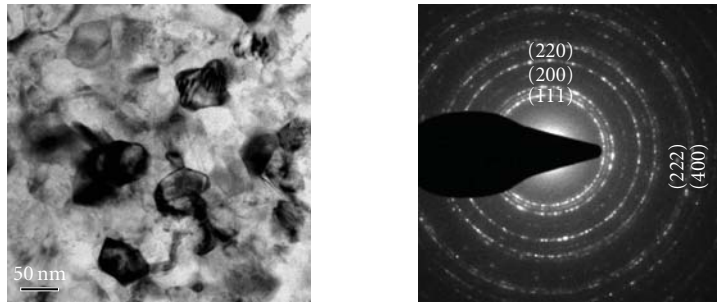


(a) (b)

Figure 5: TEM morphology of the reactive plasma sprayed TiN coating: (a) nanocrystallines, (b) the selected area electron diffraction pattern.

the RPS TiN coating in Figure 4(a) indicates that its thickness is 420 $\mu$m, which is about 100 times than that of TiN films prepared by CVD or PVD. The coating presents layer structure, which is tightly piled. The structure with few pores should be attributed to gas which exists between the TiN liquid drops and has no time to be released during coating forming. Small quantities of cracks appear in the multilayered structures of the coating (see Figure 4(b)). Further study is needed to reduce the pores and cracks, and improve the structure of the coating.

TEM is an indispensable analytical tool in the study of the microstructure of coatings. Figure 5 indicates the TEM morphology and the selected area electron diffraction (SAED) pattern of the reactive plasma sprayed TiN coating. It can be seen from Figure 5(a) that the most of grain size of the coating is smaller than 100 nm. The SAED pattern of the coating is given in Figure 5(b). The grain size of 82 ± 10 nm was measured by linear intercepting, which is approximate to the result obtained by calculation, and smaller than that of the original Ti powders, which is 30~40 $\mu$m. The diffraction rings of the SAED pattern in Figure 5(b) are continuous, dense, and broader, which indicates the (111), (200), and (220) orientation. (311) orientation is not clear. The diffraction rings show that the orientation of TiN crystal grains is random. Weak diffraction spots distribute in diffraction rings because the size of small quantity of crystal grains is bigger than 100 nm. XRD and SAED examinations revealed that the TiN coating has the cubic structure of NaCl type ($a$ = 0.42 nm).

Table 1: Scherrer crystallite sizes of the TiN coatings.

| Diffraction plane ($hkl$) | (111) | (200) | (220) |
|---|---|---|---|
| $D_{hkl}$ (nm) | 92~97 | 83~88 | 78~83 |

### 3.3. Microhardness of the TiN coating

It is well known that the apparent microhardness of solid materials depends on the applied indentation test load. This phenomenon is known as the indentation size effect (ISE). Figure 6 shows the dependence of the microhardness for the

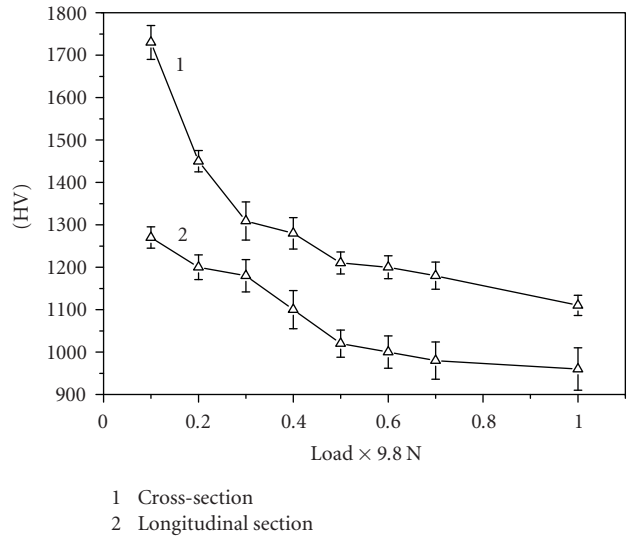


Figure 6: The microhardness of TiN coating longitudinal section and cross-section.

cross-sectional and longitudinal-sectional RPS TiN coating on the indentation loads. As the applied load ranges from 100 to 1000 g, the Vickers microhardness drops from 1735.43 to 1125.27 HV and 1267.78 to 962.26 HV, respectively, which is an evident phenomenon of ISE. When the test load is standard load of 100 g, the microhardness is 1189.36 HV.

### 3.4. Volumetric wear loss of TiN coating specimens

In order to study the wear resistance of the TiN coating, the test load changes from 100∼1470 N. For $Al_2O_3$ ceramic coating cannot resist wear of high load, when the test load is higher than 500 N, the friction coefficient increases notably, and friction noise is high. M2 high-speed steel is selected as the comparison samples when test load is above 500 N. Figure 7(a) shows the volumetric wear loss of the $Al_2O_3$ coating and TiN coating at loads between 100 and 500 N and at 0.4 $ms^{-1}$; Figure 7(b) shows the volumetric wear loss of TiN coating and M2 high-speed steel at loads between 500 and 1470 N. The volumetric wear loss of the $Al_2O_3$ coating, the TiN coating, and M2 steel increases with the loads increased. Under low loads (100∼500 N), the volumetric wear loss of the $Al_2O_3$ coating is bigger than that of the TiN coating. When the load changes from 490∼980 N, the TiN coating and M2 high-speed steel are close in wear loss. With the continuous increase of the loads, the TiN coating remained a mild increase in wear loss, and reached 6.86 $mm^3$ when the load is up to 1470 N, while the curve of the M2 steel's volumetric wear loss versus loads presents distinctly moving up tend. The volumetric wear loss of the TiN coating is approximately half under 1225 N and two-fifths of that of the M2 high-speed steel under 1470 N, respectively. Figure 7 indicated that the wear resistance of the TiN coating is better than $Al_2O_3$ coating and M2 high-speed steel.

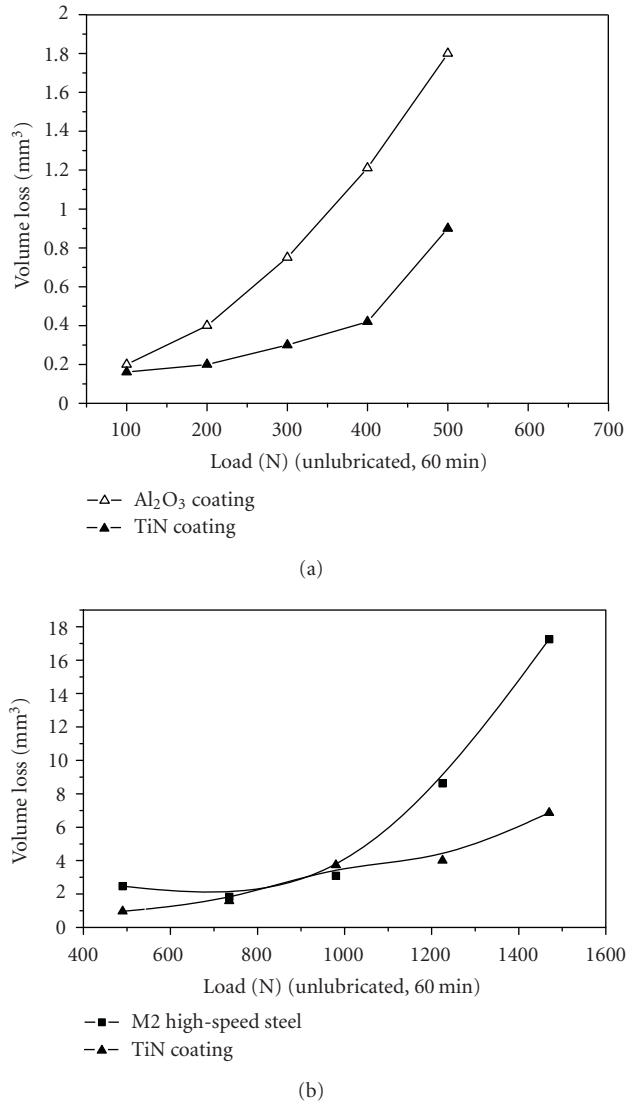


Figure 7: Wear volume loss of the TiN coating, $Al_2O_3$ coating, and M2 steel plotted as a function of loads: (a) load is smaller than 500 N, (b) load is bigger than 500 N.

### 3.5. Friction coefficient of TiN coating and M2 high-speed steel

Figure 8 presents the dependence of friction coefficient on loads of both the TiN coating and the M2 steel under dry sliding wear. It can be seen from the curves that with the increase of loads, the FC of the TiN coating and AISI M2 steel generally changes in a small range of about 0.372∼0.412 and 0.331∼0.375, respectively. The two are close in friction coefficient when load is 1470 N. Therefore, the antifriction property of TiN coating is close to that of the AISI M2 steel at dry sliding wear under heavy loads.

### 3.6. Analyses and discussion

Figure 9 shows the surface layer morphologies of a few TiN drops sprayed on the surface of glass and the TiN coating

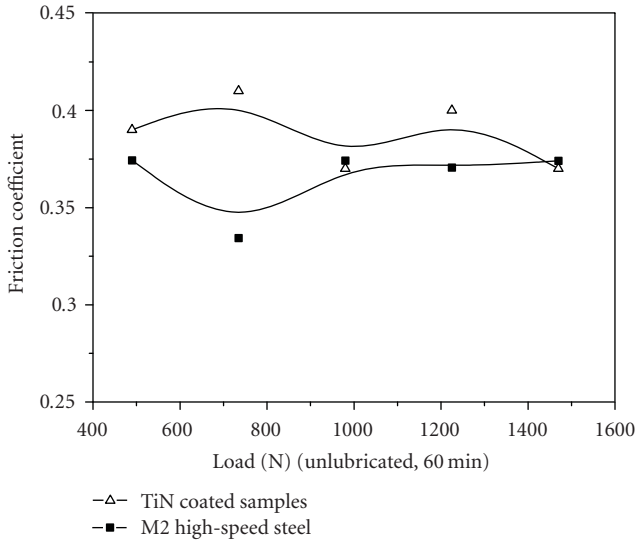


Figure 8: Friction coefficients of the TiN coating and M2 steel plotted as a function of loads.

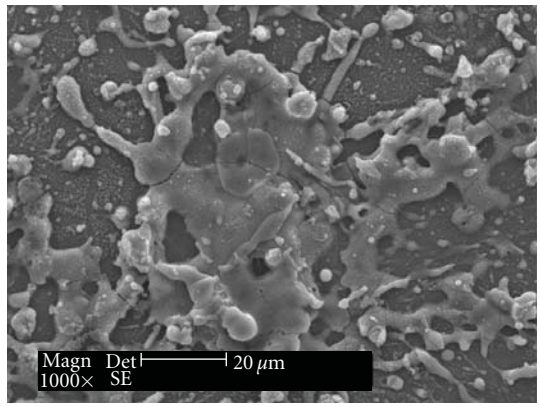


(a)

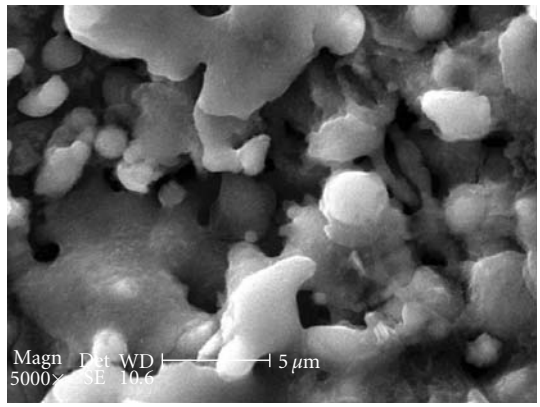


(b)

Figure 9: Surface morphologies of the TiN sprayed on the glass and the TiN coating: (a) the TiN on the glass, (b) the TiN coating.

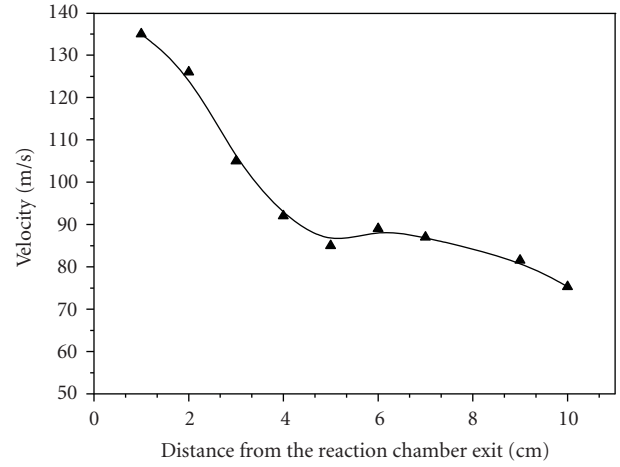


(a)

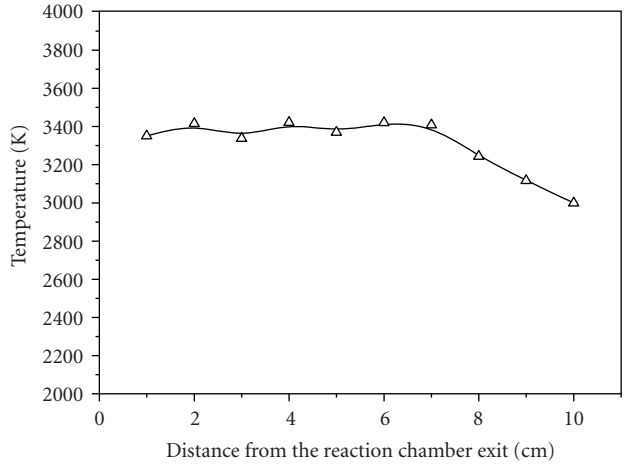


(b)

Figure 10: The velocity and temperature of the particles in plasma jet when the RPS state is steady, which are measured by Spray Watch: (a) the velocity of the particle, (b) the temperature of the particle.

under same spraying condition. Obviously, the topography of TiN drops on the glass surface presents the character of high-temperature molten drop spattering. It is indicated that the coating is deposited with molten drops. The forming process of the TiN coating is that the molten reactants remain in liquid state in the plasma jet, spatter, spread, deform, and freeze on the sample surface. Owing to the fact that the temperature gradient from plasma jet to the sample surface is so big that the molten drops nucleate quickly, but nucleates have no time to grow, therefore the grain of the TiN is refined.

Solid Ti particles are melted in high temperature plasma jet and acutely reacted with $N_2$ ion gas and $N_2$ gas in reactive chamber, while a great deal of reaction heat is given out. The reaction belongs to combustion synthesis [25]. As a result, the temperature of the liquid particle increases. When the spraying state is steady, the velocity and temperature of the particles in plasma jet are measured by Spray Watch. Figure 10 shows the temperature and the velocity of the

particles flying in plasma jet. It can be seen that the velocity of particle decreases with its flying distance to reactive chamber exit increasing, while the temperature of the particles remains steady, which is different to normal plasma spray. For normal plasma spray, the temperature of particle decreases with the distance increasing. The reaction heat reinforces the heat of the plasma jet and has particles remained liquid before it reaches to metal substrate. The measured average velocity and temperature of particles arriving to substrate are 105 m/s and 3360 K, respectively (see Figure 10). The molten point of TiN is 3223 K, which is lower than 3360 K. During spraying, the distance ($l$) from metal substrate to spray gun exit is 100 mm. The time ($t$) in which a particle arrives to substrate from reactive chamber is

$$t = \frac{l}{v} = \frac{100 \times 10^{-3}\, m}{105\, m/s} = 0.95 \times 10^{-3}\, s. \quad (4)$$

In so short time, the TiN drops quench from 3360 K to about 800 K and quickly freeze; the cooling rate is higher than general plasma spraying. The Huge cooling velocity and undercooling increase the nucleation rate. The reason for forming nanocrystal TiN coating is that combustion synthesis between Ti and $N_2$ and plasma spraying condition coacts. Combustion synthesis reaction in plasma jet fabricates liquid TiN with high temperature. TiN liquid drops, shock-cooling under the plasma spraying condition, solidify and form nanocrystal TiN coatings on substrates.

## 4. CONCLUSIONS

(1) The TiN coating, prepared via RPS Ti powders using spraying gun with self-made reactive chamber, is mainly composed of two phases, TiN and small quantities of $Ti_3O$. TiN coatings present typical layer structure. The size of most of crystal grains in the TiN coating is smaller than 100 nm.

(2) The forming mechanism of the nanostructure coating is that Ti powders are melted and reacted with $N_2$ in plasma jet and in the chamber. Heat given out by combustion synthesis reaction increases the temperature of molten drops. The Huge cooling velocity and degree of supercooling under plasma spraying condition have the drops quench, nucleate quickly, and form nanostructure.

(3) The highest hardness of the TiN coating is 1735 .43 $HV_{100\,g}$; the wear resistance of the coating is better than that of $Al_2O_3$ coating and M2 high-speed steel.

## ACKNOWLEDGMENT

This work was supported by the National Natural Science Foundation of China (no. 50472033).

## REFERENCES

[1] H. Dingjun, H. Shejun, and X. Guangrong, "Application and research development of TiN coating," *Transaction of Guangdong University of Technology*, vol. 22, no. 2, 2005.

[2] H. A. Jehn, "Multicomponent and multiphase hard coatings for tribological applications," *Surface and Coatings Technology*, vol. 131, no. 1–3, pp. 433–440, 2000.

[3] J. G. Han, J. S. Yoon, H. J. Kim, and K. Song, "High temperature wear resistance of (TiAl)N films synthesized by cathodic arc plasma deposition," *Surface and Coatings Technology*, vol. 86-87, part 1, pp. 82–87, 1996.

[4] L. Jiwen and Y. Li, "Characteristics of low temperature ion plating TiN coatings," *Chinese Journal of Mechanical Engineering*, vol. 11, no. 2, pp. 136–140, 1998.

[5] L. Wenmei and H. Jiawen, "Oxidation resistant properties of vapor deposited TiN, Ti (C, N) coatings," *Materials for Mechanical Engineering*, vol. 21, no. 4, 1997.

[6] C. Jimenez, S. Gilles, R. Doppelt, et al., "CVD of TiN and other barrier metals," *Surface and Coatings Technology*, vol. 31, pp. 33–46, 1995.

[7] S. Wilson and A. T. Alpas, "Wear mechanism maps for TiN-coated high speed steel," *Surface and Coatings Technology*, vol. 120-121, pp. 519–527, 1999.

[8] T. S. Li, H. Li, and F. Pan, "Microstructure and nanoindentation hardness of Ti/TiN multilayered films," *Surface and Coatings Technology*, vol. 137, no. 2-3, pp. 225–229, 2001.

[9] A. Kobayashi, "Formation of TiN coatings by gas tunnel type plasma reactive spraying," *Surface and Coatings Technology*, vol. 132, no. 2-3, pp. 152–157, 2000.

[10] R. Motte, M. Proust, J. Torres, et al., "TiN-CVD process optimization for integration with Cu-CVD," *Microelectronic Engineering*, vol. 50, no. 1–4, pp. 369–374, 2000.

[11] M. Kawamura, K. Kumagai, Y. Abe, K. Sasaki, and H. Yanagisawa, "Characterization of TiN films prepared by rf sputtering using metal and compound targets," *Vacuum*, vol. 51, no. 3, pp. 377–380, 1998.

[12] R. M. Marin-Ayral, C. Pascal, F. Martinez, and J. C. Tedenac, "Simultaneous synthesis and densification of titanium nitride by high pressure combustion synthesis," *Journal of the European Ceramic Society*, vol. 20, no. 14-15, pp. 2679–2684, 2000.

[13] P. V. Ananthapadmanabhan, P. R. Taylor, and W. Zhu, "Synthesis of titanium nitride in a thermal plasma reactor," *Journal of Alloys and Compounds*, vol. 287, no. 1-2, pp. 126–129, 1999.

[14] H. Kuwahara, N. Mazaki, M. Takahashi, T. Watanabe, X. Yang, and T. Aizawa, "Mechanical properties of bulk sintered titanium nitride ceramics," *Materials Science and Engineering A*, vol. 319–321, pp. 687–691, 2001.

[15] T. Valente and F. P. Galliano, "Corrosion resistance properties of reactive plasma-sprayed titanium composite coatings," *Surface and Coatings Technology*, vol. 127, no. 1, pp. 86–92, 2000.

[16] D. S. Rickerby and P. J. Burnett, "The wear and erosion resistance of hard pvd coatings," *Surface and Coatings Technology*, vol. 33, pp. 191–211, 1987.

[17] P. V. Ananthapadmanabhan and P. R. Taylor, "Titanium carbide-iron composite coatings by reactive plasma spraying of limonite," *Journal of Alloys and Compounds*, vol. 287, no. 1-2, pp. 121–125, 1999.

[18] A. Kobayashi, "New applied technology of plasma heat source," *Welding International*, vol. 4, no. 4, pp. 276–282, 1990.

[19] T. Valente and F. P. Galliano, "Corrosion resistance properties of reactive plasma-sprayed titanium composite coatings," *Surface and Coatings Technology*, vol. 127, no. 1, pp. 86–92, 2000.

[20] E. Galvanetto, F. P. Galliano, F. Borgioli, U. Bardi, and A. Lavacchi, "XRD and XPS study on reactive plasma sprayed titanium-titanium nitride coatings," *Thin Solid Films*, vol. 384, no. 2, pp. 223–229, 2001.

[21] W. Feng, D. Yan, J. He, et al., "Microhardness and toughness of the TiN coating prepared by reactive plasma spraying," *Applied Surface Science*, vol. 243, no. 1–4, pp. 204–213, 2005.

[22] Y. Dianran, H. Jining, and D. Yanchun, "Plasma spraying reactive chamber equipment (P) Cina," Patent no. ZLCN200410072552.X, 2007.

[23] A. Akbari, J. P. Riviere, C. Templier, et al., "Structural and mechanical properties of IBAD deposited nanocomposite Ti-Ni-N coatings," *Surface and Coatings Technology*, vol. 200, pp. 6298–6302, 2006.

[24] S. Malinov, W. Sha, and C. S. Voon, "*In situ* high temperature microscopy study of the surface oxidation and phase transformations in titanium alloys," *Journal of Microscopy*, vol. 207, no. 3, pp. 163–168, 2002.

[25] Y. Sheng, *Combustion Synthesis*, vol. 7, Metallurgical Industry, Beijing, China, 1999.

Hindawi Publishing Corporation
Journal of Nanomaterials
Volume 2008, Article ID 638947, 9 pages
doi:10.1155/2008/638947

*Research Article*

# Nanomechanics of Single Crystalline Tungsten Nanowires

**Volker Cimalla,[1] Claus-Christian Röhlig,[1] Jörg Pezoldt,[1] Merten Niebelschütz,[1] Oliver Ambacher,[1] Klemens Brückner,[1] Matthias Hein,[1] Jochen Weber,[2] Srdjan Milenkovic,[3] Andrew Jonathan Smith,[3] and Achim Walter Hassel[3]**

[1] *Institut für Mikro- und Nanotechnologien, Technische Universität Ilmenau, Gustav-Kirchhoff-Strasse 7, 98693 Ilmenau, Germany*
[2] *Max-Planck-Institut für Festkörperforschung, HeisenbergStrasse 1, 70569 Stuttgart, Germany*
[3] *Max-Planck-Institut für Eisenforschung, Max-Planck-Strasse 1, 40237 Düsseldorf, Germany*

Correspondence should be addressed to Achim Walter Hassel, hassel@elchem.de

Received 2 September 2007; Accepted 29 January 2008

Recommended by Jun Lou

Single crystalline tungsten nanowires were prepared from directionally solidified NiAl-W alloys by a chemical release from the resulting binary phase material. Electron back scatter diffraction (EBSD) proves that they are single crystals having identical crystallographic orientation. Mechanical investigations such as bending tests, lateral force measurements, and mechanical resonance measurements were performed on 100–300 nm diameter wires. The wires could be either directly employed using micro tweezers, as a singly clamped nanowire or in a doubly clamped nanobridge. The mechanical tests exhibit a surprisingly high flexibility for such a brittle material resulting from the small dimensions. Force displacement measurements on singly clamped W nanowires by an AFM measurement allowed the determination of a Young's modulus of 332 GPa very close to the bulk value of 355 GPa. Doubly clamped W nanowires were employed as resonant oscillating nanowires in a magnetomotively driven resonator running at 117 kHz. The Young's modulus determined from this setup was found to be higher 450 GPa which is likely to be an artefact resulting from the shift of the resonance frequency by an additional mass loading.



## 1. INTRODUCTION

Tungsten is a brittle refractory metal that crystallises in the BCC form [1]. It has high-tensile strength and good creep resistance. However, it suffers from poor low-temperature ductility and strong reactivity in air [2]. Like the other BCC metals, tungsten also undergoes a brittle-to-ductile transition (BDTT) above 205°C. Below the BDTT it is very brittle exhibiting only few percents of elongation. The BDTT can only be lowered by heavy warm or cold deformation at temperatures below the room temperature. Due to its high stability this material is used in various applications in engineering. The trend for miniaturization of devices increases the demands for the selected materials to consider size effects of their properties. Most of the mechanical phenomena are well-known on a macroscopic scale, however, they are hard to determine on a nanoscopic scale. There is a variety of theoretical predictions of hardness and Young's modulus; mainly for carbon nanotubes [3], but only a few for nanowires (e.g., Au [4, 5]) which could not be confirmed experimentally up to date. Many metals are known to have oxidised surfaces under environmental conditions. This is also the case for tungsten, and the high surface to volume ratio in nanostructures amplifies the importance to consider this process [6]. Thus, a remarkable influence of the oxidised surface on the properties of the nanowires can be expected, which complicates the mechanical analysis of metal nanowires. Mechanical studies on nanowires are of interest as their diameter is already smaller than the average dislocation distance. The dislocations will therefore accumulate at the nanowires surface generating virtually dislocation free structures. These structures exhibit mechanical strength that may reach the theoretical limit. This is especially true if the wires are single crystalline [7]. Cutting of those structures from bulk material by means of a focused ion beam is one method to prepare the necessary test objects [8]. The FIB preparation often generates a large number of surface defects which limits the applicability of this method. Wang [9] has reviewed

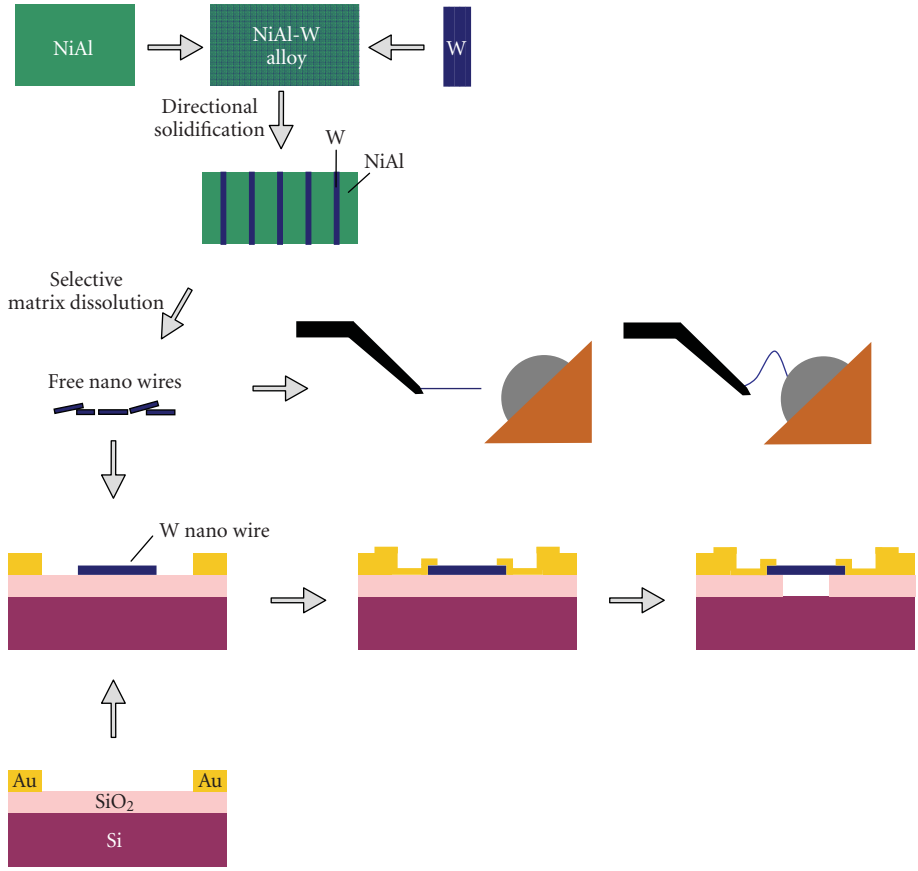


Figure 1: Roadmap of the processing steps employed in this work. A detailed description of the processing steps is given in the text.

the mechanical properties of nanowires and nanobelts characterised by techniques developed for mechanical characterisation using in situ transmission electron microscopy (TEM).

Recently, a method was established that allows producing single crystalline Re [10], W [11], Mo [12], Cu [13], and Au [14, 15] nanowires with a high-aspect ratio from directionally solidified eutectic alloys. By controlling the growth parameters and the dissolution conditions, the diameter [16] and the released length [15, 17], respectively, are well adjustable. The advantage of this system is that an array of nanowires is produced which allows studying the anisotropy of the mechanical properties. This was demonstrated for the Re system [18]. It is also possible to perform compression tests on Mo [19]. Since the release of the wires is done chemically or electrochemically, the surface of the wires is not mechanically affected, on the contrary deformations will be preferentially dissolved. This is well known and the reason why electropolishing is used for surface preparations for TEM samples.

The focus of this study lays in the investigation of stability and the mechanical properties of the tungsten nanowires. Different static and dynamic analysis approaches will be presented to extract one basic elastic property of the nanowires in comparison to the bulk material—the Young's modulus. The influence of the contamination and oxidation in air on the elastic behaviour is studied qualitatively in static bending experiments as well as in resonant oscillating nanomechanical devices.

## 2. EXPERIMENTAL

### 2.1. Preparation of the nanowires

The complete fabrication process from source material up to the mechanical test structure is schematically shown in Figure 1. The single steps are described in more detail in the following paragraph. Prealloys were prepared from nickel (99.97 wt%), electrolytic aluminium (99.9999 wt%), and tungsten (99.99 wt%) by induction melting under an inert atmosphere. They were drop cast into a cylindrical copper mould and subsequently fitted into alumina crucibles. Directional solidification was performedin a Bridgman-type crystal growing facility. The solidification was conducted at a temperature of $1700 \pm 10^{\circ}$C, a thermal gradient of approximately 40 K cm$^{-1}$, and a growth rate of 30 mm h$^{-1}$. Mechanical cutting and a standard metallographic preparation yielded the sample shown in Figure 2 in which the cross sections of the nanowires appear darker. This sample was further investigated by EBSD as discussed in the results section.

### 2.2. Nanowire release

In order to extract the tungsten wires from the matrix, the conditions under which both matrix elements—nickel and

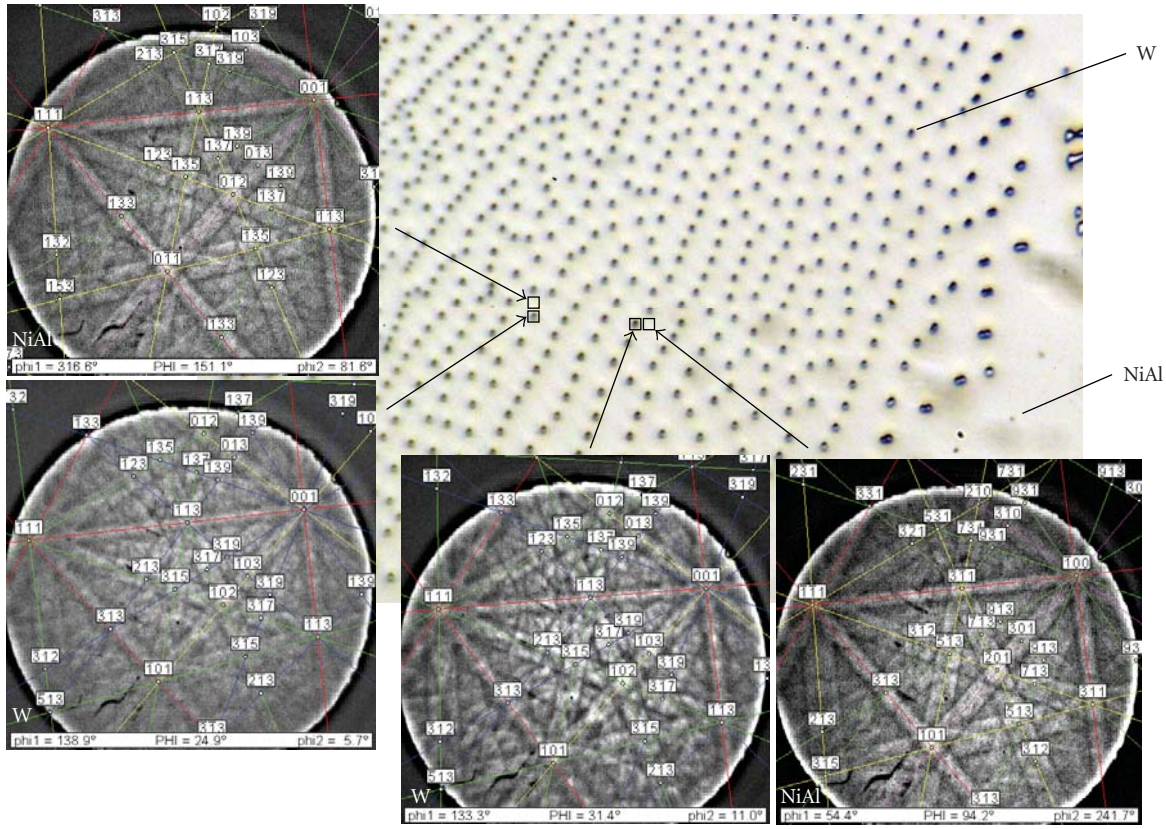


Figure 2: Optical image of a cross section through a directionally solidified NiAl-W eutectic. The W nanowires appear as darker spots in a bright NiAl matrix. Inserts: EBSD patterns at the marked positions with well-defined Kikuchi lines.

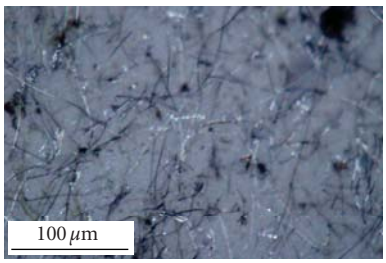


Figure 3: Bunch of tungsten nanowires on a filter paper with an approximate diameter of 200 nm, the tungsten nanowires become visible in an optical microscope due to the strong light scattering of the metal.

aluminium—corrode, while passivating tungsten was chosen, the details of which are described in [11]. Both a chemical and an electrochemical route are available to release these wires from the matrix. The chemical route pieces of the sample were immersed in a solution of HCl and $H_2O_2$ which leads to the selective digestion of the matrix phase [11]. The appropriate potential could also be applied electrochemically. By continuing the dissolution process for a few hours, the matrix was completely digested. In both cases, a subsequent filtration yielded free nanowires on a filter paper (see Figure 3). It clearly shows the extreme aspect ratio of these wires. All potentials in the electrolyte are given versus the standard hydrogen electrode (SHE). The chemicals were of p.a. grade and purchased from VWR, Germany.

### 2.3. Preparation of nanowires for mechanical investigation

For the processing of nanowire-based nanomechanical devices and test structures, no reliable technology for the large-scale fabrication exists and every structure can be considered as a handmade single device. Moreover, classical processes often damage or destroy bottom up nanomaterials [20]. In this work, two variants of a process technology were used, both bridging classical top down and novel bottom up methods.

The first method combines photolithography and electron-beam lithography as shown schematically in Figure 1. The basis is a silicon wafer with thermally grown $SiO_2$ and a matrix of large gold pads as well as alignment marks as in Figure 1. The pads are defined by photolithography and are used as interface between external wiring (bonding or attached tips) and the nanocontacts to the nanowires. The $SiO_2$ surface provides electrical isolation between the contacts and is also utilised to be etched by HF (hydrofluoric acid)-vapour-etching [21] to obtain freestanding nanowires.

The tungsten nanowires collected on filter paper (see Section 2.4) were transferred into a suspension of isopropanol or methanol after etching. After drying out on the substrate, the nanowires are randomly distributed on

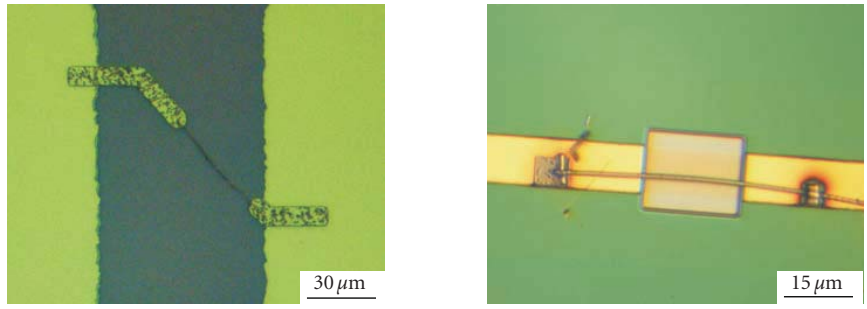


(a) (b)

Figure 4: Optical micrographs of contacted tungsten nanowires: (a) by electron beam lithography and (b) by FIB.

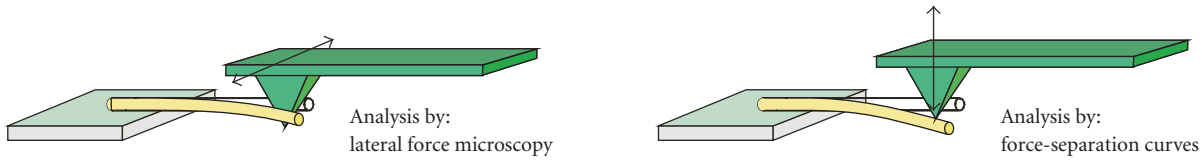


(a) (b)

Figure 5: Principles of static analysis of mechanical properties of nanowires by AFM.

the surface (Figure 1). Due to their light scattering properties, they can be localised in an optical microscope. Afterwards the position is mapped relative to the alignment marks, and the obtained coordinates are used to create a mask for the electrical contacts. The nanocontacts are prepared by e-beam lithography, Au evaporation, and lift off processing (Figure 1). A thin layer of chromium (Cr) is deposited first in order to improve the adhesion of gold on the $SiO_2$-surface.

Finally, the freestanding nanowires are realized by the undercut of the $SiO_2$. The sample is heated 13°C relative to the room temperature and is then placed into a chamber containing HF-vapour for 10 minutes (Figure 1). An example of a tungsten nanowire and the prepared Au nanocontacts is shown in Figure 4(a).

In a second method, nanowires can be contacted directly by writing the pads using Pt deposition by the focused ion beam (FIB) technique (see Figure 4(b)). A major disadvantage of the method is the possibility to contaminate the nanowires with Pt and carbon, which may alter the mechanical properties.

### 2.4. Chemical and structural characterisation

Chemical analysis of the solutions was performed by inductively-coupled plasma optical emission spectrometry (ICP-OES). Scanning electron microscopy was performed using a Leo 1550 VP apparatus (Leo Elektronenmikroskopie GmbH, Oberkochen, Germany) fitted with an INCA energy dispersive system (EDS) (Oxford Instruments, Oxford, UK).

A scanning electron microscope model JSM6500F from JEOL, Japan equipped with an EBSD detector from TSL was used for electron back scatter diffraction (EBSD) measurements. The patterns were recorded by a CCD camera (DigiView) 12 under a tilting angle of the sample stage of 70°. The acceleration voltage was 15 kV. The analysis of the individual EBSD patterns yielded the crystallographic orientations of the crystal at each position of the electron beam. In the present study, ACOM has been applied in a high-resolution, high-intensity SEM with field emission gun (JEOL JSM 6500 F). For pattern analysis, the TSL OIM analysis software was used.

### 2.5. Mechanical characterisation

#### 2.5.1. Bending (static) experiments

Static bending experiments were performed on singly clamped nanowires by exposing a force on a nanowire clamped on one side only. As a qualitative test of mechanical properties of the tungsten nanowires, a micromanipulator was used for bending experiments, which were observed by optical microscopy. Quantitative analysis was performed using an atomic force microscope (AFM) in order to obtain the Young's modulus. This analysis was performed on laterally aligned nanowires (Figure 5).

#### 2.5.2. Analysis of resonant oscillating nanowires

Dynamic studies can be performed on oscillating nanowires by analysis of the resonant frequency, which is given by the Euler-Bernoulli theory [22]:

$$f_{\text{res}} = \frac{\kappa^2}{2\pi l^2}\sqrt{\frac{EI}{\rho A}}, \tag{1}$$

with $k$ being a constant depending on the oscillation mode. For the singly and doubly clamped oscillators (Figure 6), the

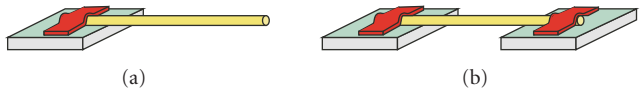


Figure 6: Basic configuration of nanowire-based resonators.

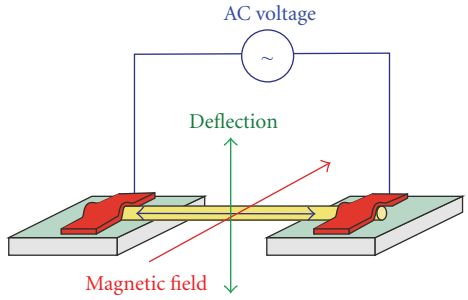


Figure 7: Magnetodynamic operation principle of doubly clamped nanowires with magnetomotive actuation and inductive sensing.

resonant frequency of the first flexural is then given by

$$f_{\text{res}} \approx 0.28\sqrt{\frac{E}{\rho}}\frac{R}{L^2}, \tag{2}$$

for singly clamped nanowires (cantilever), and

$$f_{\text{res}} \approx 1.78\sqrt{\frac{E}{\rho}}\frac{R}{L^2}, \tag{3}$$

for doubly clamped nanowires (bridge), with $E$ being the Young's modulus and $p$ the mass density of the resonator material, $R$ and $L$ are radius and length of the resonator beam, respectively. Consequently, resonators are powerful test structures for the determination of the Young's modulus on the nanoscale as long as the geometry can be determined accurately.

In this study, only doubly clamped nanowires were investigated. These resonators were operated by magneto motive actuation, the principle of which is shown in Figure 7. The conducting actuator was positioned in a static magnetic field, and the current through the actuator causes a Lorentz force to bring the device into motion [23, 24]. It is one of the most popular actuation mechanisms for NEMS devices [25].

## 3. RESULTS AND DISCUSSION

### 3.1. Nanowire crystallography

There are several methods available to produce tungsten nanowires. However, none of the techniques is able to yield a self-organised array of the single crystalline tungsten nanowires except the method presented here.

Figure 2(a) shows an array of tungsten nanowires embedded in the NiAl matrix. In order to establish whether they are single crystalline as well as determine the growth direction of the two eutectic phases (NiAl and W) and their interfacial planes, orientation imaging microscopy (OIM) was used. EBSD patterns taken from the NiAl matrix and the W nanowires at different locations of the sample are depicted in Figure 2(b). First of all, the identity of the patterns from the NiAl matrix shows that the matrix is single crystalline. Also, the patterns obtained from different nanowires show well-defined Kikuchi lines, proving that they are single crystalline. Moreover, the symmetry and parallelism of the patterns indicate that the nanowires have the same crystallographic orientation, even azimuthally. This practically proves that this method surpasses the drawbacks of the other available methods and is capable of yielding self-organised arrays of the single crystalline tungsten nanowires.

An interesting aspect of directionally solidified eutectics is a preferred crystallographic orientation relationship between the phases. The existence of such specific crystallographic relationships is ascribed to the minimisation of the interface energy between the phases. Cantor [26] has reviewed the evidence for the development of special crystallographic relationships during directional solidification of eutectic alloys and shown that behaviours ranging from strict epitaxial to completely independent growth can occur.

The crystallographic orientation relationship was found to be cube-on-cube, which is characteristic for eutectic alloys containing phases with similar structures, such as NiAl-Cr, Mo, and V. As W also has a BCC structure which is crystallographically identical to the B2 ordered structure of NiAl, they also adopt identical growth textures and form a unique orientation relationship.

### 3.2. Flexibility

As a qualitative test of the mechanical properties of the tungsten nanowires, bending with a micromanipulator was carried out. The sequence of images (Figures 8(a)–8(d)), comprised of snapshots from a video, demonstrates totally elastic bending of a nanowire, even after several load-unload cycles, which is unusual for a brittle material like tungsten. Both high elasticity and ductility of the nanowires observed during bending experiments brought up a necessity for more accurate and quantitative measurements of the mechanical properties which are described in the following sections.

### 3.3. Young's modulus of nanowires by static bending

A singly clamped tungsten nanowire prepared by the FIB technique is shown in Figure 9. An example for the analysis of lateral positioned nanowires by lateral force microscopy (LFM) is presented in Figure 10. The singly clamped nanowire (see Figure 9) is scanned at different points along the nanowire and lateral deflection of the AFM cantilever is recorded. Figure 10(b) shows three selected line scans separated by about 300 nm. It can clearly be seen that the lateral deflection, and thus the applied force increases when scanning approximate the anchor point, and that the nanowire is released after stronger bending.

Consequently, as expected the stiffness (spring constant) of the nanowire increases with decreased distance to the anchor point, that is, with shorter nanowires. The stiffness value is used to calculate the Young's modulus. A major difficulty in LFM, however, is the accurate determination of the

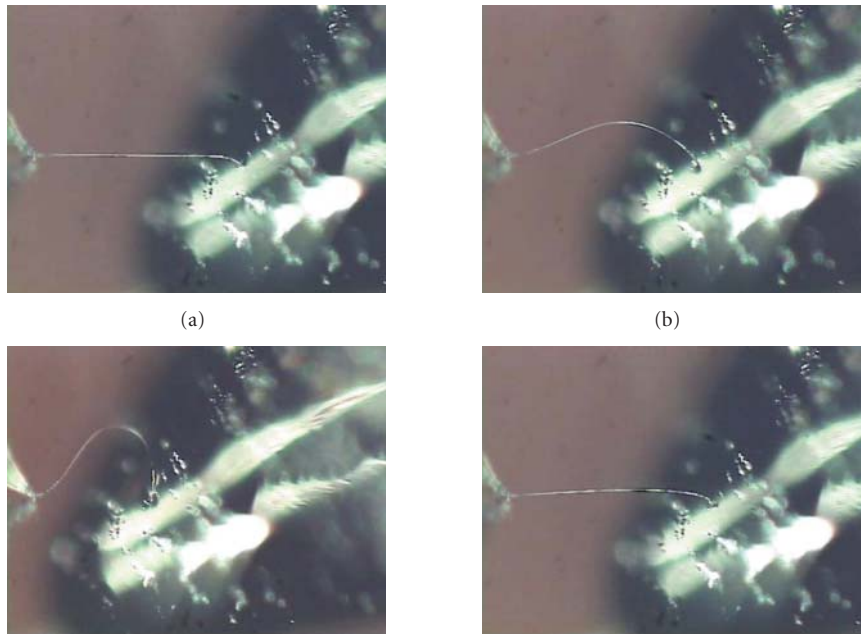


Figure 8: Series of optical images showing the flexibility of tungsten nanowires.

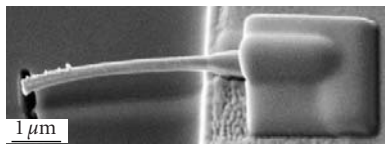


Figure 9: Typical singly clamped lateral aligned tungsten nanowire prepared by FIB on $SiO_2$/Si substrates with Au pads.

lateral force in Figure 10(b), since the torsional lattice constant of the AFM cantilever cannot be determined with the required accuracy. In contrast, the vertical bending lattice constant of the AFM cantilevers can be obtained with much higher accuracy (e.g., from the resonant frequency), the application of force-displacement curves is much more reliable for the determinations of the Young's modulus. Figure 11 shows the force-displacement curves on the same tungsten nanowire. Similar to the LFM analysis, the stiffness $k_{\text{eff}}$ of the system can be determined from the slope in Figure 11(b). The lattice constant $k_{\text{NW}}$ of the tungsten nanowire is

$$k_{\text{NW}} = \frac{k_{\text{eff}}\, k_{\text{cantilever}}}{k_{\text{eff}} - k_{\text{cantilever}}}, \tag{4}$$

with the spring constant $k_{\text{cantilever}}$ of the silicon cantilever. Finally, the Young's modulus of the tungsten nanowire is given by

$$E = \frac{4L^3}{3\pi R_{\text{NW}}^4} k_{\text{NW}}. \tag{5}$$

The determined values in dependence on the position on the nanowire are shown in Figure 12. For this nanowire, an average Young's modulus of $E_0 = 332$ GPa was extracted. The analysis of several nanowires results in an average Young's modulus of $E_0 = 362 \pm 62$ GPa, which is very close to the bulk value of $E_0 = 355$ GPa [27]. Nanowires prepared by the e-beam-based technology had a slightly smaller value, however, this difference is within the accuracy of the measurements. As a consequence, nanowires down to 100 nm diameter exhibit a Young's modulus, which does not show dependence on the diameter and is not different from the bulk value.

### 3.4. Young's modulus from resonant oscillating nanowires

In the case of oscillating nanowires, the Young's modulus is calculated from the measured resonant frequency of magnetomotively driven, doubly clamped nanowires as described in Section 2.5.2. Figure 13 shows the resonant curve of a nanoresonator (insert) prepared by FIB-contacting of a tungsten nanowire.

The calculated Young's modulus (E~450 GPa) for this structure strongly differs from the bulk value. Generally, the dynamic measurements yield to higher values for the Young's modulus (400–650 GPa). The main reason for this phenomenon is the high contamination during the processing. All the resonator bridges were prepared by the FIB technique, and Auger electron spectroscopic investigations have shown that these nanowires were higher contaminated with carbon and traces of Pt then the singly-clamped nanowires used for the static measurements. As a consequence, the highest values for the apparent Young's modulus were obtained for the nanowires with the highest contamination level. These contaminations affect the resonant behaviour of the nanowire by simple mass loading $\Delta m$ according to

$$\Delta f_{\text{res}} = -\frac{1}{2} f_{\text{res}} \frac{\Delta m}{m}, \tag{6}$$

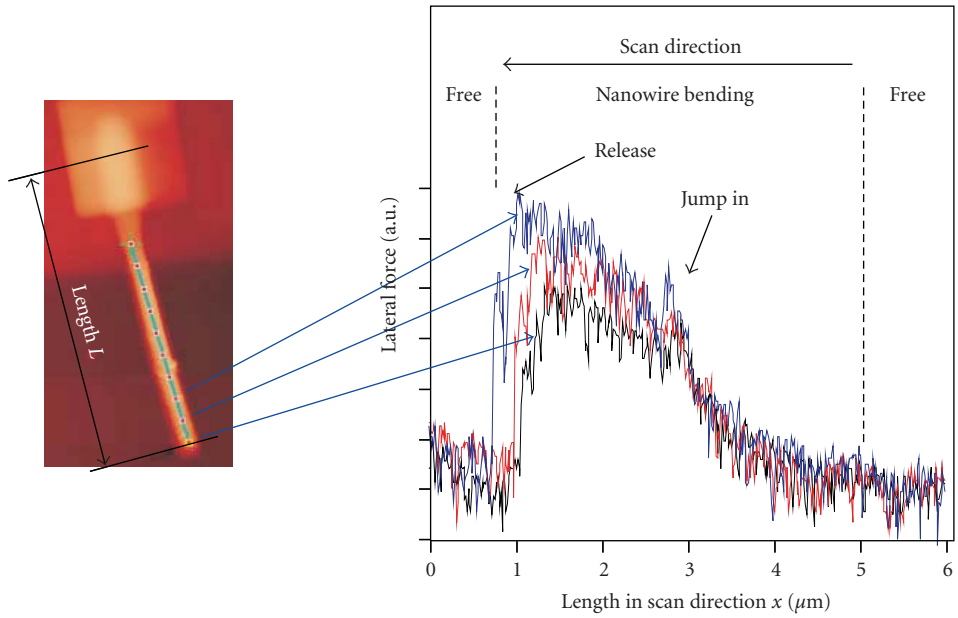


FIGURE 10: LFM analysis on a tungsten nanowire: (a) AFM topography image, (b) 3 selected LFM line scans, recorded crossing the marked points on the nanowire.

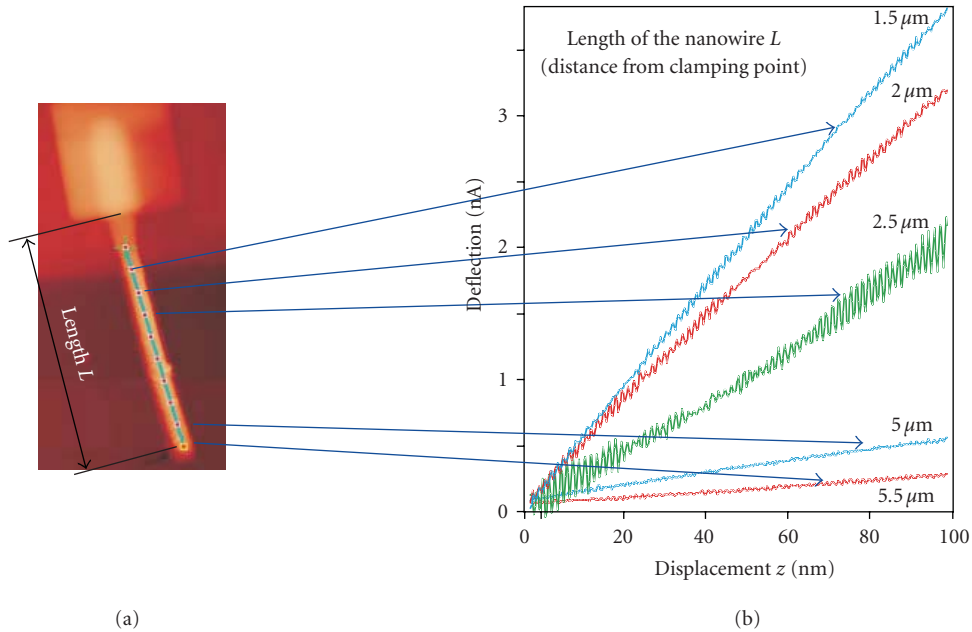


FIGURE 11: Force displacement analysis of a W nanowire: (a) AFM topography image, (b) selected *F*-*z* curves, recorded crossing the marked points on the nanowire.

or by introducing additional strain, which also alters the resonant frequency [28–30]. Consequently, the apparent Young's modulus is not representative for the pure tungsten nanowire but an effective value for the processed nanoresonator. This observation underlines the importance of controlling the processing technologies, the nanowire surfaces, and the environment with highest accuracy while maintaining absolute cleanliness. On the other hand, this phenomenon gives rise to an attractive possibility of using nanowires as highly sensitive sensors [31]. For further qualitative analysis of this effect, two coupled resonators on the same nanowire were investigated (Figure 14).

After bending of a single tungsten nanowire, the original resonator with a resonant frequency of $f_{res}$ = 117 kHz

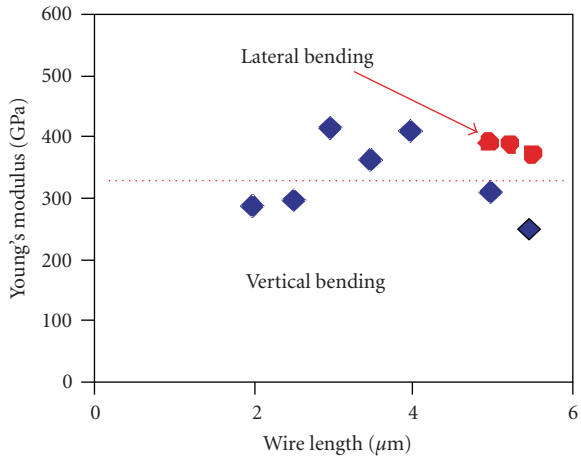


FIGURE 12: Calculated values for the Young's modulus of tungsten nanowires in dependence on the measurement point. The dashed line represents the average value from all measurements.

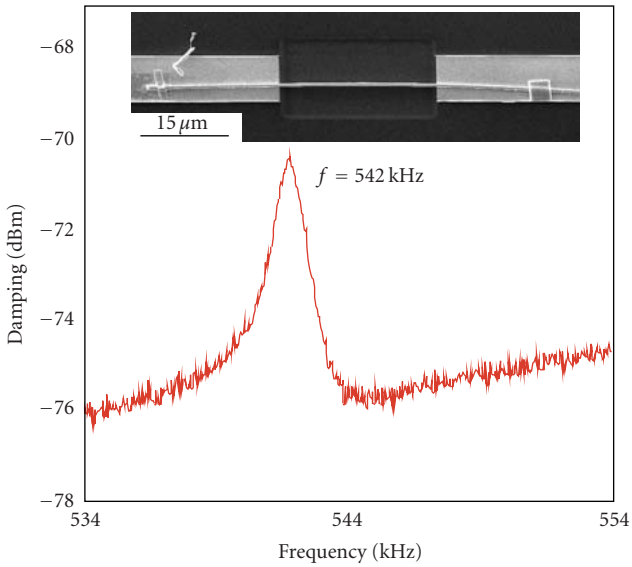


FIGURE 13: Resonance curve of a tungsten nanowire measured by the magnetomotive principle.

(I) splits into two resonators with each with its own resonant frequency (II). After a long-term exposure of the nanowires to air, these two resonant frequencies shift further to higher values (III) indicating a modified structure. Auger electron spectroscopy showed an increased amount of oxygen and carbon on the nanowire surface demonstrating again the high sensitivity of the properties of nanowires to surface modifications. Thus, in contrast to the almost constant behaviour in static bending experiments, contamination and oxidation have a strong influence on the resonant oscillation behaviour of the nanowire, which leads one to expect a discontinuous surface film. The quantification of the influence of these additional surface layers on the mechanical properties of the nanowires and the development of a corresponding analytical model is the subject of the ongoing studies.

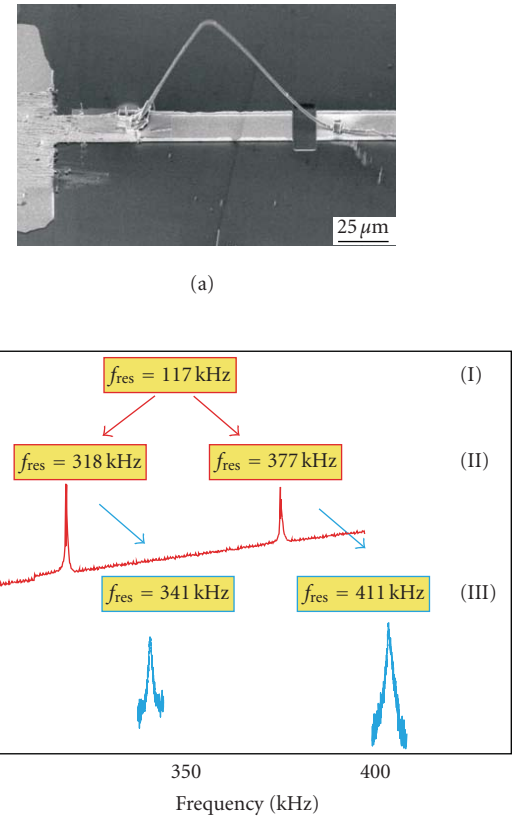


FIGURE 14: (a) Bended, doubly clamped tungsten nanowire resonator and (b) corresponding resonant curves: (I) single resonant frequency before bending, (II) two resonant peaks after bending, and (III) two shifted resonant peaks after 2 months exposure to air.

## 4. SUMMARY

In this study, single crystalline tungsten nanowires were grown by directional solidification of NiAl-W alloys and were chemically released. Single crystallinity and parallel crystallographic orientation were proven by EBSD. These nanowires were further processed to realise freestanding structures for mechanical characterisation. By different mechanical analysis techniques, it was shown that single crystalline tungsten nanowires with diameters down to 100 nm exhibit a Young's modulus, which is comparable to the bulk value. In bending experiments, these tungsten nanowires have shown a high stability. However, particularly the analysis of resonant nanowire structures revealed that the mechanical properties can be drastically altered by the processing technology and the exposure to the ambient environment. In contrast to semiconducting nanowires such as ZnO, the effective Young's modulus increases. These observations have a high impact on the design of nanowire-based nanomechanical devices. The increased effective Young's modulus is the consequence of the observed contamination and the formation of a surface oxide on the tungsten wire, which alters the geometry as well as the internal strain. A quantitative analysis of this effect will be the subject of future investigations.

## ACKNOWLEDGMENTS

The financial support of the DFG through the projects CI 148/2 and HA 3118/4-2 within the frame of the priority programme SPP 1165 "Nanowires and Nanotubes, from controlled synthesis to function" and AM 105/1 within the frame of the priority programme SPP 1157 "Integrierte Elektrokeramische Funktionsstrukturen" is gratefully acknowledged.

## REFERENCES

[1] P. Villars and L. D. Calvert, *Pearson's Handbook of Crystallographic Data for Intermetallic Phases*, American Society for Metals, Metals Park, Materials Park, Ohio, USA, 1985.

[2] J. B. Lambert and J. J. Rausch, "Refractory metals and alloys," in *Metals Handbook Vol. 2. Properties and Selection: Nonferrous Alloys and Special-Purpose Materials*, pp. 558–585, ASM International, Materials Park, Ohio, USA, 10th edition, 1990.

[3] A. V. Melechko, V. I. Merkulov, T. E. McKnight, et al., "Vertically aligned carbon nanofibers and related structures: controlled synthesis and directed assembly," *Journal of Applied Physics*, vol. 97, no. 4, Article ID 041301, 39 pages, 2005.

[4] D.-L. Chen and T.-C. Chen, "Mechanical properties of Au nanowires under uniaxial tension with high strain-rate by molecular dynamics," *Nanotechnology*, vol. 16, no. 12, pp. 2972–2981, 2005.

[5] H. S. Park and J. A Zimmerman, "Modelling inelasticity and failure in gold nanowires," *Physical Review B*, vol. 72, no. 5, Article ID 054106, 9 pages, 2005.

[6] Y. S. Kwon, A. A. Gromov, A. P. Ilyin, et al., "Features of passivation, oxidation and combustion of tungsten nanopowders by air," *International Journal of Refractory Metals and Hard Materials*, vol. 22, no. 6, pp. 235–241, 2004.

[7] B. Wu, A. Heidelberg, J. J. Boland, J. E. Sader, X. Sun, and Y. Li, "Microstructure-hardened silver nanowires," *Nano Letters*, vol. 6, no. 3, pp. 468–472, 2006.

[8] M. D. Uchic, D. M. Dimiduk, J. N. Florando, and W. D. Nix, "Sample dimensions influence strength and crystal plasticity," *Science*, vol. 305, no. 5686, pp. 986–989, 2004.

[9] Z. L. Wang, "Mechanical properties of nanowires and nanobelts," in *Dekker Encyclopedia of Nanoscience and Nanotechnology*, pp. 1773–1786, Marcel Dekker, New York, NY, USA, 2004.

[10] A. W. Hassel, B. Bello-Rodriguez, S. Milenkovic, and A. Schneider, "Electrochemical production of nanopore arrays in a nickel aluminium alloy," *Electrochimica Acta*, vol. 50, no. 15, pp. 3033–3039, 2005.

[11] A. W. Hassel, A. J. Smith, and S. Milenkovic, "Nanostructures from directionally solidified NiAl-W eutectic alloys," *Electrochimica Acta*, vol. 52, no. 4, pp. 1799–1804, 2006.

[12] S. Milenkovic, A. J. Smith, and A. W. Hassel, "Single crystalline Mo nanowires, nanowire arrays and nanopore arrays in nickel-aluminum," *Journal of Nanoscience and Nanotechnology*. In press.

[13] S. Brittman, A. J. Smith, S. Milenkovic, and A. W. Hassel, "Copper nanowires and silver micropit arrays from the electrochemical treatment of a directionally solidified silver-copper eutectic," *Electrochimica Acta*, vol. 53, no. 2, pp. 324–329, 2007.

[14] S. Milenkovic, A. W. Hassel, and A. Schneider, "Gold nanostructures by directional solid-state decomposition," *Gold Bulletin*, vol. 39, no. 4, pp. 185–191, 2006.

[15] Y. Chen, S. Milenkovic, and A. W. Hassel, "Arrays of isooriented gold nanobelts," *Nano Letters*, vol. 8, no. 2, pp. 737–742, 2008.

[16] S. Milenkovic, A. W. Hassel, and A. Schneider, "Effect of the growth conditions on the spatial features of Re nanowires produced by directional solidification," *Nano Letters*, vol. 6, no. 4, pp. 794–799, 2006.

[17] A. W. Hassel, S. Milenkovic, U. Schürmann, et al., "Model systems with extreme aspect ratio, tuneable geometry, and surface functionality for a quantitative investigation of the lotus effect," *Langmuir*, vol. 23, no. 4, pp. 2091–2094, 2007.

[18] L. Philippe, I. Peyrot, J. Michler, A. W. Hassel, and S. Milenkovic, "Yield strength of monocrystalline rhenium nanowires," *Applied Physics Letters*, vol. 91, no. 11, Article ID 111919, 3 pages, 2007.

[19] H. Bei, S. Shim, E. P. George, M. K. Miller, E. G. Herbert, and G. M. Pharr, "Compressive strengths of molybdenum alloy micro-pillars prepared using a new technique," *Scripta Materialia*, vol. 57, no. 5, pp. 397–400, 2007.

[20] M. Niebelschütz, V. Cimalla, O. Ambacher, T. Machleidt, J. Ristic, and E. Calleja, "Electrical performance of gallium nitride nanocolumns," *Physica E*, vol. 37, no. 1-2, pp. 200–203, 2007.

[21] W. I. Jang, C. A. Choi, M. L. Lee, C. H. Jun, and Y. T. Kim, "Fabrication of MEMS devices by using anhydrous HF gas-phase etching with alcoholic vapour," *Journal of Micromechanics and Microengineering*, vol. 12, no. 3, pp. 297–306, 2002.

[22] W. Weaver Jr., S. P. Timoshenko, and D. H. Young, *Vibration Problems in Engineering*, John Wiley & Sons, New York, NY, USA, 5th edition, 1990.

[23] A. N. Cleland and M. L. Roukes, "Fabrication of high frequency nanometer scale mechanical resonators from bulk Si crystals," *Applied Physics Letters*, vol. 69, no. 18, pp. 2653–2655, 1996.

[24] K. Brückner, V. Cimalla, F. Niebelschütz, et al., "Strain- and pressure-dependent RF response of microelectromechanical resonators for sensing applications," *Journal of Micromechanics and Microengineering*, vol. 17, no. 10, pp. 2016–2023, 2007.

[25] K. L. Ekinci and M. L. Roukes, "Nanoelectromechanical systems," *Review of Scientific Instruments*, vol. 76, no. 6, Article ID 061101, 12 pages, 2005.

[26] B. Cantor, "Interphase interfaces," in *Grain Boundary Structure and Properties*, G. A. Chadwick and D. A. Smith, Eds., Academic Press, London, UK, 1976.

[27] D. Mende and G. Simon, *Physik—Gleichungen und Tabellen*, VEB Fachbuchverlag, Leipzig, Germany, 1986.

[28] V. Cimalla, F. Will, K. Tonisch, et al., "Nanoelectromechanical devices for ultra sensitive sensors," *Sensors and Actuators B*, vol. 126, no. 1, pp. 24–34, 2006.

[29] V. Cimalla, Ch. Föerster, F. Will, et al., "Pulsed mode operation of strained microelectromechanical resonators in air," *Applied Physics Letters*, vol. 88, no. 25, Article ID 253501, 3 pages, 2006.

[30] S. S. Verbridge, J. M. Parpia, R. B. Reichenbach, L. M. Bellan, and H. G. Craighead, "High quality factor resonance at room temperature with nanostrings under high tensile stress," *Journal of Applied Physics*, vol. 99, no. 12, Article ID 124304, 8 pages, 2006.

[31] X. M. H. Huang, M. Manolidis, S. C. Jun, and J. Hone, "Nanomechanical hydrogen sensing," *Applied Physics Letters*, vol. 86, no. 14, Article ID 143104, 3 pages, 2005.

Hindawi Publishing Corporation
Journal of Nanomaterials
Volume 2008, Article ID 849745, 7 pages
doi:10.1155/2008/849745

*Research Article*

# Synthesis and Elastic Characterization of Zinc Oxide Nanowires

**M. P. Manoharan, A. V. Desai, G. Neely, and M. A. Haque**

*Department of Mechanical and Nuclear Engineering, The Pennsylvania State University, University Park, PA 16802, USA*

Correspondence should be addressed to M. A. Haque, mah37@engr.psu.edu

Received 20 August 2007; Accepted 24 January 2008

Recommended by Jun Lou

Zinc oxide nanowires, nanobelts, and nanoneedles were synthesized using the vapor-liquid-solid technique. Young's modulus of the nanowires was measured by performing cantilever bending experiments on individual nanowires in situ inside a scanning electron microscope. The nanowires tested had diameters in the range of 200–750 nm. The average Young's modulus, measured to be 40 GPa, is about 30% of that reported at the bulk scale. The experimental results are discussed in light of the pronounced electromechanical coupling due to the piezoelectric nature of the material.



## 1. INTRODUCTION

Zinc oxide (ZnO) exhibits several unique properties, such as being a semiconductor and a piezoelectric material [1], and consequently, is used in a wide variety of sensors and actuators. ZnO nanostructures are being explored for a wide range of applications in nanoscale devices, such as nanogenerators [2], gas sensors [3], field emission transistors [4], nanocantilevers [5], and in biomedical systems, such as ultrasensitive DNA sequence detectors [6]. Apart from the technological significance of ZnO nanostructures, their quasi one-dimensional structure with diameters in the range of tens of nanometers to hundreds of nanometers makes them interesting from a scientific point of view. In this size range, they are expected to possess interesting physical properties and pronounced coupling that are quite different from their bulk counterpart [7].

Although ZnO nanowires are touted as the next generation materials for use in nanoscale systems [8], very few experimental investigations on their mechanical properties are reported in literature. The lack of experimental studies is mainly due to the challenges of material characterization at the nanoscale, such as (i) specimen manipulation, alignment, and gripping to achieve the desired boundary conditions, and (ii) application and measurement of force and displacement with very high resolution [1]. Additionally, ability to perform in situ experiments is important for nanoscale materials characterization. In situ experiments, usually conducted in analytical chambers such as the scanning or transmission electron microscope (SEM or TEM), enable direct visualization of the events as they occur, thus providing qualitative information along with quantitative data. In situ experiments also ensure accuracy of the experimental procedures, which is challenging to supervise at the nanoscale.

In this paper, we study the effect of temperature and gas flow rate on the growth of different zinc oxide nanostructures synthesized using the vapor-liquid-solid (VLS) technique and present experimental results on Young's modulus of single ZnO nanowires. The modulus was measured by bending the nanowire in a cantilever configuration inside a SEM, enabled for in situ observations. In Section 2, we review the main techniques in literature for mechanical characterization at the nanoscale, and experimental results on Young's modulus of zinc oxide nanostructures.

## 2. REVIEW OF NANOMECHANICAL EXPERIMENTAL TECHNIQUES AND YOUNG'S MODULUS VALUES FOR ZINC OXIDE NANOSTRUCTURES

One of the direct techniques to measure Young's modulus of materials is uniaxial tensile testing. However, it is difficult to adapt this technique for nanoscale material characterization, due to the reasons mentioned in Section 1. Microelectromechanical systems (MEMS) are used as test beds for characterizing the mechanical properties of nanostructures to circumvent some of these problems at the cost of complexity in

Table 1: Young's modulus values of ZnO nanostructures reported in literature.

| No. | Young's modulus (GPa) | Nanostructure type | Reference | Technique |
|---|---|---|---|---|
| (1) | 52 | Nanobelts | [9] | Mechanical resonance in TEM |
| (2) | 50 | Nanobelts | [10] | TEM resonance |
| (4) | 29 ± 8 | Nanowire | [11] | AFM bending (vertical nanowires) |
| (5) | 140–210 (size effect reported) | Nanowire | [12] | SEM resonance |
| (6) | 58 | Nanowire | [13] | TEM resonance |
| (7) | 90–100 | Nanowire | [14] | Nanoindentation |
| (8) | 38.2 by AFM<br>31.3 by nanoindentation | Nanobelt | [15] | Nanoindentation and 3-point AFM bending |
| (9) | 106 ± 25 | Nanowire | [16] | Detecting resonance under an optical microscope |
| (10) | 97 ± 18 | Nanowire | [17] | Tensile and cantilever bending experiments, measured modulus only at fracture |
| (11) | 117, 229 (100 nm diameter)<br>232, 454 (30 nm diameter) | Nanowire | [18] | Buckling of nanowires using nanoindentation |

device design and fabrication [19–21]. Desai and Haque [1] have used the uniaxial tensile testing technique to measure Young's modulus of ZnO nanowires. It is interesting to note that the authors reported fracture strains as high as 15% for the nanowires, which is unusual considering that bulk ZnO is a brittle material at the bulk scale [22]. Young's modulus of nanowires can also be extracted from the resonant frequency of a single nanowire, induced by an alternating electric field. As examples, researchers have used this dynamic characterization technique to measure the modulus of zinc oxide nanowires [13], carbon nanotubes [23], and gallium nitride nanowires [24].

The quasi-static counterpart of the dynamic experiments essentially involves bending the nanowire specimen with a very soft spring (e.g., cantilever beam). The experiment is generally performed using an Atomic Force Microscope (AFM). Here, the deformation is primarily strain gradient dominant at the rigid support. Song et al. [11] and Hoffmann et al. [17] have used this technique to measure Young's modulus of ZnO nanowires. It is important to note that the effect of varying levels of strain gradient in these experiments (caused by bending) may result in significant deviation in the mechanical properties, because of the piezo-electric nature of the material. AFM-based experiments are popular techniques for mechanical characterization, because the stiffness of the tip is very small, and hence, the force measurement resolution is very high (on the order of nano-Newtons). However, understanding the tip-nanowire interaction is crucial for accurate and reliable experimental studies. For instance, friction (due to slipping) and van der Waals forces between the nanowire and tip will introduce errors in the measurement of mechanical properties [25]. The influence of these surface forces on the mechanical properties will be more significant in the case of smaller diameter (less than 30–40 nm) or high aspect ratio nanowires (greater than 100), where the magnitude of forces is very small (on the order of pico-Newtons to few nano-Newtons). It is also important to note that specimen geometry, crystallographic orientation, synthesis process, and the nature of experimental technique–uniform strain versus strain gradient-dominant and static versus dynamic deformation, all significantly affect the experimental results. Consequently, a huge spread is observed in Young's modulus values reported in literature for zinc oxide nanowires, as summarized in Table 1.

In this paper, we present results on in situ cantilever bending experiments inside a Focused Ion Beam–Scanning Electron Microscope (FIB-SEM) on ZnO nanowires. These experiments provide information on the elasticity of ZnO nanowires determined using a quasi-static and strain gradient-dominated technique. In situ experiments enabled us to observe the nanowires-tip interaction during the experiment. In Section 3, we discuss the synthesis process of zinc oxide nanowires.

## 3. NANOWIRE SYNTHESIS PROCESS

We synthesized the zinc oxide nanowires by the vapor-liquid-solid (VLS) mechanism [26] using gold as a catalyst. The

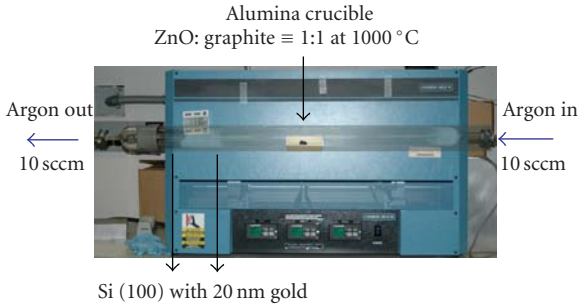


Figure 1: Vapor-liquid-solid synthesis chamber and process description.

Lindberg Anneal single tube furnace (Blue M) was used for the nanowire growth process; the schematic of the furnace is shown in Figure 1. We started with ZnO powder (Alfa Aesar, 99.99%) and graphite powder (Alfa Aesar, 99.99%) in 1 : 1 ratio by weight in an alumina crucible inside the furnace. Argon gas was allowed to flow in the tube (from right to left in Figure 1) at 10 sccm. The silicon (Si) substrates with 20 nm gold (Au) films (on [100] silicon surface) were placed downstream from the crucible, and served as the platform for nanowire growth.

As the temperature of the crucible increases to approximately 1000°C, the ZnO powder is reduced by graphite to form zinc (Zn), carbon monoxide (CO), and carbon dioxide ($CO_2$) vapors. The argon gas carries these vapor-phase products to the silicon samples placed at different temperatures. Meanwhile, gold and silicon droplets form a eutectic alloy at each catalyst site. The gaseous products produced by the reduction reaction adsorb and condense on the alloy droplets. Subsequently, the ZnO nanowire synthesis reaction is catalyzed by the Au-Si alloy at solid-liquid interface to form zinc oxide nanowires [27]. The ZnO vapor saturates the alloy droplet, followed by the nucleation and growth of solid ZnO nanowire, due to the super saturation of the liquid droplet. Incremental growth of the nanowire taking place at the droplet interface, constantly pushes the catalyst upwards until no more zinc vapor is available, or all the gold is used up. We observed nanowire growth from around 500°C to 900°C, the diameters of the nanowire ranged from 30 nm to 750 nm and the lengths were up to 100 $\mu$m. Some of the nanowires had a gold tip on the end (Figure 2(c)), indicating VLS mechanism for the growth process. We also observed nanobelt (Figure 2(a)) and nanoneedles (Figure 2(b)) formation in the lower-temperature regions. In Section 4, we discuss the sample preparation techniques for mechanical characterization experiments (cantilever bending) of nanowires.

## 4. SPECIMEN PREPARATION

The ZnO nanowires grown by VLS mechanism generally occurred as clusters, but individual nanowires are required for the experiments. Individual ZnO nanowires were picked using a micromanipulator (Creative Devices Inc., NJ, USA) fitted with an electrochemically sharpened tungsten probe tip. The nanowires adhere to the probe tip due to both short- and

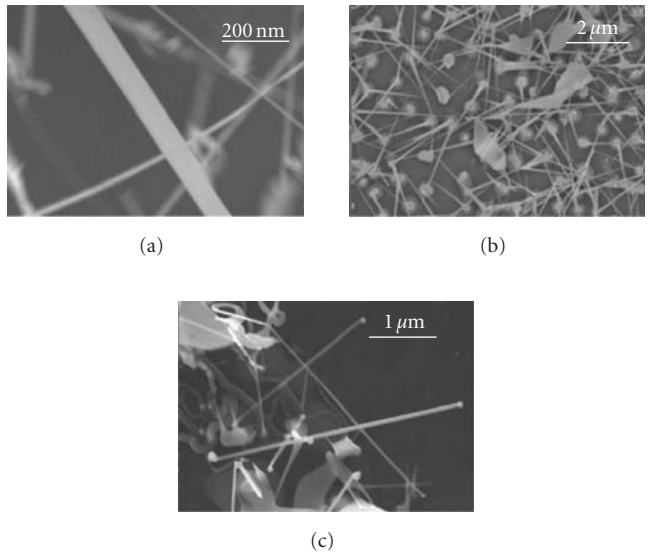


Figure 2: Effect of synthesis temperature on the geometry of nanostructures: (a) nanobelts at 650–700°C, (b) nanoneedles at 825–875°C, (c) nanowires at 900–950°C.

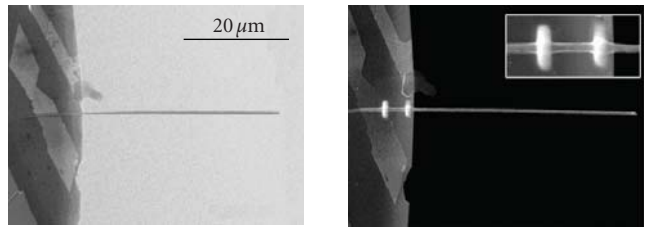


Figure 3: Zinc oxide nanowire (a) before and (b) after "gluing" with platinum in FIB-SEM. Inset in (b) shows platinum deposition on the nanowire near the edge of the wafer.

long-range attractive forces, which we generically term as van der Waal's forces. The nanowire was then placed on the edge of a chip of silicon wafer (coated with 100 nm thick gold film to improve imaging in SEM), as shown in Figure 3(a). The nanowire was oriented perpendicular to the edge of the silicon wafer using the probe tip. We "glued" the end of the nanowire near the edge of the silicon wafer by platinum deposition using a focused ion beam (FIB) (FEI Quanta 3D 200 FIB/SEM), as shown in Figure 3(b). The inset in Figure 3(b) shows the platinum deposition or "glue" on the nanowire near the edge of the silicon wafer. The microscale version of the pick-and-place technique is time intensive, but enables us to consistently prepare long nanowire specimens for the experiments. In Section 5, we discuss the experimental technique and results on Young's modulus of ZnO nanowires.

## 5. EXPERIMENTAL SETUP AND RESULTS

We performed cantilever-bending experiments to estimate Young's modulus of the nanowires. Bending loads were applied on the nanowires using an AFM cantilever with a

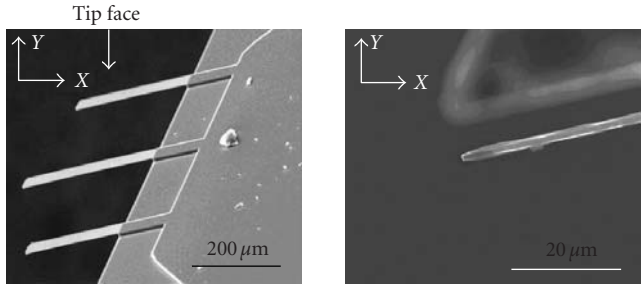


(a) (b)

Figure 4: (a) Tipless AFM cantilever (b) when mounted on the tungsten tip in the omniprobe.

known spring constant. The AFM cantilever (MikroMasch, CSC12) was mounted on the tungsten probe tip in the omniprobe (a three-axis piezoelectric actuator in the FIB-SEM) along the $x$-axis (Figure 4(a), probe is not shown in image). The SEM image plane is the $X$-$Y$ plane.

We then tilted the probe such that the tip face was aligned perpendicular to the viewing screen (parallel to the $Z$-axis) (Figure 4(b)). This ensures that the loading direction is in the desired plane ($X$-$Y$ plane).

We then mounted the nanowire specimen inside the SEM chamber, and rotated the SEM stage (about the $Z$-axis) to align the longitudinal axis (length) of the nanowire parallel to the length of the AFM cantilever (Figure 5(a)). This ensures that the central axis of the nanowire and AFM tip are parallel before loading. We then tilted the stage (around the $x$-axis) to verify that the nanowire is completely in the $X$-$Y$ plane. After ensuring that the nanowire and the AFM tip were aligned, we performed the cantilever-bending experiment inside the SEM. The schematic of the bending experiment is shown in Figure 5(a). Note that Figure 5(a) is not to scale and in reality, the nanowire is thinner than the AFM cantilever. Figure 5(b) shows the in situ bending experiment inside the SEM.

The AFM cantilever moves vertically downwards (negative $Y$ direction) to vertically load the nanowire and the deflection of the AFM cantilever and nanowire tip are the same. We can estimate Young's modulus of the nanowire from the deflections of the AFM cantilever base and nanowire tip.

We assume the following conditions for the cantilever bending experiments:

(1) clamped fixed end,
(2) small nanowire tip deflections (valid for $y_{nw}/l \leq 0.1$, where $y_{nw}$ and $l$ are the tip deflection and length of the nanowire, resp.).

Based on these assumptions, the normal or tensile bending stress ($\sigma$) and the normal or tensile bending strain ($\varepsilon$) on the nanowire, during the cantilever bending are given by

$$\sigma = \frac{32k_{tip}(y_{base} - y_{nw})l}{\pi d^3}, \qquad \varepsilon = \frac{3y_{nw}d}{2l^2}, \tag{1}$$

where $k_{tip}$ is the stiffness of the AFM cantilever tip, $y_{base}$ is the displacement of the AFM cantilever base, $y_{nw}$ is the displacement of the nanowire, $d$ is the diameter of the nanowire, and the stresses and strains are the maximum values that occur on the outermost diameter of the nanowire at the clamped end. The deflections of the nanowire and AFM cantilever base are estimated from processing the SEM images during the loading experiments. Thus, using the deflection values of the AFM cantilever base and nanowire tip and (1), we can estimate the normal stress and strain on the nanowire, and plot a stress-strain diagram. The slope of the stress-strain curve (linear fit) is Young's modulus of the nanowire. We performed cantilever bending experiments inside the SEM on ZnO nanowires specimens with diameters ranging from 350–750 nm and did not observe any dependence of Young's modulus on the diameter of the nanowire. Figure 6 shows a representative stress-strain diagram. Young's modulus values of the nanowires (five specimens) ranged from 35 GPa to 44 GPa, which is within the expected error in the experimental data. In some of the bending experiments, the deflections of the nanowires were large and the expressions for stress and strain (1) are not accurate. In those cases, the nonlinear moment curvature differential equation is numerically solved to match the bending profile of the nanowire to obtain more accurate values of the stresses and strains (details in [25]).

For mechanical measurements, the boundary condition of the cantilever support is critical for an accurate estimation of the properties. Typically, the nanowire specimen is clamped with electron-beam-induced deposition [28, 29] or the focused ion beam-based platinum deposition (FIB-Pt) [19], which might introduce ion beam induced stresses [25]. However, our in situ SEM observations show that for nanoscale bending experiments on specimens without deposition-based clamping, there is no observable rotation of the nanowire at the fixed end. This suggests that specimen-substrate adhesion could be strong enough to work as a clamping mechanism.

In order to study the effect of boundary conditions, we repeated the experiment on adhesion-clamped specimens prepared using the technique employed by Ding et al. [29]. From the experiments on adhesion-clamped specimens, we measured Young's modulus of the nanowires to vary from 18 GPa to 27 GPa (four specimens), and the range of diameters was from 200 nm to 330 nm. This discrepancy can be attributed largely to the difference in boundary conditions in the two specimen clamping techniques. If the applied bending force is comparable to the adhesion and friction forces, the rigid support boundary condition is no longer valid, as the nanowire has free boundary conditions on a significant part of its outer surface. In Section 6, the synthesis process and the experimental results are discussed.

## 6. DISCUSSION

We studied the effects of temperature on the synthesis of ZnO nanostructures using the VLS technique, and subsequently characterized their elastic properties. We observed no nanowire growth at gas flow rates higher than 10 sccm implying that the zinc, carbon monoxide, and carbon dioxide

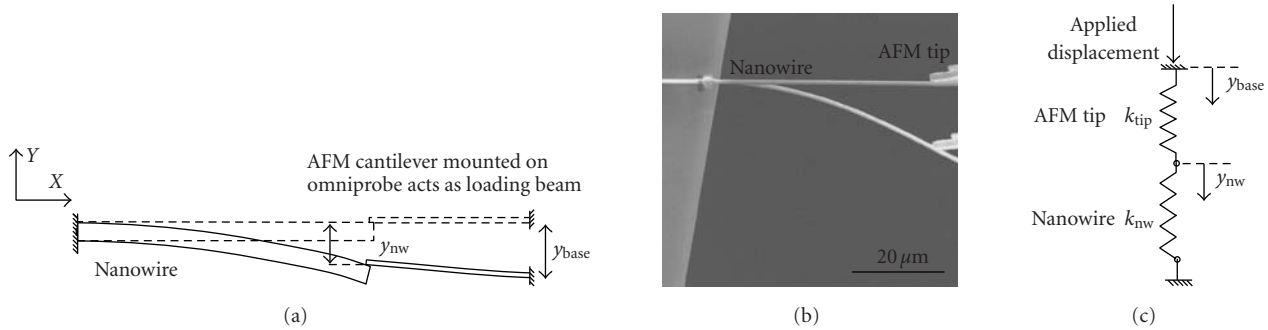


Figure 5: (a) Schematic of nanowire-bending experiment, (b) superimposed images from the in situ bending experiment inside the SEM showing the specimen and only the tip of the loading structure and (c) "spring" equivalent of the experimental setup.

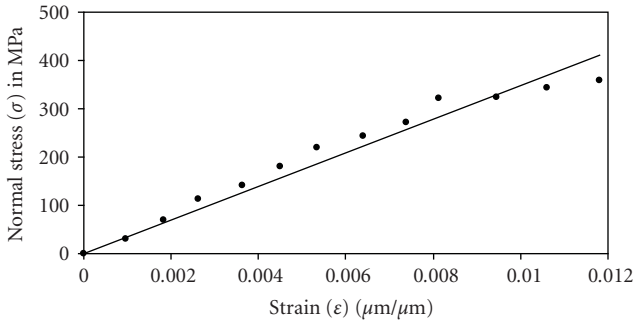


Figure 6: Stress-strain diagram for a ZnO nanowire specimen.

vapors are carried away rapidly from the substrates and do not have enough time to react at the silicon-gold interface. In most of the cases, the nanowire growth temperatures were between 500 and 800°C, which is consistent with the binary phase diagram of gold and zinc [30]. Ideally, the nanowire growth temperatures should be set between the eutectic temperature (683°C) for gold and zinc and melting point of zinc (420°C), reaching a maximum of 750°C [31]. However, it should be noted that the equilibrium phase diagrams at the nanoscale might be different from bulk and could result in different preferential growth temperatures for the nanowires. In some cases, we observed the growth of different nanostructures of zinc oxide such as nanobelts and nanoneedles (Figures 2(a) and 2(b)), similar to observations by other researchers [32, 33].

From transmission electron microscope (TEM) images, the growth direction of the nanowire was determined to be [0001], and the nanowires had a wurtzite crystal structure (single crystal) with lattice constants close to those of bulk crystals. At the bulk scale, Young's modulus of zinc oxide in the [0001] direction is 140 GPa [34], which is significantly higher than the modulus value reported in this paper. This is commonly attributed to the surface stress effects in the literature. Due to the lower coordination number of surface atoms compared to bulk atoms, there exist intrinsic surface stresses in materials [35, 36], and the mechanical properties of surfaces are different from bulk. The effects of surface stresses are significant when the size of the material is on the order of $h_0 = S/E$, where $S$ is the surface elastic constant and $E$ is the modulus of the bulk material [37]. For zinc oxide, the order of $h_0$ is approximately a few angstroms, which implies that the surface effects cannot alone explain the size effects observed in Table 1.

One of the reasons for the observed scatter in the modulus values (Table 1) is the difference in experimental techniques used to estimate Young's modulus. The dynamic experiments performed by Huang et al. [13], Chen et al. [12], and Zhou et al. [16] are expected to show slightly higher, unrelaxed ($E_U$) modulus, whereas in this paper we report modulus values estimated by quasi-static experiments ($E_R$). In dynamic experiments, the time period of motion of the nanowire is much lower than the relaxation time, and hence, the modulus values estimated during dynamic experiments tend to be higher than the values estimated during static or quasi-static experiments ($E_U > E_R$) [38]. Also, the oscillating electric field applied to the specimen induces charges on the nanowire surface, which can significantly overestimate the elastic properties [39]. For aspect ratios of around 100 for copper nanowires, the measured modulus could be 1.5 times the actual modulus.

The modulus value reported in this paper is less than the modulus value estimated by Feng et al. [14] (90–100 GPa), using nanoindentation. They estimated the modulus of the nanowires from the hardness values of the nanowires, which were measured during nanoindentation. In order to estimate the hardness of the nanowire, they had to make assumptions about the elastic properties of the nanoindenter tip and the nanowire material. In their experiments, they assumed that the elastic properties of bulk ZnO are applicable to ZnO nanowires, and this may have influenced the final estimated modulus value of the ZnO nanowire. Ni and Li [15] estimated the bending Young's modulus of ZnO nanobelts as 38.2 GPa and nanoindentation modulus as 31.1 GPa, which compare favorably with the modulus values reported in this paper.

A possible mechanism to explain the reduction in modulus of ZnO nanowire compared to bulk is the strong electromechanical coupling in zinc oxide. Due to its noncentrosymmetric wurtzite structure and ionic nature of the interatomic bond, internal electric fields are induced in ZnO when the material is strained [40, 41]. The positive sign

of the electromechanical coupling coefficient, $e_{33}$, along the [0001] direction implies that the induced electric field tends to reduce the measured modulus of the nanowire. Additional electrical polarization is introduced in the nanowire during flexural deformation due to the flexoelectric effect which arises because of the high-strain gradient at the nanoscale [42]. For piezoelectric materials with low dielectric constant, such as zinc oxide, quasi-static tests are not recommended for measurements of elastic constants (Young's modulus) because of the uncertainties in electrical boundary conditions [43]. As a result, the measured modulus values in quasi-static nanomechanical characterization (e.g., the technique reported in this paper) are influenced by the electromechanical coupling resulting in Young's modulus of ZnO nanowire being different from bulk. Another approach for explanation of reduction in modulus is that the elastic properties of a material can be described at the atomistic level, where the bond length, bond energy, and arrangement of atoms influence the overall elastic behavior of the material [44, 45]. In case of ZnO, the effective charge ($e^*$) on the zinc-oxygen changes due to charge redistribution when the material is strained [46]. Since Young's modulus of the material depends on $e^*$, the modulus of the material should change at higher strains. The techniques used for measuring the elastic properties at bulk scale involve negligible strains compared to nanoscale bending experiments. As a result, the measured modulus values of nanoscale zinc oxide are different from bulk due to strain-dependent modulus.

## 7. CONCLUSION

Zinc oxide nanostructures (nanobelts, nanoneedles, and nanowires) were synthesized using the vapor-liquid-solid technique. Young's modulus of the nanowires was estimated by bending experiments performed in situ in a scanning electron microscope on individual nanowires. Young's modulus was measured to be about 40 GPa, which is about 30% of the modulus value at the bulk scale (140 GPa). It was observed that the specimen preparation technique influences the boundary conditions, which affects the measured modulus value. The observed size effect was discussed on the basis of the pronounced electromechanical coupling and strain gradient at the nanoscale.

## ACKNOWLEDGMENTS

The authors acknowledge support from the National Science Foundation (CMMI-0555420 and ECCS-0501436). This publication was supported by the Pennsylvania State University Materials Research Institute Nano Fabrication Network and the National Science Foundation Cooperative Agreement no. 0335765, National Nanotechnology Infrastructure Network, with Cornell University.

## REFERENCES

[1] A. V. Desai and M. A. Haque, "Mechanical properties of ZnO nanowires," *Sensors and Actuators A*, vol. 134, no. 1, pp. 169–176, 2007.

[2] X. Wang, J. Song, and Z. L. Wang, "Nanowire and nanobelt arrays of zinc oxide from synthesis to properties and to novel devices," *Journal of Materials Chemistry*, vol. 17, no. 8, pp. 711–720, 2007.

[3] E. Comini, G. Faglia, G. Sberveglieri, Z. Pan, and Z. L. Wang, "Stable and highly sensitive gas sensors based on semiconducting oxide nanobelts," *Applied Physics Letters*, vol. 81, no. 10, pp. 1869–1871, 2002.

[4] M. S. Arnold, P. Avouris, Z. W. Pan, and Z. L. Wang, "Field-effect transistors based on single semiconducting oxide nanobelts," *Journal of Physical Chemistry B*, vol. 107, no. 3, pp. 659–663, 2003.

[5] W. L. Hughes and Z. L. Wang, "Nanobelts as nanocantilevers," *Applied Physics Letters*, vol. 82, no. 17, pp. 2886–2888, 2003.

[6] N. Kumar, A. Dorfman, and J.-I. Hahm, "Ultrasensitive DNA sequence detection using nanoscale ZnO sensor arrays," *Nanotechnology*, vol. 17, no. 12, pp. 2875–2881, 2006.

[7] M. Law, J. Goldberger, and P. Yang, "Semiconductor nanowires and nanotubes," *Annual Review of Materials Research*, vol. 34, no. 1, pp. 83–122, 2004.

[8] Y. Xia, P. Yang, Y. Sun, et al., "One-dimensional nanostructures: synthesis, characterization, and applications," *Advanced Materials*, vol. 15, no. 5, pp. 353–389, 2003.

[9] Z. L. Wang, "Zinc oxide nanostructures: growth, properties and applications," *Journal of Physics: Condensed Matter*, vol. 16, no. 25, pp. R829–R858, 2004.

[10] X. D. Bai, P. X. Gao, Z. L. Wang, and E. G. Wang, "Dual-mode mechanical resonance of individual ZnO nanobelts," *Applied Physics Letters*, vol. 82, no. 26, pp. 4806–4808, 2003.

[11] J. Song, X. Wang, E. Riedo, and Z. L. Wang, "Elastic property of vertically aligned nanowires," *Nano Letters*, vol. 5, no. 10, pp. 1954–1958, 2005.

[12] C. Q. Chen, Y. Shi, Y. S. Zhang, J. Zhu, and Y. J. Yan, "Size dependence of Young's modulus in ZnO nanowires," *Physical Review Letters*, vol. 96, no. 7, Article ID 075505, 4 pages, 2006.

[13] Y. Huang, X. Bai, and Y. Zhang, "*In situ* mechanical properties of individual ZnO nanowires and the mass measurement of nanoparticles," *Journal of Physics: Condensed Matter*, vol. 18, no. 15, pp. L179–L184, 2006.

[14] G. Feng, W. D. Nix, Y. Yoon, and C. J. Lee, "A study of the mechanical properties of nanowires using nanoindentation," *Journal of Applied Physics*, vol. 99, no. 7, Article ID 074304, 10 pages, 2006.

[15] H. Ni and X. Li, "Young's modulus of ZnO nanobelts measured using atomic force microscopy and nanoindentation techniques," *Nanotechnology*, vol. 17, no. 14, pp. 3591–3597, 2006.

[16] J. Zhou, C. S. Lao, P. Gao, et al., "Nanowire as pico-gram balance at workplace atmosphere," *Solid State Communications*, vol. 139, no. 5, pp. 222–226, 2006.

[17] S. Hoffmann, F. Östlund, J. Michler, et al., "Fracture strength and Young's modulus of ZnO nanowires," *Nanotechnology*, vol. 18, no. 20, Article ID 205503, 5 pages, 2007.

[18] L.-W. Ji, S.-J. Young, T.-H. Fang, and C.-H. Liu, "Buckling characterization of vertical ZnO nanowires using nanoindentation," *Applied Physics Letters*, vol. 90, no. 3, Article ID 033109, 3 pages, 2007.

[19] Y. Zhu and H. D. Espinosa, "An electromechanical material testing system for *in situ* electron microscopy and applications," *Proceedings of the National Academy of Sciences of the United States of America*, vol. 102, no. 41, pp. 14503–14508, 2005.

[20] B. G. Demczyk, Y. M. Wang, J. Cumings, et al., "Direct mechanical measurement of the tensile strength and elastic modulus of multiwalled carbon nanotubes," *Materials Science and Engineering A*, vol. 334, no. 1-2, pp. 173–178, 2002.

[21] M. A. Haque and M. T. A. Saif, "*In situ* tensile testing of nanoscale freestanding thin films inside a transmission electron microscope," *Journal of Materials Research*, vol. 20, no. 7, pp. 1769–1777, 2005.

[22] S. Boggs, J. Kuang, H. Andoh, and S. Nishiwaki, "Electro-thermal-mechanical computations in ZnO arrester elements," *IEEE Transactions on Power Delivery*, vol. 15, no. 1, pp. 128–134, 2000.

[23] R. Ciocan, J. Gaillard, M. J. Skove, and A. M. Rao, "Determination of the bending modulus of an individual multiwall carbon nanotube using an electric harmonic detection of resonance technique," *Nano Letters*, vol. 5, no. 12, pp. 2389–2393, 2005.

[24] C.-Y. Nam, P. Jaroenapibal, D. Tham, D. E. Luzzi, S. Evoy, and J. E. Fischer, "Diameter-dependent electromechanical properties of GaN nanowires," *Nano Letters*, vol. 6, no. 2, pp. 153–158, 2006.

[25] A. V. Desai and M. A. Haque, "Sliding of zinc oxide nanowires on silicon substrate," *Applied Physics Letters*, vol. 90, no. 3, Article ID 033102, 3 pages, 2007.

[26] P. Yang, H. Yan, S. Mao, et al., "Controlled growth of ZnO nanowires and their optical properties," *Advanced Functional Materials*, vol. 12, no. 5, pp. 323–331, 2002.

[27] C. Y. Lee, T. Y. Tseng, S. Y. Li, and P. Lin, "Growth of zinc oxide nanowires on silicon (100)," *Tamkang Journal of Science and Engineering*, vol. 6, no. 2, pp. 127–132, 2003.

[28] D. A. Dikin, X. Chen, W. Ding, G. Wagner, and R. S. Ruoff, "Resonance vibration of amorphous $SiO_2$ nanowires driven by mechanical or electrical field excitation," *Journal of Applied Physics*, vol. 93, no. 1, pp. 226–230, 2003.

[29] W. Ding, L. Calabri, X. Chen, K. M. Kohlhaas, and R. S. Ruoff, "Mechanics of crystalline boron nanowires," *Composites Science and Technology*, vol. 66, no. 9, pp. 1112–1124, 2006.

[30] H. Okamoto and T. B. Massalski, *Phase Diagrams of Binary Gold Alloys*, ASM International, Materials Park, Ohio, USA, 1987.

[31] Y. Wu, H. Yan, M. Huang, B. Messer, J. H. Song, and P. Yang, "Inorganic semiconductor nanowires: rational growth, assembly, and novel properties," *Chemistry: A European Journal*, vol. 8, no. 6, pp. 1261–1268, 2002.

[32] Z. L. Wang, "Nanostructures of zinc oxide," *Materials Today*, vol. 7, no. 6, pp. 26–33, 2004.

[33] J. Y. Lao, J. Y. Huang, D. Z. Wang, and Z. F. Ren, "ZnO nanobridges and nanonails," *Nano Letters*, vol. 3, no. 2, pp. 235–238, 2003.

[34] I. B. Kobiakov, "Elastic, piezoelectric and dielectric properties of ZnO and CdS single crystals in a wide range of temperatures," *Solid State Communications*, vol. 35, no. 3, pp. 305–310, 1980.

[35] R. Dingreville, J. Qu, and M. Cherkaoui, "Surface free energy and its effect on the elastic behavior of nano-sized particles, wires and films," *Journal of the Mechanics and Physics of Solids*, vol. 53, no. 8, pp. 1827–1854, 2005.

[36] W. Haiss, "Surface stress of clean and adsorbate-covered solids," *Reports on Progress in Physics*, vol. 64, no. 5, pp. 591–648, 2001.

[37] V. B. Shenoy, "Atomistic calculations of elastic properties of metallic fcc crystal surfaces," *Physical Review B*, vol. 71, no. 9, Article ID 094104, 11 pages, 2005.

[38] A. S. Nowick and B. S. Berry, *Analelastic Relaxation in Crystalline Solids*, Academic Press, New York, NY, USA, 1972.

[39] X. Zheng and L. Zhu, "Theoretical analysis of electric field effect on Young's modulus of nanowires," *Applied Physics Letters*, vol. 89, no. 15, Article ID 153110, 3 pages, 2006.

[40] A. Sakamoto and T. Ogawa, "Effective charge in the IIVI and IIIV compounds with zincblende or wurtzite type structure," *Journal of Physics and Chemistry of Solids*, vol. 36, no. 6, pp. 583–589, 1975.

[41] R. Kato and J. Hama, "First-principles calculation of the elastic stiffness tensor of aluminium nitride under high pressure," *Journal of Physics: Condensed Matter*, vol. 6, no. 38, pp. 7617–7632, 1994.

[42] R. Maranganti, N. D. Sharma, and P. Sharma, "Electromechanical coupling in nonpiezoelectric materials due to nanoscale nonlocal size effects: Green's function solutions and embedded inclusions," *Physical Review B*, vol. 74, no. 1, Article ID 014110, 14 pages, 2006.

[43] ANSI/IEEE Std 176-1987, "IEEE standard on piezoelectricity," The Institute of Electrical and Electronics Engineers: New York, NY, USA, 1987.

[44] R. M. Martin, "Elastic properties of ZnS structure semiconductors," *Physical Review B*, vol. 1, no. 10, pp. 4005–4011, 1970.

[45] R. M. Martin, "Relation between elastic tensors of wurtzite and zincblende structure materials," *Physical Review B*, vol. 6, no. 12, pp. 4546–4553, 1972.

[46] J. C. Phillips and J. A. Van Vechten, "Charge redistribution and piezoelectric constants," *Physical Review Letters*, vol. 23, no. 19, pp. 1115–1117, 1969.

Hindawi Publishing Corporation
Journal of Nanomaterials
Volume 2008, Article ID 352109, 7 pages
doi:10.1155/2008/352109

*Research Article*

# Atomic Force and Optical Microscopy Characterization of the Deformation of Individual Carbon Nanotubes and Nanofibers

**Terry P. Bigioni[1,2] and Brett A. Cruden[1]**

[1] *NASA Ames Research Center, University Affiliated Research Center (UARC), Moffett Field, California, CA 94035, USA*
[2] *Department of Chemistry, The University of Toledo, Toledo, OH 43606, USA*

Correspondence should be addressed to Brett A. Cruden, brett.a.cruden@nasa.gov

Received 4 September 2007; Revised 31 December 2007; Accepted 12 January 2008

Recommended by Jun Lou

A popular technique for characterizing the mechanical properties of carbon nanotubes is to apply a one-dimension axial compression and measure its response to the compressive force. At some critical compression, a dramatic decrease in the force is observed. This has previously been attributed to Euler buckling, allowing the elastic modulus to be calculated from the Euler buckling force. We have attached individual plasma enhanced chemical vapor deposition (PECVD) grown carbon nanofibers (CNFs) and thermal chemical vapor deposition (CVD) grown carbon nanotubes (CNTs) to the apex of an atomic force microscope (AFM) cantilever to examine this mechanical response. By combining the force measurements and simultaneous video microscopy, we are able to observe the mechanical deformation and correlate points in the force curve with phenomena such as slipping and bending. Analysis of the mechanical response must therefore be interpreted in terms of bending and/or slipping of a tube compressed by an off-normal force.



## 1. INTRODUCTION

Carbon nanotubes (CNTs) have recently generated intense interest due to a combination of remarkable electrical, thermal, and mechanical properties. The mechanical properties have generated interest for producing high-strength lightweight composite materials [1]. The mechanical properties are also relevant for operation of CNTs as resonators [2], electromechanical relays [3, 4], or atomic force microscope (AFM) probe tips [5, 6]. Other applications utilizing CNTs as interfacial materials, such as thermal interface [7], dry adhesive [8], or super-compressible films [9], rely on the mechanical deformation and stiction properties of the CNT within an array or mat of CNTs.

Varied attempts have been made to measure the moduli and strengths of carbon nanotubes via approaches such as natural and driven resonance measurements and bending deformation under AFM measurement. The modulus of CNTs is measured at around 1.2 TPa with some studies suggesting a reduction in modulus as diameter and structural defects increase [10, 11]. A variation on the carbon nanotube, often called a carbon nanofiber (CNF), which is grown by plasma enhanced chemical vapor deposition (PECVD), should show a significant reduction in modulus relative to the CNT due to its stacked cone graphene morphology [12]. Still the CNF is of interest as it may be grown as a free standing, vertically aligned cylindrical nanostructure. While the data available on the mechanical properties of the CNF is fairly limited, they are still of interest for applications such as thermal interface materials [7, 13], AFM tips [5], and cellular probes [14].

The mechanical deflection behavior of these nanostructures needs to be understood in much broader terms than the basic modulus measurement. Specifically, it is not well known what the mechanical behavior and deformation modes of CNTs and CNFs are at an interface under compression. The nanotubes may deform by buckling, or they may slip at the interface. Local defects on the CNTs and CNFs may lead to a kinking behavior. These different modes of deformation are important in understanding

performance of the material in applications such as thermal interface and dry adhesives, where the actual areal overlap of the CNT with its contacted surface is likely the determining factor for thermal conduction or adhesion strength. CNTs present at a high packing may act as a metamaterial, where the bending, buckling, or slip of one tube may influence the motion and contact of neighboring tubes. Finally, phenomena such as plastic deformation and work hardening have also been observed in CNT and CNF arrays which are presently not well characterized or understood [9, 15].

While single CNTs have been attached to AFM tips and measured under a compressive load [16, 17], misalignments of the CNT with respect to the substrate and imperfections in the tubes themselves, such as curvature and lattice defects, can lead to bending, slipping, and kinking during compression. Measurement of the force response curve alone is not sufficient, in general, to distinguish these different modes of compressive response. This has been accomplished previously by visualizing deformation modes of CNTs under tensile and compressive loads in a scanning electron microscope (SEM) [18, 19] or transmission electron microscope (TEM) [20, 21].

We have devised a technically simpler method wherein we observe the tube motion using optical video microscopy while simultaneously measuring its compressive behavior. Our approach requires no specialized equipment, making it accessible to many more laboratories and applicable to a wide range of materials. Additionally, the approach can provide insight into how these systems behave under ambient conditions, rather than under vacuum. Although optical imaging provides only a two-dimensional projection of a three-dimensional geometry, and with limited spatial resolution, it serves as a qualitative guide for identifying events such as bending, kinking, and slipping for the purposes of interpreting force data. This allows for correlation of force response curves with the actual compressive responses of individual CNTs and CNFs.

## 2. EXPERIMENTAL

Carbon nanotubes were grown by thermal chemical vapor deposition on NiCr substrates as described in [22]. Carbon nanofibers were produced by PECVD in acetylene ammonia mixtures as described in [23]. The CNTs and CNFs were then attached to Ni-coated AFM tips as described in [24], as shown in Figure 2. In the case of the CNF, it was found that a side attachment of the CNF to the pyramid did not result in a strong attachment, and the CNF could be removed from the pyramid under repeated cycling. To address this issue, the CNF was brought into contact solely at the tip of the AFM pyramid, as shown in Figure 2(a). This resulted in a strong attachment of the CNF to the AFM tip. We believe this approach was effective because it increased the contact resistance between the CNF and AFM tip, producing sufficient contact heating to spot weld the CNF to the AFM tip. This process was not required in the case of the CNT due to a smaller cross-sectional area of the contact and/or a lower-electrical resistance for the CNT itself resulting in heat dissipation primarily at the contact rather than being divided between the contact and the interior of the CNT. The insets in Figures 2(a) and 2(c) highlight the differences in the attachment techniques for CNTs and CNFs.

Measurements were made on a Molecular Imaging Pico, scanning probe microscope operating in tapping mode. For the purposes of the measurement, the head was moved at a constant rate while monitoring the change in resonance amplitude as the tip moved in and out of contact with a Si wafer. It should be noted that the driving frequency was held constant near the free-resonance frequency of the cantilever throughout the experiment, such that the changing response is attributable to a combination of damping and resonance shift. A CCD camera coupled with a long working distance lens was used to image the motion of the AFM tip and attached CNT/CNF at a magnification of 500×. Images were $208 \times 160$ pixels and were captured at a frame rate of 20 fps. A customized sample plate holder was designed with a notch to accommodate the positioning of the objective lens. The scanner was also lowered to provide adequate clearance for the objective below the AFM body. A red filter was required to remove scattered laser light from the optical image. A fiber optic light source was positioned at each side of the AFM head to provide oblique illumination for dark-field imaging. The experimental set up is shown in Figure 1. The CCD camera output was sent to a computer for data storage and analysis.

The CNTs/CNFs were repeatedly cycled through compressions and generally reproduced each cycle, often in detail. These experiments were preferred for analysis. Occasionally, a tip-fiber weld would fail, as confirmed later by SEM, and the measurements would drastically change for subsequent cycles (not shown). It was possible to correlate video microscopy data with the AFM scanning by identifying sudden movements of the AFM cantilever that were coincident with scan start and stop commands from the AFM software. Logger Pro Software was employed to track motion of images collected.

It is well known that CNTs can be visualized in an optical microscope [25]. This is the predominant method used to attach CNTs to AFM tips as first demonstrated by Dai et al. [26]. While their paper claimed to visualize bundles, it has later been realized that individual tubes are also viewable this way [27]. An optical microscope cannot resolve the diameter of the CNT because it is smaller than the diffraction limit. The CNT can scatter light, however, and so can be routinely visualized in the dark field. This is analogous to visualizing individual metal nanoparticles by imaging the light scattered by their plasmon modes under darkfield illumination [28]. Namely, the diameter of the nanoparticles cannot be determined optically, but light scattered from single nanoparticles can be measured if they are isolated on a substrate. In contrast, the length of the CNT is several microns and is therefore well within the resolution limits of optical microscopy. In our system, the optical imaging corresponds to approximately 100 nm per pixel, therefore the deflections of the CNTs and CNFs under compression are also easily detected.

(a) (b)

Figure 1: Images of the setup. The long-working-distance microscopic lens is pointed at the AFM cantilever.

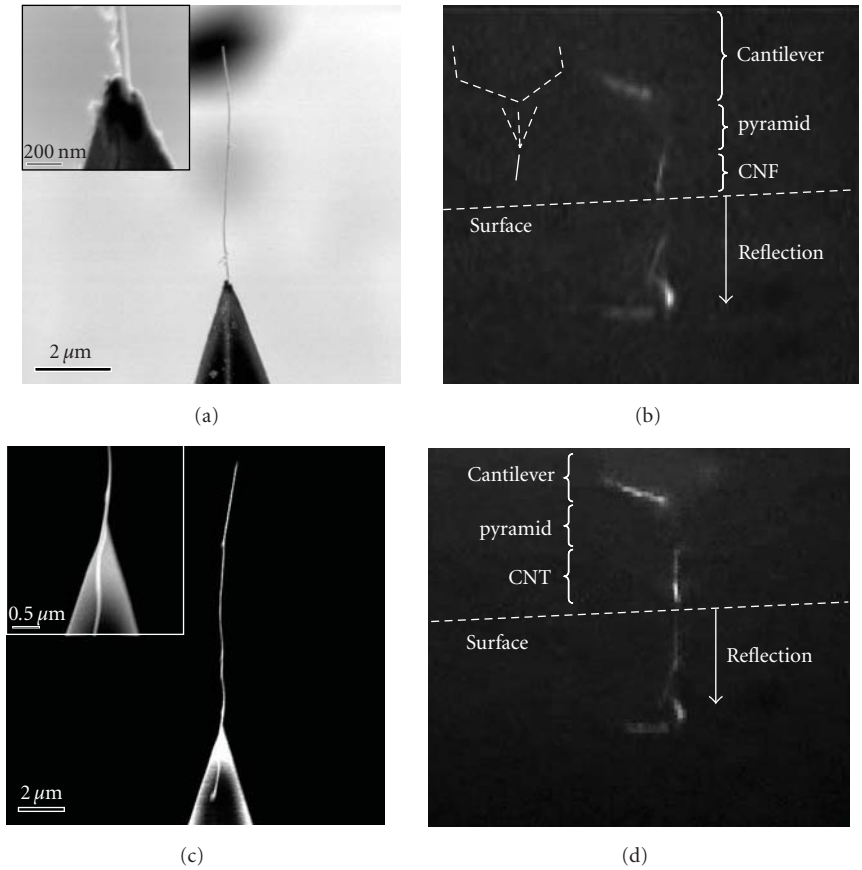


(a) (b)

(c) (d)

Figure 2: (a), (c) SEM and (b), (d) optical microscopy images of the AFM tips with attached nanostructures. Insets show close-up of the attachment points. Parts of the video image are labeled for clarity. The dashed lines in (b) show the profile of the cantilever, only part of which scatters light into the optical microscope. (a), (b) are for the carbon nanofiber and (c), (d) are for the carbon nanotube.

## 3. RESULTS AND DISCUSSION

Two representative data sets for CNT- and CNF-based deflection measurements will be discussed to illustrate the application of the technique. It should be noted that the difference between these measurements is not indicative of a difference between CNTs and CNFs per se, but is instead meant to illustrate different deformation modes observed through this approach. Further analysis and quantification would be required to gain a full understanding of the behaviors of CNTs and CNFs under compression, but this is beyond the scope of the current letter. Figure 2 shows SEM images of the CNT and CNF as attached to the AFM cantilever, along with the complimentary video capture images. The CNT is approximately 12 $\mu$m long while the CNF is approximately 6.5 $\mu$m long. This was sufficient for imaging under video capture (approximately 50–100 pixels per tube). Actual videos of the deflection during measurement are available as supplementary material online.

We must note that each mounted CNT and CNF has its own shape and structural defects and approaches the substrate at a different angle. Since dark-field imaging relies on

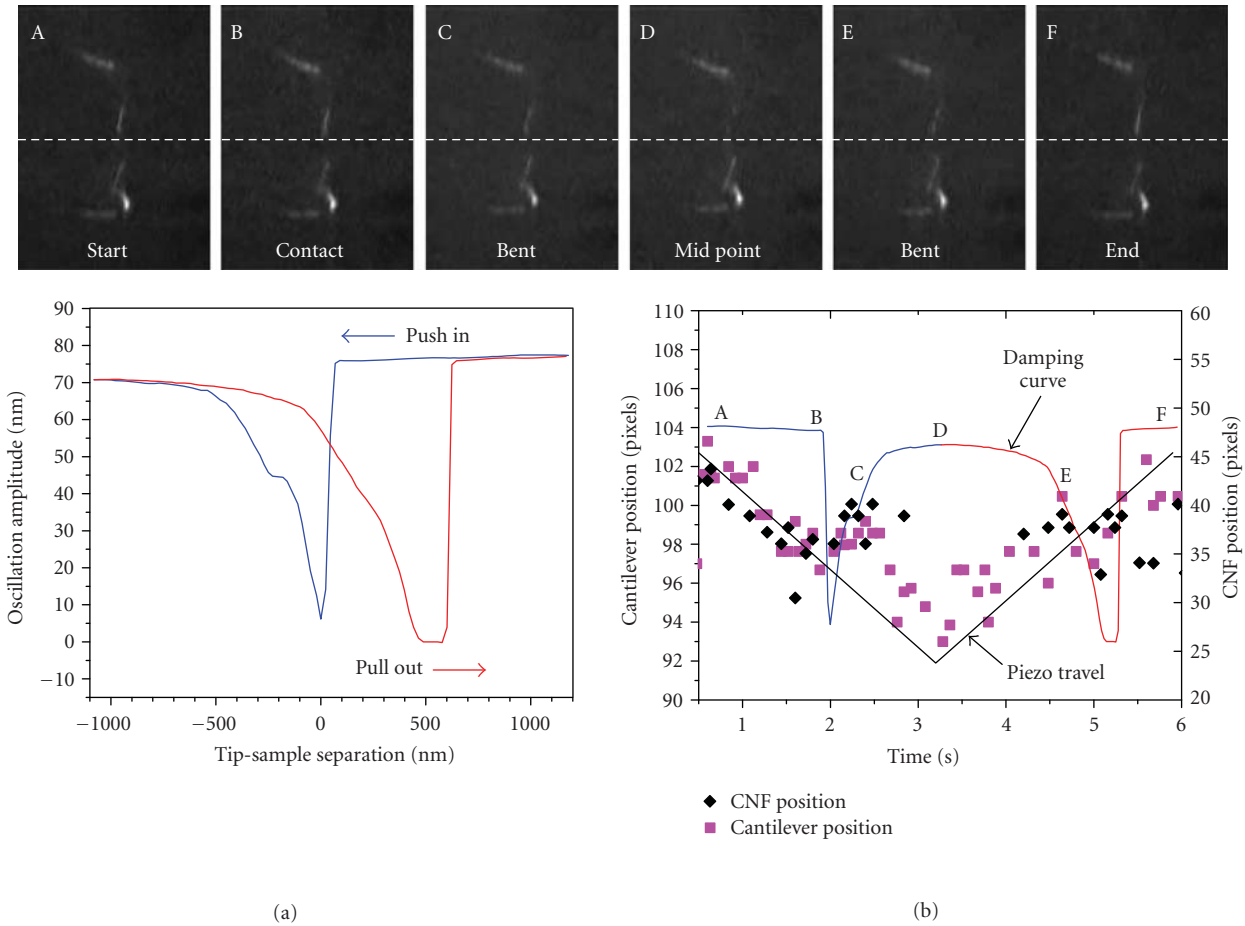


Figure 3: (a) Trace from the tapping mode AFM data for a carbon nanofiber tip, showing oscillation damping as tip sample separation is varied. (b) The same trace as a function of time, showing the AFM data and piezo travel. Several major points on the curve are labeled and the corresponding stills from the video are shown at these points. Also shown are points tracked during video capture, including cantilever position and position of the carbon nanofiber.

oblique light being scattered into the objective, each CNT and CNF looks different. The ability to identify bending, slipping, and kinking naturally differed for different experiments. In general, however, our observations indicate certain consistent optical behaviors, namely, (i) bending results in a slow change in illumination, (ii) slipping a discontinuous change, and (iii) kinking a slow change in one part of the tube and little in the other. Often a sharp bend is also observed for kinks. Similar observations are made during withdrawal, but occasionally the tube/fiber will appear to straighten and scatter more light than usual. This is likely due to tension, although it is difficult to distinguish exactly when contact is broken due to the short length scales and the imaging mode. These three different modes are demonstrated in supplemental video S1.

Figure 3, together with corresponding supplemental video S2, displays the response of the CNF under compression of up to 1.1 $\mu$m. Figure 3(a) shows the displacement-damping curve with corresponding video capture images from various points in the displacement cycle. Figure 3(b) shows $y$-axis pixel locations for tracking two prominent points in the video data—the end of the AFM cantilever and the upper end of the CNF. At initial contact, the CNF tip still appears fairly straight in the video microscopy and the AFM oscillation is immediately damped as the CNF is pressed into the surface. Under further depression, the system stiffness is reduced and oscillation amplitude begins to increase. This increase is accompanied by an apparent upward motion of both the cantilever and CNF tip. In this stage, deflection of the CNF is barely perceptible and the force is apparently being absorbed primarily by the cantilever. A brief plateau in the displacement-damping curve corresponds to the maximum deflection of the cantilever as load is transferred to the CNF. Following this plateau, a more visible bending of the CNF is apparent and the upward trend of displacement reverses. The cantilever displacement then follows the trend of the piezo displacement, while the separation between the CNF tip and piezo/cantilever decreases, corresponding to bending or buckling of the CNF.

At around 500 nm of compression, the CNF shape is distorted such that it is no longer trackable in the video, indicating that it is bent in such a way as to no longer scatter light

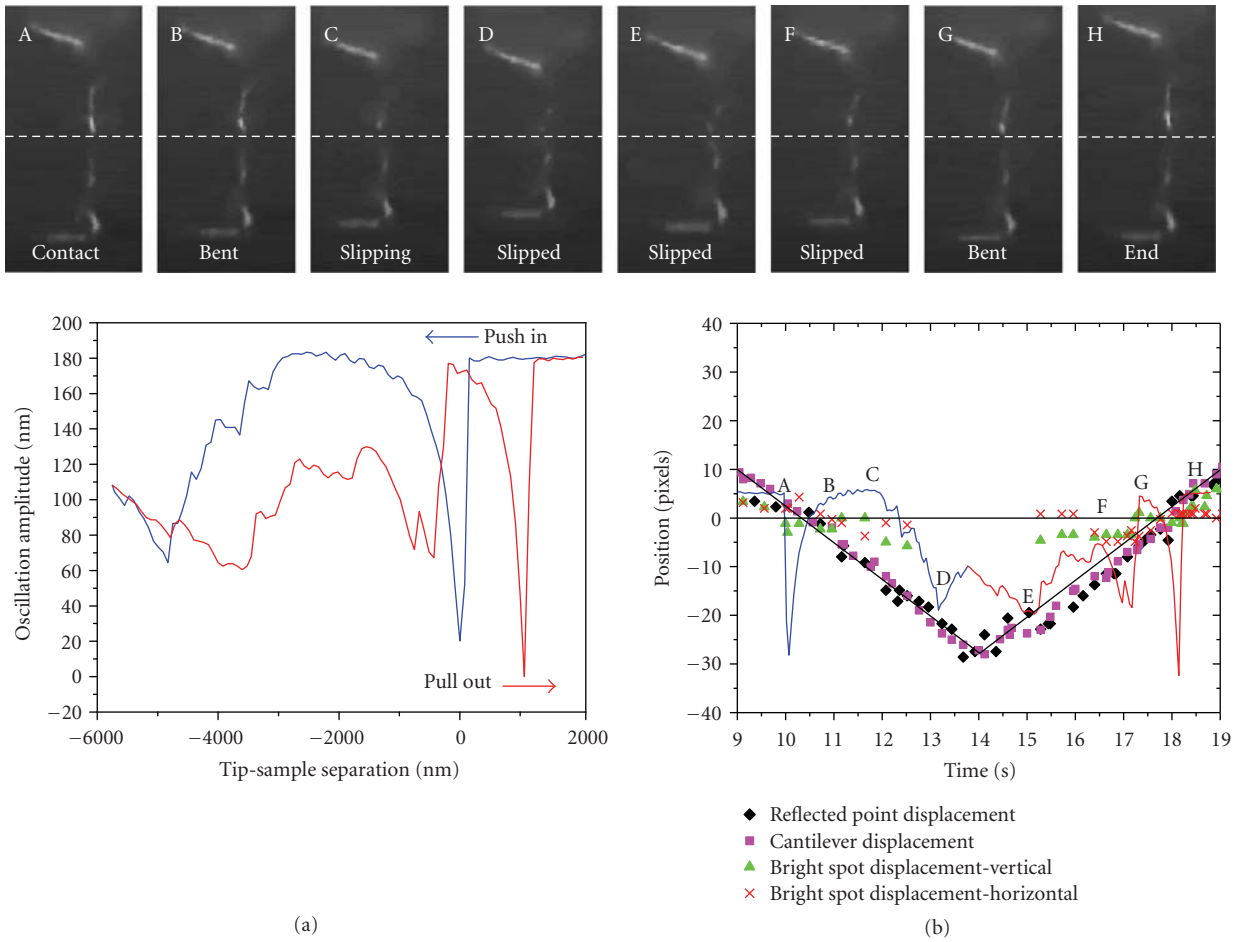


FIGURE 4: The same measurement as for Figure 3 for a carbon nanotube attached tip at higher degrees of compression. The points in (b) include motion tracked on the cantilever, the reflection of the cantilever, and horizontal and vertical displacements of the carbon nanotube.

into the objective. During this stage, the oscillation amplitude has reached a constant value close to the free oscillation amplitude. This indicates that the CNF is presenting a very low stiffness, consistent with a strongly bowed fiber. On pull-out, the CNF becomes visible again and the oscillation amplitude begins to decrease. Very little bending is observable on pull out—the CNF appears to be straight when the piezo displacement returns to zero, even though the oscillation amplitude is still decreasing. This hysteresis observed between scanning probe push-in and pull-out is often attributed to the properties of a water bridge formed between the tip and the substrate [29]. In this case, the water bridge provides an adhesion force and therefore tension on the CNF once the tip passes the initial contact point during withdrawal. The CNF may straighten under tension and reposition on the surface such that the contact angle approaches 90 degrees and the tip-substrate separation is maximized while still in contact. This could provide additional travel beyond the initial contact point, after which the water bridge collapses and separation is achieved.

Figure 4, together with supplemental video S3, shows similar data to Figure 3 for the CNTs under higher compression. The initial trends of the CNTs are nearly identical to that of the CNF. As the unbent CNT first makes contact with the surface the oscillation amplitude is immediately damped. As opposed to the previous case, no plateau in the damping curve or cantilever deflection is observed. This is attributed primarily to the curvature of the CNT reducing its resistance to buckling relative to the straighter CNF. The greater length of the CNT will reduce its stiffness by almost 8×, though this is expected to be compensated by a higher modulus in the CNT relative to the CNF. Further pushing of the tube results in buckling and a corresponding reduction in stiffness until, at 2 $\mu$m of compression, the oscillation amplitude has returned to nearly the free-oscillation amplitude and the CNT is clearly bowed. Further pushing leads to slip of the tube along the surface, and the CNT is no longer visible in the images. This results in a stiffening of the CNT as it slides along the surface in a stick-slip mode, leading to several ridges in the damping curve. Outside of the first slip event, this stick-slip action is inferred rather than observed directly because the CNT is not visible. Pull-out shows a similar series of ridges as the CNT unsticks and slides, eventually returning to a single point contact near the original cantilever position. Close inspection of Figure 4(b) shows that during pull-out these ridges are reflected in the motion of the cantilever

relative to the piezo line, which is not observed during push-in. At the point of zero tip-sample separation, the damping characteristics are determined by the water bridge and the cantilever is pulled approximately 1 $\mu$m further away than the initial contact separation when the water bridge collapses.

## 4. CONCLUSIONS

We have shown that it is possible to track motions of CNFs and CNTs with optical video microscopy during mechanical measurements of CNFs and CNTs that were mounted to AFM tips. Motions of the CNF/Ts and cantilevers in the optical images can be correlated with features in AFM measurements. Reductions in stiffness were correlated with bending modes and increases in stiffness can be attributed to slipping on the Si substrate. These measurements demonstrate that optical characterization of the mechanical response of nanotubes and fibers can aid in the interpretation of mechanical measurements, such as those demonstrated with AFM. Performing contact-mode AFM force measurements coupled with an inverted optical microscope that is equipped with dark-field optics should improve the quality of the data and may provide some unique insights into the mechanics of nanoscale objects.

## ACKNOWLEDGMENTS

The authors would like to thank Drs. Cattien Nguyen, Joseph Leung, and Alan Cassell for helpful discussions. Funding for the project was provided by the University of California Discovery Grant Program.

## REFERENCES

[1] O. Breuer and U. Sundararaj, "Big returns from small fibers: a review of polymer/carbon nanotube composites," *Polymer Composites*, vol. 25, no. 6, pp. 630–645, 2004.

[2] J. F. Davis, M. Bronikowski, D. Choi, et al., "High-Q mechanical resonator arrays based on carbon nanotubes," in *Proceedings of the 3rd IEEE Conference on Nanotechnology (NANO '03)*, vol. 2, pp. 635–638, San Francisco, Calif, USA, August 2003.

[3] S. W. Lee, D. S. Lee, R. E. Morjan, et al., "A three-terminal carbon nanorelay," *Nano Letters*, vol. 4, no. 10, pp. 2027–2030, 2004.

[4] B. A. Cruden and A. M. Cassell, "Vertically oriented carbon nanofiber based nanoelectromechanical switch," *IEEE Transactions on Nanotechnology*, vol. 5, no. 4, pp. 350–355, 2006.

[5] Q. Ye, A. M. Cassell, H. Liu, K.-J. Chao, J. Han, and M. Meyyappan, "Large-scale fabrication of carbon nanotube probe tips for atomic force microscopy critical dimension imaging applications," *Nano Letters*, vol. 4, no. 7, pp. 1301–1308, 2004.

[6] C. V. Nguyen, K.-J. Chao, R. M. D. Stevens, et al., "Carbon nanotube tip probes: stability and lateral resolution in scanning probe microscopy and application to surface science in semiconductors," *Nanotechnology*, vol. 12, no. 3, pp. 363–367, 2001.

[7] Q. Ngo, B. A. Cruden, A. M. Cassell, et al., "Thermal interface properties of Cu-filled vertically aligned carbon nanofiber arrays," *Nano Letters*, vol. 4, no. 12, pp. 2403–2407, 2004.

[8] Y. Zhao, T. Tong, L. Delzeit, A. Kashani, M. Meyyappan, and A. Majumdar, "Interfacial energy and strength of multiwalled-carbon-nanotube-based dry adhesive," *Journal of Vacuum Science and Technology B*, vol. 24, no. 1, pp. 331–335, 2006.

[9] A. Cao, P. L. Dickrell, W. G. Sawyer, M. N. Ghasemi-Nejhad, and P. M. Ajayan, "Materials science: super-compressible foamlike carbon nanotube films," *Science*, vol. 310, no. 5752, pp. 1307–1310, 2005.

[10] E. W. Wong, P. E. Sheehan, and C. M. Lieber, "Nanobeam mechanics: elasticity, strength, and toughness of nanorods and nanotubes," *Science*, vol. 277, no. 5334, pp. 1971–1975, 1997.

[11] Z. L. Wang, P. Poncharal, and W. A. de Heer, "Nanomeasurements of individual carbon nanotubes by *in situ* TEM," *Pure and Applied Chemistry*, vol. 72, no. 1-2, pp. 209–219, 2000.

[12] A. V. Melechko, V. I. Merkulov, T. E. McKnight, et al., "Vertically aligned carbon nanofibers and related structures: controlled synthesis and directed assembly," *Journal of Applied Physics*, vol. 97, no. 4, Article ID 041301, 39 pages, 2005.

[13] J. Xu and T. S. Fisher, "Enhancement of thermal interface materials with carbon nanotube arrays," *International Journal of Heat and Mass Transfer*, vol. 49, no. 9-10, pp. 1658–1666, 2006.

[14] T. D. B. Nguyen-Vu, H. Chen, A. M. Cassell, R. Andrews, M. Meyyappan, and J. Li, "Vertically aligned carbon nanoflber arrays: an advance toward electrical-neural interfaces," *Small*, vol. 2, no. 1, pp. 89–94, 2006.

[15] Y. Zhang, E. Suhir, and Y. Xu, "Effective Young's modulus of carbon nanofiber array," *Journal of Materials Research*, vol. 21, no. 11, pp. 2948–2954, 2006.

[16] S. I. Lee, S. W. Howell, A. Raman, R. Reifenberger, C. V. Nguyen, and M. Meyyappan, "Nonlinear tapping dynamics of multi-walled carbon nanotube tipped atomic force microcantilevers," *Nanotechnology*, vol. 15, no. 5, pp. 416–421, 2004.

[17] H. W. Yap, R. S. Lakes, and R. W. Carpick, "Mechanical instabilities of individual multiwalled carbon nanotubes under cyclic axial compression," *Nano Letters*, vol. 7, no. 5, pp. 1149–1154, 2007.

[18] W. Ding, L. Calabri, K. M. Kohlhaas, X. Chen, D. A. Dikin, and R. S. Ruoff, "Modulus, fracture strength, and brittle vs. plastic response of the outer shell of arc-grown multi-walled carbon nanotubes," *Experimental Mechanics*, vol. 47, no. 1, pp. 25–36, 2007.

[19] M. F. Yu, M. J. Dyer, G. D. Skidmore, et al., "Three-dimen sional manipulation of carbon nanotubes under a scanning electron microscope," *Nanotechnology*, vol. 10, no. 3, pp. 244–252, 1999.

[20] T. Kuzumaki and Y. Mitsuda, "Nanoscale mechanics of carbon nanotube evaluated by nanoprobe manipulation in transmission electron microscope," *Japanese Journal of Applied Physics, Part 1*, vol. 45, no. 1, pp. 364–368, 2006.

[21] M. Nakajima, F. Arai, and T. Fukuda, " *In situ* measurement of Young's modulus of carbon nanotubes inside a TEM through a hybrid nanorobotic manipulation system," *IEEE Transactions on Nanotechnology*, vol. 5, no. 3, pp. 243–248, 2006.

[22] B. Ribaya, J. Leung, M. Rahman, and C. V. Nguyen, "A study on the mechanical and electrical reliability of individual carbon nanotube field emission cathodes," to appear in *Nanotechnology*.

[23] B. A. Cruden, A. M. Cassell, Q. Ye, and M. Meyyappan, "Reactor design considerations in the hot filament/direct current plasma synthesis of carbon nanofibers," *Journal of Applied Physics*, vol. 94, no. 6, pp. 4070–4078, 2003.

[24] C. V. Nguyen, R. M. D. Stevens, J. Barber, et al., "Carbon nanotube scanning probe for profiling of deep-ultraviolet and 193 nm photoresist patterns," *Applied Physics Letters*, vol. 81, no. 5, pp. 901–903, 2002.

[25] J. Gaillard, M. Skove, and A. M. Rao, "Mechanical properties of chemical vapor deposition-grown multiwalled carbon nanotubes," *Applied Physics Letters*, vol. 86, no. 23, Article ID 233109, 3 pages, 2005.
[26] H. Dai, J. H. Hafner, A. G. Rinzler, D. T. Colbert, and R. E. Smalley, "Nanotubes as nanoprobes in scanning probe microscopy," *Nature*, vol. 384, no. 6605, pp. 147–150, 1996.
[27] C. V. Nguyen, Q. Ye, and M. Meyyappan, "Carbon nanotube tips for scanning probe microscopy: fabrication and high aspect ratio nanometrology," *Measurement Science and Technology*, vol. 16, no. 11, pp. 2138–2146, 2005.
[28] J. J. Mock, D. R. Smith, and S. Schultz, "Local refractive index dependence of plasmon resonance spectra from individual nanoparticles," *Nano Letters*, vol. 3, no. 4, pp. 485–491, 2003.
[29] J. Jang, M. Yang, and G. Schatz, "Microscopic origin of the humidity dependence of the adhesion force in atomic force microscopy," *Journal of Chemical Physics*, vol. 126, no. 17, Article ID 174705, 6 pages, 2007.

Hindawi Publishing Corporation
Journal of Nanomaterials
Volume 2008, Article ID 874213, 18 pages
doi:10.1155/2008/874213

*Review Article*

# Toward a Detailed Understanding of Si(111)-7 × 7 Surface and Adsorbed Ge Nanostructures: Fabrications, Structures, and Calculations

**Ye-Liang Wang, Hai-Ming Guo, Zhi-Hui Qin, Hai-Feng Ma, and Hong-Jun Gao**

*Nanoscale Physics & Devices Laboratory, Institute of Physics, Chinese Academy of Sciences, P.O. Box 603, Beijing 100080, China*

Correspondence should be addressed to Hong-Jun Gao, hjgao@aphy.iphy.ac.cn

Received 30 August 2007; Accepted 11 January 2008

Recommended by Jun Lou

Firstly, both the rest atoms and the adatoms of Si(111)-7×7 surface are observed simultaneously by scanning tunneling microscopy (STM) when the sample bias voltages are kept less than − 0.7 V. The visibility of the rest atoms is rationalized by first-principle calculations and a very sharper tip can resolve them. Secondly, the behaviors of various Ge nanostructures fabricated on Si(111)-7 × 7, ranging from the initial adsorption sites of individual Ge atoms to the aggregation patterns of Ge nanoclusters, and then to 2D extended Ge islands, are comprehensively investigated by STM. The individual Ge atoms tend to substitute for Si adatoms at Si(111)-7 × 7 with the preference of corner adatoms in the faulted half unit when keeping substrate at 150°C. With increasing Ge coverage, individual Ge atoms and Ge nanoclusters coexist on the substrate. Subsequently, the density of Ge nanoclusters increase and cluster-distribution becomes gradually regular with the formation of final 2D extended hexagonal configuration. When keeping the substrate at 300°C, Ge islands consisting of more complicated reconstructions with intermixing Ge/Si components are present on the substrate. The detail structural characterizations and the bonding nature of the observed Ge nanostructures are enunciated by the first-principle calculations.



## 1. "ULTIMATE" STM IMAGES OF THE Si(111)-7 × 7 SURFACE

Si(111)-7 × 7 surface as one of the most complicated and fascinating objectof study is being extensively used invarious research fields ranging from surface science and material science to nanotechnology. As a classic example, this reconstructed surface provides a platform for the testing of the unprecedented resolution of STM as a novel powerful apparatus in the early 1980s [1]. The first real space atomic image of this surface was obtained by Binnig et al. in their landmark STM experiment [2], in which twelve bright spots corresponding to the topmost adatoms are revealed.

Since then, with this powerful tool and the later family of scanning probe microscope, the structure of Si(111)-7 × 7 surface has been extensively investigated [3–8]. The demonstrations on the atomic topography of clean Si(111)-7 × 7 surface commonly show the topmost adatoms. On the mapping of rest atoms of Si(111)-7 × 7 surface, some saddle points at the position expected for the rest atoms were reported by Avouris and Wolkow [3] and Nishikawa et al. [4] using STM. Recently, some special techniques were used to obtain the images of Si(111)-7 × 7 surface with atomic scale resolution, such as Lantz et al. [5] using scanning force microscopy and Giessibl et al. [6, 7] using atomic force microscopy. Sutter et al. [8] have mapped selectively the rest atoms at a price of suppressing the adatom spots with a monocrystalline semiconductor tip since its energy gap can suppress the tunneling from the adatoms at certain sample bias. STM is very sensitive to states closest to the sample Fermi Energy ($E_F$). The state of dangling bonds of the adatoms is about 0.4 eV below $E_F$ and that of rest atoms is about 0.8 eV below $E_F$ [9], so it is difficult to map the rest atoms whose dangling bonds state is far from $E_F$. Up till now, the adatoms and the rest atoms of Si(111)-7×7 surface are still not clearly distinguished simultaneously by using conventional tungsten tip. This inability has led to the perception that the measured tunneling current for semiconductor materials comes mostly from states near the Fermi level instead of the states further away, due to the

exponential dependence of the tunneling probability on the energy level position [10]. We revisit this surface by using STM. The resultant images simultaneously reveal that not only the 12 adatoms but also the 6 rest atoms per (7 × 7) unit cell of Si(111) surface have high contrast. A careful preparation of the STM tips (reducing the radius of the apex) may bethe key to the success, as our first-principle calculations reveal a geometric hindrance effect of the tip apex for imaging of such complex surfaces.

### 1.1. Experimental

The experiments were performed by using an ultra-high-vacuum (UHV) STM system with a base pressure of ∼5 × $10^{-11}$ mbar. The sample was an antimony-doped *n*-type Si(111) wafer (resistance ∼ 0.03 Ω·cm, thickness ∼0.5 mm). Before being introduced into the vacuum chamber, the sample is cleaned by ethanol in an ultrasonic bath and rinsed thoroughly by deionized water. It was degassed at about 600°C in the chamber for several hours. Then, the sample was annealed by direct current heating while keeping the pressure below $10^{-10}$ mbar. The annealing cycle consisted of flashing the sample to 1200°C for 20 seconds, rapidly lowering the temperature to about 900°C, and then slowly decreasing the temperature at a pace of 1∼2°C/s to room temperature. Nearly perfect (7 × 7) reconstruction was obtained by this method. Sharp STM tips made of a polycrystalline tungsten wire were etched electrochemically in NaOH solution and subsequently cleaned in ethanol and distilled water. Out of many tips used, however, only three had the ability to produce repeatedly the eighteen-spot STM images (Figure 1) while the others produce only the standard twelve-spot images.

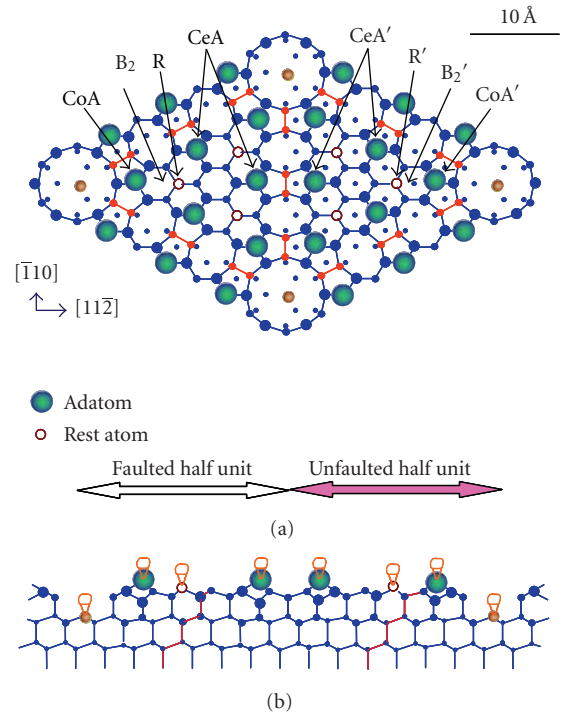


Figure 1: Schematic diagram for Si(111)-7 × 7 "DAS" model [2]. (a) Top view: atoms on (111) layers with the decreasing heights indicated by dots of decreasing sizes. The sites of corner adatom, center adatom, and rest atom in FHUC (labeled CoA, CeA, and R, resp.), and in UHUC (labeled CoA′, CeA′ and R′, resp.), are identified by arrows. Positions $B_2$ in FHUC, and $B_2'$ in UHUC are also denoted by arrows. (b) Side view: dangling bonds are located at the topmost of all adatoms, rest atoms, and holes.

### 1.2. Imaging simultaneously the rest atoms and adatoms

The atomic arrangement of the Si(111)-7 × 7 reconstructed surface can be described by a commonly accepted dimer-adatom-stacking (DAS) fault model [11], as schematically shown in Figure 1. This model consists of twelve adatoms and six rest atoms, which are evenly distributed in the faulted half unit cell (FHUC) and unfaulted half unit cell (UHUC). Each unit cell contains nineteen dangling bonds perpendicular to the surface, twelve for the adatoms and six for rest atoms and one for corner atom below the vacancy. The tunneling current in STM of the Si(111)-7 × 7 surface originates from these dangling bonds. A stacking fault exists between the second and third atom layers in the FHUC side (the interlayer bonding rotates 60°), which makes the FHUC more reactive than the UHUC. The large unit cell size (2.7 nm×2.7 nm) makes this surface an ideal template for the growth of well-ordered nanostructures.

Figures 2(a) and 2(b) show STM images with high contrast. They demonstrate simultaneously the adatoms and the rest atoms, that is, 18 topographic maxima per (7 × 7) unit cell. The high-resolution image (Figure 2(b)) presents more clearly all of them. In the UHUC side, the rest atoms appear to have almost the same brightness as the central adatoms, whereas in the FHUC, the rest atoms appear to have considerably less brightness than the central adatoms. The line profile in Figure 2(c) showed the positions and height differences of the six distinct types of atoms (labeled 1 to 6) along the solid line depicted in Figure 2(b). The ranking of height of these atoms is as follows: 1 is the highest, then 3 and 6 follow, with 2, 4, and 5 being the lowest. The rest atom (site 2) in the FHUC side is at the same level as the rest atom (site 5) in the UHUC side, and they are both even at the same level as the central adatom (site 4) in the UHUC half side. The high contrast between rest atoms and adatoms is even better than the previous results obtained by using scanning force microscopies [5–7]. Very recently, Bassi et al. reported the extremely similar topography of this surface at −1.5 V by using Cr tip [12], they claimed that the Cr tip reduced its convolution effects and enhanced its resolving capability. Here, for the first time, all the rest atoms and adatoms of the Si(111)-7 × 7 surface are simultaneously revealed with high contrast by the conventional W tips. The emergence of rest atoms will be further rationalized below by theoretic analysis.

Noting the defect with the missing of one corner adatom (close to the hole at the left-upper corner of the panel) in Figure 2(b), it shows no influence on its adjacent rest atom, which is still visible and stays its normal position without any lateral distortion. So the absence of local adatom does not

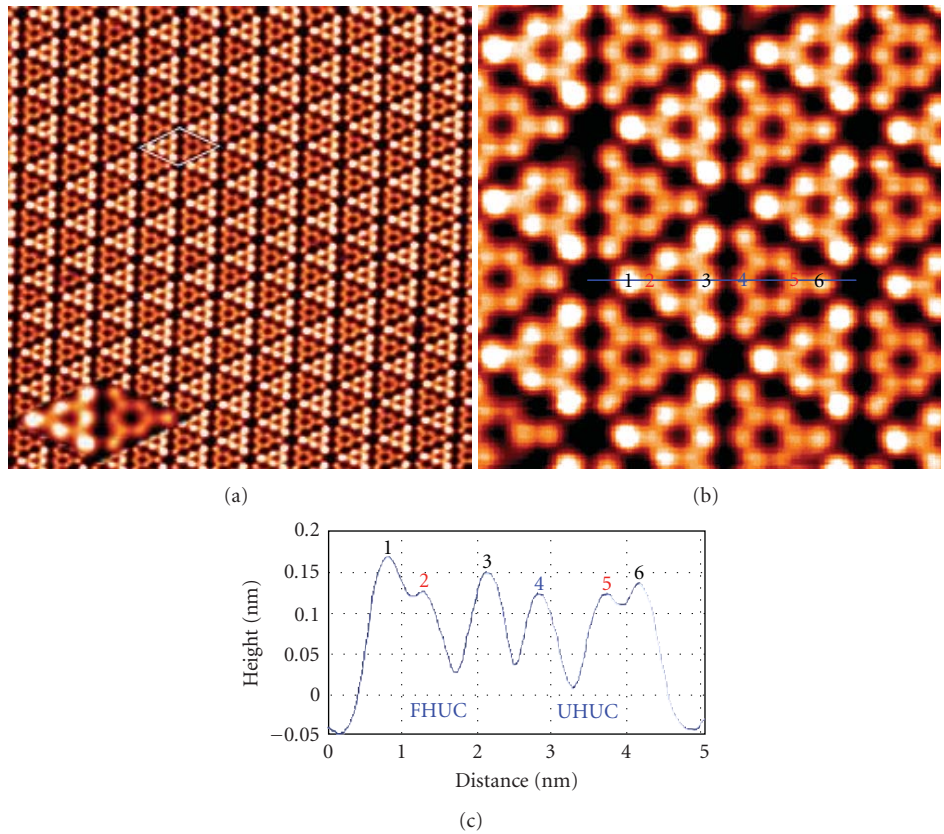


Figure 2: Filled-state STM images of Si(111)-7 × 7 surface reveal 12 adatoms and 6 rest atoms per (7 × 7) unit cell. (a) The image extends over an area of 30 nm × 30 nm. The amplificatory (7 × 7) unit cell was indicated in the inset. (b) Amplified image with scanning area of 8 nm × 8 nm. Both images are recorded by sample bias voltage of −1.5 V and tunneling current of 0.3 nA. (c) The line profile taken along the line in (b). Labels "1," "2," and "3" denote the corner adatom, the rest atom, the center adatom in the FHUC, and labels "4", "5", and"6" denote the center adatom, the rest atom, the corner adatom in the UHUC, respectively.

affect the geometric structures of its surrounding atoms in (7 × 7) unit cell. This result coincides with the recent reports about the local structures of adatom vacancies in Si(111)-7 × 7 surface [13]. There, Chen et al. conducted STM dI/dV mappings on adatom vacancies and found that the adatom vacancies showed different local electronic structures but no effect to the geometric or electronic structures of the nearby rest atoms.

### 1.3. The emergence of rest atoms is dependent on the bias voltage

A sequential STM snapshots obtained at different sample bias voltages, as shown in Figure 3, illustrate that the emergence of rest atoms is dependent on the sample bias voltage. At lower bias voltages of −0.5 and −0.6 V, the images (Figures 3(a) and 3(b)) only show 12 adatoms in each (7 × 7) unit cell. It suggests that the electronic states of adatoms are closer to Fermi level than those of the rest atoms. The absence of the rest atoms ascribes to the electronic states of the rest atoms which are outside the range of the bias when the value of sample bias keeping very low. By further decreasing the value of bias voltage less than −0.7 V, the rest atom spots can be visible, as shown in Figures 3(c)–3(f). It clearly reveals that the dangling bond states of the rest atoms are located at about 0.7 eV below the $E_F$, which is in excellent agreement with the experimental results measured by the method of current imaging tunneling spectroscopy (CITS). In the year 1989, Hamers et al. measured the electronic banding structure of Si(111)-7 × 7 surface by using CITS. They provided knowledge of the dangling bonds states of the adatoms (about 0.35 eV below the $E_F$) and the rest atoms (about 0.8 eV below the $E_F$) [9]. Here, the rest atoms appear to have almost the same brightness as the central adatoms on the UHUC when the bias voltages are less than −0.9 V (see Figures 3(e) and 3(f)).

The STM observations presented here are in sharp contrast to previous STM studies, which in most cases showed images similar to that in Figure 3(a) with 12 protrusions in each (7 × 7) unit, irrespective of the bias voltages (somewhere between −2 V to 2 V). A common explanation for the absence of the rest atom spots in the images relies on the fact that the tunneling probability depends on the thickness of the tunneling barrier [10]. Because the tunneling current is inversely proportional to the exponential of the thickness, the lower-electronic state located in the valence band corresponds to the smaller tunneling current. The rest atoms are invisible but the adatoms are visible may be

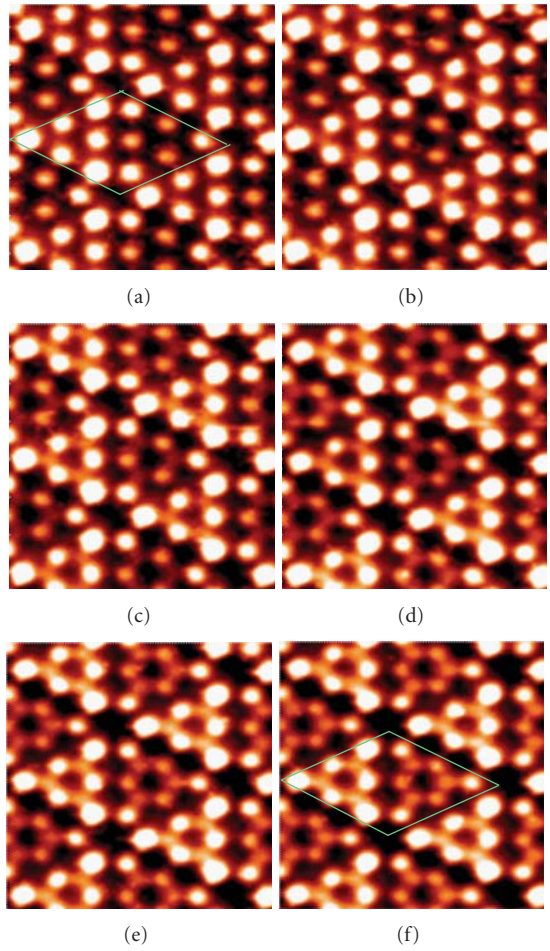


FIGURE 3: STM images of Si(111)-7×7 surface with different sample bias voltages: (a) −0.5, (b) −0.6, (c) −0.7, (d) −0.8, (e) −0.9, (f) −1.0 V, respectively. The rest atoms appear when the sample voltages are less than −0.7 V. All images are taken at tunneling current 0.4 nA in the scanning area of 5 nm × 5 nm.

because the former has significant lower energies than the latter. This argument, however, contradicts the theoretical prediction that the dangling bond states of the rest atoms extended into the vacuum region like the adatoms [14]. Also, because the rest atoms are about 4.6 Å away from the nearest adatoms, if one has an infinitely sharp tip positioned right above the rest atom, there is no reason to believe that the adatoms have effect to screen the rest-atom tunneling. If the tunneling currents from the rest atom were indeed weak, one can move the tip closer to the surface in a constant current STM mode. Thus, this common explanation is probably questionable.

Another possible explanation concerns tip contamination, that is, a few silicon atoms might be accidentally picked up by the tungsten tip during the scan, resulting in a semiconductor tip instead of the original metallic tip. Indeed, recently it has been shown that an InAs semiconductor tip [8] could be used to enhance rest-atom visibility by utilizing the second gap above the fundamental gap (both lie in the Brillouin zone center) of InAs material to suppress tunneling current from the high-lying adatom states. However, a previous study [15] also showed that the local electronic structure of a typical metal/semiconductor interface remains metallic until several monolayers are in the semiconductor. Thus, this is unlikely in the present case with Si atoms adsorption unless the thickness of the contaminant layer exceeds the effective screening length of Si.

### 1.4. First-principle calculations are in remarkable agreement with experiments

It is impractical for us to experimentally determine what might have happened to the few tips that worked so remarkably well. Instead, we look for a plausible explanation from theory calculations. Our collaborators carried out the calculation by using first-principle density function theory (DFT) [16], as implemented in the VASP codes [17]. The Vanderbilt ultrasoft pseudopotential [18] was used with a cutoff energy equal to 170 eV and one special k-point in the Brillouin zone sum. The surface unit cell contains a slab of six Si layers (without counting the Si adatoms) and a vacuum layer equivalent to six Si layers. The front surface contains the (7×7) reconstruction in the Takayanagi model [11], whereas the back surface is passivated by hydrogen. Except for the bottom layer, all the Si atoms are fully relaxed to minimize the system total energy.

Apparently, the actual tip morphology is complex, possibly with additional atoms adsorbed at the end of the apex, as shown schematically in the inset in Figure 4(f). Because only the lower semispherical part of the tip can be in close proximity with the surface, here the tip is replaced by a sphere of radius $r$. To further simplify the calculations, only the linescans along the diagonal of the (7×7) unit cell are considered in our simulations.

Figure 4(a) shows the STM image of the Si(111)-7 × 7 surface at a sample bias of −0.57 V. The appearance shows a significant contrast between the FHUC and UHUC of the (7 × 7) unit. At this low sample bias, the electronic states of the rest atoms are outside the range of the bias, as demonstrated in Figures 3(a) and 3(b). Thus, the STM topography here reveals only the twelve topmost adatoms. The adatoms in the FHUC appear noticeably brighter than those in the UHUC. In each half, the adatoms at the corners appear also slightly brighter than those near the center. These qualitative features are in good agreement with the calculated real-space charge distribution at this particular bias (Figure 4(b)). Figure 4(c) shows the STM image at a sample bias −1.5 V. Images of similar quality can be repeatedly reproduced over large area up to 30 nm × 30 nm (Figure 2(a)). We can clearly see both the adatoms and the rest atoms. On the UHUC, they appear to have almost the same brightness as the central adatoms, whereas on the FUHC, the rest atoms appear to have considerably less brightness than the central adatoms. These observations are again in excellent agreement with the calculated real-space charge distribution at the experimental bias in Figure 4(d).

Figure 4(e) shows the calculated linescan at −1.5 V with an infinitely sharp tip, that is, $r = 0$, as has been done

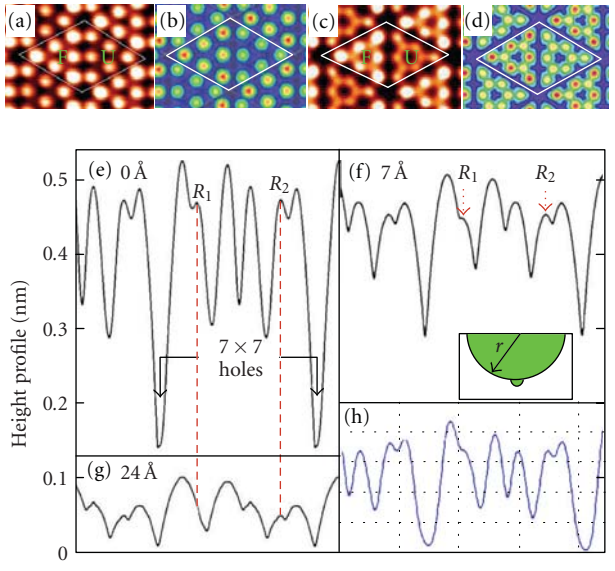


FIGURE 4: (a), (c) Experimental STM images with bias voltage of −0.57 and −1.5 V, and tunneling current of 0.3 and 0.41 nA, respectively. F and U depict the FHUC and UHUC, respectively. (b), (d) Calculated STM images for Si(111)-7 × 7 at − 0.57 and −1.5 V, respectively. The red peaks are about 2 Å above the dark blue borderlines. (e), (f), and (g) are the calculated height profiles along the diagonal of the (7 × 7) unit cell with a tip apex radius $r$ = 0.0, 7.0, and 24.0 Å, respectively. (h) The experimental profile. The inset in (f) schematically shows an STM tip with an adsorbed cluster beneath the apex.

before in most STM image simulations [19]. A sharp tip is also assumed in calculating the images in Figures 4(b) and 4(d). Now, we trace this $r = 0$ curve with a disk of radius $r$, which is a two-dimensional representation of the three-dimensional sphere, to explore geometric hindrance. It is assumed that at each tip position, tunneling takes place at only one spot on the disk. This is reasonable in most cases because tunneling probability diminishes exponentially with distance. However, there are a few exceptions where the disk is nearly or equally distanced from the $r = 0$ curve, that is, at or near the local symmetry points. For simplicity, however, such a tunneling-current double effect is ignored in our simulation.

Our results show that for small disk radius mimicking adsorbed clusters, the line-scan is essentially the same as in Figure 4(e). Figure 4(f) shows the simulated result for $r$ = 7 Å. At this radius, while none of the main surface topological features have been lost, the overall shape of the linescan has been significantly modified, noticeably the depth of the profile, and the size of the atoms being noticeably larger than those in Figure 4(e). Figure 4(g) shows the simulated result for $r = 24$ Å. At this radius, the rest atom on the FHUC has completely vanished. Even for the UHUC, the contrast between the rest atom spots and the adatom spots has been greatly reduced. Thus, it is clear that the attainable size of the tip apex is the crucial factor in imaging the true charge distribution on the (7×7) surfaces. Figure 4(h) shows the corresponding linescan determined by our experiment. Despite the simplicity of the model, the calculated result for $r = 7$ Å in Figure 4(f) is in quantitative agreement with experimental observation. Some of the subtle differences between Figures 4(f) and 4(h) could probably ascribe to the tunneling-current double effect.

It is now understood that STM probes the real-space charge distribution near the $E_F$ in a rather delicate way that may or may not reveal the unperturbed real-space charge distribution of the surfaces. Here, For the Si(111)-7 × 7 surface, we show the calculated and experimental voltage-dependent charge distributions of the Si(111)-7 × 7 surface, which reveal simultaneously both the twelve adatoms and six rest atoms in each (7×7) unit cell [20]. The emergence of rest atom is dependent on the bias voltage and the rest atom spots can be visible at the sample bias voltages less than −0.7 V. The first-principle electronic structure calculations also show a strong dependence of the charge distribution on the bias voltage: twelve spots at −0.57 V for the twelve adatoms (see Figure 4(b)), whereas eighteen spots at −1.5 V for the twelve adatoms plus six rest atoms (see Figure 4(d)). Our results suggest that a geometric hindrance due to the finite size of the tip apex could be the reason for the invisibility of the rest atoms in the past experiments. This finding should invoke significant research interest in the design and fabrication of the STM tip and its applications in exploring more detailed information about surface reconstructions and nanostructures.

## 2. Ge NANOSTRUCTURES ON Si(111)-7 × 7 SURFACES

Low-dimensional structures can provide interesting physical and chemical properties due to their tiny size and shape. The growth of nanostructures with reduced dimensions has been extensively studied, driven by the intrinsic interest in structures as well as the potential technological applications in quantum devices [21]. Recent studies demonstrated the feasibilities and possibilities of growing self-organized nanostructures on periodic solid surfaces. The Si(111)-7 × 7 surface offers unique template for the self-assembly growth of divers nanostructures because of the large number of distinct bonding sites. Recently, "magic" islands and nanoclusters of semiconductor or metal have been grown on this surface [22–26]. Ordered arrays of two-dimensional nanodots/nanoclusters, including Al, Ga, In, Tl, Si, Ge, Sn, Pb, Na, Cu, Au, Ag, were successfully fabricated [27–51]. These self-organized structures are expected to have a smaller size and stronger confinement potentials compared to the lithographically defined clusters [52].

The adsorption of Germanium on the Si(111)-7 × 7 surface has been extensively studied in recent years [40–51, 53–83], because Ge-based nanostructures have potential applications in microelectronics and optoelectronics. Indeed, Ge/Si system naturally has advantage compatible with Si technology. In addition, being currently incorporated in Si structures, Ge can be used to fabricate strained Si layers with enhanced mobility. Therefore, there are renewed activities in Ge-based nanostructures grown on Si surface in expectation of functional devices with unique electronic and optoelectronic properties [53].

The microscopic understanding of the bonding nature of the adsorbed Ge atoms is an essential issue for the controlled fabrication of desired nanostructures, since the initial adsorption nature may affect the growth behaviors of Ge-based quantum dots and films. In spite of numerous investigations, a unified picture for the bonding structures of Ge atoms on Si(111)-7 × 7 surface has not been established. Meanwhile, the formation and transformation process of various Ge nanostructures during the initial growth stages is far from being well understood. Without doubt, they impede the further control of the growth process of Ge nanostructures.

Here, we provide an STM investigation on various Ge nanostructures on Si(111)-7 × 7 surface with different size and geometry, ranging from individual Ge atoms (adsorption sites) to Ge nanoclusters (evolution and aggregation patterns), and then to 2D extended Ge islands (components and bondings). Especially, we go inside the structural characterizations as well as the transformation process and possible mechanisms of the observed Ge nanostructures in association with first-principle calculations.

The preparation of Si(111)-7×7 surface was conducted as described in the part 1. Then Germanium (99.9999% purity) was deposited onto the as-prepared Si(111)-7 × 7 surface by resistive evaporation. The substrate was kept above room temperature (ranging from 100 to 300°C) to facilitate the formation of ordered structures since at room temperature, Ge atoms do not have enough mobility to span the dimer wall after arriving on the Si(111)-7 × 7 surface [59, 61, 68]. During evaporation, the system pressure was better than $5 \times 10^{-10}$ mbar. A typical deposition rate of 0.01 ML/min was routinely achieved. One monolayer is defined as the atomic density of the unreconstructed Si(111) surface (1 ML = $7.83 \times 10^{14}$ atoms/cm$^2$). Each sample was cooled down to room temperature, and then transferred to STM chamber for measurements. All images were acquired in a constant-current mode with an electrochemically etched tungsten tip.

### 2.1. Direct STM observations of the adsorption sites of Ge atoms

For the adsorption sites of Ge atoms on Si(111)-7×7 surfaces reported in the literatures, X-ray standing wave (XSW) studies of submonolayer Ge deposited on Si(111)-7 × 7 at 300°C done by Patel et al. in 1985 suggested that Ge atoms might occupy substitutional-like sites on the Si(111) plane [69]. However, the precise Ge sites and the bonding structures were not possible to determine in their studies. Also based on XSW measurements, Dev et al. in 1986 proposed that at low coverages (~ 0.5 ML) Ge atoms would prefer to occupy the ontop sites and to bond directly to the Si adatoms and rest atoms which were just below the adsorbed Ge atoms [70]. Reflection electron microscopy and transmission electron diffraction investigations on Ge/Si(111)-7 × 7 prepared at 640°C by Kajiyama et al. in 1989 found evidence that Ge atoms randomly substituted any Si atoms at the top three layers [71]. Core-level photoemission spectroscopy measurements by Carlisle et al. in 1994 provided indirect observations that there was some preference for Ge to replace the Si adatoms for the annealed Ge/Si(111)-7 × 7 samples [72]. More recent measurements using near-edge X-ray absorption spectroscopy and STM did not provide conclusive descriptions of Ge bonding sites on this surface [56, 73, 74].

Some theoretical calculations have also been reported on Ge bonding sites on the Si(111)-7 × 7 surface, however, the calculations provided limited information and showed contradictory results. Early work was semiempirical $X_\alpha$ and extended Hückel calculations with limited predictive capabilities, which provided support for the notion that Ge atoms bond directly to rest atoms or Si adatoms [75–77]. In contrast to the semiempirical calculations, on the other hand, using first-principle density functional calculations, Cho and Kaxiras in 1998 reported a limited exploration of bonding possibilities and found that the most stable adsorption position for Ge on Si(111) is the high-coordination bridge $B_2$ site (see Figure 1 for pertinent terminology of the Si(111)-7 × 7 surface), which was a bonding site that had not been proposed on the basis of experimental data [78]. They introduced the so-called basins of attraction, which contain stable adsorbate positions as high-coordination sites rather than surface dangling bond sites. Their calculations showed that the rest atoms or intrinsic Si adatoms sites (dangling bond $T_1$ sites) of substrate were the high-energy sites, and the low-energy sites were the $B_2$-type sites for Si and Ge adsorption.

Here, we report STM observations and first-principle calculations for the structure of the Ge-adsorbed Si(111)-7 × 7 surface at low Ge coverages. Figure 5 shows STM image of the Si(111)-7 × 7 surface with Ge coverages of 0.02, 0.08, and 0.10 ML, respectively. These images show that the surface lattice retains the original (7 × 7) reconstruction with the dimers and the adatoms. The FHUC and the UHUC of the (7 × 7) reconstruction are distinguished due to the different contrast. The deposited Ge atoms appear as bright protrusions. Three significant features are presented in the STM images. First, the deposited Ge atoms are clearly resolved as individual atoms on the surface. Second, the adsorbed Ge atoms reside on the sites that were occupied by the Si adatoms on Si(111)-7 × 7. Finally, more Ge atoms occupy the corner Si adatom sites in the FHUC than the other Si adatom sites. No Ge atoms are found at either the rest atom or the high-coordination surface sites. Furthermore, profile lines through the bright dots show that the height difference between the Ge atoms and the original Si adatoms is about 0.2 Å in the STM images. This data clearly show that the Si adatom does not stay in its original position (on a clean Si(111)-7 × 7 surface, the Si adatom occupies a so-called $T_4$ site just above a second-layer Si atom) [11, 79, 80]. As the bond length of Si-Ge is about 2.36 Å, the increased height due to addition of one Ge atom should be reflected in the STM image.

Therefore, the addition mechanism of Ge atop Si adatom is supposed as a questionable explanation. Moreover, the number of dangling bonds will increase to three if a Ge atom adds on the top of one Si adatom, and it is not considered having a suitable total energy. The topographic height undulations of adatom sites in STM images caused by Ge-Si exchange on Si(111)-5 × 5-Ge reconstructions

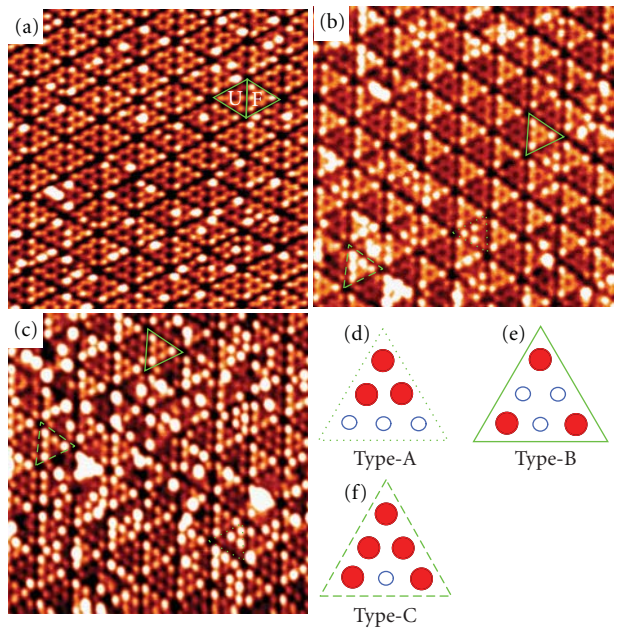


Figure 5: Filled-state STM images (20 nm × 20 nm) of the Si(111)-7 × 7 surface with Ge coverages of (a) 0.02 ML; (b) 0.08 ML; and (c) 0.10 ML. Sample bias: −2.2 V in (a), and −1.5 V in (b) and (c); tunneling current: 0.5 nA in (a), and 0.2 nA in (b) and (c). Three different configurations of Ge protrusion distributions are denoted in (b) and (c) by solid-line triangle, dotted-line triangle, and dashed-line triangle, respectively. The schematics for the three typical Ge patterns, named type-A, type-B, and type-C, are shown in (d), (e), and (f), respectively.

have been proposed by Becker et al. [81] and Fukuda [82], and were also investigated by Rosei et al. [83] with current imaging tunneling spectroscopy. The feature of Ge-Si exchange is confirmed by our recent results, which will be introduced in the following section. Here, we suggest that Ge-Si exchange can also occur during the initial adsorption stage of Ge/Si epitaxy growth due to the structures similarity of Ge and Si. We thus conclude that Ge would prefer to substitute the Si adatoms in its initial adsorption stages.

As shown in Figures 5(b) and 5(c), there are three types of Ge protrusions patterns on the Si(111)-7 × 7 surface. The schematics of these three types patterns, named as type-A, type-B, type-C, are given in Figures 5(d), 5(e), and 5(f), respectively. Type-A illustrates three Ge atoms (red spheres) locating at one corner adatom site and two adjacent center adatom sites in a HUC. Type-B indicates the configuration with three Ge atoms occupying corner adatom sites in a HUC. Type-C refers to the adsorption structure with five Ge atoms residing on the sites of three corner adatoms and two center adatoms in a HUC. Type-B and Type-C distribute preferentially in the FHUCs, as shown in Figures 5(b) and 5(c).

The sites distribution of the bright protrusions at the corner and center adatom sites in both the FHUCs and the UHUCs is illustrated in Figure 6. At the Ge coverage of 0.02 ML, the site preference ratio is about 5.6 : 4.4 for the FHUC to the UHUC, and 6.1 : 3.9 for the corner to the center adatom sites, respectively. When the Ge coverage increases to 0.08 ML, the site preference ratios are about 9 : 1 for the FHUC to the UHUC, and 4 : 1 for the corner to the center adatom sites. The site distribution for the coverage of

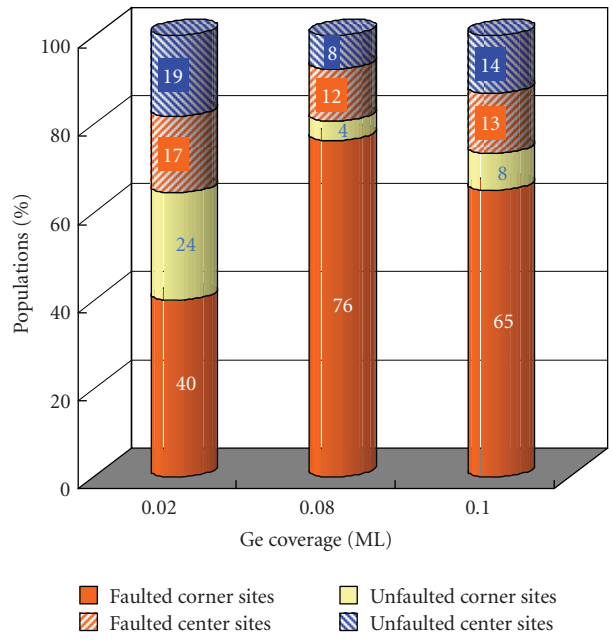


Figure 6: Site distributions of Ge at various adatom positions at coverages of 0.02 ML, 0.08 ML, and 0.10 ML.

0.10 ML is similar to that for the coverage of 0.08 ML. The overall conclusion is that after an initial random occupation of Si adatom sites, corner adatom sites in the FHUC are preferred and gradually type-B patterns become dominant. Type-A and Type-C patterns are more discernible at slightly higher coverages, and finally, small islands begin to appear.

Our collaborators performed first-principle DFT calculations using the pseudopotential method and a plane-wave basis set [16, 17]. The Si(111) surface was modeled by repeated slabs with 4 layers of Si atoms (each layer contained 16 Si atoms, corresponding to a $4 \times 4$ surface unit cell) and 4 Si adatoms, separated by a vacuum region of 12 Å. Two of the four rest atoms were saturated by hydrogen, so that the ratio of the number of the adatoms to that of the rest atoms is the same as for the $7 \times 7$ surface. Except for the Si atoms in the bottom layer, which were fixed and saturated by H atoms, all the atoms were relaxed until the forces on them were less than 0.05 eV/Å. The exchange-correlation effects were treated with the generalized gradient-corrected exchange-correlation functions given by Perdew and Wang [84]. The Vanderbilt ultrasoft pseudopotentials are adopted [18]. A plane-wave energy cutoff of 14.7 Ry and the point for reciprocal space sampling were used for all the calculations.

All the possible configurations with a Ge atom near an adatom or/and a rest atom were calculated. Two lowest energy configurations, as shown in Figure 7, were found to have essentially the same total energy (the difference in total energy is smaller than 0.02 eV). The first one consists of Ge at a $B_2$ site (Figure 7(a)), as identified earlier by Cho and Kaxiras [85]. In the second configuration (Figure 7(b)), the adsorbed Ge atom substitutes for an Si adatom and the substituted Si adatom occupies a nearby $B_2$ site. We refer to the Ge position in the second configuration as $S_4$ (substitutional site with four nearest-neighboring silicon atoms). The total energies of the configurations with Ge bonded at the ontop positions of adatoms and rest atoms are significantly higher (2.3 and 1.6 eV, resp.) than the $B_2$ and $S_4$ configurations. So we can clearly rule out the possibility of such configurations, which were suggested previously on the basis of semiempirical calculations [70, 75, 76].

For both lowest energy configurations ($B_2$ and $S_4$), the atom (Si or Ge) at a bridge site may diffuse within a basin (to occupy any of the six $B_2$ sites near the rest atom) and across basins (to occupy the $B_2$ sites near different rest atoms). The diffusion barriers within a basin and across basins are about 0.5 eV (0.6 eV) and 1.0 eV (1.0 eV) for the Ge (Si) atoms, respectively, which is in agreement with previous first-principle calculations [77, 86]. Therefore, Ge atoms in the $S_4$ configurations are thermodynamically more stable than in the $B_2$ configurations. In particular, after the atoms initially bonded at the $B_2$ sites migrate to step edges and/or to form islands, the surface exhibits a stable Ge-$S_4$ configuration, in which Ge atoms substitute for some of the Si adatoms and no atoms are bonded at any of the $B_2$ sites (Figure 7(c)), as shown by our STM observations. The Ge-$S_4$ configuration is coincided with the recent results reported by two research groups [46, 61]. They prepared the sample with the same experimental conditions as the current work. In their STM measurements, they also confirmed that Ge replaced Si adatoms on the Si(111)-$7 \times 7$.

It is well known that the backbonds of the Si adatoms of the Si(111)-$7 \times 7$ surface are under considerable strain [11, 79, 86]. We therefore suggest that the adsorbed Ge atoms are able to break the backbonds and further replace the Si adatoms at elevated temperatures. Previous studies have established that the corner adatoms in the FHUCs are under more strain than the other adatoms, which implies that backbonds of the corner adatoms in the FHUCs are broken easier than those of the other adatoms [85, 86]. When Ge atoms are deposited on the surface, the chance for the Ge atoms occupying the $B_2$ sites near a center adatom is larger than that near a corner adatom (the center adatom has two nearby rest atoms while the corner adatom has only one). Thus, the Ge–$S_4$ bonding structure tends to be preferentially formed at the corner adatom sites and in the FHUCs of the Si(111)-$7 \times 7$ surface [87].

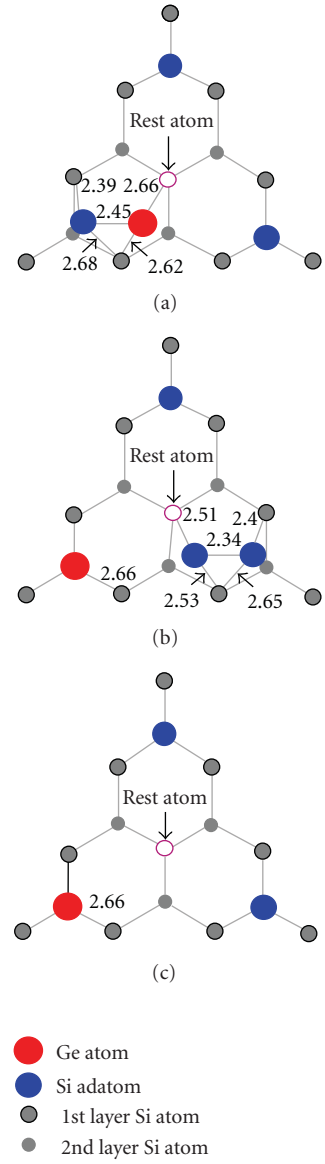


Figure 7: Schematic top view of the calculated lowest energy configurations of a Ge atom on the Si(111) surface: (a) Ge at a $B_2$ site and the nearby Si adatom at the position of its original site. (b) Ge at the substitutional $S_4$ site and the Si adatom at a $B_2$ site. (c) Ge atoms substitute for some of the Si adatoms and no atoms are bonded at any of the $B_2$ sites. The bond lengths are shown with unit of Å.

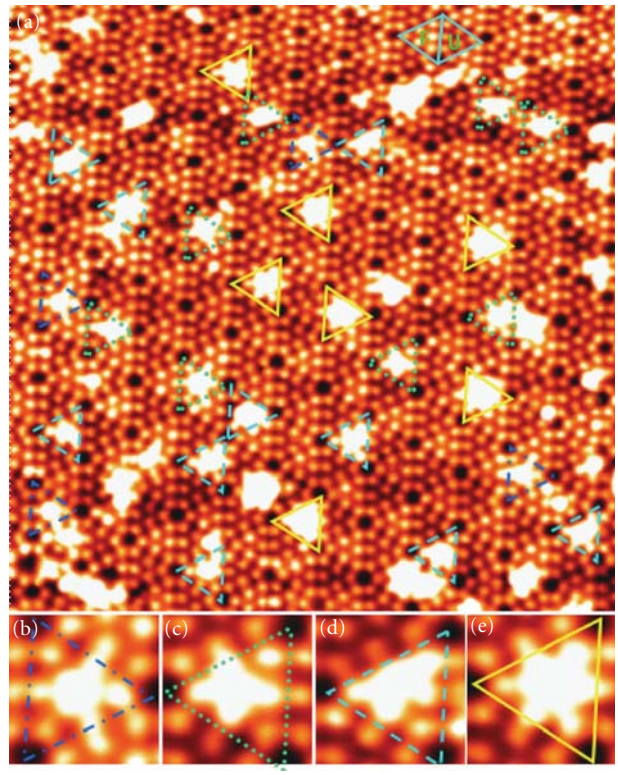


FIGURE 8: (a) Empty-state STM image ($U_b$ = 2.0 V, $I_t$ = 0.3 nA, 30 nm × 30 nm) of the Si(111)-7 × 7 surface with Ge coverage ~ 0.12 ML. The substrate temperature is held at ~100°C for the Ge deposition. Ge clusters with four typical geometrical configurations, named as type-Tr (triangle), type-Te (tetragonal), type-P (pentagonal), and type-H (hexagonal), are denoted by the triangles with the dotted dash-line, dotted-line, dashed-line, and solid-line, and their magnified images (3 nm × 3 nm) are shown in (b), (c), (d), and (e), respectively.

Finally, the relaxed Ge–$S_4$ configuration obtained from our calculations shows that the Ge atom resides at the position higher by 0.24 Å than the original Si adatom that has been replaced by Ge, which is in good agreement with our STM data.

### 2.2. Formation and transformation of Ge clusters

It is of course interesting to study the possible configurations of Ge nanostructures in subsequent Ge depositions. Indeed, with increasing Ge coverage, some novel structures, like small Ge clusters with varying geometrical configurations appear on the Si(111)-7 × 7 surface. The representative image is shown in Figure 8(a) with Ge coverage about 0.12 ML deposited at the substrate temperature ~ 100°C. A remarkable feature in the image is the emergence of Ge clusters with special configurations. Dimer rows and corner-holes of the surface are left uncovered, indicating a strong preference of the Ge clusters to locate in (7 × 7) unit cell. Deposited Ge clusters are imaged as bright bumps and four typical bump structures are distinguished, as named type-Tr, type-Te, type-P, and type-H. Figures 8(b)–8(e) show their magnified images.

Type-Tr (triangle-star-like) cluster emerges like a bright triangle star in a HUC, in this structure three center adatoms and their adjacent high-coordination sites are covered by Ge atoms. Similarly, in the type-Te (tetragonal-star-like), type-P (pentagonal-star-like), and type-H (hexagonal-star-like) clusters, Ge atoms occupy an increasing area in a HUC: type-Te covers one more rest-atom region, type-P covers another one, and type-P covers all three rest-atoms regions.

Four kinds of Ge cluster configurations appear in the same image, it suggests a formation process of Ge clusters from triangle to tetragonal, then to pentagonal, and at last to mature hexagonal-star-like structure despite the fact that we do not observe the real-time evolution of single Ge cluster from simple to complex. Each kind of Ge cluster is observed both in the FHUCs and UHUCs, as shown in Figure 8(a), and there is no clear preference for locating positions of Ge clusters in the FHUCs and UHUCs (37 clusters in the FHUCs and 34 clusters in the UHUCs).

Although the Ge cluster structures on the Si(111)-7 × 7 surface represent the majority in Figure 8(a), while lots of individual Ge atoms locating on the Si adatoms still can be resolved with bright spots at the positions of some Si adatoms in the empty-state STM image. As we know, the STM empty-state images are taken at positive sample bias voltage, corresponding to tunneling electrons from the occupied state of tip to sample. On clean Si(111)-7 × 7 surface, each adatom has a dangling bond and has the same probability to accept the tunneling electrons from tip, so all the adatoms on clean Si(111)-7 × 7 surface have the same brightness in STM empty-state images. By this rule, we can affirm that the brighter protrusions at the sites of Si

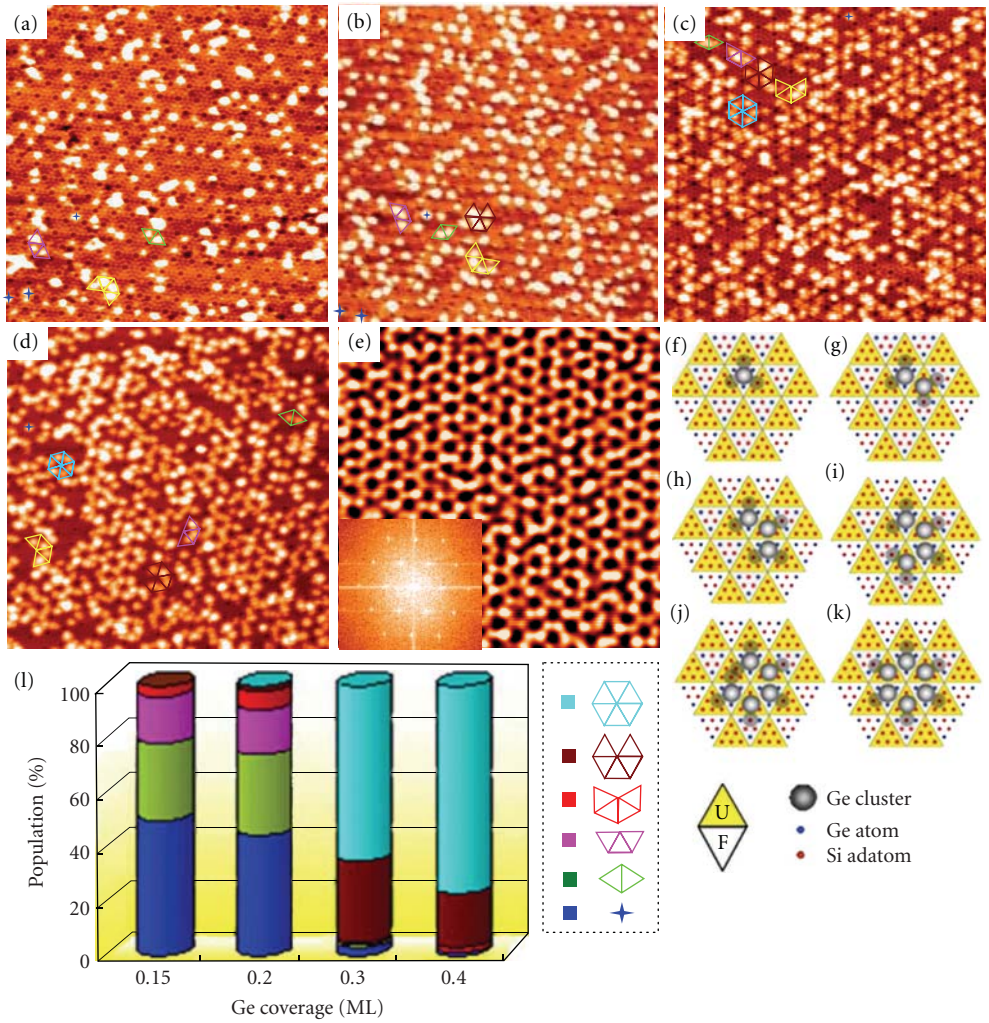


Figure 9: (a)–(e) Series of STM images of Ge-deposited Si(111)-7 × 7 surface show the formation process of hexagonal superlattice with increasing Ge coverages ranging from 0.15, 0.2, 0.3, 0.4 to 0.5 ML, respectively. The substrate temperature is held at ~150°C for Ge deposition. All image sizes are 50 nm × 50 nm. The inset in (e) shows a Fourier transform of the hexagonal arrays. (f)–(k) Schematics illustrating the evolution of cluster structures from open to close hexagonal ring. The Si-center adatoms that transfer charge are shaded in gray. (l) Histograms for the distributions of different local Ge nanostructures at varying coverages. Six distinct local nanostructures are depicted by symbols with different shapes and colors in the STM images.

adatoms are Ge atoms. Thus, individual Ge atoms and some Ge clusters coexist on the Si(111)-7 × 7 surface at proper substrate temperature and Ge coverage.

### 2.3. *Evolution of hexagonal Ge cluster superlattice*

The above results showed that most Ge atoms form correlated patterns at very low Ge coverages less than 0.1 ML, by replacing the Si adatoms of the Si(111)-7 × 7. With the further increasing of Ge coverage, deposited Ge atoms are constrained inside the HUC and aggregate into the form of clusters with different geometry and atom numbers. In addition, previous results reported the existence of hexagonal Ge nanostructures on Si(111)-7 × 7 [57, 60], however, the detail process and driving force are still not clear. Here, we will further reveal the evolution of hexagonal Ge clusters with increasing Ge coverages. The driving mechanism and the atomic geometry of Ge clusters will be enunciated by STM observations and first-principle calculations.

In Figures 9(a)–9(e), a sequence of STM images at varying Ge coverages show the continuing evolution of the Ge clusters from isolated ones into hexagonal patterns. The appearance illustrates that the density of Ge clusters gradually increases with the increasing Ge coverages. The cluster distribution becomes much regular from disordered arrangement to high-symmetric hexagonal superlattice. Six distinct local cluster patterns can be distinguished in STM images, as marked by different symbols. The schematics in Figures 9(f)–9(k) simply depict the structures of these local cluster patterns, ranging from single Ge clusters, to pair of clusters, to open cluster ring, and finally a close cluster ring with six clusters surrounding a hole in Si(111)-7 × 7 surface. The histograms in Figure 9(l) reveal the distribution feature of six different local Ge nanostructures at varying

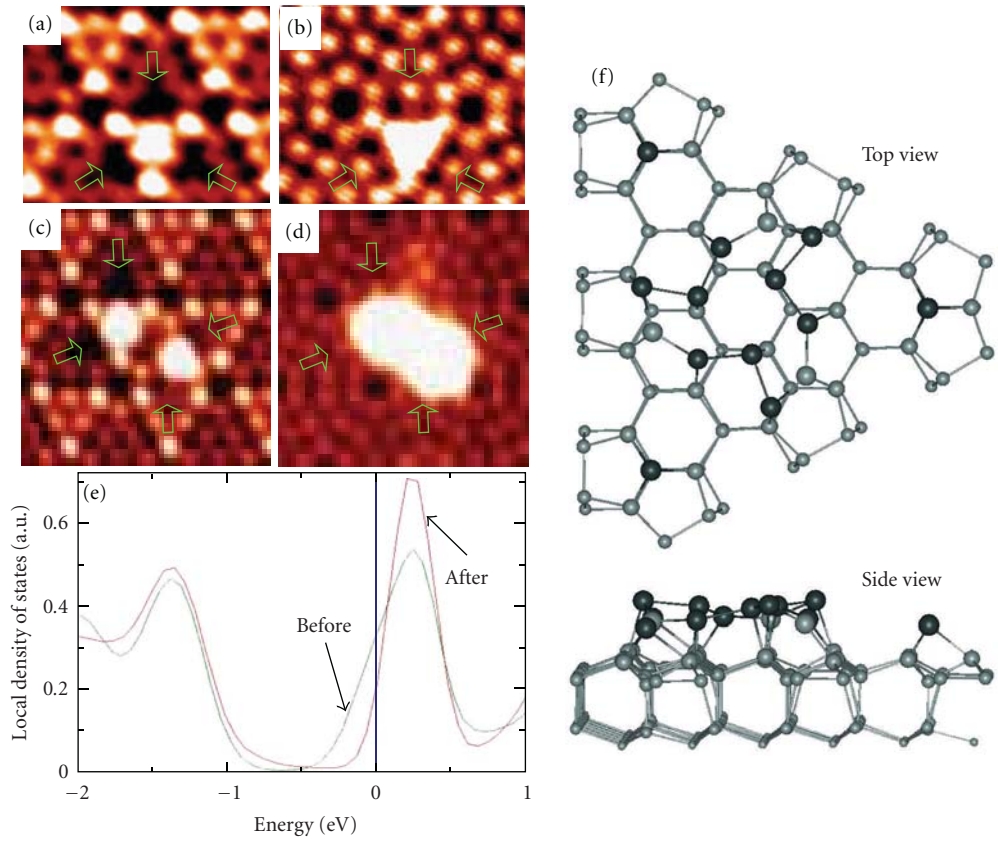


FIGURE 10: Local STM images show the different appearance of Ge-deposited Si(111)-7 × 7 surface with filled-state images (−2.5 V) in (a) and (c) and empty-state image (+2.5 V) in (b) and (d). Single Ge cluster presents in (a) and (b) and double clusters in (c) and (d). The centers Si adatoms, as indicated by the arrows, are invisible in (a) and (c) but visible in (b) and (d). (e) Local density of states projected onto a center Si adatom in a UHUC before and after Ge deposition. The Fermi level is at 0 eV. (f) The corresponding relaxed minimum energy configuration (only the FHUC is shown). The Si and Ge atoms are depicted by gray and dark spheres, respectively. Spheres of decreasing size represent the Si atoms with increasing distances from the surface. The dotted lines show weak bonds.

coverages. The evident tendency is that the ratio of simple cluster pattern reduces with the increase of complex ones.

The distribution tendency suggests the evolution of hierarchical cluster patterns from dispersing clusters to close cluster rings. Most of clusters discretely emerge on the substrate at low coverage of 0.10 ∼ 0.15 ML with an initial preference in the FHUCs (see Figure 9(a)). And then open cluster rings containing three, four, and five clusters, nucleated on the Si(111)-7 × 7 surface at a Ge coverage of ∼ 0.2 ML (Figure 9(b)). Afterwards closed Ge hexagonal rings consisting of six clusters begin to form at a Ge coverage of ∼ 0.3 ML (Figure 9(c)). When the Ge coverage approaches to 0.4 ML, most of the HUCs of both FHUC and UHUC are occupied by Ge clusters. The underlying (7 × 7) surface periodicity and the hexagonal superstructures coexist. Finally, the high-regular hexagonal superlattice forms at a Ge coverage of ∼0.5 ML and covers the entire (7 × 7) surface (Figure 9(e)). The driving mechanism for the cluster evolution, ascribing to the charge transfer from Si center adatoms to Ge clusters, will be further discussed as following in association with DFT calculations.

In Figures 10(a) and 10(b), we show contrasted filled-state STM image at sample bias −2.5 V, and empty-state image at +2.5 V, respectively. The Ge clusters look more compact in the former than in the latter, and they show strong brightness in the center region of the FHUC. An obvious feature is that Ge cluster has a strong effect on its three neighboring UHUCs. The closest Si-center adatoms in the nearest-neighbor UHUCs are invisible in the filled-state image. However, these Si adatoms do exist at their original places in the (7 × 7) reconstruction, as shown by the empty-state image. This fact suggests that the Si-center adatoms in the nearest-neighbor UHUCs transfer charge to the Ge clusters.

As we known, the tunneling electrons transfer from sample to tip for the filled-state imaging, in reverse, they transfer from tip to sample for the empty-state imaging. Here in our measurements, in the filled-state images, the darkened areas (center adatoms) surround the clusters. One reason is due to geometric defect, that is, no adatoms exist at these positions. But the empty-state images prove the existence of the adatoms at the original positions. So, the only reason is that the charge of center adatoms transfers to nearby Ge clusters and resulting in the absence of tunneling electrons from center adatoms in the filled-state images. Thus, the STM measurements demonstrate lateral charge redistributions in Ge-Si system.

The charge transferring from center adatoms to Ge cluster is further revealed by first-principle DFT calculations. For all the minimum-energy configurations, Ge clusters contain 6 ∼ 12 Ge atoms in the FHUC of a (7 × 7) unit cell, and the dangling bond state of the center Si adatoms nearby the FHUC is almost empty, indicating charge transfer of neighboring Si adatoms. Figure 10(e) shows the projected electronic density of states (local density of states, DOS) onto the center Si adatom in an adjacent UHUC before and after the formation of a nine-Ge cluster in an FHUC, see the minimum-energy configuration in Figure 10(f). For clean Si(111)-7 × 7 surface before Ge deposition, the dangling bond state of the center Si adatom is partially occupied and crosses the Fermi level [80, 88, 89]. After the formation of Ge clusters, the occupation of the dangling-bond state is reduced significantly, confirming a charge transfer from the central Si adatom. Such a charge transfer occurs because it can lower the total energy of the system. Self-assembled clusters of various metals formed on Si(111)-7 × 7, which have similar network as Ge clusters, have been reported [24, 27, 28, 90–92]. Several groups suggested that the interaction between the substrate and the metal clusters might play a role for the self-organization [24, 27, 28], and other researchers had emphasized the interaction between the clusters themselves [93]. Charge transfer and its role have not been reported before.

When local coverage is higher, a second Ge clusters may form at the center of an UHUC adjacent to an FHUC already containing a Ge cluster, as shown in Figures 10(c) and 10(d). Similar to the first one, the second Ge cluster darkens the center Si atoms in the two neighboring FHUCs in the filled-state image (Figure 10(c)), which again indicate charge transfer, though the charge transfer is not as effective as in the UHUC. Charge transfer helps us understand the formation of a cluster in an UHUC nearby an existing particle in a FHUC, and further explain the evolution of Ge cluster patterns from isolated one to closed hexagonal patterns [94].

The above results show that a new cluster forms adjacent to an existing FHUC cluster in a neighboring UHUC, and electron transfer occurs from the two new surrounding FHUCs. The two clusters remain distinct with a "dimer wall" separating them as shown in Figure 9(h). First-principle calculations confirm the depletion of charge associating with the dangling bonds of center Si adatoms in the three UHUCs surrounding a Ge cluster in an FHUC, and also a decrease in electronic energy by such a charge transfer. The energy gain can be attributed to "local Madelung energy", which is used in determining the energy of a single ion in a crystal.

Assuming that the amount of charge transferring from any of the center Si adatom is the same $q_0$, then a single cluster has a central charge of $-3q_0$ (Figure 9(f)). The total energy is lowered by a local Madelung energy of the cluster, that is roughly $(-9/d_1 + 3/d_2)q_0^2$, where $d_1$ (∼11 Å) is the distance between the Ge clusters and an adjacent Si adatom that has been depleted of charge, and $d_2$ (∼19 Å) is the distance between two such Si adatoms. Because $d_1$ is smaller than $d_2$, the local Madelung energy is negative ($-0.66q_0^2$). When a second cluster forms in an adjacent UHUC, as in Figure 9(h), the charge on each cluster is reduced from $-3q_0$ to $-2q_0$ and the local Madelung energy is approximately $(-8/d_1 + 2/d_2 + 4/d_3)q_0^2 \approx -0.36q_0^2$, where $d_3$ (∼15.5 Å) is the distance between the two Ge clusters. The local Madelung energy in the Ge cluster pair is smaller than that of single cluster. The reduction in the Madelung energy is used to overcome the factors that inhibit the formation of isolated clusters in UHUCs, and the residual Madelung energy stabilizes the cluster pair. The energy is substantial, and from the DOS curves of Figure 10(e), we estimate $q_0 \approx (0.3–0.5)$ $e$, whereby the Madelung energy stabilizing a pair is ∼ 0.5–1.3 eV. With the emergence of new Ge clusters, the net charge on each Ge cluster decreases gradually from $3q_0$ in the case of an isolated cluster to $2q_0$, $5/3q_0$, $3/2q_0$, $7/5q_0$, and finally $1q_0$ if a complete isolated hexagon is formed as in the schematic of Figures 9(f)–9(k), and the effective Madelung energy per cluster also gradually reduces. So the reduction of the local Madelung energies contributes to the stabilization of the local cluster structures. Thus here we quantitatively revealed how the charge transfer sustains the evolution of cluster patterns from isolated ones to ordered hexagonal arrays.

### 2.4. Formation of Ge islands and Ge-Si intermixing at high temperature

The further increase of the substrate temperature causes the coarsening of clusters and intermixing between Ge and Si atoms, which is believed to be due to the enhancing mobility of Ge atoms [43, 44]. When the substrate temperature is increased to about 300°C or even higher temperature, the Ge islands begin epitaxial growth. Deposition of Ge atoms on Si(111)-7 × 7 at room temperatures following by annealing treatment also results in 2D extended Ge islands. Figure 11(a) shows a typical surface morphology of a Ge island with submonolayer Ge coverage. There are three distinct features in this image. First, the reconstruction of the island is (7 × 7), same as the configuration of original substrate, see the close-up STM image in Figure 11(c). Second, the dimer directions of the Ge island are same as that of the substrate which, revealing the supercell of Ge island, has the same alignment as the substrate. Third, the shape of Ge islands is usually close to triangle, similar to the shape of HUC triangle of the substrate. All these features reveal the modulation effect of the substrate to the epitaxy growth of Ge islands.

During the growth of an island, the substrate (7 × 7) reconstruction has to be removed and the surface Si atoms will rearrange to the bulk (1 × 1) structure [95]. It needs to overcome different energy barriers for the removal of the reconstruction in the UHUCs and in the FHUCs [96]. In the UHUC triangles, only the atoms in the topmost layer rearrange, which is associated with a relatively low-energy barrier. However, in the FHUC triangles, the removal of the stacking faults (see the schematic in Figure 1) in the deeper layer below the adatoms is associated with a larger energy barrier. The activation barrier for Ge overgrowth in the FHUCs is clearly higher than in the UHUCs. Thus, the edges of Ge island are comprised of UHUC triangles and surrounded by FHUC triangles of the substrate, as shown in Figures 11(c) and 11(d).

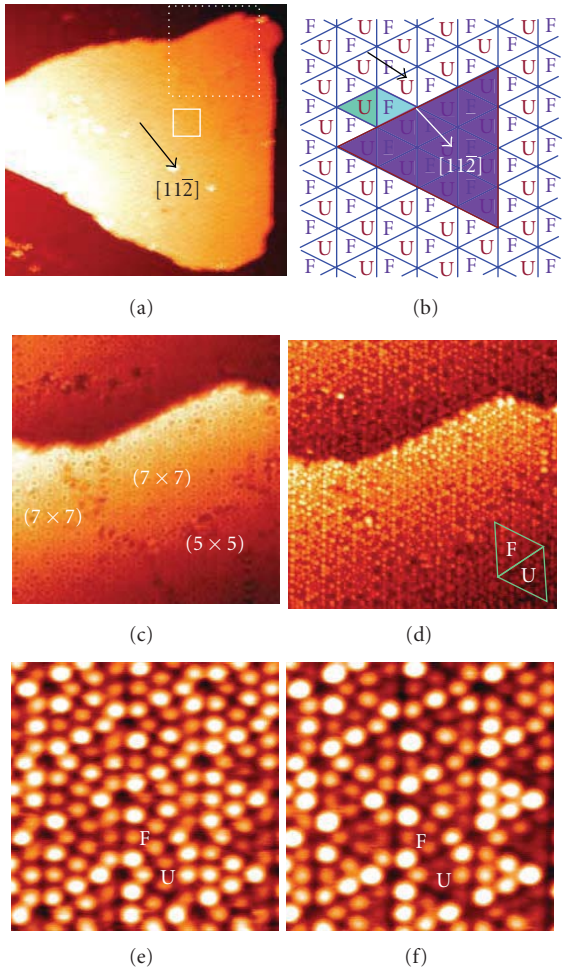


FIGURE 11: (a) STM image shows a typical Ge island on the Si(111)-7 × 7 surface. The substrate temperature was kept at 300°C for Ge deposition. (b) The schematic drawing of the Ge island on (7 × 7) reconstruction. (c) and (d) are amplified images of the area in (a) depicted with a dotted-line square. (7 × 7) and (5 × 5) reconstructions coexist in the island. (e) and (f) are the close-up images of area in (a) depicted with a solid-line square. These images, with the irregular distribution of the brighter atoms, illustrate the intermixing between Ge and Si atoms. Scanning parameters: (a) 120 nm × 100 nm, 1.8 V, 0.15 nA; (c) 45 nm × 45 nm, 1.2 V, 0.15 nA; (d) 45 nm × 45 nm, −1.2 V, 0.15 nA; (e) 9 nm × 9 nm, −1.0 V, 0.15 nA; (f) 9 nm × 9 nm, −1.5 V, 0.15 nA.

Figure 11(b) is the schematic drawing for the Ge island on (7 × 7) reconstruction. FHUC triangles surrounding the Ge island as a high-energy barrier hinder the further growth in them. Ge will nucleate on the UHUC triangle near the FHUC triangle, as denoted by the black arrow in Figure 11(b), where it has low energy barrier. The energy barrier of FHUC triangle will be reduced by a gain of edge energy, thus the FHUC triangle between the island edge and the UHUC triangle with Ge nucleation will be attached by epitaxy Ge atoms. As a result, the Ge island shows a lateral growth model along its edge, and the shape of Ge islands usually is triangle, which is due to the modulation by the substrate reconstruction.

Figures 11(c) and 11(d) show the island involving in several domains with two different reconstructions, (7 × 7) and (5 × 5). The domain boundaries (defect area) are very clear. Their formation is due to the strains between the substrate and the Ge epitaxy island. The defects on the substrate (like the missing of adatoms and vacancies) will deform the period of (7 × 7) reconstruction and give rise to strain [47, 97]. In addition, the mismatch of the lattice constant of Ge and Si (Ge is 4% larger than Si) will also bring strain. The strains can be effectively released by the formation of the domain boundaries and the different kinds of reconstruction such as the (7 × 7) and (5 × 5) domains shown here.

The (5 × 5) reconstruction also can be described by DAS model [53, 68], as the model shown in Figure 1 for the (7 × 7). Each (5 × 5) unit cell includes one triangle FHUC and one UHUC, and there are three adatoms and one rest atom distributing on the topmost layer in each HUC.

The close-up filled-state STM images in Figures 11(e) and 11(f) show an irregular distribution of brighter adatoms in (7 × 7) unit cell. The arrangement of adatoms, however, is very regular on pure Si(111)-7×7 surface, where the adatoms in the FHUC are imaged brighter than the adatoms in the UHUC, and the corner adatoms are brighter than the center adatoms in both FHUC triangle and UHUC triangle [98]. Here, the brightness and contrast features between adatoms disappear. In Figures 11(e) and 11(f), the corner (or center) adatoms in the same HUC show different brightness, and even some spots at the center adatoms sites are bright close to that of the spots at the corner adatoms sites, so it clearly suggests the mixing condition of Ge and Si atoms. According to the contrast feature of single Ge atoms on Si surface at very low coverage (Figure 5), the brighter protrusions at the center adatoms sites in Figure 11(e) are Ge atoms, and the dimmer ones are Si atoms. These observations are coincided with the findings reported in the earlier literatures [81, 82, 99, 100], where the Ge-Si exchange in Si(111)-5 × 5 Ge reconstructions has been proposed. Most recent results by Voigtländer et al. provided evidences for the exchange and intermixing of Ge/Si in Si(111)-7 × 7 surface at high temperatures by their special techniques [43, 44]. They showed the chemical contrast images between Si and Ge in their STM observations (Ge is much brighter than Si) obtained on Bi-covered Ge/Si(111) surfaces. Thus, the Ge-Si exchanging and intermixing happen at high temperature, and play an important role in the epitaxial growth of Ge islands.

In our high-temperature deposition experiments, when Ge coverage keeps at the range of 0.2 to 0.5 ML, a novel local reconstruction with an ordered arrangement of Ge atoms on the Si(111) surfaces is obtained. Figure 12 shows the STM images of such Ge-induced reconstruction, which coexists with the Si(111)-7 × 7 reconstruction. The local reconstruction emerges not only inside the Ge island (Figure 12(a)) but also inside the original (7 × 7) surface (Figure 12(b)). The triangle domain runs over 30 nm in edge length. The close-up image in Figure 12(c) illustrates the local atomic structure with a hexagonal arrangement. The atomic density is higher than the normal (7 × 7)

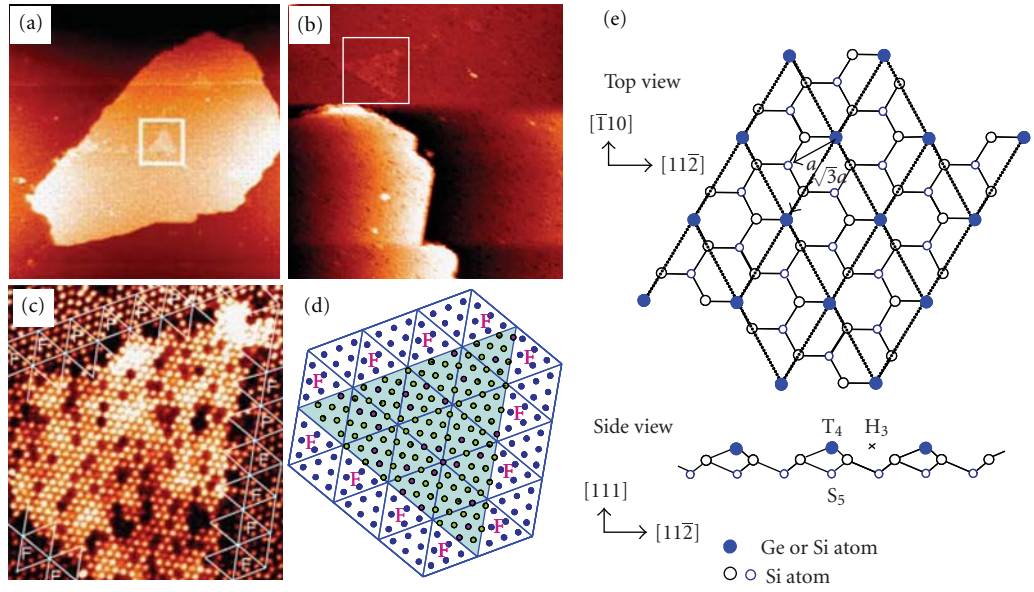


FIGURE 12: STM images of 0.45 ML Ge on the Si(111)-7 × 7 surface. The substrate temperature was held at 300°C for the Ge deposition. Local $(\sqrt{3} \times \sqrt{3})R30^\circ$ reconstruction (marked by the white squares) emerges inside the Ge island in (a) and the Si(111)-7 × 7 substrate in (b). (c) High-resolution image of triangle domain. (d) Schematic of the atomic arrangement of the $(\sqrt{3} \times \sqrt{3})R30^\circ$ domain surrounded by FHUC triangles. (e) Schematic top and side views of the atomic arrangement for the $(\sqrt{3} \times \sqrt{3})R30^\circ$ reconstruction with the adatoms at the $T_4$ sites. The images are recorded at 2.0 V, 0.10 nA in (a), and 1.4 V, 0.20 nA in (b) and (c). Image sizes: (a) 236 nm × 236 nm, (b) 123 nm × 123 nm, and (c) 22 nm × 24 nm.

reconstruction and the orientation of atom rows is different from the surrounding (7 × 7) lattice alignment. The distance between the neighbor atoms is 0.65 ± 0.01 nm, that is, about $\sqrt{3}$ times the length of the basis vector (0.38 nm) for the ideal bulk-terminated Si(111)-1 × 1 unit cell. In addition, we measured the angle between the main direction of the new local reconstruction and the boundary of the nearby (7 × 7) unit cells and found it to be 30°. Thus, the local reconstruction shows a $(\sqrt{3} \times \sqrt{3})R30^\circ$ arrangement.

The appearance of images in Figures 12(a) and 12(b) demonstrates that Ge-induced $(\sqrt{3} \times \sqrt{3})R30^\circ$ reconstruction replaces some of the (7 × 7) unit cells, and it does not cover the whole surface or the whole island. The local Ge nanostructures thus coexist with the Si(111)-(7 × 7) reconstruction. In addition, several dimmer features at some atom positions exist within the $(\sqrt{3} \times \sqrt{3})R30^\circ$ reconstruction (Figure 12(c)), suggesting that Si atoms are mixed with the Ge atoms.

The schematic in Figure 12(d) shows the atomic arrangement of the $(\sqrt{3} \times \sqrt{3})R30^\circ$ domain surrounded by the FHUC triangles of (7 × 7) unit cells. As the above-mentioned analysis for the similar structure of Ge island boundary in Figure 11(b), removing the reconstruction of the FHUC triangles requires to overcome a larger energy barrier [96]. The activation energy for atom rearrangement in FHUC halves is higher than that in UHUC halves. Thus, the $(\sqrt{3} \times \sqrt{3})R30^\circ$ domain propagates energy preferentially in UHUC triangles.

We further go inside the bonding structure of the local $(\sqrt{3} \times \sqrt{3})R30^\circ$ arrangement with support from the first-principle calculations. When the top-layer atoms form a $(\sqrt{3} \times \sqrt{3})R30^\circ$ reconstruction on Si(111), the underlying substrate changes its original (7 × 7) reconstruction to (1 × 1) arrangement. On an ideal unreconstructed Si(111) surface, there are two types of threefold symmetric adsorption sites, known as $T_4$, a filled position directly above a second-layer Si atom and $H_3$, a hollow site above a fourth-layer Si atom sites [88, 90], as shown in Figure 12(e). The adsorbed atoms at either $T_4$ or $H_3$ sites are bonded to three first-layer Si atoms. When the dangling bonds of all the first-layer Si atoms are saturated in this way, the adsorbed atoms form a $(\sqrt{3} \times \sqrt{3})R30^\circ$ reconstruction. Such a reconstruction could also be formed when the adsorbed atoms occupy the so-called $S_5$ site (Figure 12(e)), in which an adsorbed atom substitutes a second-layer Si atom while the replaced Si atom is at the $T_4$ site directly above $S_5$ [16, 101, 102]. Our collaborators have performed the first-principle DFT calculations for a $(\sqrt{3} \times \sqrt{3})R30^\circ$ reconstruction. In the case of the Ge-$S_5$ configuration, Ge or Si forms an adlayer with a Ge coverage of 1/3 monolayer for each of the three bonding configurations [103].

The calculations show that the $T_4$ configuration is the most stable structure. Its total energy is lower than both the $H_3$ and the $S_5$ configurations by 0.60 and 0.68 eV per unit cell, respectively. This is consistent with the general picture that the adatoms prefer to occupy the $T_4$ sites on almost all of the Si(111)-$(\sqrt{3} \times \sqrt{3})R30^\circ$ surfaces induced by chemisorptions of groups III, IV, and V atoms [101]. The occurrence of Ge atoms in the subsurface substitutional $S_5$ sites is usually adopted by small atoms such as boron and carbon [104–107], and is energetically unfavorable. Occupation of a Ge atom at the subsurface $S_5$ site would

introduce significant strain energy due to its larger size than Si. In addition, for the Ge-$S_5$ configuration, fully filled Ge-associated bands do not warrant a charge transfer from the Si dandling bond to the subsurface to decrease the surface energy as observed in the boron-induced $S_5$ configuration [108]. Therefore, Ge atoms would prefer to stay on the surface. While the underlying substrate supporting the Ge-induced $(\sqrt{3} \times \sqrt{3})R30^\circ$ structure has an unreconstructed Si(111) configuration, and significant structural relaxation is also found.

## 3. CONCLUSIONS

Firstly, we reported UHV-STM experiments and first-principle total energy calculations which are combined to determine the STM images of Si(111)-7×7 surface. Both the rest atoms and adatoms were observed simultaneously with high contrast by using the conventional W tips. The emergence of the rest atoms was dependent on the sample bias voltage. The rest atom spots could be visible at the bias voltages less than $-0.7$ V, and their brightness is even comparable to that of the center Si adatoms when the voltage is less than $-0.9$ V. The possible explanations for the visibility of rest atoms in our STM images were discussed and a very sharper tip could resolve them, which were enunciated by first-principle calculations.

Secondly, we investigated the structural characterizations and the bonding nature of diverse Ge nanostructures on Si(111)-7×7 surface at different deposition stages. We performed STM measurements of the adsorption site of single Ge atom on the Si(111)-7×7 surfaces for a sequence of submonolayer coverages deposited at 150°C. The observations suggested that individual Ge atoms replaced the so-called Si adatoms rather than being adsorbed directly atop of the Si adatoms. Initially, the replacements were random, but distinct patterns emerged when increasing the Ge coverages, until small clusters are formed on the substrate. The first-principle density-functional calculations revealed that Ge/Si substitution configuration was more energetically favorable and thermodynamically stable than the arrangements of Ge locating at the high-coordination surface sites.

Further deposited Ge atoms generated nanoclusters with varying geometrical configurations. Individual Ge atoms and Ge clusters coexisted on the Si(111)-7×7 surfaces. Ge nanoclusters gradually produced in both the faulted and unfaulted half unit cells of (7×7) units with an initial preference in the faulted halves, and ultimately self-organized into the form of well-ordered hexagonal superlattice corresponding to the geometry of one Ge cluster per triangle half unit of original (7×7) lattice. Charge transfer from Si adatoms to Ge nanoclusters played a key role in the self-organization of the superlattice, which was proved by experimental observations and theoretic calculations.

Two-dimensional extended Ge islands with triangle shape were formed on the substrate when its temperature was kept at 300°C for Ge deposition. The irregular distribution of brighter topmost adatoms suggested the intermixing status of Ge/Si components in the islands, and the intermixing ascribed to the exchanging of Ge atoms with the substrate Si atoms at higher temperatures. Several local domains with different reconstructions like (5×5) and $(\sqrt{3} \times \sqrt{3})R30^\circ$ arrangements were found on the substrates. The configuration of the Ge adatoms residing at the $T_4$ sites rather than $S_5$ or $H_3$ positions in the $(\sqrt{3} \times \sqrt{3})R30^\circ$ reconstruction was proposed according to the first-principle calculations.

## ACKNOWLEDGMENTS

The authors are grateful for H. W. Liu, D. X. Shi, and M. C. Xu for experimental assistance, and I. G. Batyrev, W. E. McMahon, S. B. Zhang, A. S. Rao, S. W. Wang, and S. T. Pantelides for theoretic simulations and calculations. This research is supported by the Natural Science Foundation of China (Grants 07JC021N41 and 07JH011N41) and the Chinese National "973" Project.

## REFERENCES

[1] G. Binning, H. Rohrer, Ch. Gerber, and E. Weibel, "Surface studies by scanning tunneling microscopy," *Physical Review Letters*, vol. 49, no. 1, pp. 57–61, 1982.

[2] G. Binnig, H. Rohrer, Ch. Gerber, and E. Weibel, "7 × 7 reconstruction on Si(111) resolved in real space," *Physical Review Letters*, vol. 50, no. 2, pp. 120–123, 1983.

[3] Ph. Avouris and R. Wolkow, "Atom-resolved surface chemistry studied by scanning tunneling microscopy and spectroscopy," *Physical Review B*, vol. 39, no. 8, pp. 5091–5100, 1989.

[4] O. Nishikawa, M. Tomitori, F. Iwawaki, and N. Hirano, "Correlation between scanning tunneling microscopy/spectroscopy images and apex profiles of scanning tips," *Journal of Vacuum Science & Technology A*, vol. 8, no. 1, pp. 421–424, 1990.

[5] M. A. Lantz, H. J. Hug, P. J. A. van Schendel, et al., "Low temperature scanning force microscopy of the Si(111)-(7×7) surface," *Physical Review Letters*, vol. 84, no. 12, pp. 2642–2645, 2000.

[6] F. J. Giessibl, S. Hembacher, H. Bielefeldt, and J. Mannhart, "Subatomic features on the silicon (111)-(7 × 7) surface observed by atomic force microscopy," *Science*, vol. 289, no. 5478, pp. 422–425, 2000.

[7] F. J. Giessibl, "Atomic resolution of the silicon (111)-(7 × 7) surface by atomic force microscopy," *Science*, vol. 267, no. 5194, pp. 68–71, 1995.

[8] P. Sutter, P. Zahl, E. Sutter, and J. E. Bernard, "Energy-filtered scanning tunneling microscopy using a semiconductor tip," *Physical Review Letters*, vol. 90, no. 16, Article ID 166101, 4 pages, 2003.

[9] R. J. Hamers, R. M. Tromp, and J. E. Demuth, "Surface electronic structure of Si (111)-(7×7) resolved in real space," *Physical Review Letters*, vol. 56, no. 18, pp. 1972–1975, 1986.

[10] R. S. Becker, B. S. Swartzentruber, J. S. Vickers, and T. Klitsner, "Dimer-adatom-stacking-fault (DAS) and non-DAS (111) semiconductor surfaces: a comparison of Ge(111)-c(2×8) to Si(111)-(2×2), -(5×5), -(7×7), and -(9×9) with scanning tunneling microscopy," *Physical Review B*, vol. 39, no. 3, pp. 1633–1647, 1989.

[11] K. Takayanagi, Y. Tanishiro, M. Takahashi, and S. Takahashi, "Structural analysis of Si(111)-7 × 7 by UHV-transmission

electron diffraction and microscopy," *Journal of Vacuum Science & Technology A*, vol. 3, no. 3, pp. 1502–1506, 1985.

[12] A. Li Bassi, C. S. Casari, D. Cattaneo, et al., "Bulk Cr tips for scanning tunneling microscopy and spin-polarized scanning tunneling microscopy," *Applied Physics Letters*, vol. 91, no. 17, Article ID 173120, 3 pages, 2007.

[13] L. Chen, B. C. Pan, H. Xiang, et al., "Observation of local electronic structures of adatom vacancies in Si (111)-(7 × 7) surface in real space," *Physical Review B*, vol. 75, no. 8, Article ID 085329, 5 pages, 2007.

[14] R. Wiesendanger, *Scanning Probe Microscopy and Spectroscopy: Methods and Applications*, Cambridge University Press, Cambridge, UK, 1994.

[15] S. B. Zhang, M. L. Cohen, and S. G. Louie, "Structural and electronic properties of the Al-GaAs(110) interface," *Physical Review B*, vol. 34, no. 2, pp. 768–772, 1986.

[16] W. Kohn and L. J. Sham, "Self-consistent equations including exchange and correlation effects," *Physical Review*, vol. 140, no. 4A, pp. A1133–A1138, 1965.

[17] G. Kresse and J. Furthmüller, "Efficiency of ab-initio total energy calculations for metals and semiconductors using a plane-wave basis set," *Computational Materials Science*, vol. 6, no. 1, pp. 15–50, 1996.

[18] D. Vanderbilt, "Soft self-consistent pseudopotentials in a generalized eigenvalue formalism," *Physical Review B*, vol. 41, no. 11, pp. 7892–7895, 1990.

[19] J. Tersoff and D. R. Hamann, "Theory of the scanning tunneling microscope," *Physical Review B*, vol. 31, no. 2, pp. 805–813, 1985.

[20] Y.-L. Wang, H.-J. Gao, H.-M. Guo, et al., "Tip size effect on the appearance of a STM image for complex surfaces: theory versus experiment for Si(111)-(7 × 7)," *Physical Review B*, vol. 70, no. 7, Article ID 073312, 4 apges, 2004.

[21] H. Brune, M. Giovannini, K. Bromann, and K. Kern, "Self-organized growth of nanostructure arrays on strain-relief patterns," *Nature*, vol. 394, no. 6692, pp. 451–453, 1998.

[22] I.-S. Hwang, M.-S. Ho, and T. T. Tsong, "Dynamic behavior of Si magic clusters on Si(111) surfaces," *Physical Review Letters*, vol. 83, no. 1, pp. 120–123, 1999.

[23] J.-L. Li, J.-F. Jia, X.-J. Liang, et al., "Spontaneous assembly of perfectly ordered identical-size nanocluster arrays," *Physical Review Letters*, vol. 88, no. 6, Article ID 066101, 4 pages, 2002.

[24] J. Jia, J.-Z. Wang, X. Liu, et al., "Artificial nanocluster crystal: lattice of identical Al clusters," *Applied Physics Letters*, vol. 80, no. 17, pp. 3186–3188, 2002.

[25] J.-F. Jia, X. Liu, J.-Z. Wang, et al., "Fabrication and structural analysis of Al, Ga, and in nanocluster crystals," *Physical Review B*, vol. 66, no. 16, Article ID 165412, 10 pages, 2002.

[26] B. Voigtländer, M. Kästner, and P. Šmilauer, "Magic islands in Si/Si(111) homoepitaxy," *Physical Review Letters*, vol. 81, no. 4, pp. 858–861, 1998.

[27] K. Wu, Y. Fujikawa, T. Nagao, et al., "Na Adsorption on the Si(111)-(7 × 7) surface: from two-dimensional gas to nanocluster array," *Physical Review Letters*, vol. 91, no. 12, Article ID 126101, 4 pages, 2003.

[28] L. Vitali, M. G. Ramsey, and F. P. Netzer, "Nanodot formation on the Si(111)-(7 × 7) surface by adatom trapping," *Physical Review Letters*, vol. 83, no. 2, pp. 316–319, 1999.

[29] H. Hibino and T. Ogino, "Substitution of In for Si adatoms and exchanges between In and Si adatoms on a Si(111)-7 × 7 surface," *Physical Review B*, vol. 55, no. 11, pp. 7018–7022, 1997.

[30] I. Chizhov, G. Lee, and R. F. Willis, "Initial stages of Au adsorption on the Si(111)-(7×7) surface studied by scanning tunneling microscopy," *Physical Review B*, vol. 56, no. 19, pp. 12316–12320, 1997.

[31] Ph. Sonnet, L. Stauffer, and C. Minot, "Adsorption and diffusion mechanisms of Pb on Si(111)-(7 × 7) in the initial stages of Pb chemisorption," *Surface Science*, vol. 407, no. 1–3, pp. 121–132, 1998.

[32] J. M. Gómez-Rodríguez, J. J. Sáenz, A. M. Baró, J.-Y. Veuillen, and R. C. Cinti, "Real-time observation of the dynamics of single Pb atoms on Si(111)-(7 × 7) by scanning tunneling microscopy," *Physical Review Letters*, vol. 76, no. 5, pp. 799–802, 1996.

[33] O. Custance, S. Brochard, I. Brihuega, et al., "Single adatom adsorption and diffusion on Si(111)-(7 × 7) surfaces: scanning tunneling microscopy and first-principles calculations," *Physical Review B*, vol. 67, no. 23, Article ID 235410, 4 pages, 2003.

[34] M. Yoon, X. F. Lin, I. Chizhov, H. A. Mai, and R. F. Willis, "Self-assembled nanodot arrays on Si(111)-(7 × 7) surfaces," *Physical Review B*, vol. 64, no. 8, Article ID 085321, 5 pages, 2001.

[35] X. F. Lin, I. Chizhov, H. A. Mai, and R. F. Willis, "Interaction of Sn atoms with the intrinsic dangling-bond states of Si(111)-(7 × 7)," *Surface Science*, vol. 366, no. 1, pp. 51–59, 1996.

[36] O. Custance, I. Brihuega, J. M. Gómez-Rodríguez, and A. M. Baró, "Initial stages of Sn adsorption on Si(111)-(7 × 7)," *Surface Science*, vol. 482–485, no. 2, pp. 1406–1412, 2001.

[37] Y. P. Zhang, L. Yang, Y. H. Lai, G. Q. Xu, and X. S. Wang, "Formation of ordered two-dimensional nanostructures of Cu on the Si(111)-(7 × 7) surface," *Surface Science*, vol. 531, no. 3, pp. L378–L382, 2003.

[38] H. F. Hsu, L. J. Chen, H. L. Hsiao, and T. W. Pi, "Adsorption and switching behavior of individual Ti atoms on the Si(111)-7 × 7 surface," *Physical Review B*, vol. 68, no. 16, Article ID 165403, 10 pages, 2003.

[39] B. Voigtländer and T. Weber, "Growth processes in Si/Si(111) epitaxy observed by scanning tunneling microscopy during epitaxy," *Physical Review Letters*, vol. 77, no. 18, pp. 3861–3864, 1996.

[40] B. Voigtländer, "Scanning tunneling microscopy studies during semiconductor growth," *Micron*, vol. 30, no. 1, pp. 33–39, 1999.

[41] B. Voigtländer, "Fundamental processes in Si/Si and Ge/Si epitaxy studied by scanning tunneling microscopy during growth," *Surface Science Reports*, vol. 43, no. 5–8, pp. 127–254, 2001.

[42] B. Voigtländer, M. Kawamura, N. Paul, and V. Cherepanov, "Formation of Si/Ge nanostructures at surfaces by self-organization," *Journal of Physics Condensed Matter*, vol. 16, no. 17, pp. S1535–S1551, 2004.

[43] M. Kawamura, N. Paul, V. Cherepanov, and B. Voigtländer, "Nanowires and nanorings at the atomic level," *Physical Review Letters*, vol. 91, no. 9, Article ID 096102, 4 pages, 2003.

[44] N. Paul, S. Filimonov, V. Cherepanov, M. Çakmak, and B. Voigtländer, "Identification of Ge/Si intermixing processes at the Bi/Ge/Si(111) surface," *Physical Review Letters*, vol. 98, no. 16, Article ID 166104, 4 pages, 2007.

[45] T. Sekiguchi, S. Yoshida, K. M. Itoh, J. Mysliveček, and B. Voigtländer, "One-dimensional ordering of Ge nanoclusters along atomically straight steps of Si(111)," *Applied Physics Letters*, vol. 90, no. 1, Article ID 013108, 3 pages, 2007.

[46] Z. A. Ansari, M. Tomitori, and T. Arai, "Evidence of temperature dependence of initial adsorption sites of Ge atoms on Si (111)-7 × 7," *Applied Physics Letters*, vol. 88, no. 17, Article ID 171902, 3 pages, 2006.

[47] M. Suzuki, R. Negishi, and Y. Shigeta, "Strain and electronic structure of Ge nanoislands on Si(111)-7×7 surface," *Physical Review B*, vol. 72, no. 23, Article ID 235325, 5 pages, 2005.

[48] Y. P. Zhang, L. Yan, S. S. Xie, S. J. Pang, and H.-J. Gao, "Self-assembled growth of ordered Ge nanoclusters on the Si(111)-(7 × 7) surface," *Surface Science*, vol. 497, no. 1–3, pp. L60–L64, 2002.

[49] J. Bęben, I.-S. Hwang, T.-C. Chang, and T. T. Tsong, "Model for surfactant-mediated growth of Ge on Pb-covered Si(111) surfaces," *Physical Review B*, vol. 63, no. 3, Article ID 033304, 4 pages, 2001.

[50] K. Wang, C. Zhang, M. M. T. Loy, and X. Xiao, "Time-dependent tunneling spectroscopy for studying surface diffusion confined in nanostructures," *Physical Review Letters*, vol. 94, no. 3, Article ID 036103, 4 pages, 2005.

[51] C. Zhang, G. Chen, K. Wang, et al., "Experimental and theoretical investigation of single Cu, Ag, and Au atoms adsorbed on Si(111)-(7×7)," *Physical Review Letters*, vol. 94, no. 17, Article ID 176104, 4 pages, 2005.

[52] P. M. Petro, A. Lorke, and A. Imamoglu, "Epitaxially selfassembled quantum dots," *Physics Today*, vol. 54, no. 5, pp. 46–52, 2001.

[53] N. Motta, "Self-assembling and ordering of Ge/Si(111) quantum dots: scanning microscopy probe studies," *Journal of Physics Condensed Matter*, vol. 14, no. 35, pp. 8353–8378, 2002.

[54] Y. P. Zhang, L. Yan, S. S. Xie, S. J. Pang, and H.-J. Gao, "Formation of ordered Ge quantum dots on the Si(111)-(7 × 7) surface," *Applied Physics Letters*, vol. 79, no. 20, pp. 3317–3319, 2001.

[55] A. Lobo, S. Gokhale, and S. K. Kulkarni, "Surface morphology and electronic structure of Ge/Si(111)-7 × 7 system," *Applied Surface Science*, vol. 173, no. 3-4, pp. 270–281, 2001.

[56] L. Yan, H. Yang, H.-J. Gao, S. S. Xie, and S. Pang, "Initial adsorption of Ge on Si(111)- (7 × 7) surface at room temperature," *Surface Science*, vol. 498, no. 1-2, pp. 83–88, 2002.

[57] L. Yan, Y. Zhang, H.-J. Gao, S. S. Xie, and S. Pang, "Formation of two dimension Ge cluster superlattice on Si(111)- (7 × 7) surface," *Surface Science*, vol. 506, no. 1-2, pp. L255–L260, 2002.

[58] F. Ratto, F. Rosei, A. Locatelli, et al., "Composition of Ge(Si) islands in the growth of Ge on Si(111)," *Applied Physics Letters*, vol. 84, no. 22, pp. 4526–4528, 2004.

[59] H.-M. Guo, Y.-L. Wang, H. W. Liu, H.-F. Ma, Z.-H. Qin, and H.-J. Gao, "Formation of Ge nanoclusters on Si(111)-7 × 7 surface at high temperature," *Surface Science*, vol. 561, no. 2-3, pp. 227–232, 2004.

[60] Z. A. Ansari, T. Arai, and M. Tomitori, "Hexagonal arrangement of Ge clusters self-organized on a template of half unit cells of Si(111) -7 × 7 observed by scanning tunneling microscopy," *Surface Science*, vol. 574, no. 2-3, pp. L17–L22, 2005.

[61] A. Zhao, X. Zhang, G. Chen, M. M. T. Loy, and X. Xiao, "Initial stages of the adsorption of Ge atoms on the Si (111) - (7 × 7) surface," *Physical Review B*, vol. 74, no. 12, Article ID 125301, 8 pages, 2006.

[62] F. Ratto, A. Locatelli, S. Fontana, et al., "Diffusion dynamics during the nucleation and growth of Ge/Si nanostructures on Si(111)," *Physical Review Letters*, vol. 96, no. 9, Article ID 096103, 4 pages, 2006.

[63] T. P. Pearsall, "Si-Ge alloys and superlattices for optoelectronics," *Materials Science and Engineering B*, vol. 9, no. 1–3, pp. 225–231, 1991.

[64] L. J. Schowalter, "Heteroepitaxy and strain: applications to electronic and optoelectronic materials," *MRS Bulletin*, vol. 21, no. 4, pp. 18–19, 1996.

[65] A. P. Alivisatos, "Semiconductor clusters, nanocrystals, and quantum dots," *Science*, vol. 271, no. 5251, pp. 933–937, 1996.

[66] C. Westphal, "The study of the local atomic structure by means of X-ray photoelectron diffraction," *Surface Science Reports*, vol. 50, no. 1–3, pp. 1–106, 2003.

[67] F. Boscherini, G. Capellini, L. Di Gaspare, F. Rosei, N. Motta, and S. Mobilio, "Ge-Si intermixing in Ge quantum dots on Si(001) and Si(111)," *Applied Physics Letters*, vol. 76, no. 6, pp. 682–684, 2000.

[68] U. Köhler, O. Jusko, G. Pietsch, B. Müller, and M. Henzler, "Strained-layer growth and islanding of germanium on Si(111)-(7 × 7) studied with STM," *Surface Science*, vol. 248, no. 3, pp. 321–331, 1991.

[69] J. R. Patel, J. A. Golovchenko, J. C. Bean, and R. J. Morris, "X-ray-standing-wave interface studies of germanium on Si(111)," *Physical Review B*, vol. 31, no. 10, pp. 6884–6886, 1985.

[70] B. N. Dev, G. Materlik, F. Grey, R. L. Johnson, and M. Clausnitzer, "Geometrical structures of the Ge/Si(111) interface and the Si(111) (7 × 7) surface," *Physical Review Letters*, vol. 57, no. 24, pp. 3058–3061, 1986.

[71] K. Kajiyama, Y. Tanishiro, and K. Takayanagi, "Reconstructions and phase transitions of Ge on the Si(111)-7×7 surface: II. 7×7 and 5×5 structures stabilized by Ge," *Surface Science*, vol. 222, no. 1, pp. 47–63, 1989.

[72] J. A. Carlisle, T. Miller, and T.-C. Chiang, "Ge chemisorption and alloying on the Si(111)-(7 × 7) surface," *Physical Review B*, vol. 49, no. 19, pp. 13600–13606, 1994.

[73] P. Castrucci, R. Gunnella, M. De Crescenzi, M. Sacchi, G. Dufour, and F. Rochet, "Electronic density of empty states of Ge/Si(111) epitaxial layers: theory and experiment," *Physical Review B*, vol. 60, no. 8, pp. 5759–5769, 1999.

[74] G. H. Takaoka, T. Seki, K. Tsumura, and J. Matsuo, "Scanning tunneling microscope observations of Ge deposition on Si(111)-7×7 surfaces irradiated by Xe ions," *Thin Solid Films*, vol. 405, pp. 141–145, 2002.

[75] M. Grodzicki and M. Wagner, "Cluster molecular-orbital calculations on germanium adsorbed on Si(111) surfaces," *Physical Review B*, vol. 40, no. 2, pp. 1110–1120, 1989.

[76] L. Stauffer, S. Van, D. Bolmont, J. J. Koulmann, and C. Minot, "First stages of Ge adsorption on the Si (111)-7 × 7 surface: experimental and theoretical studies," *Surface Science*, vol. 307–309, part 1, pp. 274–279, 1994.

[77] L. Stauffer, P. Sonnet, and C. Minot, "Electronic and atomic structure of Ge/Si(111)-7 × 7 in the initial stages of Ge chemisorption," *Surface Science*, vol. 371, no. 1, pp. 63–78, 1997.

[78] K. Cho and E. Kaxiras, "Diffusion of adsorbate atoms on the reconstructed Si(111) surface," *Surface Science*, vol. 396, no. 1–3, pp. L261–L266, 1998.

[79] S. Y. Tong, H. Huang, C. M. Wei, et al., "Low-energy electron diffraction analysis of the Si(111)-7 × 7 structure," *Journal of Vacuum Science & Technology A*, vol. 6, no. 3, pp. 615–624, 1988.

[80] S. Wang, M. W. Radny, and P. V. Smith, "First-principles electronic structure studies for the cluster modeled Si/Si(111) chemisorption system," *Journal of Chemical Physics*, vol. 114, no. 1, pp. 436–444, 2001.

[81] R. S. Becker, J. A. Golovchenko, and B. S. Swartzentruber, "Tunneling images of the $5\times5$ surface reconstruction on Ge-Si(111)," *Physical Review B*, vol. 32, no. 12, pp. 8455–8457, 1985.

[82] T. Fukuda, "Random adatom heights in Ge/Si(111)-$5\times5$ surfaces," *Surface Science*, vol. 351, no. 1–3, pp. 103–110, 1996.

[83] F. Rosei, N. Motta, A. Sgarlata, G. Capellini, and F. Boscherini, "Formation of the wetting layer in Ge/Si(111) studied by STM and XAFS," *Thin Solid Films*, vol. 369, no. 1, pp. 29–32, 2000.

[84] J. P. Perdew and Y. Wang, "Accurate and simple analytic representation of the electron-gas correlation energy," *Physical Review B*, vol. 45, no. 23, pp. 13244–13249, 1992.

[85] K. Cho and E. Kaxiras, "Intermittent diffusion on the reconstructed Si(111) surface," *Europhysics Letters*, vol. 39, no. 3, pp. 287–292, 1997.

[86] I.-W. Lyo and Ph. Avouris, "Atomic scale desorption processes induced by the scanning tunneling microscope," *Journal of Chemical Physics*, vol. 93, no. 6, pp. 4479–4480, 1990.

[87] Y.-L. Wang, H.-J. Gao, H.-M. Guo, S. Wang, and S. T. Pantelides, "Bonding configurations and collective patterns of Ge atoms adsorbed on Si(111)-$(7\times7)$," *Physical Review Letters*, vol. 94, no. 10, Article ID 106101, 4 pages, 2005.

[88] J. E. Northrup, "Origin of surface states on Si(111)-$(7\times7)$," *Physical Review Letters*, vol. 57, no. 1, p. 154, 1986.

[89] K. D. Brommer, M. Galvan, A. Dal Pino Jr., and J. D. Joannopoulos, "Theory of adsorption of atoms and molecules on Si(111)-$(7\times7)$," *Surface Science*, vol. 314, no. 1, pp. 57–70, 1994.

[90] M. Y. Lai and Y.-L. Wang, "Self-organized two-dimensional lattice of magic clusters," *Physical Review B*, vol. 64, no. 24, Article ID 241404, 4 pages, 2001.

[91] H. H. Chang, M. Y. Lai, J. H. Wei, C. M. Wei, and Y.-L. Wang, "Structure determination of surface magic clusters," *Physical Review Letters*, vol. 92, no. 6, Article ID 066103, 4 pages, 2004.

[92] M. A. K. Zilani, H. Xu, T. Liu, et al., "Electronic structure of Co-induced magic clusters grown on Si(111)-$(7\times7)$ : scanning tunneling microscopy and spectroscopy and real-space multiple-scattering calculations," *Physical Review B*, vol. 73, no. 19, Article ID 195415, 5 pages, 2006.

[93] E. Vasco, C. Polop, and E. Rodríguez-Cañas, "Aggregation mechanisms in the adsorption of metals on Si(111)-$7\times7$," *Physical Review B*, vol. 67, no. 23, Article ID 235412, 10 pages, 2003.

[94] H.-F. Ma, Z.-H. Qin, M. C. Xu, et al., "Formation and evolution of a self-organized hierarchy of Ge nanostructures on Si (111)-$(7\times7)$: STM observations and first-principles calculations," *Physical Review B*, vol. 75, no. 16, Article ID 165403, 5 pages, 2007.

[95] M. Suzuki and Y. Shigeta, "Growth of nanoscale Ge magic islands on Si(111)-$7\times7$ substrate," *Surface Science*, vol. 539, no. 1–3, pp. 113–119, 2003.

[96] W. Shimada and H. Tochihara, "Step-structure dependent step-flow: models for the homoepitaxial growth at the atomic steps on Si(111)-$7\times7$," *Surface Science*, vol. 311, no. 1-2, pp. 107–125, 1994.

[97] M. Itoh, H. Tanaka, Y. Watanabe, M. Udagawa, and I. Sumita, "Classification and structure analyses of domain boundaries on Si(111)," *Physical Review B*, vol. 47, no. 4, pp. 2216–2227, 1993.

[98] L. Andersohn, Th. Berke, U. Köhler, and B. Voigtländer, "Nucleation behavior in molecular beam and chemical vapor deposition of silicon on Si(111)-$(7\times7)$," *Journal of Vacuum Science &Technology A*, vol. 14, no. 2, pp. 312–318, 1996.

[99] N. Motta, A. Sgarlata, R. Calarco, et al., "Growth of Ge-Si(111) epitaxial layers: intermixing, strain relaxation and island formation," *Surface Science*, vol. 406, no. 1–3, pp. 254–263, 1998.

[100] P. Martensson, W-X. Ni, G. V. Hansson, J. M. Nicholls, and B. Reihl, "Surface electronic structure of Si(111)$7\times7$-Ge and Si(111)$5\times5$-Ge studied with photoemission and inverse photoemission," *Physical Review B*, vol. 36, no. 11, pp. 5974–5981, 1987.

[101] W. Mönch, *Semiconductor Surfaces and Interfaces*, Springer, New York, NY, USA, 2001.

[102] S. Wang, M. W. Radny, and P. V. Smith, "Ab initio HF/DFT studies of the chemisorption of hydrogen on the cluster simulated Si(111)-$(\sqrt{3}\times\sqrt{3})$R30°-A1 and -Ga surfaces," *Surface Science*, vol. 396, no. 1–3, pp. 40–51, 1998.

[103] Z.-H. Qin, D. X. Shi, H.-F. Ma, et al., "STM observation and first-principles determination of Ge nanoscale structures on Si(111)," *Physical Review B*, vol. 75, no. 8, Article ID 085313, 5 pages, 2007.

[104] P. Castrucci, A. Sgarlata, M. Scarselli, and M. De Crescenzi, "STM study of acetylene reaction with Si(111): observation of a carbon-induced Si(111)-$(\sqrt{3}\times\sqrt{3})$R30° reconstruction," *Surface Science Letters*, vol. 531, no. 1, pp. 329–334, 2003.

[105] X. Peng, L. Ye, and X. Wang, "Carbon induced $(\sqrt{3}\times\sqrt{3})$R30° reconstruction on Si(111) surface: a theoretical study," *Surface Science*, vol. 548, no. 1–3, pp. 51–58, 2004.

[106] C. A. Pignedoli, A. Catellani, P. Castrucci, et al., "Carbon induced restructuring of the Si(111) surface," *Physical Review B*, vol. 69, no. 11, Article ID 113313, 4 pages, 2004.

[107] G. Profeta, L. Ottaviano, and A. Continenza, "$(\sqrt{3}\times\sqrt{3})$R30°$\rightarrow3\times3$ distortion on the C/Si(111) surface," *Physical Review B*, vol. 69, no. 24, Article ID 241307, 4 pages, 2004.

[108] S. Wang, M. W. Radny, and P. V. Smith, "Mechanisms for the stability of Al and B adatoms on the Si(111)-$(\sqrt{3}\times\sqrt{3})$R30° surface," *Physical Review B*, vol. 59, no. 3, pp. 1594–1597, 1999.

Hindawi Publishing Corporation
Journal of Nanomaterials
Volume 2008, Article ID 659397, 10 pages
doi:10.1155/2008/659397

*Research Article*

# Improving the Performance of Lithium-Ion Batteries by Using Spinel Nanoparticles

**J. C. Arrebola, A. Caballero, L. Hernán, and J. Morales**

*Departamento de Química Inorgánica e Ingeniería Química, Universidad de Córdoba, Campus de Rabanales, Edificio Marie Curie, 14071 Córdoba, Spain*

Correspondence should be addressed to L. Hernán, iq1hepal@uco.es

Received 31 July 2007; Revised 21 January 2008; Accepted 10 March 2008

Recommended by Jun Lou

In this work, we examined the use of nanospinels to construct batttery electrodes. We chose two spinels suitable as cathode materials ($LiMn_2O_4$ and $LiNi_{0.5}Mn_{1.5}O_4$, which are representative of 4 and 5 V versus Li metal, resp.) and one providing good results as anode ($Li_4Ti_5O_{12}$). In order to ensure good cell performance, nanometric particles must meet another requirement; thus they should contain few surface or bulk defects (i.e., they should be highly crystalline). Because the synthesis of such spinels usually requires a thermal treatment, ensuring that they will meet both requirements entails accuratly controlling in the synthesis conditions. Thermal decomposition of nanooxalate in the spinel-conaining elements obtained by mechanochenical activation in the presence of polymers provides a simple, effective route for this purpose. We prepared two types of hybrid lithium-ion batteries using $LiMn_2O_4$ and $LiNi_{0.5}Mn_{1.5}O_4$ as cathode materials, and $Li_4Ti_5O_{12}$ as anode material. The electrochemical properties of these cells were compared with those of a similar configuration made from micrometric particles. The nano-nano configuration exhibited higher reversibility and better performance than the micro-micro configuartion in both types of cells, possibly as a result of lithium ions in the former being able to migrate more easily into the electrode material.



## 1. INTRODUCTION

Some properties of nanometric materials differ markedly from those of micrometric materials of identical composition by effect of mere simple size effects or differences in electronic structure. This has aroused great expectations in many fields including the production of electrochemical energy storage systems. Thus, the use of nanometric materials to prepare electrodes for lithium-ions batteries has gained substantial interest in the last few years [1–6]. Trivial size effects (e.g., an increased surface-to-volume ratio and shorter length displacements for lithium ions) can lead to an improved rate capability and cycle life of cells.

On the other hand, the increased surface area of the electrode and also the increased area of the electrode/electrolyte interface provide additional advantages for nanometric particles over the bulk material [7] such as (i) an improved reaction kinetics that increases the extent of development and reversibility of the lithium insertion/extraction process and results in increased cell capacity and better capacity retention, and (ii) the ability to use high charge/discharge rates. However, the increased reactivity of nanometric materials can raise some problems derived from a greater vulnerability to attack by the electrolyte (particularly at low charge/discharge rates). Under these conditions, the lithium insertion/extraction process takes a long time and contact between the active material and electrolyte prolonged. This situation can be detrimental when the electrolyte is capable of decomposing the electrode. Such is the case with the release of HF from $LiPF_6$ promoted by the presence of water traces. Coating particle surfaces with a protective agent can help overcome this drawback [8]. However, the main disadvantage of nanometric materials is probably the typical labour intensity and high cost of their synthetic procedures. Developing simple affordable synthetic methods will be one of the keys for nanometric materials to prevail in the design of electrochemical devices for energy storage and conversion.

Another valuable property of lithium-ion batteries is their ability to operate at the highest availablevoltages. Provided cells retain their capacity, this can be used to increase their specific energy. Cell voltage is determined by the difference in Li chemical potential between the two

insertion electrodes. The greater the difference is, the higher will be the cell voltage. This can be accomplished by using anodic and cathodic materials with the lowest and highest potentials versus the lithium reference electrode, respectively. The presence of Li ions that can be extracted during charging and inserted on discharging the cell is an indispensable condition for cathodic materials to be active in this respect. The most attractive and widely studied compounds in this context are the layered oxide $LiCoO_2$ [9] (commercial lithium-ion batteries are based on it, but its high cost and toxicity can compromise its leading position), and the spinel $LiMn_2O_4$, which is more inexpensive and environmentally benign than $LiCoO_2$ but has poorer cycling properties [10]. The spinel gains stability when Mn is partly replaced with other elements such as V [11], Cr [12], Fe [13], Co [14], Cu [15], or Ni [16]. A spinel of composition $LiNi_{0.5}Mn_{1.5}O_4$ has been prepared which affords complete reversible extraction of $Li^+$ at ca. 4.7 V (i.e., more than 0.5 V above the potential for the unsubsituted spinel). This compound has started a new generation of lithium-ion batteries capable of operating at higher voltages.

All these compounds share a common feature: introducting $Li^+$ in their structures usually requires a thermal treatment. Hence, the most common procedure used for their synthesis in nanometric size is based on combustion [17]. There is, however, an alternative procedure alike to a ceramic method which starts from nanometric precursors and involves a rapid heating. The preparation of nanometric precursors, which can be obtained by mechanochemical activation at room temperature [18], is a key factor. Activation in the presence of a polymer provides highly crystalline nanoparticles [19], otherwise it is difficult to obtain with other methods that require prolonged heating and/or higher heating temperatures.

Polymer-assisted nanoparticles possess significant advantages, namely, (i) they are more resistant to electrolyte attack than are those obtained in the absence of polymer, probably because of lower crystallinity, and (ii) they exhibit a better electrochemical response when operated in the voltage window close to 5 V. All these factors combine to give nanocompounds which can be cycled at high currents [20]. This was comfirmed here by highly crystalline Li-containing nanospinels (viz. $LiMn_2O_4$ and $LiNi_{0.5}Mn_{1.5}O_4$, which were used as cathode materials and $Li_4Ti_5O_{12}$ as anode material). The hybrid lithium batteries made from these compounds were found to exhibit good performance under a wide range of charge/discharge rates.

## 2. EXPERIMENTAL

The above-describe synthetic method is effective for any Li-containing oxide. We prepared the following spinels in this work: $LiMn_2O_4$ (LMO), $Li_4Ti_5O_{12}$ (LTO), and $LiNi_{0.5}Mn_{1.5}O_4$ (LNMO). In previous work [21], the method was used to prepare of $LiCoO_2$ and $LiNi_{0.5}Mn_{0.5}O_2$ layered oxides. The method is based on the synthesis of nanometric oxalates followed by rapid calcination up to 800°C at a high heating rate (ca. 20°C/min). Then, the furnace is shutoff, and the material is allowed to cool to room temperature inside. The formation of nanometric oxalate is boosted by the presence of highly hydrated precursors in excess oxalic acid dihydrate. Mechanical activation was done in a planetary high-energy ball mill in the air at room temperature in two steps, first under dryness for 15 minutes and then in ethanol for another 15 minutes. This sufficed to obtain oxalate particles less than 10 nm in size.

Mechanical activation can be done in the presence of a polymer in order to tailor particle size and shape. Two polymers were tested: polyethyleneglycol (PEG) in molecular weight 400 and polymethylmethacrylate (PMMA). Mechanical activation for 1 hour sufficed to obtain a homogeneous mixture of polymer and precursors. Further heating at 800°C yielded highly crystalline nanoparticles.

X-ray diffraction (XRD) patterns were recorded on a Siemens D5000 X-ray diffractometer using nonmonochromated Cu K$\alpha$ radiation and a graphite monochromator for the diffracted beam. Thermogravimetric measurements were made under ambient conditions, using a Cahn 2000 thermobalance at a heating rate of 10°C/min. Transmission electron microscopy (TEM) images were obtained with a Phillips TEM operating at 100 keV and SEM images with a Jeol 6400 scanning electron microscope.

Electrochemical measurements were carried out with CR2032 two-electrodecoin cells supplied by Hohsen Corporation. Powdered pellets 13 mm in diameter were prepared by pressing, in a stainless steel grid, ca. 10 mg of active material with acetylene black (15 wt%). The electrolyte, supplied by Merck, was 1 M anhydrous $LiPF_6$ in a 1 : 1 mixture of ethylene carbonate and dimethyl carbonate. Cells were assembled in an M-Braun glovebox. Cycling tests were performed on a McPile II (biologic) potentiostat-galvanostat system under a galvanostatic regime. The Li-ion batteries were anode limited [22], and the specific capacity and rate of the batteries referred to the mass of the negative electrode.

## 3. RESULTS AND DISCUSSION

### 3.1. Morphological properties

As stated above, thermal treatment of an appropriate precursor for a short time provides a simple route for obtaining an Li-containing oxide of nanometric size. The suitability of the precursor is a key factor here. We started from hydrated acetates (except for the synthesis of $Li_4Ti_5O_{12}$, where the Ti source was acetylacetonate). On contact with oxalic acid dihydrate and mechanochemical activation, the acetates become nanometric oxalates (see Figure 1). The increased reactivity of these oxalates compared with micrometric particles affords the use of milder thermal conditions to obtain the spinel framework. The combination of TG curves and XRD patterns revealed that the spinel is formed at 400°C, albeit with low crystallinity. Heating at 800°C for a short time results in improved particle crystallinity as revealed the reduction in the broadening of the X-ray diffraction lines. Figure 2 shows some XRD patterns representative of the different conditions used in the spinel synthesis. At this temperature, the spinel peaks are quite well resolved, and peaks assigned to transition metal oxide-based impurities are

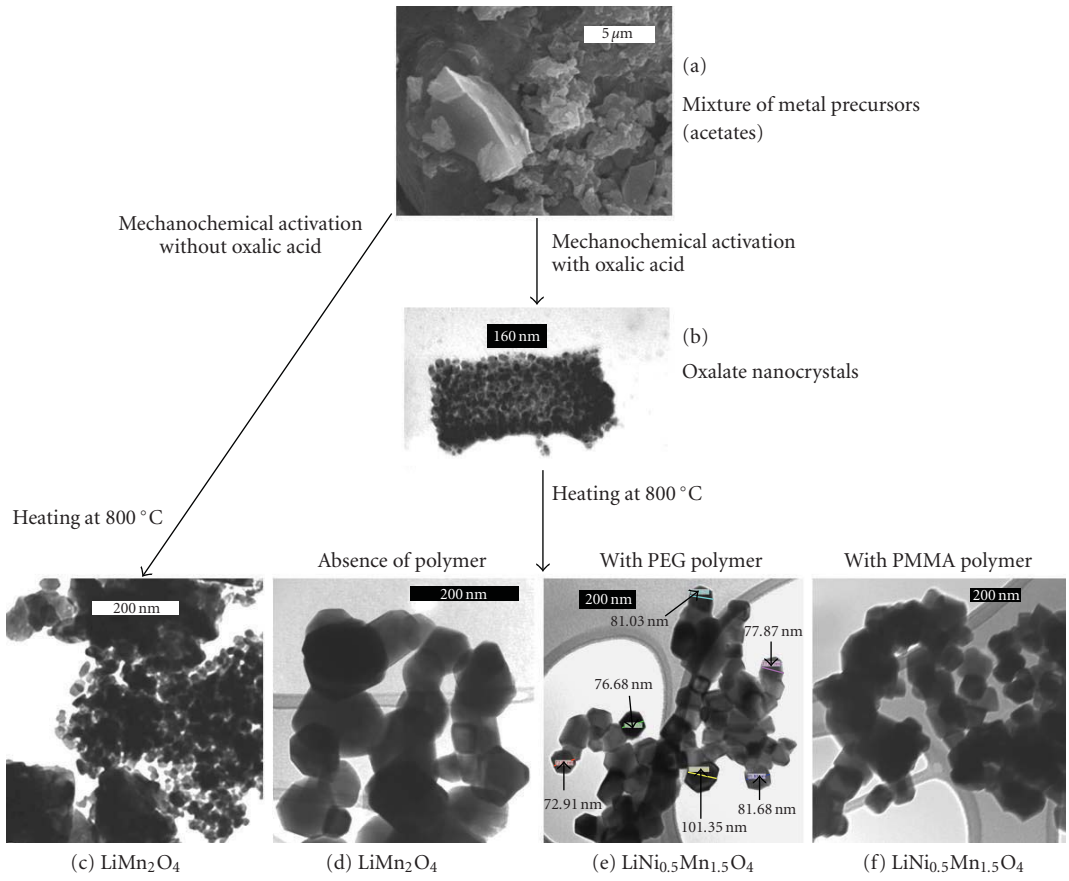


Figure 1: Steps of the method used to synthesize the nanospinels.

hardly perceptible. The role played by oxalic acid is shown in Figures 1(c) and 1(d). The presence of oxalic acid dihydrate in the medium plays a key role in the final particle size of the mixed oxide by means of the formation of oxalate nanocrystals on grinding (see Figure 1(b)). Nucleation and growth of these reaction products are facilitated by the presence of hydration water. Thus, this precursor-like route enhances the uniform distribution of the elements resulting in a well-defined morphology and quite homogeneous particle size. By contrast, direct synthesis from the acetates in the absence of oxalic acid resulted in wider particle size distribution and nanoparticles coexisted with microparticles (see Figure 1(c)).

The use of polymers in the synthetic procedure has two main effects, namely, (i) particle size is reduced (compare Figures 1(d), 1(e), and 1(f)) and (ii) an improvement in spinel crystallinity, as shown below. The polymer helps to adopt a more homogeneous distribution of metal ions on an atomic scale as a result of its ability to coordinate to the metal ions forming the spinel. The functional groups of the polymer capable of acting as Lewis basic sites—atoms with nonbonding electron pairs—may bind to the ions, thereby bringing them closer and shortening diffusion paths to adopt the spinel framework. This model is consistent with the results obtained by using a polymer such as poly(divydilene fluoride) (PVDF), where no functional oxygen atoms are present, with which the spinel synthesis failed. Thus, the functional groups of the polymer are key factors for the spinel synthesis and should be able to approach and stabilize the metal ions via their chelating properties. Thus, the presence of the polymer, in addition to tailoring the particle shape, helps maintain connectivity between nanocrystals, thereby facilitating the release of strains as the temperature is raised. Nanoparticles adopt a well-defined octahedral morphology typical of the spinel structure (see Figure 3(a)). Also, lattice defects are insignificant as revealed by HREM images (see Figure 3(b)). The interplanar spacing was calculated to be ca. 0.46, which corresponds to the orientation of (111) atomic planes. The high crystallinity observed by TEM, a highly localized technique, was confirmed from X-ray broadening analysis, more suitable to examine bulk properties of a material. The lattice distortion was estimated from the full width at half maximum (FWHM), using the Williamson and Hall equation [23]:

$$\beta \cos\theta = \frac{2\langle e\rangle \operatorname{sen}\theta + 0.9\lambda}{D}, \tag{1}$$

where $\beta$ is the integral breadth after correction for instrumental broadening from highly crystalline quartz and k$\alpha_2$ elimination using the Rachinger method [24], $\langle e\rangle$ denotes

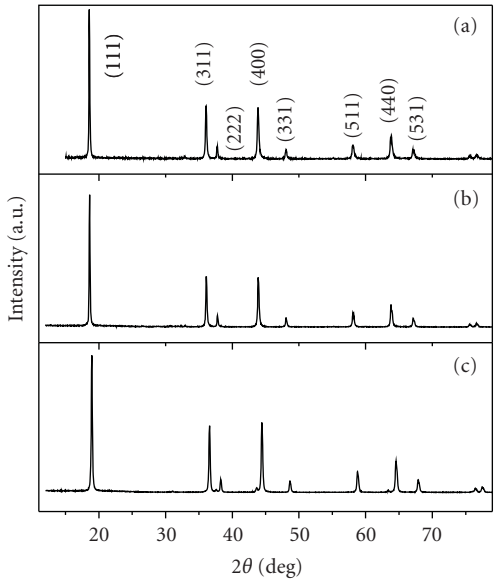


Figure 2: XRD patterns for the spinels. Samples: (a) and (b) $LiMn_2O_4$ in the absence and presence of oxalic acid, (c) $LiNi_{0.5}Mn_{1.5}O_4$ in the presence of oxalic acid and PEG400.

local strains (defined as $\Delta d/d$, where $d$ is the interplanar space), and $D$ is crystallite size. Equation (1) was applied to the strongest reflections that do not overlap with other reflections. Figure 4 shows the plots of the above equation for different spinels, and Table 1 lists the crystallite sizes and strains calculated from the intercepts and slopes, respectively. Both the presence of oxalic acid and especially polymer in the synthesis improved particle crystallinity as microstrain content decreased under these conditions. The lower crystallite size for the $LiMn_2O_4$ spinel prepared in the absence of oxalic acid compared with that of the same spinel obtained in the presence of oxalic acid could be due to the wider particle size distribution of the former sample. Figure 1(c) shows the presence of ill-defined particles of few tens nanometer with others exceeding 200 nm. In any case, highly crystalline particles of small size are quite appropriate to cycle at high charge/discharge rates as Li-ion displacement is enhanced by effect of the reduced probability to find defects potentially truncating their movement.

### 3.2. Electrochemical properties

#### 3.2.1. Nanometric $LiMn_2O_4$ versus Li

The essential condition for a material to be useful in lithium-ion battery cathodes is that it should be able to react in a reversible manner with lithium at high potentials. This requirement is met by the spinel $LiMn_2O_4$, for which a vast amount of literature is available [25]. This spinel can extract and insert lithium above 4 V versus Li. Figure 5 shows the variation of the specific capacity delivered by half-cells made from nanometric particles as a function of the number of cycles. Galvanostatic data were recorded at different charge/discharge rates from C/4 to 4C (C representing 1 $Li^+$ ion exchanged in 1 hour, equivalent to 148 mA/g). The initial capacities obtained ranged from 108 at C/4 to 100 mAh/g at 4C. The difference in capacity was in fact rather small (8%) in spite of the significant difference in rate (16 times). On further cycling, the half cells exhibited good capacity retention, irrespective of the rate capability used. With the electrode made from micrometric particles, the initial capacity delivered by the half-cell was 107 mAh/g at C/4 and 95 mAh/g at 1C, which is close to the value for the electrode made from nanometric particles. However, capacity fading with cycling was more pronounced than in the half cell made from nanometric particles. The capacity loss was particularly significant at 1C. Under these cycling conditions, the capacity fell from 95 to 40 mAh/g over the first twenty cycles; in the half-cell made from nanometric particles, however, the capacity only decreased from 105 to 100 mAh/g. The origin of this striking behavior may be associated to the way lithium diffusion is affected by particle size. The time $\tau$ taken to travel a distance $r$ can be calculated from the equation:

$$\tau = \frac{r^2}{\pi D}, \tag{2}$$

where $D$ is the diffusion coefficient of $Li^+$. Thus, for nanoscale materials (viz. those having a size of 1−100 nm in at least one direction), Li ions take few minutes to cross nanoparticles (the average value of $D$ for $Li^+$ is ca. $10^{-4}$ $cm^2/s$). Thus, reducing the average diffusion distances delays concentration polarization and allows cells to operate at high currents and hence electrode rate capabilities to be improved [7]. Obviously, reducing the distance for $Li^+$ ions travel must be also beneficial when the cell anode is made from an insertion electrode, as shown below.

Table 1: Crystallite size and microstrain content of Li-Mn spinels.

| Sample | $D$ (nm) | Microstrain ($\times 10^{-4}$) |
|---|---|---|
| $LiMn_2O_4$ [(a)] | 92 | 19.3 |
| $LiMn_2O_4$ [(b)] | 116 | 10.7 |
| $LiNi_{0.5}Mn_{1.5}O_4$ [(c)] | 79 | 2.1 |

Synthesis conditions: [(a)]absence of oxalic acid, [(b,c)]with oxalic acid, [(c)]with PEG400.

#### 3.2.2. Nanometric $LiMn_2O_4$ versus $Li_4Ti_5O_{12}$ (hybrid batteries)

In most commercial batteries the positive and negative electrodes are made from $LiCoO_2$ and graphite, respectively. These components have two major shortcomings. Graphite operates at a very low voltage (ca. 50 mV versus Li). Under these conditions, the electrolyte is thermodynamically unstable and can decompose releasing gases which detract from battery safety. On the other hand, cobalt is a toxic and expensive element. In this context, Li-based spinels provide interesting prospects for circumventing these shortcomings. The spinels $Li_4Ti_5O_{12}$ and $LiMn_2O_4$ are good choices for this purpose as they can act as anode and cathode materials, respectively, for batteries. LTO is one of the few lithium intercalation compounds known that

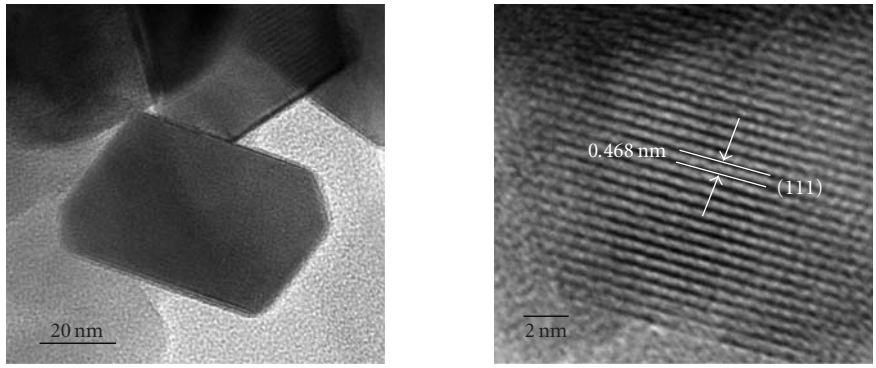


Figure 3: (a) TEM and (b) HREM images of $LiNi_{0.5}Mn_{1.5}O_4$ nanocrystals synthesized in the presence of PEG400.

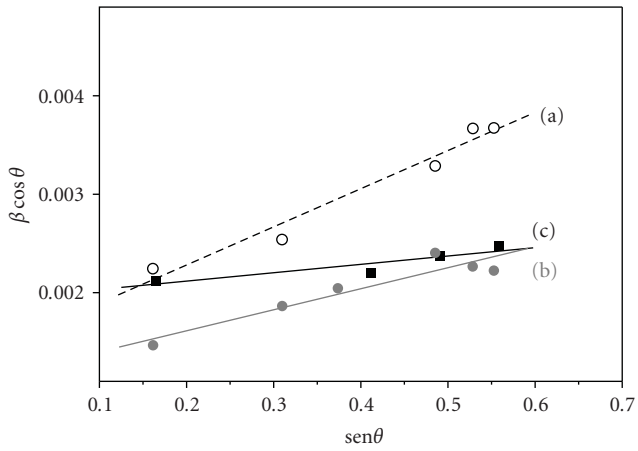


Figure 4: Plots of the Williamson and Hall equation for various (hkl) reflections. Samples calcined at 800°C: $LiMn_2O_4$ in the absence (a,○) and presence (b,•) of oxalic acid, $LiNi_{0.5}Mn_{1.5}O_4$ in the presence (c, ■) of oxalic acid and PEG400.

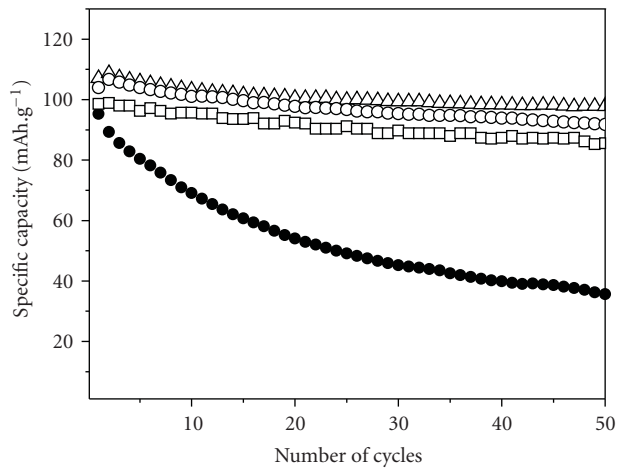


Figure 5: Variation of cell capacity in $LiMn_2O_4$/Li half-cells as a function of the number of cycles. Rate: (Δ) C4, (○) 1C, (□) 4C, and m-$LiMn_2O_4$/Li half-cell at (•) 1C.

undergoes little expansion or contraction during the lithium insertion/reinsertion process [26]. We have found battery performance to be significantly improved by using both compounds as nanoparticles [27]. Hybrid batteries made from such particles exhibit enhanced rate capabilities and surpass batteries made from larger particles (microparticles) in performance.

Figure 6 shows the charge/discharge curves for two batteries made from the spinels obtained as nano(n)- and micropaticles (m). The curve shapes are typical for $LiMn_2O_4$, with two pseudoplateaux consistent with the two-step mechanism for lithium extraction and insertion [28]. The capacity values delivered by the cells in the 1st and 10th cycle as measured at C/4 and 1C are shown in Table 2.

The initial capacity delivered by the cell was higher when the electrodes were made from nanoparticles, irrespective of the discharge rate used. However, the greater differences were observed at 1C, consistent with the better electrochemical response of nanometric particles cycled at high rates. On cycling at a low rate (C/4), capacity retention of this cell was

Table 2: Capacity values delivered by the hybrid cells (mAh/g).

| Battery | 1st discharge | | 10th discharge | |
|---|---|---|---|---|
| | C/4 | 1C | C/4 | 1C |
| n-LMO–n-LTO | 134 | 120 | 133 | 108 |
| m-LMO–m-LTO | 107 | 76 | 96 | 66 |

quite good. By contrast, the capacity of the cell made from microparticles decreased by about a 10%. At higher rates (1C), the capacity of the two batteries faded with cycling, but capacity retention in the battery made from nanoparticles was better (its capacity loss was 10% versus 26%). Clearly, as previously found for the half cell, a nanometric size helps in improving battery performance.

### 3.2.3. *Nanometric $LiNi_{0.5}Mn_{1.5}O_4$ versus Li*

The highest cathode potentials achieved to date are in the region of 5 V versus Li, value which is on the verge of

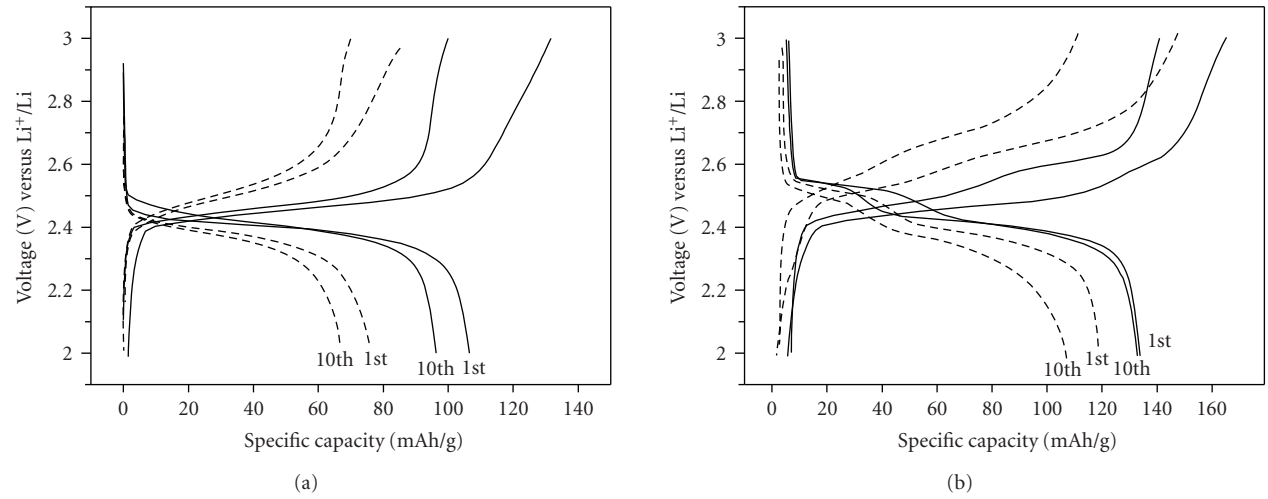


Figure 6: Galvanostatic profiles for the first and tenth charge/discharge of (a) m-$LiMn_2O_4$/m-$Li_4Ti_5O_{12}$ and (b) n-$LiMn_2O_4$/n-$Li_4Ti_5O_{12}$ hybrid batteries. Rates: C4 (solid line) and 1C (dash line).

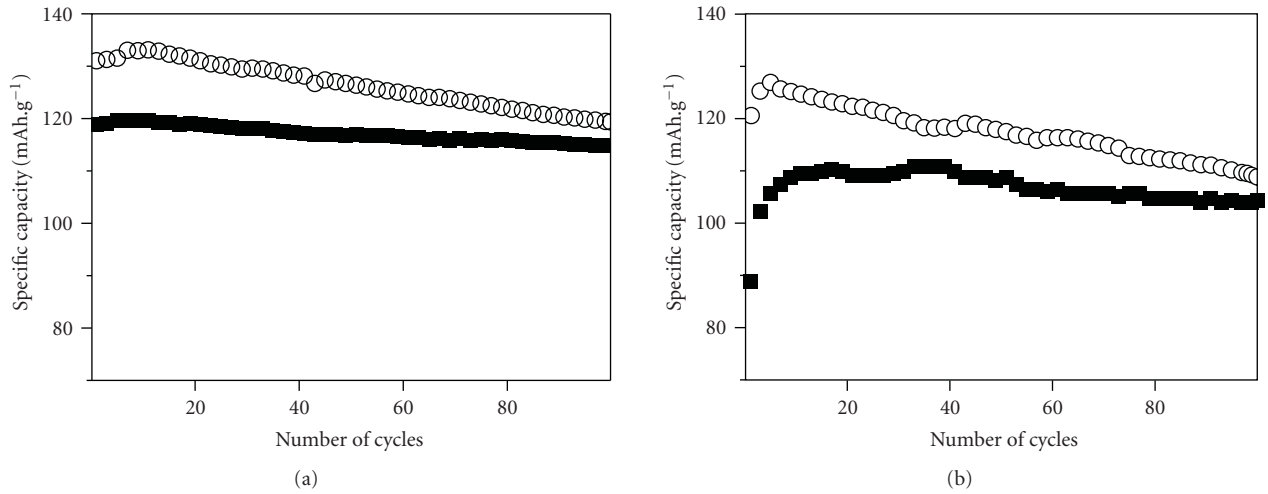


Figure 7: Variation of cell capacity as a function of the number of cycles in half-cells made from m-$LiNi_{0.5}Mn_{1.5}O_4$ spinel (■) and a mixture of 50/50 wt% n-$LiNi_{0.5}Mn_{1.5}O_4$/m-$LiNi_{0.5}Mn_{1.5}O_4$ (∘). Charge/discharge rate: (a) C/4, (b) 2C.

the potential window for liquid-based electrolytes. Some Li-based spinels (e.g., $LiNi_{0.5}Mn_{1.5}O_4$) possess this property and are the best candidates for future applications [22]. Li is removed from this compound between 4.5 and 4.8 V, and charge neutrality is maintained by oxidizing $Ni^{2+}$ to $Ni^{4+}$ [29]. In order to ensure good reversibility in the electrochemical reaction at high voltages, the electrode must be made from a highly crystalline spinel. The conditions used to obtain nanometric particles usually provide solids with a high defect content. In other words, particles are poorly crystalline as revealed by X-ray line broadening analysis [19]. This is so because the heating temperature cannot be too high and the heating time should be as short as possible in order to avoid sintering. Spinels prepared as microparticles are not subject to this drawback and possess a high crystallinity. As stated above, however, microparticles exhibit a limited electrochemical response in lithium cells, particularly at high rates. One way of overcoming this restriction is by using composite electrodes made from a mixture of nano- and micrometric particles. In this way, cells can exploit the advantages of nanoparticles (high rate capabilities) and microparticles (good reversibility in the electrochemical reaction).

Figure 7 shows the capacity delivered by various half cells as a function of the number of cycles. Two types of electrodes were studied that were prepared from (i) microparticles and (ii) a 50 : 50 w/w mixture of micro- and nanoparticles (composite electrode) obtained by mechanochemical activation for 15 minutes [30]. Tests were conducted at two different rates (C/4 and 2C). As can be seen, the best performance

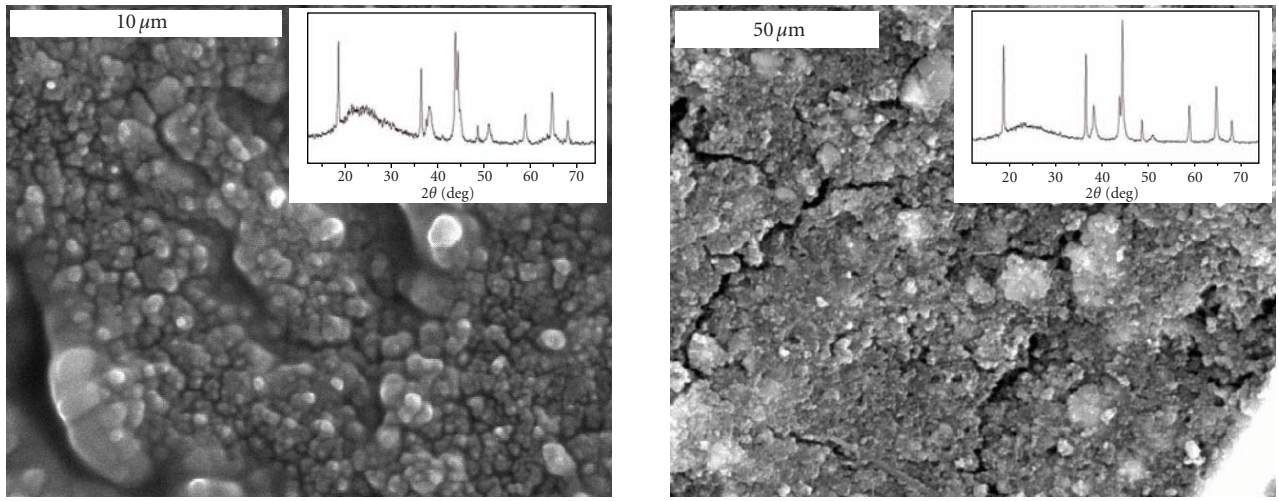


(a) (b)

Figure 8: SEM images of electrodes tested at C/4 after the hundredth discharge. (a) Micrometric spinel and (b) 50/50 composite electrode.

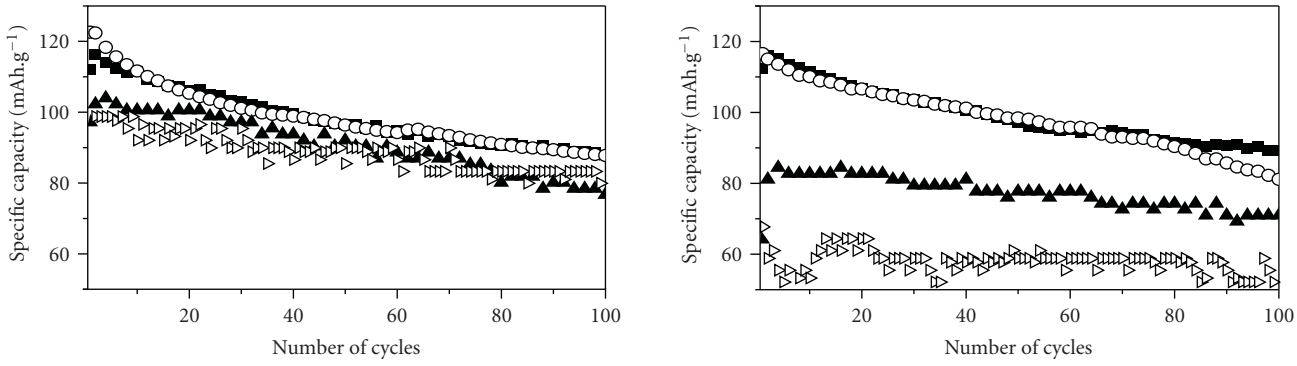


(a) (b)

Figure 9: Variation of cell capacity as a function of the number of cycles at a variable charge/discharge rate. Half-cells made from the n-$LiNi_{0.5}Mn_{1.5}O_4$ spinel prepared in (a) the presence and (b) the absence of PEG-800. Charge/discharge rate: C/4 (■), 2C (∘), 8C (▲), 15C (▷).

was obtained for the composite electrode, irrespective of the charge/discharge rate used. This electrode delivered a higher capacity over the one hundred cycles measured. Differences in textural properties of the electrodes rather than in the structural properties of the spinels seem to be the origin of the enhanced performance of the composite electrode. As can be seen in the insets of Figure 8, the particles maintained the spinel structure with similar unit cell dimensions to those of the pristine compounds on cycling. However, the SEM images (see Figure 8) revealed significant differences between the two electrodes. Thus, the composite electrode was the better at retaining its integrity. Also, it was the electrode exhibiting the best electrochemical performance (see Figure 7(a)). The appearance of the electrode made from the m-spinel (see Figure 7(b)) was quite different. As expected, particles were clearly larger and not so closely bound as in the composite electrode. The nanoparticles probably occupy the cavities formed upon compaction of the microparticles. Therefore, the nanoparticles seem to act as binders between the microparticles, thereby improving connectivity between particles and facilitating transport of charge carriers. This must decrease cell polarization and increase the reversibility of the reaction with lithium, thereby improving cell performance.

As stated above, one alternative route for improving cell performance involves preparing electrodes from highly crystalline nanoparticles. The use of polymers in the synthetic procedure has proved an excellent method for obtaining highly crystalline nanosized spinels. The beneficial effect on their electrochemical properties is apparent from Figures 9(a) and 9(b), which compare the performance of half cells made from nanoparticles of $LiNi_{0.5}Mn_{1.5}O_4$ obtained in the presence and absence of polymer (PEG800). The influence of the charge/discharge rate on the capacity delivered by

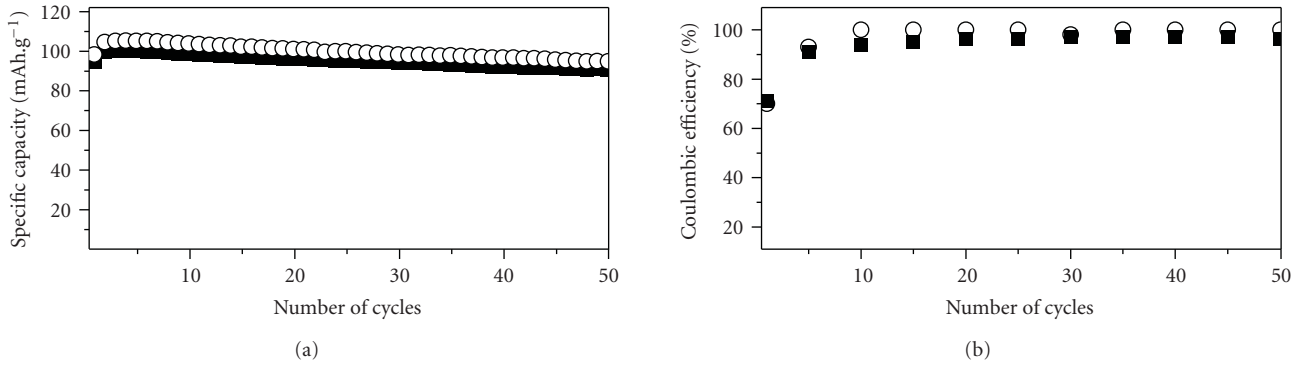


Figure 10: (a) Variation of the specific capacity delivered by the half-cell made from n-$LiNi_{0.5}Mn_{1.5}O_4$ spinel prepared in the presence of PEG-800 under different charge/discharge regimes. (∘) Charge 2C, discharge C/4; (■) charge 4C, discharge C/4. (b) Coulombic efficiency.

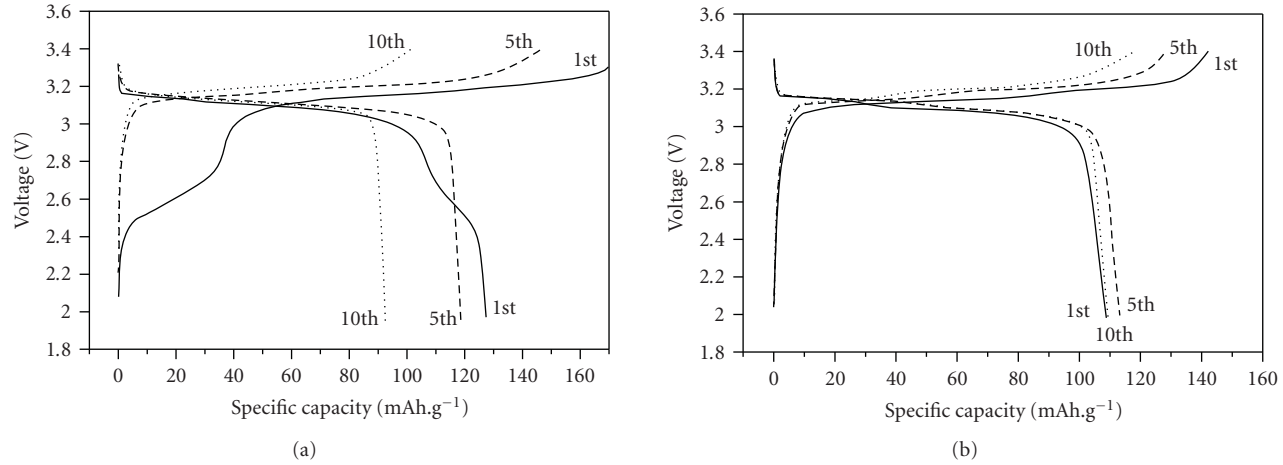


Figure 11: Galvanostatic profiles for the first (solid line), fifth (dash line), and tenth (dot line) charge/discharge of (a) m-$LiNi_{0.5}Mn_{1.5}O_4$/m-$Li_4Ti_5O_{12}$ and (b) n-$LiNi_{0.5}Mn_{1.5}O_4$/n-$Li_4Ti_5O_{12}$ hybrid batteries.

the half-cells is weaker when the electrode is prepared from nanoparticles obtained in the presence of polymer. The initial capacity values range from 120 at C/4 to 100 mAh/g at 15C. In the electrode made from the nanospinel obtained in the absence of polymer, the delivered capacity shifts from 120 to 60 mAh/g. Although particle size was similar for the two spinels, the use of a polymer facilitated the release of defects and internal strains, thereby incrasing the crystallinity of the nanoparticles [31].

Another interesting property of the cells made from nanometric $LiNi_{0.5}Mn_{1.5}O_4$ spinel is their ability to be charged at high current densities and discharged slowly. This is interesting as they approach the requirements of commercial batteries. This property was tested in a spinel prepared in the presence of PEG and calcined at 800°C; cells were charged under two fast regimes (2C and 4C) and further discharged under one slow regime (C/4). Figure 10(a) shows the variation of the capacity as a function of the number of cycles. As can be seen, capacity retention by the cells was quite good (the capacity faded less than 5% after fifty cycles). Moreover, the coulombic efficiency approached 100% upon cycling (see Figure 10(b)). Therefore, the spinel exhibited an excellent electrochemical response under such drastic operating conditions.

#### 3.2.4. *Nanometric $LiNi_{0.5}Mn_{1.5}O_4$ versus $Li_4Ti_5O_{12}$ (hybrid batteries)*

The electrochemical properties of $LiNi_{0.5}Mn_{1.5}O_4$ spinel versus $Li_4Ti_5O_{12}$ were also studied. Figure 11 shows the charge/discharge curves obtained in the 1st, 5th, and 10th cycles for the two types of hybrid batteries examined, with electrodes made from nano (n)- and microparticles (m). All cells were cycled at C/4. The shape of the curves of the cells made from nanometric particles was similar to that observed for the $LiNi_{0.5}Mn_{1.5}O_4$/Li half cell (viz. two pseudoplateaux between 3.0 and 3.3 V associated to the $Ni^{2+} \rightarrow Ni^{4+}$ process, the mechanism of which involves two cubic/cubic two-phase reactions [32]). By contrast, the first charge and discharge curve for the micrometric sample exhibited a third plateau at ca. 2.5 V. This signal is comparable to that for the hybrid cell made from $LiMn_2O_4$ (see Figure 6). For this reason, it

Table 3: Capacity values delivered by the hybrid batteries (mAh/g).

| Battery | 1st discharge | 5th discharge | 10th discharge |
|---|---|---|---|
| n-LNMO−n-LTO | 110 | 116 | 111 |
| m-LNMO−m-LTO | 128 | 120 | 95 |

can be assigned to the oxidation of $Mn^{3+}$ to $Mn^{4+}$. The XRD pattern (not shown here) revealed the presence of NiO related impurities; this means that not all Ni substitutes Mn in the spinel framework, hence the presence of some $Mn^{3+}$ in the spinel framework. The presence of impurities in this spinel is a common finding when the solid is obtained using a conventional ceramic method [33]. The low-voltage plateau disappeared after the second cycle because of the excess of cathode material, and the curve shape was comparable with that for the cells made from nanometric particles except that the two pseudoplateaux were more ill-defined.

The discharge capacities delivered by the cells are shown in Table 3. Except for the capacity value obtained in the first discharge for the cell made from nanometric materials (110 mAh/g which is somewhat lower than that calculated from the spinel stoichiometry) the remaining data exhibited a well-defined trend. Thus, the capacity of the n-LNMO−n-LTO hybrid battery was retained on cycling (at least over the ten cycles measured). This behaviour is similar to that of the n-LMO−n-LTO hybrid battery at the same rate (C/4) (see Table 2). By contrast, the trend exhibited by the capacity of the cell made from micrometric particles is to significantly fade on cycling, consistent with the results for the m-LMO−m-LTO hybrid battery (see Table 2). Again, the performance of the cell made from nanometric particles was better than that of the cell obtained from micrometric particles.

## ACKNOWLEDGMENTS

This work was supported by CICYT (MAT2005-03069) and Junta de Andalucía (Group FQM 175).

## REFERENCES

[1] A. S. Aricò, P. Bruce, B. Scrosati, J.-M. Tarascon, and W. van Schalkwijk, "Nanostructured materials for advanced energy conversion and storage devices," *Nature Materials*, vol. 4, no. 5, pp. 366–377, 2005.

[2] C. R. Sides, N. Li, C. J. Patrissi, B. Scrosati, and C. R. Martin, "Nanoscale materials for lithium-ion batteries," *MRS Bulletin*, vol. 27, no. 8, pp. 604–607, 2002.

[3] C. R. Sides and C. R. Martin, "Nanostructured electrodes and the low-temperature performance of Li-ion batteries," *Advanced Materials*, vol. 17, no. 1, pp. 125–128, 2005.

[4] C. Jiang, E. Hosono, and H. Zhou, "Nanomaterials for lithium ion batteries," *Nano Today*, vol. 1, no. 4, pp. 28–33, 2006.

[5] L. F. Nazar, G. Goward, F. Leroux, et al., "Nanostructured materials for energy storage," *International Journal of Inorganic Materials*, vol. 3, no. 3, pp. 191–200, 2001.

[6] A. Singhal, G. Skandan, G. Amatucci, et al., "Nanostructured electrodes for next generation rechargeable electrochemical devices," *Journal of Power Sources*, vol. 129, no. 1, pp. 38–44, 2004.

[7] F. F. C. Bazito and R. M. Torresi, "Cathodes for lithium ion batteries: the benefits of using nanostructured materials," *Journal of the Brazilian Chemical Society*, vol. 17, no. 4, pp. 627–642, 2006.

[8] J. C. Arrebola, A. Caballero, L. Hernán, J. Morales, E. Rodríguez-Castellón, and J. R. Ramos Barrado, "Effects of coating with gold on the performance of nanosized $LiNi_{0.5}Mn_{1.5}O_4$ for lithium batteries," *Journal of the Electrochemical Society*, vol. 154, no. 3, pp. A178–A184, 2007.

[9] M. S. Whittingham, "Lithium batteries and cathode materials," *Chemical Reviews*, vol. 104, no. 10, pp. 4271–4301, 2004.

[10] M. M. Thackeray, "Manganese oxides for lithium batteries," *Progress in Solid State Chemistry*, vol. 25, no. 1-2, pp. 1–71, 1997.

[11] L. Hernán, J. Morales, L. Sánchez, J. Santos, and E. Rodríguez-Castellón, "Sol-gel derived Li-V-Mn-O spinels as cathodes for rechargeable lithium batteries," *Solid State Ionics*, vol. 133, no. 3-4, pp. 179–188, 2000.

[12] C. Sigala, D. Guyomard, A. Verbaere, Y. Piffard, and M. Tournoux, "Positive electrode materials with high operating voltage for lithium batteries: $LiCr_yMn_{2-y}O_4 (0 \leq y \leq 1)$," *Solid State Ionics*, vol. 81, no. 3-4, pp. 167–170, 1995.

[13] H. Kawai, M. Nagata, M. Tabuchi, H. Tukamoto, and A. R. West, "Novel 5 V spinel cathode $Li_2FeMn_3O_8$ for lithium ion batteries," *Chemistry of Materials*, vol. 10, no. 11, pp. 3266–3268, 1998.

[14] H. Kawai, M. Nagata, H. Tukamoto, and A. R. West, "A new lithium cathode $LiCoMnO_4$: toward practical 5 V lithium batteries," *Electrochemical and Solid-State Letters*, vol. 1, no. 5, pp. 212–214, 1998.

[15] Y. Ein-Eli, W. F. Howard Jr., S. H. Lu, et al., "$LiMn_{2-x}Cu_xO_4$ spinels ($0.1 \leq x \leq 0.5$): a new class of 5 V cathode materials for Li batteries. I. Electrochemical, structural, and spectroscopic studies," *Journal of the Electrochemical Society*, vol. 145, no. 4, pp. 1238–1244, 1998.

[16] Q. Zhong, A. Bonakdarpour, M. Zhang, Y. Gao, and J. R. Dahn, "Synthesis and electrochemistry of $LiNi_xMn_{2-x}O_4$," *Journal of the Electrochemical Society*, vol. 144, no. 1, pp. 205–213, 1997.

[17] M. G. Lazarraga, L. Pascual, H. Gadjov, et al., "Nanosize $LiNi_yMn_{2-y}O_4$ ($0 < y \leq 0.5$) spinels synthesized by a sucrose-aided combustion method. Characterization and electrochemical performance," *Journal of Materials Chemistry*, vol. 14, no. 10, pp. 1640–1647, 2004.

[18] X. R. Ye, D. Z. Jia, J. Q. Yu, X. Q. Xin, and Z. Xue, "One-step solid-state reactions at ambient temperatures—a novel approach to nanocrystals synthesis," *Advanced Materials*, vol. 11, no. 11, pp. 941–942, 1999.

[19] J. C. Arrebola, A. Caballero, M. Cruz, L. Hernán, J. Morales, and E. Rodríguez-Castellón, "Crystallinity control of a nanostructured $LiNi_{0.5}Mn_{1.5}O_4$ spinel via polymer-assisted synthesis: a method for improving its rate capability and performance in 5 V lithium batteries," *Advanced Functional Materials*, vol. 16, no. 14, pp. 1904–1912, 2006.

[20] A. Odani, A. Nimberger, B. Markovsky, et al., "Development and testing of nanomaterials for rechargeable lithium batteries," *Journal of Power Sources*, vol. 119–121, pp. 517–521, 2003.

[21] A. Caballero, M. Cruz, L. Hernán, M. Melero, J. Morales, and E. Rodríguez-Castellón, "Nanocrystalline materials obtained by using a simple, rapid method for rechargeable lithium batteries," *Journal of Power Sources*, vol. 150, pp. 192–201, 2005.

[22] G. Armstrong, A. R. Armstrong, P. Bruce, P. Reale, and B. Scrosati, "$TiO_2$(B) nanowires as an improved anode

material for lithium-ion batteries containing $LiFePO_4$ or $LiNi_{0.5}Mn_{1.5}O_4$ cathodes and a polymer electrolyte," *Advanced Materials*, vol. 18, no. 19, pp. 2597–2600, 2006.

[23] H. P. Klug and L. E. Alexander, *X-Ray Diffraction Procedures for Pollycrystalline and Amorphous Materials*, John Willey & Sons, New York, NY, USA, 1974.

[24] W. A. Rachinger, "A correction for the $\alpha_1\alpha_2$ doublet in the measurement of widths of x-ray diffraction lines," *Journal of Scientific Instruments*, vol. 25, no. 7, pp. 254–255, 1948.

[25] M. Winter, J. O. Besenhard, M. E. Spahr, and P. Novák, "Insertion electrode materials for rechargeable lithium batteries," *Advanced Materials*, vol. 10, no. 10, pp. 725–763, 1998.

[26] L. Kavan and M. Grätzel, "Facile synthesis of nanocrystalline $Li_4Ti_5O_{12}$ (spinel) exhibiting fast Li insertion," *Electrochemical and Solid-State Letters*, vol. 5, no. 2, pp. A39–A42, 2002.

[27] J. C. Arrebola, A. Caballero, and L. Hernán, "High performance hybrid lithium-ion batteries based on combinations of nanometric materials," *Nanotechnology*, vol. 18, no. 29, Article ID 295705, 5 pages, 2007.

[28] A. Ott, P. Endres, V. Klein, et al., "Electrochemical performance and chemical properties of oxidic cathode materials for 4 V rechargeable Li-ion batteries," *Journal of Power Sources*, vol. 72, no. 1, pp. 1–8, 1998.

[29] Y. Terada, K. Yasaka, F. Nishikawa, T. Konishi, M. Yoshio, and I. Nakai, "*In situ* XAFS analysis of $Li(Mn, M)_2O_4$ ($M$ = Cr, Co, Ni) 5 V cathode materials for lithium-ion secondary batteries," *Journal of Solid State Chemistry*, vol. 156, no. 2, pp. 286–291, 2001.

[30] J. C. Arrebola, A. Caballero, L. Hernán, and J. Morales, "Expanding the rate capabilities of the $LiNi_{0.5}Mn_{1.5}O_4$ spinel by exploiting the synergistic effect between nano and microparticles," *Electrochemical and Solid-State Letters*, vol. 8, no. 12, pp. A641–A645, 2005.

[31] Z. Zhang, A. J. Rondinone, J. X. Ma, J. Shen, and S. Dai, "Morphologically templated growth of aligned spinel $CoFe_2O_4$ nanorods," *Advanced Materials*, vol. 17, no. 11, pp. 1415–1419, 2005.

[32] K. Ariyoshi, Y. Iwakoshi, N. Nakayama, and T. Ohzuku, "Topotactic two-phase reactions of $Li[Ni_{1/2}Mn_{3/2}]O_4(P4_332)$ in nonaqueous lithium cells," *Journal of the Electrochemical Society*, vol. 151, no. 2, pp. A296–A303, 2004.

[33] Y. Ein-Eli, J. T. Vaughey, M. M. Thackeray, S. Mukerjee, X. Q. Yang, and J. McBreen, "$LiNi_xCu_{0.5-x}Mn_{1.5}O_4$ spinel electrodes, superior high-potential cathode materials for Li batteries. I. Electrochemical and structural studies," *Journal of the Electrochemical Society*, vol. 146, no. 3, pp. 908–913, 1999.

Hindawi Publishing Corporation
Journal of Nanomaterials
Volume 2008, Article ID 759825, 8 pages
doi:10.1155/2008/759825

*Research Article*

# Membranes of Polyvinylidene Fluoride and PVDF Nanocomposites with Carbon Nanotubes via Immersion Precipitation

**Gaurav Mago,[1] Dilhan M. Kalyon,[2] and Frank T. Fisher[1]**

[1] *Department of Mechanical Engineering, Stevens Institute of Technology, Hoboken, NJ 07030, USA*
[2] *Department of Chemical Engineering and Materials Science, Stevens Institute of Technology, Hoboken, NJ 07030, USA*

Correspondence should be addressed to Frank T. Fisher, ffisher@stevens.edu

Received 24 September 2007; Accepted 21 March 2008

Recommended by Jun Lou

Microporous polyvinylidene fluoride (PVDF) and PVDF nanocomposite membranes were prepared via an isothermal immersion precipitation method using two different antisolvents (ethanol and water). The structure and morphology of the resulting membranes were investigated by wide angle X-ray diffraction (WAXD), Fourier transform infrared spectroscopy (FTIR), scanning electron microscopy (SEM), and differential scanning calorimetry (DSC). The effects of the type of the antisolvent and the presence of multiwalled carbon nanotubes (MWNTs) on membrane morphology and the crystal structure developed within the membranes were studied. The crystallization of the PVDF upon immersion precipitation occurred predominantly in the $\alpha$-phase when water is used as the antisolvent or in the absence of the carbon nanotubes. On the other hand, $\beta$-phase crystallization of the PVDF was promoted upon the use of ethanol as the antisolvent in conjunction with the incorporation of the MWNTs. The morphology and the total crystallinity of the PVDF membranes were also affected by the incorporation of the MWNTs and the antisolvent used, suggesting that the microstructure and the ultimate properties of the PVDF membranes can be engineered upon the judicious selection of crystallization conditions and the use of carbon nanotubes.



## 1. INTRODUCTION

The physical properties of semicrystalline polymers depend upon the processing conditions [1] and can be strongly influenced by the presence of nanoparticles, which affect the crystallization behavior [2] and the resulting crystal morphology developed within the processed sample. Polyvinylidene fluoride (PVDF) is a semicrystalline thermoplastic polymer with five possible polymorphs [3]. Among these polymorphs, more attention has been paid to the $\beta$-phase due to its piezoelectric, ferroelectric, and pyroelectric properties [4–7]. Since the increase in the $\beta$-phase of PVDF has been associated with a greater piezoelectric coefficient (due to an enhancement of the electromechanical coupling coefficient), a variety of experimental techniques have been developed to induce $\beta$-phase formation in PVDF [8, 9]. For example, Matsushige and Takemura showed that crystallization from themelt at pressures which exceed 350 MPa led to the formation of the $\beta$-form of PVDF [10]. Uniaxial or biaxial drawing of PVDF films has also been shown to induce an $\alpha$-$\beta$ transition [11–13]. In addition, a number of reports also indicate that nanoclays and carbon nanotubes can induce the $\beta$-crystal formation in PVDF nanocomposites prepared via melt processing or solution processing [14–17]. Recently, Dillon et al. used a coprecipitation method to induce the $\beta$-crystal structure for PVDF samples reinforced with nanoclays [18].

Such organic-inorganic polymer nanocomposites have attracted wide interest in the research community as researchers investigate the addition of inorganic nanoparticles to impart multifunctionality to the host polymer system, for example, simultaneous enhancement of multiple properties such as electrical and thermal conductivity, mechanical toughness, and dielectric constants of composites [19–24]. Such nanocomposites can also prove to be useful for molecular separations. For example, Merkel et al. found that physical dispersion of nonporous, nanoscale, fumed silica particles in glassy amorphous poly(4-methyl-2-pentyne)

enhanced both membrane permeability and selectivity for large organic molecules over small gas molecules such as hydrogen [25]. In this regard, immersion precipitation is a commonly used technique to prepare PVDF membranes for microfiltration and ultrafiltration [26–32]. Membranes from electrospun polymer nanocomposites can also be used for sensing applications [33, 34]. The incorporation of carbon nanotubes into PVDF is especially attractive because of the significant increase in the electromechanical coefficient to enable the use of the resulting nanocomposites as actuators for artificial muscles and sensors for vibration control [35–37].

While immersion precipitation has been used for a number of pure polymer systems [38–44], lacking are studies of the effect of MWNTs and other nanoparticles on the morphology and crystal structure of PVDF nanocomposite membranes prepared using this technique. Here, we report the utilization of the immersion precipitation technique for the preparation of PVDF nanocomposite membranes. The effects of the incorporation of MWNTs on the crystallization behavior of PVDF was investigated when ethanol and water, respectively, were used as the antisolvent in the immersion precipitation process .

## 2. EXPERIMENTAL

### 2.1. Materials

Powdered PVDF (Kynar 741) was obtained from Arkema Inc., Philadelphia, PA, USA. As reported by the manufacturer, its weight average molecular weight is 250,000 and its density is 1.78 g/cm$^3$. The MWNTs (trade name: MWNT-A-P) were purchased from Sunnano, Jiangxi, China. As reported by the manufacturer, the diameter of the MWNTs was 10–30 nm, and the average bulk density was 1.5 g/cm$^3$. To examine the size and shape distributions of the MWNTs samples, an LEO 1550 scanning electron microscope (SEM) operated at 15 kV was used. Figure 1 shows a typical scanning electron micrograph of MWNTs. The scale bar is 1 $\mu$m. The solvent used was HPLC grade (99.9%) N,N-dimethylformamide (DMF) from Sigma-Aldrich (St. Louis, MO, USA). The antisolvents used were distilled water and ethanol (A.C.S grade 99.98% purity from Pharmco Inc. (Brookfield, CT, USA).

### 2.2. Membrane preparation

First, the PVDF powder and the MWNTs were mixed separately with DMF. The polymer solution was prepared by heating a mixture of PVDF and solvent (1 : 4 in weight ratio) at 70°C for 2 hours. The MWNT/DMF premix was mixed using a hot plate with magnetic stirrer at 50°C for approximately 3 hours. The final mixture was prepared by adding the contents of the MWNT/DMF premix to the PVDF solution at 70°C with continuous stirring. The result was a mixture that is approximately 5 wt% MWNT-PVDF in DMF (from here onwards, the loading of MWNTs is in wt% unless otherwise stated). This solution was cast on a glass plate and then first dried in a vacuum oven at 50°C for approximately 2 minutes for solvent pre-evaporation; and then the membrane was coagulated using ethanol or water antisolvents. After complete coagulation, the membranes were transferred to a vacuum oven for drying overnight at 50°C. A similar technique was followed to prepare pure PVDF membranes for comparison purposes. Thickness of the membranes was 100–200 $\mu$m. The morphology of the dried membranes was examined using an LEO 1550 SEM at 20 kV. The top surface of the membranes was sputter-coated with gold before analysis.

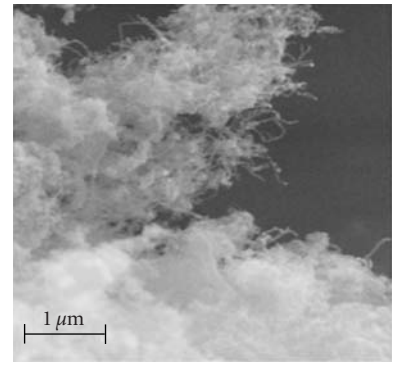


Figure 1: SEM micrograph of MWNTs.

### 2.3. Membrane characterization

Differential scanning calorimetry (DSC) studies were conducted using a TA Instruments (New Castle, DE, USA) DSC model Q1000 for pure PVDF and PVDF nanocomposite samples under a dry $N_2$ environment. The sample weight was kept at approximately 3 mg. During DSC analysis, the precipitated and dried samples were ramped from 25°C to 200°C at a rate of 10°C/min, then maintained at isothermal conditions for 5 minutes at 200°C. The specimens were then cooled at a rate of 10°C/min to ambient. The nominal melting temperature ($T_{m,p}$) was defined as the peak of the melting endotherm during first heating from 25 to 200°C, and the nominal crystallization temperature ($T_{c,p}$) was defined as the peak of the crystallization exotherm upon cooling from 200 to 25°C. Wide angle X-ray diffraction (WAXD) data were collected at room temperature by positioning the membranes on a quartz sample holder using a Rigaku Miniflex diffractometer in conjunction with a Cu$K_\alpha$ radiation source ($\lambda = 0.154$ nm) operated at 30 kV. The X-ray diffractograms were collected in the scan range, $2\theta$ of 5–50° at the scan speed of 1° min$^{-1}$ and using a step size of 0.04°. Fourier transform infrared (FTIR) spectra of the membranes were recorded on a JASCO ATR/FTIR-460 Plus over a range of 1000–550 cm$^{-1}$ with a resolution of 4 cm$^{-1}$.

## 3. RESULTS AND DISCUSSION

The morphology and the crystallinity of the PVDF and MWNT-PVDF nanocomposite membranes, prepared by the immersion precipitation technique, were investigated as a function of the incorporation of the MWNTs and the type

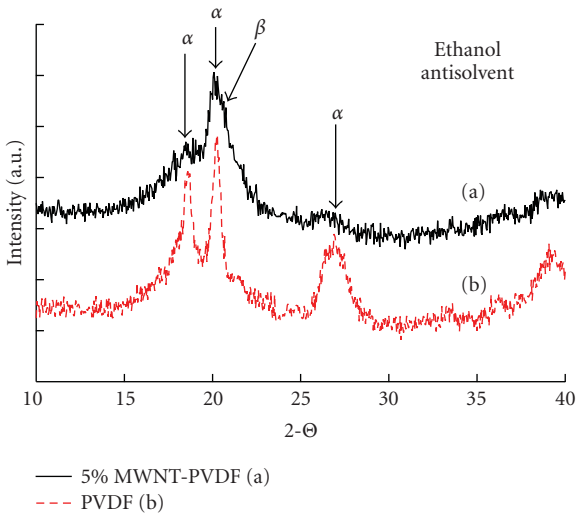


Figure 2: WAXD of PVDF and PVDF nanocomposite membranes prepared using ethanol as the antisolvent.

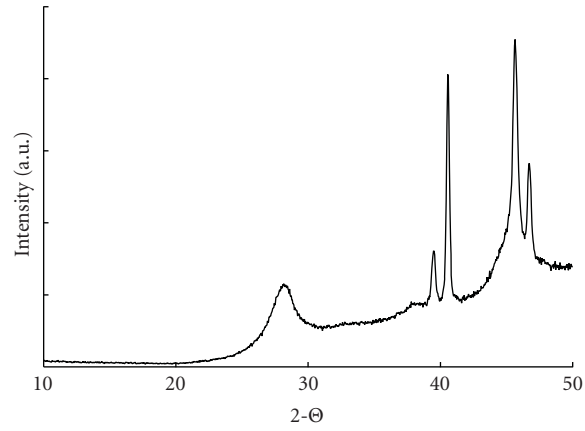


Figure 3: WAXD of pure MWNT sample.

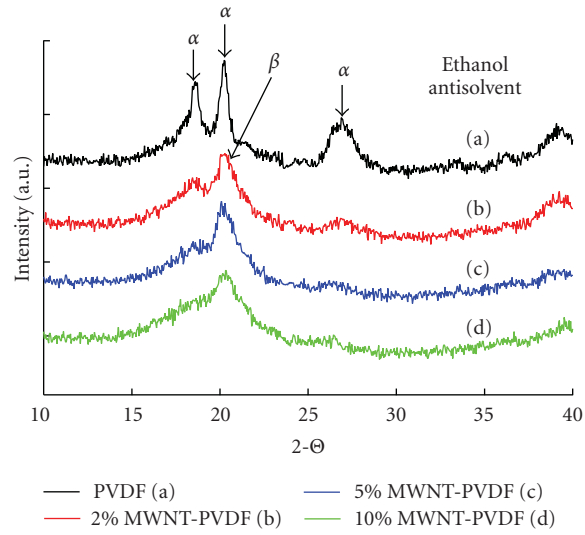


Figure 4: WAXD of nanocomposite membranes with different loadings of MWNTs prepared using ethanol as the antisolvent.

of antisolvent used. As described below, the crystallization of the PVDF upon immersion precipitation occurred predominantly in the $\alpha$-phase when water is used as the antisolvent or in the absence of the carbon nanotubes, while $\beta$-phase crystallization was favored upon the use of ethanol as the antisolvent in conjunction with the incorporation of the MWNTs.

### 3.1. *Effect of MWNTs and antisolvent on the PVDF crystal structure*

The results of WAXD analysis of PVDF and PVDF nanocomposite membranes prepared using ethanol as the antisolvent are shown in Figure 2. From the integration of the area under the crystalline peaks, it can be seen that the pure PVDF membrane contains predominantly major crystalline peaks at the $2\theta$ values of 18.6°, 20.3°, and 27°. These peaks are attributed to the crystal planes associated with the $\alpha$-phase of PVDF [18, 41]. It is significant that the addition of 5% MWNTs into PVDF promotes the crystallization of the PVDF in the $\beta$-polymorph. This is indicated from the WAXD patterns of 5% MWNT-PVDF nanocomposite membranes which exhibit the distinct feature of containing a sharp peak at 20.6° which is attributed specifically to the presence of the $\beta$ polymorph of PVDF [14–18]. In addition to this peak, the 5% MWNT-PVDF nanocomposite samples also exhibit large reductions in the areas under the peaks associated with the $\alpha$ polymorph that occur at the $2\theta$ values of 18.6° and 27°. The WAXD pattern for pure MWNTs (Figure 3) shows major peaks at 28.5°, 39.5°, and 40.6° which indicate that the crystalline peaks arising from the presence of the MWNTs are not overlapping with the crystalline peak associated with $\beta$ polymorph which occurs at 20.6°.

To further elucidate the effects of the concentration of the MWNTs on $\beta$-phase formation, PVDF membranes were prepared using 2 and 10 wt% loadings of MWNTs as shown in Figure 4. A decrease in the $\alpha$-peak area with increase in MWNT loadings can clearly be seen in the figure. It was found that the incorporation of MWNTs at both the 2 and 10 wt% levels continue to promote the crystallization of PVDF in the $\beta$-polymorph. The WAXD patterns of 2 and 10% MWNT-PVDF nanocomposites both exhibit a single sharp peak at 20.6° (Figure 4). Furthermore, the effect of the polymer concentration in the premix was also investigated by using a 10% PVDF/DMF solution (compared to the 20% PVDF solution used previously); this premix solution was then used to prepare 5% MWNT-PVDF nanocomposite membranes using ethanol as the antisolvent. X-ray data from these samples also indicated the crystallization of the PVDF predominantly in the $\beta$-phase (not shown here). This again suggests that the $\beta$-phase formation in MWNT-PVDF membranes is principally due to the presence of the nanotubes and ethanol as the antisolvent.

By comparison, the WAXD results obtained from PVDF and 5% MWNT-PVDF membranes prepared using water as the antisolvent during the precipitation process are shown in

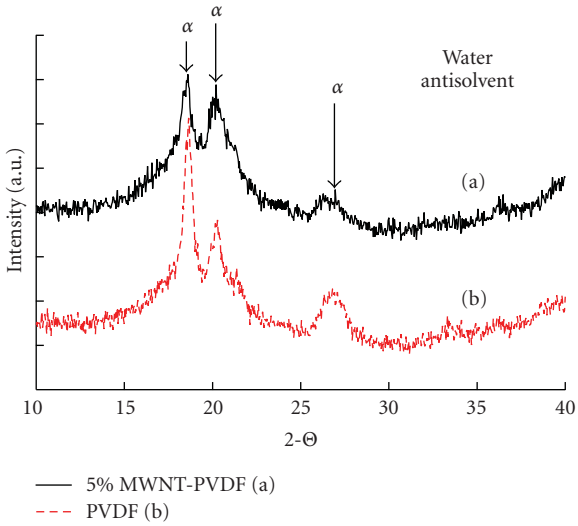


Figure 5: WAXD of PVDF and PVDF nanocomposite membranes prepared using water as the antisolvent.

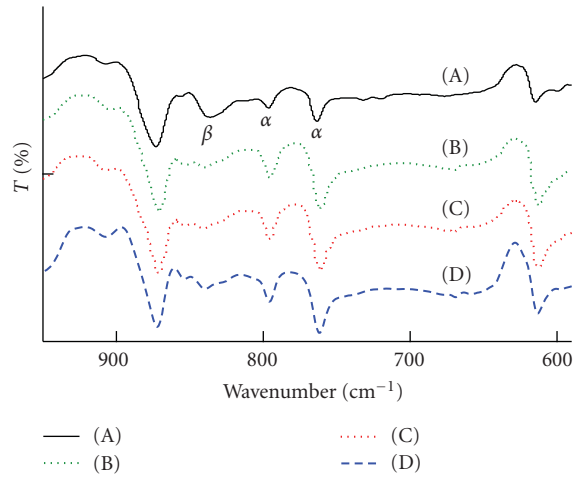


Figure 6: FTIR spectra of (A) 5% MWNT-PVDF (ethanol antisolvent), (B) pure PVDF (ethanol antisolvent), (C) 5% MWNT-PVDF (water antisolvent), and (D) pure PVDF (water antisolvent) membranes.

Figure 5. Here, it can be seen that the major peaks in both membranes correspond to the $\alpha$-form of PVDF and remain largely unchanged upon the incorporation of the MWNTs. Additional WAXD results on membranes prepared using 2 and 10 wt% MWNTs (not shown here) show similar behavior. The difference in crystal structure attained as a function of antisolvent can be attributed to the fact that ethanol gives rise to a relatively slow rate of polymer coagulation for PVDF, whereas water as the anitsolvent results in rapid coagulation of PVDF [26, 40, 42, 45]. Upon addition of ethanol solid-liquid, demixing occurs in the crystallizable segments of the polymer, which enables polymer crystallization to take place due to slow precipitation of the polymer [42]. In the case of water, the rate of polymer precipitation is very fast, leading to a relatively fast rate of crystallization, which should result in a lowered degree of crystallinity [38, 45, 46]. The principle reason that the rate of precipitation increases for the water/PVDF system should be associated with the rapid rate of interdiffusion of the solvent and the nonsolvent [45]. It is interesting to note that the nanocomposite membranes prepared using water as the antisolvent did not exhibit the $\beta$-phase (Figure 5) which can again be related to the slow coagulation rate with ethanol. Figure 3 shows that major $\alpha$-peaks in PVDF membranes are transformed to $\beta$-peak upon the incorporation of the MWNTs (5%). As discussed further in Section 3.3, the presence of the MWNTs increases the nucleation rate for crystallization (with MWNTs acting as heterogeneous nuclei sites), giving rise to an increase in the crystallinity of the membranes versus virgin PVDF and as seen here promotes crystallization in the $\beta$ phase.

The crystal phases within the membranes were further verified using FTIR analysis. The corresponding IR absorption band characteristics of the $\alpha$-phase are 766 and 796 $cm^{-1}$, whereas for $\beta$-phase peaks in the IR spectra are located at 511 and 840 $cm^{-1}$ [20, 41]. Figure 6 shows the FTIR spectra for the pure PVDF and PVDF nanocomposite membranes prepared using ethanol and water as the antisolvent. It can be seen that 5% MWNT-PVDF membrane prepared using ethanol antisolvent consists primarily of $\beta$-phase crystals (840 $cm^{-1}$), along with small amount of $\alpha$-phase crystals as well (the $\alpha$-peaks at 766 and 796 $cm^{-1}$ have low intensity). FTIR spectra of pure PVDF membrane prepared with ethanol antisolvent indicate predominantly the $\alpha$-crystal phase. Similarly, the FTIR results for membranes prepared with water antisolvent (both the pure PVDF and the 5% MWNT-PVDF nanocomposite samples) are dominated by the presence of $\alpha$-crystals (peaks at 766 and 796 $cm^{-1}$). These results along with WAXD data confirm the enhancement of $\beta$-phase crystal in 5% MWNT-PVDF membrane prepared with ethanol antisolvent.

### 3.2. Effect of MWNTs and antisolvent on morphology of PVDF membrane

SEM images of the top surface of pure PVDF and 5% MWNT-PVDF membranes precipitated from ethanol are shown in Figure 7. The effect of MWNTs on the membrane structure is significant and gives rise to the decrease in crystal size and to an increase of the microporosity of the PVDF membranes. From Figure 7(a), it can be seen that a sponge-like structure is formed to constitute the pure PVDF membrane. While a clear skin surface can be seen in the image, the structure of the membrane appears dominated by spherulitic crystallites in the 20–40 $\mu$m diameter range.

By comparison, the incorporation of the MWNTs has a profound effect on the distributions of crystallite shapes, sizes, and porosity. The morphological features shown in Figure 7(b) suggest that MWNTs are acting as heterogeneous nucleating agents, the concentration of which determines the number of nuclei. The increase of the nucleation rate and the crystallization of the PVDF on the nanotube surfaces eliminate the impinging of the relatively large spherulitic crystallites observed with pure PVDF (see Figure 7(a)). Upon

Table 1: Thermal analysis for PVDF and PVDF nanocomposite membranes.

| Sample | Antisolvent | $\Delta H_m$, J/g | $X_c^m$ (%) | $T_{m,p}$ (°C) | $\Delta H_c$, J/g | $X_c^c$ (%) | $T_{c,p}$ (°C) |
|---|---|---|---|---|---|---|---|
| PVDF | Ethanol | 51.32 ± 1.01 | 48.77 ± 0.59 | 168.03 ± 0.39 | 41.5 ± 0.56 | 39.67 ± 0.54 | 132.4 ± 0.78 |
| 5% MWNT-PVDF | Ethanol | 56.6 ± 1.62 | 54.41 ± 1.24 | 166.13 ± 0.62 | 41.33 ± 2.11 | 39.27 ± 1.89 | 142.89 ± 3.02 |
| PVDF | Water | 44.9 ± 1.06 | 42.9 ± 1.05 | 168.03 ± 0.30 | 41.16 ± 1.05 | 39.26 ± 0.99 | 133.48 ± 0.39 |
| 5% MWNT-PVDF | Water | 41.93 ± 1.52 | 40.09 ± 1.45 | 165.41 ± 0.98 | 38.35 ± 2.27 | 36.67 ± 2.17 | 136.41 ± 0.50 |

$T_{m,p}$ = nominal melting temperature, $T_{c,p}$ = nominal crystallization temperature, $\Delta H_m$ = heat of fusion, $\Delta H_c$ = heat of crystallization, $X_c^m$ = crystallinity from melting endotherm, $X_c^c$ = crystallinity from crystallization exotherm. Average values and 95% confidence intervals are reported.

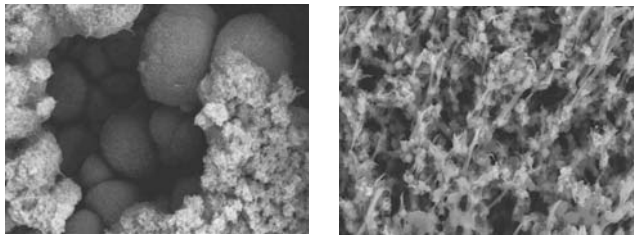


(a) PVDF (b) 5% MWNT-PVDF

Figure 7: SEM of (a) PVDF and (b) 5% MWNT-PVDF nanocomposite membranes prepared using ethanol as the antisolvent.

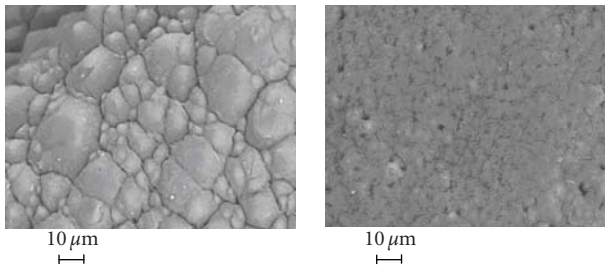


(a) PVDF (b) 5% MWNT-PVDF

Figure 8: SEM images of (a) PVDF and (b) 5% MWNT-PVDF nanocomposite membranes prepared using water as the antisolvent.

the incorporation of the MWNTs, a porous superstructure consisting of shish-kebab-like crystalline entities, forming a loose network, is observed. It also appears that the nanotubes are providing interconnections to form a continuous and open structure. The interconnectivity of the membrane will likely provide additional mechanical strength to the membrane, possibly increasing the utility of such piezoelectric membranes.

On the other hand, Figure 8 shows the PVDF and 5% MWNT-PVDF membranes prepared using water as the antisolvent. The top surface of the PVDF membrane shows a dense "skin" layer, which appears to be nonporous [38, 45]. The skin is composed of intersecting polygonal plates with clear boundaries; similar structures with crystalline polygonal plates have been observed in Nylon-6 membranes prepared via the immersion precipitation in water [39, 46]. As noted earlier, the formation of the skin layer and lack of an interconnected pore structure upon the use of water as the antisolvent is likely due to the rapid precipitation that occurs when water is used as the antisolvent, associated with the high rate of interdiffusion of DMF and water [45], where the rate of interdiffusion depends on the value of the solubility parameters of the solvent and antisolvent. In addition, small micropores can be seen on the surface of the membrane. Similar effects on morphology have been observed in mica-intercalated Nylon-6 nanocomposite membrane prepared by phase inversion method using water as the antisolvent [39]. As shown in Figure 8(b), the incorporation of MWNTs results in a similar morphology, albeit with smaller polygonal regions making up the surface of the membrane.

These initial results, together with the WAXD results presented in Section 3.1, indicate that the overall crystal morphology and porosity of the PVDF nanocomposite membranes are strongly influenced by both the antisolvent used to prepare the membrane as well as the presence of the MWNTs. Further analysis of the effects of these parameters on the crystallinity, porosity, and the availability of the targeted $\beta$ crystalline phase in PVDF nanocomposite membranes is necessary to allow the optimization of the microstructure and associated ultimate properties of such membranes.

### 3.3. Effects of MWNTs and antisolvent on melting and crystallization behavior of PVDF membrane

DSC analysis of pure PVDF and PVDF nanocomposite membranes was conducted to examine the effect of MWNTs and antisolvents on the degree of crystallinity $X_c$ of the membranes upon precipitation and the melting/crystallization temperatures observed upon the heating and the subsequent cooling of the membranes. Representative DSC heating and cooling curves are shown in Figures 9 and 10, respectively, while the results for four samples tested at each condition are summarized in Table 1. The heat of fusion ($\Delta H_m$) data obtained for nanocomposite samples was corrected due to the presence of MWNTs in the sample (such that $\Delta H_{\text{corrected}} = \Delta H_{\text{measured}}/W_p$, where $W_p$ is the weight fraction of polymer in the sample). Similarly, the heat of crystallization ($\Delta H_c$) data for PVDF nanocomposite samples was also corrected for true heat of crystallization of PVDF.

There are significant differences in the heat of fusion values for the four cases (with and without the MWNTs, and with ethanol or water). The use of ethanol as the antisolvent versus water gives rise to a greater heat of fusion as shown in Table 1. The percent crystallinity of PVDF and PVDF nanocomposites, based on either the melting ($X_c^m$)

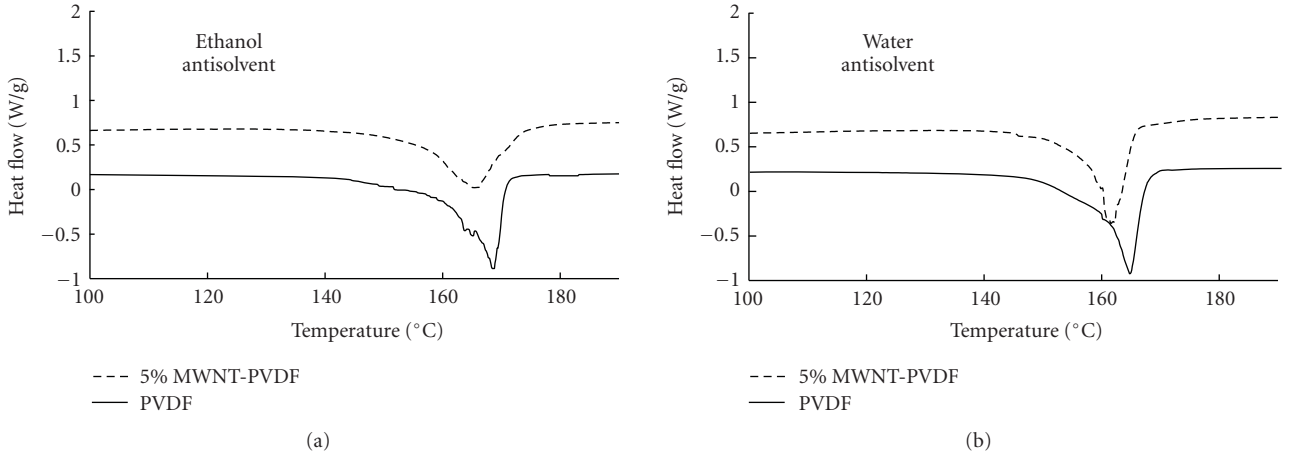


Figure 9: DSC endotherms of PVDF and 5% MWNT-PVDF nanocomposite membranes scanned at 10°C/min (a) using ethanol as the antisolvent and (b) using water as the antisolvent.

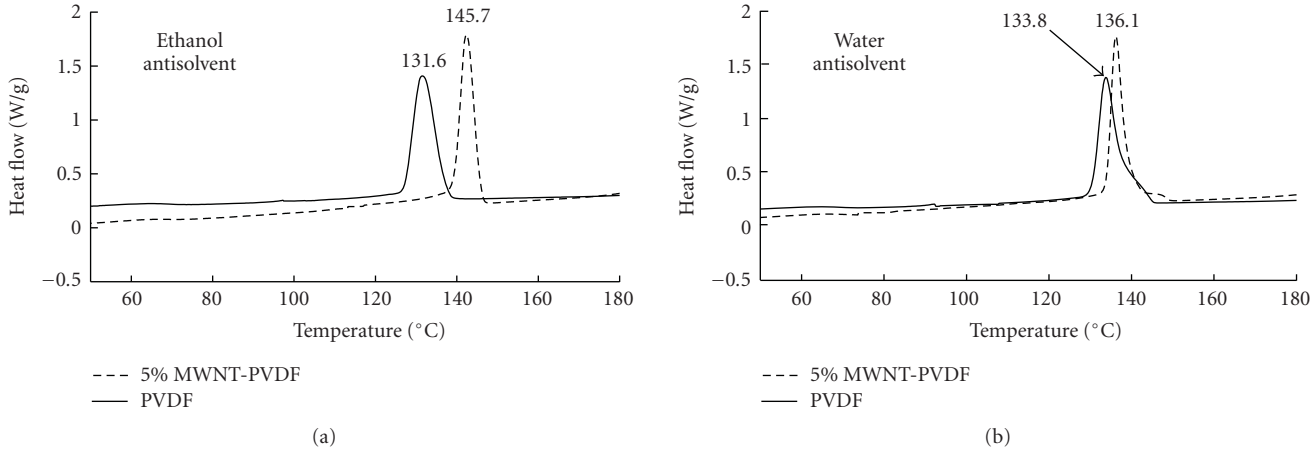


Figure 10: DSC exotherms for PVDF and 5% MWNT-PVDF nanocomposite membrane scanned at 10°C/min (a) using ethanol antisolvent and (b) using water antisolvent.

or crystallization ($X_c^c$) DSC scans, can be obtained from the expressions:

$$X_c^m = \frac{\Delta H_m * 100}{\Delta H_{100\%,\text{crystalline}}}, \qquad X_c^c = \frac{\Delta H_c * 100}{\Delta H_{100\%,\text{crystalline}}}, \tag{1}$$

where $\Delta H_{100\%,\text{crystalline}}$ is the heat of fusion of pure crystalline PVDF, which is reported to be 104.6 J/g [14], and $\Delta H_m$ and $\Delta H_c$ are the heat of fusion and the heat of crystallization of the sample. As shown in Table 1, the degree of crystallinity $X_c^m$ of the PVDF is greater when ethanol is used as the antisolvent. As indicated earlier, experimental studies of interdiffusion rates of ethanol and water in similar solvents have suggested that the interdiffusion rate of water in the solvent would be significantly higher than that of ethanol [45], giving rise to a significantly higher rate of precipitation in water and thus restricting the degree of crystallinity of PVDF.

The role played by the nanotubes in the crystallization process is interesting and again depends on which antisolvent is utilized during the precipitation. With ethanol, the favorable relatively slow rate of precipitation allows the MWNTs to act as nucleating agents to induce an increase in the nucleation and enables crystallization to take place to a greater extent. The presence of the MWNTs further increases the degree of the crystallinity $X_c^m$ of PVDF (Table 1), which is consistent with the SEM micrographs showing a decrease in the size of the crystallites upon the incorporation of the MWNTs (Figure 7(b)). On the other hand, the MWNTs incorporated into the PVDF membranes upon using water as the antisolvent have no favorable effect on the crystallization of PVDF and are even detrimental, that is, a reduction in the heat of fusion and hence the degree of crystallinity is observed. It appears that during the rapid precipitation process associated with water as the antisolvent, the MWNTs presumably remain as clusters and immobilize some of the PVDF, preventing their crystallization and thus reducing the degree of crystallinity $X_c^m$ of PVDF upon precipitation.

The data associated with the crystallization peak temperature further reinforce this understanding associated with

the roles of the rate of precipitation and the effects of the MWNTs (Table 1). The nominal crystallization temperature ($T_{c,p}$) was found to increase upon the addition of MWNTs, which is attributed to the heterogeneous nucleation induced by the presence of the MWNTs and the associated increase in the rate of nucleation/crystallization [47]. The increase in $T_{c,p}$ is significantly higher in the case of nanocomposite membranes prepared using ethanol. In contrast, a small change in crystallization temperature and a comparatively small decrease in polymer crystal size in nanocomposite membranes are observed when water is used as the antisolvent. In addition, little change is observed in the percent crystallinity $X_c^c$ based on the DSC cooling scans.

## 4. CONCLUSIONS

MWNT-PVDF nanocomposite membranes were prepared using ethanol and water antisolvents. The desirable $\beta$-phase crystallization of PVDF was promoted using MWNTs and ethanol as the antisolvent. The crystal size of the polymer was found to decrease due to addition of MWNTs, using ethanol, while the degree of crystallinity and the crystallization temperature increased. Further tests to correlate the mechanical and piezoelectric properties of the membranes as a function of the processing parameters are ongoing. These results indicate that the microstructure and the ultimate properties of the PVDF membranes can be engineered upon the judicious selection of crystallization conditions and the use of carbon nanotubes, with applications in the engineering of surfaces and structures for targeted applications such as sensors, filters, and artificial muscles.

## ACKNOWLEDGMENTS

Financial support from the Department of Mechanical Engineering at Stevens (for GM) is greatly appreciated. The authors would like to thank Dr. Halil Gevgilili from the Highly Filled Materials Institute (HfMI) at Stevens for his contributions to this work. Arkema Inc. (USA) is acknowledged for providing Kynar 741 PVDF powder. We also thank Dr. Jim Quinn, SUNY Stony Brook, for his help with the SEM imaging.

## REFERENCES

[1] M. R. Kamal, D. M. Kalyon, and J. Dealy, "An integrated experimental study of the injection molding behavior of some polyethylene resins," *Polymer Engineering & Science*, vol. 20, no. 17, pp. 1117–1125, 1980.

[2] G. Mago, F. T. Fisher, and D. M. Kalyon, "Effect of shearing on the crystallization behavior of poly(butylene terephthalate) and PBT nanocomposites," in *Proceedings of the ASME International Mechanical Engineering Congress and Exposition (IMECE '06)*, Chicago, Ill, USA, November 2006.

[3] A. J. Lovinger, "Ferroelectric polymers," *Science*, vol. 220, no. 4602, pp. 1115–1121, 1983.

[4] X. He, K. Yao, and B. K. Gan, "Phase transition and properties of a ferroelectric poly(vinylidene fluoride-hexafluoropropylene) copolymer," *Journal of Applied Physics*, vol. 97, no. 8, Article ID 084101, 6 pages, 2005.

[5] A. Ambrosy and K. Holdik, "Piezoelectric PVDF films as ultrasonic transducers," *Journal of Physics E*, vol. 17, no. 10, pp. 856–859, 1984.

[6] M. G. Broadhurst and G. T. Davis, "Physical basis for piezoelectricity in PVDF," *Ferroelectrics*, vol. 60, pp. 3–13, 1984.

[7] A. J. Lovinger, "Crystallization of the $\beta$ phase of poly(vinylidene fluoride) from the melt," *Polymer*, vol. 22, no. 3, pp. 412–413, 1981.

[8] J. Scheinbeim, C. Nakafuku, B. A. Newman, and K. D. Pae, "High-pressure crystallization of poly(vinylidene fluoride)," *Journal of Applied Physics*, vol. 50, no. 6, pp. 4399–4405, 1979.

[9] G. T. Davis, J. E. McKinney, M. G. Broadhurst, and S. C. Roth, "Electric-field-induced phase changes in poly(vinylidene fluoride)," *Journal of Applied Physics*, vol. 49, no. 10, pp. 4998–5002, 1978.

[10] K. Matsushige and T. Takemura, "Melting and crystallization of poly(vinylidene fluoride) under high pressure," *Journal of Polymer Science B*, vol. 16, no. 5, pp. 921–934, 1978.

[11] B. Mohajir and N. Heymans, "Changes in structural and mechanical behavior of PVDF with processing or thermal treatment—2: evolution of mechanical behavior," *Polymer*, vol. 42, no. 16, pp. 7017–7023, 2001.

[12] B. Mohajir and N. Heymans, "Changes in structural and mechanical behavior of PVDF with processing and thermomechanical treatments—1: change in structure," *Polymer*, vol. 42, no. 13, pp. 5661–5667, 2001.

[13] C.-H. Du, B.-K. Zhu, and Y.-Y. Xu, "Effects of stretching on crystalline phase structure and morphology of hard elastic PVDF fibers," *Journal of Applied Polymer Science*, vol. 104, no. 4, pp. 2254–2259, 2007.

[14] J. Buckley, P. Cebe, D. Cherdack, et al., "Nanocomposites of poly(vinylidene fluoride) with organically modified silicate," *Polymer*, vol. 47, no. 7, pp. 2411–2422, 2006.

[15] N. Levi, R. Czerw, S. Xing, P. Iyer, and D. L. Carroll, "Properties of polyvinylidene difluoride-carbon nanotube blends," *Nano Letters*, vol. 4, no. 7, pp. 1267–1271, 2004.

[16] Y. W. Nam, W. N. Kim, Y. H. Cho, et al., "Morphology and physical properties of binary blend based on PVDF and multi-walled carbon nanotube," *Macromolecular Symposia*, vol. 249-250, no. 1, pp. 478–484, 2007.

[17] L. Priya and J. P. Jog, "Polymorphism in intercalated poly(vinylidene fluoride)/clay nanocomposites," *Journal of Applied Polymer Science*, vol. 89, no. 8, pp. 2036–2040, 2003.

[18] D. R. Dillon, K. K. Tenneti, C. Y. Li, F. K. Ko, I. Sics, and B. S. Hsiao, "On the structure and morphology of polyvinylidene fluoride-nanoclay nanocomposites," *Polymer*, vol. 47, no. 5, pp. 1678–1688, 2006.

[19] Z.-M. Dang, S.-H. Yao, and H.-P. Xu, "Effect of tensile strain on morphology and dielectric property in nanotube/polymer nanocomposites," *Applied Physics Letters*, vol. 90, no. 1, Article ID 012907, 3 pages, 2007.

[20] D. Shah, P. Maiti, E. Gunn, et al., "Dramatic enhancements in toughness of polyvinylidene fluoride nanocomposites via nanoclay-directed crystal structure and morphology," *Advanced Materials*, vol. 16, no. 14, pp. 1173–1177, 2004.

[21] D. Shah, P. Maiti, D. D. Jiang, C. A. Batt, and E. P. Giannelis, "Effect of nanoparticle mobility on toughness of polymer nanocomposites," *Advanced Materials*, vol. 17, no. 5, pp. 525–528, 2005.

[22] Z.-M. Dang, Y.-H. Lin, and C.-W. Nan, "Novel ferroelectric polymer composites with high dielectric constants," *Advanced Materials*, vol. 15, no. 19, pp. 1625–1629, 2003.

[23] M. Wang, J. Shi, K. P. Pramoda, and S. H. Goh, "Microstructure, crystallization and dynamic mechanical behavior of poly(vinylidene fluoride) composites containing poly(methyl methacrylate)-grafted multiwalled carbon nanotubes," *Nanotechnology*, vol. 18, Article ID 235701, 7 pages, 2007.

[24] K. Peng, L. Hornbergera, C. V. Nguyena, and U. Sopory, "Processing of dispersed and aligned multi-walled carbon nanotubes in polyvinylidene fluoride," *Journal of Advanced Materials*, vol. 39, no. 2, pp. 24–31, 2007.

[25] T. C. Merkel, B. D. Freeman, R. J. Spontak, et al., "Ultrapermeable, reverse-selective nanocomposite membranes," *Science*, vol. 296, no. 5567, pp. 519–522, 2002.

[26] S. P. Deshmukh and K. Li, "Effect of ethanol composition in water coagulation bath on morphology of PVDF hollow fibre membranes," *Journal of Membrane Science*, vol. 150, no. 1, pp. 75–85, 1998.

[27] K.-Y. Lin, D.-M. Wang, and J.-Y. Lai, "Nonsolvent-induced gelation and its effect on membrane morphology," *Macromolecules*, vol. 35, no. 17, pp. 6697–6706, 2002.

[28] W.-H. Seol, Y. M. Lee, and J.-K. Park, "Enhancement of the mechanical properties of PVDF membranes by non-solvent aided morphology control," *Journal of Power Sources*, vol. 170, no. 1, pp. 191–195, 2007.

[29] K. Li, J. F. Kong, D. Wang, and W. K. Teo, "Tailor-made asymmetric PVDF hollow fibers for soluble gas removal," *AIChE Journal*, vol. 45, no. 6, pp. 1211–1219, 1999.

[30] M. Ulbricht, "Advanced functional polymer membranes," *Polymer*, vol. 47, no. 7, pp. 2217–2262, 2006.

[31] H. Kataoka, Y. Saito, T. Sakai, E. Quartarone, and P. Mustarelli, "Conduction mechanisms of PVDF-type gel polymer electrolytes of lithium prepared by a phase inversion process," *Journal of Physical Chemistry B*, vol. 104, no. 48, pp. 11460–11464, 2000.

[32] A. Akthakul, R. F. Salinaro, and A. M. Mayes, "Antifouling polymer membranes with subnanometer size selectivity," *Macromolecules*, vol. 37, no. 20, pp. 7663–7668, 2004.

[33] K. Laxminarayana and N. Jalili, "Functional nanotube-based textiles: pathway to next generation fabrics with enhanced sensing capabilities," *Textile Research Journal*, vol. 75, no. 9, pp. 670–680, 2005.

[34] C. Seoul, Y.-T. Kim, and C.-K. Baek, "Electrospinning of poly(vinylidene fluoride)/dimethyl formamide solutions with carbon nanotubes," *Journal of Applied Polymer Science B*, vol. 41, no. 13, pp. 1572–1577, 2003.

[35] T. Mirfakhrai, J. D. W. Madden, and R. H. Baughman, "Polymer artificial muscles," *Materials Today*, vol. 10, no. 4, pp. 30–38, 2007.

[36] A. Ramaratnam, N. Jalili, and H. Rajoria, "Development of a novel strain sensor using nanotube-based materials with applications to structural vibration control," in *6th International Conference on Vibration Measurements by Laser Techniques: Advances and Applications*, vol. 5503 of *Proceedings of SPIE*, pp. 478–485, Ancona, Italy, June 2004.

[37] A. Ramaratnam and N. Jalili, "Reinforcement of piezoelectric polymers with carbon nanotubes: pathway to next-generation sensors," *Journal of Intelligent Material Systems and Structures*, vol. 17, no. 3, pp. 199–208, 2006.

[38] L.-P. Cheng, D.-J. Lin, C.-H. Shih, A.-H. Dwan, and C. C. Gryte, "PVDF membrane formation by diffusion-induced phase separation-morphology prediction based on phase behavior and mass transfer modeling," *Journal of Polymer Science B*, vol. 37, no. 16, pp. 2079–2092, 1999.

[39] L.-P. Cheng, D.-J. Lin, and K.-C. Yang, "Formation of mica-intercalated-Nylon 6 nanocomposite membranes by phase inversion method," *Journal of Membrane Science*, vol. 172, no. 1-2, pp. 157–166, 2000.

[40] L.-P. Cheng, T.-H. Young, L. Fang, and J.-J. Gau, "Formation of particulate microporous poly(vinylidene fluoride) membranes by isothermal immersion precipitation from the 1-octanol/dimethylformamide/poly(vinylidene fluoride) system," *Polymer*, vol. 40, no. 9, pp. 2395–2403, 1999.

[41] M. G. Buonomenna, P. Macchi, M. Davoli, and E. Drioli, "Poly(vinylidene fluoride) membranes by phase inversion: the role the casting and coagulation conditions play in their morphology, crystalline structure and properties," *European Polymer Journal*, vol. 43, no. 4, pp. 1557–1572, 2007.

[42] L.-P. Cheng, "Effect of temperature on the formation of microporous PVDF membranes by precipitation from 1-octanol/DMF/PVDF and water/ DMF/PVDF systems," *Macromolecules*, vol. 32, no. 20, pp. 6668–6674, 1999.

[43] M. L. Yeow, Y. T. Liu, and K. Li, "Isothermal phase diagrams and phase-inversion behavior of poly(vinylidene fluoride)/solvents/additives/water systems," *Journal of Applied Polymer Science*, vol. 90, no. 8, pp. 2150–2155, 2003.

[44] A. J. McHugh and D. C. Miller, "The dynamics of diffusion and gel growth during nonsolvent-induced phase inversion of polyethersulfone," *Journal of Membrane Science*, vol. 105, no. 1-2, pp. 121–136, 1995.

[45] T.-H. Young, L.-P. Cheng, D.-J. Lin, L. Fane, and W.-Y. Chuang, "Mechanisms of PVDF membrane formation by immersion-precipitation in soft (1-octanol) and harsh (water) nonsolvents," *Polymer*, vol. 40, no. 19, pp. 5315–5323, 1999.

[46] T.-H. Young, D.-J. Lin, J.-J. Gau, W.-Y. Chuang, and L.-P. Cheng, "Morphology of crystalline Nylon-610 membranes prepared by the immersion-precipitation process: competition between crystallization and liquid-liquid phase separation," *Polymer*, vol. 40, no. 18, pp. 5011–5021, 1999.

[47] I. Pillin, S. Pimbert, and G. Levesque, "Influence of additives on the crystallization kinetics of semicrystalline polymers. II: selective polymer-additive interaction in poly(vinylidene difluoride)-poly(methylmethacrylate) blends," *Polymer Engineering & Science*, vol. 42, no. 11, pp. 2193–2201, 2002.

Hindawi Publishing Corporation
Journal of Nanomaterials
Volume 2008, Article ID 786405, 15 pages
doi:10.1155/2008/786405

*Research Article*

# Morphology and Properties of Aminosilane Grafted MWCNT/Polyimide Nanocomposites

**Siu-Ming Yuen,[1] Chen-Chi M. Ma,[1] Chin-Lung Chiang,[2] and Chih-Chun Teng[1]**

[1] *Department of Chemical Engineering, National Tsing Hua University, Hsinchu 30043, Taiwan*
[2] *Department of Industrial Safety and Health, Hung Kuang University, Salu, Taichung 443, Taiwan*

Correspondence should be addressed to Chen-Chi M. Ma, ccma@che.nthu.edu.tw

Received 2 April 2007; Revised 2 September 2007; Accepted 4 October 2007

Recommended by Jun Lou

This investigation presents a novel method for modifying multiwalled carbon nanotubes (MWCNTs). The morphology, electrical resistivity, and percolation threshold of MWCNT/Polyimide nanocomposites were studied. Acid-modified MWCNTs reacted with (3-aminopropyl)triethoxysilane by ionic bonding, and were then mixed with polyamic acid via imidization. TEM microphotographs reveal that silane-grafted MWCNTs were connected to each other. The electrical resistivity of silane-grafted MWCNT/polyimide decreased substantially below than that of acid-treated MWCNTs when the silane-modified MWCNT content was lower than 2.4 wt%. The percolation threshold of the MWCNT/polyimide composites is 1.0 wt% for silane-modified MWCNT and exceeds 7.0 wt% for acid-modified MWCNT. The acid-modified MWCNT/polyimide composites possess slightly higher glass transition temperatures than that of pure polyimide. The glass transition temperature of the polyimide increased significantly with silane-modified MWCNT content. Tensile properties of the polyimide have been improved with the MWCNTs content.



## 1. INTRODUCTION

Polyimide is a high-performance polymer with high thermal stability, favorable dielectric properties, and chemical resistance. It has been found applications in the microelectronics and composites industries [1]. Carbon nanotubes (CNTs) have attracted much research interest in various areas since their structures were identified in 1991 [2]. They exhibit excellent mechanical and electrical properties, low density, high-surface area, and high chemical resistance [3–8]. CNT/polymer composites are interesting materials whose mechanical properties and electrical conductivity can be improved by the addition of CNT [9–13]. CNT/polyimide composites are interesting materials and have been extensively studied [14–17]. In our previous investigation, [17] unmodified-, acid-modified-, and amine-modified-MWCNT/polyimide nanocomposites were prepared and their morphology and electrical, thermal, and mechanical properties were examined .

CNT can be modified by refluxing with strong acid or a strong oxidizing agent. Carboxyl and hydroxyl functional groups are formed on the surface of CNTs during acid modification [18]. Acid-modified MWCNT can be modified with silane [19–23]. Shanmugharaj et al. [20] grafted 3-aminopropyltriethoxysilane (APTES) to acid-modified MWCNT and prepared silane-modified MWCNT/natural rubber composites. They suggested that silane can be reacted with the hydroxyl groups (−OH) on the surface of MWCNTs [19–23]. The oxidation of MWCNT may generate carboxylic groups (−COOH) rather than hydroxyl groups. Valentini et al. [23] modified SWCNTs using $CF_4$ plasma to obtain fluorinated SWCNT (f-SWCNT). The f-MWCNT then reacted with APTES and the amine functional group of APTES was grafted on the f-MWCNT. Our previous study has successfully modified MWCNT with silane [24–26]. The silane-modified MWCNTs/Poly (urea urethane) composites have been prepared. The molecular structure and molecular mobility of the carbon-nanotube/PUU nanocomposites have been investigated [26]. These references indicated that carbon nanotube may be dispersed effectively. Increase the dispersion does not improve the electrical conductivity nor decrease the percolation threshold effectively.

In this study, acid-modified MWCNT was mixed with (3-aminopropyl)triethoxysilane(APTES). Silane functional groups are grafted on the acid-modified MWCNT (APTES-MWCNT) by ionic bonding or amide bonding, and some ungrafted APTES may react with polyamic acid to form a complex [1]. After modification of the MWCNT, silane functional groups were remained. The APTES-MWCNT was dispersed in the polyamic acid which was imidized at 300°C. When the APTES-MWCNT/polyamic acid was heated to 300°C, the silane reacted on the MWCNT surface, and this reaction was examined. This work studies the electrical resistivity, the percolation threshold, and the thermal properties of the MWCNT/polyimide.

## 2. EXPERIMENTAL SECTION

### 2.1. Materials

Multiwalled carbon nanotubes were obtained from the Nanotech Port Company, Shenzhen, China. The diameters of the MWCNTs were 40–60 nm; their lengths were 0.5–40 $\mu$m, and their special surface areas were 40–3000 $m^2$/g. Both 4,4′-oxydianiline (ODA) and 3,3′,4,4′-benzophenone tetracarboxylic dianhydride (BTDA) were obtained from Chris KEV Company, Inc. Terrance Leawood, KS, USA. (3-Aminopropyl)triethoxysilane (APTES) was obtained from Lancaster Synthesis Co., Morecambe, England. N,N-Dimethylacetamide (DMAc) was obtained from Tedia Company Inc., Fairfield, OH, USA.

### 2.2. Synthesis of polyamic acid

The precursor of polyimide (polyamic acid) was prepared by reacting 4,4′-oxydianiline (ODA) with 3,3′,4,4′-benzophenone tetracarboxylic dianhydride (BTDA) in N,N-Dimethylacetamide (DMAc). The mole ratio of ODA to BTDA was 1 : 1. 4,4′-Oxydianiline (ODA) was dissolved in DMAc and then 3,3′,4,4′-benzophenone tetracarboxylic dianhydride (BTDA) was added to the 4,4′-oxydianiline (ODA) solution with an ice bath. The polyamic acid was imidized at 300°C to yield polyimide (as shown in Scheme 1).

### 2.3. Modification of MWCNT

Pristine MWCNTs were functionalized by refluxing with a mixture of $H_2SO_4$ and $HNO_3$ (weight ratio of $H_2SO_4$ to $HNO_3$ is 3 : 2) at 50°C for 24 hours. After acid treatment, the MWCNTs were washed using deionized water, filtered and dried at 100°C. Then, the modified MWCNT was dispersed in DMAc and then (3-aminopropyl)-triethoxysilane (APTES) added to the mixture and was stirred for 1 hour (as presented in Scheme 2). Table 1 presents the mass ratio of APTES to MWCNT. The APTES-treated MWCNT is denoted APTES-MWCNT.

### 2.4. Preparation of carbon nanotubes/polyimide nanocomposites

APTES-MWCNT was added to polyamic acid then put on to a plastic plate and heated to 60°C to remove the solvent (DMAc). The mixture was then heated to 300°C to produce MWCNT/polyimide composites.

Table 1: The ratios of APTES to acid-modified MWCNT for APTES-MWCNT.

| ID | APTES : MWCNT (in weight) |
|---|---|
| APTES-MWCNT-1 | 1 : 1 |
| APTES-MWCNT-2 | 2 : 1 |
| APTES-MWCNT-3 | 3 : 1 |

### 2.5. Measurement of properties

#### 2.5.1. Fourier transform infrared spectroscopy

The Fourier transform infrared spectroscopy (FT-IR) spectra of unmodified and acid-modified MWCNT were recorded between 800 and 4000 $cm^{-1}$ using a Nicolet Avatar 320 FT-IR spectrometer, from the Nicolet Instrument Corporation, Madison, WI, USA. The sample was dispersed in THF solvent and then coated on a $CaF_2$ plate and dried in a vacuum oven at 120°C before it was tested. The *spectra* from a minimum of 32 scans were averaged with a signal resolution of 2 $cm^{-1}$ within the range 400–4000 $cm^{-1}$.

#### 2.5.2. X-ray photoelectron spectroscopy (XPS)

The XPS spectra of MWCNTs were obtained using a ULVAC-PHI, PHI Quantera with scanning monochromated A1 anode high-resolution X-ray photoelectron spectrometer.

#### 2.5.3. CP/MAS solid state $^{29}$Si nuclear magnetic resonance (NMR) spectroscopy

High-resolution $^{29}$Si solid-state NMR was conducted using a Bruker DSX 400 MHz NMR. The samples were ground into fine powder. The $^{29}$Si CP/MAS NMR spectra of the composites were obtained to characterize the degree of condensation of the APTES-MWCNT/polyimide interpenetrating network with various Multiwalled carbon nanotube contents.

#### 2.5.4. Morphological properties

Morphological properties were studied using an FE-SEM (S-4200) scanning electron microscope from Hitachi, Japan, and a JEOL-2000EX transmission electron microscope (TEM) from Japan.

#### 2.5.5. Measurement of electrical properties

Surface and volume electrical resistivity were measured using a ULTRA Mesohmeter SM-8220, from the DKK TOA Corporation, Tokyo, Japan. The Surface and volume electrical resistivities of the MWCNT/polyimide composites were measured after various MWCNT contents were added. The charge time was 30 s, and the current voltage of the measurements was 100 V. An average value was obtained from five to six measurements for each sample.

Table 2: Percentages of T and Q substitution of APTES-MWCNT/polyimide composites.

| APTES : MWCNT (in weight) | MWCNT content, wt% | % of T substituted | % of Q substituted |
|---|---|---|---|
| 1 : 1 | 0.99 | 97.12 | 2.88 |
| 1 : 1 | 6.98 | 84.02 | 15.98 |
| 2 : 2 | 0.99 | 88.41 | 11.59 |
| 2 : 2 | 6.98 | 86.50 | 13.50 |
| 3 : 3 | 0.99 | 87.27 | 12.73 |
| 3 : 3 | 6.98 | 86.56 | 13.44 |

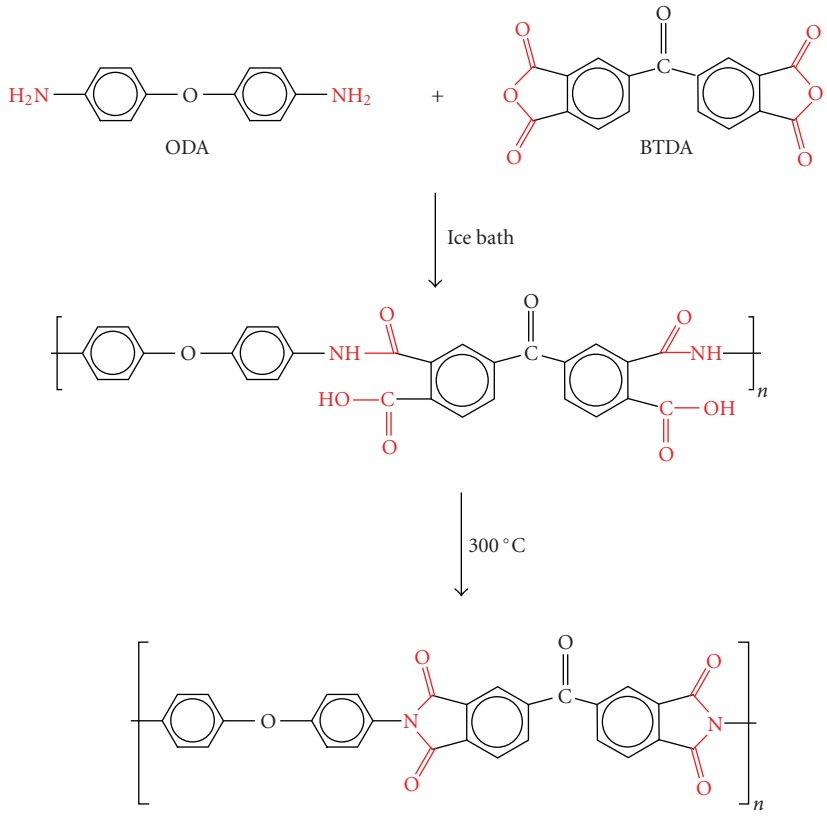


Scheme 1: Preparation of the polyimide.

#### 2.5.6. Glass transition temperature (Tg)

Glass transition temperatures (Tgs) were measured using a differential scanning calorimeter (DSC) (TA Instruments DSC Q-10). Test data were obtained from 50°C to 350°C at a heating rate of 10°C/min. A minimum of three specimens of each composition were tested.

#### 2.5.7. Measurements of tensile properties

Tensile strength test was carried out by using an instron machine model 4488 at room temperature. Test procedure followed the ASTM-D882. Dimensions of test specimens were 50 mm × 5 mm × 0.1 mm. The crosshead speed was 5 mm/min.

## 3. RESULTS AND DISCUSSION

### 3.1. Fourier transfer infrared spectroscopy

Figure 1(a) shows the FTIR spectrum of unmodified carbon nanotubes; the wavenumbers 3000 and 2800 $cm^{-1}$ corresponded to −CH stretching and 1711 $cm^{-1}$ corresponded to c=O stretching. The FTIR result (−CH stretching) demonstrates that MWCNTs contain defects, which may be formed during the manufacturing of MWCNT. Figure 1(b) presents the FTIR spectrum of acid-modified carbon nanotubes. The wavenumbers 3000 and 2800 $cm^{-1}$ corresponded to the stretching of −CH. Carboxylic group stretching (COOH) occurred at 1720 $cm^{-1}$. Absorption peaks at wavenumbers 1610 $cm^{-1}$ and 3430 $cm^{-1}$ correspond to COO− asymmetric stretching and −COO− stretching, respectively. The FTIR

Table 3: Surface electrical resistivity of MWCNT/polyimide composites.

| MWCNT content | Surface electrical resistivity of unmodified MWCNT/PI, $\Omega/cm^2$ | Surface electrical resistivity of acid-modified MWCNT/PI, $\Omega/cm^2$ | Surface electrical resistivity of APTES-MWCNT-1/PI, $\Omega/cm^2$ | Surface electrical resistivity of APTES-MWCNT-2/PI, $\Omega/cm^2$ | Surface electrical resistivity of APTES-MWCNT-3/PI, $\Omega/cm^2$ |
|---|---|---|---|---|---|
| 0 | $1.28 \times 10^{15}$ | $1.27 \times 10^{15}$ | $1.27 \times 10^{15}$ | $1.27 \times 10^{15}$ | $1.27 \times 10^{15}$ |
| 0.5 | $6.75 \times 10^{14}$ | $2.99 \times 10^{13}$ | $1.94 \times 10^{15}$ | $2.46 \times 10^{13}$ | $7.88 \times 10^{12}$ |
| 1.0 | $2.03 \times 10^{14}$ | $2.65 \times 10^{13}$ | $2.06 \times 10^{13}$ | $1.70 \times 10^{13}$ | $5.61 \times 10^{12}$ |
| 2.4 | $3.03 \times 10^{12}$ | $2.73 \times 10^{13}$ | $8.07 \times 10^{12}$ | $1.29 \times 10^{13}$ | $5.29 \times 10^{12}$ |
| 4.8 | $8.82 \times 10^{7}$ | $2.31 \times 10^{13}$ | $1.53 \times 10^{12}$ | $2.35 \times 10^{12}$ | $5.58 \times 10^{11}$ |
| 7.0 | $7.59 \times 10^{6}$ | $2.53 \times 10^{13}$ | $8.64 \times 10^{10}$ | $8.58 \times 10^{11}$ | $4.53 \times 10^{11}$ |

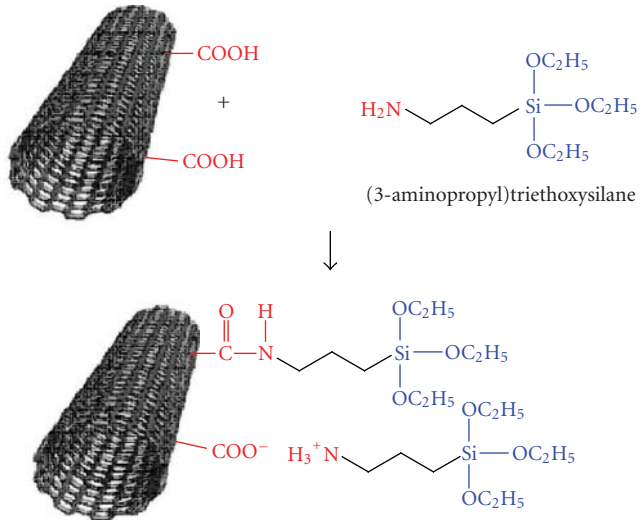


Scheme 2: Attachment of APTES with acid-modified MWCNT.

spectrum of acid-modified carbon nanotubes confirmed that pristine MWCNT was modified by $H_2SO_4/HNO_3$ mixed acid generating carboxylic groups. Figure 1(c) presents the FTIR spectrum of the APTES-MWCNT. The wavenumbers at 3000 and 2800 $cm^{-1}$ corresponded to stretching of $-CH$. Carboxylic groups stretching ($-COO^-$) appeared at 1400 $cm^{-1}$. Stretch of amine salt ($-NH-$) appeared at 3100 $cm^{-1}$. Bend of the amine salt ($-NH_3^+$) appeared at 1610 $cm^{-1}$ and 1500 $cm^{-1}$. Absorption peaks at wavenumbers 1110 $cm^{-1}$ and 956 $cm^{-1}$ corresponded to $-SiO-$ stretching. The FTIR spectrum of APTES-MWCNT confirmed that MWCNT was modified with APTES.

### 3.2. X-ray photoelectron spectroscopy (XPS)

Figure 2 presents XPS spectra of the silane-modified MWCNT. Figures 2(a), 2(c), and 2(e) reveal that silane-modified MWCNTs have peaks at about 103eV, 154eV, 285eV, 400eV, and 531eV. The peak appeared at 103eV was Si2p, 154eV was Si2s, 285eV was C1s, 400eV was N1s, and 531eV was O1s, respectively. Figure 2(b) presents the peaks of APTES-MWCNT-1 at 400eV, (N1s) can be separated as 400.0eV, 401.4eV, and 402.6eV. The peak at 400.0eV was amide and peaks at 401.4eV, and 402.6eV were amino ions. The ratio of 400.0eV : 401.4eV : 402.6eV was 1 : 0.26 : 0.06. Figures 2(d) and 2(f) present the peaks of APTES-MWCNT-2 and APTES-MWCNT-3 at 400eV, (N1s) can be separated as 400.0eV and 401.4eV. The ratio of 400.0eV : 401.4eV of APTES-MWCNT-2 and APTES-MWCNT-3 were 1 : 0.08 and 1 : 0.13, respectively. The XPS data confirm the most of the silane bonding with the acid-modified MWCNT with amide functional groups and some of them bonded with amino ion.

### 3.3. CP/MAS solid state $^{29}Si$ nuclear magnetic resonance (NMR) spectroscopy

Figures 3(a) to 3(f) present the $^{29}Si$ solid-state NMR spectra of APTES-MWCNT/polyimide composites. They reveal that trisubstituted siloxane bonds (chemical shift of $T^2$, $\delta$ − 59.84 ppm, and $T^3$, $\delta$ − 67.002 ppm) [27] and some tetrasubstituted siloxane bonds (associated with chemical shifts $Q^2$, $Q^3$ and $Q^4$ of −91, −101 and −109.13 ppm, resp.) [27] are present in APTES-MWCNT/polyimide composites. Trisubstituted siloxane bonds are defined as a silicon atom possesses four bonds, three of them are bonded with three oxygen atoms and the fourth bond may be bonded with another

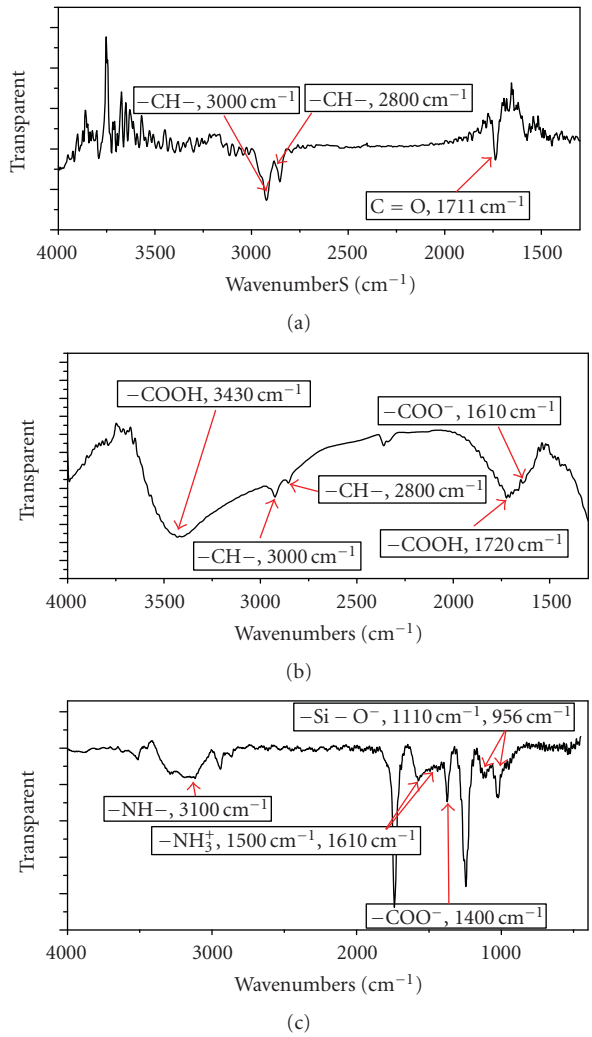


Figure 1: FTIR spectra of (a) unmodified MWCNT, (b) acid modified MWCNT, (c) APTES-MWCNT.

atom, such as carbon atom (Figure 4(a)). Tetrasubstituted siloxane bonds are the four bonds of the silicon atom bonded to oxygen atoms (Figure 4(b)).

Table 2 summarizes the percentages of T and Q substitution of the composites. The tetrasubstituted bond may have been formed when the composites were heated to 300°C and the Si−C bonds of the APTES may have been broken. When the MWCNT content was low (1.0 wt%), the percentage of Q-substitution was proportional to the ratio of APTES to MWCNT. When the ratio of APTES to MWCNT was excessive, most APTES do not graft on the MWCNT. The ungrafted APTES may be responsible for a lower thermal stability, since the Si−C bond of the ungrafted APTES is weak. Hence, the proportion of tetrasubstitution increased with the ratio of APTES to MWCNT. When the MWCNT content was high (7.0 wt%), the percentage of Q-substitution decreased as the ratio of APTES to MWCNT increased. When the MWCNT content and the silane content were both high, the $SiO_x$ network was easily formed. APTES grafted on the SiOx network and increased the thermal stability.

Regarding T substitution (Figure 4), the peak height of $T^3$ of the sample with higher MWCNT content was higher than that with a lower MWCNT content. When the APTES-MWCNT content was low, since the silane in the nanocomposites could not easily react with the other silane because the APTES-MWCNT intermolecular distance was very large, the interpenetrating network could not easily be formed. However, when the APTES-MWCNT content was high, the silane more easily reacted with the other silane, because the ATPES-MWCNT intermolecular distance was shortened.

### 3.4. Morphology of MWCNT/polyimide composites

Figures 5(a)–5(f) present SEM microphotographs of the APTES-MWCNT/polyimide composites. The MWCNT was dispersed in the polymer matrix. Most of the MWCNTs were embedded in the polyimide matrix. Figures 5(a) and 5(b) show SEM microphotographs of the APTES-MWCNT-1/polyimide composites. Most APTES-MWCNT were embedded in the polyimide matrix and only a few were pulled out from the matrix. Figures 5(c) and 5(d) indicate that most of the MWCNTs in APTES-MWCNT-2/polyimide composites were embedded in the polyimide matrix and some of the MWCNTs were pulled out from the matrix. Figures 5(e) and 5(f) reveal that most of the MWCNT in APTES-MWCNT-2/polyimide composites were also embedded. However, it can be seen that more MWCNTs were pulled out than those of the APTES-MWCNT-1/polyimide composites and APTES-MWCNT-2/polyimide composites. The imprint of the MWCNT on the polyimide matrix (indicated by the arrow in Figure 5(f)) was observed.

Figures 6(a) to 6(f) display the TEM microphotographs of the ATPES-MWCNT/polyimide composites. Figures 6(a) and 6(b) present the TEM microphotographs of the APTES-MWCNT-1/polyimide composites. The MWCNTs were coated with $SiO_x$ layers, which looked like "needles" and were dispersed in the polymer matrix. Some of the MWCNTs were connected to each other. Some of the $SiO_x$ was not coated on the MWCNT surface and was aggregated in the shape of cotton balls.

Figures 6(c) and 6(d) show the TEM microphotographs of the APTES-MWCNT-2/polyimide composites. The MWCNTs were also coated with $SiO_x$ layers and dispersed in the polymer matrix. Some of the MWCNTs were also connected to each other. The MWCNTs were assembled in an "H" shape or a "Ψ" shape.

Figures 6(e) and 6(f) display TEM microphotographs of the APTES-MWCNT-3/polyimide composites. The $SiO_x$ was aggregated on the MWCNT surface. Figure 6(e) reveals that the MWCNTs were assembled in the shapes of longer needles which differed from those in Figures 6(a), 6(b). The "needle-shaped" MWCNTs in Figures 6(e), 6(f) were longer and thinner than those in Figures 6(a), 6(b). Figure 6(f) shows that some of the MWCNT have been connected. When the ratio of APTES to MWCNT was high, most of the APTES were not grafted on the surface of acid-modified MWCNTs. Some of the APTES reacted with the polyamaric acid to form a complex [1, 28]. The ungrafted APTES bonded with the grafted APTES, and could

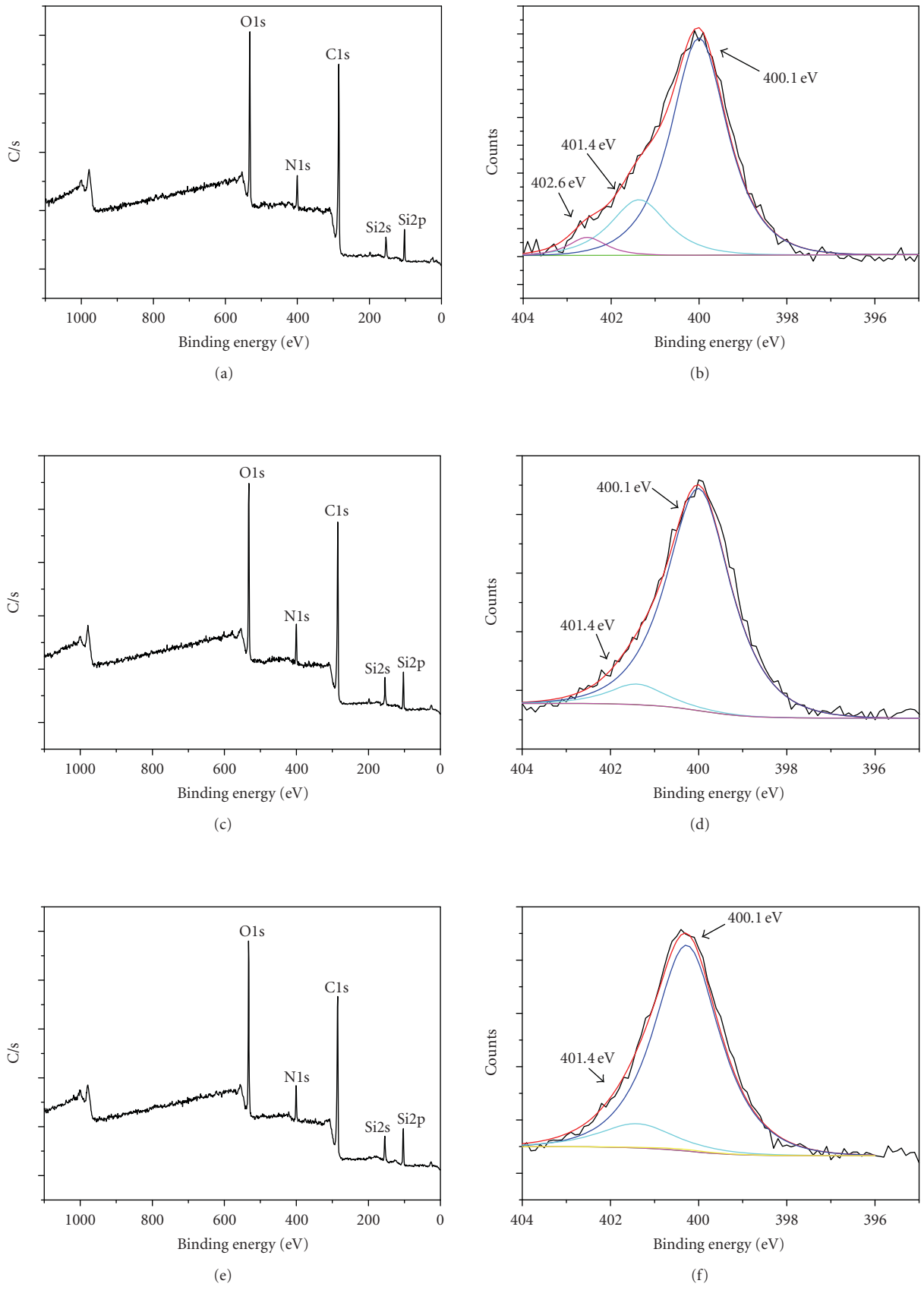


Figure 2: X-ray photoelectron spectroscopy (XPS) spectra of (a, b) APTES-MWCNT-1, (c, d) APTES-MWCNT-2, and (e, f) APTES-MWCNT-3.

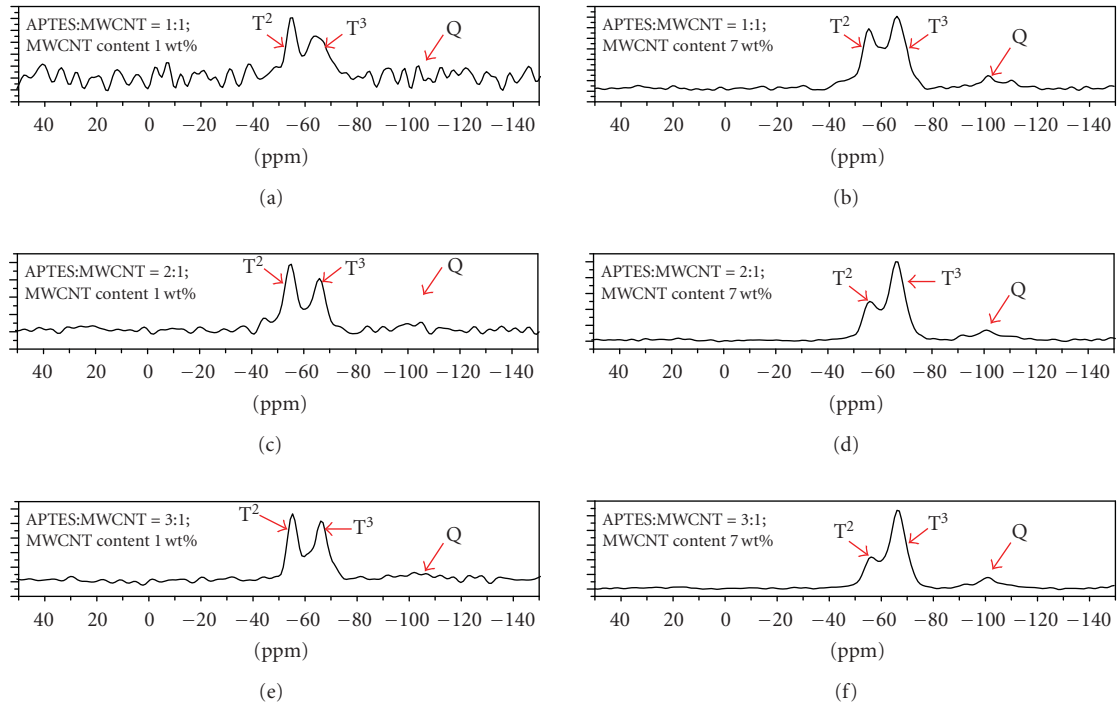


Figure 3: $^{29}$Si solid-state NMR spectra of cured APTES-MWCNT/polyimide composites.

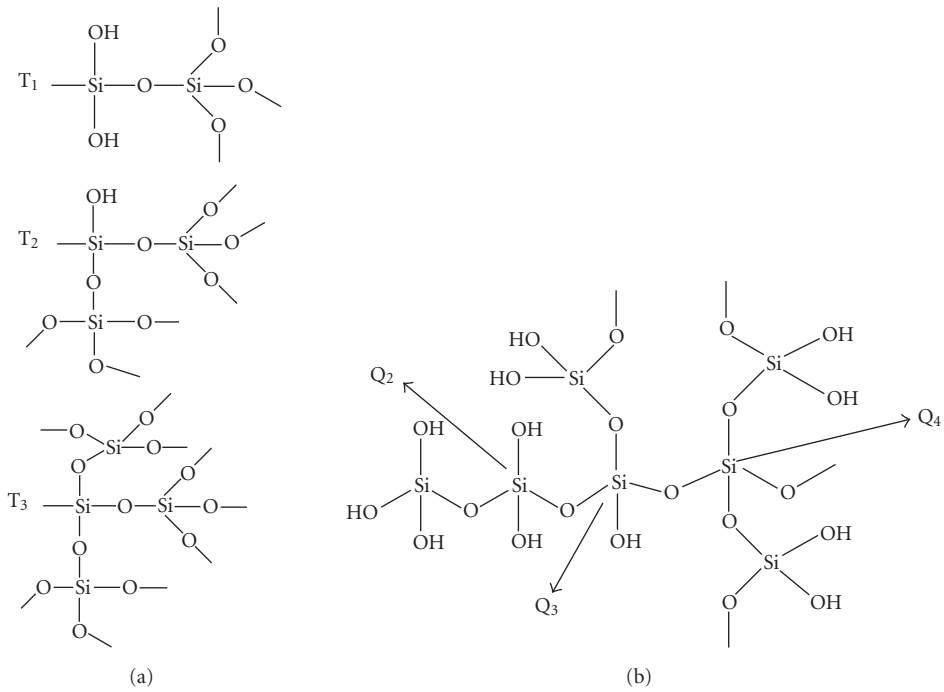


Figure 4: Structure of (a) trisubstituted siloxane bonds (T shift) [27] and (b) tetrasubstituted siloxane bonds (Q shift) [27].

not easily form an interpenetrating network. The TEM microphotograph shows that concentrations were different even with the same content (7.0 wt%) APTES-MWCNT. APTES-MWCNT-3 show less concentrated than that of APTES-MWCNT-1 and APTES-MWCNT-2 in polyimide matrix with 7.0 wt% MWCNT content. APTES-MWCNT-1 and APTES-MWCNT-2 show similar concentration in polyimide matrix with 7.0 wt% MWCNT content. However, the lengths of the assembled MWCNT were different. Assembled APTES-MWCNT-3 is longer than that of

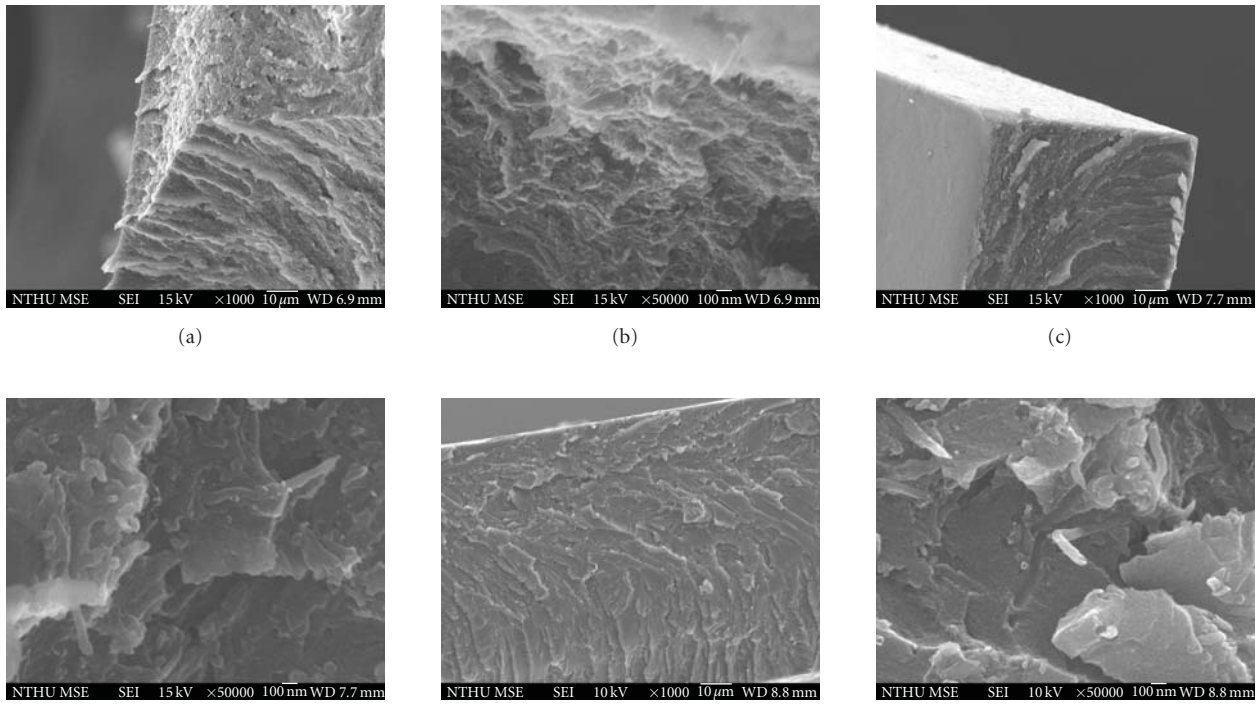


Figure 5: SEM microphotograph of 7.0 wt% APTES-MWCNT/polyimide composites: (a) APTES-MWCNT-1 (×1000), (b) APTES-MWCNT-1 (×50 000), (c) APTES-MWCNT-2 (×1000), (d) APTES-MWCNT-2 (×50 000), (e) APTES-MWCNT-3 (×1000), and (f) APTES-MWCNT-3 (×50 000).

APTES-MWCNT-2 and APTES-MWCNT-1 in the polyimide matrix. APTES-MWCNT-3 was connected with "head-to-tail" and the APTES-MWCNT-3 assembled to long, thin "needle shaped." The quantity of MWCNT of 7.0 wt% APTES-MWCNT-3 in polyimide matrix was similar to the 7.0 wt% APTES-MWCNT-2 and APTES-MWCNT-1.

### 3.5. Electrical properties

CNTs have a high aspect ratio and contain numerous $\pi$-bonds (C=C bond). Electrical charges may be transferred through the $\pi$-bond (C=C bond) of CNTs. Adding a small quantity of CNT to the polymer matrix substantially reduces the surface and volume electrical resistivities of the matrix.

Figures 7(a) and 7(b) plot the surface and volume electrical resistivities of the APTES-MWCNT/polyimide composites. The surface resistivities were summarized in Table 3 and the volume resistivities were summarized in Table 4. When unmodified and acid-modified MWCNT were utilized, the surface electrical resistivity of the composites decreased from $1.28 \times 10^{15}\ \Omega/\text{cm}^2$ (neat polyimide) to $7.59 \times 10^{6}\ \Omega/\text{cm}^2$ (a decrease of nine orders of magnitude with 7.0 wt% unmodified MWCNT) and to $2.53 \times 10^{9}\ \Omega/\text{cm}^2$ (a decrease of six orders of magnitude with 7.0 wt% acid-modified CNT) (Figure 7(a)). The volume electrical resistivity of the composites decreased from $1.53 \times 10^{17}\ \Omega\text{cm}$ (neat polyimide) to $4.09 \times 10^{4}\ \Omega\text{cm}$ (a decrease of 13 orders of magnitude with 7.0 wt% unmodified MWCNT), and $2.66 \times 10^{8}\ \Omega\text{cm}$ (a decrease in nine order of magnitude with 7.0 wt% acid-modified CNT), (Figure 7(b)). In the APTES-MWCNT system, the surface electrical resistivity of the composites decreased by five orders of magnitude from $1.28 \times 10^{15}\ \Omega/\text{cm}^2$ (neat polyimide) to $8.64 \times 10^{10}\ \Omega/\text{cm}^2$ (for 7.0 wt% APTES-MWCNT-1/polyimde composites), by four orders of magnitude to $8.58 \times 10^{11}\ \Omega/\text{cm}^2$ (with 7.0 wt% APTES-MWCNT-2/polyimide composites), and by four orders of magnitude to $4.53 \times 10^{11}\ \Omega/\text{cm}^2$ (with 7.0 wt% APTES-MWCNT-3/polyimide composites) (Figure 7(a)). The volume electrical resistivity of the composites decreased by four orders of magnitude from $1.53 \times 10^{17}\ \Omega\text{cm}$ (neat polyimide) to $5.07 \times 10^{11}\ \Omega\text{cm}$ (with 7.0 wt% APTES-MWCNT-1/polyimide composites), by eight orders of magnitude to $1.68 \times 10^{9}\ \Omega\text{cm}$ (with 7.0 wt% APTES-MWCNT-2/polyimide composites), and by seven orders of magnitude to $2.90 \times 10^{10}\ \Omega\text{cm}$ (7.0 wt% APTES-MWCNT-3/polyimide composites) (Figure 7(b)).

Acid-modified MWCNTs and APTES-MWCNTs provide less improved surface and volume electricity conductivities than unmodified MWCNTs over MWCNT/polyimide nanocomposites. The MWCNTs may be shortened and the number of defects increased during acid modification. Our previous study revealed that unmodified MWCNTs were aggregated, but acid-modified MWCNT were dispersed in the polyimide matrix [17]. The aggregated MWCNTs may connect to each other and more easily form charge-conducting pathways. The model of the

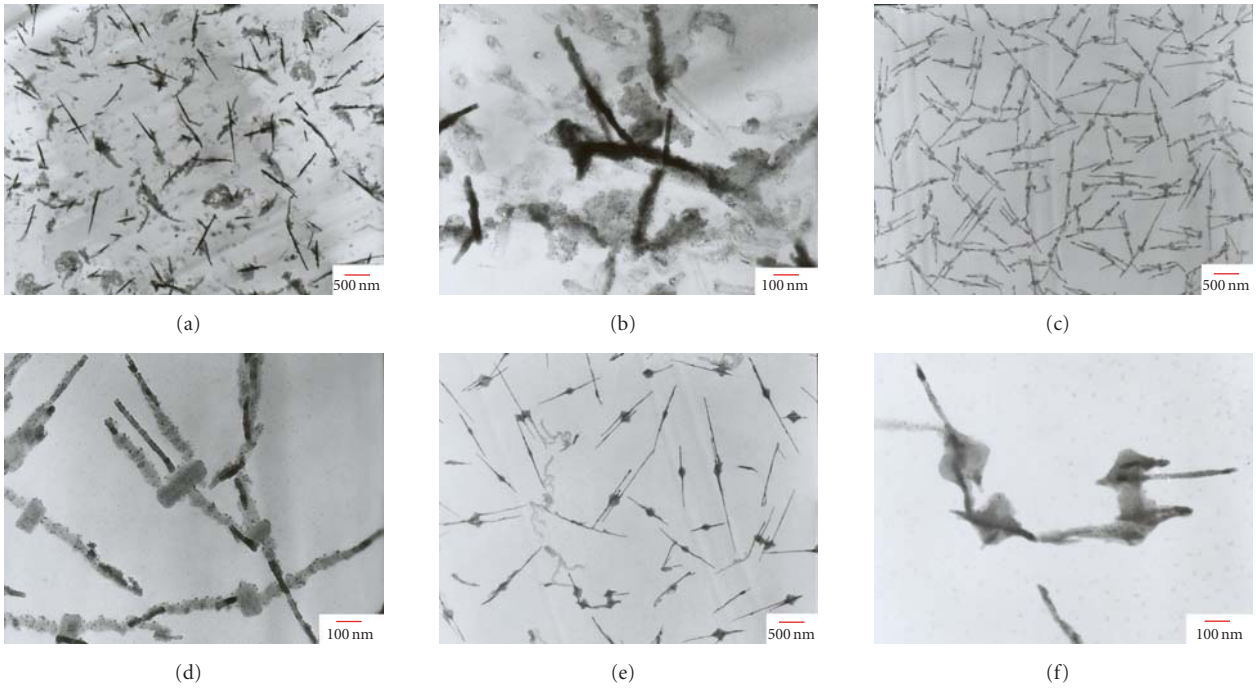


FIGURE 6: TEM microphotograph of 7.0 wt% APTES-MWCNT/polyimide composites APTES-MWCNT-1 (a) ×10 000, (b) ×50 000 APTES-MWCNT-2, (c) ×10 000, (d) ×50 000 APTES-MWCNT-3, (e) ×10 000, (f) ×50 000.

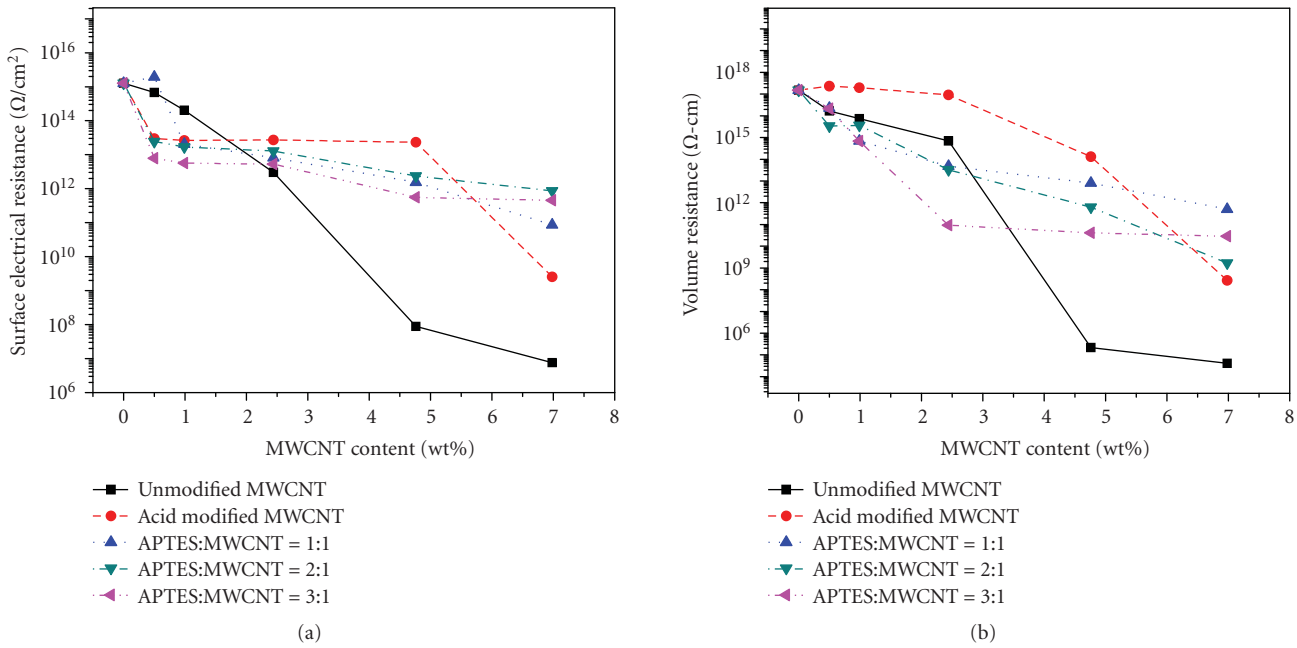


FIGURE 7: Electrical resisitivity of MWCNT/polyimide composites: (a) surface resistance and (b) volume resistance.

aggregated unmodified MWCNT is similar to that presented in Figure 8(a) and the electrical charge conducting model of the small amount of dispersed acid-modified MWCNT is similar to that shown in Figure 8(b). Figure 7(b) reveals that the APTES-MWCNT/polyimide composites have a lower percolation threshold (1.0 wt% for APTES-MWCNT-1 and APTES-MWCNT-2 and 2.4 wt% for APTES-MWCNT-3) than that of the unmodified MWCNT/polyimide (4.76 wt%) or acid-modified MWCNT/polyimide (more than 6.98 wt%). APTES-MWCNT-3 has a higher percolation threshold than APTES-MWCNT-1 and APTES-MWCNT-2 in the polyimide matrix, perhaps because

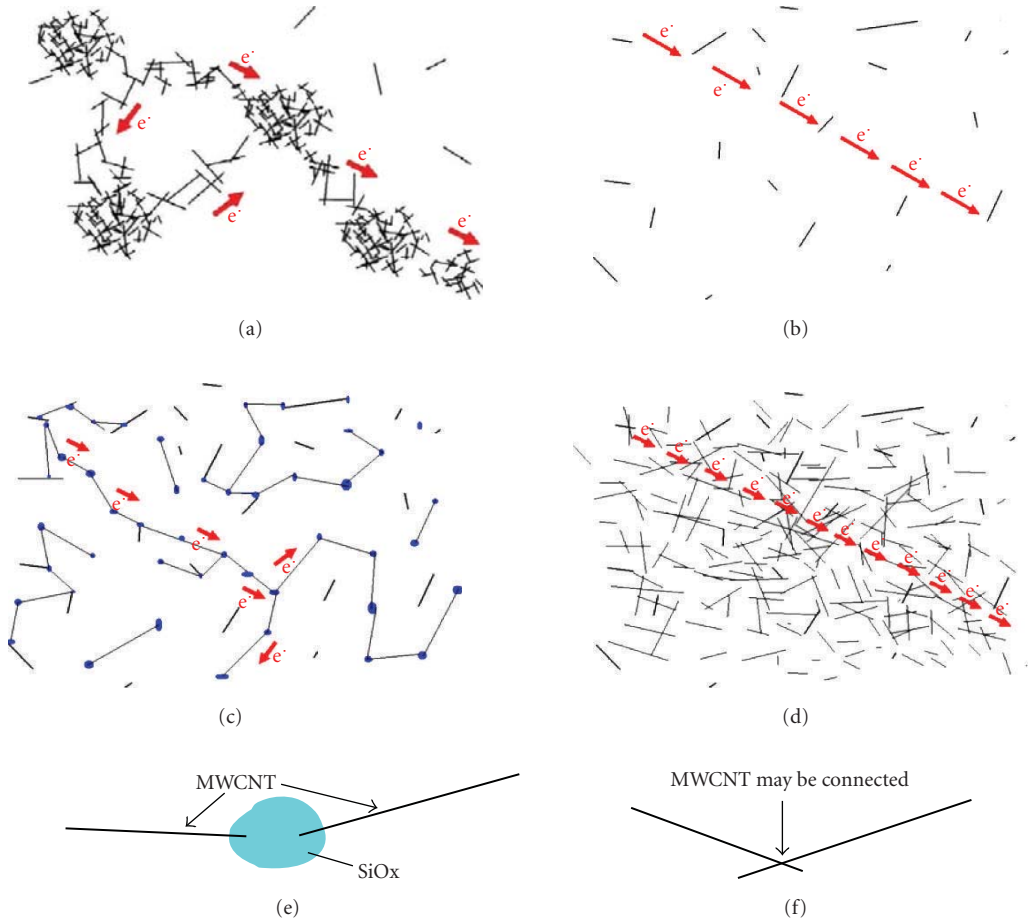


Figure 8: Diagram of electrical charge transfer on (a) aggregated conductivity material, (b) small amount of dispersed conductivity material, (c) conductivity material connect each other, (d) large amount of dispersed conductivity material, (e) Junction of connected APTES-MWCNT, (f) Junction of connected unmodified or acid-modified MWCNT over percolation threshold.

Table 4: Volume electrical resistivity of MWCNT/polyimide composites.

| MWCNT content | Volume electrical resistivity of unmodified MWCNT/PI, Ω-cm | Volume electrical resistivity of acid-modified MWCNT/PI, Ω-cm | Volume electrical resistivity of APTES-MWCNT-1/PI, Ω-cm | Volume electrical resistivity of APTES-MWCNT-2/PI, Ω-cm | Volume electrical resistivity of APTES-MWCNT-3/PI, Ω-cm |
|---|---|---|---|---|---|
| 0 | $1.53 \times 10^{17}$ | $1.53 \times 10^{17}$ | $1.53 \times 10^{17}$ | $1.53 \times 10^{17}$ | $1.53 \times 10^{17}$ |
| 0.5 | $1.69 \times 10^{16}$ | $2.33 \times 10^{17}$ | $2.30 \times 10^{16}$ | $3.37 \times 10^{15}$ | $2.13 \times 10^{16}$ |
| 1.0 | $7.52 \times 10^{15}$ | $1.95 \times 10^{17}$ | $6.94 \times 10^{14}$ | $3.61 \times 10^{15}$ | $6.90 \times 10^{14}$ |
| 2.4 | $7.08 \times 10^{14}$ | $9.25 \times 10^{16}$ | $4.82 \times 10^{13}$ | $3.27 \times 10^{13}$ | $9.24 \times 10^{10}$ |
| 4.8 | $219 \times 10^{5}$ | $1.33 \times 10^{14}$ | $8.11 \times 10^{12}$ | $6.19 \times 10^{11}$ | $4.07 \times 10^{10}$ |
| 7.0 | $409 \times 10^{4}$ | $2.66 \times 10^{8}$ | $5.07 \times 10^{11}$ | $1.68 \times 10^{9}$ | $2.90 \times 10^{10}$ |

APTES-MWCNT-3 cannot form an interpenetrating network easier than APTES-MWCNT-1 and APTES-MWCNT-2 can.

When the MWCNT content is high (7.0 wt%), the volume electrical resistivities of APTES-MWCNT/polyimide composites exceed those of unmodified and acid-modified MWCNT/polyimide composites. Figures 7(a) and 7(b) show that when the MWCNT content was lower than 7.0 wt%, APTES-MWCNT/polyimide composites had a lower surface and volume electrical resistivity than those of acid-modified MWCNT/polyimide composites. The electrical charge transfer model of the APTES-MWCNT in polyimide matrix is similar to that presented in Figure 8(c). The TEM microphotograph indicates that some of the APTES-MWCNTs are connected to each other in the polyimide matrix and the charge transfer pathways may be more effective than

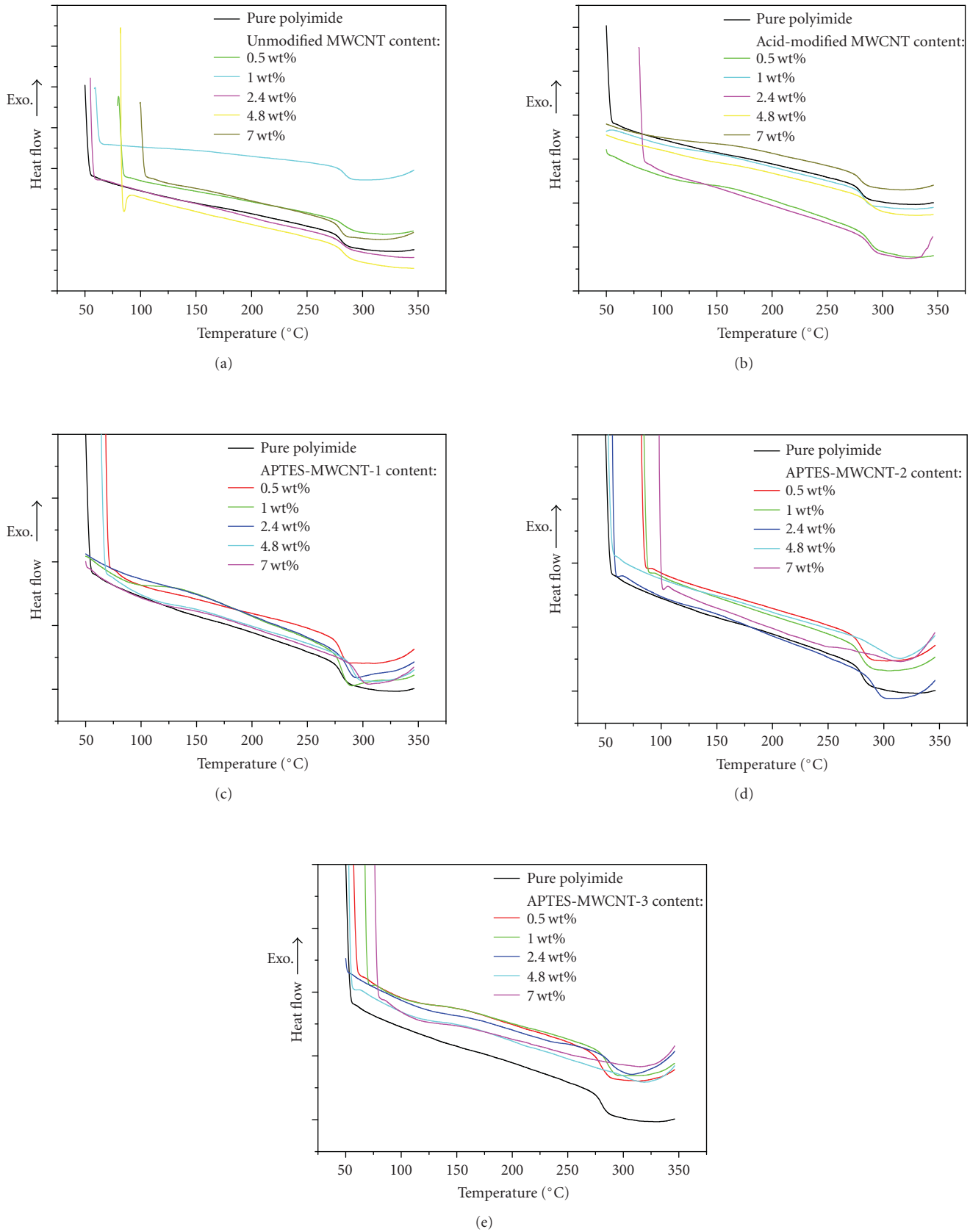


Figure 9: DSC data of the MWCNTs/polyimide composites: (a) unmodified MWCNT, (b) acid-modified MWCNT, (c) APTES-MWCNT-1, (d) APTES-MWCNT-2, (e) APTES-MWCNT-3.

Table 5: Tg of MWCNT/polyimide composites.

| MWCNT content | Tg of unmodified MWCNT/PI, °C | Tg of acid-modified MWCNT/PI, °C | Tg of APTES-MWCNT-1/PI, °C | Tg of APTES-MWCNT-2/PI, °C | Tg of APTES-MWCNT-3/PI, °C |
|---|---|---|---|---|---|
| 0 | 281.1 | 281.1 | 281.1 | 281.1 | 281.1 |
| 0.5 | 280.2 | 281.8 | 280.5 | 279.9 | 279.0 |
| 1.0 | 278.6 | 284.8 | 280.6 | 279.9 | 285.7 |
| 2.4 | 278.7 | 285.3 | 285.7 | 290.7 | 288.5 |
| 4.8 | 278.4 | 285.2 | 290.8 | 293.9 | 303.7 |
| 7.0 | 276.5 | 288.4 | 295.2 | 294.9 | — |

Table 6: Tensile strength of MWCNT/polyimide composites.

| MWCNT content | Tensile strength of unmodified MWCNT/PI, MPa | Tensile strength of acid-modified MWCNT/PI, MPa | Tensile strength of APTES-MWCNT-1/PI, MPa | Tensile strength of APTES-MWCNT-2/PI, MPa | Tensile strength of APTES-MWCNT-3/PI, MPa |
|---|---|---|---|---|---|
| 0 | 101.71 ± 5.10 | 101.71 ± 5.10 | 101.71 ± 5.10 | 101.71 ± 5.10 | 101.71 ± 5.10 |
| 0.5 | 107.37 ± 5.66 | 106.91 ± 7.24 | 121.53 ± 5.21 | 125.55 ± 5.12 | 125.00 ± 8.25 |
| 1.0 | 110.67 ± 5.66 | 110.02 ± 5.23 | 126.49 ± 9.68 | 126.66 ± 9.96 | 128.03 ± 6.32 |
| 2.4 | 111.56 ± 10.00 | 115.44 ± 7.46 | 126.03 ± 7.34 | 116.90 ± 6.00 | 117.44 ± 8.46 |
| 4.8 | 118.11 ± 6.11 | 129.42 ± 6.63 | 101.01 ± 8.50 | 106.91 ± 5.02 | 109.64 ± 7.40 |
| 7.0 | 120.87 ± 10.834 | 133.84 ± 5.37 | 104.24 ± 9.07 | 82.39 ± 4.24 | Too brittle |

those of unmodified and acid-modified MWCNT. When the MWCNT content is higher than 7.0 wt%, the charge transfer pathway may be formed (Figure 8(d)) in acid-modified MWCNT polyimide composites. Some of the APTESs were not bonded with the acid-modified MWCNT, which may bond to the polyamic acid and form a complex [1, 28]. Furthermore, as presented in Figure 8(e), although the APTES-MWCNTs connected with each other in the polyimide matrix, the MWCNTs were separated by SiOx. When the unmodified and acid-modified MWCNT contents were very high, the MWCNTs may be interconnected (Figure 8(f)). The results show that when the MWCNT content exceeds 7.0 wt%, APTES-MWCNT/polyimide composites have a higher surface and volume electrical resistivity than those of acid-modified MWCNT/polyimide composites.

### 3.6. Glass transition temperature (Tg)

The glass transition temperatures (Tgs) of the polymer matrix depend on the free volume of the polymer, which is related to the affinity between the filler and the polymer matrix. A polymer with a lower free volume generally has a higher Tg. A polymer matrix with a higher affinity to filler exhibited less polymer molecular motion and reduced the free volume of the polymer molecules [32, 33]. The −COOH functional groups on the acid-modified MWCNT surface can form hydrogen bonds with the imide functional groups of the polyimide, reducing the free volume of the polymer. When the APTES-MWCNT/polyamic acid was heated to 300°C, the silane molecules on the MWCNT surface reacted and connected with each other. The free volume of the polymer is reduced and molecular motion is restricted.

Figure 9 shows the DSC data of the MWCNT/polyimide composites. The glass transition temperatures (Tgs) of the MWCNT/polyimide composites were summarized in Table 5. When 1.0 wt% unmodified MWCNT was added to the matrix, Tg decreased slightly. The Tg of 1.0 wt% unmodified MWCNT/polyimide is 279°C. When the unmodified MWCNT content was 7.0 wt%, Tg decreased to 277°C. The affinity between the unmodified MWCNT and the polyimide was poor, so the free volume of the composites increased and Tg decreased. The glass transition temperature (Tg) of the pristine polyimide was 280.44°C. When acid-modified MWCNTs were utilized, the Tg of the MWCNT/polyimide composites increased slightly to 287.45°C (2.4 wt% acid-modified MWCNT/polyimide composites). When the acidmodified MWCNT content was 7.0 wt%, Tg decreased slightly to 284.09°C. When the APTES-MWCNT content was high, Tg increased significantly. The Tg of the APTES-MWCNT/polyimide composites increased to 295.22°C (7.0 wt% APTES-MWCNT-1/polyimide composites), 294.88°C (7.0 wt% APTES-MWCNT-2/polyimide composites), and to 303.69°C (4.8 wt% APTES-MWCNT-3/polyimide composites). The results show that Tg increased with the ratio of APTES to MWCNT, since silane may restrict the molecular motion of the polyimide matrix.

### 3.7. Tensile properties

The mechanical properties of MWCNT/polymer composites depend on the affinity of the MWCNTs to the polymer matrix. Since modified MWCNTs have a greater affinity to the polymer matrix than that of unmodified MWCNT*s*, modified MWCNTs improve the tensile properties of the polyimide significantly. Hydrogen atoms at the −COOH groups of acid-modified MWCNTs may form hydrogen bonds with the C=O bonds of the PI molecules [31, 32].

Table 7: Young's modulus of MWCNT/polyimide composites.

| MWCNT content | Young's modulus of unmodified MWCNT/PI, GPa | Young's modulus of acid-modified MWCNT/PI, GPa | Young's modulus of APTES-MWCNT-1/PI, GPa | Young's modulus of APTES-MWCNT-2/PI, GPa | Young's modulus of APTES-MWCNT-3/PI, GPa |
|---|---|---|---|---|---|
| 0 | 2.34 ± 0.12 | 2.34 ± 0.12 | 2.34 ± 0.12 | 2.34 ± 0.12 | 2.34 ± 0.12 |
| 0.5 | 2.41 ± 0.29 | 3.08 ± 0.23 | 3.71 ± 0.24 | 3.95 ± 0.25 | 3.45 ± 0.18 |
| 1.0 | 2.52 ± 0.12 | 3.20 ± 0.25 | 3.81 ± 0.19 | 4.04 ± 0.22 | 3.52 ± 0.21 |
| 2.4 | 3.05 ± 0.12 | 3.68 ± 0.11 | 3.75 ± 0.25 | 3.74 ± 0.22 | 3.48 ± 0.28 |
| 4.8 | 3.15 ± 0.18 | 3.60 ± 0.25 | 3.49 ± 0.18 | 3.62 ± 0.12 | 3.48 ± 0.30 |
| 7.0 | 3.19 ± 0.15 | 3.66 ± 0.29 | 3.54 ± 0.19 | 3.17 ± 0.21 | Too brittle |

Tables 6 and 7 exhibit the tensile properties of the MWCNT/polyimide composites. The tensile strength of neat polyimide is 101.71 MPa. The APTES-MWCNT/polyimide exhibits a maximum tensile strength at the MWCNT content of 1.0 wt%. When 1.0 wt% APTES-MWCNT was employed, the tensile strength increased to 126.49 MPa (increased 24.36%) (APTES-MWCNT-1), to 126.66 MPa (increased 24.53%) (APTES-MWCNT-2), and to 128.03 MPa (increased 25.88%) (APTES-MWCNT-3) (Table 6). However, if the MWCNT content exceeds 1.0 wt%, the tensile strength declines. Table 7 shows the Young's modulus of the APTES-MWCNT/polyimide composites. The Young's modulus of neat polyimide was 2.34 GPa. When 1.0 wt% acid-modified MWCNT was used, the Young's modulus increased to 3.68 GPa (increased 57.73%). When 1.0 wt% APTES-MWCNT was used, the Young's modulus increased to 3.81 GPa (increase 62.82%) (APTES-MWCNT-1), to 4.04 GPa (increase 71.79%) (APTES-MWCNT-2), and to 3.51 GPa (increase 50.00%) (APTES-MWCNT-3) (Table 7). When the APTES-MWCNT (APTES-MWCNT-1 and APTES-MWCNT-2) content exceeds 1.0 wt%, the Young's modulus decreased. When the APTES-MWCNT-1 and APTES-MWCNT-2 contents were 7.0 wt%, Young's modulus decreased to 3.54 GPa (APTES-MWCNT-1) and 3.17 GPa (APTES-MWCNT-2). When the APTES-MWCNT-3 contents were 4.8 wt%, Young's modulus increased to 3.48 GPa.

TEM microphotograph shows that some of the APTES-MWCNTs were connected together in the polyimide matrix. MWCNT network may be formed in the polyimide matrix. When MWCNTs networks were formed in the polyimide matrix, it can be improve the tensile strength more significantly than that of acid-modified MWCNT. Tai et al. [36] reported that the network MWCNT improved the mechanical properties significantly more than that of dispersed MWCNT. They proposed that the lengths of MWCNTs in network were longer [33]. When APTES-MWCNT content was higher than 2.4 wt%, the composites possess lower tensile strength and Young's modulus decreased slightly. The composites became brittle when APTES-MWCNT content is high.

## 4. CONCLUSION

Aminosilane-modified MWCNT/polyimide nanocomposites have been prepared. $^{29}$Si solid state NMR demonstrates that T substituted and Q substituted siloxane bonds are present in APTES-MWCNT/polyimide composites. A TEM microphotograph shows that MWCNTs may connect to each other in the polyimide matrix, MWCNT network, and that polyimide molecules may interpenetrate the crosslinked MWCNT network.

The surface and volume electrical resistivity of the APTES-MWCNT/polyimide composites decreased more significantly than that of acid-modified MWCNT/polyimide composites when the APTES-MWCNTs content was lower than 4.8 wt%, the percolation threshold of the APTES-MWCNT/polyimide composites was lower than that of the unmodified and acid-modified MWCNT/polyimide composites. The surface electrical resistivity of the polyimide decreased from $1.28 \times 10^{15}\ \Omega/\text{cm}^2$ (neat polyimide) to $2.73 \times 10^{13}\ \Omega-\text{cm}$ (2.4 wt% acid modified MWCNT) and $8.07 \times 10^{12}\ \Omega-\text{cm}$ (2.4 wt% APTES-MWCNT-1). The volume electrical resistivity of the polyimide decreased from $1.53 \times 10^{17}\ \Omega\text{cm}$ (neat polyimide) to $9.25 \times 10^{16}\ \Omega\text{cm}$ (2.4 wt% acid modified MWCNT) and $9.23 \times 10^{10}\ \Omega\text{cm}$ (2.4 wt% APTES-MWCNT-2). The percolation thresholds of the unmodified MWCNT/polyimde, acid-modified MWCNT/polyimide, APTES- MWCNT-1/polyimide, APTES-MWCNT-2/polyimide, and APTES-MWCNT-3/polyimide were 4.76 wt%, more than 7.0 wt%, 1.0 wt%, 1.0 wt%, and 2.4 wt%, respectively.

The glass transition temperature (Tg) of the APTES-MWCNT/polyimide composites increased more than those of unmodified and acid-modified MWCNT/polyimide composites. The Tg of polyimide increased from 281.1°C (neat polyimide) to 303.7°C (4.8 wt% APTES-MWCNT-3).

Tensile strength of MWCNT/polyimide increase form 101.71 MPa (neat polyimide) to 120.87 MPa (7.0 wt% unmodified MWCNT, increased 18.8%), 132.87 MPa (7.0 wt% acid modified MWCNT, increased 30.6%), 126.49 MPa (1.0 wt% APTES-MWCNT-1, increased 24.4%), 126.66 MPa (1.0 wt% APTES-MWCNT-2 increased, 24.5%), and 128.03 MPa (1.0 wt% APTES-MWCNT-3, increased 25.9%)

## ACKNOWLEDGMENTS

The authors would like to acknowledge the National Science Council of Taiwan for the financial support under Contract no. NSC 95-2221-E-007-081.

## REFERENCES


[1] D. Wilson, H. D. Stenzenberger, and P. M. Hergenrother, *Polyimides*, Chapman & Hall, New York, NY, USA, 1990.

[2] S. Iijima, "Helical microtubules of graphitic carbon," *Nature*, vol. 354, no. 6348, pp. 56–58, 1991.

[3] J. Sandler, M. S. P. Shaffer, T. Prasse, W. Bauhofer, K. Schulte, and A. H. Windle, "Development of a dispersion process for carbon nanotubes in an epoxy matrix and the resulting electrical properties," *Polymer*, vol. 40, no. 21, pp. 5967–5971, 1999.

[4] H. Geng, R. Rosen, B. Zheng, et al., "Fabrication and properties of composites of poly(ethylene oxide) and functionalized carbon nanotubes," *Advanced Materials*, vol. 14, no. 19, pp. 1387–1390, 2002.

[5] M. S. Dresselhaus, G. Dresselhaus, and P. C. Eklund, *Science of Fullerenes and Carbon Nanotubes*, Academic Press, San Diego, Calif, USA, 1996.

[6] F. Béguin and P. Ehrburger, "Special issue on carbon nanotubes," *Carbon*, vol. 40, no. 10, p. 1619, 2002.

[7] S. Subramoney, "Novel nanocarbons—structure, properties, and potential applications," *Advanced Materials*, vol. 10, no. 15, pp. 1157–1171, 1998.

[8] B. I. Yakobson and R. E. Smalley, "Fullerene nanotubes: C1,000,000 and beyond," *American Scientist*, vol. 85, no. 4, pp. 324–337, 1997.

[9] T. McNally, P. Pötschke, P. Halley, et al., "Polyethylene multiwalled carbon nanotube composites," *Polymer*, vol. 46, no. 19, pp. 8222–8232, 2005.

[10] W. Tang, M. H. Santare, and S. G. Advani, "Melt processing and mechanical property characterization of multi-walled carbon nanotube/high density polyethylene (MWNT/HDPE) composite films," *Carbon*, vol. 41, no. 14, pp. 2779–2785, 2003.

[11] M.-K. Seo, J.-R. Lee, and S.-J. Park, "Crystallization kinetics and interfacial behaviors of polypropylene composites reinforced with multi-walled carbon nanotubes," *Materials Science and Engineering A*, vol. 404, no. 1-2, pp. 79–84, 2005.

[12] Z. Yang, B. Dong, Y. Huang, L. Liu, F.-Y. Yan, and H.-L. Li, "A study on carbon nanotubes reinforced poly(methyl methacrylate) nanocomposites," *Materials Letters*, vol. 59, no. 17, pp. 2128–2132, 2005.

[13] H. Zeng, C. Gao, Y. Wang, et al., "In situ polymerization approach to multiwalled carbon nanotubes-reinforced nylon 1010 composites: mechanical properties and crystallization behavior," *Polymer*, vol. 47, no. 1, pp. 113–122, 2006.

[14] A. Yu, H. Hu, E. Bekyarova, et al., "Incorporation of highly dispersed single-walled carbon nanotubes in a polyimide matrix," *Composites Science and Technology*, vol. 66, no. 9, pp. 1190–1197, 2006.

[15] D. M. Delozier, K. A. Watson, J. G. Smith Jr., T. C. Clancy, and J. W. Connell, "Investigation of aromatic/aliphatic polyimides as dispersants for single wall carbon nanotubes," *Macromolecules*, vol. 39, no. 5, pp. 1731–1739, 2006.

[16] B.-K. Zhu, S.-H. Xie, Z.-K. Xu, and Y.-Y. Xu, "Preparation and properties of the polyimide/multi-walled carbon nanotubes (MWNTs) nanocomposites," *Composites Science and Technology*, vol. 66, no. 3-4, pp. 548–554, 2006.

[17] S.-M. Yuen, C.-C. M. Ma, Y.-Y. Lin, and H.-C. Kuan, "Preparation, morphology and properties of acid and amine modified multiwalled carbon nanotube/polyimide composite," *Composites Science and Technology*, vol. 67, no. 11-12, pp. 2564–2573, 2007.

[18] A. Hirsch, "Functionalization of single-walled carbon nanotubes," *Angewandte Chemie International Edition*, vol. 41, no. 11, pp. 1853–1859, 2002.

[19] C. Velasco-Santos, A. L. Martínez-Hernández, M. Lozada-Cassou, A. Alvarez-Castillo, and V. M. Castaño, "Chemical functionalization of carbon nanotubes through an organosilane," *Nanotechnology*, vol. 13, no. 4, pp. 495–498, 2002.

[20] A. M. Shanmugharaj, J. H. Bae, K. Y. Lee, W. H. Noh, S. H. Lee, and S. H. Ryu, "Physical and chemical characteristics of multiwalled carbon nanotubes functionalized with aminosilane and its influence on the properties of natural rubber composites," *Composites Science and Technology*, vol. 67, no. 9, pp. 1813–1822, 2007.

[21] P. C. Ma, J.-K. Kim, and B. Z. Tang, "Functionalization of carbon nanotubes using a silane coupling agent," *Carbon*, vol. 44, no. 15, pp. 3232–3238, 2006.

[22] L. Vast, G. Philippin, A. Destrée, et al., "Chemical functionalization by a fluorinated trichlorosilane of multi-walled carbon nanotubes," *Nanotechnology*, vol. 15, no. 7, pp. 781–785, 2004.

[23] L. Valentini, J. Macan, I. Armentano, F. Mengoni, and J. M. Kenny, "Modification of fluorinated single-walled carbon nanotubes with aminosilane molecules," *Carbon*, vol. 44, no. 11, pp. 2196–2201, 2006.

[24] H.-L. Wu, C.-C. M. Ma, Y.-T. Yang, H.-C. Kuan, C.-C. Yang, and C.-L. Chiang, "Morphology, electrical resistance, electromagnetic interference shielding and mechanical properties of functionalized MWNT and poly(urea urethane) nanocomposites," *Journal of Polymer Science Part B*, vol. 44, no. 7, pp. 1096–1105, 2006.

[25] C.-F. Kuan, H.-C. Kuan, C.-C. M. Ma, C.-H. Chen, and H.-L. Wu, "The preparation of carbon nanotube/linear low density polyethylene composites by a water-crosslinking reaction," *Materials Letters*, vol. 61, no. 13, pp. 2744–2748, 2007.

[26] H.-L. Wu, Y.-T. Yang, C.-C. M. Ma, and H.-C. Kuan, "Molecular mobility of free-radical-functionalized carbon-nanotube/siloxane/poly(urea urethane) nanocomposites," *Journal of Polymer Science Part A*, vol. 43, no. 23, pp. 6084–6094, 2005.

[27] K. J. Shea, D. A. Loy, and O. Webster, "Arylsilsesquioxane gel and related materials. New hybrids of organic and inorganic networks," *Journal of the American Chemical Society*, vol. 114, no. 17, pp. 6700–6710, 1992.

[28] K. L. Mittal, *Polyimides: Synthesis, Characterization, and Applications*, Plenum Press, New York, NY, USA, 1984.

[29] Y. J. Kim, T. S. Shin, H. D. Choi, J. H. Kwon, Y.-C. Chung, and H. G. Yoon, "Electrical conductivity of chemically modified multiwalled carbon nanotube/epoxy composites," *Carbon*, vol. 43, no. 1, pp. 23–30, 2005.

[30] D. Stauffer, *Introduction to the Percolation Theory*, Francis & Taylor, London, UK, 1991.

[31] G. Hu, C. Zhao, S. Zhang, M. Yang, and Z. Wang, "Low percolation thresholds of electrical conductivity and rheology in poly(ethylene terephthalate) through the networks of multi-walled carbon nanotubes," *Polymer*, vol. 47, no. 1, pp. 480–488, 2006.

[32] M. I. Chipara, "The glass transition phenomenon in macromolecular systems," *Physica B*, vol. 234–236, pp. 263–265, 1997.

[33] L. H. Sperling, *Introduction to Physical Polymer Science*, Wiley-Interscience, New York, NY, USA, 3rd edition, 2001.

[34] R. A. Nyquist, C. L. Putzig, T. L. Clark, and A. T. McDonald, "Infrared study of intramolecularly hydrogen bonded aromatic carbonyl containing compounds in various solvents," *Vibrational Spectroscopy*, vol. 12, no. 1, pp. 93–102, 1996.

[35] V. Gutmann, *The Donor-Acceptor Approach to Molecular Interactions*, Plenum Press, New York, NY, USA, 1978.

[36] N.-H. Tai, M.-K. Yeh, and J.-H. Liu, "Enhancement of the mechanical properties of carbon nanotube/phenolic composites using a carbon nanotube network as the reinforcement," *Carbon*, vol. 42, no. 12-13, pp. 2774–2777, 2004.

Hindawi Publishing Corporation
Journal of Nanomaterials
Volume 2008, Article ID 739613, 7 pages
doi:10.1155/2008/739613

*Research Article*

# Properties Enhancement of PS Nanocomposites through the POSS Surfactants

**Huei-Kuan Fu,[1] Shiao-Wei Kuo,[2] Ding-Ru Yeh,[1] and Feng-Chih Chang[1]**

[1] *Institute of Applied Chemistry, National Chiao-Tung University, Hsinchu 300, Taiwan*
[2] *Center for Nanoscience and Nanotechnology, Department of Materials Science and Optoelectronic Engineering, National Sun Yat-Sen University, Kaohsiung, 804, Taiwan*

Correspondence should be addressed to Shiao-Wei Kuo, kuosw@faculty.nsysu.edu.tw

Received 5 August 2007; Accepted 5 February 2008

Recommended by Junlan Wang

Polyhedral oligomeric silsesquioxane (POSS)-clay hybrids of polystyrene are prepared by two organically modified clays using POSS-$NH_2$ and $C_{20}$-POSS as intercalated agents. X-ray diffraction (XRD) studies show the formation of these POSS/clay/PS nanocomposites in all cases with the disappearance of the peaks corresponding to the basal spacing of MMT. Transmission electronic microscopy (TEM) was used to investigate the morphology of these nanocomposites and indicates that these nanocomposites are composed of a random dispersion of exfoliated clay platelets throughout the PS matrix. Incorporation of these exfoliated clay platelets into the PS matrix led to effectively increase in glass transition temperature ($T_g$), thermal decomposition temperature ($T_d$), and the maximum reduction in coefficient of thermal expansion (CTE) is ca. 40% for the $C_{20}$-POSS/clay nanocomposite.



## 1. INTRODUCTION

Organic-inorganic hybrid materials are recognized as a new class of advanced material because they can be synthesized or processed using versatile approaches and own tunable properties [1, 2]. Clays have been extensively used as reinforcement agents to prepare polymer-layered silicate nanocomposites with improved thermal and mechanical properties [3–9]. The incorporation of clay into polymer matrix imparts unique physical and chemical properties was first reported by the Toyota Research Lab for Nylon 6/organoclay nanocomposites [10]. These improvements are related to the dispersion of the layered silicate in the polymer matrix. Typically, the chemical structure of montmorillonite (MMT) consists of two fused silica tetrahedral sheets sandwiching an edge-shared octahedral sheet of either magnesium or aluminum hydroxide. Generally, the naturally occurring clays are hydrophilic characters and require a modification by intercalating with amino acid, alkylammonium, or phosphonium salts to become organically compatible [11, 12]. The resulting organophilic galleries of the organically modified montmorillonite (OMMT) will enhance the compatibility with polymer [13]. Several methods to make polymer clay nanocomposites have been demonstrated, including solution mixing, melt blending, and in situ polymerization [14–16]. The interaction of layered silicates with polymers leads to two classes of hybrid materials. In the first class, denoted as intercalated hybrids, one or more polymer chains are inserted between the host layers, generating ordered lamella with the distance of a few nanometers. In the second, described as delaminated hybrids, silicate layers of 1 nm thickness are exfoliated and dispersed in the polymer matrix.

Polyhedral oligomeric silsesquioxane (POSS) reagents, monomers, and polymers are emerging as new chemical feedstocks for the preparation of organic-inorganic nanocomposites [17–21]. Silsesquioxane is the term for all structures with the formula $(RSiO_{1.5})_n$, where R is hydrogen or any alkyl, alkylene, aryl, arylene, or organic functional derivative groups. POSS compounds with diameters of 1–3 nm can be possibly considered the smallest particles of silica, but unlike silica, silicones, or fillers, POSS molecules contain either functionalized or unfunctionalized substituents at each of the corner silicon atoms. These substituents can compatibilize POSS molecules with polymers or monomers. POSS macromonomer and POSS-containing polymers inspires to prepare the functionalized POSS cages, which can be used as the intercalating agents of layered silicates to prepare the nanocomposites combining the two types of

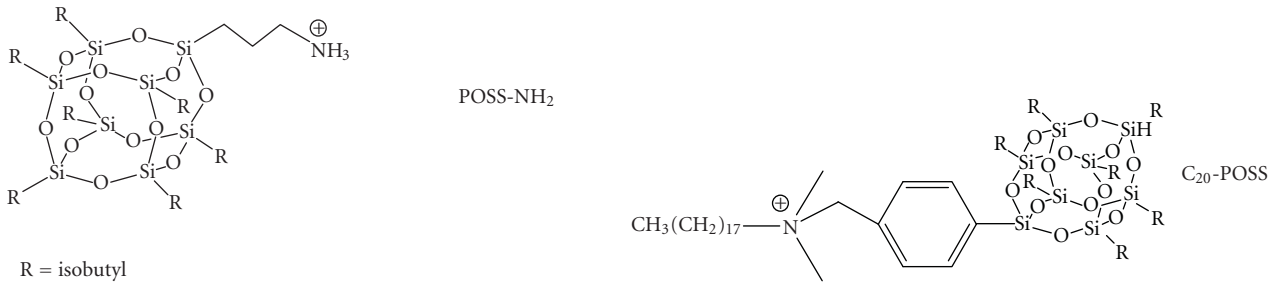


Scheme 1: Chemical structures of the intercalated agents used to prepare the modified clays.

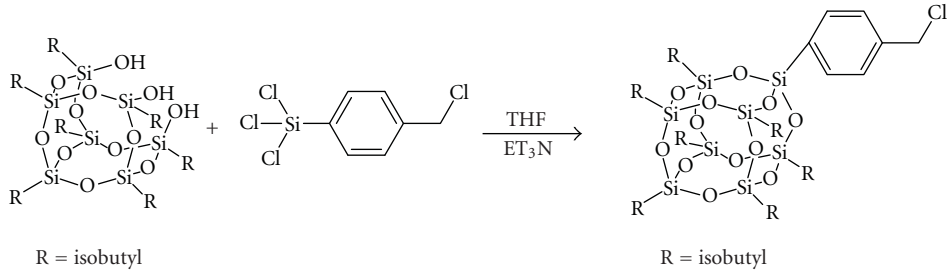


Scheme 2: Synthesis of POSS-Cl compound.

nanoreinforcement agents and improved mechanical and thermal properties.

In this study, these nanocomposites were prepared by emulsion polymerization using the POSS-$NH_2$ and $C_{20}$-POSS-treated clays as shown in Scheme 1. The morphology and the extent of delamination of the nanocomposites are elucidated using the X-ray diffraction and transmission electron microscopy. The thermal properties of these nanocomposites are characterized by thermalgravimetric analysis and differential scanning calorimetry. The coefficient of thermal expansion of virgin PS and nanocomposites are measured by thermal mechanical analyzer.

## 2. EXPERIMENTAL

### 2.1. Materials

The sodium montmorillonite ($Na^+$-MMT) with 1.45 mequiv/g cationic exchange capacity (CEC) was provided by Nanocor Co. (Ill, USA). The majority of chemicals used in this study including, acetone, methanol, tetrahydrofuran, acetonitrile, potassium hydroxide (KOH), triethylamine, and trichloro [4-(chloromethyl)phenyl] silane were acquired from Sigma-Aldrich Chemical Co., Inc. The styrene monomer was purchased from Sigma-Aldrich Chemical Co. and purified by removing the inhibitor with the aid of an inhibitor-removal column. Sodium dodecyl sulfate (SDS) and hydrochloride acid (HCl) were both obtained from Curtin Matheson Scientific, Inc. (Tex, USA). Potassium persulfate ($K_2S_2O_8$) and aluminum sulfate[$Al_2(SO_4)_3$] were acquired from Fisher Scientific, Inc. (Pittsburgh, USA). N, N-dimethyloctadecylamine ($C_{20}$) was obtained from Acros Organics, (NJ, USA). Trisilanolisobutyl polyhedral oligomeric silsesquioxane (T7-POSS) and aminopropylisobutyl polyhedral oligomeric silsesquioxane (POSS-$NH_2$) were obtained from Hybrid Plastic Corporate Headquarters Inc. (USA). All reagents, except styrene, were used as received without further purification.

### 2.2. Preparation of $C_{20}$-POSS intercalated agent

The POSS-Cl compound was prepared by the method based on Scheme 2 [22]. Trisilanolisobutyl polyhedral oligomeric silsesquioxane (3 g) and $Et_3N$ (1.26 g) were added into a 100 mL two-neck round bottom flask and stirred continuously for 3 hours under nitrogen, then 20 mL of THF was added into the flask at 0°C for 1 hour. After stirring at 0°C under nitrogen, triethylamine, and trichloro[4-(chloromethyl) phenyl]silane(1.28 g) in THF (10 mL) were added dropwisely into the solution and stirred at 0°C. The cooling bath was removed and stirred continuously for 7.5 hours under nitrogen. The POSS-Cl compound and $HNEt_3$-Cl byproduct were separated by filtration. The clear THF solution was dropped into a beaker of acetonitrile and rapidly stirred. The resulting product was collected and dried in a vacuum oven for 24 hours. $^1$H NMR (i.e., proton-NMR spectroscopy) ($CDCl_3$),$\delta$: 7.59 (d, 2H), 7.33 (d, 2H), 4.52 (s, 2H), 1.92–1.62 (m, 7H), 1.09–0.85 (m, 42H), 0.75–0.48 (m, 14H).

The intercalated agent of $C_{20}$-POSS was prepared as shown in Scheme 2. N, N-dimethyloctadecylamine ($C_{20}$, 1.49 g) and POSS-Cl compound (5.68 g) in acetone (15 mL) were refluxed 80°C under nitrogen for 24 hours. After

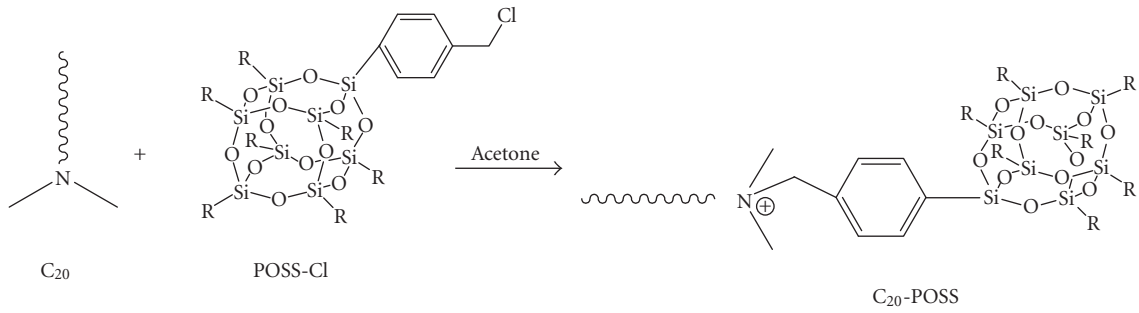


Scheme 3: Synthesis of the $C_{20}$-POSS intercalated agent.

cooling, the mixture was evaporated by a rotatory evaporator and then added $Et_2O$ (20 mL). The solution was extracted with deionized water three times (150 mL×3). The organic phase was dried with $MgSO_4$ and evaporated by arotatory evaporator to obtain the $C_{20}$-POSS intercalated agent. $^1$H NMR ($CDCl_3$), $\delta$:7.68 (d, 2H), 7.58 (d, 2H), 5.03 (s, 2H), 3.42 (t, 2H), 3.30 (s, 6H), 1.81 (m, 7H), 1.41 (m, 2H), 1.26 (m, 30H), 0.90 (m, 42H), 0.82 (t, 3H), 0.59 (m, 14H).

### 2.3. Preparation of POSS-$NH_2$ and $C_{20}$-POSS Modified Clays

$Na^+$MMT (0.3 g) in deionized water (50 mL) was stirred continuously at 80°C for 4 hours. The POSS-$NH_2$ (0.38 g) or $C_{20}$-POSS (0.63 g) in water (5 mL) was placed into another flask and then 10% hydrochloric acid (1 mL) and ethanol (5 mL) were added and stirred at 80°C for 1 hour. This intercalated solution was poured slowly into the clay suspension solution and stirred vigorously at 80°C for 4 hours. The resulting white precipitate was separated by filtration and then washed thoroughly with warm deionized water. The final product was dried in a vacuum oven at room temperature overnight.

### 2.4. Preparation of Polystyrene/Clay Nanocomposites

$Na^+$-MMT (0.3 g) was dispersed in 40 mL of deionized water and stirred at 80°C for 4 hours. Based on the CEC value (145mequiv/100g) of the $Na^+$-MMT and the Mw of the intercalated agent, the calculated weight (the weight of the intercalated agent needed to fully replace the $Na^+$ of the clay) of the intercalated agent was added and stirred for 4 hours. KOH (0.02 g), SDS (0.4 g), $K_2S_2O_8$ (0.05 g), and styrene monomer (10 g) were added into the solution. After emulsification, the dispersion was flushed with nitrogen for 30 minutes while the temperature was raised to 80°C under nitrogen protection. Polymerization was carried out at 80°C for 8 hours. After cooling, 10 mL of the 2.5% aqueous aluminum sulfate was added into the polymerized emulsion, followed by dilute hydrochloric acid (10 mL) with stirring. Finally, acetone was added to break down the emulsion completely and then the polymer product was washed several times with methanol and deionized water. The white powder was filtered and dried in a vacuum oven at 80°C for 24 hours. Similar procedures were employed to prepare the virgin polystyrene.

### 2.5. Instrumentations

#### 2.5.1. Measurement of the molecular weights characterization

Molecular weight (Mw), number-average(Mn) molecular weight, and polydispersity index (Mw/Mn) were measured using a Waters 410 gel permeation chromatography (GPC) system equipped with RI and UV detectors and a series of styragel columns (100, 500, and $10^3$ Å). The system was calibrated using polystyrene standards. These polymer chains were extracted from the clay surface using a reverse ion exchange reaction with LiCl/DMF to determine the molecular weight and molecular weight distribution.

#### 2.5.2. Structure analysis characterization

$^1$H NMR spectra were recoded in $CDCl_3$ on a Bruker AM 500 (500 MHz) spectrometer using the solvent signal as an internal standard. FT-IR spectra were recorded using a Nicolet Avatar 320 FT-IR spectrometer; 32 scans were collected at a spectral resolution of 1 $cm^{-1}$. The modified clay was mixed with KBr pellets to press into the small flakes and dried at 70°C for 24 hours. The holder was placed in the sample chamber and spectrum was recorded under $N_2$ purge to maintain the test of the sample dryness.

Transmission electron microscopy (TEM) images were obtained on a Hitachi H-7500 operating at 100 kV. The sample was thin section to ~70 nm by a Leica ultracut UCT microtome. Wide-angle X-ray diffraction (WAXD) experiments were carried on a Rigaku D/max-2500 type X-ray diffraction instrument with Cu K$\alpha$ radiation ($\lambda$ = 1.54 Å) using an Ni-filter. Data were recorded in the range of $2\theta$ = 1 to 20 at the scanning rate of 0.6°/min.

#### 2.5.3. Thermal and mechanical analysis characterization

Thermal stability of nanocomposite was investigated by a TA Instruments Q50 apparatus. The sample ~5 mg was placed in a Pt cell with scan rate of 20°C/min from 30 to 800°C under a 40 mL/min flow of nitrogen gas. Thermal analysis through differential scanning calorimetry (DSC) was performed using a Du-Pont (DSC-2010) to measure the glass transition temperature ($T_g$) of the nanocomposite. The sample was preheated at a scan rate of 20°C/min from 30 to 150°C under

a nitrogen atmosphere. A small sample (ca. 5–10 mg) was weighted and sealed in an aluminum pan. The sample was quickly cooled to 10°C from the first scan and then scanned between 30 and 150°C at the scan rate of 20°C/min. The glass transition temperatures are taken as the midpoint of the heat capacity transition between the upper and lower points of deviation from the extrapolated glass and liquid lines. The coefficient of thermal expansion (CTE) was measured using a thermomechanical analyzer (TMA TA 2940) by recording the change in dimension of the specimen with temperature. The specimen was heated from 25 to 150°C at a heating rate of 5°C/min.

## 3. RESULTS AND DISCUSSION

### 3.1. Morphologies of modified clays and nanocomposites

Microstructures of polymer-layered silicate nanocomposites were characterized by XRD and TEM. Figure 4 shows the X-ray diffraction curves of the pristine clay and modified clays in the $2\theta$ region of 2–10°. For the pristine clay, the Bragg diffraction peak at $2\theta = 6.92°$ corresponds to $d$-spacing of 1.28 nm. For the POSS-$NH_2$/clay and $C_{20}$-POSS/clay, the $2\theta$ value shifts from 6.92° (1.28 nm) to 5.51° (1.61 nm) and 2.33° (3.80 nm) after ion exchange, indicating that the basal spacing is expanded as the sodium cations in the interlayer galleries are replaced by intercalated agents of POSS-$NH_2$ and $C_{20}$-POSS. The increase of the basal spacing indicates that the clay can be efficiently intercalated by POSS-$NH_2$ and $C_{20}$-POSS. The $d$-spacing of the $C_{20}$-POSS-modified clay is substantially greater than the POSS-$NH_2$-modified clay. Larger interlayer spacing favors the penetration of styrene monomer and the formation of exfoliated nanocomposite by providing more hydrophobic environment. The pure POSS-$NH_2$ has characteristic diffraction peaks arising from the aggregation of the POSS [23]. Figure 5 shows XRD patterns of the unmodified clay and the $C_{20}$-POSS modified clay. The pure $C_{20}$-POSS has a broad peak in the region of 5–12° arising from the $C_{20}$ long aliphatic chain. When the $C_{20}$-POSS is inserted between the galleries of the clay, the $d$ spacing is increased from 1.28 nm for original clay to 3.80 nm, implying that the organic modifier is incorporated between and pushing the clay layers. Both nanocomposites do not show XRD diffraction peak as shown in Figure 6, indicating the silicate layers are exfoliated in the polymer matrix. TEM images for POSS-$NH_2$/clay and $C_{20}$-POSS/clay nanocomposites at 3% inorganic clay loading are shown in Figures 7(a) and 7(b), indicating that the exfoliated clay platelets are distributed in the matrix homogeneously and randomly.

### 3.2. Fourier transfer infrared analyses

The representative FT-IR spectra of the organophilic clay, POSS-$NH_2$-modified and $C_{20}$-POSS modified clays are given in Figure 1. After ion exchange, FT-IR spectroscopy can provide important information regarding the difference between intercalated agents and modified clays. In Figure 1(a), characteristic vibration bands of the pure clay are 1030 $cm^{-1}$(Si–O), 520 $cm^{-1}$ (Al–O), and 470 $cm^{-1}$ (Mg–O) [24–26]. In Figure 1(b), the absorption peaks in the region of 2950–2800 is assigned to the stretching vibration of aliphatic C–H. The symmetrical Si–O–Si band in the silsequioxane cage is characterized by the stretching band at 1109 $cm^{-1}$. In Figure 1(d), $C_{20}$-POSS contains both alkyl chain and POSS moiety where the POSS moiety exhibits characteristic absorption peaks at 2950–2800 $cm^{-1}$ (C–H bonds), 1230 $cm^{-1}$ (Si–C bonds), 1109 $cm^{-1}$ (Si–O–Si bonds of the cage structure). The characteristics of the vibration band of alkyl chain appear at 2920, 2850, and 1475 $cm^{-1}$ (–$CH_2$–vibration bands). Figures 1(c) and 1(e) show the features of combination of characteristic bands of pure clay, POSS-$NH_2$, and $C_{20}$-POSS. IR analysis further confirms the existence of these intercalated agents in

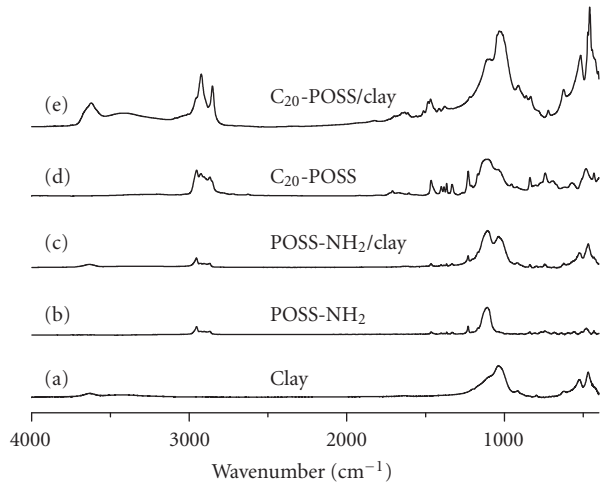


Figure 1: IR spectra of the two intercalated agent, intercalated clay, and pure clay.

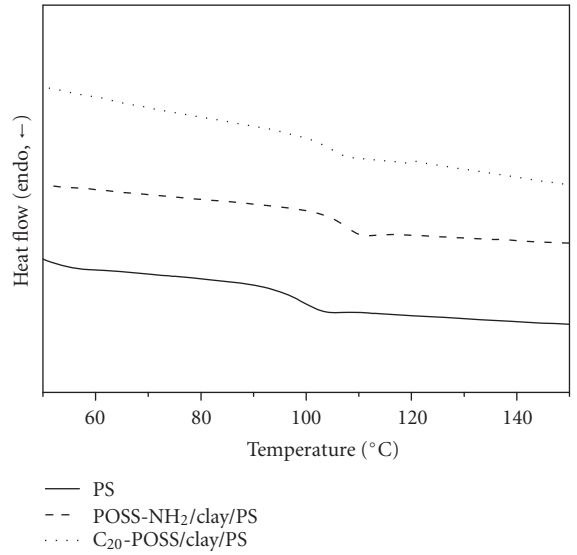


Figure 2: DSC curves glass transition temperature of (a) PS, (b) the nanocomposites formed used POSS-$NH_2$, and (c) the nanocomposites formed used $C_{20}$-POSS.

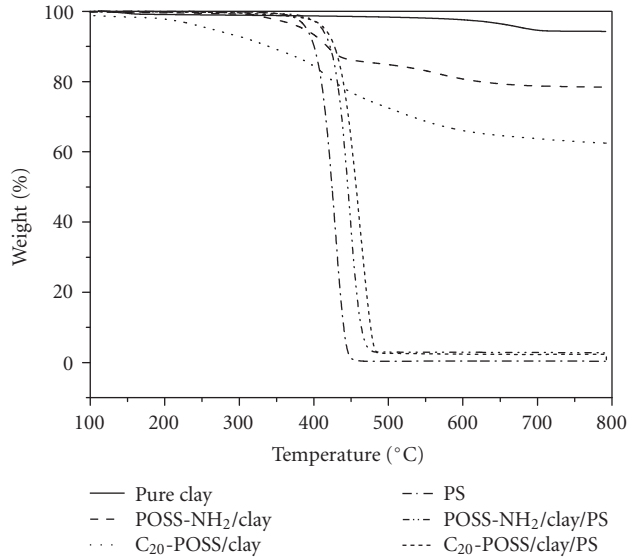


Figure 3: TGA curves of (a) pure Clay, (b) POSS-$NH_2$/Clay, (c) $C_{20}$-POSS/Clay, (d) pure PS, (e) the nanocomposite formed with POSS-$NH_2$, and (f) the nanocomposite formed with $C_{20}$-POSS.

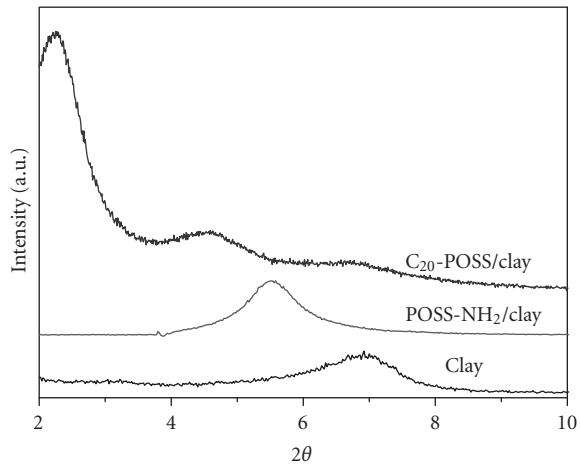


Figure 4: X-Ray diffraction patterns of pure clay, and intercalated clay.

these intercalated clay samples, implying that these intercalations of the intercalated agents are indeed present within the gallery gap. These observations support the explanation in the earlier observation from XRD.

### 3.3. Thermal properties

Figure 2 presents DSC traces of these nanocomposites with different intercalated agents. All DSC thermograms display single glass transition temperatures in the experimental temperature range. The glass transition temperature of PS occurs at 100°C. With the addition of the POSS and $C_{20}$-POSS modified MMT to the polymer matrix, the glass transition temperatures ($T_g$s) of the POSS-$NH_2$/clay/PS and $C_{20}$-

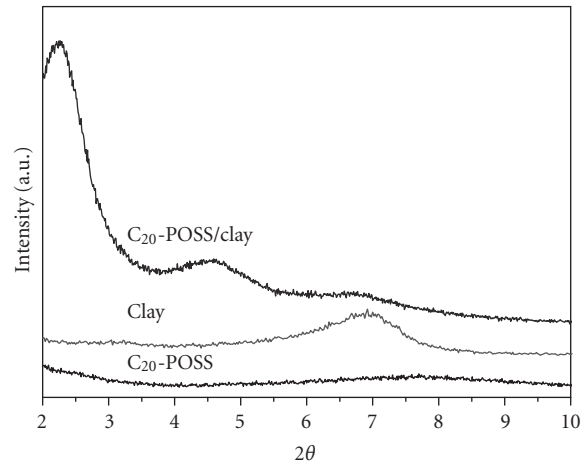


Figure 5: XRD spectra of $C_{20}$-POSS, pure clay, and $C_{20}$-POSS/Clay.

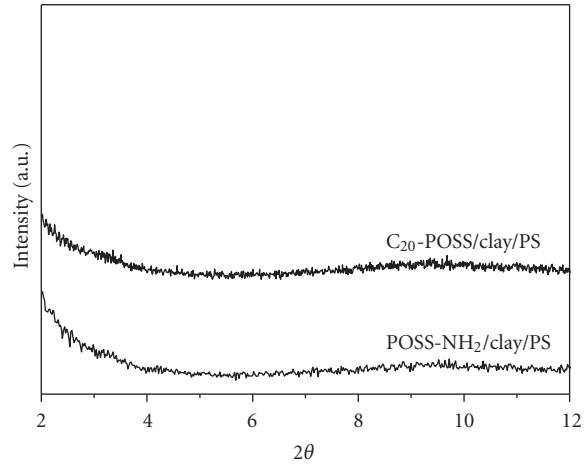


Figure 6: XRD spectra of the two surfactant-containing nanocomposites indicating the extent of delamination.

POSS/clay/PS are 108, and 105°C, respectively. From the DSC results that the incorporation of the organoclay resulted in an increase in the $T_g$ relative to virgin PS, as summarized in Table 1. The addition of clay results in $T_g$ increase which can be attributed to the retardation of PS chain movement.

Figure 3 presents the thermal stabilities of POSS-$NH_2$- and $C_{20}$-POSS-modified clays and nanocomposites investigated by TGA. Both nanocomposites show improved thermal stabilities than the virgin PS. The improvement in the degradation temperature is mainly due to the homogeneous dispersion of silicate nanoplatelets in the PS matrix [27–30]. In Figure 3, the $C_{20}$-POSS/clay decomposes at 262°C while the POSS-$NH_2$/clay decomposes at higher temperature of 38°C. The POSS-$NH_2$-modified clay is relatively more stable than the $C_{20}$-POSS-modified clay. Essentially, all nanocomposites give higher decomposition temperatures than the pristine PS and the improved thermal stability can be attributed to the diffusion hindrance of the decomposited volatiles. The values of 5% and 50% weight loss temperatures and the char yields are summarized in Table 1.

Table 1: Results of thermal and mechanical properties of polystyrene and polystyrene nanocomposites.

| Sample | $T_g$,(°C)[a] | $T_{0.05}$,(°C)[b] | $T_{0.5}$,(°C)[c] | Char at 600(°C) % | CTE($\mu$m/m°C) |
|---|---|---|---|---|---|
| PS | 100 ± 0.5 | 390 ± 1.7 | 424 ± 0.8 | 0 | 164 ± 2 |
| POSS/Clay/PS | 108 ± 0.6 | 411 ± 1.3 | 446 ± 1.2 | 2.9 | 98 ± 1 |
| $C_{20}$-POSS/Clay/PS | 105 ± 0.3 | 415 ± 1.1 | 457 ± 0.9 | 2.4 | 100 ± 3 |

[a] Glass transition temperature ($T_g$).
[b] 5% Degradation temperature ($T_{0.05}$).
[c] 50% Degradation temperature ($T_{0.5}$).

Table 2: Molecular weights of polystyrene and polystyrene nanocomposites.

| Sample | Mn ($\times 10^4$)[a] | Mw ($\times 10^4$)[b] | PDI (Mw/Mn)[c] |
|---|---|---|---|
| PS | 34.5 | 53.1 | 1.54 |
| POSS-$NH_2$/Clay/PS | 40.9 | 54.0 | 1.32 |
| $C_{20}$-POSS/Clay/PS | 47.7 | 58.7 | 1.23 |

[a] Number-average molecular weights (Mn).
[b] Weight-average molecular weights (Mw) were determined by GPC.
[c] Polydispersity index, Mw/Mn.

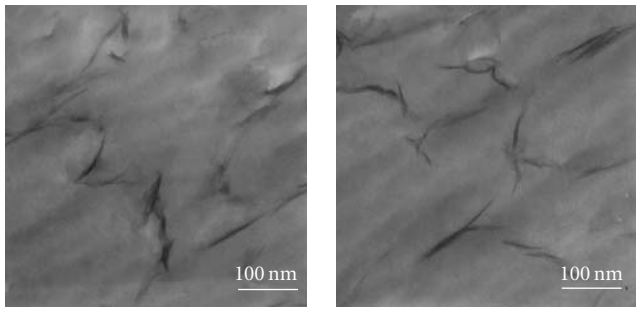


(a) (b)

Figure 7: TEM images of (a) POSS-$NH_2$ and (b) $C_{20}$-POSS-treated nanocomposites.

### 3.4. Molecular weights of the nanocomposites

Molecular weight and molecular weight distribution (PDI) by GPC analyses of polymer samples recovered after excluding all clay content are listed in Table 2. From Table 2, molecular weight (Mw or Mn) of the PS in the PS/clay nanocomposites is higher than the pure PS, suggesting that clay may act as a catalytic agent responsible for the observed higher molecular weight of the PS with the proceeding emulsion polymerization.

### 3.5. Coefficient of thermal coefficient

Thermal mechanical analyzer (TMA) was used to determine the coefficient of thermal expansion of the POSS/clay nanocomposites. The thermal expansion coefficient is an important issue for polymers in engineering applications. The CTE was measured from the initial linear slope of the thermal strain-temperature plot. A low thermal expansion coefficient is often desirable to achieve dimensional stability and can be achieved by incorporation of a rigid and low CTE filler material. From the data in Table 1, the CTE of the virgin PS is 164 $\mu$m/m°C and the addition 3 wt% organically modified clays reduces the CTE values to 98 and 100 $\mu$m/m°C for POSS/clay/PS and $C_{20}$-POSS/clay/PS approximately 40% reduction relative to the virgin PS.

In general, the extent of CTE reduction depends on the particle rigidity and fine dispersion of the clay platelets in the PS matrix and also due to efficient stress transfer to clay layers. The retardation of PS chain segmental movement through incorporation of organically modified clays also leads to decrease in the coefficient of thermal expansion (CTE). The incorporation of the organically modified clays results in significant improvement in dimensional stability of the PS matrix.

## 4. CONCLUSIONS

The POSS-clay hybrids of polystyrene are prepared via emulsion polymerization using two organically modified clays, POSS-$NH_2$ and $C_{20}$-POSS, as intercalated agents. X-ray diffraction (XRD) results indicate that the clay is successfully intercalated by POSS-$NH_2$ and $C_{20}$-POSS. The random dispersion of these exfoliated silicate layers in these nanocomposites are identified by XRD and TEM. These well dispersed clay platelets in PS matrix result in improved thermal properties in terms of thermal decomposition temperature ($T_d$) and glass transition temperature ($T_g$). In addition, the incorporation of these organoclay results in significant reduction in coefficient of thermal expansion of virgin PS.

## ACKNOWLEDGMENT

This work was financially supported by the National Science Council, Taiwan , under Contracts no. NSC-96-2120-M-009-009 a nd NSC-96-2218-E-110-008.

## REFERENCES


[1] H.-A. Klok and S. Lecommandoux, "Supramolecular materials via block copolymer self-assembly," *Advanced Materials*, vol. 13, no. 16, pp. 1217–1229, 2001.

[2] C. Sanchez, G. J. de A. A. Soler-Illia, F. Ribot, T. Lalot, C. R. Mayer, and V. Cabuil, "Designed hybrid organic-inorganic nanocomposites from functional nanobuilding blocks," *Chemistry of Materials*, vol. 13, no. 10, pp. 3061–3083, 2001.

[3] C. Park, J. G. Smith Jr., J. W. Connell, S. E. Lowther, D. C. Working, and E. J. Siochi, "Polyimide/silica hybrid-clay nanocomposites," *Polymer*, vol. 46, no. 23, pp. 9694–9701, 2005.

[4] D.-R. Yei, S.-W. Kuo, H.-K. Fu, and F.-C. Chang, "Enhanced thermal properties of PS nanocomposites formed from montmorillonite treated with a surfactant/cyclodextrin inclusion complex," *Polymer*, vol. 46, no. 3, pp. 741–750, 2005.

[5] W. Xie, J. M. Hwu, G. J. Jiang, T. M. Buthelezi, and W.-P. Pan, "A study of the effect of surfactants on the properties of polystyrene-montmorillonite nanocomposites," *Polymer Engineering & Science*, vol. 43, no. 1, pp. 214–222, 2003.

[6] D.-R. Yei, S.-W. Kuo, Y.-C. Su, and F.-C. Chang, "Enhanced thermal properties of PS nanocomposites formed from inorganic POSS-treated montmorillonite," *Polymer*, vol. 45, no. 8, pp. 2633–2640, 2004.

[7] C.-R. Tseng, J.-Y. Wu, H.-Y. Lee, and F.-C. Chang, "Preparation and characterization of polystyrene-clay nanocomposites by free-radical polymerization," *Journal of Applied Polymer Science*, vol. 85, no. 7, pp. 1370–1377, 2002.

[8] S. Su and C. A. Wilkie, "Exfoliated poly(methyl methacrylate) and polystyrene nanocomposites occur when the clay cation contains a vinyl monomer," *Journal of Polymer Science A*, vol. 41, no. 8, pp. 1124–1135, 2003.

[9] M. H. Kim, C. I. Park, W. M. Choi, et al., "Synthesis and material properties of syndiotactic polystyrene/organophilic clay nanocomposites," *Journal of Applied Polymer Science*, vol. 92, no. 4, pp. 2144–2150, 2004.

[10] A. Okado, M. Kawasumi, T. Kurauchi, and O. Kamigaito, "Synthesis and characterization of a nylon 6-clay hybrid," *Polymer Preprints*, vol. 28, pp. 447–448, 1987.

[11] D. Kong and C. E. Park, "Real time exfoliation behavior of clay layers in epoxy-clay nanocomposites," *Chemistry of Materials*, vol. 15, no. 2, pp. 419–424, 2003.

[12] W.-B. Xu, S.-P. Bao, and P.-S. He, "Intercalation and exfoliation behavior of epoxy resin/curing agent/montmorillonite nanocomposite," *Journal of Applied Polymer Science*, vol. 84, no. 4, pp. 842–849, 2002.

[13] A. Akelah, "Nanocomposites of grafted polymers onto layered silicates," in *Polymers and Other Advanced Materials: Emerging Technologies and Business Opportunities*, P. N. Prasad, J. E. Mark, and J. F. Tung, Eds., pp. 625–644, Plenum Press, New York, NY, USA, 1995.

[14] R. A. Vaia, S. Vasudevan, W. Krawiec, L. G. Scanlon, and E. P. Giannelis, "New polymer electrolyte nanocomposites: melt intercalation of poly(ethylene oxide) in mica-type silicates," *Advanced Materials*, vol. 7, no. 2, pp. 154–156, 1995.

[15] E. P. Giannelis, "Polymer layered silicate nanocomposites," *Advanced Materials*, vol. 8, no. 1, pp. 29–35, 1996.

[16] J. W. Gilman, A. B. Morgan, R. H. Harris, P. C. Trulove, H. C. Delong, and T. E Sutto, "Polymer layered silicate nanocomposites: thermal stability of organic cationic treatments," *Polymeric Materials Science and Engineering*, vol. 83, pp. 59–60, 2000.

[17] J. D. Lichtenhan, N. Q. Vu, J. A. Carter, J. W. Gilman, and F. J. Feher, "Silsesquioxane-siloxane copolymers from polyhedral silsesquioxanes," *Macromolecules*, vol. 26, no. 8, pp. 2141–2142, 1993.

[18] J. D. Lichtenhan, Y. A. Otonari, and M. J. Carr, "Linear hybrid polymer building blocks: methacrylate-functionalized polyhedral oligomeric silsesquioxane monomers and polymers," *Macromolecules*, vol. 28, no. 24, pp. 8435–8437, 1995.

[19] T. S. Haddad and J. D. Lichtenhan, "The incorporation of transition metals into polyhedral oligosilsesquioxane polymers," *Journal of Inorganic Organometallic Polymer*, vol. 5, no. 3, pp. 237–246, 1995.

[20] R. A. Mantz, P. F. Jones, K. P. Chaffee, et al., "Thermolysis of polyhedral oligomeric silsesquioxane (POSS) macromers and POSS-siloxane copolymers," *Chemistry of Materials*, vol. 8, no. 6, pp. 1250–1259, 1996.

[21] T. S. Haddad and J. D. Lichtenhan, "Hybrid organic-inorganic thermoplastics: styryl-based polyhedral oligomeric silsesquioxane polymers," *Macromolecules*, vol. 29, no. 22, pp. 7302–7304, 1996.

[22] C.-F. Huang, S.-W. Kuo, F.-J. Lin, et al., "Influence of PMMA-chain-end tethered polyhedral oligomeric silsesquioxanes on the miscibility and specific interaction with phenolic blends," *Macromolecules*, vol. 39, no. 1, pp. 300–308, 2006.

[23] H. Zhang, C. Wang, M. Li, X. Ji, J. Zhang, and B. Yang, "Fluorescent nanocrystal-polymer composites from aqueous banocrystals: methods without ligand exchange," *Chemistry of Materials*, vol. 17, no. 19, pp. 4783–4788, 2005.

[24] J.-M. Yeh, S.-J. Liou, C.-Y. Lai, P.-C. Wu, and T.-Y. Tsai, "Enhancement of corrosion protection effect in polyaniline via the formation of polyaniline-clay nanocomposite materials," *Chemistry of Materials*, vol. 13, no. 3, pp. 1131–1136, 2001.

[25] J.-M. Yeh, S.-J. Liou, C.-Y. Lin, C.-Y. Cheng, Y.-W. Chang, and K. R. Lee, "Anticorrosively enhanced PMMA-clay nanocomposite materials with quaternary alkylphosphonium salt as an intercalating agent," *Chemistry of Materials*, vol. 14, no. 1, pp. 154–161, 2002.

[26] J.-M. Yeh, C.-L. Chen, Y.-C. Chen, et al., "Enhancement of corrosion protection effect of poly(*o*-ethoxyaniline) via the formation of poly(*o*-ethoxyaniline)-clay nanocomposite materials," *Polymer*, vol. 43, no. 9, pp. 2729–2736, 2002.

[27] P. Uthirakumar, K. S. Nahm, Y. B. Hahn, and Y.-S. Lee, "Preparation of polystyrene/montmorillonite nanocomposites using a new radical initiator-montmorillonite hybrid via in situ intercalative polymerization," *European Polymer Journal*, vol. 40, no. 11, pp. 2437–2444, 2004.

[28] T. K. Chen, Y. I. Tien, and K. H. Wei, "Synthesis and characterization of novel segmented polyurethane/clay nanocomposite via poly(ε-caprolactone)/clay," *Journal of Polymer Science A*, vol. 37, no. 13, pp. 2225–2233, 1999.

[29] J. G. Doh and I. Cho, "Synthesis and properties of polystyrene-organoammonium montmorillonite hybrid," *Polymer Bulletin*, vol. 41, no. 5, pp. 511–518, 1998.

[30] X. Fu and S. Qutubiddin, "Polymer-clay nanocomposites: exfoliation of organophilic montmorillonite nanolayers in polystyrene," *Polymer*, vol. 42, no. 2, pp. 807–813, 2001.

Hindawi Publishing Corporation
Journal of Nanomaterials
Volume 2008, Article ID 459093, 4 pages
doi:10.1155/2008/459093

*Research Article*

# Effect of Rare Earth Y on Properties of Nanosized 90W-7Ni-3Fe Composite Powder Fabricated by Spray Drying-Hydrogen Reduction

**Y.-Z. Ma, Liu Wensheng, Huang Baiyun, and Fan Jinglian**

*State Key Laboratory of Powder Metallurgy, Central South University, Changsha 410083, China*

Correspondence should be addressed to Y.-Z. Ma, yunzhum@163.com

Received 6 July 2007; Accepted 11 January 2008

Recommended by Jun Lou

(W,Ni,Fe) composite oxide powder synthesized by spray drying was reduced at 700°C for 90 minutes in $H_2$ atmosphere. The effect of rare earth Y on $H_2$ reduction of (W,Ni,Fe) composite oxide powder was studied. Phase composition, crystalline size, and particle morphology of the reduced powder have been measured by X-ray diffraction and scanning electron microscope (SEM). Fsss particle size and special surface area of the reduced powder were also measured and analyzed. The result showed that new phase $Y(Ni_{0.75}W_{0.25})O_3$ appeared in the reduced powder and particle morphology was nearly spherical or polyhedron by Y additions. The higher the rare earth element content was, the bigger the influencing on particle morphology was. When the rare earth Y content was under 0.8%, with the increase of the rare earth element content, $d_{BET}$, Fsss, and crystal sizes of the reduced powder decreased greatly.



## 1. INTRODUCTION

Tungsten-based heavy alloys, which are used as kinetic energy penetrators, counter weights, radiation shields, and electrical contacts due to their high density, strength, and ductility, are two-phase composites produced by liquid phase sintering mixed elemental tungsten, nickel, and iron powders. Typical compositions have 90 wt% tungsten with the balance nickel and iron, usually in the ratio of 7 : 3 [1].

Nanostructured tungsten-based alloys possess very high properties, which put high demands on the manufacture process for both powders and bulk alloys. High-energy ball milling, which is a well-known process for preparing amorphous alloyed powders, has been considered as a powderful technique due to relative inexpensive equipment [2]. However, it takes tens of hours to fabricate nanosized W-Ni-Fe composite powder for high-energy milling technique [3], so the milling efficiency is very low. Meanwhile, high-energy milling could bring inclusions. Spray drying process is a useful technique for synthesizing numerous nanostructured materials due to its simplicity and various elements homogeneous dispersibility [4, 5]. Previous studies have discussed preparation and reduction mechanisms of (W,Ni,Fe) composite oxide powder by spray drying [6–8]. In this paper, effects on the reduced powder properties with Y additions were studied by previous reduced conditions optimized at 700°C for 90 minutes.

## 2. EXPERIMENTAL

The raw materials in this experiment included the $(NH_4)_6H_2W_{12}O_{40} \cdot xH_2O$, $Ni(NO_3)_2 \cdot 6H_2O$, $Fe(NO_3)_3 \cdot 9H_2O$, $Y(NO_3)_2 \cdot 6H_2O$, and surfactant PEG-1000. First, the $(NH_4)_6H_2W_{12}O_{40} \cdot xH_2O$, $Ni(NO_3)_2 \cdot 6H_2O$, and $Fe(NO_3)_3 \cdot 9H_2O$ were added in distilled water by a composition ratio of 90 wt%W-7 wt%Ni-3 wt%Fe and produced solution with 0.2, 0.4, 0.6, 0.8 wt% Y additions by $Y(NO_3)_2 \cdot 6H_2O$ (theoretical content calculation), respectively. Secondly, the solution was changed into solution colloid by adjusting pH value, and $0.5\,g \cdot L^{-1}$ PEG-1000 was added. Finally, the (W,Ni,Fe) precursor oxide powder was fabricated by drying spraying of solution colloid, then the nanosized 90W-7Ni-3Fe composite powder including different Y additions was fabricated by reduction of the (W,Ni,Fe) precursor oxide powder in the hydrogen-atmosphere at 700°C for 90 minutes.

Special surface areas of the reduced powder were measured by the nitrogen adsorption method. The Fsss sizes of the reduced powder were measured by the Fisher testing method. The phase compositions and crystal sizes of the reduced powder were tested and analyzed with Rigaku D/max2550VB$^+$18 Kw X-ray diffraction made in Japan. The reduced powders were dispersed by ultrasonic wave for 30 minutes, whose morphology images were observed with the JSM-5600LV type scanning electron microscope (SEM) made by JEOL cop.

## 3. RESULTS AND DISCUSSION

### 3.1. Effect of rare earth Y on phase composition of 90W-7Ni-3Fe composite powder

Figure 1 showed curves between the Y additions and phase compositions of the reduced composite powder at 700°C for 90 minutes. It was seen from Figure 1 that the phase compositions of the reduced powder were W and $\gamma$-(Ni,Fe) without the rare earth Y addition, new phase $Y(Ni_{0.75}W_{0.25})O_3$ was appeared when adding 0.4 wt% Y. With the increase of Y additions from 0.4 wt% to 0.8 wt%, intensity of new phase $Y(Ni_{0.75}W_{0.25})O_3$ raised in X-ray diffraction graph.

### 3.2. Effect of rare earth Y on properties of 90W-7Ni- 3Fe composite powder

Figure 2 showed curves between the $d_{BET}$ particle sizes, Fsss particle sizes, and crystal sizes of the reduced powder and the Y additions. The crystal sizes of the reduced powder were decreased with increase of the Y additions from Figure 2(a). High Y addition has better effect on inhibition for crystal size than low Y addition. The $d_{BET}$ and Fsss particle sizes of the reduced powder with some Y additions were much smaller than those of the reduced powder without Y addition from Figures 2(b) and 2(c). Even if 0.2 wt% Y was added, the $d_{BET}$ and Fsss particle sizes of the reduced powder declined obviously. With the increase of water vapor produced during reduction process, tungsten oxide and water vapor synthesized volatiling $WO_x \cdot H_2O$, that is $WO_2(OH)_2$, which deposited on the surface of metal tungsten powder by vapor transference, and led to growth of particles [9]. The process sequenced as

$$WO_3(\text{solid}) \longrightarrow WO_{2.9}(\text{solid}) \longrightarrow WO_2(\text{solid}) \longrightarrow W(\text{solid})$$
$$WO_2(OH)_2(\text{gas}) \longrightarrow W(\text{solid})$$

When rare earth Y was added, new phase $Y(Ni_{0.75}W_{0.25})O_3$ formed and adsorbed on the surface of tungsten particles. Meanwhile, new phase $Y(Ni_{0.75}W_{0.25})O_3$ can effectively prevent $WO_2(OH)_2$ from producing and decreasing vapor transference, which inhibited effectively W particles from growing up.

### 3.3. Effect of rare earth Y on morphology images of 90W-7Ni-3Fe composite powder

SEM morphology images of the reduced composite powder were listed in Figure 3. From Figure 3, the reduced W-Ni-Fe

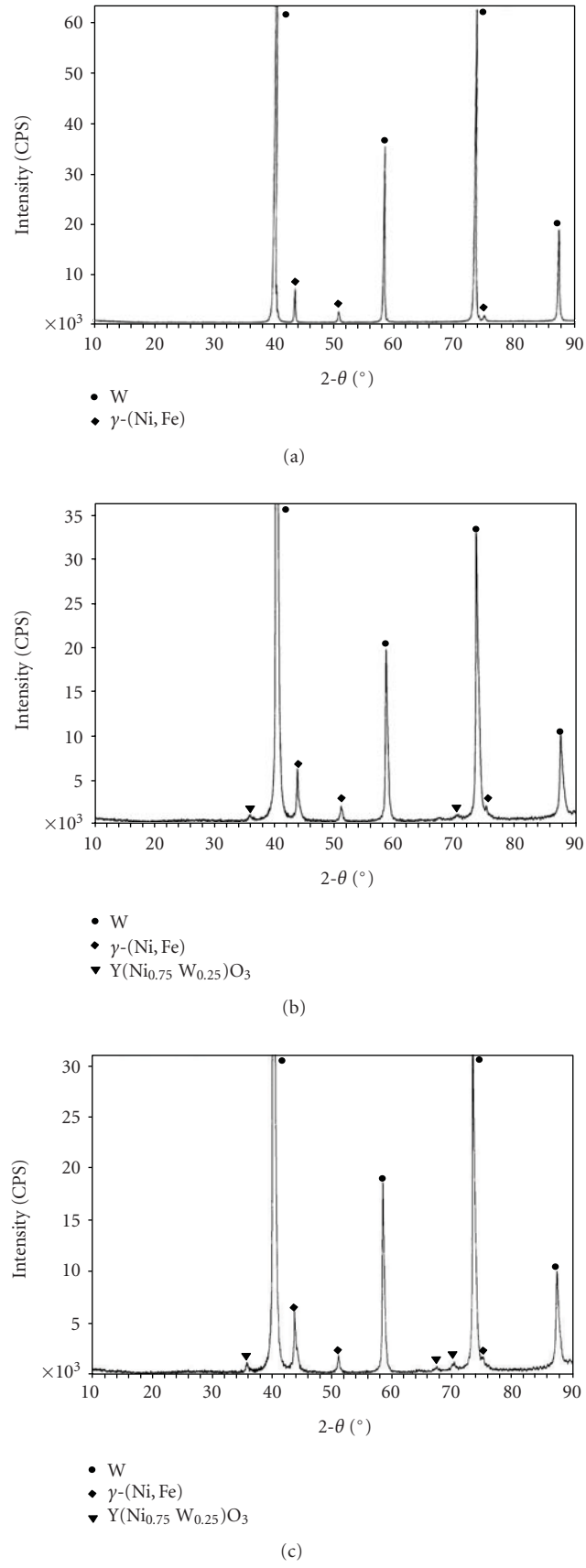


Figure 1: X-ray diffraction images of W-Ni-Fe composite powder reduced: (a) no Y addition; (b) 0.4 wt% Y; (c) 0.8 wt% Y.

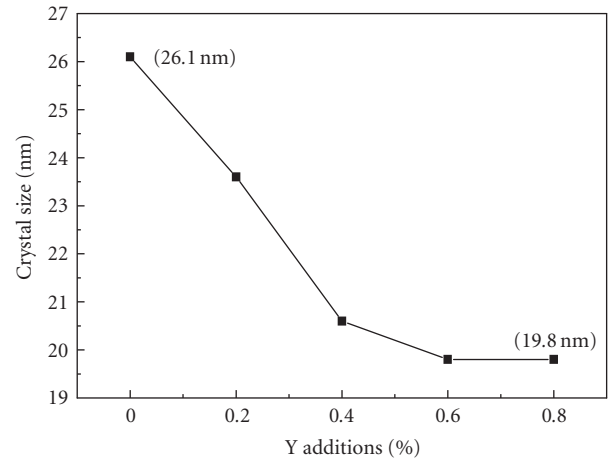


(a)

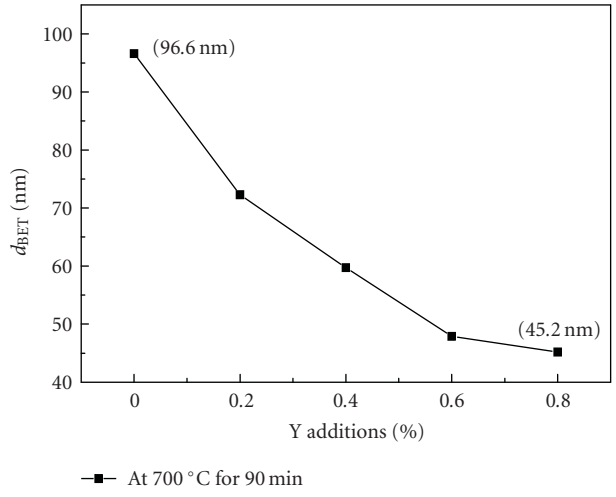


(b)

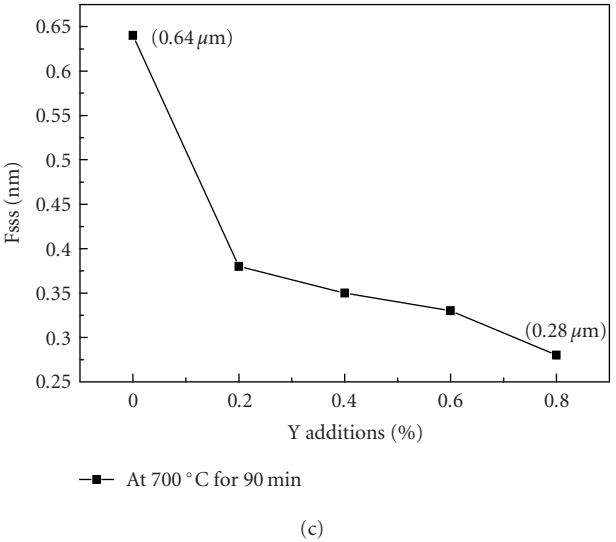


(c)

Figure 2: Properties curves of the reduced powder for different Y additions: (a) crystal sizes; (b) $d_{BET}$; (c) Fsss.

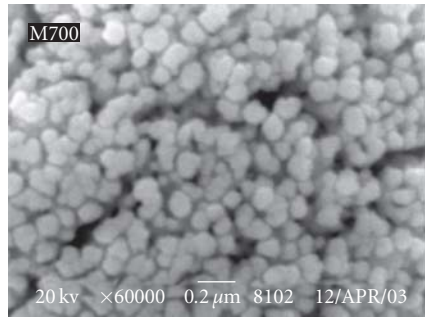


(a)

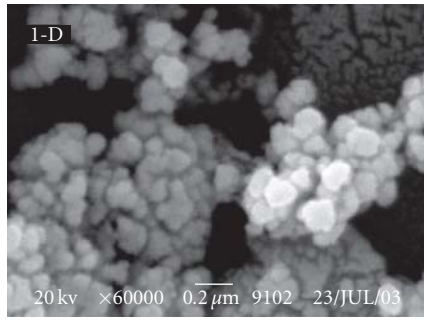


(b)

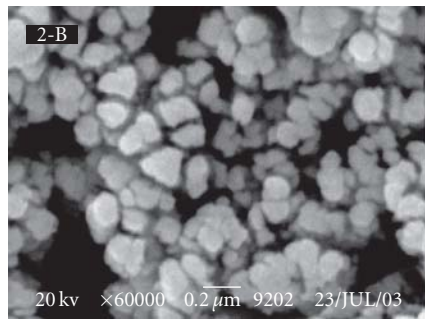


(c)

Figure 3: Morphology images of the reduced powder for different Y additions (SEM): (a) no Y addition; (b) 0.4 wt% Y; (c) 0.8 wt.% Y.

composite powder by rare earth Y additions was more homogeneous dispersibility than that of no Y addition. Meanwhile, with the increase of Y addition, effect of rare earth on dispersibility of the reduced powder enlarged obviously. It was also seen clearly from Figure 3 that, powder particle morphology with rare earth Y addition has changed, the particle morphology was spherical without rare earth Y, but the powder particle morphology was nearly spherical with 0.4 wt% Y and polyhedral with 0.8 wt% Y. The higher the Y additions were, the greater the effect on powder particle morphology was. Because energy state of some crystal interface has changed when some rare earth Y were added, which forced crystal quickly growth up at some directions and inhibited other directions from growthing up. With the increase of rare earth Y, tendency of preferential orientation growthing was more obvious [10, 11].

## 4. CONCLUSION

(1) The phase compositions of the reduced powder were W and $\gamma$-(Ni,Fe) without the rare earth Y addition, but new phase $Y(Ni_{0.75}W_{0.25})O_3$ was appeared by adding 0.4 wt% Y. With the increase of Y additions from 0.4 wt% to 0.8 wt%, intensity of new phase $Y(Ni_{0.75}W_{0.25})O_3$ raised in X-ray diffraction graph.

(2) With increase of Y additions in the range of 0.8 wt%, the crystal, $d_{BET}$, and Fsss sizes of the reduced W-Ni-Fe composite powder were decreased from 26.1 nm, 96.6 nm, 0.64 $\mu$m to 19.8 nm, 45.2 nm, 0.28 $\mu$m, respectively.

(3) Rare earth Y possessed great influence on powder particle morphology. The particle morphology is spherical without rare earth Y, but the particle morphology is nearly spherical by adding 0.4 wt% Y or polyhedron with 0.8 wt% Y addition. The higher rare earth content is, the bigger influencing on particle morphology is.

## ACKNOWLEDGMENTS

The authors thank the National Natural Science Foundation of China (Grant no. 50774098) and the Creative research group of National Natural Science Foundation of China (Grant no. 50721003) for the financial support.

## REFERENCES

[1] Y. Weihong, "Processing industry of refractory metals in our country between centuries," *Rare Metal Materials and Engineering*, vol. 27, supplement 1, pp. 1–8, 1998, (Chinese).

[2] H. J. Ryu, S. H. Hong, and W. H. Baek, "Mechanical alloying process of 93W-5.6Ni-1.4Fe tungsten heavy alloy," *Journal of Materials Processing Technology*, vol. 63, no. 1–3, pp. 292–297, 1997.

[3] J. Sun, F. Zhang, and J. Shen, "Characterizations of ball-milled nanocrystalline WC-Co composite powders and subsequently rapid hot pressing sintered cermets," *Materials Letters*, vol. 57, no. 21, pp. 3140–3148, 2003.

[4] M. H. Manusson and K. Deppert, "Single-crystalline of tungsten nanoparticles produce by thermal decomposition of tungsten exacarbonyl," *Journal of Materials Research*, vol. 15, no. 7, pp. 1564–1569, 2000.

[5] L. E. McCandlish, B. H. Kear, and S. J. Bhatia, World Patent, WO91/07244, 1991.

[6] M. Yunzhu, H. Baiyun, F. Jinglian, et al., "Reduction procedure study of (W,Ni,Fe) composite oxide powder," *Journal of Central South University*, vol. 35, no. 1, pp. 16–20, 2004, (Chinese).

[7] W. D. Schubert, "Kinetics of the hydrogen reduction of tungsten oxides," *International Journal of Refractory Metals & Hard Materials*, vol. 9, no. 4, pp. 178–191, 1990.

[8] A. Lackner, "Hydrogen reduction of blue tungsten oxide," *International Journal of Refractory Metals & Hard Materials*, vol. 14, no. 5-6, pp. 383–391, 1996.

[9] W. Zunan, "Summarizing of modern times reduction theory of tungsten," *Cemented Carbide*, vol. 8, no. 1, pp. 14–21, 1991, (Chinese).

[10] Y. Yang, Z. Meiling, and L. Hanguang, "Effect of La and Y on hydrogenolysis of blue W oxide," *Rare Metal Materials and Engineering*, vol. 23, no. 5, pp. 52–55, 1994, (Chinese).

[11] Z. Jiuxing, L. Xinyu, Z. Tieyong, et al., "The effect of rare earth element La on the doped tungsten powder morphology and the properties of the bars," *Rare Metal Materials and Engineering*, vol. 20, no. 6, pp. 28–32, 1991, (Chinese).

Hindawi Publishing Corporation
Journal of Nanomaterials
Volume 2008, Article ID 286069, 5 pages
doi:10.1155/2008/286069

*Research Article*

# Structure and Property Investigation of Composite $ZnO/SnO_2$ Nanocrystalline Particles after High-Pressure Treatment

**Sun Zhenya,[1] Deng Yundi,[2] and Zhang Weiying[2]**

[1] *Center for Material Research and Analysis, Wuhan University of Technology, Wuhan 430070, China*
[2] *School of Science, Wuhan University of Technology, Wuhan 430070, China*

Correspondence should be addressed to Deng Yundi, dirkdean@163.com

Received 26 September 2007; Revised 21 January 2008; Accepted 20 February 2008

Recommended by Junlan Wang

Composite $ZnO/SnO_2$ nanocrystalline particles ($ZnO/SnO_2$) were synthesized by sol-gel method and with treatment of high pressure at 6 GPa. The crystallinity and the particle size of the prepared samples were analyzed by X-ray diffraction (XRD) spectroscopy. The results indicated that all the samples had the good crystallinity, and the particle size of ZnO and $ZnO/SnO_2$ decreased after high-pressure treatment. The infrared (IR) spectra showed that the distance of crystal lattice was shortened after high-pressure treatment, and the size distribution became more uneven after $SnO_2$ doping. With the high-resolution transmission electron microscope (HRTEM), we got some morphology information and evidence to support the IR and XRD analysis results. The results of ultraviolet-visible absorption (UV-Vis) spectra showed that $ZnO/SnO_2$ might improve the photocatalytic property of the samples after high-pressure treatment.



## 1. INTRODUCTION

People gradually realize that pollutants in water should be removed urgently. There are two common techniques to treat such wastewater: one is adsorption and the other is chemical coagulation. However, these methods merely transfer pollutants from the liquid to the solid phase causing secondary pollution and requiring further treatment.

On the other hand, as a new technique the photocatalytic method can be conveniently applied toward the degradation of pollutants such as dye, without causing secondary pollution. Photogenerated carriers (electrons and holes) in a semiconductor particle can tunnel to a reaction medium and can participate in chemical reactions. Photocatalysis depends on the energy of the electron-hole pairs and the extent of their separation. While $TiO_2$ is widely employed as a photocatalyst, composite material may be more suitable than $TiO_2$ attributing to different band gap which can effectively reduce the recombination of electron-hole pairs [1]. High-pressure treatment is a new attempt to improve photocatalytic property which may change particle structure and excite particle quantum effect to induce decreasement of the recombination of electron-hole pairs.

$ZnO/SnO_2$ is a kind of excellent photocatalyst [2]. Many experiments proved that simple $ZnO/SnO_2$ mixture system [3, 4] and complex system (e.g., $SnO_2$ gel/ZnO system [5], $Zn_2SnO_4(ZnSnO_3)$ nanocrystal [6, 7]) both have very good effect. However, their structure and properties after high-pressure treatment were not reported so far. In this study, $ZnO/SnO_2$ was prepared by sol-gel method, using zinc acetate dihydrate, oxalic acid, and stannous chloride as raw materials. Then, samples were treated under high pressure at 6 GPa.

## 2. EXPERIMENTAL

### 2.1. Preparation of $ZnO/SnO_2$

$ZnO/SnO_2$ was prepared by the following method. Oxalic acid ($(COOH)_2 \cdot 2H_2O$) solution and stannous chloride($SnCl_2 \cdot 2H_2O$) solution were prepared with absolute ethyl alcohol as the solvent. The stannous chloride solution was slowly added to the oxalic acid solution with stirring. Then, zinc acetate dihydrate solution was slowly added to the mixture solution (with the molar ratio of $ZnO : SnO_2 = 100 : 3$). The resultant solution was aged for 2 hours to obtain the required sol. The sol was heated at 75°C for 12 hours to produce the gel which should be dried over for at least one day, followed by annealing in air at 500°C for 2

hours and cooling to room temperature at last. Pure ZnO was also prepared by a similar method [8].

### 2.2. High-pressure procedure

Cubic anvil press was used as high-pressure equipment which can generate a pressure up to 6 GPa. The samples were assembled in a cube block, and the assembly steps were as follows [9]. At first, powder was processed into a rotund piece using low-pressure molding which was then put into the carbon pipe center with the sodium chloride (NaCl) piece filled in. At last, assembled pipe was put into pyrophyllite block center and also was covered with pyrophyllite. Figure 1 shows the overall assembled cube block.

Assembled sample was put into the center of the cubic anvil press, boosted for 2 minutes, kept pressure for 30 minutes, decompressed for 3 minutes, and then was taken out.

### 2.3. Characterization of assynthesized samples

The mean crystallite size, $d$, was measured from the XRD (D/MAX-YB, RIGAKU) peaks at a scanning rate of 15°/min based on Scherrer's equation:

$$d = \frac{0.89\lambda}{\beta\cos\theta}, \quad (1)$$

where $\lambda$ is the wavelength of the X-rays, $\theta$ is the diffraction angle, and $\beta$ is the full width at half maximum.

IR spectra (60SXB, Nexus) were also used to characterize the samples, and the crystal morphology and micromechanism of the asprepared powder were characterized by HRTEM (JEM-2100F, JEOL Corporation). Absorption spectra were recorded with a spectrophotometer (UV-Vis Spectrophotometer 754PC, Shanghai Spectrophotometer Instruments Co, LTD). The band gap energy was calculated by the following equation:

$$\lambda_g = \frac{1240}{E_g}, \quad (2)$$

where $\lambda_g$ is the wavelength of the characteristic absorption peak value; $E_g$ is the band gap energy.

## 3. RESULTS AND DISCUSSION

### 3.1. XRD spectra analysis

Figure 2 shows the XRD spectra of different samples: pure ZnO, pure ZnO after high-pressure procedure, ZnO/$SnO_2$, and ZnO/$SnO_2$ after high-pressure procedure. The Sn peaks were not observed in the spectra because the concentration of Sn was too low. The diffraction peaks were in good agreement with those given in the standard data (PCPDF, 79-0207) for ZnO and showed a good crystallinity. This means that asprepared materials had crystallized in a hexagonal wurtzite ZnO (see Table 1).

As shown in Figure 2, the peak width of pure ZnO/6G and ZnO($SnO_2$)/6G is obviously wider than that of ZnO and

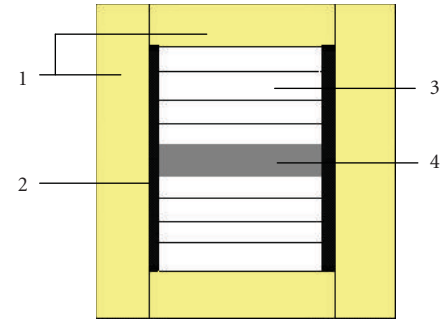


Figure 1: sketch diagram of assembled cube block (1) pyrophyllite, (2) carbon pipe, (3) NaCl piece, and (4) sample piece.

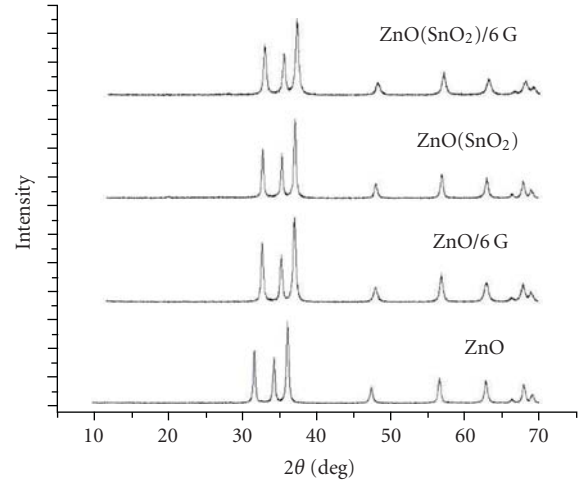


Figure 2: X-ray diffraction spectra of pure ZnO, pure ZnO after high pressure, ZnO/$SnO_2$, and ZnO/$SnO_2$ after high-pressure procedure.

ZnO($SnO_2$) because of high-pressure effect. For the mean crystallite size, $d$ is in inverse proportion to the full width at half maximum $\beta(d = 0.89\lambda/(\beta\cos\theta))$, indicating that the high-pressure procedure can cause the initial grain size to decrease. Table 2 lists the calculation results of the average particle size of the samples. About the reason for the particle size decreasing, there are two possibilities. One is that the high pressure can smash the particles and the other is that the high pressure can make the crystallite more dense by grain squeeze.

The peak intensity of pure ZnO and ZnO/$SnO_2$ also changed after high-pressure procedure, which reveals that the high pressure may affect the orientation of the samples, but this part needs further in-depth study.

### 3.2. IR spectra analysis

Figure 3 shows the IR spectra of different samples. From the figure, it can be seen that peaks occur around wavenumber 400 $cm^{-1}$ and 500 $cm^{-1}$ which are due to stretching mode of ZnO. After high-pressure treatment, the characteristic peak of ZnO moved from wavenumber 438 $cm^{-1}$ to 451 $cm^{-1}$, and

Table 1: the XRD parameters of (h k l), and *d*-value of standard wurtzite phase ZnO and samples.

| (h k l) | Int-f | PCPDF79-0207 d(nm) | ZnO d(nm) | ZnO/6G d(nm) | $ZnO/SnO_2$ d(nm) | $ZnO/SnO_2$/6G d(nm) |
|---|---|---|---|---|---|---|
| (1 0 0) | 570 | 0.28204 | 0.28220 | 0.28272 | 0.28220 | 0.28203 |
| (0 0 2) | 416 | 0.26062 | 0.26107 | 0.26151 | 0.26092 | 0.26078 |
| (1 0 1) | 999 | 0.24806 | 0.24820 | 0.24860 | 0.24820 | 0.24793 |
| (1 0 2) | 210 | 0.19141 | 0.19140 | 0.19163 | 0.19140 | 0.19133 |
| (1 1 0) | 291 | 0.16284 | 0.16268 | 0.16284 | 0.16268 | 0.16263 |
| (1 0 3) | 251 | 0.14793 | 0.14784 | 0.14801 | 0.14788 | 0.14835 |
| (1 1 2) | 203 | 0.13810 | 0.13796 | 0.13803 | 0.14082 | 0.14052 |

Table 2: Average particle size of different sample.

| Sample | ZnO | ZnO/6G | $ZnO(SnO_2)$ | $ZnO(SnO_2)$/6G |
|---|---|---|---|---|
| Size | 17.22 | 16.20 | 19.68 | 14.50 |

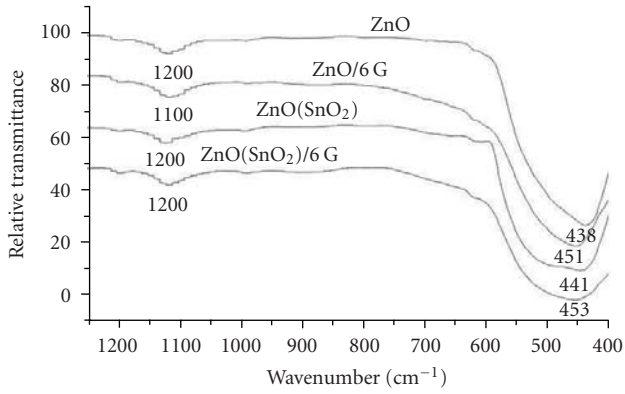


Figure 3: IR spectra of pure ZnO, pure ZnO after high-pressure procedure, $ZnO/SnO_2$ and $ZnO/SnO_2$ after high-pressure procedure.

the characteristic peak of $ZnO/SnO_2$ moved from wavenumber 441 $cm^{-1}$ to 453 $cm^{-1}$. It was said that the characteristic peaks of both pure ZnO and $ZnO/SnO_2$ showed blue shift after high-pressure treatment. It was also noticed that the characteristic peak width of ZnO/6G is broader than that of ZnO, and the peak width of $ZnO(SnO_2)$ and $ZnO(SnO_2)$/6G is wider than that of ZnO and ZnO/6G.

There are a few reasons to explain the above two phenomena. Peaks occurred with blue shift indicate that high pressure may improve the samples crystallinity and shorten the distance of crystal lattice, which causes enhancing of the field effect of crystal and increasing of the band vibration frequency. In this theory, we exclude the assumption that the decrease of particle size is caused by smashing effect. On the peaks width, it may be caused by interfacial effect and size distribution effect. After high-pressure treatment, the particle interface defects increased, and the size distribution was more disordered. The characteristic peaks of $ZnO(SnO_2)$ and $ZnO(SnO_2)$/6G are wider than those of ZnO and ZnO/6G, respectively, because of interfacial effect and size distribution effect.

### 3.3. Morphology and micromechanism

From the HRTEM image of ZnO (a), it can be seen that the particles show a homogeneous size of 18 nm, consistent with the XRD results (17.22 nm). Figure 4(b) shows the good crystallinity of ZnO, also consistent with the XRD results.

Compared with ZnO images, there was some difference in ZnO/6G images (Figures 4(c) and 4(d)). Deformation area near the crystal grain boundary is obvious in Figures 4(c) and 4(d). Maybe it was caused by squeezing between crystals. From Figure 4(c), it can be seen that the crystal lattice was distorted by the grain squeeze below, while the area in Figure 4(d) was distorted by the grain squeeze above, which reveals that deformation always occurs around crystalline exterior. So, it can be supposed that the decrease of particle size was caused partially by particle squeeze.

Figures 5(a) and 5(b) show the $ZnO/SnO_2$ morphology and microstructure. In Figure 5(a), the big particles are ZnO which are about 20 nm, while $SnO_2$ particles are much smaller about several nanometers. The ZnO particles were surrounded by $SnO_2$ particles. So, this microstructure could improve photocatalytic properties [1]. Because of uneven size, the characteristic peak of $ZnO/SnO_2$ in IR spectra was wider than that of pure ZnO.

In Figures 5(c) and 5(d), the deformation areas of $ZnO/SnO_2$ particles were obvious. Compared with pure ZnO after high-pressure treatment, the deformation area of $ZnO/SnO_2$ was more complicated. Probably, the particle size of $ZnO/SnO_2$ was more uneven than that of pure ZnO, and the grain squeeze was more complicated. Moreover, the particle gap was smaller than that of pure ZnO, indicating a greater degree of compression, which was in agreement with the XRD result (Table 2).

### 3.4. UV-Vis spectra and band gap energy

The UV-Vis spectra of the samples are displayed in Figure 6. The top absorption peak of both ZnO and $ZnO/SnO_2$ occurs at the wavelength of 380 nm (3.26 eV). The band gap energy of $ZnO/SnO_2$ was little changed after doping $SnO_2$ particles, and the intrinsic absorption peak of $SnO_2$ did not appear, which may be due to the reunion phenomenon of the $SnO_2$ particles. For the composite structure, the UV absorption strength of $ZnO/SnO_2$ was higher than that of ZnO. After high-pressure treatment, the characteristic absorption peak values of ZnO and $ZnO/SnO_2$ increased

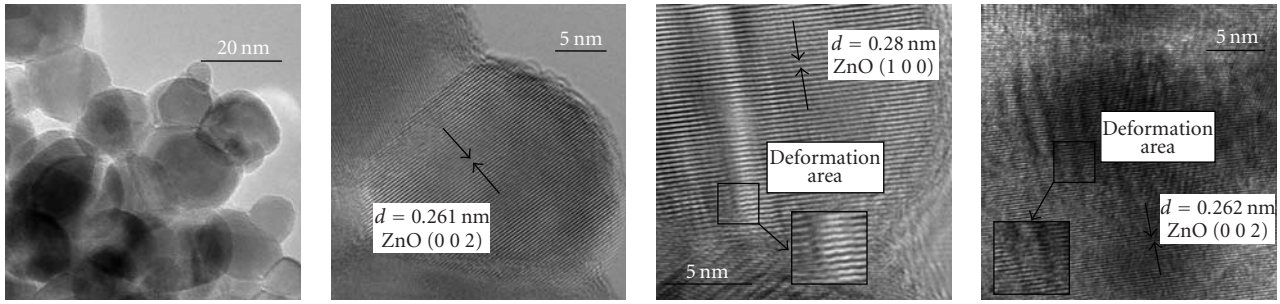


Figure 4: HRTEM images of different samples. (a) ZnO morphology image, (b) ZnO crystal lattice image, (c) ZnO/6G crystal lattice image, (d) ZnO/6G crystal lattice image.

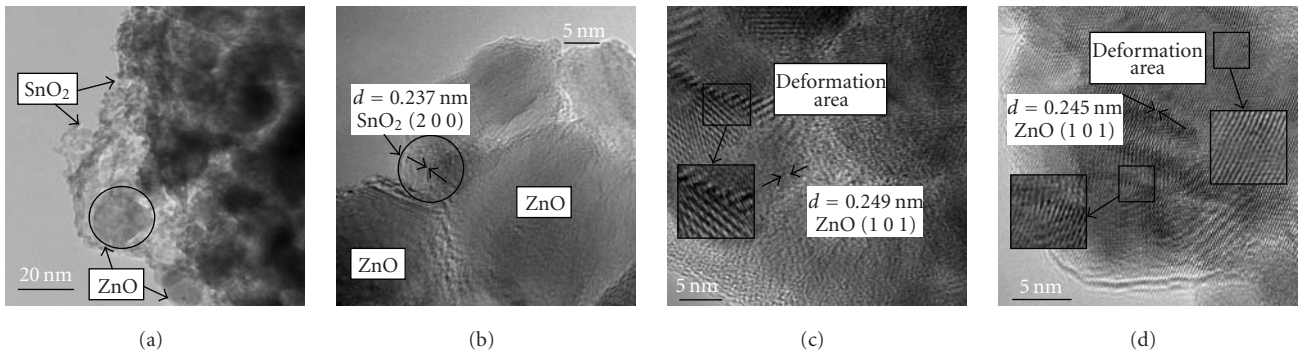


Figure 5: HRTEM image of different samples. (a) ZnO/$SnO_2$ morphology image, (b) ZnO/$SnO_2$ crystal lattice image, (c) ZnO ($SnO_2$)/6G crystal lattice image, and (d) ZnO ($SnO_2$)/6G crystal lattice image.

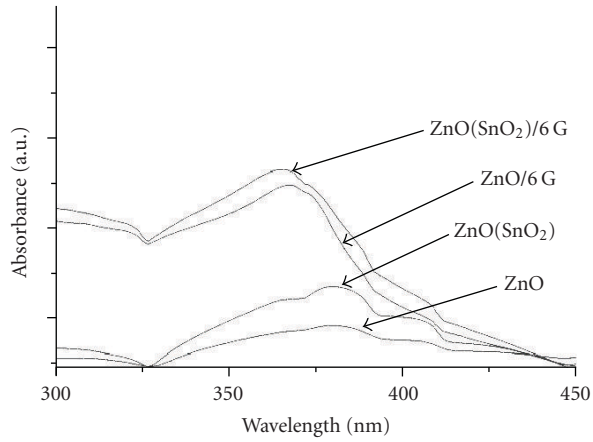


Figure 6: UV-Vis absorption spectra of pure ZnO, pure ZnO after high-pressure procedure, ZnO/$SnO_2$, and ZnO/$SnO_2$ after high-pressure procedure.

with obvious blue shift, which are at wavelength of 368 nm (3.37 eV) and 366 nm (3.39 eV), respectively. It revealed that after high-pressure procedure, the band gap energy of ZnO and ZnO/$SnO_2$ increased so that it can decrease the recombination of electron-hole pairs effectively. For the inverse relationship between the recombination efficiency of electron-hole pairs and the photocatalytic property, it can be inferred that after high-pressure procedure ZnO/$SnO_2$ has some benefits for photocatalytic property.

## 4. CONCLUSION

In this work, the ZnO/$SnO_2$ powders were synthesized by sol-gel method and treated by high-pressure procedure. The X-ray diffraction (XRD) spectra of the samples showed that the nanocrystals had good crystallinity, and the size decreased after high-pressure treatment. The infrared (IR) spectra showed that the distance of crystal lattice was shortened after high-pressure treatment, and the size distribution became more uneven after doping. Through high-resolution transmission electron microscope (HRTEM), some morphology information and evidence support to IR spectroscopic analysis results were obtained. The UV-Vis spectra of the samples showed that ZnO/$SnO_2$ has some benefits for photocatalytic property after high-pressure procedure.

## ACKNOWLEDGMENT

This work was supported by the National Natural Science Foundation of China Grants no. 40672028 and 40372028.

## REFERENCES


[1] K. Tennakone and J. Bandara, "Photocatalytic activity of dye-sensitized tin(IV) oxide nanocrystalline particles attached to zinc oxide particles: long distance electron transfer via ballistic transport of electrons across nanocrystallites," *Applied Catalysis A*, vol. 208, no. 1-2, pp. 335–341, 2001.

[2] J. Bandara, K. Tennakone, and P. P. B. Jayatilaka, "Composite Tin and Zinc oxide nanocrystalline particles for enhanced charge separation in sensitized degradation of dyes," *Chemosphere*, vol. 49, no. 4, pp. 439–445, 2002.

[3] M. Zhang, G. Sheng, J. Fu, T. An, X. Wang, and X. Hu, "Novel preparation of nanosized ZnO-$SnO_2$ with high photocatalytic activity by homogeneous co-precipitation method," *Materials Letters*, vol. 59, no. 28, pp. 3641–3644, 2005.

[4] C. Wang, X. Wang, B.-Q. Xu, et al., "Enhanced photocatalytic performance of nanosized coupled ZnO/$SnO_2$ photocatalysts for methyl orange degradation," *Journal of Photochemistry and Photobiology A*, vol. 168, no. 1-2, pp. 47–52, 2004.

[5] K. Melghit, M. S. Al-Rubaei, and I. Al-Amri, "Photodegradation enhancement of Congo red aqueous solution using a mixture of $SnO_2 \cdot xH_2O$ gel/ZnO powder," *Journal of Photochemistry and Photobiology A*, vol. 181, no. 2-3, pp. 137–141, 2006.

[6] X. Lou, X. Jia, J. Xu, S. Liu, and Q. Gao, "Hydrothermal synthesis, characterization and photocatalytic properties of $Zn_2SnO_4$ nanocrystal," *Materials Science & Engineering A*, vol. 432, no. 1-2, pp. 221–225, 2006.

[7] J. Xu, X. Jia, X. Lou, and J. Shen, "One-step hydrothermal synthesis and gas sensing property of $ZnSnO_3$ microparticles," *Solid-State Electronics*, vol. 50, no. 3, pp. 504–507, 2006.

[8] J. Cao, "Study on nanometer ZnO prepared by sol-gel method," *Chemical Engineer*, vol. 4, pp. 5–8, 2005.

[9] Z.-Y. Wu, L. Cao, Z.-X. Bao, C.-X. Liu, Q.-S. Li, and B.-S. Zou, "The properties and structural investigation of ZnO nanocrystals under pressure," *Chinese Journal of High Pressure Physics*, vol. 1, pp. 45–49, 2003.

Hindawi Publishing Corporation
Journal of Nanomaterials
Volume 2008, Article ID 749508, 8 pages
doi:10.1155/2008/749508

*Research Article*

# Synthesis of Nanostructured Nanoclay-Zirconia Multilayers: a Feasibility Study

**Hao Chen,[1] Guoping Zhang,[2] Kathleen Richardson,[1,3] and Jian Luo[1,3]**

[1] *School of Materials Science and Engineering, College of Engineering & Science, Clemson University, Clemson, SC 29634, USA*
[2] *Department of Civil and Environmental Engineering, College of Engineering, Louisiana State University, Baton Rouge, LA 70803, USA*
[3] *Center for Optical Materials Science and Engineering Technologies (COMSET), Clemson University, Clemson, SC 29634, USA*

Correspondence should be addressed to Jian Luo, jianluo@clemson.edu

Received 2 September 2007; Accepted 5 February 2008

Recommended by Junlan Wang

This paper reports the first effort to synthesize a new class of inorganic nanostructured materials consisting of alternating ultrathin layers of nanoclays and oxide ceramics. A novel solution-based layer-by-layer (LBL) deposition technique was developed to prepare multilayers of hydrated Zr cations and nanoclays. This LBL deposition technique is devised by integrating an electrostatic-mediated dip coating method for making nanoclay-polymer multilayers with a successive ionic layer adsorption and reaction method for making ultrathin oxide films. Nanostructured clay-zirconia multilayer composites formed through subsequent annealing. Characterization by scanning electron microscopy, energy dispersive X-ray spectroscopy, and X-ray diffraction confirmed that these films are uniform and crack-free, consist of no detectable impurities, and possess nanoscale-layered structure. The incorporation of nanoclays facilitates the electrostatic-mediated assembling of multilayers, enhances the structural integrity, and provides a generic framework to construct functionally graded materials. Potential applications are envisaged.



## 1. INTRODUCTION

The last decade has seen tremendous developments in the "wet" colloid chemical synthesis of nanosized and nanostructured materials, which was inspired by "biomineralization and hierarchically organized self-assembly" [1]. This wet synthesis technique utilizes alternating layer-by-layer (LBL) deposition process, which is enhanced by electrostatic assembling or surface-mediated adsorption and reaction. It has several major advantages, such as relative ease of preparation, low cost, and high versatility. Through this technique, a variety of nanostructured materials with improved properties or enhanced functionalities have been developed, including inorganic [2, 3] or hybrid organic-inorganic [4] films. In particular, inspired by the special mortar-brick nanostructure of nacre and its superior mechanical properties, hybrid multilayers consisting of alternating organic polymer and inorganic nanoclay layers have been made by an LBL deposition and assembly method [5, 6]. This method was modified from a more general method for making polyelectrolyte multilayers where substrates are alternately dipped into polycation and polyanion solutions to form polyelectrolyte thin films [7].

In parallel, a successive ionic layer adsorption and reaction (SILAR) method [8–10] was developed initially for the deposition of sulfide films. The SILAR method grows sulfide thin films by repeating deposition cycles consisting of four steps: dipping in cationic precursor solutions for adsorption of cations, rinsing to remove physisorbed cations, dipping into anionic ($S^{2-}$) solutions to form a monolayer or submonolayer of sulfides, and rinsing again. This SILAR technique has recently been adapted to deposit oxide (e.g., ZnO) films [9, 10]. Notably, this technique has been used for making ultrathin (e.g., 1–10 nm) gate dielectric oxide films [11, 12] and combined with a hydrothermal annealing process for low-temperature synthesis of nanocrystalline oxide films [13]. More recently, the feasibility of a modified SILAR technique without rinsing steps to prepare thin zirconia films has been reported [14] and the associated film growth kinetics has been studied [15]. The latter approach can be regarded as a surface hydrolysis and precipitation process assisted by electrostatic interactions [14, 15].

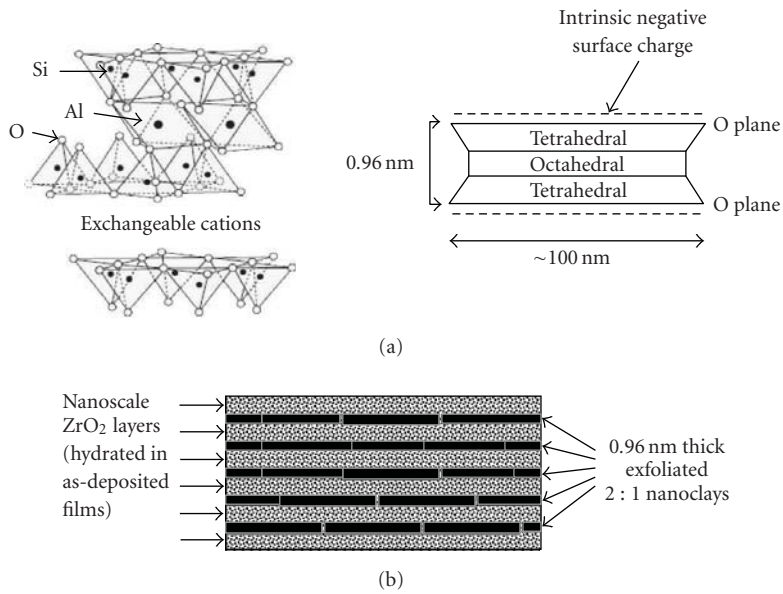


Figure 1: (a) The structure of 2 : 1 clay nanoplatelets exfoliated from MMT. (b) A targeted multilayer structure to be synthesized using a new LBL assembling technique via making use of the intrinsic negative surface charges and unique platy shape of nanoclays (as shown in (a)). In principle, the thickness and chemical composition of each nanometer-thick oxide layer can be tuned individually, offering versatility in engineering these nanostructured films with a wide range of potential applications to be explored in future studies.

A key underlying mechanism in the wet chemical construction of nanomaterials is the solution-based self-assembly aided by electrostatic attraction force between oppositely charged components (e.g., ions, polyions). The use of platy-shaped clay nanoplatelets with intrinsic, permanent negative surface charges in constructing nanostructured multilayers is an innovation to extend the capabilities of the conventional ion/polyion aided self-assembly techniques. Clay minerals are hydrous layered aluminosilicates, and montmorillonite (MMT) is a swelling clay mineral consisting of 2 : 1 layers (i.e., 2 tetrahedral and 1 octahedral sheets per layer, as shown in Figure 1(a)). These 2 : 1 layers can be separated in $Na^+$ or $Li^+$ rich solutions forming exfoliated clay nanoplatelets of ~1 nm in thickness. The permanent negative surface charges of nanoclays not only promote the electrostatic self-assembly process and its efficiency, but also render a high lateral bond strength within the constructed multilayers or their precursors [1]. In addition, the high aspect ratio of platy nanoclays provides an ideal planar surface for self-assembly and growth of other nanomaterials. To date, hybrid inorganic clay and organic polymer (including biopolymer) nanostructured multilayers have been developed [16], but development in making nanoclay-based inorganic nanocomposites or multilayers has not been reported. Due to the inherent thermal and chemical instability of organic polymers, hybrid organic and inorganic multilayers have limitations in some specialized applications, such as in high-temperature environments. In this study, we attempt to develop a new class of inorganic oxide-clay nanostructured multilayers.

The paper presents the preliminary findings of this research with a particular focus on the feasibility of making hydrated inorganic oxide-clay nanostructured multilayers using the newly developed solution-based LBL synthesis technique. The ultimate goal of this study is to develop purely inorganic, nanostructured nanoclay-oxide multilayers, as shown in Figure 1(b). Zirconia is chosen as the model oxide because we have recently developed a modified SILAR technique to make pure or doped zirconia films [14] and a relevant film growth model [15]. Zirconia thin films have a wide variety of applications, such as protective coatings, insulating or dielectric ceramic layers, and other functional ceramics.

## 2. EXPERIMENTAL

### 2.1. Materials

Silicon wafers with thermally oxidized surface layers ($Si/SiO_2$) were purchased and cut into pieces of $1 \times 2\,cm^2$, which are used as substrates. The $Si/SiO_2$ wafers were ultrasonically cleaned in 0.1 M NaOH solution for 20 minutes, immersed into piranha solution (3 vol. of 95–98 wt.% $H_2SO_4$:1 vol. of 30 wt.% $H_2O_2$) for 20 minutes, rinsed with deionized water 4 times and dried in air. A Na-MMT clay (Cloisite® $Na^+$) was purchased from Southern Clay Products (Gonzales, Tex, USA). The 0.03 wt.% clay suspension (pH = 7.24) was prepared by stirring clays with magnet at 1000 rpm speed in deionized water for 20 minutes and then ultrasonicated for 20 minutes to achieve complete dispersion and exfoliation. Other chemicals were purchased from Sigma (Sigma-Aldrich, Saint Louis, MO, USA). Two different zirconium cationic precursor solutions were used to examine their suitability for growing the zirconia nanolayers on clay nanoplatelets, including 0.1 M zirconium chloride solution ($ZrCl_4$, pH = 1.32) prepared from zirconium

(IV) oxychloride octahydrate and zirconium acetate solution ($ZrAc_4$, pH = 4.14) prepared from zirconium (IV) acetate hydroxide. Sodium poly(styrenesulfonate) (PSS) and poly(ethyleneimine) (PEI) were dissolved in deionized water at concentrations of 1.5 mg/mL for the preparation of polymer-clay multilayers.

### 2.2. Wet chemical synthesis and annealing

Two steps were involved in the synthesis of oxide-clay multilayers: (1) wet chemical construction of multilayer precursors (termed as-deposited films), and (2) thermal dehydration and crystallization at elevated temperatures to form the annealed films. This preliminary study particularly focused on demonstrating the feasibility of the first step, which is more critical for developing the targeted clay-oxide multilayers. Thus the dehydration and thermal annealing conditions were preselected as a rule of thumb to be 600°C in air for 2 hours under 1 atmospheric pressure, since most MMTs can maintain their crystal structure intact (i.e., no dehydroxylation) below temperatures of 600–650°C. However, the control parameters of thermal annealing or hydrothermal treatment (i.e., the second step of synthesis) will be further optimized in future studies.

A computer-controlled programmable Nima dip coater (Nima Technology Ltd., Coventry, UK) was used to synthesize nanostructured as-deposited multilayers. To verify the LBL deposition method and the functions of the dip coater, nanoclay-polymer films were prepared following the recipe in Lvov et al. [17]. The $Si/SiO_2$ substrates were pretreated by dipping into PEI, PSS, and PEI solutions each for 20 minutes. The pretreated substrates were then dipped into a clay suspension for 20 minutes, rinsed with water for 2 minutes, dipped into a PEI solution for 20 minutes, and rinsed again with water for 2 minutes to complete one deposition cycle. This four-step deposition cycle was repeated 8 times to make nanoclay-polymer multilayers, denoted as (PEI-PSS-PEI)-$(MMT\text{-}PEI)_8$. Both the dipping and withdrawing speeds were controlled at 20 mm per minute.

To prepare nanoclay-oxide multilayers, the precleaned silicon substrates were dipped into a zirconium cationic precursor solution ($ZrCl_4$ or $ZrAc_4$) and the exfoliated nanoclay suspension alternately without interdipping rinsing. The deposition cycle was repeated 15 to 30 times to prepare the as-deposited multilayers. Both the dipping and withdrawing speeds were controlled at 20 mm per minute. The holding time was kept 45 seconds in air, Zr precursor solution and clay suspension. After completing a certain number ($n$) of deposition cycles, the substrates were then air-dried at room temperature to form the as-deposited films or annealed isothermally to 600°C for 2 hours to form the annealed films, denoted as $(\text{clay-oxide})_n$. A constant heating and cooling rate of 5°C per minute was used during annealing.

### 2.3. Characterization

Both as-deposited (i.e., air-dried) and annealed films were characterized by a Hitachi S4800 field-emission scanning electron microscope (FE-SEM) equipped with an energy dispersive X-ray spectroscopy (EDXS) analyzer. SEM specimens were coated with Pt/Au for increased conductivity. In addition, a Hitachi S3500 variable-pressure SEM was employed to examine specimens without conductive coating. Both in-plane and cross-sectional surfaces of the multilayers were studied. Fresh cross-sectional surfaces were created by carefully cleaving the Si wafers, while protecting the films with soft filter paper. Multiple measurements on different points were conducted to obtain the film thickness on cross-sectional surfaces under SEM. EDXS was also performed to analyze both qualitatively and quantitatively the elemental composition of the multilayers.

X-ray diffraction (XRD) was performed on both as-deposited and annealed films in a Scintag diffractometer using Cu-$K_\alpha$ radiation ($\lambda = 1.5418$ Å) generated at 40 kV and 35 A at a scan speed of $1^\circ(2\theta)$ per minute, step size of 0.01°, and a scan range of $1\text{–}60^\circ 2\theta$. In addition, a bare $Si/SiO_2$ substrate was scanned by XRD to examine any potential influence of the substrate on the observed diffraction patterns of the ultrathin multilayers.

## 3. RESULTS AND DISCUSSION

### 3.1. Clay-polymer multilayers

SEM images of the planar and cross-sectional surfaces of the as-deposited nanoclay-polymer multilayers [(PEI-PSS-PEI)-$(MMT\text{-}PEI)_8$] are shown in Figure 2. Some unevenly piled or protruded MMT platelets can be observed in the planar surfaces, as shown in Figure 2(a). The cross-sectional surface, as shown in Figure 2(b), exhibits nacre-like layered structure, which is similar to that observed in the films developed by Tang et al. [18]. The average measured film thickness is 40 ± 9 nm, of which 10 nm is from the precursor polymer film [17]. Thus the thickness of a single $(MMT\text{-}PEI)_1$ layer formed through a complete deposition cycle is approximately ~3.75 nm, which is consistent with the previously reported value of 3.3 nm per deposition cycle [17]. It was postulated that the highly branched polycation PEI works as "electrostatic glue" [17] to assemble clay platelets. In conclusion, polymer-nanoclay multilayers with similar nanostructure were reproduced in our laboratory. This verified our equipment and procedures and enabled further exploration of synthesizing the new nanoclay-oxide multilayers.

### 3.2. Clay-zirconia multilayers

The SEM images of as-deposited films prepared by $ZrCl_4$ and $ZrAc_4$ cationic precursor solutions are shown in Figures 3 and 4, respectively. The as-deposited films were dried in air, thus either nanoclays or hydrated Zr cations are not completely dehydrated, and water molecules exist within the interface of clay nanoplatelets and Zr cations. Both films appear to be reasonably uniform and crack-free. Furthermore, they both exhibit observable layered structures in cross-sectional surfaces under SEM (Figures 3(b) and 4(b)).

Evidently, the films made by $ZrAc_4$ cationic precursor solutions have significantly smoother surface and more regularly (parallel) layered structure than those by $ZrCl_4$

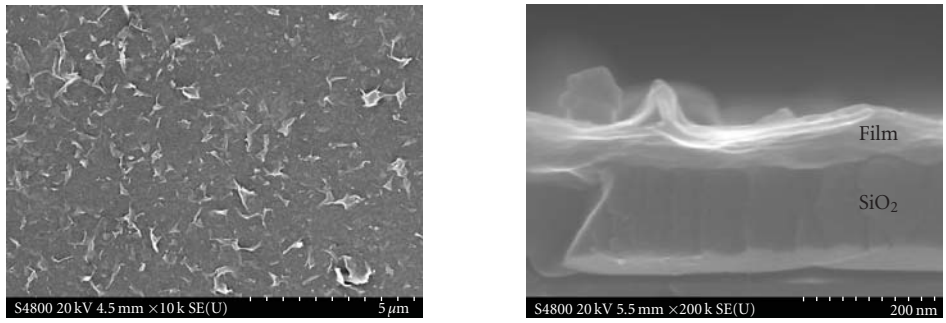


(a) (b)

Figure 2: (a) Planar surface and (b) cross-sectional surface SEM images of as-deposited nanoclay-polymer [(PEI-PSS-PEI)-(nanoclay-PEI)$_8$] films.

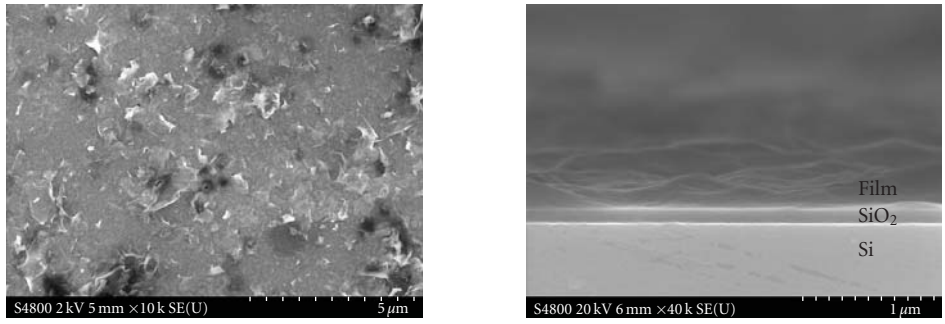


(a) (b)

Figure 3: (a) Planar surface and (b) cross-sectional surface SEM images of as-deposited nanoclay-zirconia multilayers made via $ZrCl_4$ cationic solution.

precursor solutions (Figure 3 versus Figure 4). The clay nanoplatelets are better oriented in the films prepared by $ZrAc_4$ cationic solutions, while peeled and protruded edges of clay platelets are frequently observed in the $ZrCl_4$ prepared films, as shown in Figure 3(a). For films prepared by $ZrCl_4$ precursor solutions, the layered structure is less close-packed with occasional, sparsely distributed open voids, as shown in Figure 3(b). The nanoclay-oxide multilayers prepared using $ZrAc_4$ precursor solutions also appear to have lower surface roughness than those polymer-nanoclay multilayers prepared in this and prior [17] studies. Based on these results, $ZrAc_4$ cationic precursor solutions are used exclusively to make multilayers in further studies.

SEM images of the planar and cross-sectional surfaces of annealed films are shown in Figure 5. The annealed films appear to be denser and more uniform than the as-deposited ones. Some indications of the layered structure can be observed in the cross-sectional surfaces under SEM, as shown in Figures 5(a) and 5(b). It should be noted that the observed cross-sectional surfaces were influenced by the actual (somewhat random) cleaving process and hence the layered structure is not always clearly visible. The surfaces of annealed films, as shown in Figure 5(c) are also smoother than those of as-deposited films, as shown in Figure 4(a); yet, some clay nanoplatelets can still be seen in Figure 5(c).

EDXS analysis of as-deposited and annealed films found the presence of Al, Si, and Zr, without other metal impurities. A representative EDXS spectrum is shown in Figure 6. Quantitative elemental analysis was also attempted with results shown in Table 1. We believe that the excess amounts of Si and O measured by EDXS are from the Si/$SiO_2$ substrates. Since the films are thin (less than 100 nm) and the penetration depth of an electron beam into a nonmetallic material is usually about 1 $\mu$m, the beam must be smeared. Although the quantitative compositional measurements are probably not accurate due to the beam spreading effect, it can be concluded that these films consist of oxides (or hydroxides) of Al, Si, and Zr without significant impurities of other elements.

XRD patterns of as-deposited and annealed multilayers are shown in Figure 7, in which the $d$-spacings are labeled for all peaks. As-deposited films appeared to be largely amorphous, but a series of low-angle peaks were observed. The 1.2 nm peak should result from hydrated montmorillonite, which usually exhibits the first peak (001) around 1.0–2.0 nm, depending on the degree of hydration (e.g., relative humidity) and the types of interlayer cations [19]. The as-deposited films were air-dried (i.e., the relative humidity is unknown) and contain $Zr^{4+}$ as interlayer cations. Therefore, the montmorillonite in the air-dried films is likely to have a basal spacing of 1.2 nm. The presence of this peak indicates

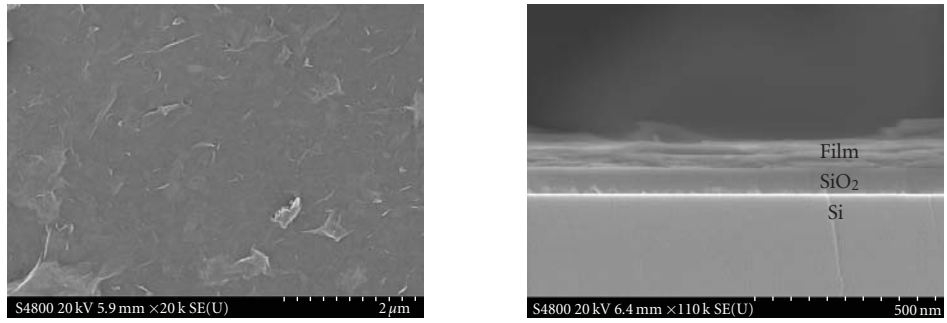


(a) (b)

Figure 4: (a) Planar surface and (b) cross-sectional surface SEM images of as-deposited nanoclay-zirconia multilayers made by $ZrAc_4$ cationic solutions.

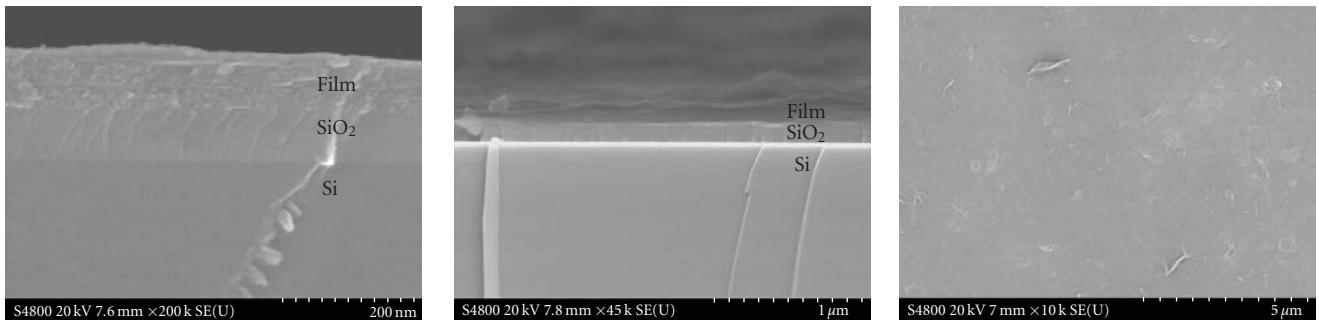


(a) (b) (c)

Figure 5: (a), (b) cross-sectional surface, and (c) planar surface SEM images of annealed nanoclay-zirconia films made by $ZrAc_4$ precursor solutions with 25 deposition cycles.

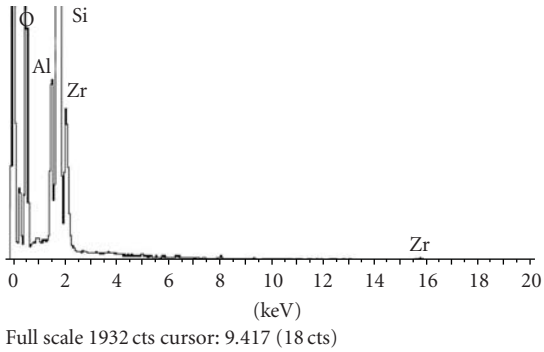


Figure 6: A representative EDXS spectrum for an annealed film.

Table 1: EDXS compositional analysis. Each value is the average of three measurements. The measured excessive amounts of Si and O are from $Si/SiO_2$ substrates, an artifact due to the spread of electron beams.

| Element | Atomic % | |
|---|---|---|
| | As-deposited | Annealed |
| O | 61.7 | 35.3 |
| Al | 3.6 | 1.2 |
| Si | 30.6 | 59.9 |
| Zr | 4 | 3.6 |

that some multiple layers of clay nanoplatelets are absorbed in dipping, which is not desired. The 5.7 nm peak represents the periodic thickness formed by each deposition cycle for the multilayers without annealing. The origin of the 2.3 nm peak is currently unclear and worth further investigation. It is noteworthy that the 1.2 nm peak is the sharpest of all peak, as shown in Figure 7(a). Given the low crystallinity of clay minerals, all other broad peaks suggest that the as-deposited multilayers possess much less ordered atomic structure or crystallinity, as expected. Nevertheless, a good layered nanostructure is clearly present in the as-deposited film with a periodic thickness of ~5.7 nm, as shown in Figure 7, indicating the success of the LBL deposition.

For annealed specimens Figure 7(b), only two peaks are observed. A broad weak peak at 1.6 nm is probably caused by the (002) reflection of the periodic thickness of 3.2 nm (see Section 3.3). The shape of the peak also indicates that the periodicity of the layers is not perfect, which is probably caused by the crystallization process during annealing. The low-angle scan did not find the (001) reflection at 3.2 nm, and the reason is unclear at present. The second peak at $d$ = 0.3 nm matches $ZrO_2$ (111) reflection, indicating the formation of nanocrystalline $ZrO_2$. (It is noted that a broad weak peak whose intensity varies with the specific experimental

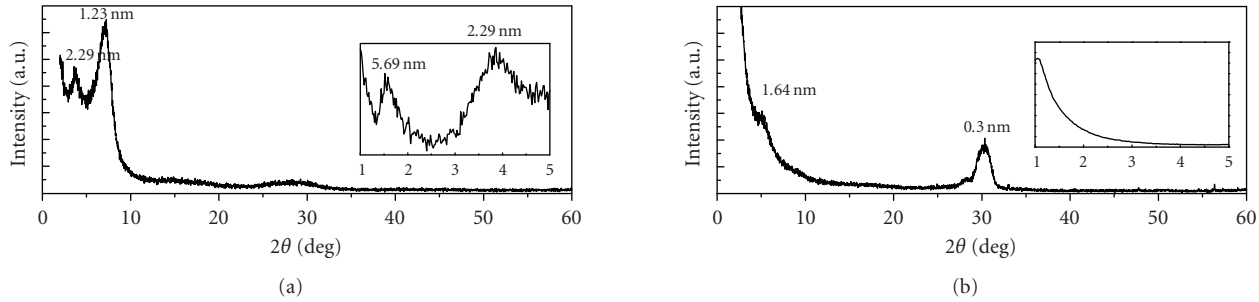


Figure 7: XRD patterns of (a) as-deposited and (b) annealed films formed by 20 deposition cycles and $ZrAc_4$ cationic solutions. The two XRD scans were carried out at the same conditions (scan rate and slit size) and the patterns are shown in the same intensity scale. The insets (which are shown in different intensity scales) are additional scans at low angles with a smaller slit.

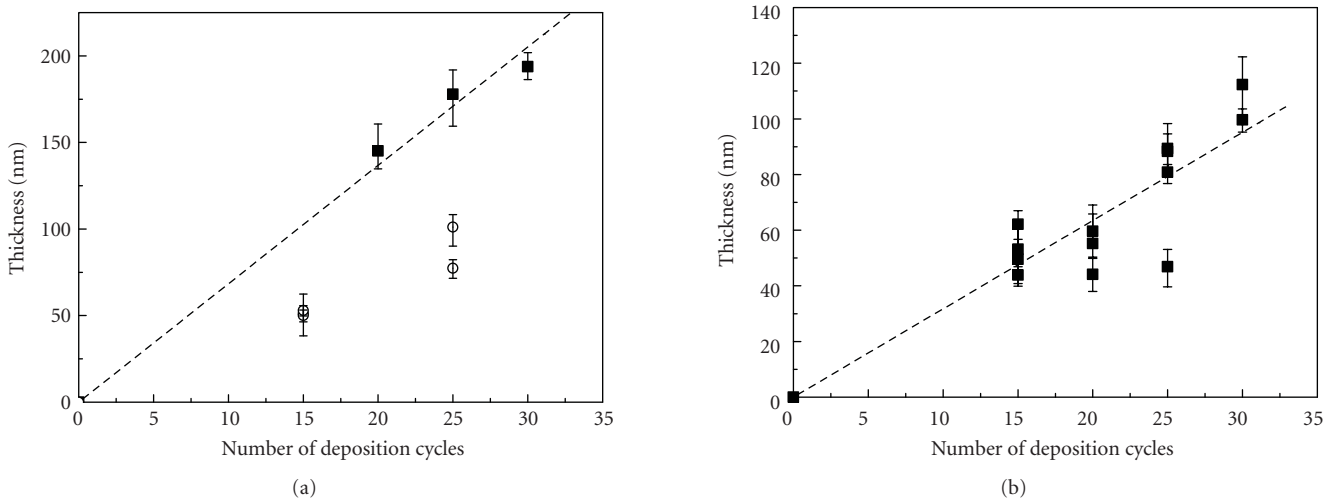


Figure 8: Thickness versus the number of deposition cycles for (a) as-deposited and (b) annealed films made by $ZrAc_4$ precursor solutions. In (a), it is assumed that open circles represent measurement artifacts (as-deposited films where the part of layered films peeled off during cleaving of the substrates). Error bars represent the data range. Lines represent the best linear fits.

conditions was sometimes observed around 30° $2\theta$, which is believed to be caused by the $Si/SiO_2$ substrates [14, 15]. This is also seen in the XRD patterns of the as-deposited films, although a lower intensity was observed. Although these two measurements were made in the same conditions, it is still uncertain whether or not this peak at ~30° $2\theta$ is an artifact from the substrate). Assuming that this peak at ~30° $2\theta$ is indeed from $ZrO_2$ (111) reflection, the mean grain size of the nanocrystalline $ZrO_2$ was estimated to be ~9.7 nm based on the peak width. Given that periodic thickness in the annealed film is approximately 3.2 nm (see Section 3.3), the $ZrO_2$ crystallite size of 9.7 nm indicates that the growth of nanocrystals may start to break the parallel multilayer structure (by displacing or heaving up nanoclay platelets which should act as barriers between two adjacent oxide layers), which is consistent with the absence of or week low-angle reflections from the annealed multilayers. Nonetheless, the existence of some layered structures is evident by SEM observations on the cross-sectional surfaces, as shown in Figures 5(b) and 5(c), but the layered structure is probably less regular, presumably due to the growth of $ZrO_2$ nanocrystals.

It is generally expected that montmorillonites are chemically stable for heating or annealing at 600°C [20]. More annealing experiments will be conducted to investigate how nanoclays react with Zr complexes during high temperatures, which will help form high temperature endurable nanoclay-oxide multilayers.

It is worth emphasizing that the annealed films still remained layered structure after cutting and no significant cracking or delaminating was observed in Figure 5, in spite of up to 50% linear shrinkage occurred during annealing, as discussed below.

### 3.3. Film growth rate through LBL deposition

The thickness of as-deposited and annealed films versus the number of deposition cycles prepared through $ZrAc_4$ cationic precursor solutions are shown in Figures 8(a) and 8(b), respectively. As-deposited multilayers are expected to exhibit low cohesion between layers, and part of the multilayers might fall off when they were cut along with the substrate for cross-sectional surface observations. This may be

responsible for the measured unusually small thickness values (i.e., the three open circles shown in Figure 8(a)). If these data are excluded, the measured film thickness for both as-deposited and annealed films increase almost linearly with the number of deposition cycles. Through linear regression, the average film growth rates of as-deposited and annealed multilayers are ~6.8 nm and ~3.2 nm per cycle, respectively. In other words, annealing at 600°C for 2 hours caused a ~50% linear shrinkage of film thickness, which is nearly the same as that previously observed for pure $ZrO_2$ films [14, 15]. The shrinkage also indicates dehydration and sintering have occurred during annealing. The periodic layer spacing of the as-deposited multilayers was ~5.7 nm, as measured by XRD, as shown in Figure 7, which should be more accurate than the value (~6.8 nm) obtained by SEM measurement. However, the XRD and SEM measurements (5.7 nm versus 6.8 nm) are rather consistent.

### 3.4. Issues, future studies, and potential applications

As discussed above, the preliminary results are promising. However, the combined XRD, SEM, and EDXS characterization indicates that the multilayers synthesized in this study are not yet perfect, and there are some deviations from the targeted nanostructure shown in Figure 1(b). First, the 1.2 nm peak in XRD patterns in Figure 7(b) indicates that nanoclays are not completely exfoliated into single 2 : 1 layers and multiple layers of clay nanoplatelets are deposited within the films. This can be further improved by fine tuning the clay suspension chemistry, exfoliation method, and dipping process. Second, while as-deposited films exhibit fairly good layered structure, the thermally annealed films appear to possess relatively poor periodicity, as evident by both SEM and XRD. Annealing at 600°C for 2 hours in air was the only dehydration process that has been tested so far (since this study focused more on the feasibility of the LBL deposition). Further optimization of the annealing procedure will be conducted to identify optimal conditions based on a trade-off between dehydration and the structure integrity. Hydrothermal annealing [13] may be an alternative method to crystallize the oxides while maintaining the stability of clays and multilayered structure.

Nonetheless, this study has clearly demonstrated the basic feasibility of this new LBL technique for making this new class of nanostructured nanoclay-oxide multilayers. Further research should be conducted to finely tune the thickness and composition of each individual oxide layers (i.e., oxides other than $ZrO_2$) by changing the deposition parameters and precursor solutions, which offers significant versatility for making nanostructured films with diverse functionalities and applications.

The clay-oxide multilayers are expected to have many potential applications, which include but are not limited to coatings and free-standing membranes (made by using sacrificial substrates) for MEMS/NEMS and sensors. This is, in part, owing to the unique-layered nanostructure, as demonstrated by the organic-inorganic hybrid counterparts—nanoclay-polymer multilayers. In particular, a purely inorganic nanostructured composite consisting of zirconia and nanoclays has high thermal resistance (e.g., stable up to 800°C) and high hardness and is chemically inert. Thus, it can be used as protective and hard coatings. In addition to the high hardness of nanocrystalline $ZrO_2$, the presence of platy nanoclay layer within the structure increases fracture toughness by deflecting cracks, rendering even higher hardness of the multilayers. The high lateral bond strength of nanoclays ensures the integrity of free-standing films and membranes, and hence enhances the dynamic or vibrational performance. Potential applications in cantilever sensing components can be envisioned. Finally, it is expected that this purely inorganic nanostructured composite consisting of zirconia and nanoclays exhibits much higher thermal and chemical stability than their hybrid counterparts.

## 4. CONCLUSIONS

A novel layer-by-layer deposition technique has been developed for manufacturing nanoclay-zirconia multilayers by sequentially dipping a substrate in an exfoliated nanoclay suspension and a zirconia cationic precursor solution followed by annealing at 600°C for 2 hours. Nanoscale layer-by-layer growth is achievable, as evidenced by a linear film growth rate per deposition cycle measured on the cross-sectional surfaces under SEM and by X-ray diffraction. It is found that $ZrAc_4$ is a better cationic precursor solution for growing more uniformly layered films. The growth rate of as-deposited films is ~5.7 nm per cycle; the growth rate can be further tuned by changing the deposition parameters and dipping settings. Denser dehydrated films form after annealing at 600°C for 2 hours in air and the film thickness shrinks by ~50%; yet, the annealed films remain uniform and crack-free, and still possess nanoscale layered structure (although less clearly observable under SEM). In summary, the feasibility of the new LBL deposition technique has been clearly demonstrated, but the postdeposition dehydration and annealing processing should be further optimized.

The success of this study enables further endeavors to make a variety of novel oxide-based nanostructured films. This LBL deposition technique can be conveniently adapted for making periodic multilayers or functionally graded oxide films via changing the composition or concentration of oxide cationic precursor solutions periodically or continuously. Nanoclays with permanent surface charges are used to further assist electrostatic assembling, serve as diffusion barriers for functionally graded films, and incorporate other functional materials. It is expected that such purely inorganic nanostructured thin films exhibit unique mechanical properties, permeability, and corrosion resistance. Further research to optimize the synthesis methods (particularly the postdeposition dehydration process) and investigate their mechanical and physical properties is currently in progress.

## ACKNOWLEDGMENTS

H. C. and J. L. are supported in part by a research initiation grant from South Carolina Space Grant Consortium and a National Science Foundation CAREER award (DMR-0448879). G. Z. is supported by Ralph Powe Junior Faculty

Enhancement Award from Oak Ridge Associated Universities and the LSU Faculty research grant. The authors thank A. Kumbhar, Dr. J. Hudson, and D. Cash for assistance in using SEM, and Dr. van Derveer for assistance in using XRD.

## REFERENCES

[1] J. H. Fendler, "Self-assembled nanostructured materials," *Chemistry of Materials*, vol. 8, no. 8, pp. 1616–1624, 1996.

[2] K. Ariga, Y. Lvov, I. Ichinose, and T. Kunitake, "Ultrathin films of inorganic materials ($SiO_2$ nanoparticle, montmorillonite microplate, and molybdenum oxide) prepared by alternate layer-by-layer assembly with organic polyions," *Applied Clay Science*, vol. 15, no. 1-2, pp. 137–152, 1999.

[3] M. Isayama and T. Kunitake, "Self-supporting films of clay minerals and metal oxides: molecular ceramics," *Advanced Materials*, vol. 6, no. 1, pp. 77–78, 1994.

[4] P. Podsiadlo, Z. Liu, D. Paterson, P. B. Messersmith, and N. A. Kotov, "Fusion of seashell nacre and marine bioadhesive analogs: high-strength nanocomposite by layer-by-layer assembly of clay and L-3,4-dihydroxyphenylalanine polymer," *Advanced Materials*, vol. 19, no. 7, pp. 949–955, 2007.

[5] M. Rubner, "Materials science: synthetic sea shell," *Nature*, vol. 423, no. 6943, pp. 925–926, 2003.

[6] Z. Tang, N. A. Kotov, S. Magonov, and B. Ozturk, "Nanostructured artificial nacre," *Nature Materials*, vol. 2, no. 6, pp. 413–418, 2003.

[7] P. T. Hammond, "Form and function in multilayer assembly: new applications at the nanoscale," *Advanced Materials*, vol. 16, no. 15, pp. 1271–1293, 2004.

[8] Y. F. Nicolau, "Solution deposition of thin solid compound films by a successive ionic-layer adsorption and reaction process," *Applications of Surface Science*, vol. 22-23, pp. 1061–1074, 1985.

[9] T. P. Niesen and M. R. De Guire, "Review: deposition of ceramic thin films at low temperatures from aqueous solutions," *Journal of Electroceramics*, vol. 6, no. 3, pp. 169–207, 2001.

[10] T. P. Niesen and M. R. De Guire, "Review: deposition of ceramic thin films at low temperatures from aqueous solutions," *Solid State Ionics*, vol. 151, no. 1–4, pp. 61–68, 2002.

[11] Y. Aoki and T. Kunitake, "Solution-based fabrication of high-$\kappa$ gate dielectrics for next-generation metal-oxide semiconductor transistors," *Advanced Materials*, vol. 16, no. 2, pp. 118–123, 2004.

[12] Y. Aoki, T. Kunitake, and A. Nakao, "Sol-gel fabrication of dielectric $HfO_2$ nano-films; formation of uniform, void-free layers and their superior electrical properties," *Chemistry of Materials*, vol. 17, no. 2, pp. 450–458, 2005.

[13] S. Park, B. L. Clark, D. A. Keszler, et al., "Low-temperature thin-film deposition and crystallization," *Science*, vol. 297, no. 5578, p. 65, 2002.

[14] P. K. Arcot and J. Luo, "Layer-by-layer deposition of zirconia thin films from aqueous solutions," *Materials Letters*, vol. 62, no. 1, pp. 117–120, 2008.

[15] P. K. Arcot and J. Luo, "Solution-based synthesis of oxide thin films via a layer-by-layer deposition method: feasibility and a phenomenological film growth model," *Surface and Coatings Technology*, vol. 202, no. 12, pp. 2690–2697, 2008.

[16] N. A. Kotov, T. Haraszti, L. Turi, et al., "Mechanism of and defect formation in the self-assembly of polymeric polycation-montmorillonite ultrathin films," *Journal of the American Chemical Society*, vol. 119, no. 29, pp. 6821–6832, 1997.

[17] Y. Lvov, K. Ariga, I. Ichinose, and T. Kunitake, "Formation of ultrathin multilayer and hydrated gel from montmorillonite and linear polycations," *Langmuir*, vol. 12, no. 12, pp. 3038–3044, 1996.

[18] Z. Tang, N. A. Kotov, S. Magonov, and B. Ozturk, "Nanostructured artificial nacre," *Nature Materials*, vol. 2, no. 6, pp. 413–418, 2003.

[19] G. Borchardt, *Minerals in Soil Enviroments*, SSSA Book Series 1, Soil Science Society of America, Madison, Wis, USA, 2nd edition, 1989.

[20] G. W. Brindley, "Invited review: ethylene glycol and glycerol complexes of smectites and vermiculite," *Clay Minerals*, vol. 6, p. 273, 1966.

Hindawi Publishing Corporation
Journal of Nanomaterials
Volume 2008, Article ID 271763, 12 pages
doi:10.1155/2008/271763

*Research Article*

# Mechanisms of Nanoindentation on Multiwalled Carbon Nanotube and Nanotube Cluster

**Ling Liu, Guoxin Cao, and Xi Chen**

*Columbia Nanomechanics Research Center, Department of Civil Engineering and Engineering Mechanics, Columbia University, New York, NY 10027-6699, USA*

Correspondence should be addressed to Xi Chen, xichen@civil.columbia.edu

Received 6 August 2007; Accepted 3 January 2008

Recommended by Junlan Wang

Nanoindentation is a promising technique for deducing the elastic property of carbon nanotubes (CNTs). The paper presents an atomistic study on the nanoindentation mechanisms of single-walled and multiwalled CNTs and CNT clusters, through which the deformation characteristics are linked with CNT elastic stiffness. The assembly of individual single-walled CNTs (SWCNTs) into multiwalled CNTs (MWCNTs) and CNT clusters would significantly increase the buckling resistance in terms of withstanding the indentation load. Reverse analysis algorithms are proposed to extract the CNT stiffness by utilizing the indentation force-depth data measured from the prebuckling regimes. The numerical studies carried out in this paper may be used to guide the nanoindentation experiments, explain and extract useful data from the test, as well as stimulate new experiments.



## 1. INTRODUCTION

### 1.1. Carbon nanotube elastic property and available experimental techniques

Carbon nanotubes (CNTs) [1] are perceived to receive a wide range of potential applications thanks to their unique combinations of mechanical and electrical properties: (i) as structural components with extraordinary mechanical performances [2]; (ii) as conducting or semiconducting wires in nanoelectronic components [3]; (iii) as probes in scanning-probe microscopy with the added advantage of a chemically functionalized tip [4]; (iv) as high-sensitivity microbalances [5]; (v) as gas detectors [6]; (vi) as hydrogen storage devices by utilizing its large specific area [7]; (vii) as field-emission-type displays [8]; (viii) as electrodes in organic light-emitting diodes [9], and (ix) as tiny tweezers for nanoscale manipulation [10], among others.

The mechanical properties of the CNTs must be fully understood in order to fulfill their promises. Perhaps the most fundamental phenomenological mechanical property of CNTs is its Young's modulus $E$ upon elastic deformation. A variety of experimental attempts have been put together to measure Young's modulus of carbon nanotubes: Treacy et al. [2] have pioneered the measurement of thermally induced vibration amplitudes of multiwalled carbon nanotube (MWCNT) cantilevers and have reported a range of Young's modulus from 0.40 TPa to 4.15 TPa. Young's moduli of single-walled carbon nanotubes (SWCNTs) were measured by the same technique, varying from 0.9 TPa to 1.9 TPa [11]. Alternatively, by using an atomic force microscope (AFM) tip to impose lateral forces to bend an MWCNT cantilever deposited on a low-friction substrate, Young's moduli of MWCNTs were found to be $1.28 \pm 0.59$ TPa [12]. The elasticity of CNTs was also found to be size-dependent; by measuring the electromechanical resonances of CNTs, Poncharal et al. have discovered that the stiffness of MWCNTs decreases quickly when their diameter exceeds about 10 nm [5]. Such phenomenon was not observed in the static bending experiments with AFM [12]. These diverse experimental measurements suggest that when viewed as a structure, the mechanical properties of CNTs vary with different radius, length, and the number of walls, which are affected by various manufacturing techniques adopted by different research groups; and it was speculated that the measurement of elastic modulus may also be affected by the magnitude and type of loading [13]. In addition, all of these experimental techniques mentioned above were very challenging at the nanoscale, in particular the sample preparation, mounting, and testing setup.

New experimental methods need to be developed to quickly and effectively measure the mechanical properties of CNTs. Among them, nanoindentation is an ultralow-load indentation technique that has been widely used to measure the constitutive relationships of material structures at very small scales [14]. It is arguably the simplest and most direct way of probing the mechanical properties of materials of very small volumes, thus suitable and attractive for CNTs [15]. In nanoindentation experiments, an indenter tip is driven into and then withdrawn from a specimen. High-resolution depth-sensing instruments are used to continuously control and monitor the penetration and reaction force on the indenter. In some commercial systems, indentation forces as small as several nN and displacements less than 1 nm can be accurately measured. One of the great advantages of nanoindentation is that the test can be performed quickly on any specimen and does not require the removal of the specimen from its substrate. This simplifies specimen preparation and makes indentation measurements easier on CNTs compared with other methods.

Recently, we carried out a preliminary study on the buckling mechanisms induced by nanoindentation on an isolated, vertically aligned SWCNT [16]. An important finding is that the buckling behavior of an SWCNT is shell-like if its dimensionless ratios $R/L$ and $R/t$ are large (with $L$, $R$, and $t$ the length, radius, and effective thickness, resp.), beam-like when the ratios are small, and show an interesting transition behavior in between. For nanoindentation experiment on CNTs, it is important to note that first, MWCNTs are easier to fabricate since they do not require stringent catalyst particle preparation [17], and thus they are more popular than SWCNTs. The equilibrium spacing between neighboring layers of MWCNT is approximately 3.4 Å, and they interact with each other through van der Waals forces when the tube is deformed. Second, most CNTs prepared using chemical vapor deposition (CVD), and plasma-enhanced CVD can take the form of a cluster, or sometimes referred to as vertically aligned carbon nanotube forests [17]. In some cases when seeds are used [18], the CNTs are separated far apart during deposition and the nanoindentation experiment can be regarded as that carried out on an isolated tube—the indentation behavior of SWCNT was covered by [16] while the mechanism of MWCNT was yet to be explored. More frequently, the equilibrium spacing between the neighboring tubes is also several Å in the cluster and the CNTs are *closely packed*, forming a dense forest [19]. In fact, the van der Waals interactions between nanotubes help to keep the tubes aligned [17]. Thus, as the indentation depth increases, the bending and buckling behaviors of the tube are strongly influenced by its neighbors.

In order to take advantage of nanoindentation with minimum sample preparation, an experiment carried out directly on the vertically aligned MWCNT and/or CNT cluster is more desired than the isolated SWCNT. Therefore, it is critical to extend out previous study [16] to the nanoindentation mechanisms of both MWCNT and CNT clusters, where the interactions between tube layers and neighboring tubes play an essential role [15]. For example, it is expected that due to the nonbonded interactions, all tube layers in MWCNT and all tubes in a CNT cluster are forced to deform at the same time, which would make them become more resistant to buckling—such hypothesis will be verified quantitatively through the atomistic studies in this paper. We note that the detailed characteristics of the nonbonded interactions may be revealed through molecular mechanics simulations, which serve as the main vehicle in this study. Since the mechanical properties of CNTs are only implicitly related with the indentation response, the establishment of such relationship must be also based on a thorough understanding of the mechanism of nanoindentation—this is the focus of the present paper, and the numerical study may be used to guide nanoindentation experiments, explain and extract useful data (such as the effective stretching stiffness of CNT) from the tests, explore the strengthening mechanism (e.g., determine whether concentric assembly or array assembly is more efficient for increasing the buckling resistance), as well as stimulate new experiments.

### 1.2. Modeling and simulation of carbon nanotubes

With the development of better force field and numeric algorithms, molecular mechanics (MM) simulations have been shown to play an important role in revealing precise constitutive mechanisms of CNTs. In fact, MM simulations have been widely used to study tension, bending, and torsion behaviors of CNTs [20–22] as well as buckling caused by uniaxial compression, torsion, and bending [20, 23–29]. It should be noted that buckling initiated from uniaxial compression is radically different from buckling induced by indentation in the present study. In uniaxial compression, the lateral displacements of atoms in the end layers are constrained and they are only allowed to move along the axis of CNT. In nanoindentation, however, the CNT atoms in the top layer are initially free, and their subsequent interactions with indenter atoms are dominated by the van der Waals force. In this paper, our previous work on SWCNT [16] will be extended to explore the nanoindentation mechanisms of MWCNT and CNT clusters through atomic detailed MM simulation, where the interactions among tube layers of MWCNT and neighbors in tube cluster are also taken into account.

One of the important goals of nanoindentation test is to measure Young's modulus of nanotube—since $E$ is a phenomenological parameter, it must be established via a continuum approach. Perhaps the simplest and most convenient model is to roll a SWCNT from a planar graphite sheet, and by comparing the rolling and stretching energies obtained from both the thin plate theory and atomistic simulations [20, 30–32], an effective Young's modulus $E = 3.9$–$5.5$ TPa and effective nanotube thickness $t = 0.066$–$0.089$ nm were fitted. In general, the SWCNT can then be effectively modeled as a cylindrical elastic thin shell. By comparing critical buckling loads and total strain energy for SWNTs under axial compression and bending obtained from atomistic simulation and finite element method, Pantano et al. [33] obtained $E = 4.84$ TPa and $t = 0.075$ nm for the equivalent continuum shell. A comprehensive study of SWCNTs at small deformation was carried out in our previous work [21], where by

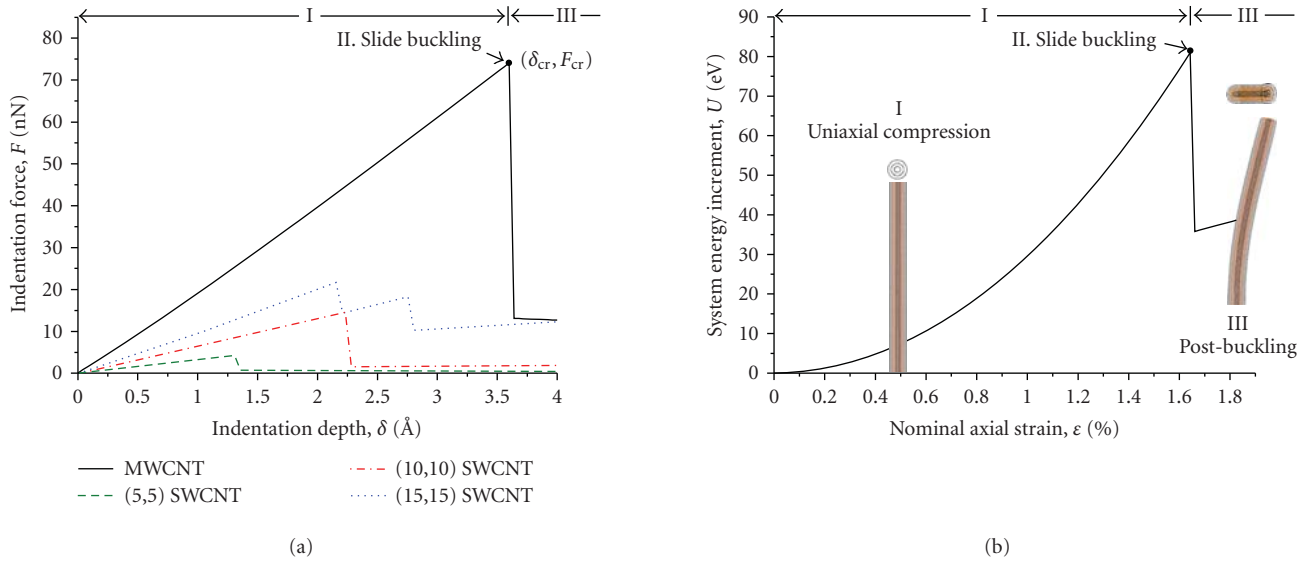


FIGURE 1: MM simulation of indentation on a (5,5)-(10,10)-(15,15) MWCNT: (a) Indentation force $F$-indentation depth $\delta$ relationship, and comparison with $F$-$\delta$ curves of its subunit SWCNTs. (b) System energy $U$-nominal axial strain $\varepsilon$ relationship, and the top view and side view of deformed configurations of MWCNT in different regimes.

fitting the MM simulations of uniaxial tension, bending, and torsion of SWCNTs of various chirality, $E = 6.85$ TPa and $t = 0.08$ nm were derived and also validated from the lateral and axial thermal vibration frequencies.

The variation of CNT Young's moduli obtained from previous theoretical and experimental studies is partly due to the following reasons. First, $E$ is closely associated with the effective shell thickness used in different approaches, which is required to provide both the required stretching and bending rigidity in the continuum shell model. In some approaches in the literature, $t = 0.34$ nm is taken according to the interlayer spacing of graphite and thus the resulting Young's moduli of 0.9–1.9 TPa [34–37] is much smaller than those obtained from other theoretical studies [20, 21, 33]. However, when $E$ and $t$ are combined, the stretching stiffness $Et$ obtained from most previous studies are reasonably close. In addition, a recent analytical study by Huang et al. [13] verified that $t$, and therefore $E$, is dependent on the type and magnitude of loading, nanotube radius $R$, and also chirality when $R < 1$ nm. As a result, it may be inappropriate to take the results of $t$ and $E$ derived from a particular SWCNT under certain loading conditions as universal parameters. For example, the $t$ and $E$ derived from our recent work [21] may be regarded as the averaged parameters when the SWCNTs (with varying chirality) are subjected to several basic small deformation modes. Based on such consideration, the present paper aims to use nanoindentation to derive the nanotube stretching stiffness $Et$ for both MWCNT and CNT clusters, from the established relationships among indentation force, displacement, and intrinsic tube deformation using MM simulations. The numerical studies not only underpin the indentation mechanics of CNTs and serve as the basis of measuring their mechanical properties, but also help to advance understanding on the mechanical behavior of CNTs.

## 2. COMPUTATIONAL METHOD

The molecular mechanics (MM) simulations may be readily employed to explore CNTs containing hundreds of thousands of atoms, by ignoring the electron motions and expressing the system potential energy as a function of the nuclear positions of atoms. The COMPASS force field, which is the first ab initio force field that enables an accurate and simultaneous prediction of various gas-phase and condensed-phase properties of organic and inorganic materials [38] (including carbon nanotubes [16, 23–25, 29, 39–45]), is used in this paper. Simulations are performed at 0 K, so as to not involve the kinetic energy term and to obtain more intrinsic buckling behavior of the tube, since buckling would be otherwise very sensitive to thermal fluctuations [20, 24–28]. The CNT radius is much smaller than the radius of any commercial diamond indenter tip (~100 nm); moreover, the diamond bulk is much stiffer than the nanotube. Therefore, the indenter is modeled as a flat plane consists of rigid diamond atoms, and during the simulation, such plane continuously moves down with a displacement increment of 0.05 Å, so as to simulate a displacement-controlled experiment with a prescribed rate. The tube (or tube cluster) is aligned perpendicular to the indenter plane (e.g., see Figure 1). All degrees of freedom of atoms in bottom layers of the CNTs are fixed to simulate clamped end conditions in mechanical analyses; the atoms in the top of CNT interact with the diamond atoms via nonbonded forces, and there is no displacement boundary condition imposed on those atoms. Breakage of C–C bonds in CNT is not considered in the present study because the strain induced by nanoindentation loading is not that large (see below).

Tubes with various chirality and structures (multiwalled and cluster) are used in the simulation. The long, beam-like

tubes are chosen in this study because they are more practical. The initial atomic structure is first optimized such that the total potential energy is minimized and all atoms are located in their equilibrium states. Due to the complicated bonded and nonbonded interactions, the carbon atoms are not exactly at their ideal positions after optimization. For instance, all SWCNT atoms at the same height may not align precisely along a circle even though the deviation from ideal positions is very small. Such small perturbation will be accumulated during the indentation process and contribute to the instability of CNTs [16, 25].

The initial separation $d_0$ between the top layer of CNT atoms and the indenter plane is set such that no net force acts on the tube at the starting point. The magnitude of $d_0$ slightly depends on the tube chirality. As the indenter plane moves down with a displacement $\delta$, normally termed as indentation depth, the separation $d$ falls below $d_0$, and the overall van der Waals repulsion between indenter and carbon atoms acts as an indentation force ($F$), to compress and deform the nanotube. The deformed configuration of CNT(s) at the current indentation depth is obtained by structural optimization in search for the minimum system potential. The total potential energy of the atomic system, $\Pi$, varies during the indentation process. Since no heat exchange is considered in the MM studies, the work done by indentation force ($F$) is the only external work, which is responsible for the variation of system potential energy with respect to its reference state

$$F = \frac{dU}{d\delta} \quad \text{or} \quad U = \int_0^{\delta} F d\delta, \tag{1}$$

where $U = \Pi\text{-}\Pi_0$ can be interpreted as the deformation energy of the whole system, which includes the strain energy of the nanotube $U_{\text{CNT}}$, and the van der Waals interaction energy $U_{vdW}$ (arises from that between the indenter layer and CNT, between neighboring CNT layers of MWCNT, and between neighboring CNTs of a cluster):

$$U = U_{\text{CNT}} + U_{vdW}. \tag{2}$$

With a state-of-the-art commercial nanoindenter, both indentation force $F$ and indentation depth $\delta$ can be readily measured, and $U$ may be integrated following (1). $F$-$\delta$ and $U$-$\delta$ curves will be explored extensively in this study to obtain valuable insights, such as their links to the deformation modes and elastic constants of CNTs. Moreover, since CNTs are slender structures having the possibility of buckling under indentation load, so $F$ may attain the peak value termed as the critical indentation force, $F_{\text{cr}}$, when the buckling occurs at the critical indentation depth, $\delta_{\text{cr}}$. $F_{\text{cr}}$ will be used as an index to evaluate the specimen's capability of withstanding the indentation load. Such buckling resistance will be compared among CNT clusters, MWCNTs, and their subunit SWCNTs.

## 3. NANOINDENTATION ON MWCNT

### 3.1. Deformation mechanisms

Although the SWCNT is more fundamental, MWCNTs are easier to make and they can be used as an AFM tip or as a reinforcement phase in nanocomposites. As a slender structure in nature, MWCNT may buckle under indentation load and/or axial compression, although one would typically suspect that the MWCNTs should have higher resistance to buckle compared with their single-walled counterparts, thanks to the van der Waals interactions between neighboring layers.

The indentation response of a representative (5,5)-(10,10)-(15,15) MWCNT is analyzed using MM simulation. The length of MWCNT is relatively long, $L = 216.77$ Å, such that it would exhibit beam-like buckling mechanisms, elaborated below; the long CNTs are more practical and their buckling behaviors are easier to analyze (as opposed to shell-like characteristics of short tubes) [16]. Figure 1 shows the sequential snap shots of the deformed configurations as the indentation depth $\delta$ (or equivalently, the *nominal* axial strain $\varepsilon = \delta/L$) is increased; both side and top views are given. The relationships between $F$ and $\delta$, and that between $U$ and $\varepsilon$, are given in Figures 1(a) and 1(b), respectively. The loading process may be divided into three mechanism zones based on system responses that correspond to different deformation modes.

During regime (I) when $\delta$ is sufficiently small ($\varepsilon$ smaller than about 1.6% for the current case), the MWCNT undergoes uniaxial compression. However, the $F$-$\delta$ curve is in fact not linear in this stage although the MWCNT deformation is supposed to be linear elastic at small strain. Note that $\delta$ is the displacement of the indenter tip and thus it includes contributions from both the compression of nanotube and the distance change between indenter and nanotube's top layer due to nonbonded interactions—the force-displacement relationship of the nonbonded component is nonlinear, which will be analyzed in detail in Section 3.3.

When the axial compressive strain becomes critical, the buckling regime (II) happens, which is marked by the sudden slide buckling of MWCNT, a characteristic of continuum beam. At this critical point, $F_{\text{cr}} = 73.5$ nN. Due to the slide buckling, most of the compression energy is relieved, leading to 85% drop of indentation force (Figure 1(a)) and substantial reduction of system energy (Figure 1(b)); the system configuration changes from compression-dominated before buckling to bending-dominated after buckling, and such structural change is mainly responsible for the sudden decrease of indentation force. After the nanotube bounces out, the van der Waals interaction between MWCNT and indenter tip exerts a bending moment on the MWCNT, which slides the MWCNT with respect to the indenter plane as indentation depth is increased. This is the postbuckling regime (III). The applied force is observed to maintain almost a constant value when the MWCNT remains in its buckled (bending) state, which is consistent with the classical beam theory (when the buckle mode is fixed).

The three subunit SWCNTs are of the same length but have different aspect ratios ($L/R$) of 63.6, 31.8, and 21.2, respectively, and their indentation force-depth curves are also plotted in Figure 1(a). It is readily seen that the curves for (5,5) and (10,10) SWCNTs exhibit the same trend (sharp reduction of load after buckle) as the MWCNT, while the $F$-$\delta$ curve of (15,15) SWCNT is characterized with two

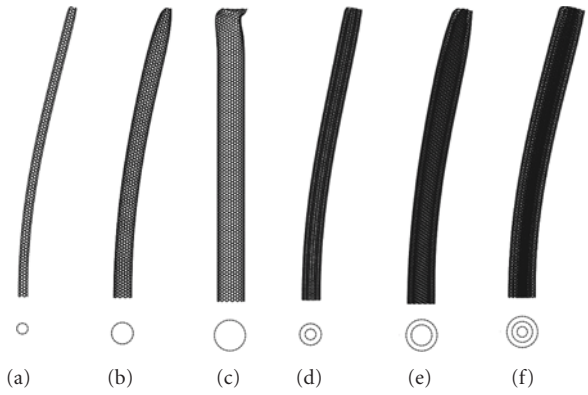


Figure 2: Side view of the structural configurations in postbuckling regimes: (a) (5,5) SWCNT, (b) (10,10) SWCNT, (c) (15,15) SWCNT, (d) (5,5)-(10,10) DWCNT, (e) (10,10)-(15,15) DWCNT, and (f) (5,5)-(10,10)-(15,15) MWCNT.

peaks. This difference in indentation response curves can be explained by the postbuckling configurations shown in Figure 2, where the examined three SWCNTs are found to have different deformation modes: beam-like slide buckling deformation for (5,5) and (10,10) SWCNTs and shell-like snap buckling deformation for (15,15) SWCNT, due to their different $L/R$ and $R/t$ ratios [16].

Note that at the present length, the MWCNT contains one subunit SWCNT having shell-like buckling characteristic if individually indented, yet the overall buckling behavior of MWCNT is still beam-like. This observation indicates that the interlayer van der Waals interactions must have coordinated the subunit deformation and thus *strengthened* the MWCNT during the indentation process, without which the outer SWCNT should have experienced snap buckling before the MWCNT collapses. In view of the system energy, considerable van der Waals energy between MWCNT layers would be generated if the deformation of each subunit SWCNT does not conform to those of the others, which is unfavorable to stabilize the system. In other words, the individual walls of MWCNTs are integrated by the interlayer van der Waals interactions, which make the MWCNT a reinforced structure analogous to a composite beam (the property of the intermediate *material* that accounts for the interlayer van der Waals interactions is anisotropic, which is much stronger in the radial direction than in the hoop direction).

### 3.2. Strengthening of buckling resistance

The three armchair SWCNTs examined above can also construct two double-walled CNTs (DWCNTs): (5,5)-(10,10) DWCNT and (10,10)-(15,15) DWCNT. In order to compare the buckling resistance of MWCNT with its subunits, the following groups of combination are considered, where in each group, the performance of an MWCNT is compared with its subunit SWCNTs and/or DWCNTs:

(i) (5,5) SWCNT, (10,10) SWCNT, and (5,5)-(10,10) DWCNT;

(ii) (10,10) SWCNT, (15,15) SWCNT, and (10,10)-(15,15) DWCNT;

(iii) (15,15) SWCNT, (5,5)-(10,10) DWCNT, and (5,5)-(10,10)-(15,15) MWCNT;

(iv) (5,5) SWCNT, (10,10)-(15,15) DWCNT, and (5,5)-(10,10)-(15,15) MWCNT.

The first two groups represent the assembly of two SWCNTs into a DWCNT, and the last two groups are examples of assembly of a SWCNT and a DWCNT into a three-layered MWCNT. Nanoindentation experiments are carried out on all these nanotubes, generating a series of $F$-$\delta$ curves for both the subunit and assembled structures, shown in Figure 3 with respect to these four groups. In addition, the summation of the $F$-$\delta$ curves of subunits is also shown, referred to as the superposition curve.

For the assembled structures, the two DWCNTs are found to have beam-like buckling behaviors (Figure 2), and their $F$-$\delta$ curves also show a sharp declination of the load after $F_{cr}$ is reached (Figure 3). This is consistent with the assembled 3-layer MWCNT. In other words, among the selected assembled CNTs and their subunits, only the (15,15) SWCNT undergoes snap buckling because its low $L/R$ aspect ratio of 21.2 falls into the shell-like region [16].

When $\delta$ is sufficiently small such that the assembled CNTs and their subunits are under uniaxial compression, the linear $F$-$\delta$ response of a MWCNT or DWCNT equals to the superposition of that of its subunits—this also indicates that the concentric assembly of CNTs (or interlayer van der Waals interactions) has essentially no influence on the elastic properties of CNTs during the axial compression regime, and the interlayer distance of MWCNT is essentially unchanged.

When $\delta$ is increased to a critical value, one of the subunit SWCNTs buckles first (usually the shell-like SWCNT, or the more slender member of SWCNTs in the beam-buckling region), leading to a sharp reduction of the load on the superposition curve; meanwhile, the other subunit can still hold the load and $F$ keeps rising on the superposition curve. Note that at this instant, the assembled multiwalled structure shows no sign of buckle. As $\delta$ is further increased, the other subunit CNT is observed to buckle at its critical force, making the force on superposition curve suddenly decrease again, yet the assembled DWCNT or MWCNT structure still holds. For all groups, the critical force of the assembled tube is observed to be 30%–90% larger than the peak value of the superposition curve. This significant enhancement of $F_{cr}$ implies that the concentric assembly of CNTs could dramatically strengthen the system in resisting buckling when subjected to indentation load. This conclusion is also supported by the increase of critical nominal strain $\varepsilon_{cr}$ of the assembled structure.

Such strengthening effect of MWCNT may be attributed to the van der Waals interactions between subunits. Consider any atom in the inner or outer tube layer of a DWCNT, the net van der Waals force acting on this atom should be small enough in the pure compression regime so as to keep the tube straight. However, just before buckling occurs when the atom attempts to move radially, the corresponding van der Waals

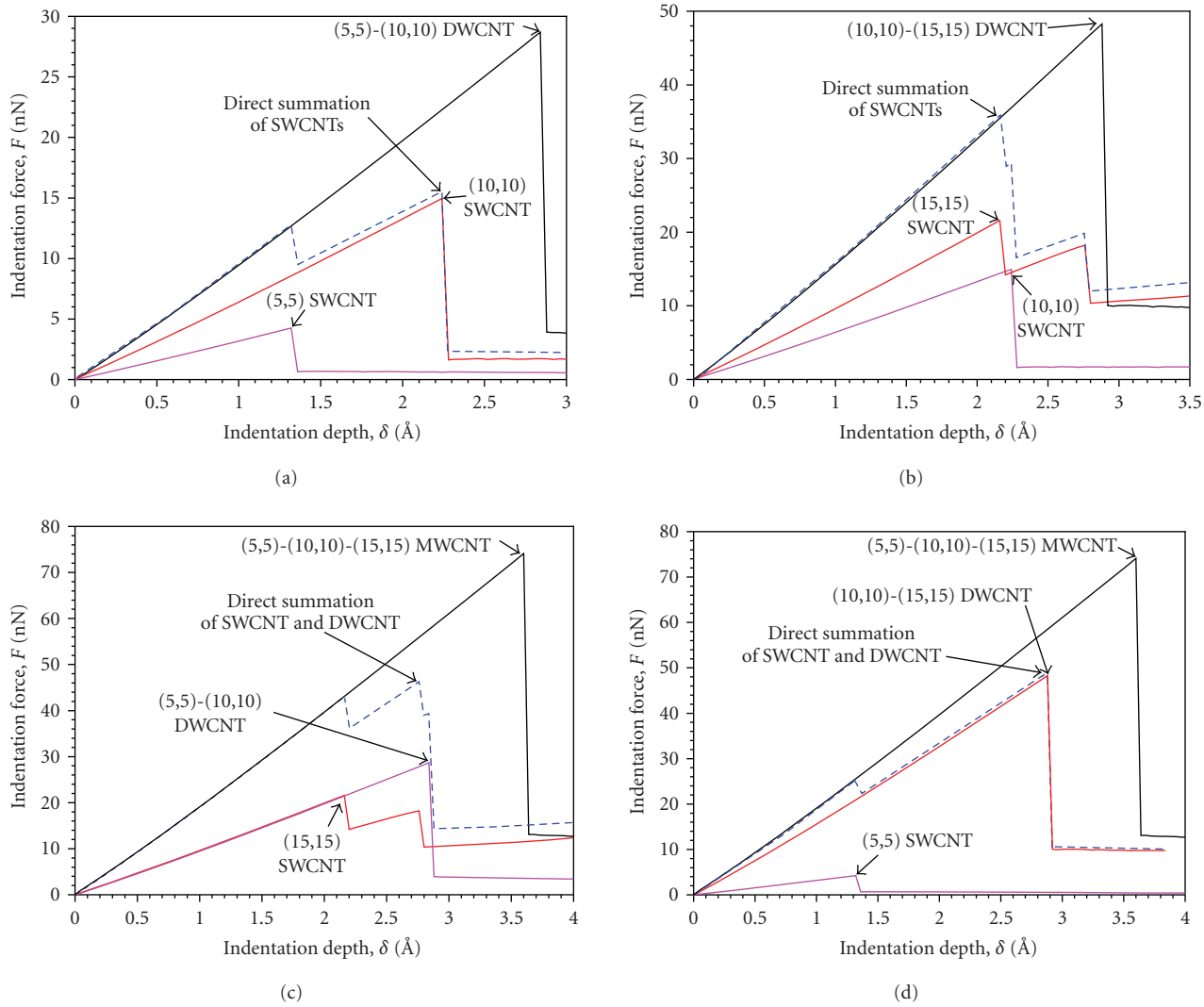


Figure 3: $F$-$\delta$ relationships of (5,5) SWCNT, (10,10) SWCNT, (15,15) SWCNT, and their combinations divided into four groups. The results are compared with the superposition curves of subunits.

repulsion or attraction will be developed in the normal (radial) direction; in other words, the van der Waals interactions between neighboring tube layers serve as an invisible nonlinear spring-like *material* which makes the assembled structure behave like a sandwich tube. The sandwich tube, with an equivalent tube thickness larger than the combined thicknesses of subunits, has a higher bending stiffness and therefore a higher critical buckling force compared to the superposition of subunits (where such van der Waals strengthening effect is absent).

The strengthening efficiency may be evaluated by the increase of critical force per reference tube, divided by the reference number of strengthening tubes. Note that subunit SWCNTs in any MWCNT must have distinct chirality with different numbers of C atoms, so in order to ensure a fair comparison, the MWCNT can be regarded as an assembly of several reference SWCNTs with same total number of atoms. For example, if we take the (10,10) SWCNT as the reference tube, a (10,10)-(15,15) DWCNT has 2.5 reference tubes in terms of equivalent number of C atoms (the reference number of (10,10) is 1 and that of (15,15) is 1.5). In this case, the critical buckling force per reference tube is increased by 28%: from 15 nN for an isolated (10,10) SWCNT to 19.2 nN (= 48 nN/2.5) per reference tube for the (10,10)-(15,15) DWCNT. In other words, 28% is the increase of buckling resistance for the (10,10) SWCNT when a (15,15) SWCNT is used to *strengthen* it by forming a DWCNT. For that matter, a strengthening efficiency for the reference subunit SWCNT can be defined, which is the percentage of increase of buckling resistance divided by the total reference number of other subunit tubes used for strengthening the MWCNT (i.e., the *cost* required for promoting the buckling resistance of the reference tube). For the (10,10) reference SWCNT under consideration, its strengthening efficiency is 18.7% (28% divided by 1.5). Following this procedure, the strengthening efficiency of all MWCNTs examined above is calculated to vary from 18.7% to 75% by choosing different reference tubes.

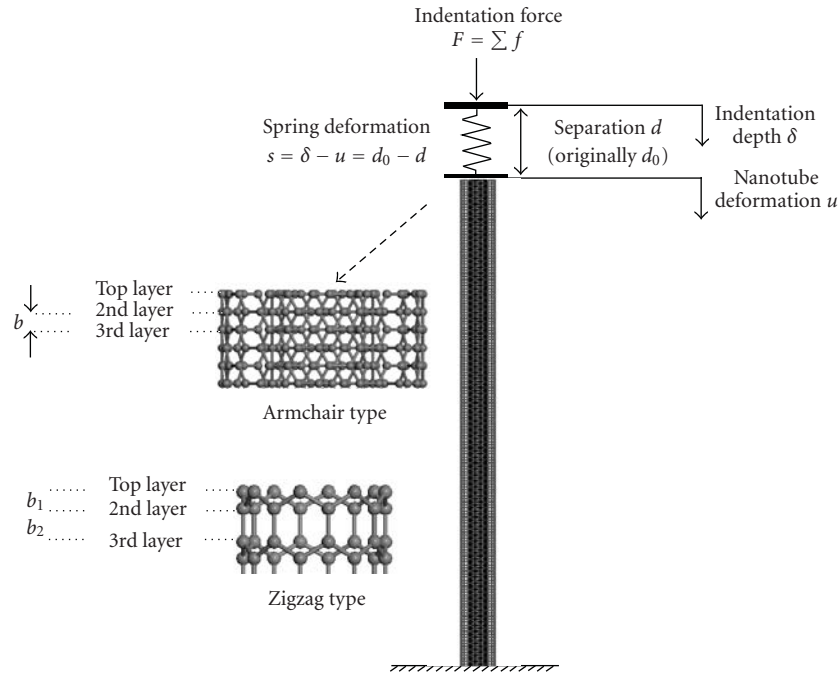


Figure 4: Schematic of the model for the axial compression regime (I), where the van der Waals interaction is simplified as a nonlinear spring, whose constitutive relationship is generalized from MM simulation.

### 3.3. Reverse analysis to deduce the elastic stiffness

As shown in Figure 1, the MWCNT is kept straight in the pure compression regime (I), which makes it possible to deduce its elastic stiffness from nanoindentation test before the tube buckles (when the nominal axial strain is less than about 1.6%). However, due to the van der Waals interaction, the displacement of the indenter tip, $\delta$, which is a measurable quantity from experiment, does not equal exactly to the intrinsic axial compression of SWCNT, $u$, which is defined as the downward displacement of carbon atoms in the top layer. In fact, the separation between indenter plane and top layer of MWCNT atoms changes nonlinearly with respect to the indentation force, sketched in Figure 4, where the van der Waals interaction between MWCNT and indenter is simplified as a nonlinear spring. The force acting on the nonlinear spring and MWCNT equals to the indentation force $F$ in this regime, and the indentation depth is

$$\delta = u + s, \tag{3}$$

where $s = d_0 - d$ with $d$ defined as the deformed *spring* length, and the undeformed length $d_0$ depends on the chirality of tube ($d_0 = 3.31$ Å for armchair tubes). Since the $F$-$\delta$ curve is a measurable characteristic system response, the contribution of $s$ needs to be subtracted off from $\delta$ in order to obtain the intrinsic elastic deformation of MWCNT.

Without losing generality, $F$ can be regarded as the summation of normal component of nonbonded interaction forces between the indenter plane and every C atom in CNT, which may be effectively modeled by the pairwise relationship

$$f(\Delta) = C \cdot \left[\left(\frac{\Delta_0}{\Delta}\right)^m - \left(\frac{\Delta_0}{\Delta}\right)^n\right], \tag{4}$$

where $\Delta_0 = 3.5$ Å represents the equilibrium separation between a C atom and indenter plane, $\Delta$ denotes the separation after indenter penetration, and $C$, $m$, and $n$ are constants to be determined. It should be emphasized that $f(\Delta)$ is constructed to characterize the interaction between any single C atom and the indenter tip, which is independent of the CNT chirality and the lateral position of the C atom with respect to the indenter tip. In other words, $\Delta$ is the distance between a C atom and the indenter plane, which is different from the variable $d$ used before, since $d$ represents the separation between the CNT top layer consisting a set of C atoms and the indenter plane, and thus $d$ is chirality-dependent. Note that $\Delta_0$ is different from $d_0$, since $d_0$ is the equilibrium separation between the top layer of CNT (a set of C atoms) and indenter plane. By moving an isolated carbon atom with respect to the indenter tip, the net van der Waals force $f$ acting on the carbon atom can be obtained and fitting of (4) leads to $C = 0.79$ nN, $m = 8$, and $n = 5$. Therefore, the nonbonded force per carbon atom may be calibrated as

$$f(\Delta) = 0.79 \cdot \left[\left(\frac{3.5}{\Delta}\right)^8 - \left(\frac{3.5}{\Delta}\right)^5\right], \tag{5}$$

where the dimension of $\Delta$ is Å.

For any $N$-walled armchair MWCNT assembly with chirality $(m_i, m_i)$ $(i = 1, \ldots, N)$, assuming that the top layers of

subunit SWCNTs are aligned in the same plane, one could obtain its total nonbonded force as a summation of the interaction forces between indenter and carbon atoms in different layers near the top of MWCNT. Note that for the topmost layer, $d$ is its distance to indenter, for other layers, their distances to the indenter plane also include relevant projections of bond length in the axial direction. Therefore, the total interaction force between indenter and MWCNT can be written as

$$F = \Phi(d) = 2 \cdot \left(\sum_{i=1}^{N} m_i\right) \cdot \left(\sum_{j=1}^{M} f\left(d + (j-1) \cdot b\right)\right), \quad (6)$$

where $2 \cdot (\sum_{i=1}^{N} m_i)$ yields the number of atoms in each layer, $b$ denotes the length projection of a C–C bond in the axial direction (shown in Figure 4), and $M$ is the number of layers interacting with the indenter plane. Note that the nonbonded interaction (c.f. (5)) decays quickly as $\Delta$ gets above $\Delta_0$, thus $M = 4$ is ensured to generate converged solution; the results are also insensitive to the lateral alignment of CNT with respect to indenter lattice. Relationships similar to (6) may be developed for other chirality of CNTs, by taking into account different positions of carbon atoms near the top of subunit SWCNTs (see Section 4.3 for the example of zigzag tubes).

From (3) and (6), the compressive displacement of examined MWCNT can be written as

$$u = \delta + \Phi^{-1}(F) - d_0. \quad (7)$$

Based on the $F$-$\delta$ curve measured from either numerical or experimental indentation study, the constitutive relationship for MWCNT can be established at small strain. For the numerical example of (5,5)-(10,10)-(15,15) MWCNT presented in Figure 1, after removing the contribution of the MWCNT-indenter interaction using (7), the predicted $F$-$u$ curve is shown in Figure 5, which is in excellent agreement with that measured directly from MM simulation.

Since the resulting $F$-$u$ relationship is almost linear, the MWCNT mechanical property is linear elastic when the nominal axial strain is smaller than about 1.6%. If each subunit SWCNT is modeled as a continuum thin shell, the linear relationship between $F$ and $u$ at small axial strain can be written as

$$F = ku = \frac{EA}{L}u = \left(\frac{2\pi Et}{L} \cdot \sum_{i=1}^{N} R_i\right) \cdot u, \quad (8)$$

where $L$ is the tube length, $E$ Young's modulus, $t$ the wall thickness, $R_i$ the radius of the $i$th subunit SWCNT, and $A$ denotes the total area of MWCNT cross section. Thus, the elastic stiffness of SWCNT, $Et$, can be measured from the slope ($k$) of $F$-$u$ curve as

$$Et = \frac{L}{2\pi \sum_{i=1}^{N} R_i} k. \quad (9)$$

For the present (5,5)-(10,10)-(15,15) SWCNT, $k$ = 231.89 N/m, $L$ = 216.77 Å, $R_1$ = 3.41 Å, $R_2 = 2R_1$, and $R_3 = 3R_1$, which leads to $Et$ = 391.35 Pa m (the same approach can also be applied to either (5,5)-(10,10) or (10,10)-(15,15) DWCNT studied in this paper and the results are almost the same). This value is fairly close to that reported by [20], where $Et$ = 363 Pa m, and by [33], where $Et$ = 363 Pa m.

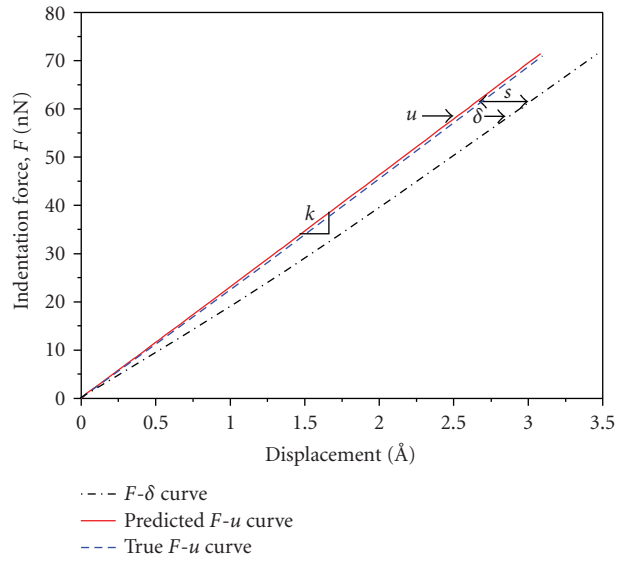


Figure 5: Comparison between $F$-$\delta$ and $F$-$u$ curves in the axial compression regime; the difference is the deformation of nonlinear spring. The predicted $F$-$u$ curve based on (7) agrees well with that measured from MM simulation (true solution).

## 4. NANOINDENTATION ON SWCNT CLUSTER

### 4.1. Deformation mechanisms

Besides forming the concentric MWCNT, SWCNTs of the same chirality and length may assemble into clusters. The initial (undeformed) cluster configuration, that is, the arrangement of SWCNTs in lateral directions, is obtained by minimizing the system potential energy of the unit cell. Upon nanoindentation on an $n$-tube cluster, the indentation force per tube $\overline{F} = F/n$ is compared with that of isolated tubes. For a representative 7-tube (8,0) cluster, the $\overline{F}$-$\delta$ curve is presented in Figure 6 whose characteristic is very similar to its component SWCNT (with $L/R$ = 24.4), as well as being similar to other long SWCNTs and MWCNTs shown in Figure 3. Based on both $\overline{F}$-$\delta$ curve and sequential snap shots of the deformed cluster in Figure 6, the indentation process can also be divided into three main regimes associated with distinct deformation modes: (I) uniaxial compression where all the tubes remain straight as the nominal axial stress is smaller than 1.4% for the cluster under investigation; (II) slide buckling where all subunit SWCNTs buckle toward the same direction after $F_{cr}$ is attained; (III) postbuckling where the top layers of subunit SWCNTs are pushed to slide with respect to the indenter plane after the indentation force is significantly reduced.

In Figure 6, the $\overline{F}$-$\delta$ curve of the 7-tube cluster is compared with that of an isolated (8,0) component, as well as

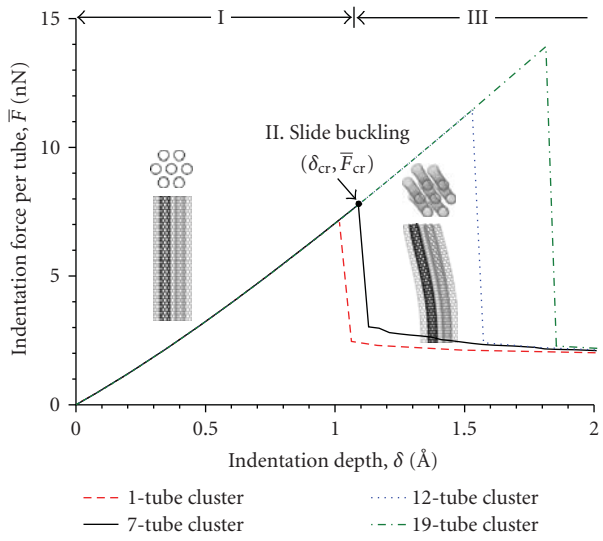


FIGURE 6: MM simulation of indentation on (8,0) SWCNT clusters with different tube numbers: $\overline{F}$-$\delta$ curves and top and side views of the deformed configurations of 7-tube clusters in different regimes.

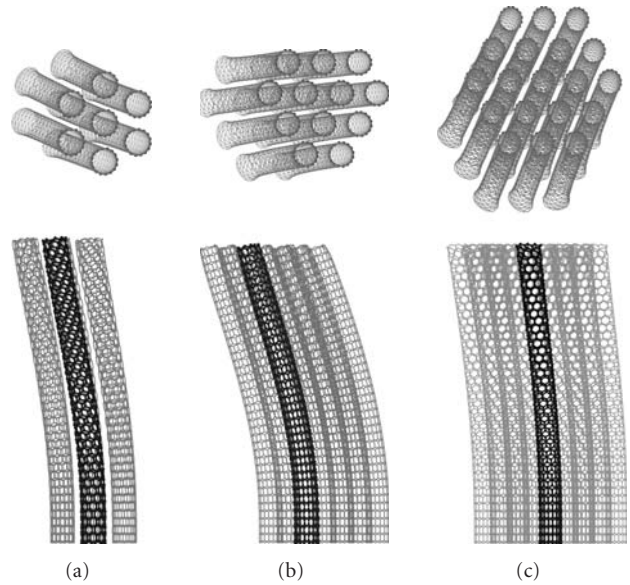


FIGURE 7: Side view and top view of the structural configurations in postbuckling regimes: (a) 7-tube cluster, (b) 12-tube cluster, and (c) 19-tube cluster.

that of 12-tube and 19-tube clusters made by the same subunit. The buckled configurations of the clusters are shown in Figure 7, where all tubes seem to buckle into the same shape. From Figure 6, the $\overline{F}$-$\delta$ curve of an isolated tube is very different than that of a subunit tube in a cluster—as a part of a cluster, the same tube could sustain much higher load before it buckles (compare with the isolated tube), and only when the nominal axial strain is smaller than 1.4% does the subunit tube has the same constitutive relationship as its isolated counterpart. Such increased buckling resistance per tube is attributed to the van der Waals interactions among neighboring tubes, elaborated below.

### 4.2. Strengthening of buckling resistance

Figure 6 clearly indicates that with the increase of tube numbers in a cluster, each tube could sustain a higher force. Before buckling, the intertube distance remains essentially unchanged and thus the van der Waals interaction among neighboring tubes is not activated in the pure compression regime. With the help of both normal and lateral nonbonded interactions, the coordinated deformation of subunit tubes increases the bending stiffness of the cluster. With reference to Figure 6, with the assistance of the normal van der Waals interaction, the deformed shape of all buckled subunit tubes is almost identical and therefore in order to overcome the relative sliding between the neighboring tubes (mainly along the axial direction), the indentation force must be increased. In other words, when a SWCNT slides with respect to a nearby counterpart, any atom in the tube has to overcome a *frictional* axial van der Waals force.

The strengthening efficiency can still be computed by the same definition in Section 3.2, that is, the increased buckling resistance divided by the *cost* of additional reference tube number. Take the 7-tube (8,0) cluster as an example, the increase of critical force per tube is 14% (from 7 nN to 8 nN), and therefore the strengthening efficiency turns out to be 2.3% (= 14%/6). Following the same procedure, the strengthening efficiency of all clusters examined above is found to be in the range between 2.3% and 5%, which is less significant than that of MWCNTs (18.7% ~ 75%). The lower level of strengthening efficiency indicates that the concentric assembly of SWCNTs into MWCNTs is able to provide higher promotion of buckling resistance than the assembly leading to clusters, since the effective area of the nonbonded interaction in a MWCNT is larger.

The intertube cohesive forces can also explain some unique features in the indentation response of SWCNT clusters. Compared with an isolated SWCNT and MWCNTs for which the indentation force maintains almost a constant value during postbuckling region (c.f. Figures 1(a) and 3), the SWCNT clusters are observed in Figure 6 to have a decreasing indentation force after buckle. This phenomenon may be attributed to the different degrees of lateral interactions between subunit tubes as the bending curvature is varied: the slide motion during each loading step is slowed down with the increase of indentation depth and curvature of subunit SWCNTs, leading to a gradual reduction of intertube *friction* and thus smaller bending resistance.

In order to investigate the influence of tube length on the strengthening effect of SWCNT clusters, (8,0) SWCNTs with $L/R$ = 12.2 are compared with their counterparts discussed above (with doubled aspect ratio). As shown in Figure 8, it is much harder to buckle the shorter specimens, which matches well with the beam theory where shorter beams always have higher buckling resistance than longer beams. Although the longer cluster should have more atoms involved in interaction and therefore higher intertube cohesion is expected, it is observed from Figure 8 that the percentage of increase of critical force per tube is nearly the same for both clusters. Here, the shorter specimens have larger critical nominal strain and therefore larger axial slide motion is initiated

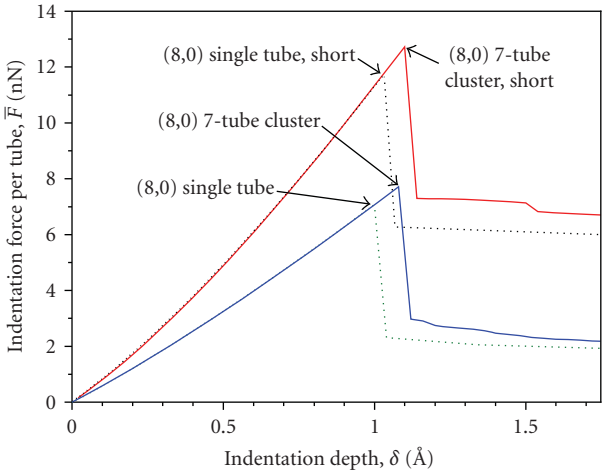


Figure 8: The effect of tube length: $\overline{F}$-$\delta$ relationships of short and long (8,0) SWCNTs and 7-tube clusters.

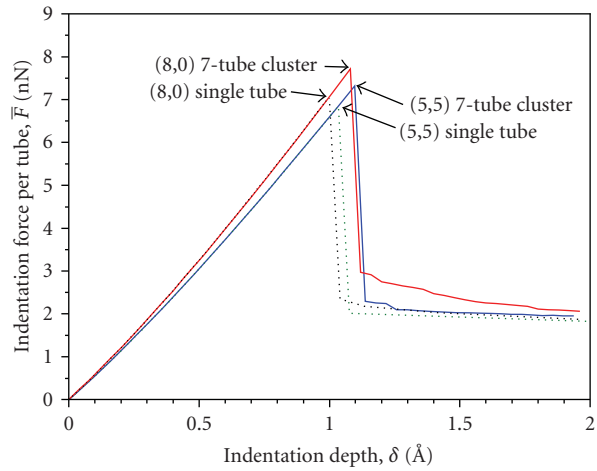


Figure 9: The effect of tube chirality: $\overline{F}$-$\delta$ relationships of (8,0) and (5,5) SWCNTs and 7-tube clusters.

during the buckling process, which leverages the smaller *interaction area* and leads to almost the same strengthening efficiency when compared with the longer cluster.

The effect of chirality is also investigated. The armchair (5,5) tube with $L/R = 25.7$ is selected to compare with zigzag (8,0) tube with similar aspect ratio. Nanoindentation responses of both SWCNTs and their 7-tube bundles are shown in Figure 9. It is found that compared to the results for (8,0) SWCNTs, the assembly of (5,5) SWCNTs into clusters does not significantly enhance the buckling resistance per tube. This phenomenon indicates that allocation of atoms in tube surface has a profound effect on the magnitude of *frictional* axial van der Waals force. This conclusion is also supported by MM simulations showing that more force is required to slide a zigzag SWCNT along the axial direction (with respect to a nearby identical neighbor) than an armchair SWCNT.

### 4.3. Reverse analysis to deduce the elastic constants

A procedure similar to that outlined in Section 4.3 is used to derive CNT elastic stiffness $Et$ based on the prebuckling indentation response of zigzag SWCNT clusters. The pairwise C–C interaction law, (5), holds for any chirality; nevertheless, analogous to (6) for armchair CNT, a new geometrical relationship needs to be established for zigzag tubes. For any $n$-tube zigzag SWCNT cluster with chirality $(m, 0)$, assuming the top layers of subunit SWCNTs are aligned in the same plane, and denote the separation between this plane and the indenter as $d$, one could obtain the force per tube as

$$\overline{F} = \frac{F}{n} = \Phi(d) = m \cdot \left( \sum_{j=1}^{M} f(d + d_j) \right), \qquad (10)$$

where $m$ is also the number of atoms per layer per tube, $d_j$ denotes the distance between the $j$th layer and the top layer, and $M$ is the number of layers to be considered. The zigzag SWCNTs have two types of layer separations in the axial direction as illustrated in Figure 4: one is associated with the inclined

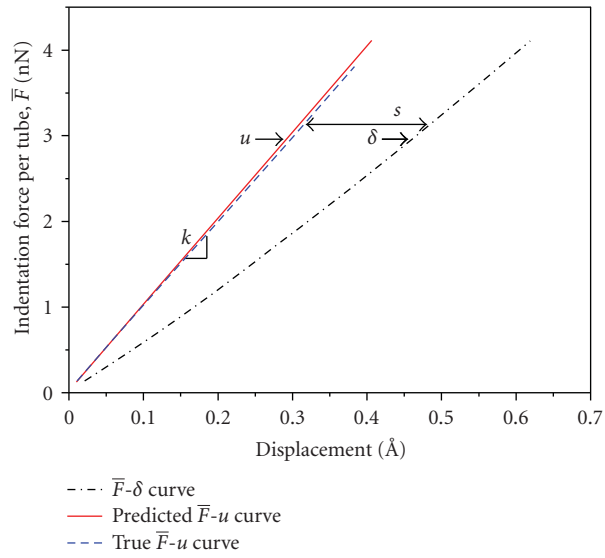


Figure 10: Comparison between the $\overline{F}$-$\delta$ and $\overline{F}$-$u$ curves in the axial compression regime; the difference is the deformation of nonlinear spring. The predicted $\overline{F}$-$u$ curve based on (7) agrees well with that measured from MM simulation (true solution).

C–C bonds whoselength projection in the axial direction is denoted as $b_1$, and the other one is due to the vertical (axial) C–C bonds having the length of $b_2$. Consequently, one can derive $d_1 = 0$, $d_2 = b_1$, $d_3 = b_1 + b_2$, $d_4 = 2b_1 + b_2$, and so forth. Again, due to the fading nature of van der Waals interaction, $M = 4$ is adequate to obtain a converged CNT cluster-indenter relationship with reasonable accuracy. By the virtue of (7) and (10) with $d_0 = 3.27$ Å for zigzag tubes, the constitutive relationship for SWCNT cluster can be established at small strain: for the numerical example of 7-tube (8,0) cluster presented in Figure 6, after removing the variation of cluster-indenter van der Waals distance, the $\overline{F}$-$u$ curve can be predicted in Figure 10. Again, the predicted relationship is almost linear and in excellent agreement with that measured

from MM simulation. Denote $k$ as the slope of $\overline{F}$-$u$ relationship, the elastic stiffness of CNT can be extracted as

$$Et = \frac{L}{2\pi R}k. \tag{11}$$

For the present cluster, $k = 100.63$ N/m, $L = 76.97$ Å, and $R = 3.16$ Å, which leads to $Et = 390.29$ Pa m (the same result is obtained for clusters containing different number of tubes). This value is very close to the result reported in Section 3.3 ($Et = 391.35$ Pa m) based on nanoindentaion experiment on the MWCNTs, and also very close to those reported by Yakobson et al. and Pantano et al. [20, 33].

## 5. CONCLUSION

In this study, MM is used to simulate nanoindentation experiments on SWCNTs, MWCNTs, and SWCNT clusters. In both cases, the buckling deformations are beam-like despite of some of the very small overall aspect ratios of MWCNTs or CNT clusters; in other words, while their subunits may individually snap buckle like a shell, when assembled into a structure, even short MWCNTs or SWCNT clusters slide buckle like beams due to the nonbonded reinforcement among subunits. In terms of both critical buckling load and critical buckling strain, the assembled structures (MWCNT and cluster) are found to have higher buckling resistance than their subunit SWCNTs, thanks to the van der Waals interactions between either neighboring layers or neighboring tubes. For MWCNTs, the normal (radial) van der Waals interaction between neighboring layers significantly enhances the bending stiffness; whereas for SWCNT clusters, the resistance to the sliding motion between nearby SWCNTs (required for buckling) is dominated by the *frictional* axial van der Waals interaction—both mechanisms give rise to higher load required for buckle. Consequently, both MWCNTs and SWCNT clusters are found to be sturdier than their subunit components in withstanding buckling, although the strengthening efficiency is significantly higher for MWCNTs than clusters.

With the penetration of indenter, both MWCNTs and SWCNT clusters composed of SWCNTs undergo three sequential deformation regimes: uniaxial compression, slide buckling, and postbuckling. The indentation responses in the first regime are utilized to deduce the elastic constant $Et$. A nonlinear spring model generalized from MM simulation is proposed to simulate the van der Waals interaction between indenter and MWCNT/cluster. By utilizing the proposed model, contribution of the van der Waals interaction is excluded from the measured indentation force-depth curve, leading to a linear relationship between the applied compression and intrinsic sample deformation. The obtained elastic stiffnesses for both MWCNT and SWCNT clusters are in good agreement with each other, as well as with that in the literature, which demonstrates the potential of using the proposed nonlinear spring model and algorithm to deduce elastic constants of CNTs via nanoindentation experiment.

## ACKNOWLEDGMENTS

The work is supported in part by NSF CMS-0407743 and CMMI-0643726, and in part by the Department of Civil Engineering and Engineering Mechanics, Columbia University.

## REFERENCES

[1] S. Iijima, "Helical microtubules of graphitic carbon," *Nature*, vol. 354, no. 6348, pp. 56–58, 1991.

[2] M. M. J. Treacy, T. W. Ebbesen, and J. M. Gibson, "Exceptionally high Young's modulus observed for individual carbon nanotubes," *Nature*, vol. 381, no. 6584, pp. 678–680, 1996.

[3] S. J. Tans, A. R. M. Verschueren, and C. Dekker, "Room-temperature transistor based on a single carbon nanotube," *Nature*, vol. 393, no. 6680, pp. 49–52, 1998.

[4] H. Dai, J. H. Hafner, A. G. Rinzler, D. T. Colbert, and R. E. Smalley, "Nanotubes as nanoprobes in scanning probe microscopy," *Nature*, vol. 384, no. 6605, pp. 147–150, 1996.

[5] P. Poncharal, Z. L. Wang, D. Ugarte, and W. A. de Heer, "Electrostatic deflections and electromechanical resonances of carbon nanotubes," *Science*, vol. 283, no. 5407, pp. 1513–1516, 1999.

[6] S. Chopra, K. McGuire, N. Gothard, A. M. Rao, and A. Pham, "Selective gas detection using a carbon nanotube sensor," *Applied Physics Letters*, vol. 83, no. 11, pp. 2280–2282, 2003.

[7] A. C. Dillon, K. M. Jones, T. A. Bekkedahl, C. H. Kiang, D. S. Bethune, and M. J. Heben, "Storage of hydrogen in single-walled carbon nanotubes," *Nature*, vol. 386, no. 6623, pp. 377–379, 1997.

[8] W. B. Choi, D. S. Chung, J. H. Kang, et al., "Fully sealed, high-brightness carbon-nanotube field-emission display," *Applied Physics Letters*, vol. 75, no. 20, pp. 3129–3131, 1999.

[9] C. M. Aguirre, S. Auvray, S. Pigeon, R. Izquierdo, P. Desjardins, and R. Martel, "Carbon nanotube sheets as electrodes in organic light-emitting diodes," *Applied Physics Letters*, vol. 88, no. 18, Article ID 183104, 3 pages, 2006.

[10] P. Kim and C. M. Lieber, "Nanotube nanotweezers," *Science*, vol. 286, no. 5447, pp. 2148–2150, 1999.

[11] A. Krishnan, E. Dujardin, T. W. Ebbesen, P. N. Yianilos, and M. M. J. Treacy, "Young's modulus of single-walled nanotubes," *Physical Review B*, vol. 58, no. 20, pp. 14013–14019, 1998.

[12] E. W. Wong, P. E. Sheehan, and C. M. Lieber, "Nanobeam mechanics: elasticity, strength, and toughness of nanorods and nanotubes," *Science*, vol. 277, no. 5334, pp. 1971–1975, 1997.

[13] Y. Huang, J. Wu, and K. C. Hwang, "Thickness of graphene and single-wall carbon nanotubes," *Physical Review B*, vol. 74, no. 24, Article ID 245413, 9 pages, 2006.

[14] G. M. Pharr, "Measurement of mechanical properties by ultra-low load indentation," *Materials Science and Engineering A*, vol. 253, no. 1-2, pp. 151–159, 1998.

[15] H. J. Qi, K. B. K. Teo, K. K. S. Lau, et al., "Determination of mechanical properties of carbon nanotubes and vertically aligned carbon nanotube forests using nanoindentation," *Journal of the Mechanics and Physics of Solids*, vol. 51, no. 11-12, pp. 2213–2237, 2003.

[16] G. Cao and X. Chen, "Mechanisms of nanoindentation on single-walled carbon nanotubes: the effect of nanotube length," *Journal of Materials Research*, vol. 21, no. 4, pp. 1048–1070, 2006.

[17] A. V. Melechko, V. I. Merkulov, T. E. McKnight, et al., "Vertically aligned carbon nanofibers and related structures:

controlled synthesis and directed assembly," *Journal of Applied Physics*, vol. 97, no. 4, Article ID 041301, 2005.

[18] V. I. Merkulov, D. H. Lowndes, Y. Y. Wei, G. Eres, and E. Voelkl, "Patterned growth of individual and multiple vertically aligned carbon nanofibers," *Applied Physics Letters*, vol. 76, no. 24, pp. 3555–3557, 2000.

[19] M. Chhowalla, K. B. K. Teo, C. Ducati, et al., "Growth process conditions of vertically aligned carbon nanotubes using plasma enhanced chemical vapor deposition," *Journal of Applied Physics*, vol. 90, no. 10, pp. 5308–5317, 2001.

[20] B. I. Yakobson, C. J. Brabec, and J. Bernholc, "Nanomechanics of carbon tubes: instabilities beyond linear response," *Physical Review Letters*, vol. 76, no. 14, pp. 2511–2514, 1996.

[21] X. Chen and G. Cao, "A structural mechanics approach of single-walled carbon nanotubes generalized from atomistic simulation," *Nanotechnology*, vol. 17, pp. 1004–1015, 2006.

[22] P. Liu, Y. W. Zhang, C. Lu, and K. Y. Lam, "Tensile and bending properties of double-walled carbon nanotubes," *Journal of Physics D*, vol. 37, no. 17, pp. 2358–2363, 2004.

[23] G. Cao and X. Chen, "Buckling of single-walled carbon nanotubes upon bending: molecular dynamics simulations and finite element method," *Physical Review B*, vol. 73, no. 15, Article ID 155435, 10 pages, 2006.

[24] G. Cao and X. Chen, "The effect of the displacement increment on the axial compressive buckling behaviours of single-walled carbon nanotubes," *Nanotechnology*, vol. 17, no. 15, Article ID 040, 3844–3855, 2006.

[25] G. Cao and X. Chen, "Buckling behavior of single-walled carbon nanotubes and a targeted molecular mechanics approach," *Physical Review B*, vol. 74, no. 16, Article ID 165422, 10 pages, 2006.

[26] S. Iijima, C. Brabec, A. Maiti, and J. Bernholc, "Structural flexibility of carbon nanotubes," *Journal of Chemical Physics*, vol. 104, no. 5, pp. 2089–2092, 1996.

[27] T. Ozaki, Y. Iwasa, and T. Mitani, "Stiffness of single-walled carbon nanotubes under large strain," *Physical Review Letters*, vol. 84, no. 8, pp. 1712–1715, 2000.

[28] A. Sears and R. C. Batra, "Buckling of multiwalled carbon nanotubes under axial compression," *Physical Review B*, vol. 73, no. 8, Article ID 085410, 11 pages, 2006.

[29] G. Cao and X. Chen, "The effects of chirality and boundary conditions on the mechanical properties of single-walled carbon nanotubes," *International Journal of Solids and Structures*, vol. 44, no. 17, pp. 5447–5465, 2007.

[30] K. N. Kudin, G. E. Scuseria, and B. I. Yakobson, "C2F, BN, and C nanoshell elasticity from ab initio computations," *Physical Review B*, vol. 64, no. 23, Article ID 235406, 10 pages, 2001.

[31] Z.-C. Tu and Z.-C. Ou-Yang, "Single-walled and multiwalled carbon nanotubes viewed as elastic tubes with the effective Young's moduli dependent on layer number," *Physical Review B*, vol. 65, no. 23, Article ID 233407, 4 pages, 2002.

[32] X. Zhou, J. Zhou, and Z.-C. Ou-Yang, "Strain energy and Young's modulus of single-wall carbon nanotubes calculated from electronic energy-band theory," *Physical Review B*, vol. 62, no. 20, pp. 13692–13696, 2000.

[33] A. Pantano, D. M. Parks, and M. C. Boyce, "Mechanics of deformation of single- and multi-wall carbon nanotubes," *Journal of the Mechanics and Physics of Solids*, vol. 52, no. 4, pp. 789–821, 2004.

[34] E. Hernández, C. Goze, P. Bernier, and A. Rubio, "Elastic properties of C and $B_xC_yN_z$ composite nanotubes," *Physical Review Letters*, vol. 80, no. 20, pp. 4502–4505, 1998.

[35] Y. Jin and F. G. Yuan, "Simulation of elastic properties of single-walled carbon nanotubes," *Composites Science and Technology*, vol. 63, no. 11, pp. 1507–1515, 2003.

[36] C. Li and T.-W. Chou, "A structural mechanics approach for the analysis of carbon nanotubes," *International Journal of Solids and Structures*, vol. 40, no. 10, pp. 2487–2499, 2003.

[37] J. P. Lu, "Elastic properties of carbon nanotubes and nanoropes," *Physical Review Letters*, vol. 79, no. 7, pp. 1297–1300, 1997.

[38] H. Sun, P. Ren, and J. R. Fried, "The COMPASS force field: parameterization and validation for phosphazenes," *Computational and Theoretical Polymer Science*, vol. 8, no. 1-2, pp. 229–246, 1998.

[39] G. Cao, X. Chen, and J. W. Kysar, "Thermal vibration and apparent thermal contraction of single-walled carbon nanotubes," *Journal of the Mechanics and Physics of Solids*, vol. 54, no. 6, pp. 1206–1236, 2006.

[40] G. Cao, X. Chen, and J. W. Kysar, "Apparent thermal contraction of single-walled carbon nanotubes," *Physical Review B*, vol. 72, no. 23, Article ID 235404, 6 pages, 2005.

[41] G. Cao, X. Chen, and J. W. Kysar, "Strain sensing with carbon nanotubes: numerical analysis of the vibration frequency of deformed single-walled carbon nanotubes," *Physical Review B*, vol. 72, no. 19, Article ID 195412, 6 pages, 2005.

[42] G. Cao, Y. Tang, and X. Chen, "Elastic properties of carbon nanotubes in radial direction," *Journal of Nanoengineering and Nanosystems*, vol. 219, no. 2, pp. 73–88, 2006.

[43] G. Cao, X. Chen, and J. W. Kysar, "Numerical analysis of the radial breathing mode of armchair and zigzag single-walled carbon nanotubes under deformation," *Journal of Applied Physics*, vol. 100, no. 12, Article ID 124305, 10 pages, 2006.

[44] X. Chen and G. Cao, "Review: atomistic studies of mechanical properties of carbon nanotubes," *Journal of Theoretical and Computational Nanoscience*, vol. 4, no. 5, pp. 823–839, 2007.

[45] Y. Qiao, G. Cao, and X. Chen, "Effect of gas molecules on nanofluidic behaviors," *Journal of the American Chemical Society*, vol. 129, pp. 2355–2359, 2007.

Hindawi Publishing Corporation
Journal of Nanomaterials
Volume 2008, Article ID 132728, 11 pages
doi:10.1155/2008/132728

*Research Article*

# Buckling of Single-Crystal Silicon Nanolines under Indentation

**Min K. Kang,[1] Bin Li,[2] Paul S. Ho,[2] and Rui Huang[1]**

[1] *Department of Aerospace Engineering and Engineering Mechanics, University of Texas, Austin, TX 78712, USA*
[2] *Microelectronics Research Center, University of Texas, Austin, TX 78758, USA*

Correspondence should be addressed to Rui Huang, ruihuang@mail.utexas.edu

Received 1 October 2007; Accepted 27 December 2007

Recommended by Junlan Wang

Atomic force microscope-(AFM-) based indentation tests were performed to examine mechanical properties of parallel single-crystal silicon nanolines (SiNLs) of sub-100-nm line width, fabricated by a process combining electron-beam lithography and anisotropic wet etching. The SiNLs have straight and nearly atomically flat sidewalls, and the cross-section is almost perfectly rectangular with uniform width and height along the longitudinal direction. The measured load-displacement curves from the indentation tests show an instability with large displacement bursts at a critical load ranging from 480 $\mu$N to 700 $\mu$N. This phenomenon is attributed to a transition of the buckling mode of the SiNLs under indentation. Using a set of finite element models with postbuckling analyses, we analyze the indentation-induced buckling modes and investigate the effects of tip location, contact friction, and substrate deformation on the critical load of mode transition. The results demonstrate a unique approach for the study of nanomaterials and patterned nanostructures via a combination of experiments and modeling.



## 1. INTRODUCTION

Silicon (Si)-based nanomaterials [1–9] have drawn much attentionrecently due to continual miniaturization of semiconductor devices in microelectronics and development of nanoelectromechanical systems (NEMSs). One of the persisting challenges for practical applications of nanomaterials has been the measurement of their mechanical properties, which as well known can be different from their counterparts of bulk materials. A variety of metrology methodologies have been developed, such as nanoscale tensile tests [10–12], resonance methods [13, 14], bending techniques [1, 2, 4–6], and nanoindentation tests [7, 15]. In particular, the nanoindentation tests have been well established for measuring mechanical properties such as elastic modulus, hardness, and fracture toughness, for both bulk and thin-film materials [16, 17], with very high force/displacement resolution and excellent controllability. Recently, the nanoindentation technique has been adopted for mechanical characterization of various nanomaterials [15], including nanotubes [18, 19], nanowires [20, 21], nanobelts [22], and nanoparticles [7]. However, interpretation of the nanoindentation results for nanomaterials is nontrivial and often requires sophisticated modeling effort [7, 21, 23, 24].

In this paper, we carry out nanoindentation experiments to characterize the mechanical properties of single-crystal Si nanolines (SiNLs). These SiNLs are fabricated by a process combining electron beam lithography (EBL) and anisotropic wet etching [25, 26]. They have atomically flat sidewalls and almost perfectly rectangular cross sections. The measured indentation load-displacement curves show a peculiar character with a large displacement burst at a critical load. A finite element model is developed to simulate the indentation test, which reveals a buckling mechanism of the SiNLs under indentation. A systematic modeling effort is presented here to elucidate the effects of the indenter tip location, contact friction, and substrate deformation on the critical load. The results demonstrate a potential methodology to study buckling, friction, and fracture of nanomaterials through a combination of experiments and modeling.

## 2. EXPERIMENTAL

Figure 1 shows an array of parallel SiNLs fabricated by a process combining EBL and anisotropic wet etching. The fabrication process began with chemical vapor deposition of an oxide layer on a Si (110) wafer, followed by depositing

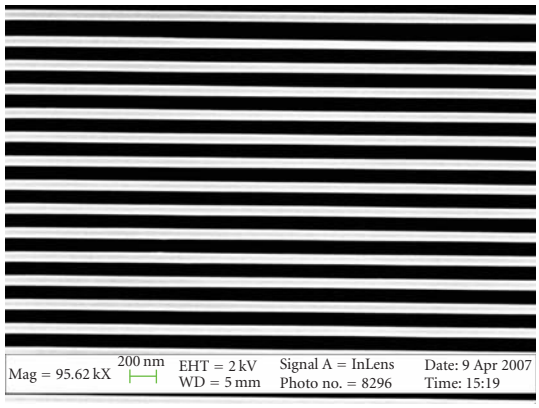


(a)

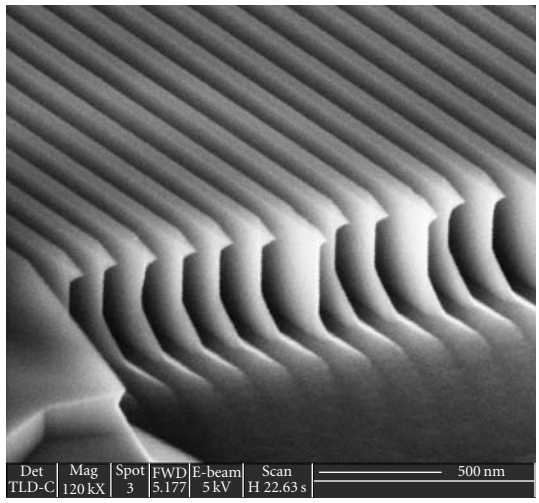


(b)

Figure 1: SEM images of parallel silicon nanolines, with 74 nm line width and 510 nm height; the pitch distance is 180 nm. (a) A plan view, (b) a perspective view with 60° tilt angle. A trench pattern is specially designed at one end of the line for the SEM image in (b), showing the cross sections of the nanolines with sharp edges due to anisotropic etching.

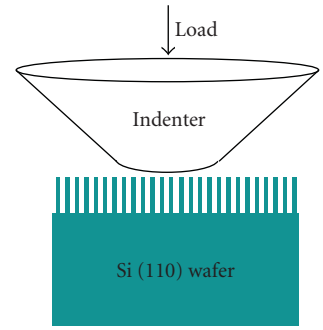


(a)

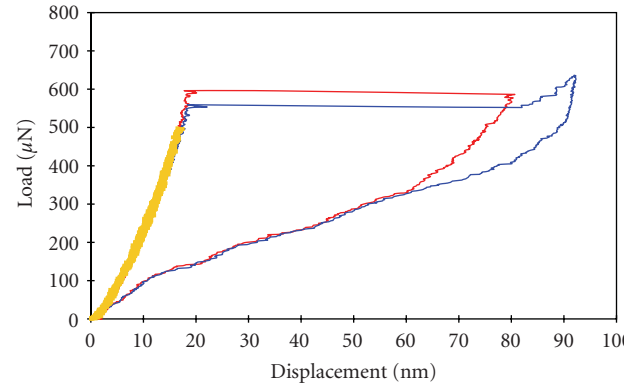


(b)

Figure 2: (a) Schematic of the nanoindentation test on parallel SiNLs. (b) A set of three load-displacement curves from the nanoindentation tests on the 74 nm SiNLs, with no residual deformation after unloading of the indenter.

a thin chromium layer. A positive photoresist was then spun on the wafer and patterned using an electron beam exposure system.Pattern transfer from the resist was performed by plasma etching of the chromiumand oxide down to the silicon surface. Subsequently, the residual resist was removed and tetra-methyl-ammonium hydroxide (TMAH) was used for anisotropic etching of the Si,with the remaining chromium and oxide layers as the hard mask. When the EBL patterned lines were aligned with one of the ⟨112⟩ directions on the Si surface, parallel SiNLs were produced by the anisotropic etchingalong the {111} crystalline planes, with vertical and atomically flat sidewalls. Finally, the residual chromium and oxide were removed by chromium etchant and bufferedoxide etchant (BOE), respectively. Figure 1(a) shows highly uniform line width along the longitudinal directions of the SiNLs, and Figure 1(b) shows a perspective view near one end of the SiNLs where a trench pattern was specially designed for the purpose of SEM imaging. The line width of the SiNLs shown in Figure 1 is 74 nm, and the height is 510 nm, corresponding to an aspect ratio of 6.9 for the rectangular cross section. The pitch distance is 180 nm. Following the same process, we have successfully fabricated SiNLs with line widths ranging from 40 nm to 500 nm. The height of the SiNLs can be controlled by TMAH etching time within the range of 100–2000 nm, and the length is defined by the exposed area for electron-beam patterning, which was 50 $\mu$m for the present study. The high crystal quality and well-defined line geometry, along with the atomically flat sidewalls and highly uniform line width, make these SiNLs well suited for accurate experimental measurements and modeling.

An atomic force microscope (AFM)-based nanoindentation system (Triboscope by Hysitron, Inc.) was used to characterize the mechanical properties of the SiNLs. A conically shaped diamond indenter with the tip radius around 5 $\mu$m was used to probe the SiNLs, as schematically illustrated in Figure 2(a). The tip radius was more precisely determined by scanning electron microscope (SEM) to be 4.6 $\mu$m. During each indentation test, the indenter was placed directly above an array of parallel SiNLs, patterned in a 50 $\mu$m by 50 $\mu$m area of the wafer surface. The indenter was

brought into contact with the SiNLs, monitored by a build-in transducer. Subsequently, loading and unloading of the indenter were performed with the force and displacement measured simultaneously. Figure 2(b) shows three load-displacement curves obtained from the indentation tests on the 74 nm SiNLs. In the first test (thick yellow curve in the plot), a small indentation load of 500 $\mu$N was applied and subsequently unloaded, which shows an elastic response with coinciding curves for loading and unloading. With the indentation load increased beyond 550 $\mu$N for the second and third tests, a large displacement burst was observed. This indicates the occurrence of instability under indentation. Similar displacement bursts were observed in nanoindentation experiments of metal films, which were attributed to a dislocation mechanism as an intrinsic material instability [24]. Here, however, the magnitude of the displacement burst is much larger (over 60 nm in comparison with a few nanometers for the metal films). As noted in a previous study [2], plastic deformation of nanoscale single-crystal Si beams was observed only at elevated temperatures (> 373 K), thus the dislocation mechanism is not expected to operate at the room temperature. Furthermore, it was found that, after the displacement burst, unloading of the indenter fully recovers the displacement, with no observable residual deformation. This suggests a likely instability mechanism due to buckling of the SiNLs, to be confirmed by modeling simulations as discussed in the later sections.

Additional indentation tests with the SiNLs were carried out with various indentation loads, as shown in Figure 3(a). Here, however, irrecoverable residual deformation was observed after unloading of the indenter. It is noted that the maximum indentation displacement for each of these tests is greater than 150 nm, while in Figure 2(a) the maximum displacement was less than 100 nm. It is thus conjectured that the larger indentation displacements in this set caused more significant bending of the SiNLs after the buckling instability, which in turn induced higher tensile stresses that eventually fractured the SiNLs. Indeed, debris of fractured Si were observed, as shown in Figure 3(b) for one of these tests. Remarkably, the debris of the fractured SiNLs are of isosceles triangular shape, with two sides well aligned in the $\langle 110 \rangle$ directions and the base in the $\langle 112 \rangle$ direction parallel to the SiNLs. This indicates a primary cleavage mechanism of the close packed $\{111\}$ planes along the $\langle 110 \rangle$ directions [17]. This opens a possibility to study fracture of Si at the nanoscale.

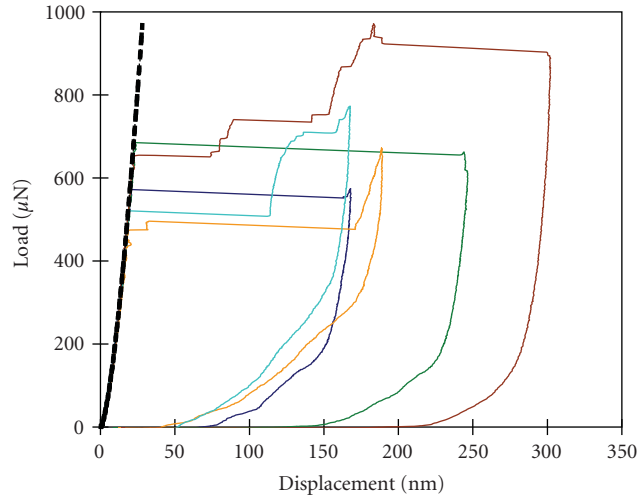


(a)

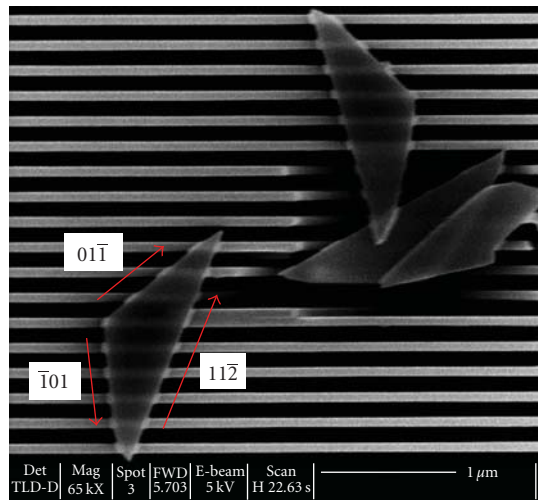


(b)

Figure 3: (a) A set of five load-displacement curves from the nanoindentation tests on the 74 nm SiNLs, with irrecoverable displacements due to fracture of the SiNLs. (b) A SEM image of the fractured SiNLs, with debris of isosceles triangular shape.

## 3. FINITE ELEMENT MODEL

In this section,we calibrate a finite element model to simulate the nanoindentation test on SiNLs. The model system consists of a spherical indenter and parallel SiNLs standing on a substrate, as illustrated in Figure 4. Since the tip radius ($R = 4.6\,\mu$m) is much greater than the line width ($w = 74$ nm) and the pitch ($S = 180$ nm), the conical indenter used in the experiments is effectively modeled by the spherical indenter of the same tip radius. Furthermore, the indenter is modeled as a rigid body. This approximation is justified by noting that Young's modulus of the diamond indenter (1140 GPa) is much greater than that of Si (e.g., 169 GPa in the [110] direction). It was confirmed that a similar model with an elastic diamond indenter predicts a load-displacement curve nearly identical to the rigid indenter model, as shown in Figure 5. On the other hand, the elastic indenter model requires significantly higher computational effort, with a larger number of elements, especially for the contact between the indenter and the SiNLs. Next, the Si substrate is modeled as a rigid foundation to the SiNLs. This approximation is made by considering that the patterned SiNLs, with air gaps in between, are more compliant than the solid substrate. The effect of elastic deformation in the substrate will be further discussed in the next section. Finally, the material of SiNLs is assumed to be linearly elastic and isotropic. As suggested by Vlassak et al. [27], modeling indentation on

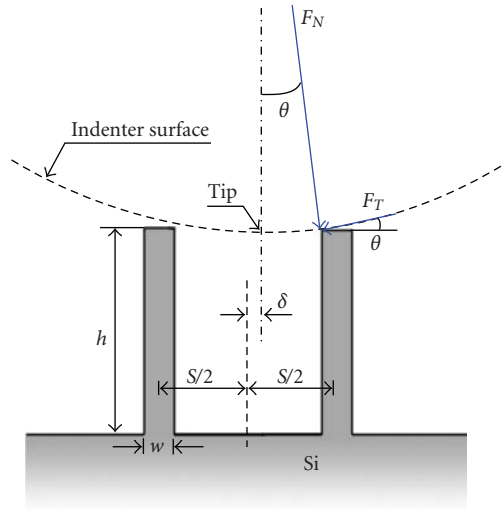


Figure 4: Illustration of the parallel SiNLs under spherical indentation (not to the scale), showing the cross sections of two lines and the contact forces. The tip alignment is indicated by an offset $\delta$ from the trench center.

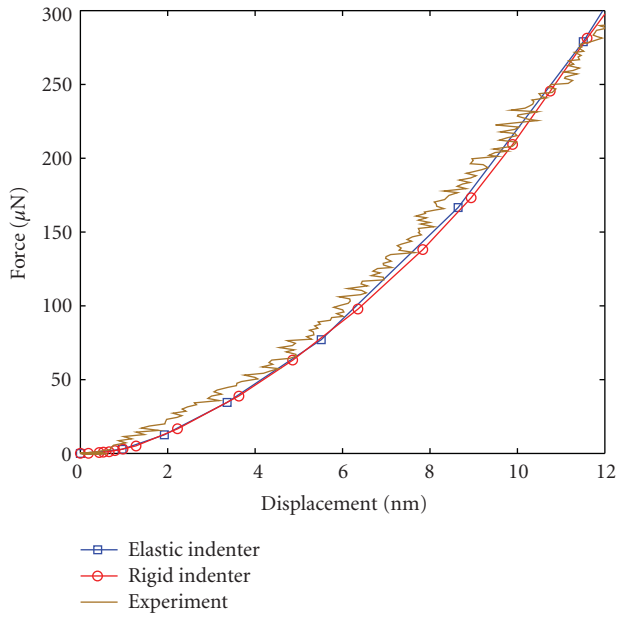


Figure 5: Calibration of the finite element model using the experimental data. The elastic indenter model and the rigid indenter model give nearly identical load-displacement curves, both in good agreement with the experimental data.

elastically anisotropic materials can be simplified by using an equivalent isotropic model. To determine the equivalent isotropic elastic modulus for the SiNLs, we compare the load-displacement curve obtained from the model to the experimental curves shown in Figure 2(b). With the Poisson's ratio fixed as 0.27, we found that a Young's modulus of 140 GPa gives a load-displacement curve in good agreement with the experimental curve, as shown in Figure 5. This

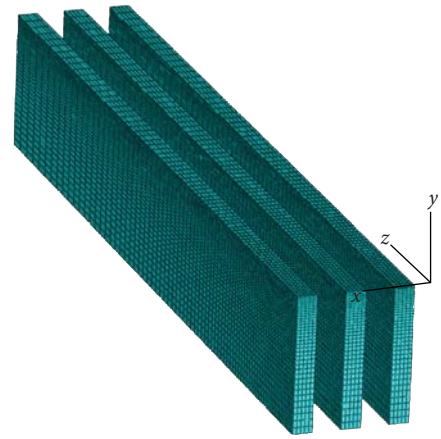


Figure 6: A finite element model of parallel SiNLs under indentation, showing three half-lines with symmetric boundary conditions at the planes $z = 0$ and $x = 0$. The tip of the indenter moves along the $y$-axis during the simulation for a symmetric trench-center loading.

modulus is lower than the Young's modulus of bulk Si in the [110] direction, but higher than that in the [001] direction.

Three-dimensional finite element (FE) models are constructed for the SiNLs using ABAQUS [28]. Figure 6 shows an example model, with the tip of the indenter aligned with a trench center (i.e., $\delta = 0$ in Figure 4). By symmetry, three half-lines on one side of the tip are modeled for indentation on six parallel SiNLs. The number of lines and the indenter tip location are varied to investigate their effects, as discussed in the next section. The length of the SiNLs in the experiments was 50 $\mu$m, much greater than the line width ($w = 74$ nm) and height ($h = 510$ nm). In the FE model, the lines are 6 $\mu$m long. The length is chosen such that the boundary condition at the ends has negligible effect on the simulation results, mimicking infinitely long lines. Only half of each line is modeled, with a symmetry boundary condition for the cross section at $z = 0$.

To model the indentation load, contact surfaces are defined between the indenter and the lines. The contact property, either frictionless or frictional, is specified. As discussed in the next section, the friction between the indenter tip and the SiNLs is very important in determining the critical buckling load. On the other hand, contact and friction among SiNLs are ignored because of the relatively large spacing between the lines ($S/w > 2$). For columnar structures with narrow spacing such as those in thermal barrier coatings [28, 29], the inter-columnar contact and friction are critical. To simulate buckling and post-buckling behavior of the SiNLs, the modified Riks method [30, 31] is adopted for the FE simulations. The essence of the Riks method is that the solution is viewed as a single equilibrium path in a space defined by both the nodal displacements and the loading parameters. This approach solves simultaneously for loads and displacements, thus providing solutions regardless of whether the response is stable or unstable. The contact between the indenter and the lines and possible loss of the contact in the present model often causes divergence in the numerical simulations. A spring-dashpot element

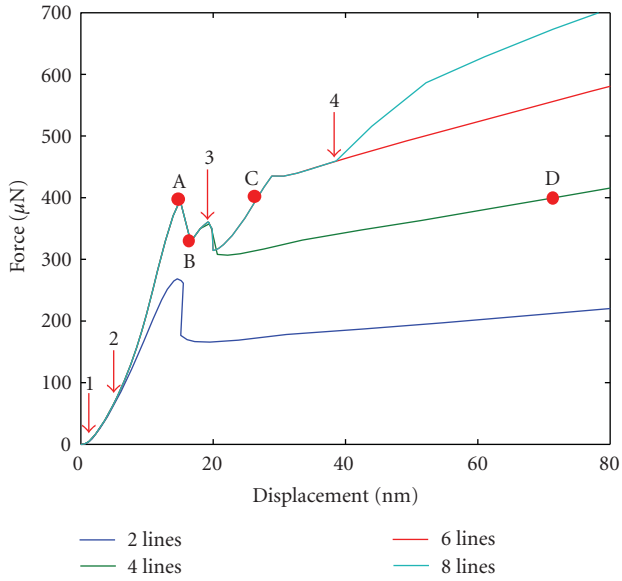


Figure 7: Indentation load-displacement curves from finite element models with different numbers of lines. The indenter tip is aligned with the trench center between two center lines. The initiation of contact with the first four pairs of the lines is indicated by the arrows with numbers 1–4.

[30] has been used as a numerical damper to stabilize the numerical simulations, which effectively adjusts the step size to relieve the sudden force change upon contact and buckle initiation.

## 4. RESULTS AND DISCUSSIONS

### 4.1. *Symmetric loading with frictionless contact*

We begin with a simplest model, assuming frictionless contact between the indenter and the lines. The tip of the indenter is aligned with a trench center between two lines (i.e., $\delta = 0$ in Figure 4). The number of lines in the model is varied from 2 to 8 by including the neighboring lines, all placed symmetrically with respect to the tip location. The condition of symmetry is used to reduce the number of elements and thus the computational time. Figure 7 plots the indentation load-displacement curves from the FE simulations. By comparing the curves for different numbers of lines, we can determine the initiation of multiple contacts at different indentation depths,as indicated by the vertical arrows in Figure 7. The first contact occurs between the indenter and the two center lines, with a very small displacement of the tip from its initial position at the same height as the lines. The indentation force is zero before the first contact and increases with the tip displacement afterwards. This part is the same for all the curves, as the first contact occurs in all the four models. The curve for the two-line model deviates from the other curves after the tip displacement reaches 5.9 nm, at which point the indenter makes contact with the next pair of lines adjacent to the center lines. This second contact is absent in the two-line model, which gives a more compliant force-displacement curve thereafter. Similarly, the curve of the four-line model deviates from the other two after the third contact at the tip displacement of 18.6 nm, and the six-line curve deviates from the eight-line curve after the fourth contact at the tip displacements of 38.4 nm. The tip displacements for the initiation of each contact can be confirmed from a pure geometric consideration using the given radius of the rigid spherical indenter along with the line width and the pitch distance.

All the force-displacement curves in Figure 7 exhibit an unstable behavior, with the force decreasing after a critical load. While the critical load for the two-line model is significantly lower, the other three models give the same critical load, as the instability occurs after the second contact but before the third contact. In other words, at the critical load, only the four lines nearest to the tip of the indenter are in contact and thus subject to the contact forces. The detail of the instability is elucidated by the six-line model in Figure 8. Figure 8(a) shows the deformation of the SiNLs and the stress distribution immediately before the instability, indicated as point A on the load-displacement curve (see Figure 7). At this point, the center two lines are bent symmetrically, with the cross section taking a half-wave shape and nearly perpendicular to the surface of the indenter at the contact. This is similar to the buckling mode of a column with one end fixed and the other end constrained of rotation (see the inset). Apparently, the frictionless contact allows lateral sliding of the lines along the spherical surface, but the compressing rigid surface constrained the rotation of the top surface of the lines. Such constraint however is lost in Figure 8(b), corresponding to point B on the load-displacement curve (see Figure 7). Now, the cross section of the center two lines takes a quarter-wave shape, similar to the buckling mode of a column with one end fixed and the other end free of any constraint (see the inset). The transition of the buckling mode is thus responsible for the instability shown in Figure 7. The quarter-wave mode is more compliant (less constrained) than the half-wave mode, leading to the force drop from A to B in the load-displacement curve. Meanwhile, the next two lines are still bent in a half-wave mode at point B. A similar transition of the buckling mode for these two lines gives the second peak in the load-displacement curve. After that, all four lines nearest to the indenter tip are bent in the quarter-wave mode, as shown in Figure 8(c). It can be seen that the transition of the buckling mode is accompanied by significant sliding and partial loss of the contact between the indenter and the SiNLs.

While the Riks method used in the numerical simulation gives a single equilibrium path for each model, experimental curves depend on the control of the load or displacement. If the experiments were under a displacement control, similar curves as shown in Figure 7 would be expected. Under a load control, however, the equilibrium path in Figure 7 would predict a displacement burst at the critical load, that is, from point A to point C for the six-line model. This qualitatively agrees with the experimental curves shown in Figure 2(b). However, it is noted that, for models with six or more lines, the displacement burst starts at point A with only four lines in contact with the indenter but stops at

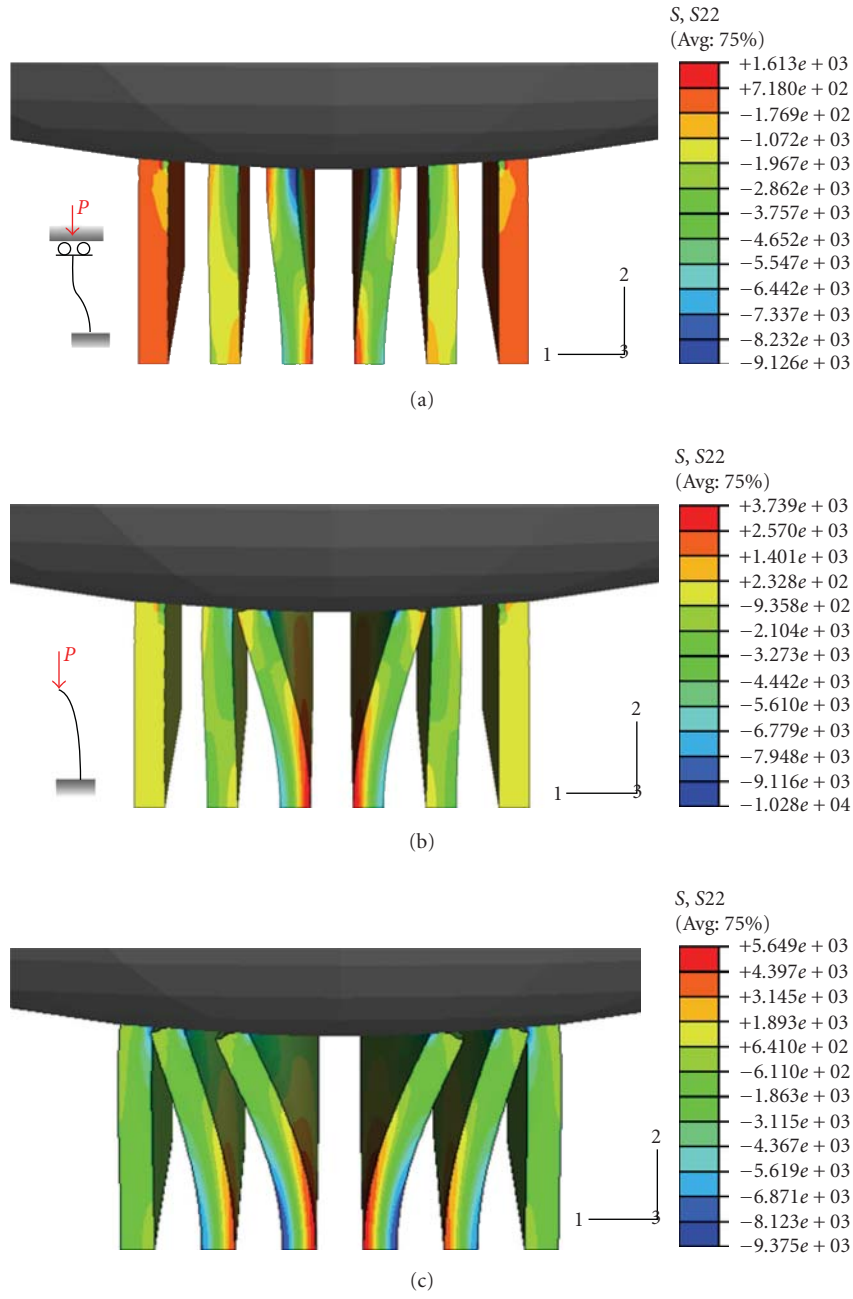


Figure 8: Buckling of SiNLs and mode transition simulated by the finite element model. The contours show the distributions of normal stress in the 2-direction. (a)–(c) correspond to the points A, B, C on the load-displacement curve in Figure 7, respectively. The insets in (a) and (b) show analogous buckling modes in columns.

point C with six lines in contact. This implies a possible dynamic contact process during the displacement burst, not captured in the present static analysis. This may account for the quantitative discrepancy in terms of the magnitude of the displacement jump between the experimental curves in Figure 2(b) and the equilibrium path in Figure 7. The former shows displacement jumps of over 60 nm, but the latter predicts only about 10 nm for the simulations with six or eight lines. Interestingly, a much larger displacement burst is predicted by the four-line model, about 55 nm from A to D. Apparently, the postbuckling behavior under the load-control experiments is complicated by the dynamic contact and friction processes, which is beyond the present static model and will be left for further investigations. In the present study, we focus on the critical load for the onset of the displacement burst, for which the static analysis of the present model suffices. Figure 7 shows that a minimum of four lines is sufficient for the modeling of the indentation test up to the critical load, because the contact with additional lines occurs only afterwards. The modeling however predicts

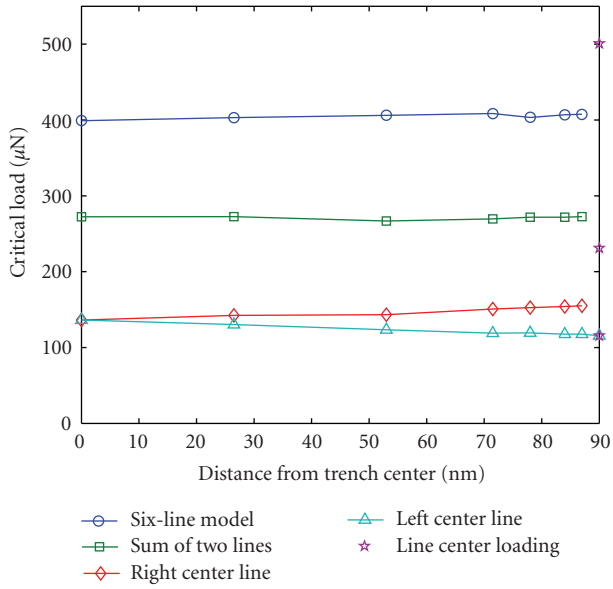


Figure 9: The critical load of buckling transition versus the indenter tip location, obtained from the finite element models. The critical loads for the left and right center lines are obtained from a single-line model.

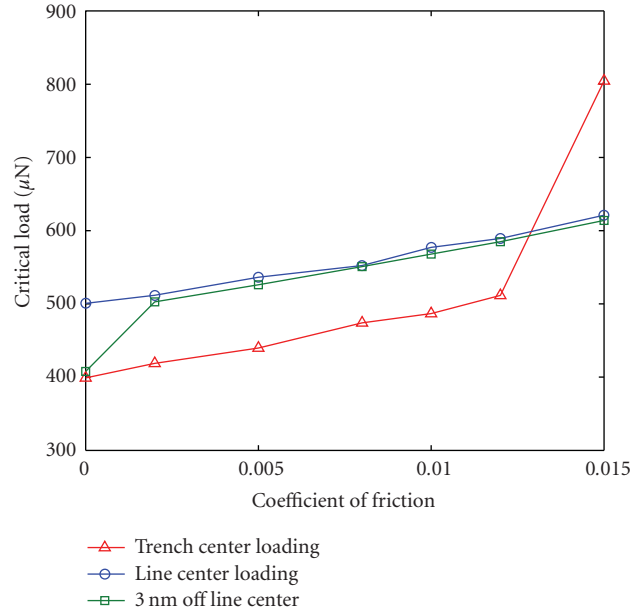


Figure 10: The critical load of buckling transition as a function of the friction coefficient at the contact, obtained from the finite element models with tip locations at the trench center, line center, and 3 nm off the line center.

a relatively low critical load at about 400 $\mu$N, while the critical load from the experimental curves (see Figures 2(b) and 3(a)) ranges from 480 $\mu$N to 700 $\mu$N. In the following, we discuss possible causes of this discrepancy by analyzing the effects of relative tip location, contact friction, and elastic deformation of the substrate.

### 4.2. *Effect of tip location*

The indentation tests of the present study were not equipped with sufficient lateral resolution for accurate positioning of the indenter with respect to individual SiNLs. The possible location of the indenter tip therefore could vary from a trench center between two lines to the center of one line (another case of symmetric loading). As illustrated in Figure 4, the eccentricity from the trench center, $\delta$, varies from 0 to $S/2$, with $S$ being the pitch distance between two adjacent lines. Figure 9 plots the critical load as a function of $\delta$ from the FE model with six lines. For the cases of asymmetric loading, six half-lines are meshed with one symmetric plane at $z = 0$ (refer to the coordinates in Figure 6). The contact between the indenter and the lines remains frictionless for the time being. It is found that shifting the relative tip location has negligible influence on the initial elastic response and the critical load. The no-effect on the elastic response before the critical load may be understood by noting the fact that the radius of the indenter is significantly larger than the pitch distance, and thus the variation of the contacts due to a shift of the tip location within the pitch distance is hardly noticeable by the large indenter. This is consistent with the experimental curves that follow a nearly identical path up to the critical load despite the uncertainty of the tip locations. On the other hand, the contact forces acting on each individual line vary asymmetrically with the tip location. For the center two lines that contribute the most to the total indentation force, the contact force is higher on the line closer to the tip and lower on the other one. Meanwhile, the critical load for each of these lines also varies with the tip location. As the tip moves closer (or farther) to the line, the contact angle $\theta$ decreases (or increases), and the critical load for the buckling mode transition of the individual line increases (or decreases). This trend has been confirmed by FE simulations with only one line under the indenter. Consequently, as the tip location shifts from the trench center towards the right side, the critical load increases for the right center lines but decreases for the left center line, as shown in Figure 9. Together with the redistribution of the contact forces on each line, the buckling instability occurs almost simultaneously for the two center lines, and the sum of the two individual critical loads is nearly independent of the tip location. The contact forces acting on the next two lines farther away from the tip account for the difference between the sum of the single-line critical loads and the total critical loads, also nearly independent of the tip location as a result of similar force redistribution.

As a special case, when the tip of the indenter is aligned exactly with the line center (i.e., $\delta = S/2$), the line directly underneath the tip is subjected to pure compression and does not buckle at all. In this case, the critical load is 500 $\mu$N, considerably higher than those for tip locations off the line center, as noted in Figure 9. A large portion of this critical load is due to the pure compression of the center line, while the buckling instability occurs for the two lines immediately adjacent to the center line. From a single-line model with the

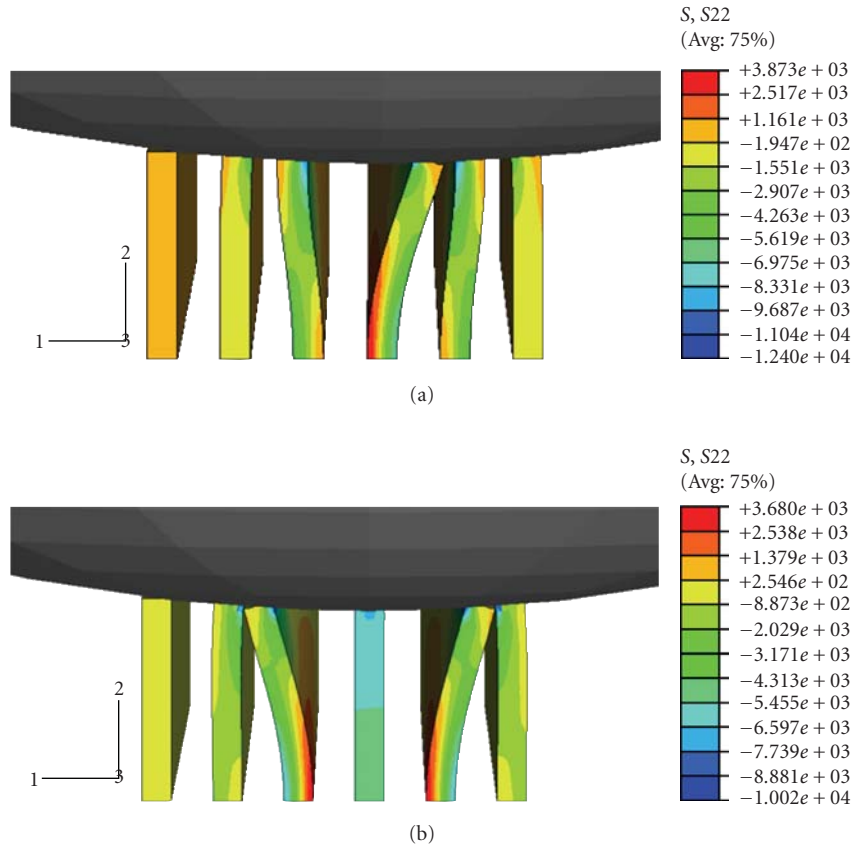


Figure 11: Simulated buckling modes of SiNLs under indentation with the indenter tip aligned 3 nm off the line center. (a) With frictionless contact between the indenter and the lines, (b) with coefficient of friction, $\mu = 0.002$, at the contact.

indenter tip located 180 nm off the line center (or, $\delta = 90$ nm for the left center line), the critical load for each of these two lines is obtained as 116 $\mu$N, twice of which contributes less than half of the total critical load from the six-line model.

### 4.3. Effect of friction

As illustrated in Figure 4, the normal contact force acting on the line tends to push the top of the line sliding against the indenter surface. This has been confirmed by the FE simulations assuming frictionless contact between the indenter and the SiNLs (see Figure 8). With friction, however, the sliding would be hindered, and thus the response of the SiNLs under indentation would be altered. By using a simple Coulomb friction model [28], we define a frictional contact surface between the indenter and the SiNLs in the FE models to analyze the effect of the friction coefficient $\mu$. First, it is noted that the frictional contact property has negligible influence on the load-displacement curve before the critical load, for the coefficients of friction between 0 and 0.02 used in the present study. On the other hand, the critical load for the buckling transition of the SiNLs increases with the friction coefficient, as shown in Figure 10. With the indenter tip aligned at the trench center, the critical load increases from 400 $\mu$N for frictionless contact to about 510 $\mu$N with a friction coefficient $\mu = 0.012$. Clearly, the friction delays the transition of the buckling model that requires significant sliding of the contact surfaces. Further increasing the friction coefficient to 0.015 sees a sudden jump of the critical load to over 800 $\mu$N. This happens because of a change in the scenario. As the sliding of the center two lines is highly constrained by the frictional force, the transition of buckling mode occurs with the next two lines farther away from the tip while the center two lines are locked underneath the indenter without buckling. The total critical load in this case thus includes a large portion from the compression of the center two lines, plus the critical load for the next two lines. It is noted that the initial contact angle between the indenter and the center lines is about 0.0115, close to the coefficient of friction that locks down the sliding of the center line. For the next two lines, the initial contact angle is around 0.05, which requires a much larger coefficient of friction to lock down their sliding.

When the indenter tip is aligned with the line center, higher critical loads are obtained except for the case with the large friction coefficient $\mu = 0.015$, as shown in Figure 10. As discussed for the frictionless contact, with the perfect alignment, the center line is under pure compression and does not buckle. The friction then delays the transition of the buckling mode for the two lines closest to the center line,

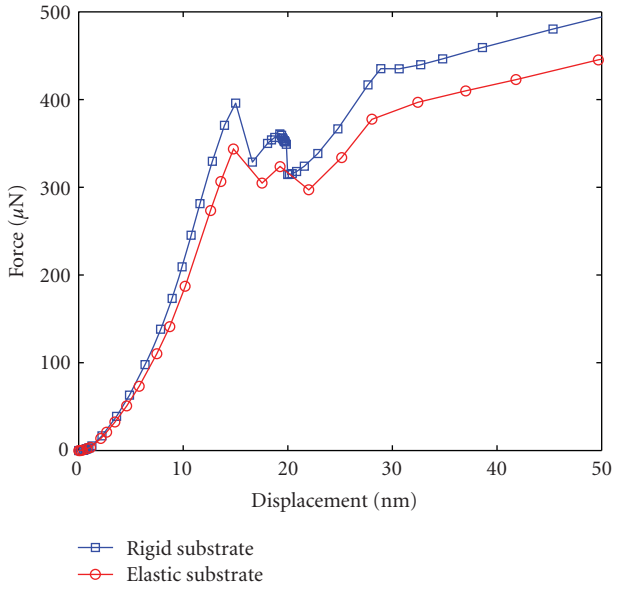


FIGURE 12: A comparison of indentation load-displacement curves from the finite element models of parallel SiNLs on a rigid substrate and on an elastic substrate, respectively.

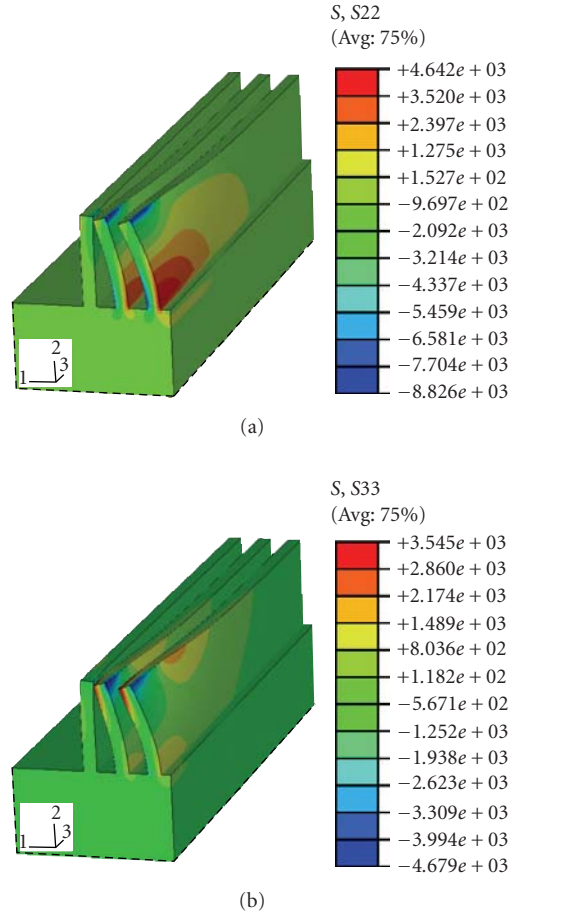


FIGURE 13: Stress distributions from a finite element model with SiNLs on an elastic substrate under a symmetric trench center loading. (a) and (b) show contours of the normal stresses in the 2- and 3-directions, respectively.

giving higher critical loads for larger coefficients of friction. For the case of the large friction coefficient ($\mu = 0.015$), the critical load for the line center indentation becomes lower than that for the trench center indentation, because the former has only one line locked underneath the indenter while the latter has two. Interestingly, when the location of the indenter tip is slightly off the line center, the center line can still be locked by the frictional contact, while it always slides and buckles with a frictionless contact. This is illustrated in Figure 11, which shows buckling of the SiNLs from the FE models with the indenter tip aligned 3 nm off the line center, one with frictionless contact and the other with a coefficient of friction $\mu = 0.002$. As shown in Figure 10, the former gives a critical load close to that under the symmetric trench-center loading, and the latter gives a critical load close to that under the exact line-center loading for the same coefficient of friction. Therefore, the friction at the contact leads to a change in the critical load and its dependence on the tip location.

The critical loads from the experiments, ranging from 480 $\mu$N to 700 $\mu$N, fall within the range shown in Figure 10 from the FE modeling. The scattering in the experimental data thus may be attributed to the combined effect of contact friction and tip location. The contact friction may vary with local surface conditions for the indenter and the SiNLs, the tip location varies from test to test due to the lack of lateral resolution for exact positioning. Therefore, refined experiments with sufficient lateral resolution would reduce the data scattering and give a better measure of the friction properties. It is noted that the coefficients of friction used in the present study are about one order of magnitude lower than those obtained from a tribological test using a spherical diamond tip (tip radius 20 $\mu$m) on single-crystal Si (100) wafers [32]. The indentation tests on the SiNLs may offer a new approach to studying friction at the nanoscales.

### 4.4. Effect of elastic substrate

In the FE simulations discussed above, the SiNLs have been assumed to be supported by a rigid foundation. Consideration of an elastic substrate requires a significant increase in the number of FE elements and the computational time. To illustrate the effect of the elastic substrate, a FE model is constructed with six lines under a symmetric loading at the trench center. The dimensions of the substrate are 490 nm (height) by 900 nm (width) by 3000 nm (length). The material properties for the substrate are the same as those for the SiNLs, with Young's modulus 140 GPa and Poisson's ratio 0.27. The contact surface is defined as frictionless for this case. Figure 12 compares the load-displacement curves from the models with the elastic and rigid substrates. Clearly, the model with the elastic substrate is more compliant, and the critical load for the onset of instability is lower. A higher Young's modulus could be used in the FE model with an elastic substrate to match the load-displacement curve with

the experimental data, which would also increase the critical load. The final result for the critical load would be close to that of the rigid substrate model.

The stress distribution after the buckling transition, obtained from the FE model with the elastic substrate, is shown in Figure 13. As expected, stress concentration near the roots of the SiNLs is observed. In addition, relatively tensile high stresses in the direction parallel to the SiNLs exist at the top of center line, due to the localized buckling deformation. The locations of high tensile stresses, along with the specific crystal orientation and cleavage planes, would be useful for understanding fracture of the SiNLs observed in the experiments (see Figure 3).

## 5. SUMMARY

A buckling instability is observed in the nanoindentation tests of the parallel silicon nanolines. A systematic analysis of the buckling modes is presented based on finite element modeling. In particular, the effects of indenter tip location and contact friction on the critical load are discussed as possible causes for the scattering of the experimental data. The result from the present study demonstrates a potential methodology to study buckling, friction, and fracture at the nanoscale via a combination of experiments and modeling.

## ACKNOWLEDGMENTS

The authors are grateful for the financial support by National Science Foundation through Grant no. CMMI-0654105. The work was performed in part at the Microelectronics Research Center of the University of Texas at Austin, a member of the National Nanofabrication Infrastructure Network supported by National Science Foundation under Award no. 0335765.

## REFERENCES

[1] T. Namazu, Y. Isono, and T. Tanaka, "Evaluation of size effect on mechanical properties of single crystal silicon by nanoscale bending test using AFM," *Journal of Microelectromechanical Systems*, vol. 9, no. 4, pp. 450–459, 2000.

[2] T. Namazu, Y. Isono, and T. Tanaka, "Plastic deformation of nanometric single crystal silicon wire in AFM bending test at intermediate temperatures," *Journal of Microelectromechanical Systems*, vol. 11, no. 2, pp. 125–135, 2002.

[3] M. S. Islam, S. Sharma, T. I. Kamins, and R. S. Williams, "A novel interconnection technique for manufacturing nanowire devices," *Applied Physics A*, vol. 80, no. 6, pp. 1133–1140, 2005.

[4] M. Tabib-Azar, M. Nassirou, R. Wang, et al., "Mechanical properties of self-welded silicon nanobridges," *Applied Physics Letters*, vol. 87, no. 11, Article ID 113102, 3 pages, 2005.

[5] S. Hoffmann, I. Utke, B. Moser, et al., "Measurement of the bending strength of vapor-liquid-solid grown silicon nanowires," *Nano Letters*, vol. 6, no. 4, pp. 622–625, 2006.

[6] T. Alan, M. A. Hines, and A. T. Zehnder, "Effect of surface morphology on the fracture strength of silicon nanobeams," *Applied Physics Letters*, vol. 89, no. 9, Article ID 091901, 3 pages, 2006.

[7] J. Deneen, W. M. Mook, A. Minor, W. W. Gerberich, and C. B. Carter, "In situ deformation of silicon nanospheres," *Journal of Materials Science*, vol. 41, no. 14, pp. 4477–4483, 2006.

[8] R. He and P. Yang, "Giant piezoresistance effect in silicon nanowires," *Nature Nanotechnology*, vol. 1, no. 1, pp. 42–46, 2006.

[9] X. L. Feng, R. He, P. Yang, and M. L. Roukes, "Very high frequency silicon nanowire electromechanical resonators," *Nano Letters*, vol. 7, no. 7, pp. 1953–1959, 2007.

[10] M.-F. Yu, O. Lourie, M. J. Dyer, K. Moloni, T. F. Kelly, and R. S. Ruoff, "Strength and breaking mechanism of multiwalled carbon nanotubes under tensile load," *Science*, vol. 287, no. 5453, pp. 637–640, 2000.

[11] Y. Zhu and H. D. Espinosa, "An electromechanical material testing system for in situ electron microscopy and applications," *Proceedings of the National Academy of Sciences of the United States of America*, vol. 102, no. 41, pp. 14503–14508, 2005.

[12] J. Y. Huang, S. Chen, Z. F. Ren, et al., "Enhanced ductile behavior of tensile-elongated individual double-walled and triple-walled carbon nanotubes at high temperatures," *Physical Review Letters*, vol. 98, no. 18, Article ID 185501, 4 pages, 2007.

[13] M. M. J. Treacy, T. W. Ebbesen, and J. M. Gibson, "Exceptionally high Young's modulus observed for individual carbon nanotubes," *Nature*, vol. 381, no. 6584, pp. 678–680, 1996.

[14] P. Poncharal, Z. L. Wang, D. Ugarte, and W. A. de Heer, "Electrostatic deflections and electromechanical resonances of carbon nanotubes," *Science*, vol. 283, no. 5407, pp. 1513–1516, 1999.

[15] X. Li, B. Bhushan, K. Takashima, C.-W. Baek, and Y.-K. Kim, "Mechanical characterization of micro/nanoscale structures for MEMS/NEMS applications using nanoindentation techniques," *Ultramicroscopy*, vol. 97, no. 1–4, pp. 481–494, 2003.

[16] W. C. Oliver and G. M. Pharr, "An improved technique for determining hardness and elastic modulus using load and displacement sensing indentation experiments," *Journal of Materials Research*, vol. 7, no. 6, pp. 1564–1583, 1992.

[17] R. F. Cook, "Strength and sharp contact fracture of silicon," *Journal of Materials Science*, vol. 41, no. 3, pp. 841–872, 2006.

[18] M.-F. Yu, T. Kowalewski, and R. S. Ruoff, "Investigation of the radial deformability of individual carbon nanotubes under controlled indentation force," *Physical Review Letters*, vol. 85, no. 7, pp. 1456–1459, 2000.

[19] H. J. Qi, K. B. K. Teo, K. K. S. Lau, et al., "Determination of mechanical properties of carbon nanotubes and vertically aligned carbon nanotube forests using nanoindentation," *Journal of the Mechanics and Physics of Solids*, vol. 51, no. 11-12, pp. 2213–2237, 2003.

[20] X. Li, H. Gao, C. J. Murphy, and K. K. Caswell, "Nanoindentation of silver nanowires," *Nano Letters*, vol. 3, no. 11, pp. 1495–1498, 2003.

[21] G. Feng, W. D. Nix, Y. Yoon, and C. J. Lee, "A study of the mechanical properties of nanowires using nanoindentation," *Journal of Applied Physics*, vol. 99, no. 7, Article ID 074304, 10 pages, 2006.

[22] S. X. Mao, M. Zhao, and Z. L. Wang, "Nanoscale mechanical behavior of individual semiconducting nanobelts," *Applied Physics Letters*, vol. 83, no. 5, pp. 993–995, 2003.

[23] X. Chen, N. Ogasawara, M. Zhao, and N. Chiba, "On the uniqueness of measuring elastoplastic properties from indentation: the indistinguishable mystical materials," *Journal of the Mechanics and Physics of Solids*, vol. 55, no. 8, pp. 1618–1660, 2007.

[24] J. Li, K. J. Van Vliet, T. Zhu, S. Yip, and S. Suresh, "Atomistic mechanisms governing elastic limit and incipient plasticity in crystals," *Nature*, vol. 418, no. 6895, pp. 307–310, 2002.

[25] R. A. Allen, B. A. am Ende, M. W. Cresswell, et al., "Test structures for referencing electrical linewidth measurements to silicon lattice parameters using HRTEM," *IEEE Transactions on Semiconductor Manufacturing*, vol. 16, no. 2, pp. 239–248, 2003.

[26] B. Li, M. K. Kang, K. Lu, et al., "Fabrication and characterization of patterned single-crystal silicon nanolines," *Nano Letters*, vol. 8, no. 1, pp. 92–98, 2008.

[27] J. J. Vlassak, M. Ciavarella, J. R. Barber, and X. Wang, "The indentation modulus of elastically anisotropic materials for indenters of arbitrary shape," *Journal of the Mechanics and Physics of Solids*, vol. 51, no. 9, pp. 1701–1721, 2003.

[28] X. Chen, J. W. Hutchinson, and A. G. Evans, "Simulation of the high temperature impression of thermal barrier coatings with columnar microstructure," *Acta Materialia*, vol. 52, no. 3, pp. 565–571, 2004.

[29] M. Watanabe, T. Xu, C. G. Levi, A. S. Gandhi, and A. G. Evans, "Shear band formation in columnar thermal barrier oxides," *Acta Materialia*, vol. 53, no. 13, pp. 3765–3773, 2005.

[30] "ABAQUS Documentation (Version 6.6)," ABAQUS, Inc., Providence, RI, USA, 2006.

[31] E. Riks, "An incremental approach to the solution of snapping and buckling problems," *International Journal of Solids and Structures*, vol. 15, no. 7, pp. 529–551, 1979.

[32] B. Bhushan and X. Li, "Micromechanical and tribological characterization of doped single-crystal silicon and polysilicon films for microelectromechanical systems devices," *Journal of Materials Research*, vol. 12, no. 1, pp. 54–63, 1997.

Hindawi Publishing Corporation
Journal of Nanomaterials
Volume 2008, Article ID 380961, 5 pages
doi:10.1155/2008/380961

*Research Article*

# Dislocation Nucleation and Pileup under a Wedge Contact at Nanoscale

**Y. F. Gao[1] and J. Lou[2]**

[1] *Department of Materials Science and Engineering, University of Tennessee, Knoxville, TN 37996, USA*
[2] *Department of Mechanical Engineering and Materials Science, Rice University, Houston, TX 77251, USA*

Correspondence should be addressed to Y. F. Gao, ygao7@utk.edu

Received 5 November 2007; Accepted 18 January 2008

Recommended by Junlan Wang

Indentation responses of crystalline materials have been found to be radically different at micrometer and nanometer scales. The latter is usually thought to be controlled by the nucleation of dislocations. To explore this physical process, a dislocation mechanics study is performed to determine the conditions for the nucleation of a finite number of dislocations under a two-dimensional wedge indenter, using the Rice-Thomson nucleation criterion. The configurational force on the dislocation consists of the applied force, the image force, and the interaction force between dislocations. Dislocations reach equilibrium positions when the total driving force equals the effective Peierls stress, giving a set of nonlinear equations that can be solved using the Newton-Raphson method. When the apex angle of the wedge indenter increases, the critical contact size for dislocation nucleation increases rapidly, indicating that dislocation multiplication near a blunt wedge tip is extremely difficult. This geometric dependence agrees well with experimental findings.



## 1. INTRODUCTION

The ability to quantitatively model mesoscopic material behavior is a critical step in understanding reliability analysis and material design for applications ranging from aerospace components to nanoelectronics. Many experimental studies in the past decade have shown that the contact plasticity is size-dependent (i.e., indentation size effects, ISEs) and thus is essentially a multiscale problem [1–7]. This phenomenon is believed to be due to the collective behavior of dislocation nucleation and storage under the contact. Statistical theories have been developed to understand the dislocation microstructures that form and evolve during contact events, but most of these theories are only applicable when the contact size is larger than micrometers. A number of recent experiments demonstrate the importance of individual dislocation nucleation events, such as pop-in excursions on the load-displacement curves [7, 8], which are thought to govern the indentation size effects at nanoscale, while the size effects at microscale are associated with strain gradient effects and geometrically necessary dislocations [1, 2, 7].

A variety of analyses have been carried out using discrete dislocation and phenomenological strain gradient plasticity to model ISE across the length scales [9, 10]. At larger length scale (submicron to micrometer scales), both strain gradient plasticity theories that are based on geometrically necessary dislocations and discrete dislocation simulations have provided important insights in understanding the dependence of microhardness on contact size. Many recent theories aim to modify these theories for nanohardness measurements [4, 10], but the connection to the dislocation microstructure still remains elusive. At sufficiently small-length scale, the size of the contact region under high stress may be comparable to the dislocation spacing, so that the indentation behavior may enter the dislocation-nucleation-controlled regime. This work attempts to explore this line from the study of the dislocation nucleation and pileup under a two-dimensional wedge contact tip.

## 2. PROBLEM FORMULATION AND SOLUTION METHOD

Figure 1 gives the problem definition where the apex half angle is $\alpha$, the applied load is $P$ (per unit length out of the plane), and the contact size is $a$. Suppose that a dislocation

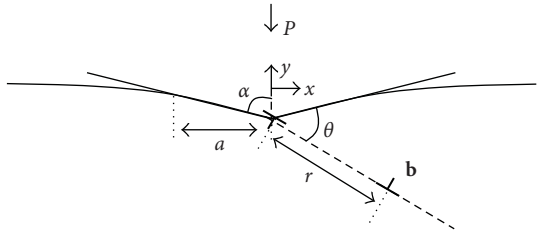


Figure 1: Schematic illustration and geometric conventions of the contact problem.

$\mathbf{b} = b(\cos\theta, \sin\theta, 0)^{\mathrm{T}}$ can be nucleated from the indenter tip, then a negative dislocation $-\mathbf{b}$ will be left. This dislocation pair will lead to tilting of the indenter, but such a modification is usually very small [11] and will be neglected in this work. The micromechanical model consists of three parts: (1) the determination of the configurational force on the dislocation, (2) the use of the Rice-Thomson criterion for dislocation nucleation, and (3) the calculation of the equilibrium dislocation positions. In the continuum dislocation modeling, we use the Rice-Thomson dislocation nucleation criterion [12, 13]. If the driving force on a dislocation at a distance $\eta$ from a stress concentration is greater than the Peierls force, the dislocation can be emitted from the step. The dislocation glides only if the driving force overcomes the Peierls force. In the Rice-Thomson model, parameter $\eta$ characterizes the size of the dislocation emission process zone. We can either regard it as a material parameter or determine it by atomistic simulations. With the information of $\eta$ and the effective Peierls stress $\tau_p$, we can easily decide whether a dislocation nucleates and where the equilibrium position of the nucleated dislocation would be, as long as the driving force on the dislocation is determined.

The driving force on the dislocation $\mathbf{b}$ has three parts:

$$J = J_{\mathrm{appl}} + J_{\mathrm{image}} + J_{\mathrm{int}}, \tag{1}$$

where $J_{\mathrm{appl}}$ is the applied driving force, $J_{\mathrm{image}}$ is the image force, and $J_{\mathrm{int}}$ is the interaction force due to the dislocation $-\mathbf{b}$ and/or other pairs of dislocations. The applied driving force can be computed from the stress field [11]:

$$\begin{aligned}
\sigma_{xx} &= \frac{2y}{\pi a}\left(\frac{\mu}{1-\nu}\right)\frac{\cot\alpha}{\pi}\int_{-1}^{1}\frac{\cosh^{-1}(1/t)(x/a-t)^2 dt}{\left[(x/a-t)^2+(y/a)^2\right]^2},\\
\sigma_{yy} &= \frac{2y^3}{\pi a^3}\left(\frac{\mu}{1-\nu}\right)\frac{\cot\alpha}{\pi}\int_{-1}^{1}\frac{\cosh^{-1}(1/t)dt}{\left[(x/a-t)^2+(y/a)^2\right]^2},\\
\sigma_{xy} &= \frac{2y^2}{\pi a^2}\left(\frac{\mu}{1-\nu}\right)\frac{\cot\alpha}{\pi}\int_{-1}^{1}\frac{\cosh^{-1}(1/t)(x/a-t)dt}{\left[(x/a-t)^2+(y/a)^2\right]^2},
\end{aligned} \tag{2}$$

and the Peach-Koehler formula:

$$J_{\mathrm{appl}} = \left[(\boldsymbol{\sigma}\cdot\mathbf{b})\times(0,0,1)^{\mathrm{T}}\right]\cdot(\cos\theta,\sin\theta,0)^{\mathrm{T}}. \tag{3}$$

Those curves of $J_{\mathrm{appl}}(1-\nu)/\mu b$ against $r/b$ will collapse onto each other by replotting $J_{\mathrm{appl}}(1-\nu)/\mu b$ against $r/a$, clearly because the indenter is self-similar. The state of stress at the apex comprises a finite shear stress superposed on an infinite hydrostatic pressure. The applied driving force at the apex can be written as

$$\frac{(1-\nu)}{\mu b}J_{\mathrm{appl}}\Big|_{r\to 0} = \frac{\cot\alpha}{\pi}f(\theta), \tag{4}$$

where $f(\theta)$ is a dimensionless function that only depends on the slip-plane angle of the order of unity. This stress state is radically different from the stress singularity caused by a crack tip, or a flat-ended punch under normal contact, or an arbitrary indenter under tangential contact [14, 15]. The implications on the dislocation nucleation behavior will be discussed shortly.

The image force can be determined by considering two opposing semi-infinite cracks in an undislocated plane, subjected to tractions that will cancel the tractions induced by the dislocation in an uncracked plane. Using the complex function analysis, the stress field at $z = x + iy$, caused by a dislocation $\mathbf{b}$ at $z_0 = x_0 + iy_0$, in an uncracked plane is given by [16]

$$\begin{aligned}
\widetilde{\sigma}_{xx} + \widetilde{\sigma}_{yy} &= 2\left[\Phi(z) + \overline{\Phi(z)}\right],\\
\widetilde{\sigma}_{yy} + i\widetilde{\sigma}_{xy} &= \overline{\Phi(z)} + \Omega(z) + (\overline{z}-z)\Phi'(z),
\end{aligned} \tag{5}$$

where the holomorphic complex functions $\Phi$ and $\Omega$ are

$$\begin{aligned}
\Phi(z) &= \frac{B}{z-z_0}, \qquad \Omega(z) = B\frac{\overline{z}_0 - z_0}{(z-z_0)^2} + \frac{\overline{B}}{z-z_0},\\
B &= \frac{\mu}{\pi i(1+\kappa)}(b_x + ib_y) = \left(\frac{\mu}{1-\nu}\right)\frac{1}{4\pi}(-ib_x + b_y),
\end{aligned} \tag{6}$$

and $\kappa = 3 - 4\nu$ for plane strain.

Now consider an undislocated plane with two opposing semi-infinite cracks, subjected to the corrected tractions $-\widetilde{\boldsymbol{\sigma}}(|x| > a,\ y = 0)$. Following Tada's solution 4.5 [17], the correction stress field can be determined by

$$\begin{aligned}
Z_{\mathrm{I}}(z) &= \left(\int_{-\infty}^{-a} + \int_{a}^{\infty}\right)dt\frac{-\widetilde{\sigma}_{yy}(t,0)}{\pi}\frac{\sqrt{t^2-a^2}}{\sqrt{a^2-z^2}}\left(\frac{1}{t-z} + \frac{2z}{a^2}\right),\\
Z_{\mathrm{II}}(z) &= \left(\int_{-\infty}^{-a} + \int_{a}^{\infty}\right)dt\frac{\widetilde{\sigma}_{xy}(t,0)}{\pi}\frac{\sqrt{t^2-a^2}}{\sqrt{a^2-z^2}}\left(\frac{1}{t-z}\right),
\end{aligned} \tag{7}$$

where $Z_{\mathrm{I}}(z)$ and $Z_{\mathrm{II}}(z)$ are the mode-I and mode-II Westergaard stress functions, respectively. The stress components inside the substrate are

$$\begin{aligned}
\widehat{\sigma}_{xx} &= \left(\mathrm{Re}Z_{\mathrm{I}} - y\mathrm{Im}Z_{\mathrm{I}}'\right) + \left(2\mathrm{Im}Z_{\mathrm{II}} + y\mathrm{Re}Z_{\mathrm{II}}'\right),\\
\widehat{\sigma}_{yy} &= \left(\mathrm{Re}Z_{\mathrm{I}} + y\mathrm{Im}Z_{\mathrm{I}}'\right) + \left(-y\mathrm{Re}Z_{\mathrm{II}}'\right),\\
\widehat{\sigma}_{xy} &= \left(-y\mathrm{Re}Z_{\mathrm{I}}'\right) + \left(\mathrm{Re}Z_{\mathrm{II}} - y\mathrm{Im}Z_{\mathrm{II}}'\right).
\end{aligned} \tag{8}$$

In (7), we have assumed that the contact region is full bonded, so that the crack analogy can be used. This is equivalent to the infinite friction condition, or to the contact between two identical solids (regardless of the friction condition). For two different materials under finite frictional contact, the shear stress inside the contact should be considered

in the calculation of image force. Finite friction usually does not change the load-displacement curve noticeably [18], but may change the stress distribution and thus lead to a large contribution to the image force.

The image force $J_{\text{image}}$ can be computed from the stress fields in (8) and the Peach-Koehler formula. The interaction force $J_{\text{int}}$ can be easily computed from (5) and (8) by substituting $-\mathbf{b}$ into $\mathbf{b}$, and 0 into $z_0$. The image force becomes less important when the contact size increases, since its magnitude decays rapidly with respect to the distance from the free surface. The interaction force decays with respect to the location of the leading dislocation.

We are concerned with the critical load or contact size to nucleate a dislocation. Using the Rice-Thomson criterion, a straightforward dimensional analysis gives that

$$\frac{a_{\text{crt}}}{b} = \Pi_a\left(\frac{\eta}{b}, \frac{\tau_p}{\mu}(1-\nu), \alpha, \theta\right). \tag{9}$$

After the dislocation is nucleated, the equilibrium position of the dislocation is determined by $J = \tau_p b$, leading to

$$\frac{r_{\text{eq}}}{a} = \Pi_r\left(\frac{a}{b}, \frac{\eta}{b}, \frac{\tau_p}{\mu}(1-\nu), \alpha, \theta\right), \tag{10}$$

with $a > a_{\text{crt}}$. It is anticipated that when $a \gg b$, the driving force is dominated by the applied stress field, so that $r_{\text{eq}}/a$ becomes size-independent since the applied stress field is self-similar. The relationship between $r_{\text{eq}}/a$ and $a/b$ gives a qualitative measure of the dislocation density under the indenter.

When there are many dislocations, the driving force on the $k$th dislocation consists of (1) and the interaction force from other pair of dislocations. The latter can be easily evaluated from (5) and (8). To determine the equilibrium positions of $N$ dislocations, we use the Newton-Raphson method to solve $N$ force-balance equations. The root finding process is very slow because of the $N$-dimensional functions and the shallow slope of driving force curves near equilibria.

## 3. RESULTS AND DISCUSSION

Figure 2 shows the total driving force with respect to the dislocation location. The zone where the interaction force dominates does not proportionally increase with the contact size. Consequently, the driving force on a fictitious dislocation at $r = \eta$ will eventually be nonzero and larger than the Peierls stress, assuming that the Peierls stress is smaller than $J_{\text{appl}}(r = 0)$.

Figure 3(a) shows the critical contact size to nucleate one and many dislocations. The Rice-Thomson model introduces a length scale $\eta$, so that the first dislocation nucleation occurs at a finite contact size for this otherwise self-similar contact problem. It is found that the larger the wedge half-angle, the more difficult to nucleate a dislocation. The image force and interaction force are independent of the wedge angle. The applied driving force, however, is proportional to $\cot\alpha$. In addition, the shear stress near the wedge tip is bounded, so that there is a critical angle above which the maximum applied driving force is lower than the Peierls stress. The second and subsequent dislocations occur

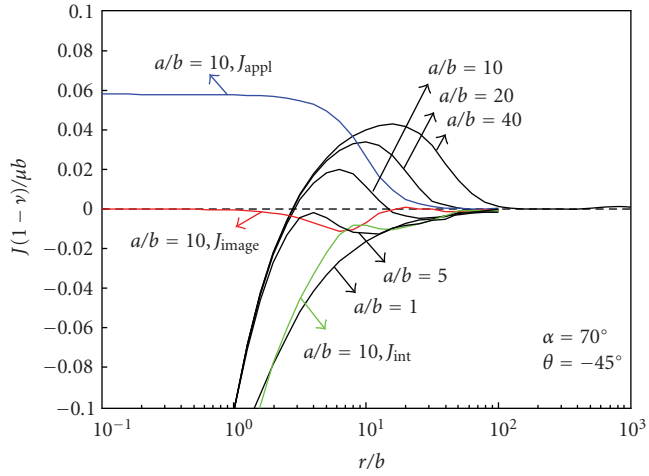


Figure 2: The configurational force on the dislocation plotted against the dislocation position with varying contact size.

at higher contact size, since the existing dislocation exerts strong back stress to prevent further dislocation nucleation. The diverging trend with respect to $\alpha$ is more evident, suggesting that dislocation multiplication for blunt wedges is extremely difficult. Consequently, when we are concerned with the effective dislocation number and density under a wedge contact, we must incorporate the bulk dislocation nucleation sources. The analysis presented in this paper is therefore only applicable for nanocontact experiments. This indenter geometry effects were also observed in a series of experiments [6, 19] where the sharper cube corner indenter tip (with half angle of $\sim 35^{\circ}$) shows higher hardness value as compared to the Berkovich indenter tip (with half angle of $\sim 70^{\circ}$) at the same indentation depth in the nanometer length scale, resulting in more dramatic indentation size effects.

Figure 3(b) shows the normalized dislocation equilibrium positions, $r_{\text{eq}}/a$, with respect to the contact size. When $a/b \to \infty$, (10) will be independent of the contact size, and the effective plasticity zone will be proportional to the contact size. Consequently, the dislocation density is approximately linear with $b/a$ at large contact size. (Of course, when the contact size is large, it is the bulk nucleation sources and the statistically stored dislocations that govern the plastic zone and contact behavior.) However, this relationship will break down for small-contact size, because of the discrete nature of the dislocation nucleation and motion, and the length scale $\eta$. It thus becomes inappropriate to estimate plastic zone size in terms of contact size and relate the dislocation density to hardness in the nanohardness measurements. A more rational treatment would require a closer look at the connection between the mean contact pressure and the dislocation microstructure evolution at nanometer length scale.

## 4. SUMMARY

A dislocation mechanics study is performed here to examine the conditions for dislocation nucleation from, and

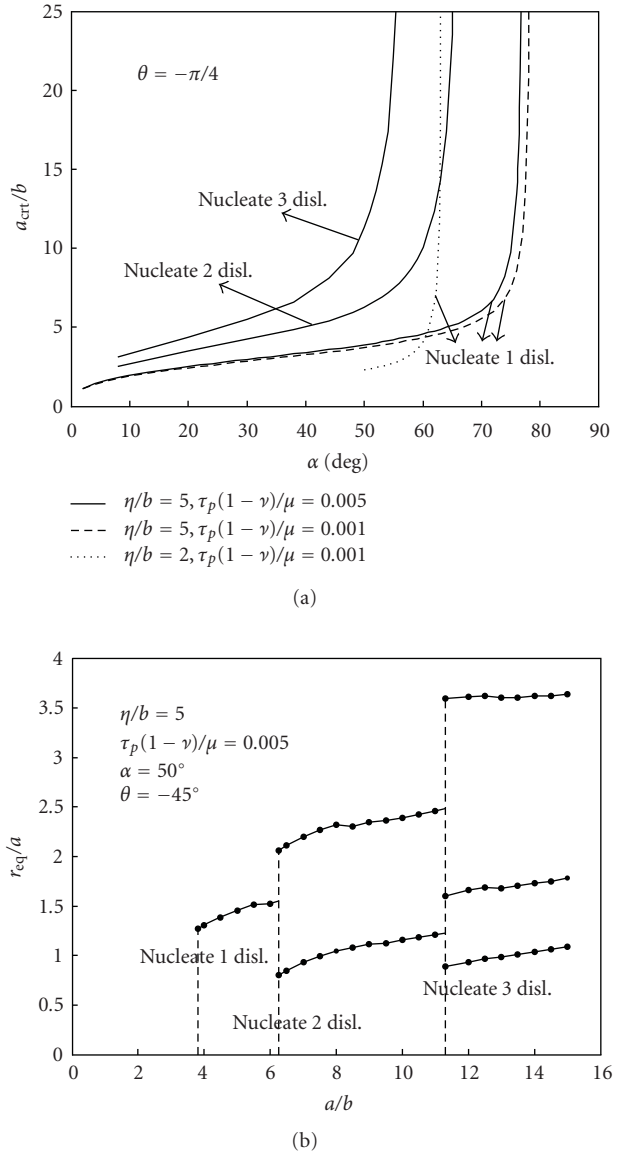


Figure 3: (a) The critical contact size to nucleate dislocations with respect to the wedge half-angle. (b) The equilibrium positions of nucleated dislocations with respect to the contact size.

pileup under, a wedge indenter. The configurational force on the dislocation is evaluated by linear elastic analysis, and the Rice-Thomson criterion is used for the dislocation nucleation. The contact strength map in Figure 3(a) shows that dislocation nucleation and multiplication are extremely difficult for blunt indenters, mainly because the stress state near the wedge tip consists of a finite shear stress and an infinite hydrostatic component. The ratio of the effective plastic zone size to the contact size is found to approach a constant when there are sufficient numbers of dislocations at large contact size. However, at nanoscale we should directly investigate the relationship between contact pressure and dislocation microstructure, instead of using dislocation-density-based hardening law.

## ACKNOWLEDGMENTS

Y. F. Gao would like to acknowledge the support from the Joint Institute of Advanced Materials at the University of Tennessee. J. Lou gratefully acknowledges the startup fund from Rice University.

## REFERENCES

[1] W. D. Nix and H. Gao, "Indentation size effects in crystalline materials: a law for strain gradient plasticity," *Journal of the Mechanics and Physics of Solids*, vol. 46, no. 3, pp. 411–425, 1998.

[2] J. G. Swadener, E. P. George, and G. M. Pharr, "The correlation of the indentation size effect measured with indenters of various shapes," *Journal of the Mechanics and Physics of Solids*, vol. 50, no. 4, pp. 681–694, 2002.

[3] J. Lou, P. Shrotriya, T. Buchheit, D. Yang, and W. O. Soboyejo, "Nanoindentation study of plasticity length scale effects in LIGA Ni microelectromechanical systems structures," *Journal of Materials Research*, vol. 18, no. 3, pp. 719–728, 2003.

[4] G. Feng and W. D. Nix, "Indentation size effect in MgO," *Scripta Materialia*, vol. 51, no. 6, pp. 599–603, 2004.

[5] Z. Zong, J. Lou, O. O. Adewoye, A. A. Elmustafa, F. Hammad, and W. O. Soboyejo, "Indentation size effects in the nano- and micro-hardness of fcc single crystal metals," *Materials Science and Engineering A*, vol. 434, no. 1-2, pp. 178–187, 2006.

[6] J. Lou, P. Shrotriya, S. Allameh, T. Buchheit, and W. O. Soboyejo, "Strain gradient plasticity length scale parameters for LIGA Ni MEMs thin films," *Materials Science and Engineering A*, vol. 441, no. 1-2, pp. 299–307, 2006.

[7] W. D. Nix, J. R. Greer, G. Feng, and E. T. Lilleodden, "Deformation at the nanometer and micrometer length scales: effects of strain gradients and dislocation starvation," *Thin Solid Films*, vol. 515, no. 6, pp. 3152–3157, 2007.

[8] H. Bei, E. P. George, J. L. Hay, and G. M. Pharr, "Influence of indenter tip geometry on elastic deformation during nanoindentation," *Physical Review Letters*, vol. 95, no. 4, Article ID 045501, 1–4, 2005.

[9] A. Widjaja, A. Needleman, and E. van der Giessen, "The effect of indenter shape on sub-micron indentation according to discrete dislocation plasticity," *Modelling and Simulation in Materials Science and Engineering*, vol. 15, no. 1, pp. S121–S131, 2007.

[10] Y. Huang, F. Zhang, K. C. Hwang, W. D. Nix, G. M. Pharr, and G. Feng, "A model of size effects in nano-indentation," *Journal of the Mechanics and Physics of Solids*, vol. 54, no. 8, pp. 1668–1686, 2006.

[11] K. L. Johnson, *Contact Mechanics*, Cambridge University Press, Cambridge, UK, 1985.

[12] J. R. Rice and R. Thomson, "Ductile versus brittle behavior of crystals," *Philosophical Magazine*, vol. 29, no. 1, pp. 73–97, 1973.

[13] H. H. Yu, P. Shrotriya, Y. F. Gao, and K.-S. Kim, "Microplasticity of surface steps under adhesive contact: part I-surface yielding controlled by single-dislocation nucleation," *Journal of the Mechanics and Physics of Solids*, vol. 55, no. 3, pp. 489–516, 2007.

[14] Y. F. Gao, B. N. Lucas, J. C. Hay, W. C. Oliver, and G. M. Pharr, "Nanoscale incipient asperity sliding and interface micro-slip assessed by the measurement of tangential contact stiffness," *Scripta Materialia*, vol. 55, no. 7, pp. 653–656, 2006.

[15] Y. F. Gao, H. T. Xu, W. C. Oliver, and G. M. Pharr, "A comparison of Coulomb friction and friction stress models based on multidimensional nanocontact experiments," to appear in *Journal of Applied Mechanics*.

[16] Z. Suo, "Singularities interacting with interfaces and cracks," *International Journal of Solids and Structures*, vol. 25, no. 10, pp. 1133–1142, 1989.

[17] H. Tada, P. C. Paris, and G. R. Irwin, *The Stress Analysis of Cracks Handbook*, ASME Press, New York, NY, USA, 2000.

[18] Y. F. Gao, H. T. Xu, W. C. Oliver, and G. M. Pharr, "Effective elastic modulus of film-on-substrate systems under normal and tangential contact," *Journal of the Mechanics and Physics of Solids*, vol. 56, no. 2, pp. 402–416, 2008.

[19] R. A. Mirshams and P. Parakala, "Nanoindentation of nanocrystalline Ni with geometrically different indenters," *Materials Science and Engineering A*, vol. 372, no. 1-2, pp. 252–260, 2004.

Hindawi Publishing Corporation
Journal of Nanomaterials
Volume 2008, Article ID 361464, 9 pages
doi:10.1155/2008/361464

*Research Article*

# Statistical Molecular Dynamics Study of (111) and (100) Ni Nanocontacts: Evidences of Pentagonal Nanowires

**P. García-Mochales,[1] R. Paredes,[2,3] S. Peláez,[3] and P. A. Serena[3]**

[1] *Departamento de Física de la Materia Condensada, Universidad Autónoma de Madrid, Cantoblanco, 28049 Madrid, Spain*
[2] *Centro de Física, Instituto Venezolano de Investigaciones Científicas Altos de Pipe, 1020-A Caracas, Venezuela*
[3] *Instituto de Ciencia de Materiales de Madrid, Consejo Superior de Investigaciones Científicas, c/ Sor Juana Inés de la Cruz 3, Cantoblanco, 28049 Madrid, Spain*

Correspondence should be addressed to P. A. Serena, pedro.serena@icmm.csic.es

Received 21 September 2007; Accepted 11 January 2008

Recommended by Jun Lou

We present molecular dynamics calculations on the evolution of Ni nanowires stretched along the (111) and (100) directions, and at two different temperatures. Using a methodology similar to that required to build experimental conductance histograms, we construct minimum crosssection histograms $H(S_m)$. These histograms are useful to understand the type of favorable atomic configurations appearing during the nanowire breakage. We have found that minimum crosssection histograms obtained for (111) and (100) stretching directions are rather different. When the nanowire is stretched along the (111) direction, monomer and dimer-like configurations appear, giving rise to well-defined peaks in $H(S_m)$. On the contrary, (100) nanowire stretching presents a different breaking pattern. In particular, we have found, with high probability, the formation of staggered pentagonal nanowires, as it has been reported for other metallic species.



## 1. INTRODUCTION

Nanotechnology involves the design, fabrication, and application of structures by controlling their composition, shape, and size at the nanometer scale [1]. In particular, the control of these properties will allow to exploit a whole set of novel physical and chemical features in future nanoelectronics development. Such development includes the study of the electron transport through different candidates to be used as nanoelectronics building blocks. Among these candidates, metallic nanowires or nanocontacts will play a relevant role [2].

The interest on metallic nanowires and nanocontacts rises from their rich phenomenology. Electron transport through metallic nanowires present ballistic features and, in addition, well-defined electron transport modes or channels appear associated to the transversal confinement of electrons for those nanowires with diameters of the order of few Fermi wavelengths $\lambda_F$. In the ballistic limit, the conductance $G$ (inverse of the nanowire resistance $R$, $G = 1/R$) is described in terms of the transmission probabilities associated to these transport channels [3, 4].

Several experimental techniques have been used to form metallic nanocontacts and nanowires. Scanning tunneling microscopy (STM) [5–7] and mechanically controllable break junction (MCBJ) [8] methods are standard approaches to study the formation and rupture of nanocontacts under different experimental conditions. Metallic nanowires are also obtained using electron-beam irradiation inside ultra-high vacuum (UHV) transmission electron microscopes (TEM) [9] or using electrochemical methods [10].

The electric characterization of a metallic nanowire is usually done during its rupture. This rupture is achieved using SPM or MCBJ methods, leading to the acquisition of a nanowire conductance trace $G(t)$. In order to obtain relevant information concerning the electronic transport through nanowires of a given metallic species, conductance histograms $H(G)$ are constructed by accumulating many different conductance traces. Usually, conductance histograms present well-defined peaked structures, reflecting

the existence of preferred conductance values. Such conductance peaks are usually interpreted in terms of conductance quantization [8] or favorable atomic arrangements [11, 12].

The interpretation of a conductance histogram is a very difficult task, since it merges mechanical and electrical information as well as information coming from different conductance channels as it happens for polyvalent metals [13]. In spite of these interpretation problems, conductance histograms have become a standard tool to analyze the properties of metallic nanowires [2].

Electronic transport in atomic-sized magnetic nanowires has been profusely studied [14–32] since magnetic nanowires are a very interesting topic for future devices and applications. However, to the presence of a new degree of freedom, "spin" requires an additional effort to study and interpret experimental conductance histograms.

Among those studies dealing with magnetic nanowires, several works have addressed the study of nickel conductance histograms. A pioneering experiment (performed at RT and without applied magnetic field) showed that Ni conductance histograms constructed with thousands of unselected conductance traces presented a featureless structure [15]. However, very different results, showing well-defined peaks, were reported for Ni conductance histograms [16] obtained in UHV. In particular, conductance histograms presented clear evidences of fractional conductance quantization. Moreover, these experiments showed that conductance histograms depend on the applied magnetic field as well as on the temperature. A different set of experiments carried out at RT showed that conductance histograms (constructed with less than 100 conductance traces) suffered strong modifications when the applied magnetic increases [17, 29]. Finally, experiments carried out at 4 K, in UHV conditions, and using thousand of conductance traces showed Ni conductance histograms with two well-defined peaks around $\sim 1.6G_0$ and $\sim 3.1G_0$, respectively [21, 22, 24, 26, 31]. The position of both peaks was not modified under application of strong magnetic fields. The position of the first peak is consistent with previous experimental results [14] and may be explained in terms of monomer and dimer configurations appearing during the last stages of the nanowire breaking process [14, 33].

Encouraged by the existence of contradictory experimental results, we have focused the present study on the role played by the mechanical behavior during the breaking process of Ni nanowires at low and room temperatures. Both situations are well below the Ni melting temperature ($T_m = 1728$ K) and, in principle, a similar mechanical behavior is expected. However, we need to exclude this thermal effect as the origin of those marked differences between low temperature and room temperature $H(G)$. The aim of the present work is to carry out a statistical study of the structural evolution of Ni nanowires under stretching at low and room temperatures following a well tested methodology [12, 34–37]. We will analyze the role of the stretching direction studying two different cases: (111) and (100). An additional motivation for carrying out the present study is also related with the different computational histograms that have been recently reported for (111) and (100) orientations in Ni nanocontacts [31, 37, 38].

The paper is organized as follows: in the following section we describe the computational approach used to construct computational histograms. In Section 3, we present the results for two temperatures as well as two nanowire stretching directions; and, finally, Section 4 summarizes our main conclusions.

## 2. COMPUTATIONAL METHODS

The main goal of the present study is to understand the role of temperature and nanowire orientation on the nanowire evolution from a statistical perspective. We follow a similar strategy to the experimental one, simulating hundreds of independent breaking events, in order to determine whether the geometry presents some preferred configurations that give rise to well-defined peaked structures in the conductance histogram.

The simulation of metallic nanowire breaking events has been carried out using standard molecular dynamics (MD) methods based on a description of the atom-atom interaction based on the atomic electron densities. MD has been extensively used to study the structure and rupture of metallic nanowires. In the past years, metallic nanowire MD simulations focused on the description of single formation or breaking events, using different interatomic potentials but neglecting the study of statistical effects [6, 7, 39–49]. More recently, several MD studies on breaking and formation processes of nanocontacts have statistically analyzed the appearance of preferred atomic configurations in order to establish correlations with these peaks found in experimental conductance histograms at different temperatures [12, 31, 34–38, 50]. Some of these statistical MD simulation studies [36, 38, 50] have been carried out using a hybrid scheme, where MD configurations are used as starting point for the calculation of the electronic transport using more sophisticated quantum methods. These studies reveal that there is a complex relation between the atomic configuration and the conductance histograms.

We have simulated the nanowire dynamics using an MD scheme where atomic interaction is represented by embedded atom method (EAM) potentials [51, 52]. In EAM, the potential energy function for the system reads

$$E = \frac{1}{2}\sum_{ij}\phi(r_{ij}) + \sum_{i}F(\overline{\rho}_i), \tag{1}$$

where $i$ and $j$ run over the number of atoms. In the first term, $\phi(r)$ corresponds to a pair potential depending only on the distance $r_{ij}$ between every pair of "different" atoms $i$ and $j$. The second term is the so-called *embedding energy*, which depends on the mean electronic density $\overline{\rho}_i$ at atom $i$'s location. This density is approximated in EAM as the sum of the contributions due to the surrounding atoms, $\overline{\rho}_i = \sum_{j\neq i}\rho(r_{ij})$. Then, the embedding energy is calculated by evaluating and summing the *embedding function* $F(\rho)$ at each atom's position. Depending on the material and the specific physical properties to be studied, different pair potential

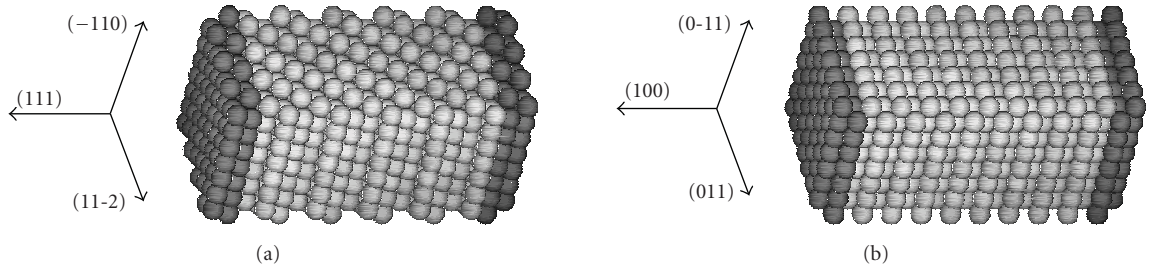


Figure 1: Initial configurations of (a) (111) and (b) (100) Ni nanowires.

$\phi(r_{ij})$, embedding $F(\rho)$, and density $\rho(r_{ij})$ functions can be defined. In the present study, we have used the EAM parameterization proposed by Mishin et al. [53]. This parameterization has been constructed by fitting almost 30 different properties obtained from experimental measurements or ab-initio calculations. These fitted properties correspond to bulk as well as surface properties, therefore taking into account low-dimensional configurations as those found during the last nanowire breaking stages.

Nanowire dynamics have been studied at constant temperature $T$ using a standard velocities scaling algorithm at every MD step. Two temperatures (4 K and 300 K) have been considered in this work in order to describe the Ni nanowire dynamics at low and room temperatures. The time interval of an MD step is $\delta t = 10^{-2}$ ps. Atomic trajectories and velocities were determined using conventional Verlet velocity integration algorithms. We have checked that the obtained minimum cross-section time evolution curves and histograms obtained with this time step are very similar to that obtained with a shorter time interval.

The simulation of a single nanowire breaking event consists of three stages. The first stage corresponds to the definition of the initial unrelaxed structure. We consider a bulk super-cell with parallelepiped shape, containing hundreds of atoms ordered according to an fcc structure with bulk Ni lattice parameter ($a = 3.52$ Å). The initial parallelepiped height will correspond to the stretching direction and is larger than the base edges. We define the $z$ axis as the stretching (pulling) direction. In the present study we have considered two different stretching directions: (111) and (100). For the (111) case we have used an initial nanowire formed by 18 layers containing 56 atoms each (i.e., a total of 1008 atoms). For the (100) case we have used a nanowire of 21 layers with 49 atoms per layer (i.e., 1029 atoms). Figure 1 shows the two initial configurations corresponding to (111) and (100) nanowires. At the beginning of the simulation, the velocity of each atom is assigned at random according to the Maxwellian distribution that correspond to the simulation temperature.

The second stage corresponds to the relaxation of the bulk-like initial structure. Firstly, we define two supporting bilayers at the top and bottom of the supercell. Atomic $x$ and $y$ coordinates within these bilayers will be kept frozen during the simulation. The nanowire will remain attached to these two bulk-like supporting bilayers during the relaxation stage. This stage lasts for 3000 MD steps in order to optimize the geometry of the isolated parallelepiped-like nanowire. Notice that the presence of both supporting frozen bilayers also avoids the appearance of phase transformation upon loading as it has been noticed for narrow Ni nanowires without such supporting bilayers [54].

During the third stage (stretching process), the $z$ coordinate of those atoms forming the top (down) frozen bilayer is forced to increase (decrease) a quantity $\Delta L_z = 10^{-4}$ Å after every MD step. This incremental process simulates the separation of the supporting bilayers in opposite directions at constant velocity of 2 m/s, giving rise to the subsequent nanowire fracture. The rest of the atoms move following the forces derived from their EAM-like interaction with the surrounding atoms. Notice that the stretching velocity is much larger than that used in experiments. However, our computational description of the nanowire breaking is comparable to that of actual experimental traces since the stretching velocity is smaller than the sound speed in nickel.

During the stretching stage, the accurate knowledge of the atomic coordinates and velocities allows the determination of the minimum cross-section $S_m$. This quantity provides information on the favorable configurations appearing during the nanowire evolution under stretching. Furthermore, $S_m$ provides a first-order approximation of the conductance $G$ [55, 56].

The minimum cross-section $S_m$ is calculated in units of atoms following standard procedures that have been successfully used in previous studies [41, 42]. In our case, we define the radius $r_0$ to be equal to half the fcc (111) interplanar distance ($r_0 = d_{111}/2$). We assign a volume $V_0 = 4\pi r_0^3/3$ to each atom. In order to calculate the cross-section $S_i$ at a given $z_i$ position, we firstly compute the total atomic volume $V_{\mathrm{tot},i}$ inside a "detecting cursor" width $\Delta z$. We have used $\Delta z = d_{111}$. The quantity $S_i = V_{\mathrm{tot},i}/V_0$ corresponds to the nanowire section (in number of atoms) at the $z_i$ position. The detecting cursor moves along the $z$-axis between the two frozen bilayers, using a step equal to $0.1 \times d_{111}$. This allows to calculate the cross-section $S_i$ along the nanowire. Finally, from the set of collected $S_i$ values, we determine the minimum cross-section value $S_m$. Note that the cursor size $\Delta z$ is kept fixed independently on the nanowire crystalline direction along the $z$ axis. This allows a true comparison between histograms obtained for different orientations, especially at the last breaking stages. In our study $S_m$ is calculated every 10 MD steps. We consider that the nanowire breaking process is completed when $S_m = 0$.

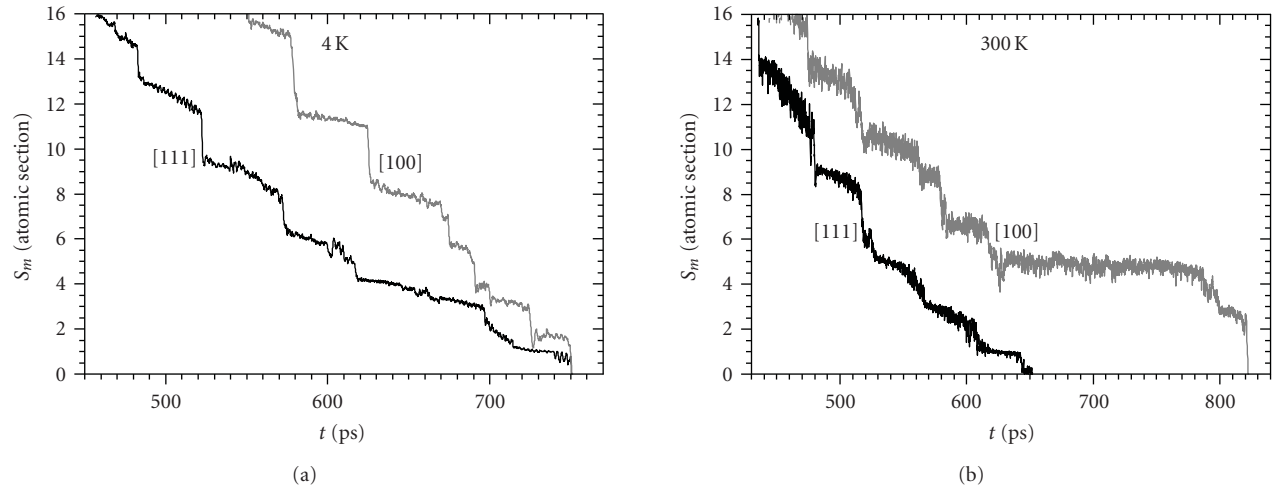


Figure 2: Minimum cross-section $S_m$ evolution of simulated breakage processes of Ni nanowires along the (111) (black curves) and (100) (grey curves) stretching directions at 4 K (a) and 300 K (b).

## 3. RESULTS AND DISCUSSION

The evolution of $S_m$ versus time shows a typical staircase trace. In Figure 2 we show four examples of $S_m(t)$ that illustrate this behaviour. $S_m(t)$ traces show a stepped profile with well-marked jumps associated to atomic rearrangements occurring at the nanowire. We have verified that these jumps are correlated with jumps in the force acting on the supporting slabs. In general, $S_m$ monotonically decreases between two subsequent jumps reflecting the existence of elastic stages. These elastic stages have been associated to the experimentally observed conductance plateaus. As it is expected, $S_m$ presents at RT larger fluctuations than at 4 K. This has been observed for both stretching orientations.

In order to visualize the possible differences between low and room temperatures and between (111) and (100) stretching directions, we have depicted in Figure 3 five atomic configurations for each trace shown in Figure 2. Although it is very difficult to make comparisons among those structural evolutions, we can see that, in general, the nanowires break-forming three types of configurations at the last stage of the breaking process: monomers, dimers, and others. The monomer structure is characterized by a central atom standing between two pyramid-like structures. This configuration usually shows a plateau around $S_m \sim 1$. In the dimer structure, the apex atoms of two opposite pyramidal configurations form a diatomic chain. The third type of final configurations presents more complex structures. In these cases we generally observe an abrupt jump from $S_m \geq 2$ (i.e., structures formed by two or more atoms) to $S_m = 0$. As expected [45], we have not found the presence of long atomic chains (formed by three or more atoms).

In our study we have found that monomer and dimer structures usually appear for nanowires stretched along (111) direction. On the contrary, more complex structures (i.e., not classifiable as monomers or dimers) appear with higher probability at the latest stages of nanowires strained along the (100) stretching directions.

The minimum cross-section histograms $H(S_m)$ have been built by accumulating $S_m(t)$ traces acquired during the simulation of hundreds of nanowire stretching processes. In Figure 4 we show the histograms $H(S_m)$ for 4 K and 300 K, constructed with 300 independent breakages for the (111) and (100) stretching directions. The different histograms are depicted in the range $0 < S_m < 12$. A first inspection of these figures reveals the existence of well-defined peaks associated to preferred nanowire configurations as it has been shown in previous works [12, 34–37].

The $H(S_m)$ histograms associated to the (111) stretching direction present a well-defined peaked structure at low and room temperature. The main difference we have found corresponds to the small increase of the peak located at $S_m \sim 5$ at RT. For the (100) case, the low-temperature histogram presents a noisy structure whereas at $T = 300$ K the histogram peaks show rounded shapes and the general structure has less noise. Small peaks at $T = 4$ K correspond to metastable configurations with slightly higher cohesive energies with respect to other metastable configurations. The increase of temperature allows the exploration of more configurations during the stretching process, and, in this way, those metastable configurations with local minimum energy are easily accessible, leading to a better definition of their associated $H(S_m)$ peaks. In addition, the (100) $H(S_m)$ histogram presents a well-marked $S_m = 5$ peak at $T = 300$ K. We will discuss later the origin of this protruding peak which is not developed at low temperatures.

Our main finding is that $H(S_m)$ histograms are very dependent on the stretching (i.e., the nanowire axis) direction. Whereas the (111) direction provides histograms with well-defined decreasing peaked structure in the low $S_m$ region, the situation dramatically changes when we consider the (100) direction. The later case presents $H(S_m)$ histograms with small peaks in the region $S_m < 2$. These differences between (111) and (100) stretching directions are consistent with previously published results [37, 38].

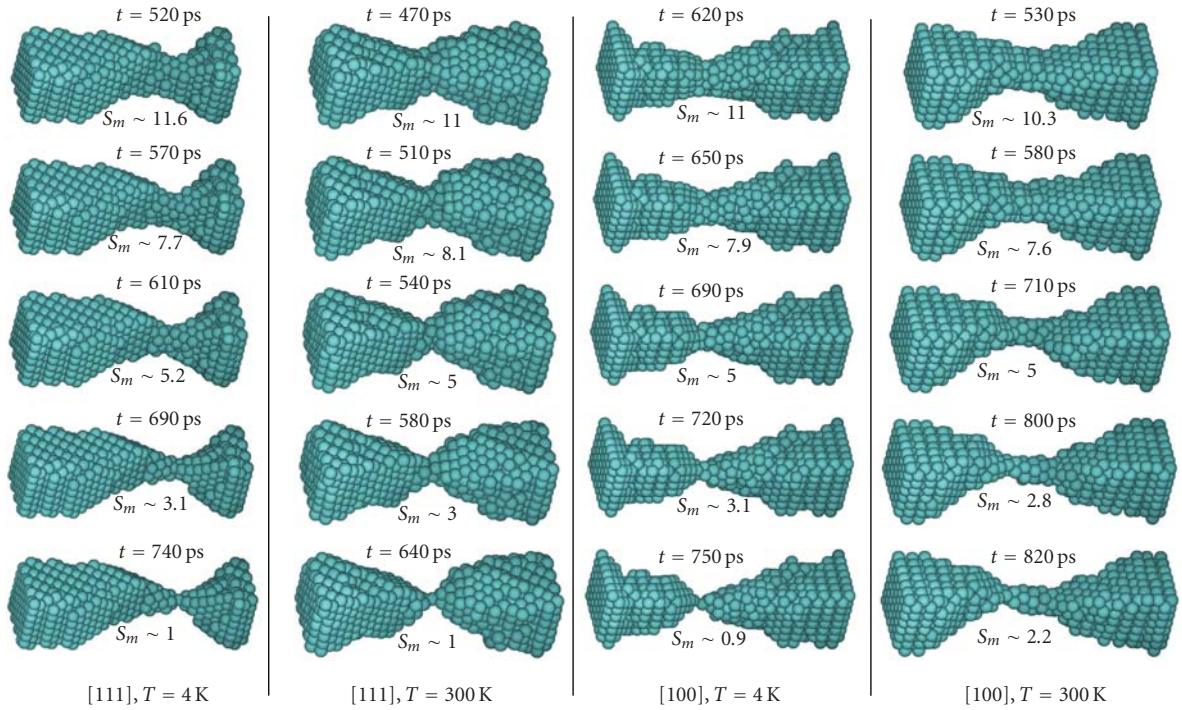


Figure 3: Snapshots at different evolution times of those nanowires whose $S_m(t)$ traces were shown in Figure 2. Each column corresponds to a given combination of the nanowire stretching direction ((111) or (100)) and temperature ($T = 4$ K or $T = 300$ K). Each snapshot includes information on the simulation time and the minimum cross-section $S_m$ at that time.

We have pointed out that the peak located at $S_m \sim 5$ of the histograms $H(S_m)$ increases when the temperature goes from $T = 4$ K to RT. This increase is small for the (111) case. The situation is rather different for the (100) case, noticing that this peak increases a factor of 2 approximately (see Figure 4). The MD simulation approach allows to monitor the evolution of the full set of atomic coordinates during the breaking process. In order to know with more detail the origin of the $S_m = 5$ peak appearing in the (100) case, we have depicted in Figure 5 a typical nanowire stretched along the (100) direction. We have chosen a snapshot corresponding to the $4.5 < S_m < 5.5$ region. It is clear that the origin of the huge peak is related to the tendency of the system to form long wires with $S_m \sim 5$. In general, this type of nanowires beaks without a progressive diminishing of its atomic section, that is, the system does not form monomers or dimers just before the rupture. At this point we should mention that these long structures are very common for the (100) stretching direction. However, these long rod-like structures appear seldom in the (111). This smaller probability agrees with the slight increase detected for the $H(S_m = 5)$ peak when $T$ increases.

A closer inspection to Figure 5 allows to determine the atomic structure of these long wires. We have found that these wires present a well-defined sequence $\cdots$–5–1–5–1–$\cdots$. This sequence does not correspond to any crystallographic fcc or bcc structure. This type of arrangement is not seen at 4 K because a larger temperature is required to explore and overcome those energy barriers leading to configurations able to develop these pentagonal chains. In addition, we can easily see that these pentagonal nanowires are formed by subsequent-staggered parallel pentagonal rings (with a relative rotation of $\pi/5$) connected with single atoms. A similar, but shorter, structure was found for Cu (111) breaking nanowires using MD simulations [57]. The stability of such pentagonal Cu nanowires was later confirmed by ab-initio calculations [58], demonstrating that staggered pentagonal nanowires are favorable configurations. More recently, MD tight-binding calculations have determined the presence of such pentagonal –5–1–5–1– nanowires during the breaking process [59] of (110) Cu nanowires although these pentagonal patterns were not frequently observed for nanowires along (100) and (111) directions. Pentagonal motives also appear in infinite Al nanowires [60]. Therefore, it seems that the formation in MD simulation of staggered pentagonal Ni nanowires follows the trend observed for other metallic species.

We have checked that formation of staggered pentagonal nanowires is favorable within the EAM scheme using the Mishin et al. potential. In fact, we have found from a set of conjugate gradients geometry minimization procedures that staggered nanowires present a cohesive energy of 3.66 eV per atom whereas the cohesive energy of the nonstaggered configuration (without the relative rotation of $\pi/5$) is 3.40 eV. The optimized geometry of the staggered pentagonal Ni nanowire presents two subsequent parallel pentagonal rings separated each other by a distance $d_{5-5} = 2.22$ Å. The optimized pentagonal ring side takes the value $l_5 = 2.55$ Å. The geometry parameters we have found for those pentagonal nanowires obtained from the stretching procedure present

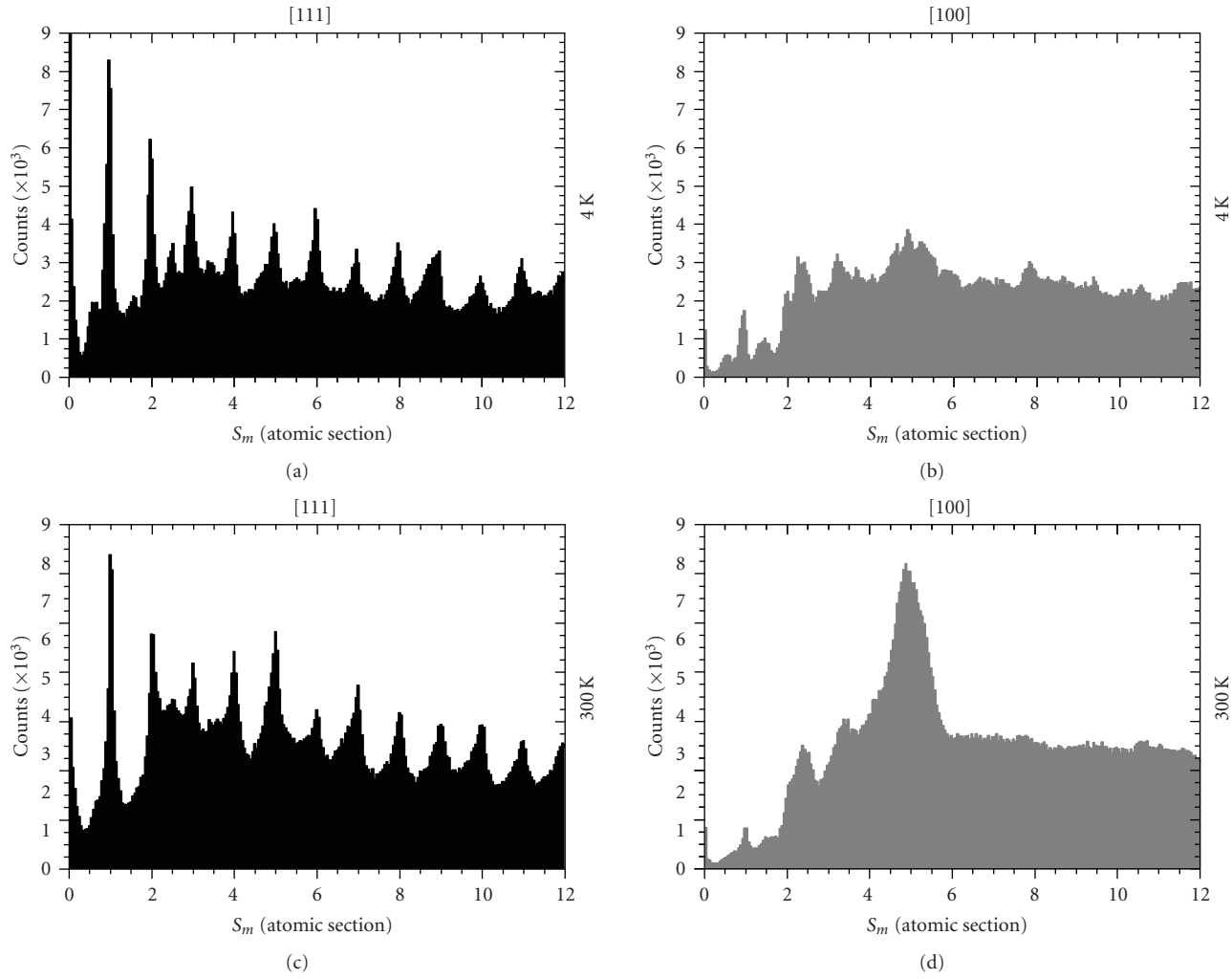


Figure 4: Minimum cross-section $S_m$ histograms built with 300 independent Ni nanowire ruptures under stretching along the (111) (a,c) and (100) (b,d) directions at $T = 4$ K (a,b) and 300 K (c,d).

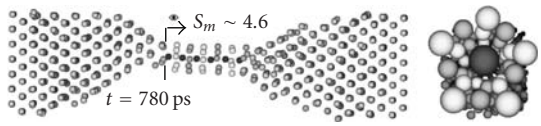


Figure 5: Longitudinal (left) and cross-section (right) views of a nanowire stretched along the (100) direction. The snapshot was acquired for an atomic configuration with minimum cross-section close to $S_m \sim 4.6$. The cross-section image shows a perspective view of the nanowire as seen from the position indicated on the longitudinal view. This image illustrates the appearance of staggered pentagonal structures –5–1–5–1–.

values of $d_{5-5}$ and $l_5$ very similar to those obtained for the free pentagonal nanowire. We have also found, using MD simulations, that the pentagonal nanowire structure is rather stable in the temperature range 3–300 K.

Therefore, it seems that the nanowire stretching along the (100) direction provides some mechanisms that allow to reach this favorable structures. In some sense, the stretching-induced formation of pentagonal nanowires is very similar to the formation of linear atomic chains (LACs) where single atoms are consecutively incorporated into the LAC from the stretched nanowire before its final breakage [2]. However, the formation of pentagonal chains involves units of 6 atoms (1 + 5 structures) and a full description of the underlying mechanical process is a very complicated task that will be afforded in a deeper study.

## 4. CONCLUSIONS

We have carried out hundreds of MD simulations of Ni nanowire breaking processes using the EAM approach to describe the interatomic many body interaction. From these simulations we are able to follow the evolution of the nanowire minimum cross-section $S_m(t)$. By adding hundreds of $S_m(t)$ traces, we have constructed computational minimum cross-section histograms $H(S_m)$ that statistically unveil the presence of preferred configuration during the elongation and breaking history. The last stages of the nanowire

breaking process are of special interest since electron transport is determined by a cross section formed by few atoms. We have found that monomers, dimers, and other more complex structures are present at the latest stages of the breaking events. We did not find linear atomic chains of three or more atoms for all the systems and stretching directions we analyzed.

We have found that $H(S_m)$ histograms do not depend dramatically on the temperature within the analyzed temperature range (below 300 K). In general, we have only noticed rounding of the peaked structure of $H(S_m)$, the suppression of small $S_m$ fluctuations, and the increase of the peak located at $S_m = 5$. This increase is larger for the (100) case. The absence of large temperature effects is consistent with the fact that bulk Ni melting temperature is rather large ($\approx$ 1728 K), and then RT is not enough to activate additional mechanisms as surface diffusion effects that could modify the nanowire breaking dynamics.

During stretching along the (111) direction, the system tends to form a bipyramid structure that forms monomers and dimers at the narrowest nanocontact region. These monomers and dimers give rise to the $S_m \sim 1$ peak appearing in $H(S_m)$.

For the (100) stretching direction, $H(S_m)$ does not present large peaks in the low $S_m$ region ($S_m < 2$), thus indicating that monomers and dimers appear with less probability than for the (111) situation. The nanowire is deformed under stretching forming elongated (rod-like) structures. The formation of these long structures increases when temperature increases from 4 K to RT. At RT we found a dramatic increase of those peaks located at $S_m \sim 5$. We have confirmed that this peak is caused by the presence of long staggered pentagonal chains with $\cdots$–5–1–5–1$\cdots$ structures. These pentagonal nanowires were also occasionally found for the (111) case (giving rise to the increase of the peak $H(S_m \sim 5)$). In relation with the formation of long chains in MD simulations, a recent work [61] points towards the higher ductibility predicted by EAM potentials in comparison with other interatomic potentials, leading to the formation of long structures. However, more detailed statistical analysis is required in order to know the actual effects of the chosen potential on the formation of elongated structures (including the pentagonal ones we have described).

In spite of our model limitations to perform the comparison with experiments, we can extract few key ideas from the present MD simulations. (i) The presence of well-marked $H(S_m)$ peaks is consistent with the appearance of preferred conductance values in the conductance histogram. (ii) The behavior of $H(S_m)$ at 4 K is rather similar to that noticed at $T = 300$ K, and this implies that mechanical aspects do not explain differences between low and room temperature experimental conductance histograms. (iii) The first broad conductance peak appearing in experiments is consistent with the presence of monomers and dimers appearing during the last stages of the breaking process associated to (111) stretching direction. (iv) We have detected the formation of long pentagonal nanowires at RT for the (100) stretching direction. These structures contribute to the formation of a large $S_m = 5$ peak. However, this large peak has not been observed in RT experimental conductance histograms. At this point we must be cautious when interpreting experimental conductance histograms, specially at RT, since the complex behavior of Ni conductance histograms may be attributed to chemiadsorbed atoms on the nanowire [26] or to ballistic magnetoresistence (BMR) effects [19, 20].

## ACKNOWLEDGMENTS

The authors thank J. L. Costa-Krämer, M. Díaz, J. J. Palacios, C. Guerrero, E. Medina, and A. Hasmy for the helpful discussions. This work has been partially supported by the CSIC-IVIC researchers exchange program and the Spanish DGICyT (MEC) through Projects FIS2005-05137, BFM2003-01167-FISI, and FIS2006-11170-C02-01, and by Madrid Regional Government through the Programs S-0505/MAT/0303 (NanoObjetos-CM) and S-0505/TIC/0191 (Microseres-CM). R.Paredes acknowledges the Spanish MEC by the financial support through its Researchers Exchange and Mobility Programme. Mochales also acknowledges Spanish MEC by its financial supprot through the RyC Programme.

## REFERENCES

[1] C. P. Poole and F. J. Owens, *Introduction to the Nanotechnology*, Wiley-VCH, Weinheim, Germany, 2003.

[2] N. Agraït, A. L. Yeyati, and J. M. van Ruitenbeek, "Quantum properties of atomic-sized conductors," *Physics Reports*, vol. 377, no. 2-3, pp. 81–279, 2003.

[3] R. Landauer, "Electrical resistance of disordered one-dimensional lattices," *Philosophical Magazine*, vol. 21, no. 172, pp. 863–867, 1970.

[4] R. Landauer, "Electrical transport in open and closed systems," *Zeitschrift für Physik B*, vol. 68, no. 2-3, pp. 217–228, 1987.

[5] J. I. Pascual, J. Méndez, J. Gómez-Herrero, A. M. Baró, N. García, and V. T. Binh, "Quantum contact in gold nanostructures by scanning tunneling microscopy," *Physical Review Letters*, vol. 71, no. 12, pp. 1852–1855, 1993.

[6] L. Olesen, E. Laegsgaard, I. Stensgaard, et al., "Quantized conductance in an atom-sized point contact," *Physical Review Letters*, vol. 72, no. 14, pp. 2251–2254, 1994.

[7] L. Olesen, E. Laegsgaard, I. Stensgaard, et al., "Olesen *et al.* reply:," *Physical Review Letters*, vol. 74, no. 11, p. 2147, 1995.

[8] J. M. Krans, J. M. van Ruitenbeek, V. V. Fisun, I. K. Yanson, and L. J. de Jongh, "The signature of conductance quantization in metallic point contacts," *Nature*, vol. 375, no. 6534, pp. 767–769, 1995.

[9] Y. Kondo and K. Takayanagi, "Gold nanobridge stabilized by surface structure," *Physical Review Letters*, vol. 79, no. 18, pp. 3455–3458, 1997.

[10] C. Z. Li and N. J. Tao, "Quantum transport in metallic nanowires fabricated by electrochemical deposition/dissolution," *Applied Physics Letters*, vol. 72, no. 8, pp. 894–896, 1998.

[11] A. I. Yanson and J. M. van Ruitenbeek, "Do histograms constitute a proof for conductance quantization?" *Physical Review Letters*, vol. 79, no. 11, p. 2157, 1997.

[12] A. Hasmy, E. Medina, and P. A. Serena, "From favorable atomic configurations to supershell structures: a new interpretation of conductance histograms," *Physical Review Letters*, vol. 86, no. 24, pp. 5574–5577, 2001.

[13] E. Scheer, P. Joyez, D. Esteve, C. Urbina, and M. H. Devoret, "Conduction channel transmissions of atomic-size aluminum contacts," *Physical Review Letters*, vol. 78, no. 18, pp. 3535–3538, 1997.

[14] C. Sirvent, J. G. Rodrigo, S. Vieira, L. Jurczyszyn, N. Mingo, and F. Flores, "Conductance step for a single-atom contact in the scanning tunneling microscope: Noble and transition metals," *Physical Review B*, vol. 53, no. 23, pp. 16086–16090, 1996.

[15] J. L. Costa-Krämer, "Conductance quantization at room temperature in magnetic and nonmagnetic metallic nanowires," *Physical Review B*, vol. 55, no. 8, pp. R4875–R4878, 1997.

[16] H. Oshima and K. Miyano, "Spin-dependent conductance quantization in nickel point contacts," *Applied Physics Letters*, vol. 73, no. 15, pp. 2203–2205, 1998.

[17] T. Ono, Y. Ooka, H. Miyajima, and Y. Otani, "$2e^2/h$ to $e^2/h$ switching of quantum conductance associated with a change in nanoscale ferromagnetic domain structure," *Applied Physics Letters*, vol. 75, no. 11, pp. 1622–1624, 1999.

[18] F. Komori and K. Nakatsuji, "Quantized conductance through atomic-sized iron contacts at 4.2 K," *Journal of the Physical Society of Japan*, vol. 68, no. 12, pp. 3786–3789, 1999.

[19] N. García, M. Muñoz, and Y.-W. Zhao, "Magnetoresistance in excess of 200% in ballistic Ni nanocontacts at room temperature and 100 Oe," *Physical Review Letters*, vol. 82, no. 14, pp. 2923–2926, 1999.

[20] H. D. Chopra and S. Z. Hua, "Ballistic magnetoresistance over 3000% in Ni nanocontacts at room temperature," *Physical Review B*, vol. 66, no. 2, Article ID 020403, 3 pages, 2002.

[21] A. I. Yanson, "Atomic chains and electronic shells: quantum mechanisns for the formation of nanowires," Ph. D. thesis, Universiteit Leiden, Leiden, The Netherlands, 2001.

[22] D. J. Bakker, Y. Noat, A. I. Yanson, and J. M. van Ruitenbeek, "Effect of disorder on the conductance of a Cu atomic point contact," *Physical Review B*, vol. 65, no. 23, Article ID 235416, 5 pages, 2002.

[23] J. Li, T. Kanzaki, K. Murakoshi, and Y. Nakato, "Metal-dependent conductance quantization of nanocontacts in solution," *Applied Physics Letters*, vol. 81, no. 1, pp. 123–125, 2002.

[24] R. H. M. Smit, "From quantum point contacts to monatomic chains: fabrication and characterization of the ultimate nanowire," Ph. D. thesis, Universiteit Leiden, Leiden, The Netherlands, 2003.

[25] V. Rodrigues, J. Bettini, P. C. Silva, and D. Ugarte, "Evidence for spontaneous spin-polarized transport in magnetic nanowires," *Physical Review Letters*, vol. 91, no. 9, Article ID 096801, 4 pages, 2003.

[26] C. Untiedt, D. M. T. Dekker, D. Djukic, and J. M. van Ruitenbeek, "Absence of magnetically induced fractional quantization in atomic contacts," *Physical Review B*, vol. 69, no. 8, Article ID 081401, 4 pages, 2004.

[27] C.-S. Yang, C. Zhang, J. Redepenning, and B. Doudin, "*In situ* magnetoresistance of Ni nanocontacts," *Applied Physics Letters*, vol. 84, no. 15, pp. 2865–2867, 2004.

[28] M. R. Sullivan, D. A. Boehm, D. A. Ateya, S. Z. Hua, and H. D. Chopra, "Ballistic magnetoresistance in nickel single-atom conductors without magnetostriction," *Physical Review B*, vol. 71, no. 2, Article ID 024412, 8 pages, 2005.

[29] K. Sekiguchi, E. Saitoh, and H. Miyajima, "Conductance quantization by the application of magnetic fields in ballistic Ni nanocontacts," *Journal of Applied Physics*, vol. 97, no. 10, p. 3 pages, 2005.

[30] M. Díaz, J. L. Costa-Krämer, and P. A. Serena, "Partial versus total conductance histograms: a tool to identify magnetic effects in nanocontacs," *Journal of Magnetism and Magnetic Materials*, vol. 305, no. 2, pp. 497–503, 2006.

[31] D. Jacob, M. J. Caturla, M. R. Calvo, C. Untiedt, and J. J. Palacios, "Mechanical and electrical properties of Ni nanocontacts," in *Proceedings of IEEE Nanotechnology Materials and Devices Conference (NMDC '06)*, vol. 1, pp. 236–237, Gyeongju, South Korea, October 2006.

[32] C. Untiedt, M. J. Caturla, M. R. Calvo, J. J. Palacios, R. C. Segers, and J. M. van Ruitenbeek, "Formation of a metallic contact: jump to contact revisited," *Physical Review Letters*, vol. 98, no. 20, Article ID 206801, 4 pages, 2007.

[33] D. Jacob, J. Fernández-Rossier, and J. J. Palacios, "Magnetic and orbital blocking in Ni nanocontacts," *Physical Review B*, vol. 71, no. 22, Article ID 220403, 4 pages, 2005.

[34] M. Díaz, J. L. Costa-Krämer, P. A. Serena, E. Medina, and A. Hasmy, "Simulations and experiments of aluminum conductance histograms," *Nanotechnology*, vol. 12, no. 2, pp. 118–120, 2001.

[35] E. Medina, M. Díaz, N. León, et al., "Ionic shell and subshell structures in aluminum and gold nanocontacts," *Physical Review Letters*, vol. 91, no. 2, Article ID 026802, 4 pages, 2003.

[36] A. Hasmy, A. J. Pérez-Jiménez, J. J. Palacios, et al., "Ballistic resistivity in aluminum nanocontacts," *Physical Review B*, vol. 72, no. 24, Article ID 245405, 5 pages, 2005.

[37] P. García-Mochales, S. Peláez, P. A. Serena, E. Medina, and A. Hasmy, "Breaking processes in nickel nanocontacts: a statistical description," *Applied Physics A*, vol. 81, no. 8, pp. 1545–1549, 2005.

[38] F. Pauly, M. Dreher, J. K. Viljas, M. Häfner, J. C. Cuevas, and P. Nielaba, "Theoretical analysis of the conductance histograms and structural properties of Ag, Pt, and Ni nanocontacts," *Physical Review B*, vol. 74, no. 23, Article ID 235106, 21 pages, 2006.

[39] U. Landman, W. D. Luedtke, N. A. Burnham, and R. J. Colton, "Atomistic mechanisms and dynamics of adhesion, nanoindentation, and fracture," *Science*, vol. 248, no. 4954, pp. 454–461, 1990.

[40] W. D. Luedtke and U. Landman, "Solid and liquid junctions," *Computational Materials Science*, vol. 1, no. 1, pp. 1–24, 1992.

[41] A. M. Bratkovsky, A. P. Sutton, and T. N. Todorov, "Conditions for conductance quantization in realistic models of atomic-scale metallic contacts," *Physical Review B*, vol. 52, no. 7, pp. 5036–5051, 1995.

[42] M. R. Sørensen, M. Brandbyge, and K. W. Jacobsen, "Mechanical deformation of atomic-scale metallic contacts: structure and mechanisms," *Physical Review B*, vol. 57, no. 6, pp. 3283–3294, 1998.

[43] H. Ikeda, Y. Qi, T. Çagin, K. Samwer, W. L. Johnson, and W. A. Goddard III, "Strain rate induced amorphization in metallic nanowires," *Physical Review Letters*, vol. 82, no. 14, pp. 2900–2903, 1999.

[44] P. S. Branício and J.-P. Rino, "Large deformation and amorphization of Ni nanowires under uniaxial strain: a molecular dynamics study," *Physical Review B*, vol. 62, no. 24, pp. 16950–16955, 2000.

[45] S. R. Bahn and K. W. Jacobsen, "Chain formation of metal atoms," *Physical Review Letters*, vol. 87, no. 26, Article ID 266101, 4 pages, 2001.

[46] J. W. T. Heemskerk, Y. Noat, D. J. Bakker, J. M. van Ruitenbeek, B. J. Thijsse, and P. Klaver, "Current-induced transition in atomic-sized contacts of metallic alloys," *Physical Review B*, vol. 67, no. 11, Article ID 115416, 5 pages, 2003.

[47] Y.-H. Wen, Z.-Z. Zhu, G.-F. Shao, and R.-Z. Zhu, "The uniaxial tensile deformation of Ni nanowire: atomic-scale computer simulations," *Physica E*, vol. 27, no. 1-2, pp. 113–120, 2005.

[48] B. Wang, D. Shi, J. Jia, G. Wang, X. Chen, and J. Zhao, "Elastic and plastic deformations of nickel nanowires under uniaxial compression," *Physica E*, vol. 30, no. 1-2, pp. 45–50, 2005.

[49] H. S. Park, K. Gall, and J. A. Zimmerman, "Shape memory and pseudoelasticity in metal nanowires," *Physical Review Letters*, vol. 95, no. 25, Article ID 255504, 4 pages, 2005.

[50] M. Dreher, F. Pauly, J. Heurich, J. C. Cuevas, E. Scheer, and P. Nielaba, "Structure and conductance histogram of atomic-sized Au contacts," *Physical Review B*, vol. 72, no. 7, Article ID 075435, 11 pages, 2005.

[51] M. S. Daw and M. I. Baskes, "Semiempirical, quantum mechanical calculation of hydrogen embrittlement in metals," *Physical Review Letters*, vol. 50, no. 17, pp. 1285–1288, 1983.

[52] S. M. Foiles, "Application of the embedded-atom method to liquid transition metals," *Physical Review B*, vol. 32, no. 6, pp. 3409–3415, 1985.

[53] Y. Mishin, D. Farkas, M. J. Mehl, and D. A. Papaconstantopoulos, "Interatomic potentials for monoatomic metals from experimental data and *ab initio* calculations," *Physical Review B*, vol. 59, no. 5, pp. 3393–3407, 1999.

[54] W. Liang and M. Zhou, "Atomistic simulations reveal shape memory of fcc metal nanowires," *Physical Review B*, vol. 73, no. 11, Article ID 115409, 11 pages, 2006.

[55] Y. V. Sharvin, "A possible method for studying fermi surfaces," *Zhurnal Eksperimental'noi i Teoreticheskoi Fiziki*, vol. 48, pp. 984–985, 1965.

[56] Y. V. Sharvin, "A possible method for studying fermi surfaces," *Soviet Physics JETP*, vol. 21, pp. 655–656, 1965.

[57] H. Mehrez and S. Ciraci, "Yielding and fracture mechanisms of nanowires," *Physical Review B*, vol. 56, no. 19, pp. 12632–12642, 1997.

[58] P. Sen, O. Gülseren, T. Yildirim, I. P. Batra, and S. Ciraci, "Pentagonal nanowires: a first-principles study of the atomic and electronic structure," *Physical Review B*, vol. 65, no. 23, Article ID 235433, 7 pages, 2002.

[59] J. C. González, V. Rodrigues, J. Bettini, et al., "Indication of unusual pentagonal structures in atomic-size Cu namwires," *Physical Review Letters*, vol. 93, no. 12, Article ID 126103, 4 pages, 2004.

[60] O. Gülseren, F. Ercolessi, and E. Tosatti, "Noncrystalline structures of ultrathin unsupported nanowires," *Physical Review Letters*, vol. 80, no. 17, pp. 3775–3778, 1998.

[61] Q. Pu, Y. Leng, L. Tsetseris, H. S. Park, S. T. Pantelides, and P. T. Cummings, "Molecular dynamics simulations of stretched gold nanowires: the relative utility of different semiempirical potentials," *Journal of Chemical Physics*, vol. 126, no. 14, Article ID 144707, 6 pages, 2007.

Hindawi Publishing Corporation
Journal of Nanomaterials
Volume 2008, Article ID 582973, 8 pages
doi:10.1155/2008/582973

*Research Article*

# Mineral and Protein-Bound Water and Latching Action Control Mechanical Behavior at Protein-Mineral Interfaces in Biological Nanocomposites

**Pijush Ghosh, Dinesh R. Katti, and Kalpana S. Katti**

*Department of Civil Engineering, North Dakota State University, Fargo, ND 58105, USA*

Correspondence should be addressed to Dinesh R. Katti, dinesh.katti@ndsu.edu

Received 9 October 2007; Revised 21 March 2008; Accepted 25 June 2008

Recommended by Junlan Wang

The nacre structure consists of laminated interlocked mineral platelets separated by nanoscale organic layers. Here, the role of close proximity of mineral to the proteins on mechanical behavior of the protein is investigated through steered molecular dynamics simulations. Our simulations indicate that energy required for unfolding protein in the proximity of mineral aragonite is several times higher than that for isolated protein in the absence of the mineral. Here, we present details of specific mechanisms which result in higher energy for protein unfolding in the proximity of mineral. At the early stage of pulling, peaks in the load-displacement (LD) plot at mineral proximity are quantitatively correlated to the interaction energy between atoms involved in the latching phenomenon of amino acid side chain to aragonite surface. Water plays an important role during mineral and protein interaction and water molecules closer to the mineral surface are highly oriented and remain rigidly attached as the protein strand is pulled. Also, the high magnitude of load for a given displacement originates from attractive interactions between the protein, protein-bound water, and mineral. This study provides an insight into mineral-protein interactions that are predominant in biological nanocomposites and also provides guidelines towards design of biomimetic nanocomposites.



## 1. INTRODUCTION

Minerals and proteins exist in close proximity and at nanoscale dimensions in biology. Interactions at these interfaces are vital to the functions of almost all structural materials in nature such as teeth, seashells, and bone. Knowledge of these interfaces, in particular, is useful in understanding the mechanical and physiochemical behavior of natural biocomposites such as bone, teeth, nacre, and so forth consisting of mineral and organic phases. The percentage constituent of mineral and organics is different in the various biological materials. In bones and teeth, the mineral content is about 60% and 90%, respectively [1], whereas, in nacre it varies from 95% to 98% [2]. The major component of the organic phase in nacre is proteins. Although organics are present in small proportion, they significantly alter the mechanical behavior of biocomposites. Nacre, for example, exhibits fracture toughness about 3 000 times more than the pure aragonite [2]. The proteins present in the natural biocomposite nacre show properties significantly different from any other bulk proteins. Our finite element modeling study, also later verified by experiments, shows that proteins present in nacre have modulus of about 15–20 GPa [3–7]. These simulations were done based on a parametric study of varying values of elastic modulus of the organic from 5 MPa to 100 GPa. This is about twenty times higher than the modulus of bulk proteins. The protein in nacre exists in a 20 nm space, between aragonite platelets of 200–250 nm thickness in an interlocked "brick and mortar" architecture [6]. Two possible factors which could cause the nacre protein to possess such high modulus are (i) its confinement in 20 nm space, and (ii) the mineral-protein interactions. Our current research focuses on the effect of mineral-protein interactions. The effect of confinement will be the focus of our future work. We have found in our previous work that the proximity of mineral influences the mechanical behavior of proteins [8]. We have reported that more energy is required to pull a protein at mineral proximity than in the absence of mineral. Recently, we have also reported the large influence of mineral on mechanical behavior of protein

through simulations of collagen-hydroxyapatite in bone [9]. Here, we present the detailed mechanisms responsible for large changes in mechanical response during protein unfolding in the proximity of the mineral. In this molecular modelling simulation, the GS domain [10, 11] of the Lustrin A, protein which is found close to mineral surface in nacre, is pulled under two conditions: (i) in the proximity of mineral aragonite, (ii) in the absence of any mineral proximity. All other conditions of simulation remain identical for the two cases. As the GS domain is pulled keeping one end constrained, the protein domain unfolds. The mechanisms involved in the unfolding pathways are significantly different under the two conditions of pulling, resulting in large differences in energy required for unfolding at mineral proximity.

Molecular dynamics is a useful technique for studying the folding/unfolding behavior of proteins [12, 13]. The reversible unfolding of individual immunoglobulin domains was successfully investigated using a combination of steered molecular dynamics (SMD) and atomic force microscopy (AFM) [14–16]. The SMD technique has been successful in reproducing the stretching events for individual solvated I27 domain [17]. This technique has also been used for studying the mechanical properties of clay minerals at nanometer length scale [18–21]. In our previous work, [21] we have used steered molecular dynamics to understand the deformational behavior of the beta barrel and beta planar sheet structures in proteins. Also, in literature, the helix-coil transition of peptide deca-alanine in vacuum was studied using molecular dynamics simulation [22]. Researchers [23] were able to investigate the different transition states of biopeptides at different temperatures.

The model protein structure used in this study is the nacre protein Lustrin A. The primary reason for this choice is that this protein is located close to the aragonite surface and thus can potentially interact with the mineral. The protein Lustrin A is made of 1428 amino acid residues and has molecular weight of about 112 KDa. The complete structure of this protein is not known. Hence, at present, this study is confined to the response of a single-domain Glycine-Serine (GS) of the protein Lustrin A. Molecular modeling techniques such as coarse-grained modeling [24] can be applied in the future to study the response of the full protein when the structure is known. Replica-exchange molecular dynamics method has been successfully used in literature to study the folding unfolding behavior of proteins and peptides [25]. There are various experimental techniques such as laser tweezers [26], florescence quenching [27], and AFM [28], which are found to be useful in characterizing the protein folding and refolding response. Most of these techniques are fairly successful in the study of single-molecule protein folding. These studies have primarily looked at the molecular mechanisms in the unfolding of proteins, however recently we have reported measurement of adhesion forces between aragonite and nacre proteins by pulling proteins off the aragonite surface using an AFM tip [29]. Experiments were conducted on freshly cleaved samples of nacre, and protein molecules were pulled in the presence of aragonite at various velocities using an AFM tip. The results indicate that protein molecules can withstand large pulling forces of the order of 6 nN before separating from the aragonite or the AFM tip [29].

## 2. MODEL CONSTRUCTION AND SIMULATION DETAILS

One of the most widely studied nacre proteins is Lustrin A. It is a domain-based protein, and is located close to the interface formed by the inorganic (aragonite) and organics (primarily proteins). Lustrin A is populated by ten cysteine rich domains with nine protein rich domains sitting in between. It has a domain made of 275 amino acids, and significantly rich in glycine and serine. It is located close to the C-terminal and named as GS domain in this work. For the sake of these simulations, GS domain is the organic entity. The details about the possible role of each of the domains in Lustrin A are discussed in our previous work [8]. From the known primary sequence of GS-domain random, structures were generated, minimized, and then solvated by "SOLVATE" module of VMD. The aragonite is built by extending its unit cell [30] to 16 units each in $X$- and $Y$-direction and 2 units in $Z$-direction. The solvated GS domain built earlier is placed next to the aragonite to build the organic inorganic model used in this study. The details of model building are discussed in our earlier paper [8]. It should also be noted that, since water has significant role in the influence of mineral proximity, appropriate solvation of protein is very important. In our model [8], before pulling the GS domain is completely solvated, thus enclosing the entire domain in a water box.

Steered molecular dynamics (SMD) is used to study the influence of mineral proximity on the mechanical response of protein (GS domain). One of the alpha-carbon atoms present close to aragonite surface is pulled to unfold the GS domain while fixing the other end located opposite to it. Same pulling and fixed atoms are used when GS is pulled in the presence and absence of aragonite. Three different magnitudes of velocity 0.25 Å/ps, 0.50 Å/ps, and 1.00 Å/ps are applied in unfolding GS domain. Using each of these velocities, the GS domain is pulled for a period of 250 ps. The stiffness of SMD spring used is 5 Kcal/mol/Å. Molecular dynamics software NAMD [31] is used for all simulations, and VMD [32] is used for visual analysis. CHARMm forcefield is applied in this work. The parameters for GS domain are obtained from standard CHARMm protein parameter file [13]. The CHARMm bonded parameters for aragonite are used from the literature whereas the non-bonded parameters are derived from existing Buckingham potential. The CHARMm aragonite parameters used in this work are shown in Table 1.

## 3. RESULTS AND DISCUSSION

It is been found from our previous work [8, 9] that the proximity of mineral influences the mechanical response of proteins as observed in both seashells and bone. More energy is required to unfold a protein when pulled in the presence of aragonite than when pulled in its absence. It is also observed that energy required to unfold at mineral proximity depends

Table 1: CHARMm forcefield parameters for aragonite.

| Bond | $K^B$ (Kcal/mol Å$^2$) | $r_o$ |
|---|---|---|
| C–$O_1$ | 9219.28 | 1.30 |
| C–$O_2$ | 9219.28 | 1.28 |
| Angle | $K^A$ (Kcal/mol rad$^2$) | $\theta_o$ |
| O1–C–O1 | 214.7613 | 119.58 |
| O2–C–O2 | 214.7613 | 120.19 |
| Nonbonded | $\sigma_{ij}$ | $\varepsilon_{ij}$ |
| Ca–$O_1$ | 2.71 | 1.52 |
| Ca–$O_2$ | 2.71 | 1.52 |
| C–$O_1$ | 2.999 | 1.5 |
| C–$O_2$ | 2.999 | 1.5 |
| $O_1$–$O_2$ | 2.855 | 0.35 |
| $\sigma_{ij} = (\sigma_i + \sigma_j)/2;\ \varepsilon_{ij} = \sqrt{\varepsilon_i * \varepsilon_j}$ | $\sigma_i$ | $\varepsilon_i$ |
| O | 2.855 | 1.6023 |
| C | 3.143 | 1.7639 |
| Ca | 2.565 | 1.4395 |

on the velocity of pulling. The specific reason for this velocity dependence is not understood yet and is a part of our future research. In the current work, studies are conducted to find mechanisms leading to large increase in energy required for unfolding of protein at mineral proximity and in the absence of the mineral.

Protein molecules exhibit a tertiary structure due to several cross links (hydrogen bond, disulphide bridge, etc.) between domains and within domains. Specific hydrogen bonds give rise to mathematically defined structures such as alpha-helix, beta-sheets. A protein has several turns (such as hairpin) between strands. When a protein is pulled (in the absence of mineral), all these bonds offer resistance to pulling. When the protein is pulled in presence of mineral the resistance comes from both structural features of the protein molecule as well as the resistance forces due to interaction of protein with mineral.

The load-displacement characteristics of the protein domain (GS domain) pulled at mineral proximity and without the mineral at a velocity of 1.00 Å/ps are shown in Figure 1. The ratio of the area under the load-displacement (L-D) curve in the presence of aragonite to the area under L-D curve in the absence of aragonite is defined as "Work Factor." The work factors obtained at three different velocities are shown in Table 2. From this table, it is observed that when the protein is pulled at velocity of 0.25 Å/ps, about ten times more energy is necessary to unfold the GS domain by same magnitude of displacement in the presence of aragonite than in the absence of it. It is observed from Figure 1 that the L-D responses are significantly different under the two conditions. The primary factors leading to the larger area under the L-D curve pulled at mineral proximity are

(a) the presence of peaks of higher magnitude in L-D response curve for mineral proximity;

(b) and the presence of higher value of load for a given displacement.

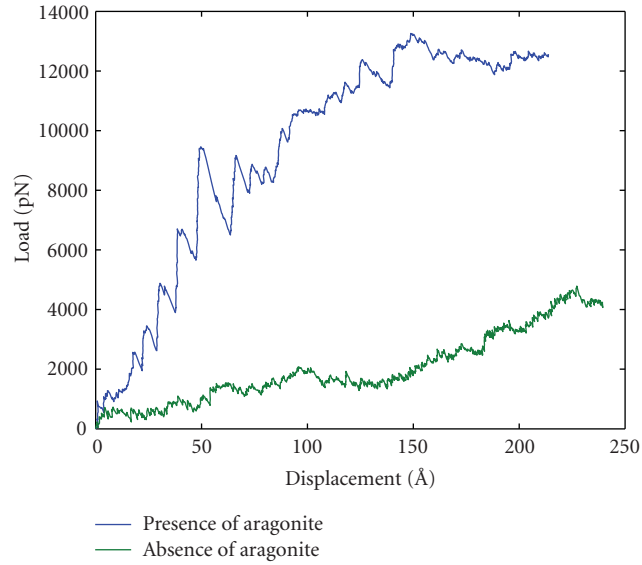


Figure 1: The L-D characteristics of the GS domain, pulled at a velocity of 1.00 Å/ps: at proximity of aragonite and in the absence of aragonite.

Table 2: "Work factor" at different velocities.

| Velocities (Å/ps) | Work factor |
|---|---|
| 0.25 | 10.50 |
| 0.50 | 8.50 |
| 1.00 | 5.00 |

In the following two sections, we present the results of our study about the mechanisms arising from the above two factors.

### 3.1. Section I

Peaks in the L-D curve are present in both plots as indicated in Figure 1. The peaks observed in the absence of mineral aragonite have a height of about 150 to 200 pN, whereas the peaks in the presence of aragonite are of larger magnitude and are in the range of 1500 to 2000 pN and have lower frequency of occurrence. The magnitude of peak heights in the absence of aragonite corresponds to the opening of loops and turns and breaking of hydrogen bonds. From the nature of peaks observed in two cases, it can be inferred that different mechanisms are involved in the formation of peaks when pulling protein at mineral proximity. From the trajectory analysis of unfolding, it is observed that peaks occur until water enters between the aragonite surface and GS strands. As pulling is continued and water enters in between, no additional peaks are observed in the L-D curve. This observation indicates that direct interaction between aragonite surface and GS strands may result in the formation of these peaks. We have investigated the peaks up to 50 Å displacement. This displacement corresponds to the point after which significant water enters in between the aragonite surface and GS strand. From the trajectory analysis, it is observed that when the GS strand is pulled

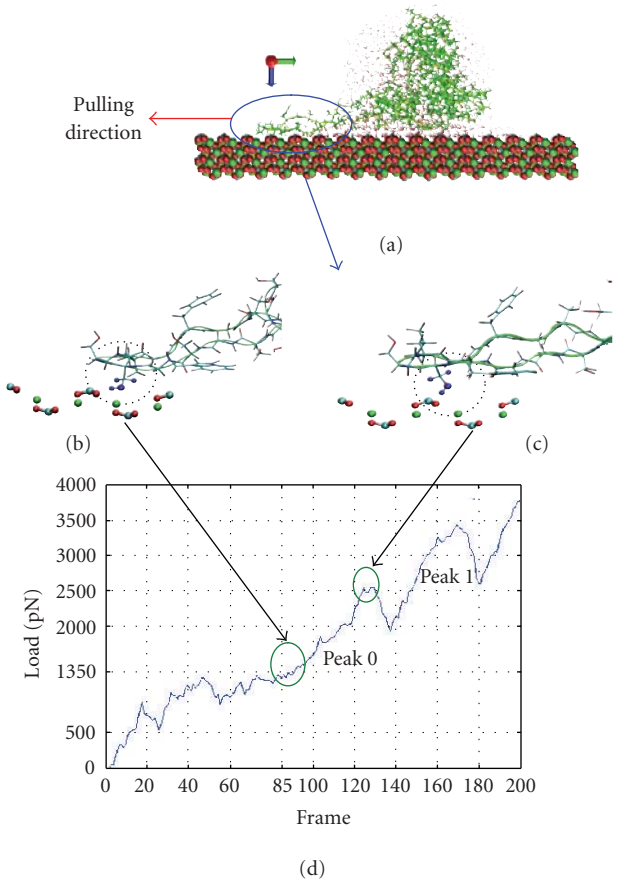


Figure 2: The mechanism of "latching" and formation of peaks: (a) latching site (b) formation of latch (c) breaking of latch (d) peaks resulting from latching mechanism.

at mineral proximity, a mechanism similar to the physical phenomenon of "latching" is observed to take place between aragonite surface and GS strand in proximity. The "latch" observed here is not a physical latch but a result of strong nonbonded interactions between an atom or a group of atoms of amino acid residues (attached to GS strand) and aragonite surface. These latches are formed when the interacting group(s) come(s) close to the aragonite surface, but as pulling is continued they are observed to break. These latches thus go through a process of "forming" and "breaking" as the GS strand is pulled along the aragonite surface, giving rise to the peaks in the L-D curve.

Further, we zoomed into a small section, circled in Figure 2(a) where, a "latch" is observed. The "forming" and "breaking" phenomenon of a latch is represented in Figures 2(b) and 2(c). The aragonite layer close to the surface is shown in the figures. The L-D characteristics of one of the peaks are shown in Figure 2(d). As the strand is pulled in the direction of the arrow in the figure, a group of atoms (marked as blue balls) comes closer to the surface, builds a strong interaction, arrives between the carbonate groups of aragonite, and gives rise to what we called as a "latch." The formation of the "latch" corresponds to the base point of the peak as marked in Figures 2(b) and 2(d). Once the latch is formed, it offers resistance to pulling, causing the magnitude of load to rise sharply. The load curve keeps rising as pulling is continued until the load level where the latch can no longer sustain the pulling force results. At that point, the latch breaks, and thus the force decreases. The apex of a peak therefore corresponds to the point where a latch breaks (Figure 2(c)).

Aragonite exhibits orthorhombic crystal symmetry. The surface formed by (001) is rich in negatively charged oxygen atoms belonging to carbonate group. The positively charged calcium atoms are located very close to the surface. The charges on the surface oxygen and calcium atoms are found to be −0.9995 and +2.000, respectively. The blue atom group constitutes mainly of hydrogen and/or oxygen atoms. The hydrogen and oxygen atoms of amino acid strongly interact with oxygen and calcium of aragonite, respectively, forming these latches. As polar water molecules enter between the aragonite surface and GS strand, these interacting groups can no longer come close enough to form the latches and thus no sharp peaks are observed. In Figure 1, no peaks are observed beyond a displacement of about 60 Å. The peaks within the same L-D curve (at mineral proximity) are different in terms of height, base width, shoulder characteristics, etc. This heterogeneity in peak characteristics depends on the number of latches formed at a given time, the atoms involved (blue group) in the "latching" action and on the presence of other interacting groups closer to the aragonite surface.

Thus, a peak in the L-D curve starts rising when a side chain group builds up a strong nonbonded interaction with aragonite surface. It falls when this interaction is broken upon further pulling. Thus, the energy stored in the rising half of the peak is due to the resistance offered by the latch and is thus expected to be approximately equal to the nonbonded energy holding these two interacting groups together. The nonbonded energy which is the summation of van der Waals and electrostatic energy between the interacting group of amino acid side chains, and the aragonite section (shown in Figure 2(b)) is determined. The variation of the electrostatic and van der Waals energy with time (frame) is shown in Figures 3(a) and 3(b). In Figure 2(d), it is observed that Peak 0 starts rising at time frame 85 (17 ps). The electrostatic and van der Waals energy corresponding to this time frame as observed in Figures 3(a) and 3(b) is 2000 pN-Å and 700 pN-Å, respectively. The area bound by the rising half of the Peak 0 ($X$, $Y$ and $Z$ in Figure 2(d)) is 2500 pN-Å, which is close to the total nonbonded interaction (2700 pN-Å) energy between the interacting groups. From a similar analysis of Peak 1 (Figure 4(a)), where the peak starts at time frame of 135 (27 ps), the total attraction energy (900 pN-Å) is found to be very close to the area bound by the rising part of the curve (1100 pN-Å). The variation of the electrostatic and van der Waals energy with time (frame) for Peak 1 is shown in Figures 4(b) and 4(c). For other major peaks, these values are also in close agreement. Thus it is quantitatively shown that the large peaks observed in the proximity of the mineral are a result of direct nonbonded interactions between the side chain atoms and the complementary atoms on the mineral surface.

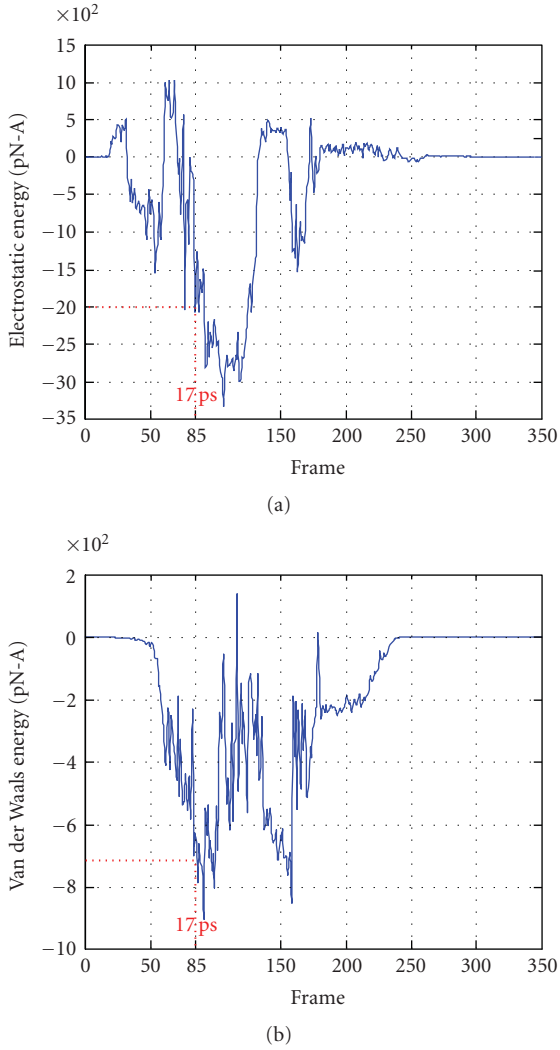


FIGURE 3: The nonbonded energy between the interacting groups giving rise to Peak 0: (a) electrostatic energy (b) van der Waals energy.

### 3.2. *Section II*

As observed in Figure 1 and also mentioned earlier, one of the factors which contribute to the work factor is the higher magnitude of load at any given displacement, when pulled at mineral proximity. The peak load observed in the figure is about 13 nN, a high magnitude, predominantly as a result of mineral protein interactions. This high magnitude of force resulting from constant velocity pulling simulations is possible without fracture of the single protein strand being pulled. Flow induced fracture of single polymer chains is reported to be between 2.5 to 13.4 nN [33, 34] and the fracture strength is dependent upon the polymer and rate of loading. In this section, the potential mechanisms involved are described. As the GS domain is pulled, the water molecules present closer to the aragonite surface orient and arrange themselves in a definite pattern and further undergo very little movement. On moving away from aragonite

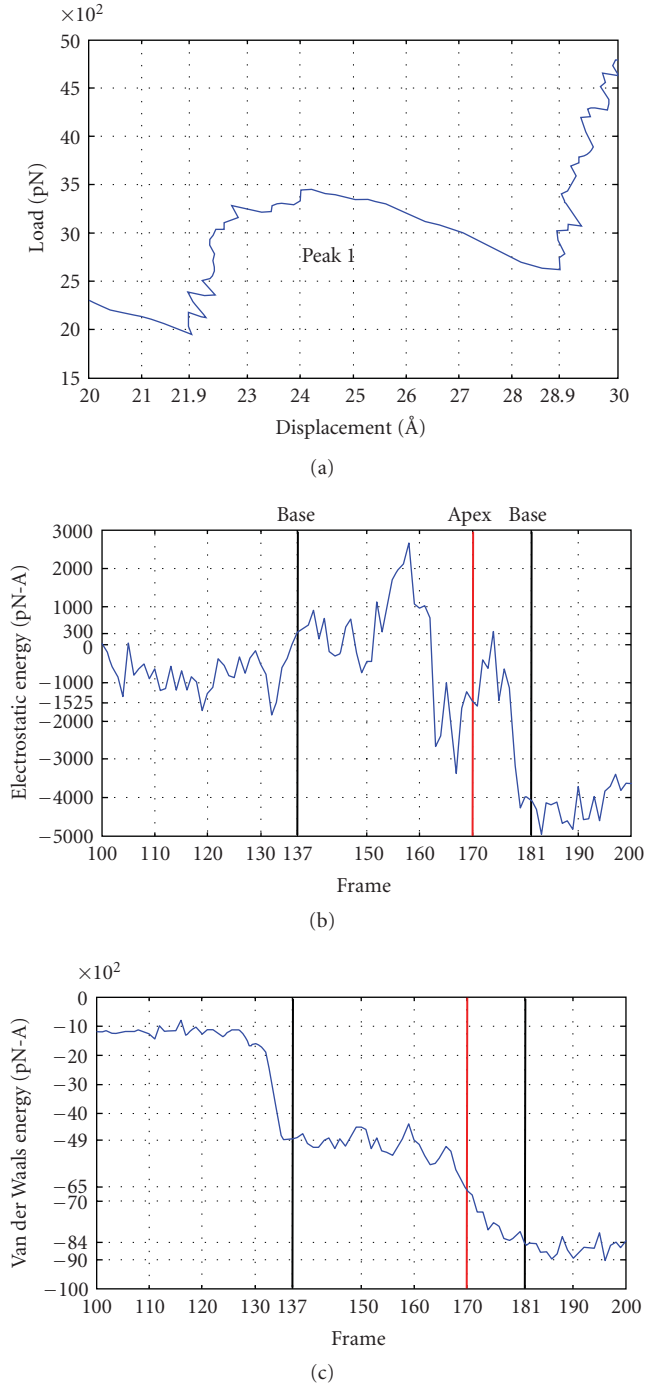


FIGURE 4: Peak 1 (a) load-displacement plot (b) electrostatic (c) van der Waals energy.

surface, the water molecules are structurally altered, and behave like "normal solvent water" attached to the protein.

A clear difference in behavior is observed between water molecules closer to the surface and away from the surface both in terms of structure and movement during pulling. We have therefore categorized the water into two types. The water molecules close to the aragonite surface are named here as Aragonite-Bound Water (A-BW), and water

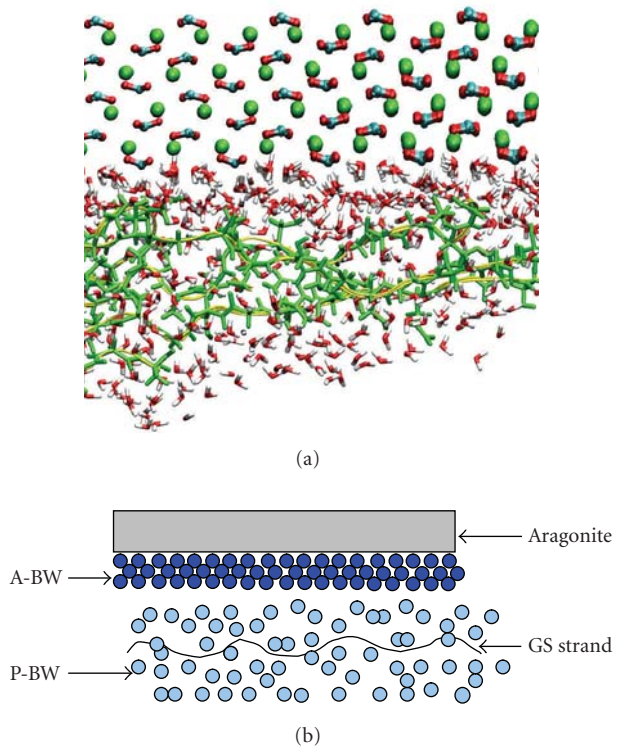


Figure 5: Two "types" of water molecules observed during pulling of GS domain (a) simulation (b) schematic representation. A-BW: aragonite bound water and P-BW: protein bound water.

molecules moving with the protein are named as Protein-Bound Water (P-BW). The schematic representation of these two types of water molecules is shown in Figure 5. At low displacement of pulling, very few water molecules are observed to be present between aragonite and GS strands. However, this number increases as pulling is continued. The strong hydrogen-bonded interaction between carbonate surface of aragonite and polar water molecules causes some of the water molecules to lie close to the aragonite surface. The water molecules form a periodic pattern which is primarily due to the periodicity of the aragonite surface in the $X$-$Y$ plane. The P-BW shows no definite pattern, with the water molecules surrounding the protein and moving freely with the protein. As the GS is pulled, the A-BW remains tightly bound to the aragonite surface and exhibits almost no movement. The P-BW on the other hand moves freely with the GS strand. On careful observation, it is observed that there is a 3-4 Å thick layer of water (about two water molecules thick) which behaves as a transition layer between A-BW and P-BW. In this layer, the slipping of P-BW is observed to happen with respect to the A-BW. The P-BW forms a sheath around the GS strands. When GS is pulled, the strands move with sheath of water around it. P-BW thus moves with GS strands and A-BW remains bound to the surface. A schematic representation of this mechanism is shown in Figure 6. This figure illustrates that when GS is pulled, the interaction contributing to resistance to displacement includes the following:

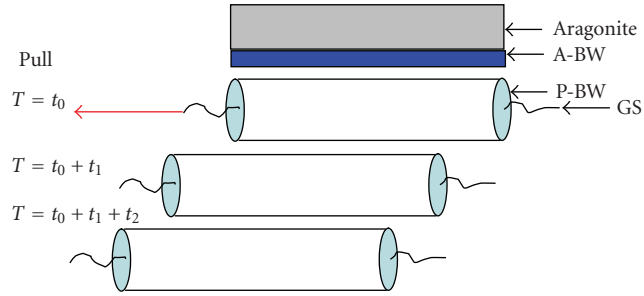


Figure 6: Schematic representation of movement of the GS domain and protein-bound-water (P-BW) when GS domain is pulled.

(i) the net attractive interactions of GS-(A-BW) and GS-aragonite;

(ii) the net attractive interaction of (P-BW)-(A-BW) and (P-BW)-aragonite and GS-(P-BW).

To study the contribution of these different interactions to the L-D characteristics of GS domain, aragonite sections of smaller $X$-$Y$ dimension and part of GS strand close to it are selected. We have used two such sections for the analysis of the interaction energy. One of them is shown in Figure 7. This section extends to 20 Å in the $X$-direction and 50 Å in the $Y$-direction. Figures 7(a) and 7(b) show this section at 180 ps and 250 ps, timeframes, respectively. The white region between A-BW and P-BW, in reality, contains water molecules, however these are not shown here for clarity. This region is the layer of transition or slippage as mentioned earlier. Figure 7(b) shows the movement of P-BW (green atoms) as the strand is pulled. The interaction energy for each of the pairs is shown in Table 3. The electrostatic interaction energy is dominant compared to the van der Waals energy. The attractive nonbonded interaction energy between mineral aragonite and A-BW is $-18 \times 10^4$ pN-Å. Thus, the A-BW is tightly bound to the aragonite surface and does not move when the GS domain is pulled alongside the mineral.

The attractive interaction energy between aragonite and P-BW is $-8.85 \times 10^4$ pN-Å, a very significant magnitude. The P-BW and the GS domain have an attractive interaction energy of $-1.30 \times 10^4$ pN-Å. In addition, aragonite and A-BW also have attractive interactions with the GS domain, although smaller magnitudes of $-0.725 \times 10^4$ pN-Å and $-0.230 \times 10^4$ pN-Å, respectively. The dominant resistance to pulling of the GS is the attractive interaction between GS domain and the P-BW, which in turn has significant interaction with the mineral. Although the direct interaction between the mineral and GS is small because of the distance, water plays a critical role in building a "bridge" between the mineral and the protein, facilitating development of a large resistance to pulling in the presence of mineral. As a result, the load experienced at the pulling end is high. This therefore results in higher magnitude of load at a given displacement in the L-D curve.

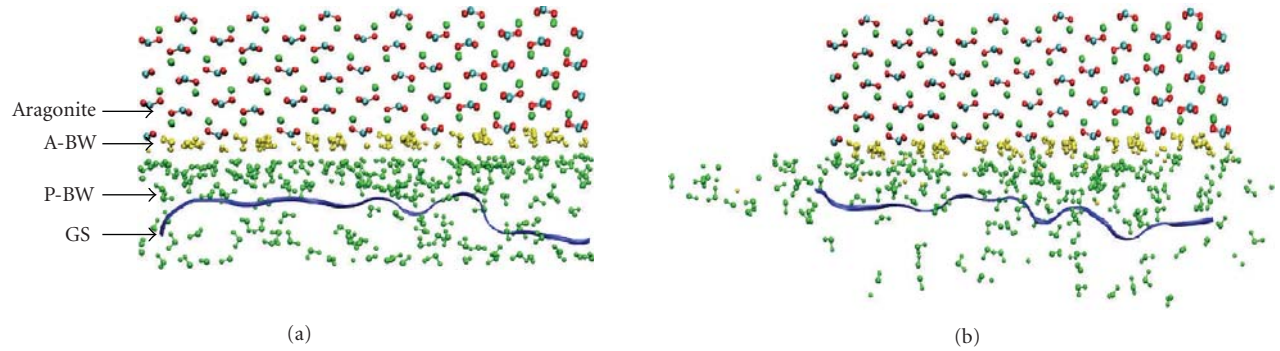


Figure 7: Snapshots taken during the steered molecular dynamics simulation of the pulling of the GS domain in the presence of aragonite mineral proximity at (a) 180 picoseconds and (b) 250 picoseconds.

Table 3: Values of interaction energies between different pairs of constituents of aragonite-water-GS domain.

| Interaction pair | Electrostatic energy (pN-Å) | van der Waals energy (pN- Å) |
|---|---|---|
| Aragonite—(A-BW) | $-17 \times 10^4$ | $-1 \times 10^4$ |
| Aragonite—(P-BW) | $-8 \times 10^4$ | $-0.85 \times 10^4$ |
| Aragonite—GS | $-0.60 \times 10^4$ | $-0.125 \times 10^4$ |
| GS—(A-BW) | $-0.20 \times 10^4$ | $-0.03 \times 10^4$ |
| GS—(P-BW) | $-1.20 \times 10^4$ | $-0.10 \times 10^4$ |
| (P-BW)—(A-BW) | $(-0.50 \text{ to } 0.50) \times 10^4$ | $-0.20 \times 10^4$ |

## 4. CONCLUSIONS

In our previous work, we have shown that the proximity of mineral influences the mechanical response of protein. More energy is required to unfold a protein in presence of aragonite than without it. The L-D curve in the presence of aragonite shows different responses from the one when pulled without mineral proximity. In the presence of aragonite, larger peaks are observed, and the magnitude of load at any given displacement is significantly higher. In this work, we have found quantitatively the mechanisms leading to the difference in load displacement response of protein at mineral proximity. The following hold.

(i) At the early stage of pulling, the peaks in the L-D plot at mineral proximity are quantitatively correlated to the interaction energy between the atoms involved in the latching phenomenon of amino acid side chain to aragonite surface.

(ii) The role of water in mineral and protein interaction is very significant.

(iii) The water closer to the mineral surface is highly oriented and does not move while the protein strand is pulled. Water layer around the strands moves with the strand as the protein is pulled.

(iv) The high magnitude of load for a given displacement originates from attractive interactions between the protein, protein-bound water, and the mineral.

Here, for the first time, quantitative description of the mechanics responsible for the large differences in the magnitude of force needed to unfold proteins in the proximity of the mineral in nacre is provided. This work provides clues as to possible reasons for extraordinary properties of organic phase such as high elastic modulus and large deformation before failure observed in nacre.

## ACKNOWLEDGMENTS

Teragrid allocation (TGDMR060001T) and NCSA supercomputing resources were used for majority of the simulations. NDSU center of supercomputing applications (CHPC) and Biomedical Research Infrastructure Network (BRIN) were used for model development. Hardware support for NAMD at NDSU was provided by Dr. Gregory Wettstein. P. Ghosh acknowledges support from ND EPSCoR for doctoral dissertation award at NDSU.

## REFERENCES

[1] A. F. von Recum, Ed., *Handbook of Biomaterials Evaluation*, Macmillan, New York, NY, USA, 1986.

[2] R. Z. Wang, Z. Suo, A. G. Evans, N. Yao, and I. A. Aksay, "Deformation mechanisms in nacre," *Journal of Materials Research*, vol. 16, no. 9, pp. 2485–2493, 2001.

[3] D. R. Katti and K. S. Katti, "Modeling microarchitecture and mechanical behavior of nacre using 3D finite element techniques—part I: elastic properties," *Journal of Materials Science*, vol. 36, no. 6, pp. 1411–1417, 2001.

[4] D. R. Katti, K. S. Katti, J. M. Sopp, and M. Sarikaya, "3D finite element modeling of mechanical response in nacre-based hybrid nanocomposites," *Computational and Theoretical Polymer Science*, vol. 11, no. 5, pp. 397–404, 2001.

[5] K. Katti, D. R. Katti, J. Tang, S. Pradhan, and M. Sarikaya, "Modeling mechanical responses in a laminated biocomposite—part II: nonlinear responses and nuances of

nanostructure," *Journal of Materials Science*, vol. 40, no. 7, pp. 1749–1755, 2005.

[6] K. S. Katti, D. R. Katti, S. M. Pradhan, and A. Bhosle, "Platelet interlocks are the key to toughness and strength in nacre," *Journal of Materials Research*, vol. 20, no. 5, pp. 1097–1100, 2005.

[7] D. R. Katti, S. M. Pradhan, and K. S. Katti, "Modeling the organic-inorganic interfacial nanoasperities in a model bio-nanocomposite, nacre," *Reviews on Advanced Materials Science*, vol. 6, no. 2, pp. 162–168, 2004.

[8] P. Ghosh, D. R. Katti, and K. S. Katti, "Mineral proximity influences mechanical responses of proteins in biological mineral-protein hybrid systems," *Biomacromolecules*, vol. 8, no. 3, pp. 851–856, 2007.

[9] R. Bhowmik, K. S. Katti, and D. R. Katti, "Mechanics of molecular collagen is influenced by hydroxyapatite in natural bone," *Journal of Materials Science*, vol. 42, no. 21, pp. 8795–8803, 2007.

[10] B. L. Smith, T. E. Schäffer, M. Viani, et al., "Molecular mechanistic origin of the toughness of natural adhesives, fibres and composites," *Nature*, vol. 399, no. 6738, pp. 761–763, 1999.

[11] X. Shen, A. M. Belcher, P. K. Hansma, G. D. Stucky, and D. E. Morse, "Molecular cloning and characterization of Lustrin A, a matrix protein from shell and pearl nacre of *Haliotis rufescens*," *The Journal of Biological Chemistry*, vol. 272, no. 51, pp. 32472–32481, 1997.

[12] M. Karplus and J. A. McCammon, "Molecular dynamics simulations of biomolecules," *Nature Structural Biology*, vol. 9, no. 9, pp. 646–652, 2002.

[13] B. R. Brooks, R. E. Bruccoleri, B. D. Olafson, D. J. States, S. Swaminathan, and M. J. Karplus, "CHARMM: a program for macromolecular energy, minimization, and dynamics calculations," *Journal of Computational Chemistry*, vol. 4, no. 2, pp. 187–217, 1983.

[14] M. Gao, M. Wilmanns, and K. Schulten, "Steered molecular dynamics studies of titin I1 domain unfolding," *Biophysical Journal*, vol. 83, no. 6, pp. 3435–3445, 2002.

[15] B. Isralewitz, M. Gao, and K. Schulten, "Steered molecular dynamics and mechanical functions of proteins," *Current Opinion in Structural Biology*, vol. 11, no. 2, pp. 224–230, 2001.

[16] H. Lu and K. Schulten, "Steered molecular dynamics simulations of force-induced protein domain unfolding," *Proteins: Structure, Function and Genetics*, vol. 35, no. 4, pp. 453–463, 1999.

[17] A. Krammer, H. Lu, B. Isralewitz, K. Schulten, and V. Vogel, "Forced unfolding of the fibronectin type III module reveals a tensile molecular recognition switch," *Proceedings of the National Academy of Sciences of the United States of America*, vol. 96, no. 4, pp. 1351–1356, 1999.

[18] D. R. Katti, S. R. Schmidt, P. Ghosh, and K. S. Katti, "Modeling the response of pyrophyllite interlayer to applied stress using steered molecular dynamics," *Clays and Clay Minerals*, vol. 53, no. 2, pp. 171–178, 2005.

[19] S. R. Schmidt, D. R. Katti, P. Ghosh, and K. S. Katti, "Evolution of mechanical response of sodium montmorillonite interlayer with increasing hydration by molecular dynamics," *Langmuir*, vol. 21, no. 17, pp. 8069–8076, 2005.

[20] D. R. Katti, S. R. Schmidt, P. Ghosh, and K. S. Katti, "Molecular modeling of the mechanical behavior and interactions in dry and slightly hydrated sodium montmorillonite interlayer," *Canadian Geotechnical Journal*, vol. 44, no. 4, pp. 425–435, 2007.

[21] P. Ghosh, D. R. Katti, and K. S. Katti, "Impact of $\beta$-sheet conformations on the mechanical response of protein in biocomposites," *Materials and Manufacturing Processes*, vol. 21, no. 7, pp. 676–682, 2006.

[22] S. Park and K. Schulten, "Calculating potentials of mean force from steered molecular dynamics simulations," *The Journal of Chemical Physics*, vol. 120, no. 13, pp. 5946–5961, 2004.

[23] S. G. Dastidar and C. Mukhopadhyay, "Unfolding dynamics of the protein ubiquitin: insight from simulation," *Physical Review E*, vol. 72, no. 5, Article ID 051928, 10 pages, 2005.

[24] M. Cieplak, T. X. Hoang, and M. O. Robbins, "Folding and stretching in a Go-like model of titin," *Proteins: Structure, Function and Genetics*, vol. 49, no. 1, pp. 114–124, 2002.

[25] Y. Sugita and Y. Okamoto, "Replica-exchange molecular dynamics method for protein folding," *Chemical Physics Letters*, vol. 314, no. 1-2, pp. 141–151, 1999.

[26] B. D. Brower-Toland, C. L. Smith, R. C. Yeh, J. T. Lis, C. L. Peterson, and M. D. Wang, "Mechanical disruption of individual nucleosomes reveals a reversible multistage release of DNA," *Proceedings of the National Academy of Sciences of the United States of America*, vol. 99, no. 4, pp. 1960–1965, 2002.

[27] X. Zhuang, T. Ha, H. D. Kim, T. Centner, S. Labeit, and S. Chu, "Fluorescence quenching: a tool for single-molecule protein-folding study," *Proceedings of the National Academy of Sciences of the United States of America*, vol. 97, no. 26, pp. 14241–14244, 2000.

[28] J. G. Forbes and G. H. Lorimer, "Unraveling a membrane protein," *Science*, vol. 288, no. 5463, pp. 63–64, 2000.

[29] B. Mohanty, K. S. Katti, and D. R. Katti, "Experimental investigation of nanomechanics of the mineral-protein interface in nacre," *Mechanics Research Communications*, vol. 35, no. 1-2, pp. 17–23, 2008.

[30] J. P. R. de Villiers, "Crystal structures of aragonite, strontianite, and witherite," *The American Mineralogist*, vol. 56, pp. 758–767, 1971.

[31] J. C. Phillips, R. Braun, W. Wang, et al., "Scalable molecular dynamics with NAMD," *Journal of Computational Chemistry*, vol. 26, no. 16, pp. 1781–1802, 2005.

[32] W. Humphrey, A. Dalke, and K. Schulten, "VMD: visual molecular dynamics," *Journal of Molecular Graphics*, vol. 14, no. 1, pp. 33–38, 1996.

[33] J. A. Odell and A. Keller, "Flow-induced chain fracture of isolated linear macromolecules in solution," *Journal of Polymer Science Part B*, vol. 24, no. 9, pp. 1889–1916, 1986.

[34] M. Grandbois, M. Beyer, M. Rief, H. Clausen-Schaumann, and H. E. Gaub, "How strong is a covalent bond," *Science*, vol. 283, no. 5408, pp. 1727–1730, 1999.